

00078493

REVIEWS ON THE PHYSICS AND CHEMISTRY
OF MATERIALS • 58

Light Scattering

Principles and Development

Edited by
WYN BROWN



OXFORD SCIENCE PUBLICATIONS



Digitized by the Internet Archive
in 2023 with funding from
Kahle/Austin Foundation

https://archive.org/details/isbn_0198517831

PROPERTY OF THE U. S. GOVERNMENT
SPACE TELESCOPE SCIENCE INSTITUTE
BALTIMORE, MARYLAND

WFO
DEC 4 1996

MONOGRAPHS ON THE
PHYSICS AND CHEMISTRY OF
MATERIALS

General Editors

R. J. BROOK ANTHONY CHEETHAM
ARTHUR HEUER SIR PETER HIRSCH
TOBIN J. MARKS JOHN SILCOX
DAVID A. SMITH MATTHEW V. TIRRELL
VACLAV VITEK

MONOGRAPHS ON THE PHYSICS AND CHEMISTRY
OF MATERIALS

- Strong solids (third edition)* A. Kelly and N. H. Macmillan
Optical spectroscopy of inorganic solids B. Henderson and G. F. Imbusch
Quantum theory of collective phenomena G. L. Sewell
Experimental high-resolution electron microscopy (second edition) J. C. H. Spence
Experimental techniques in low-temperature physics Guy K. White
Principles of dielectrics B. K. P. Scaife
Surface analytical techniques J. C. Rivière
Basic theory of surface states Sydney G. Davison and Maria Stęslicka
Acoustic microscopy Andrew Briggs
Dynamic light scattering Wyn Brown
Quasicrystals: a primer (second edition) C. Janot
Interfaces in crystalline materials A. P. Sutton and R. W. Balluffi
Atom probe field ion microscopy M. K. Miller, A. Cerezo, M. G. Hetherington,
and G. D. W. Smith
Light scattering: principles and development Wyn Brown

Light Scattering

Principles and development

Edited by

WYN BROWN

*Department of Physical Chemistry
University of Uppsala, Sweden*

CLARENDON PRESS · OXFORD
1996

101.9
1066
L54
1996
Oxford University Press, Walton Street, Oxford OX2 6DP

Oxford New York
Athens Auckland Bangkok Bombay
Calcutta Cape Town Dar es Salaam Delhi
Florence Hong Kong Istanbul Karachi
Kuala Lumpur Madras Madrid Melbourne
Mexico City Nairobi Paris Singapore
Taipei Tokyo Toronto
and associated companies in
Berlin Ibadan

Oxford is a trade mark of Oxford University Press

Published in the United States
by Oxford University Press Inc., New York

© The contributors 1996

All rights reserved. No parts of this publication may be reproduced, stored in a retrieval system, or transmitted, in any form or by any means, without the prior permission in writing of Oxford University Press. Within the UK, exceptions are allowed in respect of any fair dealing for the purpose of research or private study, or criticism or review, as permitted under the Copyright, Designs and Patents Act, 1988, or in the case of reprographic reproduction in accordance with the terms of licences issued by the Copyright Licensing Agency. Enquiries concerning reproduction outside those terms and in other countries should be sent to the Rights Department, Oxford University Press, at the address above.

This book is sold subject to the condition that it shall not, by way of trade or otherwise, be lent, re-sold, hired out, or otherwise circulated without the publisher's prior consent in any form of binding or cover other than that in which it is published and without a similar condition including this condition being imposed on the subsequent purchaser.

A catalogue record for this book is available from the British Library

Library of Congress Cataloging in Publication Data

Light scattering: principles and development / edited by Wyn Brown. – 1st ed.
(Monographs on the physics and chemistry of materials)

1. Macromolecules—Optical properties. 2. Polymers—Analysis.

3. Light—Scattering. I. Brown, Wyn. II. Series.

QD381.9.O66L54 1996 547.7'045413—dc20 95-45401

ISBN 0 19 851783 1

Typeset by Integral Typesetting, Gt. Yarmouth, Norfolk
Printed in Great Britain by Biddles Ltd, Guildford & King's Lynn

Preface

The previous volume, *Dynamic light scattering* (Clarendon Press, Oxford, 1993), was incomplete in that many topics were not included owing to obvious restrictions on the size of the volume which, as things were, already sorely tried the patience of the publishers. This second volume is a partial attempt to redress the balance and to widen the scope of the treatment to include some aspects of static light scattering as well as applications of light scattering to more complex systems. The more general title expresses this ambition. The contents include a broader spectrum of light scattering applications within a number of currently important areas of investigation in polymer physics and colloidal science.

As before, the contents reflect a personal choice and the authors were given a liberal mandate to either review or to present individual descriptions of the contribution of light scattering techniques in their chosen area. This means that the chapters are in essence independent and self-contained, although presented in a largely consistent nomenclature. While this implies an unavoidable overlap of material (not altogether a bad thing anyway), this was considered worthwhile in order to give contributors the freedom to develop and present their own viewpoints. This volume should also be viewed as complementary to the preceding volume and also as a companion to the introductory texts referred to previously. Since the inception of the first volume, a second, completely re-written version of *Laser light scattering* by Ben Chu (Academic Press, 1991) has appeared. This provides an easily accessible and very useful description of the basic principles and practice of light scattering.

The first three chapters of the present book are devoted to theoretical developments in light scattering. In Chapter 1, **Mustapha Benmouna and Wayne F. Reed** provide a timely summary of developments in static light scattering and deal with scattering from simple liquids, polymer solutions and multicomponent polymer mixtures. They also describe the role of critical fluctuations in polymer blends and mixtures of copolymers.

In Chapter 2, **Rudolf Klein and Bruno D'Aguanno** treat the static scattering properties of colloidal suspensions and derive a general equation for the scattered field. Models are discussed for the interactions between colloidal particles and methods are delineated for calculating the microstructures from pair potentials. The generalization is extended to mixtures and polydisperse suspensions of spherical particles. The microstructure of suspensions of charged rod-like particles is treated.

Chapter 3 by **Theo Odijk** provides a description of light scattering from rod-like polyelectrolytes. The case of polyelectrolytes in excess salt (Poisson-Boltzmann equation and virial equation), the structure factor and the influences of slightly attractive forces are dealt with. Weakly charged polyelectrolytes and

interference within the double layer are discussed. Molecular theory, salt-free polyelectrolyte systems and flexible polyelectrolytes are also dealt with.

Experimental aspects of polyelectrolytes in solution are considered by **Marián Sedlák** in Chapter 4. This is a companion section to that in the previous volume by Michel Mandel and the theoretical presentation by Theo Odijk in Chapter 3.

Light scattering in concentrated polymeric systems is dealt with by **Taco Nicolai** and **Wyn Brown** in Chapter 5. This is an area that has recently received considerable attention by experimentalists using light scattering techniques. Dynamic behaviour in highly concentrated solutions and extending up to the melt is considered in light of recent results, including new data elucidating the role of solvent reorientation within the polymer matrix. Free volume is a neglected but crucial concept for understanding dynamical behaviour and is discussed in this context. Finally, experimental data on cluster dynamics in polymer solutions and melts are described.

Aggregation of particles is a feature common to many systems, which has previously received less than its full share of attention. **Taco Nicolai**, **Dominique Durand** and **Jean-Christophe Gimel** deal in Chapter 6 with scattering in systems containing large particles. In particular, these authors describe the structure factor for fractal particles in the limit of infinite dilution and consider the different parameters that characterize a system. The application of the results of the calculations to real systems is discussed and recent experiments on fractal systems are described.

The phenomenon of polymer–polymer interactions is considered in Chapter 7 by **Jim Selser**, who gives a background to the application of light scattering in their elucidation, both for neutral polymers and polyelectrolytes. Recent results from studies in dilute solution are presented and a discussion of outstanding problems is given.

Redouane Borsali discusses in Chapter 8 experimental results on the scattering properties of ternary systems, focusing either on mixtures of two homopolymers in a solvent or diblock copolymer chains in solution. This section forms a complement to the theoretical discussion given by Ziya Akcasu in the first volume, as well as Chapter 11 by Petr Štěpánek and Timothy P. Lodge in this book.

Peter Schurtenberger discusses light scattering in complex micellar systems in Chapter 9: this is an area which has been the subject of much recent activity. Spherical micelles and microemulsion particles are considered, using concepts of simple liquids to describe the structure factor. Uses of optical matching and contrast variation in microemulsions are discussed. Micellar growth (the sphere-to-rod transition and giant polymer-like micelles) is dealt with as well as inter-micellar interactions and transient network formation. The subsequent application of concepts developed in polymer physics, such as scaling and renormalization group theory, is also considered. Finally, scattering from bicontinuous surfactant phases is described.

A summary of recent light scattering results on block copolymer micelle-forming systems in selective solvents is presented in Chapter 10 by **Zdeněk Tuzar** and **Pavel Kratochvíl**. In solvents which are thermodynamically good

for one block but poor for the other, the block copolymer molecules self-associate to form multi-molecular aggregates, the cores of which are the relatively insoluble blocks, with the better soluble blocks forming an outer shell.

Petr Štěpánek and **Timothy P. Lodge** discuss, in Chapter 11, various features of the recent results obtained on block copolymer liquids in ordered and disordered states. Current viewpoints on the microphase separation transition are presented both for the bulk state and in neutral solvents. Among the aspects reviewed are Semenov's theory of the dynamics of disordered block copolymer liquids, the use of the zero average contrast condition and global analysis of dynamic light scattering data as a means of studying the 'breathing' mode.

Low and very low angle intensity light scattering and its applications are described in Chapter 12 by **Francesco Mallamace** and **Norberto Micali**. This recent development has an exciting potential for experiments in condensed matter and particularly in complex systems in which the supermolecular structure can be described by scaling laws. The uses of time-resolution analysis in applications to spinodal decomposition, aggregation kinetics and percolative transitions are discussed.

In Chapter 13, **Walther Burchard** describes various uses of simultaneous static and dynamic light scattering, focusing on particle architecture-dependent parameters, and the information that can be obtained from measurement of the angular dependence in dilute solution. A section on concentrated solutions is included.

A practical aspect of light scattering concerns particle size analysis using static light scattering. Development in this area is introduced by **F. Ross Hallett** in Chapter 14. The application of inversion methods to the recovery of particle size distributions from measurement of the angle-dependence of the scattered light intensity is shown to give results which are consistent with those from other approaches, such as dynamic light scattering and electron microscopy, with the added advantage that data collection times are significantly shorter.

Chromatographic techniques used in combination with light scattering detectors are presented in Chapter 15 by **Linda L. Lloyd**, **John F. Kennedy** and **Charles J. Knill**, who summarize the developments in instrumentation together with the information which can be obtained from its utilization. The applications are reviewed in the fields of both synthetic polymers and biological macromolecules.

I would like to express my thanks to the contributors to this volume for their enthusiasm and their ready cooperation in making this book a timely reflection of the progress achieved in various theoretical aspects and application areas of light scattering methods. Without this solidarity, production of a multi-author volume on this scale would have been a traumatic experience; instead it has been a pleasure.

Contents

Contributors

xv

1 Theoretical developments in static light scattering from polymers	1
<i>Mustapha Benmouna and Wayne F. Reed</i>	
1.1 Introduction	1
1.2 Static light scattering from polymer/solvent mixtures	2
1.3 Multicomponent polymer mixtures	12
1.4 Time-dependent static scattering and critical fluctuations	19
1.5 Summary	26
Acknowledgements	27
References	27
2 Static scattering properties of colloidal suspensions	30
<i>Rudolf Klein and Bruno D'Aguanno</i>	
2.1 Introduction	30
2.2 Statistical mechanics of classical systems	32
2.3 Light scattering	48
2.4 Calculation of the microstructure	59
2.5 Solution of integral equations	63
2.6 Applications	74
2.7 Conclusions	91
Acknowledgements	92
Appendix 2.A: the Ornstein–Zernike equation and closure relations	92
Appendix 2.B: the solution of PY for polydisperse HS	96
Appendix 2.C: scattering intensity from polydisperse HS in the PY approximation	99
References	99
3 The theory of light scattering from rod-like polyelectrolytes	103
<i>Theo Odijk</i>	
3.1 Introduction	103
3.2 The Poisson–Boltzmann equation and scattering by charge fluctuations	104
3.3 Interaction between two polyions and virial coefficients	109
3.4 The virial theory of the structure factor	111
3.5 Concluding remarks	117
Appendix 3.A: the variational principle for the structure factor	117
References	118

4 Polyelectrolytes in solution	120
<i>Marián Sedlák</i>	
4.1 Polyelectrolytes: definition and classification	120
4.2 General problems of polyelectrolyte physics: definition of basic quantities for the characterization of polyelectrolytes	121
4.3 The application of static light scattering to polyelectrolyte solutions	126
References	162
5 Scattering from concentrated polymer solutions	166
<i>Taco Nicolai and Wyn Brown</i>	
5.1 Introduction	166
5.2 Time-averaged scattered intensity	167
5.3 Dynamic light scattering	173
5.4 Dynamic properties: comparison with experiments	180
5.5 Solvent relaxation in concentrated solutions	186
References	198
6 Scattering properties and modelling of aggregating and gelling systems	201
<i>Taco Nicolai, Dominique Durand, and Jean-Christophe Gimel</i>	
6.1 Introduction	201
6.2 Light scattering theory applied to aggregating systems	202
6.3 Aggregation and gelation	211
6.4 Applications to real systems	220
6.5 Conclusions	228
Appendix 6.A: list of symbols	228
References	230
7 Polymer–polymer interactions in dilute solution	232
<i>Jim Selser</i>	
7.1 Introduction and background	232
7.2 Macromolecular behaviour in dilute solutions	233
7.3 k_D^ϕ versus X ‘maps’	238
7.4 Polyethylene oxide studies	243
7.5 Intra-coil behaviour and coil–coil interactions	247
7.6 Summary	251
References	252

8 Scattering properties of ternary polymer solutions	255
<i>Redouane Borsali</i>	
8.1 Introduction	255
8.2 Historical sketch	256
8.3 General formalism	258
8.4 Experimental evidence	262
8.5 The ring diblock copolymer case	277
8.6 Extrapolation to the bulk state	285
8.7 Conclusions	287
Acknowledgements	289
References	289
9 Light scattering in complex micellar systems	293
<i>Peter Schurtenberger</i>	
9.1 Introduction	293
9.2 Spherical micelles and microemulsions: hard and soft spheres	296
9.3 Surfactant systems with extended micellar growth	308
9.4 Conclusions	322
Acknowledgements	322
References	323
10 Scattering from block copolymer micellar systems	327
<i>Zdeněk Tuzar and Pavel Kratochvíl</i>	
10.1 Introduction	327
10.2 Molecular characterization of block and graft copolymers	328
10.3 Unimer \rightleftharpoons micelle equilibrium	329
10.4 Static parameters of micelles	331
10.5 Hydrodynamic behaviour of micelles	333
10.6 Kinetics of micelle formation and dissociation	334
10.7 Anomalous micellization	337
10.8 Block copolymer micelles in aqueous solutions	339
Acknowledgement	341
References	341
11 Light scattering by block copolymer liquids in the disordered and ordered state	343
<i>Petr Štěpánek and Timothy P. Lodge</i>	
11.1 Introduction	343
11.2 Block copolymer liquids and the order-to-disorder transition	343
11.3 Static birefringence and small angle scattering of light	348

11.4	Principles of dynamic light scattering from disordered block copolymer liquids	351
11.5	Review of experiments	356
11.6	Conclusions	375
	Acknowledgement	376
	Appendix 11.A: list of symbols and abbreviations	377
	References	378
12	Low angle light scattering and its applications	381
	<i>Francesco Mallamace and Norberto Micali</i>	
12.1	Introduction	381
12.2	Historical background	382
12.3	Mie scattering	384
12.4	Fluctuation theory of light scattering	392
12.5	Scattering function for self-similar systems	411
12.6	Conclusions	434
	Acknowledgements	435
	References	435
13	Combined static and dynamic light scattering	439
	<i>Walther Burchard</i>	
13.1	Introduction	439
13.2	Time correlation functions of the scattered intensity and electric field	440
13.3	Small particles	442
13.4	Polydispersity and determination of molar mass distributions	442
13.5	Large particles	444
13.6	Special examples	445
13.7	First cumulant	448
13.8	Alternative explanation	452
13.9	Branched macromolecules	453
13.10	Shape function	454
13.11	Semi-dilute solutions	456
13.12	Association and aggregation	460
	Acknowledgments	474
	References	474
14	Size distributions from static light scattering	477
	<i>F. Ross Hallett</i>	
14.1	Introduction	477
14.2	Light scattering geometry	478
14.3	Theory	478

14.4	Experimental considerations	484
14.5	Discussion	486
14.6	Conclusions	490
	References	491
15	Light scattering and chromatography in combination	494
	<i>Linda L. Lloyd, John F. Kennedy, and Charles J. Knill</i>	
15.1	Introduction	494
15.2	Chromatographic techniques	494
15.3	Information obtainable	499
15.4	Instrumentation	501
15.5	Applications	509
15.6	Macromolecular interaction and aggregation	510
15.7	Branching	512
15.8	Copolymer analysis	514
15.9	Synthetic polymers	514
15.10	Biological macromolecules	516
15.11	Conclusions	521
	Acknowledgements	522
	References	523
	Index	524

Contributors

Bruno D'Aguanno Centro di Ricerca Sviluppo e Studi Superiori in Sardegna, CRS4, Box 1048, I-09100, Cagliari, Italy

Mustapha Benmouna University of Tlemcen, Institute of Science and Technology, Physics Department, Tlemcen, BP119, Algeria

Redouane Borsali Centre de Recherches sur les Macromolecules Végétales, C.N.R.S., P.O. Box 53, F-38041, Grenoble Cedex 9, France

Wyn Brown Department of Physical Chemistry, University of Uppsala, Box 532, 751 21 Uppsala, Sweden

Walther Burchard Institut für Makromolekulare Chemie, Sonnenstrasse 5, 79104 Freiburg i Br., Germany

Dominique Durand Laboratoire de Physico-Chimie Macromoléculaire, Université du Maine, Route de Laval, 72017 Le Mans Cedex, France

Jean-Christophe Gimel Laboratoire de Physico-Chimie Macromoléculaire, Université du Maine, Route de Laval, 72017 Le Mans Cedex, France

F. Ross Hallett Department of Physics, University of Guelph, Guelph, Ontario, Canada N1G 2W1

John F. Kennedy Birmingham Carbohydrate and Protein Technology Group, School of Chemistry, University of Birmingham, Birmingham B15 2TT, UK

Rudolf Klein Universität Konstanz, Fakultät für Physik, Universitätsstrasse 10, Postfach 5560, D-7843 Konstanz, Germany

Charles J. Knill Birmingham Carbohydrate and Protein Technology Group, School of Chemistry, University of Birmingham, Birmingham B15 2TT, UK

Pavel Kratochvíl Institute of Macromolecular Chemistry, Heyrovského n. 2, 162 06 Prague 6, Czech Republic

Linda L. Lloyd ChembioTech Ltd, Institute of Research and Development, University of Birmingham Research Park, Vincent Drive, Edgbaston, Birmingham B15 2SQ, UK

Timothy P. Lodge Department of Chemistry, University of Minnesota, Minneapolis, Minnesota 55455-0431, USA

Francesco Mallamace Dipartimento di Fisica, Università di Messina, Vill. S. Agata, P.O. Box 55, 98166 Messina, Italy

Norberto Micali Istituto Tecniche Spettroscopiche del C.N.R., Vill. S. Agata, P.O. Box 55, 98166 Messina, Italy

Taco Nicolai Laboratoire de Physico-Chimie Macromoléculaire, Université du Maine, Route de Laval 72017 Le Mans Cedex, France

Theo Odijk Delft University of Technology, Julianalaan 136, 2628 BL Delft, The Netherlands

Wayne F. Reed Department of Physics, Tulane University, New Orleans, Louisiana 70118, USA

Peter Schurtenberger Institut für Polymere, ETH-Zentrum, Universitätsstrasse 6, CH 8092 Zurich, Switzerland

Marián Sedlák Institute of Experimental Physics, Slovak Academy of Sciences, 04353 Košice, Slovakia

Jim Selser Department of Physics, University of Nevada, Las Vegas, 4505 Maryland Parkway, Las Vegas, Nevada 89154-4002, USA

Petr Štěpánek Institute of Macromolecular Chemistry, Heyrovského n. 2, 16206 Prague 6, Czech Republic

Zdeněk Tuzar Institute of Macromolecular Chemistry, Heyrovského n. 2, 16206 Prague 6, Czech Republic

Theoretical developments in static light scattering from polymers

Mustapha Benmouna and Wayne F. Reed

1.1 Introduction

The theory of light scattering was first put forward by Lord Rayleigh^[1,2] in a series of papers in which he discussed the case of particles with a small size compared to the wavelength of the incident light. Debye^[3] extended this theory to large particles, including the effects of intramolecular interference between waves scattered by different parts of the same molecule. In particular, he derived the form factor of a flexible Gaussian chain in the absence of excluded volume interaction (see eqn (1.17)). This expression is extremely useful for analysing scattering data from polymers. Rayleigh–Debye theory was extended by Zimm,^[4] who calculated the scattering intensity of a dilute polymer solution in good solvent conditions in which the excluded volume interaction is important. Zimm used the Single Contact Approximation (SCA) to derive a formula for the scattered intensity, and represented the results in terms of the reciprocal intensity as a function of the sum of the polymer concentration and the square of the scattering wavevector. The ‘Zimm plot’ has become a routine method for polymer solution characterization and provides immediate information on the size and interactions of polymers in terms of the molecular weight M , the radius of gyration R_g , and the second virial coefficient A_2 .

The theory of scattering from multicomponent polymer mixtures was worked out originally by Stockmayer,^[5] who derived a formula for the intensity at zero angle from a purely thermodynamical point of view. This formula served as a basis for the analysis of scattering and thermodynamic behaviour of polymer mixtures until the early 1980s. The generalization of Stockmayer’s result to include the wave vector dependence of the scattering intensity was proposed by Benoît and Benmouna,^[6] using the chain of single contacts method. This method is a mean field approximation equivalent to the Random Phase Approximation (RPA) or the Ornstein Zernike equation with a specific closure relation.^[7] This led to a general formula relating the static structure matrix in the interacting system, the bare structure matrix in the non-interacting system and the excluded volume interaction matrix. This result, first obtained by Benoît, has the same form as Zimm’s equation, except that it is more general and, in principle, it can be applied to systems with an arbitrary number of

components. It also reduces to the classical result obtained by de Gennes^[8] for polymer blends using the RPA.

A detailed investigation of various ternary mixtures containing two polymers and a solvent was made by Ould-Kaddour and Strazielle,^[9] using static light scattering. Benoît's equation was found to offer an appropriate framework for obtaining a large amount of thermodynamic and structural information on polymer mixtures. Recently, static light scattering measurements were made on quaternary mixtures of three polymers and a solvent, and their interpretation was also possible within this simplified theory.^[10,11] By light scattering, one could also study the changes of the thermodynamic and the structural properties of multicomponent mixtures with temperature. It is known that when the temperature of a system (i.e. a simple liquid or mixture) approaches the critical value T_c , the fluctuations become important and may drive the system into an unstable state. This results in intense light scattering, which was observed initially in simple liquids in the vicinity of the liquid–vapour transition. Early observations of this phenomenon contributed to a large extent to the development of some classical theories of light scattering by Einstein, Smoluchowski, Ornstein, Zernike and others.^[12]

Polyelectrolytes represent an important class of macromolecules where long range Coulomb forces can dominate the intra-and inter-molecular scattering properties.^[13] Strong electrostatic repulsions at extremely low or no added salt concentrations C_s lead to low osmotic compressibility and very weak scattering, with the polymer coils being highly swollen. The intermolecular interactions in this case are too strong to be described by the SCA and angular maxima are often observed in the static scattering signal. Different explanations for these maxima have been proposed, including liquid-like correlations similar to those observed in simple liquids,^[4] correlation holes,^[8,15] long range ordering and the formation of domain structures.^[16] Addition of salt leads to a sharp increase in scattering intensity and contraction of the polyelectrolyte's static dimensions (R_g) and to a decrease in interaction (A_2).

This chapter does not aim to present an exhaustive review of all these topics. Instead, it is a selection of topics concerned with static light scattering from polymers, which in our opinion represents subjects of current interest and intensive investigation.

1.2 Static light scattering from polymer/solvent mixtures

1.2.1 Density and concentration fluctuations

Light scattering has become a standard tool for polymer characterization. Its basic principles, which include the theories of electromagnetic radiation and stochastic processes, and the experimental considerations based essentially on optic and electronic systems, are described in several classic textbooks.^[2,17–20] There is no need to reproduce detailed discussions on these aspects here. Instead, we will start directly with the first application involving the simplest

example of a polymer/solvent mixture. The total scattered intensity in the forward direction is given in terms of the average square fluctuations of the dielectric constant ε_r :

$$I \propto \frac{\pi^2}{\lambda^4} \tau \langle \delta \varepsilon_r^2 \rangle, \quad (1.1)$$

where λ is the vacuum wavelength of the incident radiation and τ the scattering volume. For the binary mixture, the fluctuation $\delta \varepsilon_r$ is expressed in terms of the density fluctuation $\delta \rho$ and the polymer concentration fluctuation δc as

$$\delta \varepsilon_r = (\partial \varepsilon_r / \partial \rho)_{T,c} \delta \rho + (\partial \varepsilon_r / \partial c)_{T,\rho} \delta c. \quad (1.2a)$$

Neglecting the coupling between density and concentration fluctuations, $\langle \delta \rho \delta c \rangle \sim 0$ yields

$$\langle \delta \varepsilon_r^2 \rangle = (\partial \varepsilon_r / \partial \rho)^2 \langle \delta \rho^2 \rangle + (\partial \varepsilon_r / \partial c)^2 \langle \delta c^2 \rangle. \quad (1.2b)$$

The first term on the right-hand side (RHS) is due to volume fluctuations:

$$\langle \delta \rho^2 \rangle = \langle \rho / \tau \rangle^2 \langle \delta \tau^2 \rangle, \quad (1.2c)$$

where $(\partial \varepsilon_r / \partial \rho)$ is related to the index of refraction n ($\varepsilon_r = n^2$),

$$(\partial \varepsilon_r / \partial \rho) = (n^2 - 1)(n^2 + 2)/3\rho, \quad (1.2d)$$

whereas $\langle \delta \tau^2 \rangle$ is obtained from the theories of fluctuations:^[21,22]

$$\langle \delta \tau^2 \rangle / \tau = k_B T \chi_T, \quad (1.2e)$$

where k_B is Boltzmann's constant, T is the absolute temperature and χ_T is the coefficient of isothermal compressibility. Combining eqns (1.1) and (1.2a,b) yields the contribution to the scattered intensity from the density fluctuations. Assuming that it is entirely due to the solvent gives

$$I_{\text{solvent}} = (\pi^2 / 9\lambda^4)(n^2 - 1)^2(n^2 + 2)^2 k_B T \chi_T. \quad (1.3)$$

The second term on the RHS of (1.2b) is due to the polymer concentration fluctuations. It is calculated using $\varepsilon_r = n^2$:

$$(\partial \varepsilon_r / \partial c)_{T,\rho} = 2n(\partial n / \partial c)_{T,\rho} \quad (1.4a)$$

and from statistical thermodynamics, expressing $\langle \delta c^2 \rangle$ in terms of the solvent chemical potential μ_s :^[21,22]

$$\langle \delta c^2 \rangle = (k_B T / (\partial \mu_s / \partial c)_{T,\rho}) c v_s / \tau, \quad (1.4b)$$

where v_s is the partial molar volume of solvent. Denoting by μ_s^0 the chemical potential of a pure solvent, one has:

$$\mu_s - \mu_s^0 = \pi v_s = v_s R T c (1/M + A_2 c + \dots), \quad (1.4c)$$

where $R = N_A k_B$ is the ideal gas constant, N_A is Avogadro's number, M is the polymer molecular weight, and π is the osmotic pressure. Combining eqns

(1.4,a,b,c), (1.2b) and (1.1) yields the contribution of the concentration fluctuations to the scattered intensity. This quantity defines the excess scattering of the solution with respect to the solvent $\Delta I = I - I_{\text{solvent}}$. In light scattering, one usually uses the Rayleigh ratio (cm^{-1}), which is the fraction of incident intensity I_0 scattered per path length in the scattering medium:

$$\Delta I \equiv \frac{I_s r^2}{I_0} = \frac{Kc}{(1/M + 2A_2 c)}, \quad (1.5a)$$

where I_s is the scattered intensity per unit scattering volume at a distance r from the scattering volume. For unpolarized incident light, K is given by

$$K = \frac{2\pi^2 n^2 (\partial n / \partial c)^2 (1 + \cos^2 \theta)}{\lambda^4 N_A} \quad (1.5b)$$

and, for vertically polarized incident light,

$$K = \frac{4\pi^2 n^2 (\partial n / \partial c)^2}{\lambda^4 N_A}. \quad (1.5c)$$

This is a classical result for the scattering intensity of a binary mixture in the forward direction. At a finite angle, one should include the reduction of signal amplitude due to intra-molecular interferences for long chains and to inter-particle correlations when the mean polymer concentration increases. These two effects are discussed below.

1.2.2 The single contact approximation: Zimm's equation

At finite angles, the scattering signal is modified by the fact that the waves emitted by different parts of the same molecule or by different molecules show strong interference. The angular distribution is expressed in terms of the wave vector q , which is related to the scattering angle θ by $q = 4\pi n \sin(\theta/2)/\lambda$.

In eqn (1.4c) the interaction between particles is introduced through the second virial coefficient of the chemical potential. Here we proceed differently and introduce the second virial coefficient for the scattering intensity following Zimm's SCA.^[4] For convenience, we use a different notation and replace M , c and A_2 by the number of monomers per chain N , the volume fraction ϕ and the excluded volume parameter v , respectively. These quantities are as follows:

$$N = M/m_0, \quad \phi = cv_0 N_A / m_0, \quad v = 2A_2 m_0^2 / v_0 N_A. \quad (1.6)$$

where m_0 is the monomer molecular weight and v_0 its volume. The starting point is the definition of the scattered intensity $\Delta I(q)$:

$$\Delta I(q)/\mathfrak{R} = \phi NP(q) + \phi^2 N^2 Q(q), \quad (1.7)$$

where \mathfrak{R} is a constant proportional to K ; $P(q)$ is the chain form factor describing

its internal configuration. In general, one has

$$N^2 P(q) = \sum_{i,j} \langle e^{i\mathbf{q} \cdot (\mathbf{R}_i - \mathbf{R}_j)} \rangle. \quad (1.8a)$$

This equation embodies the approximation that the total phase difference between scattered waves arriving at the detector is due entirely to differences in geometrical path. This approximation is normally quite good for polymers, since the space between monomers is filled by solvent. After averaging over all spatial orientations, $P(q)$ can also be written in terms of the internal density distribution $\rho(\mathbf{r})$ as:

$$P(q) = \left(\int d\mathbf{r} \rho(r) \frac{\sin qr}{qr} \right) \left(\int d\mathbf{r} \rho(r) \right)^{-1}. \quad (1.8b)$$

$Q(q)$ is the inter-molecular scattering function, which describes the effects of inter-chain interactions. It is defined by

$$N^4 Q(q) = \sum_{i_1 \neq j_2} \langle e^{i\mathbf{q} \cdot (\mathbf{R}_{i1} - \mathbf{R}_{j2})} \rangle. \quad (1.9)$$

Following the standard notation, the vectors are denoted with bold face characters and are defined with respect to an origin O , which is not explicitly indicated, e.g. $\mathbf{R}_i \equiv O\mathbf{R}_i$. In eqn (1.8), monomers i and j belong to the same chain, whereas in eqn (1.9), i_1 and j_2 are on different chains 1 and 2.

Let us consider first the inter-molecular scattering function $Q(q)$. The SCA assumes that each pair of molecules has only one contact point as illustrated in Fig. 1.1. Using the following property of vector summation,

$$\mathbf{R}_{i1} - \mathbf{R}_{j2} = (\mathbf{R}_{i1} - \mathbf{R}_{\mu 1}) + (\mathbf{R}_{j2} - \mathbf{R}_{\nu 2}),$$

in eqn (1.9) and performing the average with respect to the joint probability distribution function,

$$\psi(\mathfrak{R}_1, \mathfrak{R}_2) = \psi(\mathfrak{R}_1)\psi(\mathfrak{R}_2)h(\mathfrak{R}_1, \mathfrak{R}_2), \quad (1.10a)$$

where $\mathfrak{R}_1 \equiv \{\mathbf{R}_{11}, \mathbf{R}_{21}, \mathbf{R}_{31}, \dots, \mathbf{R}_{i1}, \dots\}$ and $\mathfrak{R}_2 \equiv \{\mathbf{R}_{12}, \mathbf{R}_{22}, \mathbf{R}_{32}, \dots, \mathbf{R}_{j2}, \dots\}$ represent all the monomer coordinates of chains 1 and 2 respectively, and $h(\mathfrak{R}_1, \mathfrak{R}_2) \equiv 1 - g(\mathfrak{R}_1, \mathfrak{R}_2)$ is the total correlation function for all the monomer



FIG. 1.1. A schematic representation of the Single Contact Approximation: the continuous vertical lines represent chains 1 and 2. The dashed horizontal line represents the interaction.

coordinates of chains 1 and 2:

$$h(\mathbf{R}_1, \mathbf{R}_2) = 1 - e^{-U_{12}/K_B T} \approx -v \sum_{\mu_1, \nu_2} \delta(\mathbf{R}_{\mu_1} - \mathbf{R}_{\nu_2}). \quad (1.10b)$$

Performing the integral of the delta function over $\mathbf{R}_{\mu_1 \nu_2}$ yields:

$$N^4 Q(q) = -v \sum_{i_1, \nu_1} \langle e^{i\mathbf{q} \cdot (\mathbf{R}_{i_1} - \mathbf{R}_{\nu_1})} \rangle \sum_{\mu_2, j_2} \langle e^{i\mathbf{q} \cdot (\mathbf{R}_{\mu_2} - \mathbf{R}_{j_2})} \rangle. \quad (1.11a)$$

Then, noting that

$$\sum_{i_1, \nu_1} \langle e^{i\mathbf{q} \cdot (\mathbf{R}_{i_1} - \mathbf{R}_{\nu_1})} \rangle = \sum_{\mu_2, j_2} \langle e^{i\mathbf{q} \cdot (\mathbf{R}_{\mu_2} - \mathbf{R}_{j_2})} \rangle = N^2 P(q),$$

one obtains:

$$Q(q) = -vP^2(q). \quad (1.11b)$$

The strength of excluded volume interaction v is assumed to be independent of the position along the chain but depends strongly upon the temperature and quality of solvent. Substituting eqn (1.11b) into (1.7) yields

$$\begin{aligned} \Delta I(q)/\mathfrak{R} &= \phi NP(q) - v\phi^2 N^2 P^2(q) \approx \phi NP(q)(1 - v\phi NP(q) + \dots) \\ &= \phi NP(q)(1 + v\phi NP(q))^{-1}, \end{aligned} \quad (1.12a)$$

or, in reciprocal form:

$$\mathfrak{R}/\phi N \Delta I(q) = 1/\phi NP(q) + v. \quad (1.12b)$$

Introducing $S(q) = \phi N \Delta I(q)/\mathfrak{R}$, the total structure factor, and $S_0(q) = \phi NP(q)$, one has

$$1/S(q) = 1/S_0(q) + v. \quad (1.13)$$

In writing eqns (1.12a,b) it is assumed that the quantity $-v\phi NP(q)$ is the first term in a geometric series representing all the higher order concentration terms of multiple contact points. Equations (1.12) and (1.13) are different representations of the classical Zimm equation which, in the more familiar experimental notation, reads:

$$\frac{Kc}{\Delta I(q)} = \frac{1}{MP(q)} + 2A_2c. \quad (1.14)$$

Most modern light scattering photometers use vertically polarized incident light, so that in the horizontal detection plane K is the same as in eqn (1.5c).

1.2.3 The form factor, $P(q)$

The form factor $P(q)$ is defined in eqn (1.18). Its calculation requires knowledge of the intra-molecular distribution function characterizing the shape and architecture of the chain. There are several models of $P(q)$, and perhaps the most familiar one for unperturbed linear coils is the Debye function. Two main

assumptions are made to obtain this function. The first one is the Gaussian approximation resulting from the use of the Gaussian function for $\psi(\mathbf{R}_{ij})$,

$$\sum_{ij} \langle e^{i\mathbf{q} \cdot \mathbf{R}_{ij}} \rangle = \sum_{ij} e^{-q^2 \langle R_{ij}^2 \rangle / 6}, \quad (1.15)$$

and the second approximation is that $\langle R_{ij}^2 \rangle$ is proportional to $|i - j|$:

$$\langle R_{ij}^2 \rangle = |i - j|a^2, \quad (1.16a)$$

where a is the length of a monomer. Substituting eqn (1.16a) into (1.15) and transforming the double sum into a single one leads to:

$$N^2 P(q) = N + 2 \sum_{n=1}^{N-1} (N-n) e^{-(q^2 a^2 / 6)n}. \quad (1.16b)$$

Approximating the discrete sum by an integral, neglecting $1/N$ and introducing the radius of gyration of a Gaussian unperturbed chain, R_g , yields the classical Debye function $P_D(q)$:

$$P_D(q) = 2(e^{-u} + u - 1)/u^2, \quad \text{with} \quad u = q^2 R_g^2 = q^2 N a^2 / 6. \quad (1.17)$$

If the chain is closed in the form of a ring, the calculation of $P(q)$ proceeds in a similar way, but instead of eqn (1.16a) one should use

$$\langle R_{ij}^2 \rangle = |i - j|(1 - (|i - j|/N)a^2). \quad (1.18a)$$

Substituting this into eqn (1.15) and using similar approximations as for the open chain, one obtains Cassasa's function:^[23]

$$P_{\text{ring}}(q) = \frac{2e^{-u_r/4}}{\sqrt{u_r}} \int_0^{\sqrt{u_r/4}} dx e^{-x^2}, \quad u_r = q^2 R_{gr}^2 = q^2 N a^2 / 12, \quad (1.18b)$$

where R_{gr} is the radius of gyration of a ring. For half a ring, the result of integration is^[24]

$$P_{\text{half ring}}(q) = 4(1 - e^{-u_r/4})/u_r. \quad (1.18c)$$

Rigid polymers are another class of polymers with important applications.^[17] The most common examples of form factors for rigid polymers are the following:

the hard sphere of diameter D ,

$$P_{\text{sphere}}(qD) = [3(\sin x - x \cos x)/x^3]^2, \quad x \equiv qD/2; \quad (1.19a)$$

the rigid rod of length L ,

$$P_{\text{rod}}(qL) = \frac{2}{qL} \int_0^{qL} dx \frac{\sin x}{x} - \left(\frac{\sin(qL/2)}{qL/2} \right)^2. \quad (1.19b)$$

Other more sophisticated models of form factors were proposed for polymers with local stiffness and global flexibility. Many of these expressions have been proposed in the literature.^[25,26]

Branched polymers are interesting because of their variety of architectures and important applications. Knowledge of their conformation is crucial for an understanding of their role in these applications, their behaviour in different environments and their interactions with other species present in the solution. The simplest example of a branched polymer is the star molecule. The calculation of the form factor of a Gaussian star with N_b branches and N_0 monomers per branch can be easily carried out using:

$$(N_b N_0)^2 P_{\text{branched}}(q) = N_b N_0^2 P_b(q) + N_b(N_b - 1)N_0^2 P'_{bb}(q). \quad (1.20a)$$

$P_b(q)$ is the form factor of a single branch and $P'_{bb}(q)$ the inter-branch contribution:

$$P_b(q) = 2(e^{-u_b} + u_b - 1)/u_b^2, \quad P'_{bb}(q) = (e^{-u_b} - 1)^2/u_b^2. \quad (1.20b)$$

$u_b = q^2 R_{gb}^2$, and $R_{gb}^2 = N_b a^2/6$ is the square radius of gyration of a single branch. There are other more complicated forms of branched polymers, such as starburst dendrimers, which are being actively investigated. Their $P(q)$ values can be calculated using a similar procedure by separately evaluating the contributions from each branch and from the inter-branch interferences. This subject is also well documented in the literature and the reader is referred to the excellent review articles by Burchard^[27,28] for more details.

1.2.4 Light scattering from polyelectrolyte solutions

Different aspects of light scattering and polyelectrolyte solutions are covered in other chapters in this volume. Here we are concerned only with the effects of ionic strength on the scattering from polyelectrolytes. Light scattering from polyelectrolytes varies dramatically with the concentration of added salt C_s . When no salt is added, the intensity of scattered light is quite feeble, usually just above the solvent scattering level, the slope of $Kc/\Delta I(q)$ vs. q^2 is often negative and, at a low enough polymer concentration c , both the q -dependent inverse diffusion coefficient $1/D(q)$ and $\Delta I(q)$ manifest broad angular scattering maxima. The $\Delta I(q)$ peak is illustrated for proteoglycan subunit in SEC flow at different concentrations in Fig. 1.2 (adapted from ref. 29). As C_s increases, the peak is quickly lost, and $\Delta I(q)$ regains the qualitative shape of that for a neutral polymer. The loss of the peak and recovery of ‘neutral-like’ scattering at high C_s is also shown in Fig. 1.2.

Even though the strong interactions leading to the $\Delta I(q)$ peak have been screened by the added salt, there is, however, considerable inter- and intra-molecular repulsion, still manifested in the relatively high values of A_2 and R_g . Figure 1.3 shows $Kc/\Delta I(q)$ vs. q^2 for a dilute solution of an acrylamide/acrylate copolymer with a Manning parameter ξ (number of elementary charges per Bjerrum length) equal to 0.2 at different values of C_s (adapted from experiments presented in ref. 30). The experiment was performed by serial titration of the solution with small quantities of salt stock solutions such that c remained practically constant. As C_s increases, (i) the intercept decreases, indicating a

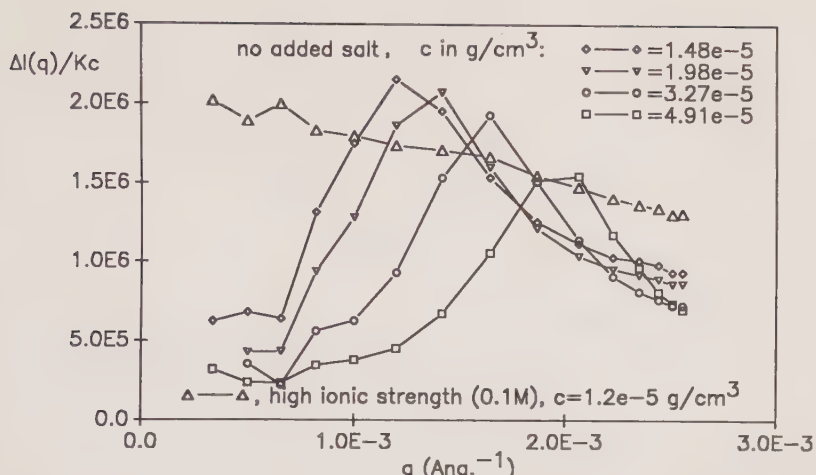


FIG. 1.2. Angular scattering peaks for proteoglycans ($M \sim 2$ million) at different concentrations under shear flow with no added salt. Addition of salt (0.1 M) leads to the loss of the peak and a monotonic decrease of scattering with q . Similar behaviour with and without salt is also obtained under no-flow conditions.

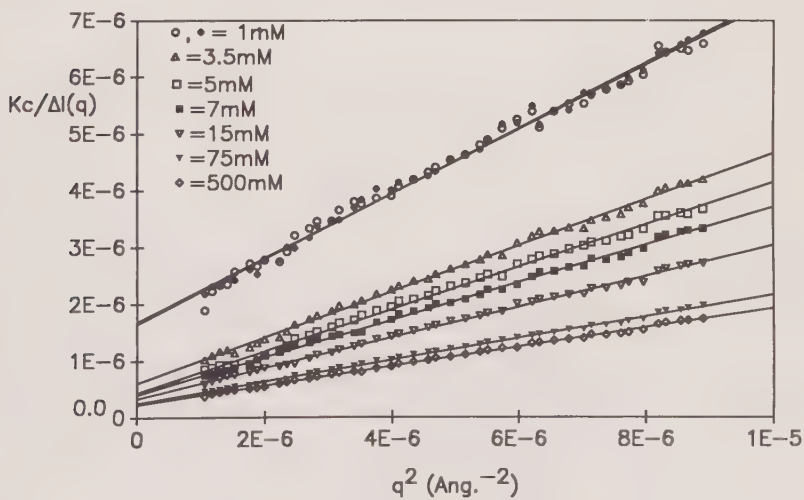


FIG. 1.3. $Kc/\Delta I(q)$ vs. q^2 for an acrylamide/acrylate copolymer at 10^{-4} g/ml and varying concentrations of added salt C_s (indicated as mM). The decreasing intercepts and slopes with increasing S_s show the decrease in both R_g and A_2 .

decrease in A_2 , and (ii) the slope decreases, indicating a decrease in R_g . If M is determined in a separate experiment (e.g. a full Zimm plot at high C_s), then A_2 vs. C_s can be determined simply from

$$A_2 = [Kc/\Delta I(q = 0) - 1/M]/2c. \quad (1.21)$$

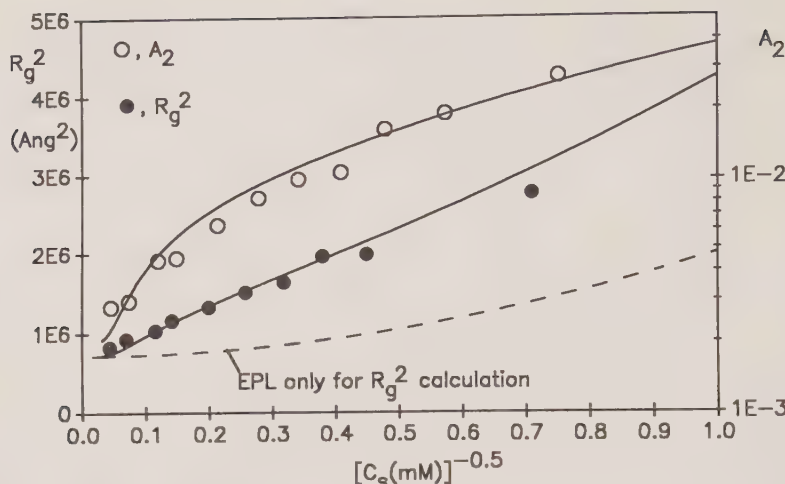


FIG. 1.4. A_2 (mole \times cm³/g²) and R_g^2 for hyaluronate ($\xi = 0.71$) as computed from eqns (1.21) and (1.22), using single concentration data similar to Fig. 3. Solid lines are the combined EPV/EEV calculations, with no adjustable parameters, using eqns (1.23)–(1.28). The dashed line shows the poor agreement with R_g^2 when only EPL effects are taken into account; i.e. EEV effects dominate the polyelectrolyte dimensions over the range of C_s studied in this case.

If the solution is sufficiently dilute that the $2A_2c$ term in eqn (1.21) is independent of q , then R_g at each C_s can be determined simply as

$$R_g^2 = 3M_w \partial[Kc/\Delta I(q)]/\partial q^2. \quad (1.22)$$

A_2 and R_g obtained in this way for hyaluronate are shown in Fig. 1.4 (adapted from ref. 31).

The combination of electrostatic persistence length (EPL) and electrostatic excluded volume theories (EEV) by Odijk^[32] and Skolnick and Fixman^[33] has proven reasonably successful in accounting for the experimentally determined ionic strength behaviour of R_g and A_2 . Namely, the total persistence length L_t is computed as $L_t = L_e + L_0$, where L_0 is the intrinsic persistence length of the polyelectrolyte, and L_e , the electrostatic persistence length, is given by

$$L_e = \frac{\xi^2}{12\lambda_B^2 \kappa_D^2} \left(3 - \frac{8}{y} + e^{-y} \left(y + 5 + \frac{8}{y} \right) \right), \quad (1.23)$$

where $y = \kappa_D L$, in which κ_D is the inverse Debye screening length, L is the polymer contour length, and λ_B is the Bjerrum length (= 7.18 Å in water at 25 °C). The unperturbed radius of gyration R_{g0} is then given by the standard worm-like chain formula

$$R_{g0}^2 = \frac{LL_t}{3} - L_t^2 + \frac{2L_t^3}{L} - 2 \frac{L_t^4}{L^2} (1 - e^{-L/L_t}). \quad (1.24)$$

The measured, perturbed R_g^2 is related to R_{g0}^2 via the static expansion factor α_s using $R_g^2 = \alpha_s^2 R_{g0}^2$. The expansion factor is related in turn to the excluded volume parameter z by one of several approximate expressions which exist.^[17] One particular form is due to Gupta and Forsman^[34] and is given as

$$\alpha_s^5 - \alpha_s^3 = \frac{134}{145}(1 - 0.885N_K^{-0.462})z, \quad (1.25)$$

with

$$z = \left(\frac{3}{2\pi L_K^2} \right)^{3/2} \beta_K N_K^{1/2}. \quad (1.26)$$

The excluded volume integral β_K has been approximated in several ways. The Fixman–Skolnick^[35] form is for that of two rods, each of one Kuhn length, interacting via the Debye–Hückel potential. This gives

$$\beta_K = 8L_T^2 \kappa_D^{-1} \int_0^{\pi/2} d\theta \sin \theta \int_0^{w/\sin \theta} dx (1 - e^{-x}), \quad (1.27a)$$

where

$$w = 2\pi \xi^2 \kappa_D^{-1} e^{-\kappa_D d} \quad (1.27b)$$

N_K being the number of rods in each polymer and d their diameter. The second virial coefficient, A_2 , is

$$A_2 = \frac{N_A N_K^2 \beta_K}{2m_0^2} h(\bar{z}), \quad \text{where} \quad h(\bar{z}) = \frac{1 - (1 + 3.9\bar{z})^{-0.468}}{1.83\bar{z}} \quad (1.28a,b)$$

and $\bar{z} = z/\alpha_s^3$ is Yamakawa's^[17] first order attempt at including intra-molecular excluded volume into the inter-molecular excluded volume problem.

Figure 1.4 shows the results of the above combined EPL and EEV calculations for R_g and A_2 for the case of hyaluronate (solid line). The calculations involve no adjustable parameters (i.e. they are not ‘fits’ to the data), and give reasonable agreement with the data over the range of C_s involved. Using L_e alone (dotted line), however, with no corrections for EEV effects, gives R_{g0}^2 , and strongly underestimates the measured R_g^2 . In fact, in the case of HA and other long, semi-flexible polyelectrolytes, the EEV effects usually dominate over EPL over the range of C_s normally accessible to light scattering. Since light scattering experiments measure R_g^2 and not R_{g0}^2 , it is not possible, *a priori*, to assess experimentally the relative contributions of EPL and EEV to the net R_g^2 .

Attempts to measure the deviation in $P(q)$ between ideal coils and coils with excluded volume have not usually been successful for electrolytes. Figure 1.3 for example, gives quite straight lines and $q^2 R_g^2$ runs from about 4 to 30 at $C_s = 1$ mM and from about 1.2 to 10 at $C_s = 500$ mM. In fact, a Monte Carlo study^[36] suggests that the curvature of $1/P(q)$ for high EEV is still slight enough over the q -range of a single wavelength light scattering experiment that deviations from the Debye $P_D(q)$ should be quite difficult to detect. Experimental tests of EPL, in which EEV effects could be minimized, would require the use of either very intrinsically stiff polyelectrolytes with few Kuhn segments, or perhaps semi-flexible polyelectrolytes at very low C_s (below 1 mM).

A recent Monte Carlo^[37] study indicates that, within the Debye–Hückel approximation, polyelectrolyte chains do in fact have worm-like character, the L_e concept is quantitatively useful and at low C_s the Debye–Hückel approximation should fail. For a chain with Manning parameter 1, for example, the energy per monomer should exceed $k_B T$ at and below around $C_s = 40$ mM, so that use of the OSF theory for L_e at low C_s should lead to an overestimation of L_e . Some experimental evidence exists for L_e being smaller than that predicted by eqn (1.23), and this is supported by a computational approach to L_e using the full Poisson–Boltzmann equation for a polyelectrolyte of finite thickness.^[38]

Finally, it should be pointed out that a meaningful measurement of static light scattering from polyelectrolytes, especially at very low C_s , requires very clean solutions. Many, though not all, polyelectrolyte solutions at low ionic strength have measurable populations of aggregates which can distort the scattering data. These can usually be permanently removed by filtration through membrane filters of the proper pore size;^[39–41] see also the discussion in Chapter 4 of this volume.

1.3 Multicomponent polymer mixtures

1.3.1 Benoît's equation

The formulation of scattering theory in the case of multicomponent polymer mixtures can be made easily and conveniently by using the matrix notation. One notes that the scattered intensity $\Delta I(q)$ in the presence of p polymer species is as follows:

$$\Delta I(q) \propto \sum_{i,j=1 \dots p} a_i S_{ij}(q) a_j, \quad (1.29)$$

where we have introduced the shorthand notation $a_i = (\partial n / \partial \phi)_i / \rho_i = (\partial n / \partial c)_i$ for the increment of refractive index of polymer i , and $\rho_i = m_i / (v_{0i} N_A)$ is the mass density. The main problem is to determine the partial structure factors $S_{ii}(q)$ and $S_{ij}(q)$ involving the interactions between pairs of polymer species. This can be done within the generalized RPA solving Benoît's^[6,7,42,43] matrix equation:

$$\mathbf{S}^{-1}(q) = \mathbf{S}_0^{-1}(q) + \mathbf{v}. \quad (1.30a)$$

This result is similar to Zimm's equation except that it is in matrix form. This similarity between the RPA and the SCA is the reason for the success of the Zimm plot analysis over a wide range of concentrations, even though the SCA applies only in the dilute regime. One should recall that the latter approximation is usually combined with the reciprocal approximation to obtain Zimm's equation as described earlier. Higher order interactions are implicitly included, giving a result which is valid beyond the SCA. The RPA is valid as long as the system does not undergo strong fluctuations if it remains far from the critical conditions.

For homopolymers, the off-diagonal elements of the bare structure matrix $S_0(q)$ are zero and the diagonal elements are

$$S_{0ii}(q) = \phi_i N_i P_i(q), \quad i = 1, \dots, p. \quad (1.30b)$$

The elements of the excluded volume matrix v are related to the Flory–Huggins interaction parameters χ_{ij} by

$$v_{ij} = (1/\phi_s - \chi_{is} - \chi_{js} + \chi_{ij}), \quad i, j = 1, \dots, p. \quad (1.30c)$$

v_{ij} are expressed here in units of the cell volume, as in the lattice model.^[44]

1.3.2 de Gennes' equation: blend A/B

In the case of an incompressible blend A/B, de Gennes^[8] obtained from the RPA:

$$1/S(q) = 1/[\phi_a N_a P_a(q)] + 1/[\phi_b N_b P_b(q)] - 2\chi_{ab}. \quad (1.31)$$

This result can be obtained as a special case of Benoît's equation. Use of the incompressibility assumption for the binary mixture A/B leads to the excluded volume $v = 1/[\phi_b N_b P_b(q)] - 2\chi_{ab}$ which, substituted into the scalar version of eqn (1.30a), gives eqn (1.31). We shall examine later the case of compressible mixtures and show how pressure can affect the scattered signal.

1.3.3 Polymer A/polymer B/solvent

The calculation of the scattered intensity for a ternary mixture A/B/solvent is straightforward. One needs to solve the two-by-two matrix equation (1.30a) and use eqn (1.29):

$$\Delta I(q) = (a^2/S_{0b}(q) + b^2/S_{0a}(q) + (a^2 v_b + b^2 v_a - 2ab v_{ab}))/\Pi(q), \quad (1.32a)$$

$$\Pi(q) = (1/S_{0a}(q) + v_a)(1/S_{0b}(q) + v_b) - v_{ab}^2, \quad (1.32b)$$

where, for simplicity, we have let $a \equiv (\partial n / \partial c)_a$ and $b \equiv (\partial n / \partial c)_b$. Several cases of practical interest are considered below.

1.3.3.1 Polymer B is isorefractive with solvent. Here $b = (\partial n / \partial c)_b = 0$ and the only contribution to the scattered light is given by the quantity $S_{aa}(q)$, which is proportional to a^2 :

$$\Delta I(q)/a^2 = S_{aa}(q) = (1/S_{0b}(q) + v_b)/[(1/S_{0a}(q) + v_a)(1/S_{0b}(q) + v_b) - v_{ab}^2] \quad (1.33a)$$

which, in the reciprocal form, reads:

$$a^2/\Delta I(q) = 1/S_{aa}(q) = 1/S_{0a}(q) + v_a - v_{ab}^2 S_{0b}(q)/(1/S_{0b}(q) + v_b). \quad (1.33b)$$

In the conventional notation of light scattering, this equation becomes:

$$\frac{K c_a M_a}{\Delta I(q, c)} = \frac{1}{P_a(q)} + 2A_{2a} M_a c_a - \frac{4A_{2ab}^2 c_a c_b M_a M_b P_b(q)}{1 + 2A_{2b} M_b c_b P_b(q)}. \quad (1.34)$$

The third term on the RHS of eqn (1.34) describes the effects of the invisible polymer on the apparent R_g and A_2 . There are several investigations of these effects by light scattering in the literature.^[9,43,45] In Benoît *et al.*,^[43] Zimm plots of polystyrene ($A \equiv$ PS)/polymethylmethacrylate ($B \equiv$ PMMA with $(\partial n/\partial c)_b = 0$) in toluene are given for polymers of molecular weights approximately equal to 1.35×10^6 and different compositions. Zimm plots were found to be substantially distorted. For example, the curve representing $Kc_a M_a / \Delta I(q=0)$ vs. c_a goes through a maximum and decreases to zero. The slope of this curve defines the apparent second virial coefficient $A_{2\text{app}}$. It is found that, for small c_a , $A_{2\text{app}}$ is positive, indicating that the matrix PMMA + toluene behaves as a good solvent; $A_{2\text{app}}$ is zero at the maximum (theta-like behaviour) and becomes negative in the upper range of c_a . The matrix consisting of the solvent and the invisible polymer behaves as a bad solvent for PS. This occurs since the polymer composition is maintained constant, meaning that c_b increases together with c_a , resulting in strong screening of the excluded volume interaction.

1.3.3.2 The optical theta condition. Expanding (1.32a) in terms of the concentration and neglecting terms of the order of ϕ^3 and higher, one obtains the scattered intensity at $q = 0$ as

$$\begin{aligned} \Delta I(q=0) = & a^2 \phi_a N_a + b^2 \phi_b N_b - (a \phi_a N_a + b \phi_b N_b)(a \phi_a N_a + b \phi_b N_b) \\ & - 2ab \chi_{ab} \phi_a \phi_b N_a N_b. \end{aligned} \quad (1.35a)$$

This expression was first reported by Fukuda *et al.*,^[46] who proposed a method of determining the Flory interaction parameter χ_{ab} based on the choice of components satisfying the so-called ‘optical theta condition’:

$$(a \phi_a N_a + b \phi_b N_b) = 0. \quad (1.35b)$$

In this case, eqn (1.35a) becomes:

$$\Delta I(q=0)/\phi = a^2(1-x)N_a + b^2xN_b - 2ab\chi_{ab}\phi x(1-x)N_a N_b, \quad (1.35c)$$

where x represents the composition of the polymer B , $x = \phi_b/\phi$ and ϕ is the total volume fraction $\phi_a + \phi_b$. Equation (1.35c) shows that the variation of the normalized intensity as a function of ϕ is linear and the slope is directly proportional to the interaction parameter χ_{ab} . With this method, one has direct access to χ_{ab} from the slope, independently of the polymer–solvent interaction parameters.

This analysis is made here in the zero q limit. At finite q , it is more difficult to obtain a simple formula which allows a direct and quick determination of the interaction parameter. The situation is greatly simplified in the case of a symmetrical mixture where $x = 1/2$, the degrees of polymerization are equal and the polymer–solvent interactions are the same:

$$x = 1/2, \quad N_a = N_b = N, \quad P_a(q) = P_b(q) = P(q), \quad \chi_{as} = \chi_{bs} = \chi_s. \quad (1.36)$$

Using these equalities in eqn (1.32a) yields, without further approximation,

$$\begin{aligned}\Delta I(q) = & [(a+b)/2]^2 \phi NP(q) / [1 + v\phi NP(q)] \\ & + [(a-b)/2]^2 \phi NP(q) [1 - \chi\phi NP(q)/2]^{-1}.\end{aligned}\quad (1.37a)$$

In the zero average contrast condition, $a\phi_a + b\phi_b = (a+b)/2 = 0$, the scattered intensity becomes

$$\Delta I(q) / [(a-b)/2]^2 = \phi NP(q) / (1 - \chi\phi NP(q)/2).\quad (1.37b)$$

This result is similar to that characterizing blends with $(a-b)_{app}^2 = (a-b)^2\phi/4$, an apparent contrast factor and $\chi_{app} = \chi\phi/4$, an apparent interaction parameter. Since the volume fraction ϕ is much smaller than 1, the compatibility of the polymers is enhanced substantially by the presence of solvent, but the contrast factor is reduced by the factor $\phi/4$. This treatment of ternary mixtures as swollen blends has been commonly applied in the literature^[47] and gives very simple results which are easy to analyse.

1.3.4 Polymer A/solvent 1/solvent 2

The above mean-field treatment can be used in the case in which only one of the three components is a polymer and the two others are low molecular weight solvents. It is sufficient to let the degree of polymerization and the form factor of one of the two polymers, say B , equal unity. For isorefractive solvents, one obtains

$$a^2/I(q) = 1/S_{aa}(q) = 1/S_{0a}(q) + 1 - 2\chi_0,\quad (1.38a)$$

$$\chi_0 = 1/2 - (1 - 2\phi_2\chi_{a2} - 2\phi_1\chi_{a1} + \phi_1\phi_2D)/2(\phi_1 + \phi_2 - 2\phi_1\phi_2\chi_{12}),\quad (1.38b)$$

$$\Pi = 2\chi_{12}\chi_{a1} + 2\chi_{12}\chi_{a2} + 2\chi_{a1}\chi_{a2} - \chi_{a1}^2 - \chi_{a2}^2 - \chi_{12}^2.\quad (1.38c)$$

This result has already been derived using a different method based on the Flory–Huggins^[44,48] free energy for the mixture. It is sometimes useful to reproduce it in terms of the parameters γ and δ , describing the preferential affinity of the solvents for the polymer and their interaction strengths, respectively:

$$\gamma = (\chi_{a1} - \chi_{a2})/\chi_{a1}, \quad \delta = \chi_{12}/\chi_{a1}.\quad (1.38d)$$

We give only the expression of χ_0 from (1.38b):

$$\begin{aligned}\chi_0 = & 1/2 - [1 - 2\chi_{a1}(\phi_1 + (1 - \gamma)\phi_2] \\ & + \phi_1\phi_2\chi_{a1}^2[4\delta - (\delta + \gamma)^2]/2(\phi_1 + \phi_2 - 2\delta\phi_1\phi_2\chi_{a1}).\end{aligned}\quad (1.38e)$$

If the parameter γ is zero, the two solvents have the same affinity for the polymer, and so

$$1/S_{aa}(q) = 1/S_{0a}(q) - 2\chi_{a1} + (1 - \phi_1\phi_2\chi_{a1}^2\delta^2)/(\phi_1 + \phi_2\delta\chi_{a1}).\quad (1.39)$$

If $\phi_2 = 0$, Zimm's equation is recovered. Studies of the preferential adsorption in various conditions of the solution using other methods are also reported.^[49]

1.3.5 Mixtures of three polymers and a solvent

Recently, Strazielle *et al.*^[10,11] reported light scattering data from several mixtures of polystyrene, polydimethylsiloxane (PDMS), polymethylmethacrylate and toluene for different concentrations, compositions and molecular weights. These polymers are characterized by special values of $\partial n/\partial c$ since $(\partial n/\partial c)_{\text{PMMA}}$ in toluene is zero, whereas those of PS and PDMS have approximately equal amplitudes but opposite signs. The data are analysed using eqns (1.32a,b) knowing that the mixture satisfies the optical theta condition:

$$\Re\varphi/S(q) = \Re\varphi/S(q=0, \varphi=0)(1 + q^2 R_g^2 \chi_{\text{app}}/3) - 2\varphi\chi_{\text{app}}, \quad (1.40\text{a})$$

$$\Re\varphi/S(q=0, \varphi=0) = 4/N, \quad (1.40\text{b})$$

$$\chi_{\text{app}} = \chi\alpha/\eta, \quad (1.40\text{c})$$

$$R_g^2 \chi_{\text{app}} = R_g^2(1 - \mu\chi\varphi N), \quad (1.40\text{d})$$

with

$$\mu = (\alpha\delta - \eta\zeta)/\eta^2,$$

$$\alpha = 1 + (\chi/2 + v)(\varphi N + \varphi_3 N_3),$$

$$\eta = 1 + (\chi/2 + v)\varphi N + (v - \chi(v + \chi/2)\varphi N/2)\varphi_3 N_3,$$

$$\delta = (\chi/2 + v)\varphi N/2 + v\varphi_3 N_3 R_{g3}^2/2R_g^2 - (1 + R_{g3}^2/R_g^2)\chi(v + \chi/2)\varphi N\varphi_3 N_3/4,$$

$$\zeta = (\chi/2 + v)(\varphi N + \varphi_3 N_3 R_{g3}^2/R_g^2)/2.$$

In these equations the parameters have their usual meanings, i.e. N , N_3 and R_g , R_{g3} are degrees of polymerization and radii of gyration of PS (or PDMS) and PMMA (component 3), respectively; φ are φ_3 , the volume fractions of (PS + PDMS) and PMMA, respectively; and χ is the interaction parameter of the pairs (PS, PDMS) and (PMMA, PDMS). Details of these approximations are given by Strazielle *et al.*^[10] These predictions fit the data as functions of the polymer concentrations, compositions and molecular weights for several systems investigated. As one can see from eqn (1.40a), the slope of $\Re\varphi/S(q=0, \varphi)$ vs. φ is proportional to the apparent interaction parameter of the blend PS/PDMS. When PMMA is added, χ_{app} increases and the blend becomes more incompatible. It is found that the incompatibility is larger for the blend having a higher molecular weight.

1.3.6 Effects of pressure and shear on the scattering properties of polymer mixtures

1.3.6.1 *Effects of pressure: the case of compressible mixtures.* The RPA, (1.31), was derived by de Gennes using the incompressibility assumption for the blend A/B . If this blend contains free volume, it becomes compressible and the above result should be modified to include the effect of pressure. This question has

been the subject of various investigations and a primary motivation was to explain the variation of the Flory–Huggins interaction parameter with the volume fraction φ . In the Flory–Huggins theory, this parameter is assumed to be constant, while experimentally it has been found to depend on various quantities, and in particular on φ . Some authors have attributed this variation to the free volume in the sample, using arguments which we examine here. First we assume that the space filled by the solvent is now a free volume and make the appropriate changes to distinguish between the properties of solvent and those of the voids. This is done by first writing Benoît's equation explicitly in the case of a mixture of polymer *A*/polymer *B*/solvent:

$$\mathbf{S}^{-1}(q) = \begin{pmatrix} S_{0a}^{-1}(q) + \varphi_s^{-1} - 2\chi_{as} & \varphi_s^{-1} - 2\chi_{ab} \\ \varphi_s^{-1} - 2\chi_{ab} & S_{0b}^{-1}(q) + \varphi_s^{-1} - 2\chi_{bs} \end{pmatrix}. \quad (1.41)$$

Changing the solvent by the free volume means that φ_s should be replaced by φ_0 , the free volume fraction, and the interaction parameters χ_{as} , χ_{bs} and χ_{ab} are replaced by the pressures βP_a^* , βP_b^* and βP_{ab}^* , with $\beta = 1/k_B T^{[50,51]}$:

$$\mathbf{S}^{-1}(q) = \begin{pmatrix} S_{0a}^{-1}(q) + \varphi_0^{-1} - 2\beta P_a^* & \varphi_0^{-1} - 2\beta P_{ab}^* \\ \varphi_0^{-1} - 2\beta P_{ab}^* & S_{0b}^{-1}(q) + \varphi_0^{-1} - 2\beta P_b^* \end{pmatrix}. \quad (1.42a)$$

P_{ab}^* is the interaction energy between monomers *A* and *B*, and P_i^* ($i = a, b$) are the characteristic pressures of components *A* and *B* which are related to their cohesive energy densities. Combining eqns (1.42a) and (1.29) yields

$$\Delta I(q) = (a - b)^2 [1 - \varphi_0/\varpi(q)]/[1/S_{0a}(q) + 1/S_{0b}(q) - 2\Theta], \quad (1.42b)$$

with

$$\begin{aligned} 1/\varpi(q) &= [2\beta(a^2P_b^* + b^2P_a^* - 2abP_{ab}^*) - a^2/S_{0b}(q) - b^2/S_{0a}(q)](a - b)^{-2}, \\ \Theta &= \beta\delta P^* + \varphi_0[2\beta^2P_{ab}^{*2} - (\beta P_a^* - 1/2S_{0a}(q))(\beta P_b^* - 1/2S_{0b}(q))], \\ \delta P^* &= P_a^*P_b^* - 2P_{ab}^*. \end{aligned}$$

In the case of incompressible blends the volume fraction of voids φ_0 goes to zero and one recovers de Gennes' result. If φ_0 is finite the system is compressible and the scattered signal is strongly modified by the pressure. The relationship between φ_0 and P is given by the equation of state, which gives the relationship between the reduced variables:

$$p' = P/P^*, \quad v' = V/V^* = 1/(1 - \varphi_0), \quad T' = T/T^*,$$

where P^* , V^* and T^* are the characteristic pressure, volume and temperature of the system. Two examples of equations of state which describe the *PVT* data of polymers well are given here: the Flory–Orwoll–Vrij^[44,52,53] equation,

$$p'/T' = \rho/(1 - \rho^{1/3}) - \rho/T', \quad (1.42c)$$

and the Sanchez–Lacombe^[54] equation,

$$\ln(1 - \rho) = -(p' + \rho^2)/T' - (1 - 1/N)\rho, \quad 1/v' = \rho = 1 - \varphi_0. \quad (1.42d)$$

For more details on the equations of state of polymers, one can refer to the review article by Rodgers.^[53] The effects of pressure on the thermodynamic properties and stability of polymer mixtures have been the subject of extensive investigations in the past. In view of the crucial importance of the pressure at various stages of polymer material processing, further efforts are being pursued^[55–57] actively to reach a better understanding of its effects on the morphology (densification, chain stretching) and phase behaviour (compatibilization) of polymer mixtures when the pressure is increased.

1.3.6.2 Effects of shear. Likewise, the effects of shear on polymer thermodynamics and structural properties are crucial in fixing the quality and strength of polymer-based materials. This is particularly true for mixtures in the vicinity of the phase boundaries, where shear is found to induce substantial shifts in the critical temperature, leading in some cases to homogenization of the mixture and in other cases to incompatibility enhancement. Hammouda *et al.*^[58,59] reported small angle neutron scattering data on high molecular weight deuterated polystyrene in dioctylphthalate solution at the polymer concentration of 3×10^{-2} g/cm³ over a wide range of shear rates. They observed a drastic increase of the scattered intensity beyond a characteristic shear rate, which is similar to the increase following a sudden temperature drop (this mixture has a UCST). The scattered intensity remains isotropic and Zimm's equation is used to extract the polymer–solvent interaction parameter. This parameter increases dramatically beyond the above characteristic shear rate up to a value at which spinodal decomposition occurs. Recently, Lai and Fuller^[60] reported small angle light scattering data for a 50/50 mixture of polystyrene and polybutadiene in dioctylphthalate under shear flow, also at 3×10^{-2} g/cm³. Their observations were quite different from those of Hammouda *et al.* The scattering patterns that they observed were rotated, stretched elliptically in the direction perpendicular to the flow and became bright. They attributed this elongation-enhancement of the signal to a distortion-increase of the fluctuations in the direction of the flow. Moreover, the quiescent structure factor $S_0(q)$ is found to fit a Gaussian form $\ln S_0(q) \sim q^2$ rather than the usual Ornstein–Zernike form, in which $S_0^{-1}(q) \sim q^2$. Hammouda *et al.*^[58] observed a strong effect of excluded volume interaction, leading to the power law $S_0^{-1}(q) \sim q^{1.67}$.

On the other hand, Reed^[29] performed light scattering measurements on extremely dilute ($C \cong 10^{-5}$ g/cm³) proteoglycan polyelectrolytes ($M \cong 2 \times 10^6$) in pure water under high steady shear (ranging from 12 s^{-1} in the scattering flow cell to over 2500 s^{-1} in other parts of the flow) in a size exclusion chromatography (SEC) set-up. He found that the usual scattering peak which is characteristic of polyelectrolytes under quiescent conditions, and obtained earlier for the same type of proteoglycan,^[61] was not significantly modified by the presence of shear. He concluded that this peak was not due to ordering in the polyelectrolyte solution but rather to liquid-like correlations.

Shear effects on viscosity, for example, are a strong function of polymer concentration. The SEC experiments of Reed were performed at concentrations

over a factor of 1000 times lower than those for the SANS measurements on polystyrene so that qualitatively different behaviour is not surprising. Nevertheless, these contrasting observations on scattering patterns in the presence of shear call for more efforts to elucidate further their origin and understand better their influence on the phase behaviour and morphology of polymer mixtures.

1.4 Time-dependent static scattering and critical fluctuations

When a polymer is degraded into fragments by some agent, the light scattering changes as the degradation proceeds. For example, if a small polymer is cut into two equal fragments, the total light scattering will drop by one half. The general problem is to determine a quantitative relationship between the time dependence of the static scattering and the kinetic and mechanistic parameters of the degradation. The problem, while theoretically straightforward, does not seem to have attracted much attention. The time-dependent forms of the static light scattering, or their ‘signatures’ are remarkably distinct for different mechanisms and polymer types, and yield much quantitative and qualitative information.

1.4.1 Random degradation of a coil

The light scattering intensity for monodisperse ideal coils undergoing random degradation was first solved by Reed and Reed.^[62] The remarkable result was found that the Debye function (eqn (1.17)) is preserved as degradation proceeds, and its initial argument $u_0 = q^2 R_{gi}^2$ is simply translated by r , the average number of random cuts per initial polymer:

$$\Delta I(q, t)/KM_0c = P(q, t) = 2(e^{-u} + u - 1)/u^2, \quad u = q^2 R_{gi}^2 + r(t), \quad (1.43a)$$

where M_0 is the initial mass of the coils. This result can be derived using the Gaussian distribution for $\psi(\mathbf{R}_{ij})$ in eqn (1.8) and multiplying it by $e^{-r(i-j)/N}$, which is the probability that after r average cuts per original polymer, the segment from i to j is still intact. The distribution of fragments, M , is given by:

$$f(r, x) = e^{-r}\delta(x - 1) + e^{-rx}(r^2 - rx + 2r), \quad x = M/M_0. \quad (1.43b)$$

Using the approximation that all fragments scatter as random coils and integrating eqn (1.43b) as $\int x f(r, x) dx$ yields the same result as in eqn (1.43a). The mass averages of the population evolve as follows:

$$\text{the number average, } M_n(t) = M_0/(1 + r), \quad (1.43c)$$

$$\text{the weight average, } M_w(t) = 2M_0(e^{-r} + r - 1)r^{-2}, \quad (1.43d)$$

$$\text{the z-average, } M_z(t) = 3M_0[2(e^{-r} - 1)/r + e^{-r} + 1][r(e^{-r}/r + 1 - 1/r)]^{-1}. \quad (1.43e)$$

For most types of random degradation the average number of cuts per original polymer per second r' will be approximately constant, and r will be proportional to time as long as the average number of cuts per polymer r is much smaller than the number of scissile bonds per polymer, i.e. if $r \ll N$, then $r = r't$. This should hold at least for the early stages of the degradation reaction.

In subsequent work, the effects of non-ideality and polydispersity on the scattering function were considered.^[63] This yielded, for an initial concentration distribution $c_0(m)$:

$$Kc/\Delta I(q, t) = \left[\int_0^\infty mc_0(m)P(u(m, t)) dm \right]^{-1} + 2A_2c, \quad (1.44a)$$

where $u(m, t) = q^2 R_{gi}^2(m) + r(m)$. For polydisperse ideal coils if $u > 3$, or if sufficient random cuts are made so that $u > 3$, the following simplifying result was obtained:

$$Kc/\Delta I(q, t) = 1/2M_{n,0} + \gamma q^2/2 + \beta't/2 + 2A_2c, \quad \gamma = R_g^2/M. \quad (1.44b)$$

This yields a *Polydispersity-independent* rate constant in terms of the average number of random cuts per original dalton of polymer:

$$\beta' = 2Kc \partial[1/\Delta I(q, t)]/\partial t. \quad (1.44c)$$

These results have been applied to the acid, base and enzymatic depolymerization of hyaluronidase.^[62-65] In addition to giving the depolymerization rate constant in each case, the asymptotic linearity of $Kc/\Delta I(q, t)$ indicated that the degradation mechanism in each case resembled random degradation of a single-stranded random coil; this latter observation weighs heavily against conjectures that hyaluronate may be double-stranded in solution. Furthermore, it was also possible to deduce from the $Kc/\Delta I(q, t)$ curves that NaOH hydrolysis rates follow a titration curve, thus pointing to an intramolecular base hydrolysis mechanism (the rate-constant titration curve was superposed by contracting radii of gyration and diminishing A_2 versus the NaOH content). Activation energies were also found for NaOH hydrolysis. The complete Michaelis–Menten–Henri parameters were rapidly and accurately determined for hyaluronidase.^[63] Concentration-dependent enzyme deactivation was also demonstrated, as well as the fact that the hyaluronidase used was an endocydase, as opposed to an exocydase.

1.4.2 Random degradation of a multistranded polymer

If random cuts are made on a polymer coil containing N_s strands bound together, then the scattered intensity does not begin to fall immediately. It is necessary for all the separate bound strands to have cuts within one ‘association length’ of each other before the molecule produces two fragments. Elementary reasoning shows that if the average number of cuts per molecule per second is constant then the probability of random cuts coinciding within an association

length grows as t^{N_s} , and the time-dependent scattering will approach the form:

$$I(t) = a + bt^{N_s}. \quad (1.45)$$

Thus monitoring the time-dependent light scattering of a polymer undergoing random degradation can determine whether the molecule is single-, double- or triple-stranded, etc. A demonstration of (1.45) was given for enzymatic degradation of DNA.^[66] It is also possible to combine expressions such as that above, to determine if a given polymer contains a fraction of variably stranded associations, e.g. a mixture of single and double coils.

1.4.3 Degradation of a simply branched polymer (comb)

Referring to Fig. 1.5, there are three ways in which to degrade a simply branched polymer: (i) sidechains may be stripped off in a first order process whereby $dM/dt = -\alpha t$; (ii) sidechains may be randomly degraded off; (iii) the backbone may be randomly degraded. In this case there may also be simultaneous sidechain degradation according to (i) and (ii).

General expressions for cases (i) and (ii) were given in Ghosh and Reed.^[67] For the case in which the sidechains are individually much less massive than the backbone and the fraction of mass in sidechain and backbone is of the same order of magnitude, the following simplifications were obtained: For the sidechain stripping (i):

$$Kc/\Delta I(q, t) = (1 + q^2 R_g^2(t)/3)/[M_{0,t}(f_p + (1 - f_p)e^{-\alpha t})^2]. \quad (1.46a)$$

Here f_p is the fraction of the total initial branched polymer mass in the backbone and $M_{0,t}$ is the initial polymer mass. When the sidechain contour

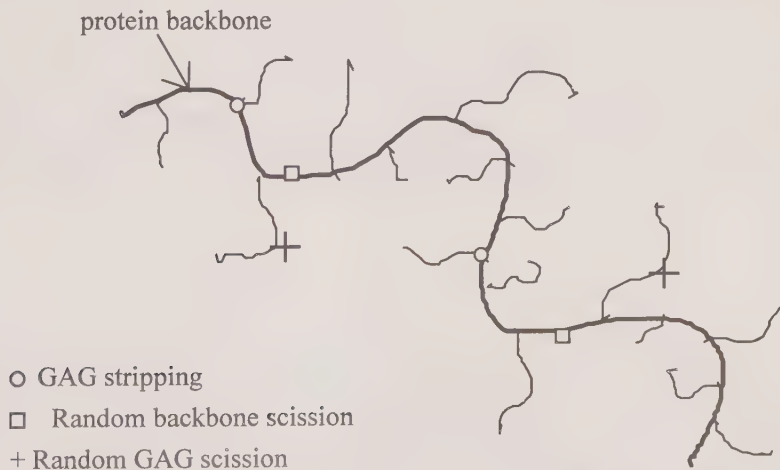


FIG. 1.5. A simply branched polymer, modelled after a proteoglycan subunit, showing the different ways it can be degraded.

length is much smaller than the backbone length, then R_g remains essentially constant in time so that α and f_p become the only fitting parameters. These conditions of short chains and massive backbone apply, for example, to proteoglycan (Aggrecan) subunits, for which mechanisms (i) and (iii) were experimentally identified. For the case in which the sidechains are randomly degraded off (ii), with M_p the backbone mass and $M_{s,0}$ the initial sidechain mass,

$$Kc/\Delta I(q, t) = (1 + q^2 R_g^2(t)/3) M_{0,t} [M_p + M_{s,0}(1 + r e^{-rt})(1 + r)^{-1}]^{-2}. \quad (1.46b)$$

For random backbone degradation (iii), where the sidechains remain intact, the result should resemble eqn (1.46a) above. If there is simultaneous sidechain stripping then, for $q^2 R_{gi}^2 + s(t) > 3$,

$$Kc/\Delta I(q, t) = \frac{1}{2}[s't + q^2 R_g^2(t)] M_{0,t} [M_p + M_{s,0} e^{-\alpha t}]^{-2}, \quad (1.46c)$$

where s' is the average number of random cuts per second per original backbone. If there is simultaneous random backbone and sidechain degradation then, for $q^2 R_{gi}^2 + r'(t) > 3$,

$$Kc/\Delta I(q, t) = \frac{1}{2}[s't + q^2 R_g^2(t)] M_{0,t} [M_p + M_{s,0}(1 + r't e^{-r't})/(1 + r't)]^{-2}. \quad (1.46d)$$

The degradation mechanisms expressed by eqns (1.46a–d) trace quite distinctive signatures in time, and hence are potentially valuable for identifying mechanisms as well as finding degradation rate constants and the fraction of material in sidechains and backbone. Figure 1.6 shows $P^{-1}(q, r)$ vs. r (i.e. vs. t) when eqn (1.46a) holds at fixed q for random coil scission (dotted line) from eqn (1.46b), sidechain stripping (dashed line) eqn (1.46b), random sidechain degradation (second line from top) eqn (1.44c) and random backbone degradation with sidechain stripping (top line) eqn (1.46d). The parameters are typical of proteoglycan subunits. The initial upwards turns on the branched polymer degradation signatures for these parameters contrast with the linearity of the asymptotic behaviour of eqn (1.46a). Ghosh and Reed established the conditions under which such characteristic upturns are experimentally observed.

1.4.4 Critical fluctuations

Light scattering is one of the most appropriate techniques to investigate the critical fluctuations in polymer mixtures because of the large size of polymers and the long range of fluctuations reached in the vicinity of the critical point. Several studies have been reported on different polymer mixtures, with or without solvent, using light scattering.^[68–73] Most of them were concerned with the critical slowing down of the dynamics of such mixtures and only a few included a description of the static scattering properties with the temperature.

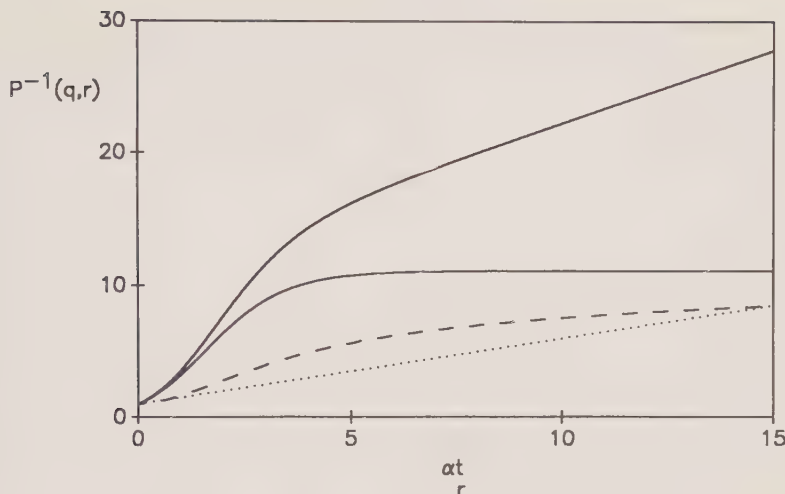


FIG. 1.6. Typical time-dependent light scattering signatures (at a fixed q), expressed as $1/P(q, r)$, for different types of degradation of polymers. From bottom to top: random degradation of a random coil (eqn (1.46a)), at high initial u_0 vs. r ; random degradation of the sidechain branches vs. r (Fig. 1.5), eqn (1.46b), where the backbone stays intact; stripping of the sidechains vs. t (Fig. 1.5), eqn (1.46a), where the backbone stays intact; simultaneous sidechain stripping and random backbone degradation vs. αt , eqn (1.46c), where $s'\alpha = 0.2$.

Here we limit ourselves to the discussion of $S(q, T)$ when T approaches the critical temperature T_c .

1.4.4.1 Polymer blends. Meier *et al.*^[73] reported static and dynamic light scattering data obtained on symmetric mixtures of poly(dimethylsiloxane) (PDMS) and poly(ethylmethylsiloxane) (PEMS). This mixture exhibits a UCST, and hence it undergoes phase separation upon cooling below T_c . The data were analysed using a mean field description supplemented with the *ad hoc* assumption that the critical exponents can have values different from the mean field predictions. They assumed that $S(q)$ is given by the Lorentzian form:

$$S^{-1}(q) = S^{-1}(q = 0)[1 + q^2 \xi_s^2], \quad (1.47a)$$

where

$$S^{-1}(q = 0) = 2(\chi_c - \chi) \quad (1.47b)$$

and

$$2\chi_c = 1/\phi_a N_a + 1/\phi_b N_b. \quad (1.47c)$$

The correlation length ξ_s is given by:

$$\xi_s^2 = \frac{1}{6} [R_{ga}^2/\phi_a N_a + R_{gb}^2/\phi_b N_b](\chi_c - \chi)^{-1}. \quad (1.47d)$$

Using the relationship between χ and T ,

$$\chi = A/T + B \quad \text{and} \quad \chi_c = A/T_c + B,$$

where A and B are constants independent of the temperature, and introducing the relative temperature shift ε :

$$\varepsilon = |T - T_c|/T,$$

one has

$$S^{-1}(q) = S_0^{-1}(q=0)\varepsilon^\gamma \quad (\gamma = 1), \quad (1.48a)$$

$$S_0^{-1}(q=0) = 2A/T_c$$

and

$$\xi_s = \xi_{s0}\varepsilon^{-\nu} \quad (\nu = 1/2), \quad (1.48b)$$

$$\xi_{s0}^2 = \frac{T_c}{6A} (R_{ga}^2/\phi_a N_a + R_{gb}^2/\phi_b N_b).$$

In the mean field limit the critical exponents are $\gamma = 1$ and $\nu = 1/2$. Relaxing this constraint, one allows the exponents γ and ν to take other values, which are obtained by fitting the experimental data to the above equations. This method has been used by Meier *et al.* to analyse their light scattering data on PDMS/PEMS over a wide range of temperatures in the vicinity of T_c . They observed that the system shows mean field behaviour above T_c but, when this temperature is approached, the exponents γ and ν show a significant deviation from the mean field values. The variation of $S^{-1}(q=0)$ as a function of T^{-1} , is linear above T_c but, when T_c is approached, a strong deviation from linearity is observed, leading the authors to introduce two different critical temperatures: the so-called ‘mean field critical temperature’, T_{MC} , which is obtained from the extrapolation of the linear part of $S^{-1}(q=0)$ vs. T^{-1} ; and the so-called Ising critical temperature, T_{IC} , which is obtained from the experimental limit when $S^{-1}(q=0) = 0$. The critical exponent γ can be determined by plotting $S^{-1}(q=0)$ as a function of $\varepsilon = |T - T_c|/T$, but the result is quite sensitive to the choice of T_c . Choosing the mean field critical temperature T_{MC} leads to the observation of a mean field behaviour in the high temperature range and a strong deviation from this behaviour as the temperature is lowered near T_c . If one defines ε in terms of the Ising critical temperature T_{IC} , one observes the Ising exponent everywhere, as observed by Meier *et al.*^[73] Likewise, the q dependence of the scattered intensity shows that $S^{-1}(q)$ varies linearly with q^2 following the Ornstein-Zernike equation. This gives the correlation length ξ_s and its scaling behaviour with ε . The results indicate that the scaling behaviour of the correlation length ξ_s with ε follows a behaviour similar to that of the forward scattering intensity and leads to the same observations.

1.4.4.2 Ternary polymer solutions.

In the presence of a low molecular weight solvent the scattering properties involve more parameters which have important

effects on the fluctuations near the critical temperature. First, one has two different contrast factors which characterize the contributions of both polymers to the scattered signal. One can tune the contrast factors in order to have access to one part or the other of the signal or to a suitable combination of different contributions. Moreover, there are three different interaction parameters: two of them characterize the polymer–solvent interactions and the third one describes the polymer–polymer incompatibility. Therefore, one needs to choose carefully the appropriate solvent for the two polymers in order to achieve favourable conditions for the observation of the critical fluctuations related to the incompatibility of the two polymers when approaching their critical temperature T_c . Some of these aspects have been discussed previously, and we only briefly comment on certain aspects here. First, we note that the scattered intensity for a ternary mixture can always be written as a linear combination of the structure factors for the concentration fluctuations $S_{cc}(q)$, the composition fluctuations $S_{xx}(q)$ and the coupling fluctuations $S_{xc}(q) = S_{cx}(q)$:

$$\Delta I(q) = [a\phi_a + b\phi_b]^2 S_{cc}(q) + (a - b)^2 S_{xx}(q) + 2(a\phi_a + b\phi_b)(a - b)S_{cx}(q), \quad (1.49a)$$

where $S_{cc}(q)$, $S_{xx}(q)$ and $S_{xc}(q)$ are the following combinations of partial structure factors:

$$S_{cc}(q) = S_{aa}(q) + S_{bb}(q) + 2S_{ab}(q), \quad (1.49b)$$

$$S_{xx}(q) = S_{aa}(q)/\phi_a^2 + S_{bb}(q)/\phi_b^2 - 2S_{ab}(q)/\phi_a\phi_b, \quad (1.49c)$$

$$S_{xc}(q) = S_{cx}(q) = (1 - x)[S_{aa}(q) + S_{ab}(q)] - x[S_{bb}(q) + S_{ab}(q)]. \quad (1.49d)$$

In the case of a symmetrical mixture satisfying the conditions of eqn (1.36), the correlations between concentration and composition fluctuations disappear ($S_{xc}(q) = 0$) and $\Delta I(q)$ becomes

$$\begin{aligned} \Delta I(q) = & [(a + b)/2]^2 \phi NP(q) [1 + v\phi NP(q)]^{-1} \\ & + [(a - b)/2]^2 \phi NP(q) / [1 - \chi\phi NP(q)/2]^{-1}. \end{aligned} \quad (1.50)$$

The first term on the RHS represents the concentration fluctuations, whereas the second describes the composition fluctuations. It is clear that the latter contribution is that which gives rise to the signal detected under the zero average contrast condition, $a + b = 0$:

$$\Delta I(q) = [(a - b)/2]^2 S(q), \quad S(q) = \phi NP(q) [1 - \chi\phi NP(q)/2]^{-1}. \quad (1.51a,b)$$

At this point the problem becomes very similar to the case of an incompressible blend with an apparent contrast factor and an apparent interaction parameter, as defined earlier. Miyashita *et al.*^[74] reported static light scattering data on solutions of PS and PMMA in d₆-benzene. They used several compositions but a constant polymer concentration (8.2 vol%). The two polymers were chosen to have approximately the same molecular weight, $M \approx 3.5 \times 10^5$. The data

show a linear variation of $S^{-1}(q = 0)$ as a function of ε , but when the temperature approaches T_c a slight deviation appears in two of the seven systems studied, corresponding to the composition of PS higher than 1/2. The temperature at which this deviation occurs is identified as the cloud point temperature, T_{Cl} , and $S^{-1}(q = 0) = 0$ gives the spinodal temperature T_s . The correlation length ξ_s was also investigated as a function of ε and its scaling behaviour determined as the temperature approaches T_c . The scaling law obtained for both $S^{-1}(q = 0)$ and ξ_s with respect to $\varepsilon = |T - T_s|/T_s$ reveals the exponents $\gamma = 1.23$ and $v = 0.65$, which are very close to the Ising model predictions of 1.23 and 0.63 respectively. Seils *et al.*^[75, 76] reported a similar investigation by static light scattering using the mixture PS/PMMA/bromobenzene. There are two important differences between this system and the one investigated by Miyashita *et al.* The first difference is that PS/PMMA/d₆-benzene has a LCST, whereas PS/PMMA/bromobenzene has UCST, which implies that the mixture undergoes a phase separation upon cooling. The second difference is related to the $\partial n/\partial c$ of the polymer species. PS and PMMA both have non-zero positive $\partial n/\partial c$ in deuterated benzene, whereas in bromobenzene these $\partial n/\partial c$ fulfil the so-called ‘optical theta condition’. The coupling between concentration and composition fluctuations vanishes and the scattered signal has similar properties to that of a polymer blend, with a modified contrast factor and a renormalized interaction parameter.

The data of Seils *et al.* show a significant difference from those of Miyashita *et al.* First, a correction for the background scattering is necessary to have a consistency data analysis. This background is due to the non-critical constant contribution, which should be subtracted from the total intensity to isolate the critical part and characterize its scaling behaviour. The necessity of subtracting this background contribution was also motivated by the observation of the dynamic light scattering correlation functions. These observations reveal a non-critical mode which appears in the vicinity of T_c with a constant amplitude equal to the static background. Their data show a transition from a mean field behaviour at high temperature to an Ising behaviour when T_c is approached. In the mean field region the exponent γ is found to be equal to 1.05, whereas in the critical region it is equal to 1.19, which is slightly lower than 1.24, the exponent of the Ising model. The second observation which indicates a difference compared to the results reported by Miyashita *et al.* has to do with the q dependence of the scattered intensity. Seils *et al.* observed that the variation of $S(q)$ with q^2 shows a deviation from the simple Ornstein-Zernike equation below 7 °C. Using the small q range to extract ξ_s in the vicinity of T_c gives an exponent of $v = 0.57$, which lies between the mean field value of 0.5 and the Ising value of 0.64.

1.5 Summary

In this chapter we have reviewed some theoretical developments of static light scattering of polymers in solution and in bulk. Attempts have been made to

cover many examples, emphasizing the way in which the formulae could be useful for experimentalists. A large section has been devoted to the application of the general formula proposed by Benoît to explain the scattering properties of multicomponent polymer mixtures. Several cases involving ternary mixtures of polymers and solvent have been considered in order to illustrate the use of this equation. In particular, we have considered the variation of the scattered signal as a function of q in various limits, which are characterized by special values of the quantity $\partial n/\partial c$. It has been shown how the scattered intensity changes in terms of relevant parameters such as the polymer concentration and composition, the temperature, the architecture of the chain and, most importantly perhaps, in terms of the interaction parameters between all the species present in the mixture. We have given examples of how Benoît's equation can be useful in treating effects of external forces such as pressure and shear on the scattering properties and phase behaviour of polymer mixtures. It must be emphasized that Benoît's equation is based on the RPA, and as such it provides a mean field description of the scattering properties. Therefore its validity is limited to regimes of weak fluctuations. In conditions in which the fluctuations become large, mean field descriptions break down and one should consider other more sophisticated methods, such as those based on renormalization group theory, which is well documented.^[77]

While many aspects of polyelectrolyte behaviour remain unresolved, their dimensions, interactions and associated scattering properties at moderate ionic strength are reasonably well understood.

Finally, time-dependent static light scattering is emerging as a powerful tool in the analysis of polymer depolymerization kinetics and mechanisms, and polymer solution structures.

Acknowledgements

M. Benmouna thanks Professor H. Benoît (Strasbourg) for his constant support and encouragement. He thanks Dr B. Hammouda (NIST, Gaithersburg) for enlightening discussions on the effects of pressure and shear. This research has been accomplished during a stay of M. Benmouna at the Physics Department of Tulane University, as a Fulbright scholar. He thanks the CIES (Washington) for making this stay possible. W. F. Reed acknowledges NSF support of his efforts on light scattering and polymers.

References

1. Lord Rayleigh (1881). *Phil. Mag.*, **XII**, 81.
2. Kerker, M. (1969). *The scattering of light and electromagnetic radiation*. Academic Press, New York.
3. Debye, P. (1954). *Collected papers*. Interscience Publishing, New York, see also *J. Appl. Phys.*, **15**, 338.
4. Zimm, B. H. (1948). *J. Chem. Phys.*, **16**, 1093.
5. Stockmayer, W. H. (1950). *J. Chem. Phys.*, **18**, 58.

6. Benoît, H. and Benmouna, M. (1984). *Polymer*, **25**, 1059.
7. Higgins, J. S. and Benoît, H. (1994). *Polymers and neutron scattering*. Clarendon Press, Oxford.
8. de Gennes, P. G. (1979). *Scaling concepts in polymer physics*. Cornell University Press, Ithaca, New York.
9. Ould-Kaddour, L. and Strazielle, C. (1987). *Polymer*, **28**, 459.
10. Strazielle, C., Duval, M. and Benmouna, M. (1994). *Macromolecules*, **27**, 4960.
11. Benmouna, M., Duval, M., Strazielle, C., Hakem, I. F. and Fischer, E. W. (1995). *Makromol. Chem. theory and simul.*, **4**, 53.
12. Cummins, H. Z. (1983). *Light scattering near phase transitions* (ed. H. Z. Cummins and A. P. Levanyuk). North-Holland, New York.
13. Katchalsky, A., Alexandrowicz, Z. and Kedem, O. (1976). *Chemical physics of ionic solutions* (ed. B. E. Conway and R. G. Barradas). John Wiley, New York.
14. Morfin, I., Reed, W., Rinaudo, M. and Borsali, R. (1994). *J. Phys. II (France)*, **4**, 1001.
15. Benmouna, M., Weill, G., Benoît, H. and Akcasu, Z. (1982). *J. Phys. (Paris)*, **43**, 1679.
16. Matsuoaka, H. and Ise, N. (1994). *Adv. Polym. Sci.*, **114**, 189.
17. Yamakawa, H. (1971). *Modern theory of polymer solutions*. Harper & Row, New York.
18. Huglin, M. B. (1972). *Light scattering from polymer solutions*. Academic Press, New York.
19. Chu, B. (1974). *Laser scattering*. Academic Press, New York.
20. Berne, B. J. and Pecora, R. (1976). *Dynamic light scattering*. Wiley-Interscience, New York.
21. Tompa, H. (1956). *Polymer solutions*. Butterworth, London.
22. Prigogine, I. (1957). *The molecular theory of solutions*. North-Holland, Amsterdam.
23. Cassasa, E. F. (1965). *J. Polym. Sci.: Part A*, **3**, 605.
24. Benmouna, M., Borsali, R. and Benoît, H. (1993). *J. Phys. II (France)*, **3**, 1041.
25. Akcasu, Z. A. and Higgins, J. S. (1977). *J. Polym. Sci., Polym. Phys. Ed.*, **15**, 1745.
26. Benmouna, M., Akcasu, Z. and Daoud, M. (1980). *Macromolecules*, **13**, 1703.
27. Burchard, W. (1983). *Adv. Polym. Sci.*, **48**, 1.
28. Hammouda, B. (1992). *Adv. Polym. Sci.*, **106**, 89.
29. Reed, W. F. (1994). *J. Chem. Phys.*, **100**, 7825.
30. Reed, W. F., Ghosh, S., Medjahdi, G. and Francois, J. (1991). *Macromolecules*, **24**, 6189.
31. Ghosh, S., Li, X., Reed, C. E. and Reed, W. F. (1990). *Biopolymers*, **30**, 1101.
32. Odijk, T. (1977). *J. Polym. Sci., Polym. Phys. Ed.*, **15**, 477.
33. Skolnick, J. and Fixman, M. (1977). *Macromolecules*, **10**, 944.
34. Gupta, S. K. and Forsman, W. C. (1972). *Macromolecules*, **5**, 779.
35. Fixman, M. and Skolnick, J. (1978). *Macromolecules*, **11**, 863.
36. Reed, C. E. and Reed, W. F. (1992). *J. Chem. Phys.*, **97**, 7766.
37. Reed, C. F. and Reed, W. F., *J. Chem. Phys.*, submitted.
38. LeBret, M. (1982). *J. Chem. Phys.*, **76**, 6243.
39. Ghosh, S., Peitzsch, R. M. and Reed, W. F. (1992). *Biopolymers*, **32**, 1105.
40. Peitzsch, R. M., Burt, M. and Reed, W. F. (1992). *Macromolecules*, **25**, 806.
41. Smits, R. G., Knil, M. E. and Mandel, M. (1994). *Macromolecules*, **27**, 5599.
42. Benoît, H., Benmouna, M. and Wu, W. L. (1990). *Macromolecules*, **23**, 1511.
43. Benoit, H., Benmouna, M., Strazielle, C., Lapp, A. and Ould-Kaddour, L. (1991). *J. Appl. Polym. Sci., Appl. Polym. Symp.*, **48**, 315.
44. Flory, P. J. (1956). *Principles of polymer chemistry*. Cornell University Press, Ithaca, New York.
45. Aven, M. R. and Cohen, C. (1990). *Macromolecules*, **23**, 476.

46. Fukuda, T., Nagata, M. and Inagaki, H. (1984). *Macromolecules*, **17**, 548.
47. Hashimoto, T., Sasaki, K. and Kawai, H. (1984). *Macromolecules*, **17**, 2812.
48. Magda, J. J., Fredrickson, G. H., Larson, R. G. and Helfand, E. (1988). *Macromolecules*, **21**, 726.
49. Nakata, M., Kawate, K. and Ishitaka, Y. (1994). *Macromolecules*, **27**, 1825.
50. Bidkar, U. R. and Sanchez, I. (1994). ACS meeting, Washington, DC.
51. Bidkar, U. R. and Sanchez, I. (1995). *Macromolecules*, **28**, 3963.
52. Sandler, S. I. (1994). *Models for thermodynamic and phase equilibria calculations*. Marcel Dekker, New York.
53. Rodgers, P. A. (1993). *J. Appl. Polym. Sci.*, **48**, 1061.
54. Sanchez, I. C. and Lacombe, R. H. (1978). *Macromolecules*, **11**, 1145.
55. Rebello, L. P. and Van Hook, W. A. (1993). *J. Polym. Sci., Polym. Phys. Ed.*, **31**, 895.
56. Janssen, S., Schwahn, D., Mortensen, K. and Spinger, T. (1993). *Macromolecules*, **26**, 5587.
57. Vanhee, S., Koningsveld, R., Berghmans, H. and Solc, K. (1994). *J. Polym. Sci., Polym. Phys. Ed.*, **32**, 2307.
58. Hammouda, B., Nakatani, H. I., Waldow, D. A. and Han, C. C. (1992). *Macromolecules*, **25**, 2903.
59. Horst, R. and Wolf, B. A. (1993). *Macromolecules*, **26**, 5676.
60. Lai, J. and Fuller, G. G. (1994). *J. Polym. Sci., Polym. Phys. Ed.*, **32**, 2461.
61. Li, X. and Reed, W. F. (1991). *J. Chem. Phys.*, **94**, 4568.
62. Reed, C. E. and Reed, W. F. (1989). *J. Chem. Phys.*, **91**, 7193.
63. Reed, W. F., Reed, C. E. and Byers, L. D. (1990) *Biopolymers*, **30**, 1073.
64. Reed, C. E. and Reed, W. F. (1990). *J. Chem. Phys.*, **93**, 9069.
65. Ghosh, S., Kobal, I., Zanette, D. and Reed, W. F. (1993). *Macromolecules*, **26**, 4685.
66. Thomas, C. A. (1956). *J. Am. Chem. Soc.*, **78**, 1861.
67. Ghosh, S. and Reed, W. F. (1995). *Biopolymers*, **5**, 435.
68. Roby, F. and Joanny, J. F. (1992). *Macromolecules*, **25**, 4612.
69. Bates, F. S., Hartney, M. A. and Wignall, G. D. (1986). *Physica*, **136B**, 196; see also Bates, F. S., Rosedale, J. H., Štěpánek, P., Lodge, T. P., Wiltzius, P., Fredrickson, G. H. and Hjelm, R. P. Jr (1990). *Phys. Rev. Lett.*, **65**, 1893.
70. Štěpánek, P., Lodge, T. P., Kedrowski, C. and Bates, F. S. (1991). *J. Chem. Phys.*, **94**, 8289.
71. Štěpánek, P. (1993). In *Dynamic light scattering* (ed. W. Brown). Clarendon Press, Oxford.
72. Hair, D. W., Hobbie, E. K., Douglas, J. and Han, C. C. (1992). *Phys. Rev. Lett.*, **68**, 2476.
73. Meier, G., Momper, B. and Fischer, E. W. (1992). *J. Chem. Phys.*, **97**, 5884.
74. Miyashita, N., Okada, M. and Nose, T. (1994). *Polymer*, **35**, 1038.
75. Benmouna, M., Seils, J., Patkowski, A., Meier, G. and Fischer, E. W. (1993). *Macromolecules*, **26**, 668.
76. Seils, J., Benmouna, M., Patkowski, A. and Fischer, E. W. (1994). *Macromolecules*, **27**, 5043.
77. Freed, K. F. (1987). *Renormalization group theory of macromolecules*. Wiley-Interscience, New York.

Static scattering properties of colloidal suspensions

Rudolf Klein and Bruno D’Aguanno

2.1 Introduction

The microstructure of colloidal suspensions is commonly studied by scattering experiments. A considerable amount of theoretical background is needed to extract information about the microstructure from the measured scattered intensity $I(k)$ and to understand such microstructure in terms of properties of the suspended particles and the solvent. It is the purpose of this chapter to provide this background and to present and discuss results for realistic systems.

The discussion will almost entirely be restricted to suspensions of spherical particles. For such systems the microstructure is mainly described by the pair distribution function $g(r)$, which is closely related to the probability of finding a particle at the distance r from another particle. The short-range structure, which is given by the particular form of $g(r)$, is the result of the interactions among the particles. It is therefore expected that the arrangement of the particles in the vicinity of a given one is rather different when the interactions are short-ranged, such as in polymer-stabilized suspensions, or when they are long-ranged, as in charged-stabilized systems. Therefore, it is necessary to have methods which provide the pair distribution function for the interacting many-body system in terms of given models of the pair interaction potentials $v(r)$.

Such methods are provided by statistical mechanics. Although there are excellent textbooks on this subject (see, for example, Hansen and McDonald,^[1] March and Tosi,^[2] Balescu^[3]), the first section of this chapter is essentially a tutorial showing how the pair distribution is formally obtained in the context of the phase space description of many-body systems. It is also shown how $g(r)$ and $v(r)$ determine thermodynamic properties such as the pressure and the compressibility.

Since size and/or charge polydispersities are often unavoidable features of colloidal suspensions, and since considerable complications arise in the interpretation of the corresponding measured scattering intensity, it is necessary to extend the statistical mechanical description to multi-component systems. In this case there are particles of differing size and/or charge so that the interactions are now characterized by a set of pair potentials $v_{\alpha\beta}(r)$, where $\alpha, \beta = 1, \dots, m$ refer to the m species of the multi-component system.

Correspondingly, there is a set of $m(m + 1)/2$ coupled pair distribution functions $g_{\alpha\beta}(r)$ describing the more complicated microstructure. Multi-component systems exhibit in general new ordering phenomena which are absent in monodisperse samples. Among these is the onset of charge-ordering in charge-stabilized systems and of depletion effects in hard-sphere-like colloids. Section 2.2 therefore provides the definition of $g_{\alpha\beta}(r)$ and explains how these functions describe density fluctuations and thermodynamic properties of multi-component systems. The reader familiar with this statistical mechanical background can omit this section.

In Section 2.3 the theory of light scattering is considered. This provides the major link between the experimentally accessible function $I(k)$ and the statistical mechanical quantities such as $g(r)$ and $g_{\alpha\beta}(r)$. The general integral equation for the scattered electromagnetic field is derived, which is then simplified to the case of single scattering. The Rayleigh Debye–Gans approximation (weak scattering) for a system of particles of different shapes and sizes is discussed, while for the Mie scattering the major results are summarized. The scattered intensity $I(k)$ is calculated for both monodisperse and polydisperse samples, and it is shown how $I(k)$ can be represented in terms of the pair distribution function $g(r)$ for the monodisperse case, and in terms of the set $g_{\alpha\beta}(r)$ for multi-component systems.

The remaining task in understanding the scattered intensity in terms of the properties of the suspended particles is therefore to calculate the pair distribution functions for given interaction potential models. This is done in Section 2.4, which introduces the Ornstein–Zernike integral equation and the so-called closure relations. These latter relations are of approximate character, and some of several existing closure schemes will be discussed.

This procedure to obtain the structure and thermodynamics from microscopic properties was originally developed to determine properties of rather crude models of simple liquids, such as the hard sphere model. More recently, these methods have been used to study systems of increasing complexity; among them there are electrolyte solutions near charged and uncharged walls, molecular fluids, cylindrical and rod-like particles, liquid crystals, micellar solutions and microemulsions and, as will be discussed in this chapter, also suspensions of monodisperse and polydisperse colloidal particles. It is considerably beyond the scope of this chapter to discuss the large variety of closure schemes and the many applications of the integral equation method. Instead, the discussion will be restricted to those schemes which have turned out to be relevant to charged and uncharged spherical colloidal particles in three-dimensional systems. Section 2.5 discusses how to solve the Percus–Yevick (PY) closure, the hypernetted-chain (HNC) approximation and the thermodynamically self-consistent integral equations. Whereas in the first case there are analytical solutions for hard sphere particles, the solutions of the other mentioned schemes are only numerical. Details of the implementation of this numerical scheme are given.

Applications of the integral equation method are presented in Section 2.6,

mostly for uncharged and charged particles, and comparisons with experimental data and computer simulation results are discussed. Some emphasis is placed on the effects of polydispersity. It will be shown that polydispersity can have dramatic effects on the scattered intensity as compared to treating the system as monodisperse. Whereas the scattered intensity of a monodisperse sample of spherical particles factorizes into a one-particle form factor and a structure factor, which is essentially the Fourier transform of the pair distribution function $g(r)$, this factorization is no longer possible in the case of polydisperse systems. Instead, one-particle properties and the functions describing the correlations are intermixed so that a simple interpretation of $I(k)$ as for monodisperse particles breaks down. The purpose of presenting detailed results for multi-component systems is to show under which circumstances the interpretation of scattering data in terms of a monodisperse model of a sample, which has some polydispersity, is misleading.

2.2 Statistical mechanics of classical systems

2.2.1 Reduced distribution functions

2.2.1.1 *Canonical ensemble.* The aim of statistical mechanics is to calculate macroscopic thermodynamic quantities and structural properties from microscopic characteristics of the constituents of the system. The most important of these characteristics is the pair interaction potential. The macroscopic equilibrium system, the state of which is characterized according to thermodynamics by a small number of macrovariables, is replaced by an ensemble of macroscopically identical systems, which differ in their microstates. In the canonical ensemble the systems are at temperature T and consist of N particles in the volume V . Then a microstate is represented as a point in $6N$ -dimensional phase space, a space spanned by the Cartesian components of the positions $\mathbf{r}^N \equiv (\mathbf{r}_1, \dots, \mathbf{r}_N)$ and the momenta $\mathbf{p}^N \equiv (\mathbf{p}_1, \dots, \mathbf{p}_N)$. Different microstates, which are compatible with the few prescribed macroscopic variables, belong to different points in phase space. Since there are very many of such different microstates, one introduces a phase space distribution function

$$f_N(\Gamma) = \frac{1}{h^{3N} N! Q_N(V, T)} \exp[-\beta H(\Gamma)] \quad (2.1)$$

for the canonical ensemble. Here $\Gamma \equiv (\mathbf{r}^N, \mathbf{p}^N)$ denotes the phase space coordinates, $h = 2\pi\hbar$ is Planck's constant, $\beta = (k_B T)^{-1}$, where k_B is Boltzmann's constant, $H(\Gamma) = T(\mathbf{p}^N) + V(\mathbf{r}^N)$ is the Hamiltonian of the system, consisting of the sum of kinetic ($T(\mathbf{p}^N)$) and potential ($V(\mathbf{r}^N)$) energies, and the canonical partition function $Q_N(V, T)$ normalizes $f_N(\Gamma)$ to unity:

$$Q_N(V, T) = \frac{1}{h^{3N} N!} \int d\Gamma \exp[-\beta H(\Gamma)]. \quad (2.2)$$

Macroscopic properties of the system are obtained by an average of the corresponding microscopic quantities, performed with the distribution function $f_N(\Gamma)$. Considering the number density as an example, the microscopic density is

$$\hat{\varrho}(\mathbf{r}) = \sum_{i=1}^N \delta(\mathbf{r} - \mathbf{r}_i), \quad (2.3)$$

which is a function of the phase space variables \mathbf{r}^N , depending parametrically on the position \mathbf{r} in physical space. The macroscopic density is

$$n(\mathbf{r}) = \langle \hat{\varrho}(\mathbf{r}) \rangle_N = \int d\Gamma \hat{\varrho}(\mathbf{r}) f_N(\Gamma), \quad (2.4)$$

which defines the (canonical) ensemble average, denoted by $\langle \dots \rangle_N$.

For the calculation of structural properties the dependence of $f_N(\Gamma)$ on the momenta is of no interest so that the kinetic energy part can be integrated, giving the distribution function in configuration space:

$$f_N(\mathbf{r}^N) = \int d\mathbf{p}^N f_N(\Gamma) = \frac{1}{Z_N(V, T)} \exp[-\beta V(\mathbf{r}^N)], \quad (2.5)$$

where

$$Z_N(V, T) = \int d\mathbf{r}^N \exp[-\beta V(\mathbf{r}^N)] \quad (2.6)$$

is the configurational integral. A similar integration over the momenta in eqn (2.2) gives the canonical partition function as

$$Q_N(V, T) = \frac{Z_N(V, T)}{N! \Lambda^{3N}}, \quad (2.7)$$

where $\Lambda = (h^2/2\pi m k_B T)^{1/2}$ is the thermal de Broglie wavelength.

It is often sufficient to have a reduced amount of information about the system. This leads to the introduction of reduced distribution functions. If one is only interested in the positions of the first n particles regardless of the positions of the other $N - n$ and regardless of all momenta, this information is contained in

$$f_N^{(n)}(\mathbf{r}^n) = \frac{1}{Z_N(V, T)} \int d\mathbf{r}^{(N-n)} \exp[-\beta V(\mathbf{r}^N)], \quad (2.8)$$

where $d\mathbf{r}^{(N-n)} = d\mathbf{r}_{n+1}, \dots, d\mathbf{r}_N$. The correlations between particles arising from the potential $V(\mathbf{r}^N)$ are fully described by these configuration space functions. For totally uncorrelated systems, such as an ideal gas, $f_N^{(n)}(\mathbf{r}^n)$ factorizes as

$$f_N^{(n)}(\mathbf{r}^n) = \prod_{i=1}^n f_N^{(1)}(\mathbf{r}_i) \quad (\text{uncorrelated particles}). \quad (2.9)$$

One is usually only interested in the probability density of finding an unspecified particle at \mathbf{r}_1 , another one at \mathbf{r}_2 , etc. Since one can put one of N

particles at \mathbf{r}_1 , one out of $N - 1$ at \mathbf{r}_2 and one out of $N - n$ at \mathbf{r}_n , one introduces the distribution functions

$$\varrho_N^{(n)}(\mathbf{r}^n) = \frac{N!}{(N-n)!} f_N^{(n)}(\mathbf{r}^n). \quad (2.10)$$

Of particular importance are the single-particle density

$$\varrho_N^{(1)}(\mathbf{r}_1) = N f_N^{(1)}(\mathbf{r}_1) \quad (2.11)$$

and the two-particle (or pair) density

$$\varrho_N^{(2)}(\mathbf{r}_1, \mathbf{r}_2) = \frac{N(N-1)}{Z_N(V, T)} \int d\mathbf{r}^{(N-2)} \exp[-\beta V(\mathbf{r}^N)], \quad (2.12)$$

where eqn (2.8) has been used. Since the functions $f_N^{(n)}(\mathbf{r}^n)$ are normalized to unity, the distributions of unspecified particles are normalized as

$$\int d\mathbf{r}^n \varrho_N^{(n)}(\mathbf{r}^n) = \frac{N!}{(N-n)!}. \quad (2.13)$$

For independent particles, $\varrho_N^{(n)}(\mathbf{r}^n)$ factorizes similarly to eqn (2.9). To describe correlations it is therefore convenient to divide out the uncorrelated parts and to introduce

$$g_N^{(n)}(\mathbf{r}^n) = \frac{\varrho_N^{(n)}(\mathbf{r}^n)}{\prod_{i=1}^n \varrho_N^{(1)}(\mathbf{r}_i)}. \quad (2.14)$$

The most important of these distributions is the one with $n = 2$, which describes pair correlations:

$$g_N^{(2)}(\mathbf{r}_1, \mathbf{r}_2) = \frac{\varrho_N^{(2)}(\mathbf{r}_1, \mathbf{r}_2)}{\varrho_N^{(1)}(\mathbf{r}_1) \varrho_N^{(1)}(\mathbf{r}_2)}. \quad (2.15)$$

In view of the definition of $\varrho_N^{(2)}(\mathbf{r}_1, \mathbf{r}_2)$ in eqn (2.12) it is emphasized that $g_N^{(2)}$ describes the correlations of two particles at \mathbf{r}_1 and \mathbf{r}_2 , respectively, in the presence of the other $N - 2$. Because of translational invariance of homogeneous systems, $\varrho_N^{(1)}(\mathbf{r}_1)$ has to be independent of \mathbf{r}_1 and $\varrho_N^{(2)}(\mathbf{r}_1, \mathbf{r}_2)$ will only depend on $\mathbf{r}_1 - \mathbf{r}_2$. It then follows from eqn (2.13) for $n = 1$ that $\varrho_N^{(1)} = N/V = n$ in homogeneous systems, where n denotes the average number density. If the system is also isotropic, the two-particle densities depend only on $r_{12} = |\mathbf{r}_1 - \mathbf{r}_2|$, so that eqn (2.15) becomes in this case

$$\varrho_N^{(2)}(r_{12}) = n^2 g_N^{(2)}(r_{12}). \quad (2.16)$$

From eqns (2.13) and (2.16) it follows that

$$n \int d\mathbf{r}_{12} g_N^{(2)}(r_{12}) = N - 1 \approx N. \quad (2.17)$$

Therefore, $\langle N(r, dr) \rangle \equiv 4\pi r^2 n g_N^{(2)}(r) dr$ is the average number of particles in a spherical shell of radius r and width dr around a particle at the origin. For non-interacting particles, for which (2.6) gives $Z_N = V^N$, eqn (2.12) shows that $\varrho_N^{(2)}(\mathbf{r}_1, \mathbf{r}_2) = n^2(1 - 1/N)$. Therefore, the pair correlation function $g_N^{(2)}(r_{12})$ goes to $1 - 1/N$ for distances r_{12} large compared to the correlation lengths.

2.2.1.2 Grand canonical ensemble. It is for many purposes more convenient and in some cases necessary to use the grand canonical ensemble, which represents systems of fixed values of volume V , temperature T and chemical potential μ . These are open systems with a variable number N of particles. The phase space distribution function of the grand canonical ensemble is

$$f(N; \Gamma) = \frac{1}{h^{3N} N! \Xi(\mu, V, T)} \exp[-\beta(H(\Gamma) - \mu N)], \quad (2.18)$$

with the normalization

$$\sum_{N=0}^{\infty} \int d\Gamma f(N; \Gamma) = 1. \quad (2.19)$$

From this condition the grand canonical partition function is given by

$$\Xi(\mu, V, T) = \sum_N \frac{e^{\beta\mu N}}{h^{3N} N!} \int d\Gamma e^{-\beta H(\Gamma)} = \sum_N \frac{z^N}{N!} Z_N(V, T), \quad (2.20)$$

where (2.2) and (2.7) have been used and where $z = \exp(\beta\mu)/A^3$.

The phase space distribution $f(N; \Gamma)$ can be expressed in terms of $f_N(\Gamma)$; from (2.1) and (2.18) one finds that

$$f(N; \Gamma) = P(N) f_N(\Gamma), \quad (2.21)$$

where

$$P(N) = \frac{e^{\beta\mu N}}{\Xi(\mu, V, T)} Q_N(V, T). \quad (2.22)$$

The meaning of $P(N)$ follows from the normalization of $f_N(\Gamma)$:

$$P(N) = \int d\Gamma f(N; \Gamma). \quad (2.23)$$

This is the probability that a system taken from the grand canonical ensemble has precisely N particles, irrespective of their positions and momenta. This allows one to express a grand canonical average over a phase-space function $B(\Gamma)$ defined by

$$\langle B \rangle = \sum_N \int d\Gamma \hat{B}(\Gamma) f(N; \Gamma), \quad (2.24)$$

in terms of the canonical one,

$$\langle B \rangle = \sum_N P(N) \int d\Gamma \hat{B} f_N(\Gamma) = \sum_N P(N) \langle B \rangle_N. \quad (2.25)$$

This relation is used to define the reduced distribution functions of the grand canonical ensemble in terms of those of the canonical ensemble, eqn (2.10), as

$$\varrho^{(n)}(\mathbf{r}^n) = \sum_{N=m}^{\infty} P(N) \varrho_N^{(n)}(\mathbf{r}^n). \quad (2.26)$$

Their normalization follows from (2.13):

$$\int d\mathbf{r}^n \varrho^{(n)}(\mathbf{r}^n) = \left\langle \frac{N!}{(N-n)!} \right\rangle. \quad (2.27)$$

By again dividing out the uncorrelated parts, similarly to (2.15), the distributions $g^{(n)}(\mathbf{r}^n)$ can be introduced; in particular,

$$g^{(2)}(\mathbf{r}_1, \mathbf{r}_2) = \frac{\varrho^{(2)}(\mathbf{r}_1, \mathbf{r}_2)}{\varrho^{(1)}(\mathbf{r}_1) \varrho^{(1)}(\mathbf{r}_2)}. \quad (2.28)$$

For homogeneous systems it follows from eqn (2.26) that $\varrho^{(1)} = \langle N \rangle / V = n$ and

$$\varrho^{(2)}(\mathbf{r}_1 - \mathbf{r}_2) = n^2 g^{(2)}(\mathbf{r}_1 - \mathbf{r}_2) \quad (2.29)$$

for this case. For non-interacting particles it is easy to show that $\varrho^{(2)} = n^2$, so that $g^{(2)}$ becomes equal to 1.

2.2.1.3 Thermodynamics. The link of the phase space description to thermodynamics is provided by the expression for the Helmholtz free energy

$$A(N, V, T) = -k_B T \ln Q_N(V, T) \quad (2.30)$$

in the case of the canonical ensemble and by

$$\Omega(\mu, V, T) = -k_B T \ln \Xi(\mu, V, T) \quad (2.31)$$

for the grand canonical ensemble, where $\Omega = -pV$ is the grand canonical potential. From these basic identifications one can obtain all thermodynamic properties in terms of the microscopic characteristics.

Considering the internal energy as an example, one uses the thermodynamic relation $U = (\partial(\beta A)/\partial\beta)_V$ to obtain

$$U = -\frac{\partial}{\partial\beta} \ln Q_N(V, T). \quad (2.32)$$

Writing the partition function (2.7) as

$$Q_N = Q_N^{id} Z_N(V, T) / V^N, \quad (2.33)$$

where $Q_N^{id} = V^N/(N! \Lambda^{3N})$ describes an ideal gas, eqn (2.32) gives

$$U = U^{id} + U^{ex}, \quad (2.34)$$

where $U^{id} = 3k_B T N/2$ is the ideal gas contribution and where, using eqn (2.6),

$$U^{ex} = \frac{1}{Z_N(V, T)} \int d\mathbf{r}^N V(\mathbf{r}^N) \exp[-\beta V(\mathbf{r}^N)] \quad (2.35)$$

is the excess part of the internal energy which arises from the interactions among the particles.

The expression (2.35), which involves the integral over the whole of configuration space, can formally be simplified by using the reduced distribution functions. If it is assumed that the total potential energy can be represented as a sum of pair interactions,

$$V(\mathbf{r}^N) = \frac{1}{2} \sum_{i,j=1}' v(r_{ij}), \quad (2.36)$$

where the prime indicates the omission of the terms with $i = j$, one can choose one pair of particles out of the $N(N - 1)/2$ different pairs and write eqn (2.35) as

$$U^{ex} = \frac{N(N - 1)}{2} \int d\mathbf{r}_1 \int d\mathbf{r}_2 v(r_{12}) \left\{ \frac{1}{Z_N(N, T)} \int d\mathbf{r}^{(N-2)} \exp[-\beta V(\mathbf{r}^N)] \right\}. \quad (2.37)$$

The factor in the curly brackets is proportional to the two-particle density $\varrho_N^{(2)}(\mathbf{r}_1, \mathbf{r}_2)$ of eqn (2.12). Using simplifications which apply to homogeneous and isotropic systems, the excess internal energy per particle becomes

$$U^{ex}/N = 2\pi n \int_0^\infty dr r^2 v(r) g_N^{(2)}(r). \quad (2.38)$$

This is a (seemingly) much simpler expression than eqn (2.35), but the difficulties have been shifted to the determination of the pair distribution function $g_N^{(2)}(r)$.

A similar procedure can be used to express the pressure. One obtains

$$p = p^{id} + p^{ex}, \quad (2.39)$$

where $p^{id} = nk_B T$ is the ideal gas part and where the excess part is essentially the configuration space average of the virial

$$p^{ex} = -\frac{1}{3V} \left\langle \sum_{i=1}^N \mathbf{r}_i \cdot \nabla_i V(\mathbf{r}^N) \right\rangle_N. \quad (2.40)$$

This result can again be rewritten by using the manipulations in going from eqn (2.35) to eqn (2.38). One finds

$$\frac{p^{ex}}{nk_B T} = \frac{p}{nk_B T} - 1 = -\frac{2\pi n}{3k_B T} \int_0^\infty dr r^3 \frac{dv(r)}{dr} g_N^{(2)}(r). \quad (2.41)$$

Another important quantity is the isothermal compressibility. It is related to density fluctuations which, at constant volume, are essentially particle number fluctuations, characterized by the mean square deviations from the average $\langle N \rangle$,

$$\sigma_N^2 = \frac{\langle N^2 \rangle - \langle N \rangle^2}{\langle N \rangle}. \quad (2.42)$$

In this case one has to use the grand canonical ensemble, since the systems of the canonical ensemble all have precisely N particles. To determine σ_N^2 one can use eqn (2.25). Since in the canonical ensemble $\langle N^\alpha \rangle_N = N^\alpha$, with $\alpha = 1, 2$, one has

$$\langle N^2 \rangle = \sum_N N^2 P(N). \quad (2.43)$$

Using eqn (2.22) for $P(N)$, eqn (2.43) becomes

$$\langle N^2 \rangle = \frac{1}{\beta \Xi} \frac{\partial}{\partial \mu} (\Xi \langle N \rangle) = k_B T \frac{\partial \langle N \rangle}{\partial \mu} + \langle N \rangle^2, \quad (2.44)$$

so that

$$\sigma_N^2 = \frac{k_B T}{\langle N \rangle} \left(\frac{\partial \langle N \rangle}{\partial \mu} \right)_{V,T}. \quad (2.45)$$

With the thermodynamic relation

$$N \left(\frac{\partial \mu}{\partial N} \right)_{V,T} = \left(\frac{\partial p}{\partial n} \right)_{N,T} = \frac{1}{n \chi_T} \quad (2.46)$$

where χ_T is the isothermal compressibility, one obtains

$$\sigma_N^2 = n k_B T \chi_T. \quad (2.47)$$

Here $\langle N \rangle$ has been identified with the thermodynamic quantity N . This is justified because eqn (2.45) shows that σ_N^2 is an intensive quantity, so that the relative number fluctuations $\sigma_N^2 / \langle N \rangle$ vanish in the thermodynamic limit $\langle N \rangle \rightarrow \infty$, $V \rightarrow \infty$ such that $\langle N \rangle / V = n$ is fixed. As a result the ensembles become equivalent in the thermodynamic limit.

The quantity σ_N^2 and therefore χ_T can easily be related to the grand canonical reduced distribution functions. From the normalization conditions (2.27) for $n = 1$ and $n = 2$ and the definition (2.28) of $g^{(2)}$, one finds that

$$\int d\mathbf{r}_1 \int d\mathbf{r}_2 \varrho^{(1)}(\mathbf{r}_1) \varrho^{(1)}(\mathbf{r}_2) \{ g^{(2)}(\mathbf{r}_1, \mathbf{r}_2) - 1 \} = \langle N^2 \rangle - \langle N \rangle - \langle N \rangle^2. \quad (2.48)$$

Specializing to homogeneous and isotropic systems and using eqn (2.47), the

compressibility is expressed as

$$nk_B T \chi_T = 1 + n \int d\mathbf{r} (g^{(2)}(\mathbf{r}) - 1). \quad (2.49)$$

Note that the result given in eqn (2.49) is more general than the results (2.38) and (2.41), since it does not rely on the assumption (2.36). The energy equation (2.38), the pressure (or virial) equation (2.41) and the compressibility equation (2.49) express the thermodynamic properties in terms of integrals of the pair distribution functions.

2.2.2 Microstructure

It will now be shown that the pair distribution functions can also be used to express the correlations of the local density at two different points \mathbf{r} and \mathbf{r}' . The canonical average of the microscopic density, eqn (2.3), follows from eqns (2.4), (2.5), (2.8) and the statistical equivalence, as

$$\langle \hat{\varrho}(\mathbf{r}) \rangle_N = \int d\Gamma N \delta(\mathbf{r} - \mathbf{r}_1) f_N(\Gamma) = N f_N^{(1)}(\mathbf{r}) = \varrho_N^{(1)}(\mathbf{r}), \quad (2.50)$$

where eqn (2.10) has been used in the last step. The same (obvious) result applies to the grand canonical ensemble without the index N because of eqns (2.25) and (2.26). The Fourier components of the microscopic density are

$$\hat{\varrho}(\mathbf{k}) = \int d\mathbf{r} e^{i\mathbf{k} \cdot \mathbf{r}} \hat{\varrho}(\mathbf{r}) = \sum_{i=1}^N e^{i\mathbf{k} \cdot \mathbf{r}_i} \quad (2.51)$$

and their canonical averages are

$$\langle \hat{\varrho}(\mathbf{k}) \rangle_N = \int d\mathbf{r} e^{i\mathbf{k} \cdot \mathbf{r}} \varrho_N^{(1)}(\mathbf{r}). \quad (2.52)$$

For homogeneous systems, for which $\varrho_N^{(1)}(\mathbf{r}) = n$,

$$\langle \hat{\varrho}(\mathbf{k}) \rangle = (2\pi)^3 n \delta(\mathbf{k}). \quad (2.53)$$

It is convenient to work with the deviations $\delta\hat{\varrho}(\mathbf{k})$ from the homogeneous case:

$$\delta\hat{\varrho}(\mathbf{k}) = \sum_i e^{i\mathbf{k} \cdot \mathbf{r}_i} - (2\pi)^3 n \delta(\mathbf{k}) = \delta\hat{\varrho}^*(-\mathbf{k}). \quad (2.54)$$

In order to investigate correlations of the densities at two points \mathbf{r} and \mathbf{r}' , one considers the function

$$\langle \hat{\varrho}(\mathbf{r}) \hat{\varrho}(\mathbf{r}') \rangle_N = \left\langle \sum_{i,j} \delta(\mathbf{r} - \mathbf{r}_i) \delta(\mathbf{r}' - \mathbf{r}_j) \right\rangle_N. \quad (2.55)$$

The diagonal part ($i = j$) gives $\varrho_N^{(1)}(\mathbf{r})\delta(\mathbf{r} - \mathbf{r}')$ and the non-diagonal contribution is

$$\begin{aligned} \left\langle \sum'_{i,j} \delta(\mathbf{r} - \mathbf{r}_i)\delta(\mathbf{r}' - \mathbf{r}_j) \right\rangle_N &= N(N-1) \langle \delta(\mathbf{r} - \mathbf{r}_1)\delta(\mathbf{r}' - \mathbf{r}_2) \rangle_N \\ &= \frac{N(N-1)}{Z_N(V, T)} \int d\mathbf{r}^N \delta(\mathbf{r} - \mathbf{r}_1)\delta(\mathbf{r}' - \mathbf{r}_2) e^{-\beta V(\mathbf{r}^N)} \\ &= \varrho_N^{(2)}(\mathbf{r}, \mathbf{r}'), \end{aligned} \quad (2.56)$$

so that

$$\langle \hat{\varrho}(\mathbf{r})\hat{\varrho}(\mathbf{r}') \rangle_N = \varrho_N^{(1)}(\mathbf{r})\delta(\mathbf{r} - \mathbf{r}') + \varrho_N^{(2)}(\mathbf{r}, \mathbf{r}'). \quad (2.57)$$

The same result applies in the grand canonical ensemble. Because of eqns (2.15) and (2.28), the correlation function defined in eqn (2.55) is closely related to the pair distribution functions $g_N^{(2)}$ and $g^{(2)}$. Furthermore, from the expression (2.56) one obtains easily another representation of $g_N^{(2)}(r)$; setting $\mathbf{r}' = \mathbf{r} + \mathbf{R}$ and integrating over \mathbf{r} gives

$$\int d\mathbf{r} \varrho_N^{(2)}(\mathbf{r}, \mathbf{r} + \mathbf{R}) = \left\langle \sum_{i \neq j} \delta(\mathbf{R} + \mathbf{r}_i - \mathbf{r}_j) \right\rangle_N. \quad (2.58)$$

Since for a homogeneous system one has $\varrho_N^{(2)}(\mathbf{r}, \mathbf{r} + \mathbf{R}) = n^2 g(R)$, independent of \mathbf{r} , it follows that

$$ng(R) = \frac{1}{N} \left\langle \sum_{i \neq j} \delta(\mathbf{R} + \mathbf{r}_i - \mathbf{r}_j) \right\rangle_N. \quad (2.59)$$

In Fourier space one considers the quantity which is known as the static structure factor,

$$S(k) = \frac{1}{N} \langle |\delta\hat{\varrho}(\mathbf{k})|^2 \rangle_N.$$

With the Fourier components of the density fluctuations, defined in eqn (2.54),

$$\begin{aligned} S(k) &= \frac{1}{N} \left\langle \sum_{i,j} e^{ik \cdot (r_i - r_j)} \right\rangle_N - \frac{1}{N} \langle \hat{\varrho}(\mathbf{k}) \rangle_N^2 \\ &= 1 + \frac{1}{N} \left\langle \sum_{i,j} e^{ik \cdot (r_i - r_j)} \right\rangle_N - \frac{1}{N} \langle \hat{\varrho}(\mathbf{k}) \rangle_N^2 \\ &= 1 + \frac{1}{N} \int d\mathbf{r} \int d\mathbf{r}' e^{ik \cdot (r - r')} \left\langle \sum'_{i,j} \delta(\mathbf{r} - \mathbf{r}_i)\delta(\mathbf{r}' - \mathbf{r}_j) \right\rangle_N - \frac{1}{N} \langle \hat{\varrho}(\mathbf{k}) \rangle_N^2 \\ &= 1 + \frac{1}{N} \int d\mathbf{r} \int d\mathbf{r}' e^{ik \cdot (r - r')} \{ \varrho_N^{(2)}(\mathbf{r}, \mathbf{r}') - \varrho_N^{(1)}(\mathbf{r})\varrho_N^{(1)}(\mathbf{r}') \}, \end{aligned} \quad (2.60)$$

where eqn (2.56) has been used. For homogeneous and isotropic systems $S(k)$

becomes

$$S(k) = 1 + n \int d\mathbf{r} e^{i\mathbf{k}\cdot\mathbf{r}} (g_N^{(2)}(\mathbf{r}) - 1). \quad (2.61)$$

The static structure factor $S(k)$ is rather directly related to the angular dependent scattered intensity of light, X-rays and neutrons. The above result therefore provides an important link between the microscopic statistical mechanical description, contained in $g_N^{(2)}(\mathbf{r})$, and the experimentally accessible scattering properties.

The limit $k \rightarrow 0$ corresponds to macroscopic thermodynamic properties. Since eqn (2.61) also applies in the grand canonical ensemble, the comparison with eqn (2.49) shows that the value $S(0)$ of the structure factor is closely related to the isothermal compressibility

$$S(0) = nk_B T \chi_T. \quad (2.62)$$

2.2.3 Multi-component systems

2.2.3.1 Distribution functions and thermodynamics. Colloidal suspensions are often polydisperse; they consist of particles with diameters, which have a certain distribution around a mean diameter, and if the particles are charged it can be expected that the charge per particle is related to the particle surface so that particles of different size will carry, in general, different charges. To understand the effects of polydispersity on the thermodynamic and structural properties it is therefore necessary to extend the statistical mechanical concepts to multi-component systems.^[4] Whereas the structure of monodisperse systems arises from density fluctuations, multi-component systems have, in addition, composition fluctuations which give rise to additional effects.

In the canonical ensemble one considers systems having the total number of particles

$$N = \sum_{\alpha=1}^m N_\alpha, \quad (2.63)$$

where N_α , $\alpha = 1, \dots, m$, is the number of particles of component α . The partition function, which replaces eqn (2.2), is

$$Q_N(V, T) = \frac{1}{\prod_{\alpha=1}^m (N_\alpha! h^{3N_\alpha})} \int d\Gamma \exp[-\beta H(\Gamma)], \quad (2.64)$$

where $\mathbf{N} = \{N_1, \dots, N_m\}$ and $d\Gamma = d\mathbf{r}^{N_1} d\mathbf{p}^{N_1} \dots d\mathbf{r}^{N_m} d\mathbf{p}^{N_m}$. The Hamiltonian of the m -component system is

$$H(\Gamma) = \sum_{\alpha=1}^m \sum_{i=1}^{N_\alpha} \frac{\mathbf{p}_{i\alpha}^2}{2m_\alpha} + \sum_{\alpha=1}^m \frac{1}{2} \sum'_{i_\alpha, j_\alpha=1}^{N_\alpha} v_{\alpha\alpha}(\mathbf{r}_{i\alpha}, \mathbf{r}_{j\alpha}) + \sum'_{\alpha, \beta=1}^m \frac{1}{2} \sum_{i_\alpha, i_\beta}^{N_\alpha, N_\beta} v_{\alpha\beta}(\mathbf{r}_{i\alpha}, \mathbf{r}_{i\beta}). \quad (2.65)$$

Here, $\mathbf{p}_{i\alpha}$ and $\mathbf{r}_{i\alpha}$ denote the momentum and the position of the i th particle of

component α , respectively. The total potential energy $V(\mathbf{r}^N)$ has already been written as a sum of pair potentials, where $v_{\alpha\beta}$ is the interaction potential of a particle of component α with a particle of component β . The prime on the double summations indicates that the terms with equal summation indices have to be omitted.

Performing the integrations over the momenta in eqn (2.64) gives

$$Q_N(V, T) = \frac{Z_N(V, T)}{\prod_{\alpha=1}^m (N_\alpha! A_\alpha^{3N_\alpha})}, \quad (2.66)$$

where $A_\alpha = (\hbar^2/2\pi m_\alpha k_B T)^{1/2}$ and

$$Z_N(V, T) = \int d\mathbf{r}^{N_1} \dots d\mathbf{r}^{N_m} \exp[-\beta V(\mathbf{r}^N)] \quad (2.67)$$

is the configurational integral; $d\mathbf{r}^{N_\alpha}$ denotes the integrations over the N_α positions of all particles of component α . For ideal gas mixtures, $Z_N = V^N$. The probability density of finding a system in the configuration

$$\mathbf{r}^N = (\mathbf{r}_{11}, \dots, \mathbf{r}_{N_1 1}, \dots, \mathbf{r}_{1m}, \dots, \mathbf{r}_{N_m m})$$

is, similarly, to eqn (2.5), given by

$$f_N(\mathbf{r}^N) = \frac{1}{Z_N(V, T)} \exp[-\beta V(\mathbf{r}^N)]. \quad (2.68)$$

The reduced distribution functions refer to a configuration with $n_1 \leq N_1$ particles of component 1, \dots , $n_m \leq N_m$ particles of component m , irrespective of the positions of the remaining particles:

$$f_N^{(n)}(\mathbf{r}^n) = \frac{1}{Z_N} \int d\mathbf{r}^{N-n} \exp[-\beta V(\mathbf{r}^N)]; \quad (2.69)$$

here, $\mathbf{r}^n = (\mathbf{r}_{11}, \dots, \mathbf{r}_{n_1 1}, \dots, \mathbf{r}_{1m}, \dots, \mathbf{r}_{n_m m})$, and the integration is over the position of all other particles. The distribution for having any n_1 particles of component 1, any n_2 particles of component 2, etc., is

$$\varrho_N^{(n)}(\mathbf{r}^n) = \prod_{\alpha} \frac{N_\alpha!}{(N_\alpha - n_\alpha)!} f_N^{(n)}(\mathbf{r}^n), \quad (2.70)$$

which generalizes eqn (2.10). Their normalization is

$$\int d\mathbf{r}^n \varrho_N^{(n)}(\mathbf{r}^n) = \prod_{\alpha} \frac{N_\alpha!}{(N_\alpha - n_\alpha)!}. \quad (2.71)$$

The grand canonical partition function is

$$\Xi(\{\mu\}, V, T) = \sum_{N_1=0}^{\infty} \dots \sum_{N_m=0}^{\infty} \lambda_1^{N_1} \dots \lambda_m^{N_m} Q_N(V, T), \quad (2.72)$$

where $\lambda_\alpha = \exp(\beta\mu_\alpha)$ and μ_α denotes the chemical potential of component α in the open system. With eqn (2.66), Ξ can be rewritten as

$$\Xi = \sum_{\mathbf{N}} \prod_{\alpha=1}^m \frac{z_\alpha^{N_\alpha}}{N_\alpha!} Z_{\mathbf{N}}, \quad (2.73)$$

where $z_\alpha = \lambda_\alpha/A_\alpha^3$. The summation on \mathbf{N} indicates the m sums as in eqn (2.72). The probability of finding in the grand canonical ensemble a system with exactly $\mathbf{N} = \{N_1, \dots, N_m\}$ particles, irrespective of their positions and momenta, is

$$P(\mathbf{N}) = \frac{\prod_\alpha \lambda_\alpha^{N_\alpha} Q_{\mathbf{N}}(V, T)}{\Xi(\{\mu\}, V, T)}, \quad (2.74)$$

which corresponds to eqn (2.22). Therefore, the reduced distributions of observing any n_1 particles of component 1, any n_2 particles of component 2, etc., are

$$\varrho^{(\mathbf{n})}(\mathbf{r}^{\mathbf{n}}) = \sum_{\mathbf{N} \geq \mathbf{n}} P(\mathbf{N}) \varrho_{\mathbf{N}}^{(\mathbf{n})}(\mathbf{r}^{\mathbf{n}}), \quad (2.75)$$

with the normalization

$$\int d\mathbf{r}^{\mathbf{n}} \varrho^{(\mathbf{n})}(\mathbf{r}^{\mathbf{n}}) = \sum_{\mathbf{N} \geq \mathbf{n}} P(\mathbf{N}) \prod_\alpha \frac{N_\alpha!}{(N_\alpha - n_\alpha)!} = \left\langle \prod_\alpha \frac{N_\alpha!}{(N_\alpha - n_\alpha)!} \right\rangle. \quad (2.76)$$

Setting $\mathbf{n} = \{0, 0, \dots, 1_\alpha, 0, \dots, 0\}$ one has, for the one-particle density of component α ,

$$\int d\mathbf{r}_\alpha \varrho_\alpha^{(1)}(\mathbf{r}_\alpha) = \langle N_\alpha \rangle, \quad (2.77)$$

which is the mean number of particles of component α in the open system. For homogeneous systems,

$$\varrho_\alpha^{(1)} = \langle N_\alpha \rangle / V = n_\alpha, \quad (2.78)$$

which is the number density of component α .

There are two types of two-particle densities; one can have both particles from the same component or one particle from component α and the other one from component β . In the first case, eqn (2.76) gives

$$\int d\mathbf{r}_{1\alpha} \int d\mathbf{r}_{2\alpha} \varrho_{\alpha\alpha}^{(2)}(\mathbf{r}_{1\alpha}, \mathbf{r}_{2\alpha}) = \langle N_\alpha(N_\alpha - 1) \rangle = \langle N_\alpha^2 \rangle - \langle N_\alpha \rangle \quad (2.79)$$

and in the second case

$$\int d\mathbf{r}_{1\alpha} \int d\mathbf{r}_{1\beta} \varrho_{\alpha\beta}^{(2)}(\mathbf{r}_{1\alpha}, \mathbf{r}_{1\beta}) = \langle N_\alpha N_\beta \rangle. \quad (2.80)$$

Since $\varrho_{\alpha\beta}^{(2)}(\mathbf{r}_{1\alpha}, \mathbf{r}_{1\beta}) = n_\alpha n_\beta$ for uncorrelated particles, one defines the generalization of the distribution functions $g^{(n)}$ to multi-component systems by dividing out

the uncorrelated parts, just as in (2.28). Therefore,

$$\varrho_{\alpha\beta}^{(2)}(\mathbf{r}_{1\alpha}, \mathbf{r}_{1\beta}) = \frac{\varrho_{\alpha\beta}^{(2)}(\mathbf{r}_{1\alpha}, \mathbf{r}_{1\beta})}{\varrho_{\alpha}^{(1)}(\mathbf{r}_{1\alpha})\varrho_{\beta}^{(1)}(\mathbf{r}_{1\beta})} \quad (2.81)$$

For homogeneous and isotropic systems $g^{(2)}$ is written as $g_{\alpha\beta}(r_{\alpha\beta})$, where $r_{\alpha\beta} = |\mathbf{r}_{1\alpha} - \mathbf{r}_{1\beta}|$.

As in the monodisperse case, it is now possible to express thermodynamic properties in terms of the functions $g_{\alpha\beta}$. The generalization of eqn (2.38) for the excess internal energy is

$$U^{ex}/N = 2\pi n \sum_{\alpha, \beta=1}^m x_{\alpha} x_{\beta} \int_0^{\infty} dr r^2 v_{\alpha\beta}(r) g_{\alpha\beta}(r) \quad (2.82)$$

and instead of using eqn (2.41) the pressure is now given by

$$\frac{p^{ex}}{nk_B T} = -\frac{2\pi n}{3k_B T} \sum_{\alpha, \beta=1}^m x_{\alpha} x_{\beta} \int_0^{\infty} dr r^3 g_{\alpha\beta}(r) \frac{dv_{\alpha\beta}(r)}{dr}. \quad (2.83)$$

Here $x_{\alpha} = \langle N_{\alpha} \rangle / \langle N \rangle = n_{\alpha} / n$ denotes the molar fraction of component α .

Whereas these last two results are fairly straightforward extensions of the previous ones, the expression for the compressibility of a multi-component system is quite different from the expressions (2.49) and (2.62) for the monodisperse case. This is due to the composition fluctuations in multi-component systems, which do not exist for monodisperse systems. From eqns (2.77) and (2.79) it follows that

$$\int d\mathbf{r}_{1\alpha} \int d\mathbf{r}_{2\alpha} [\varrho_{\alpha\alpha}^{(2)}(\mathbf{r}_{1\alpha}, \mathbf{r}_{2\alpha}) - \varrho_{\alpha}^{(1)}(\mathbf{r}_{1\alpha})\varrho_{\alpha}^{(1)}(\mathbf{r}_{2\alpha})] = \langle N_{\alpha}^2 \rangle - \langle N_{\alpha} \rangle - \langle N_{\alpha} \rangle^2, \quad (2.84)$$

which reduces to

$$\frac{1}{V} \int d\mathbf{r} [g_{\alpha\alpha}(r) - 1] = \frac{\langle N_{\alpha}^2 \rangle - \langle N_{\alpha} \rangle^2}{\langle N_{\alpha} \rangle^2} - \frac{1}{\langle N_{\alpha} \rangle} \quad (2.85)$$

in the homogeneous case. From eqns (2.77) and (2.80) one obtains, for $\alpha \neq \beta$,

$$\frac{1}{V} \int d\mathbf{r} [g_{\alpha\beta}(r) - 1] = \frac{\langle N_{\alpha} N_{\beta} \rangle - \langle N_{\alpha} \rangle \langle N_{\beta} \rangle}{\langle N_{\alpha} \rangle \langle N_{\beta} \rangle}. \quad (2.86)$$

The last two equations can be combined as

$$\frac{1}{V} \int d\mathbf{r} [g_{\alpha\beta}(r) - 1] = \frac{\langle N_{\alpha} N_{\beta} \rangle - \langle N_{\alpha} \rangle \langle N_{\beta} \rangle}{\langle N_{\alpha} \rangle \langle N_{\beta} \rangle} - \frac{\delta_{\alpha\beta}}{\langle N_{\alpha} \rangle}. \quad (2.87)$$

The first term on the right-hand side can be expressed as the derivative of a mean number of particles with respect to a chemical potential, much like going from eqn (2.42) to eqn (2.45) in the monodisperse case. The average value

of the number of particles of component α is given by

$$\langle N_\alpha \rangle = k_B T \left(\frac{\partial \ln \Xi(\{\mu\}, V, T)}{\partial \mu_\alpha} \right)_{V, T, \mu_\gamma} = \frac{1}{\Xi} \sum_{\mathbf{N}} N_\alpha \lambda_1^{N_1} \dots \lambda_m^{N_m} Q_{\mathbf{N}}(V, T), \quad (2.88)$$

where eqn (2.72) has been used. Multiplying by Ξ and taking the derivative with respect to μ_β gives

$$\frac{1}{\Xi} \frac{\partial \Xi}{\partial \mu_\beta} \langle N_\alpha \rangle + \frac{\partial \langle N_\alpha \rangle}{\partial \mu_\beta} = \frac{1}{k_B T} \frac{1}{\Xi} \sum_{\mathbf{N}} N_\alpha N_\beta \lambda_1^{N_1} \dots \lambda_m^{N_m} Q_{\mathbf{N}}. \quad (2.89)$$

The right-hand side is just $\beta \langle N_\alpha N_\beta \rangle$, so that

$$\langle N_\alpha N_\beta \rangle - \langle N_\alpha \rangle \langle N_\beta \rangle = k_B T \left(\frac{\partial \langle N_\alpha \rangle}{\partial \mu_\beta} \right)_{V, T, \mu_\gamma} = k_B T \left(\frac{\partial \langle N_\beta \rangle}{\partial \mu_\alpha} \right)_{V, T, \mu_\gamma}. \quad (2.90)$$

Therefore, eqn (2.87) can be rewritten as

$$x_\alpha \delta_{\alpha\beta} + n x_\alpha x_\beta \int d\mathbf{r} (g_{\alpha\beta}(r) - 1) = \frac{k_B T}{n} \left(\frac{\partial n_\alpha}{\partial \mu_\beta} \right)_{V, T, \mu_\gamma}. \quad (2.91)$$

To obtain the compressibility from $\chi_T^{-1} = -V(\partial p/\partial V)_T$ one uses the fact that $p = p(T, n_1, \dots, n_m)$ depends on V only through its dependence on $n_\alpha = N_\alpha/V$. Therefore,

$$\chi_T^{-1} = -V \sum_{\alpha=1}^m \frac{\partial p}{\partial n_\alpha} \frac{\partial n_\alpha}{\partial V} = \sum_{\alpha} n_\alpha \left(\frac{\partial p}{\partial n_\alpha} \right)_{V, T, n_\gamma}. \quad (2.92)$$

For the last derivative one uses the Gibbs–Duhem relation

$$dp = \frac{S}{V} dT + \sum_{\beta} n_{\beta} d\mu_{\beta}. \quad (2.93)$$

Since V and T are fixed,

$$\left(\frac{\partial p}{\partial n_\alpha} \right)_{V, T, n_\gamma} = \sum_{\beta} n_{\beta} \left(\frac{\partial \mu_{\beta}}{\partial n_\alpha} \right)_{V, T, n_\gamma}, \quad (2.94)$$

so that

$$\chi_T^{-1} = n^2 \sum_{\alpha, \beta=1}^m x_\alpha x_\beta \left(\frac{\partial \mu_{\beta}}{\partial n_\alpha} \right)_{V, T, n_\gamma}. \quad (2.95)$$

Denoting by $S_{\alpha\beta}(0)$ the symmetrical matrix on the left-hand side of eqn (2.91), one can rewrite χ_T^{-1} as

$$\frac{\beta}{n} \chi_T^{-1} = \sum_{\alpha, \beta} x_\alpha x_\beta (S^{-1}(0))_{\alpha\beta}. \quad (2.96)$$

Since the elements of the inverse matrix can be expressed as $(S^{-1})_{\alpha\beta} = |S|_{\alpha\beta}/|S|$, where $|S|_{\alpha\beta}$ is the cofactor of the $(\alpha\beta)$ element and $|S|$ the determinant of S , one

finally obtains

$$nk_B T \chi_T = \frac{|\mathbf{S}(0)|}{\sum_{\alpha, \beta=1}^m x_\alpha x_\beta |\mathbf{S}(0)|_{\alpha\beta}}. \quad (2.97)$$

This result generalizes the expression (2.62) to multi-component systems.

2.2.3.2 Microstructure. The quantities $S_{\alpha\beta}(0)$ introduced above are the $k = 0$ limits of functions $S_{\alpha\beta}(k)$, known as partial static structure factors. The static structure factor $S(k)$ for a monodisperse system was introduced in eqn (2.60) as the correlation function for the Fourier components of the density fluctuations $\delta\hat{\varrho}(\mathbf{k})$. For multi-component systems one considers the correlations of the fluctuations in the partial densities of the components $\alpha = 1, \dots, m$, which are given by

$$\delta\hat{\varrho}(\mathbf{k}) = \frac{1}{\sqrt{N}} \sum_{i=1}^{N_z} e^{i\mathbf{k}\cdot\mathbf{r}_{i\alpha}} - (2\pi)^3 n_\alpha \delta(\mathbf{k}), \quad (2.98)$$

where $\mathbf{r}_{i\alpha}$ is the position of particle i of component α . Then the $m(m+1)/2$ partial structure factors are defined by

$$S_{\alpha\beta}(k) = \langle \delta\hat{\varrho}_\alpha(\mathbf{k}) \delta\hat{\varrho}_\beta(-\mathbf{k}) \rangle. \quad (2.99)$$

Using eqn (2.98) and following steps analogous to those used in deriving eqn (2.61), one obtains

$$S_{\alpha\beta}(k) = x_\alpha \delta_{\alpha\beta} + n x_\alpha x_\beta \int d\mathbf{r} e^{i\mathbf{k}\cdot\mathbf{r}} (g_{\alpha\beta}(r) - 1). \quad (2.100)$$

Taking $k = 0$ shows that (2.100) is the left-hand side of eqn (2.91), so that the compressibility in eqn (2.97) is expressed in terms of the elements $S_{\alpha\beta}(k = 0)$ of the matrix of partial structure factors. The quantities $S_{\alpha\beta}(k)$ determine the scattered intensity from a multi-component system.

Although the fluctuations of a multi-component system are fully characterized by the quantities $\delta\hat{\varrho}_\alpha(\mathbf{k})$ introduced in eqn (2.98), it is also convenient to consider fluctuations of the total density

$$\delta\hat{\varrho}(\mathbf{r}) = \sum_{\alpha=1}^m \hat{\varrho}_\alpha(\mathbf{r}) - n, \quad (2.101)$$

where $\hat{\varrho}_\alpha(\mathbf{r})$ is the microscopic density of particles of species α and n denotes the total equilibrium density. Correlations of $\delta\hat{\varrho}(\mathbf{r})$ are characterized by

$$S_{NN}(k) = \frac{1}{N} \langle \delta\hat{\varrho}(\mathbf{k}) \delta\hat{\varrho}(-\mathbf{k}) \rangle = \sum_{\alpha, \beta=1}^m S_{\alpha\beta}(k). \quad (2.102)$$

where eqns (2.101) and (2.99) have been used. The quantity $S_{NN}(k)$, known as the number-number structure factor, is a measure of the linear response of the mixture to an external perturbation, which couples to the number density

irrespective of the size or charge of the particles. For charge-stabilized suspensions one considers, in addition, fluctuations of the normalized charge density

$$\delta\hat{\varrho}^c(\mathbf{r}) = \frac{1}{\bar{Q}} \left[\sum_{\alpha=1}^m Q_\alpha \hat{\varrho}_\alpha(\mathbf{r}) - \bar{Q} \hat{\varrho}(\mathbf{r}) \right] \quad (2.103)$$

where $\hat{\varrho}(\mathbf{r}) = \sum_{\alpha=1}^m \hat{\varrho}_\alpha(\mathbf{r})$, Q_α is the charge on the particles of component α and $\bar{Q} = \sum_{\alpha=1}^m x_\alpha Q_\alpha$ is the average charge. The correlations of $\delta\hat{\varrho}^c(\mathbf{r})$ are characterized by^[5]

$$S_{CC}(k) = \frac{1}{N} \langle \delta\hat{\varrho}^c(k) \delta\hat{\varrho}^c(-k) \rangle = \frac{1}{\bar{Q}^2} \sum_{\alpha, \beta=1}^m (Q_\alpha - \bar{Q})(Q_\beta - \bar{Q}) S_{\alpha\beta}(k). \quad (2.104)$$

The charge-charge structure factor $S_{CC}(k)$ measures the response of the mixture to an external perturbation which couples to the particle charges. Since the values of the charges on the different particles essentially determine the interactions and therefore the correlations, the structure of $S_{CC}(k)$ will indicate charge ordering. Cross-correlations of the total particle density $\delta\hat{\varrho}(\mathbf{r})$ and the charge density $\delta\hat{\varrho}^c$ are described by

$$S_{NC}(k) = \frac{1}{N} \langle \delta\hat{\varrho}(\mathbf{k}) \delta\hat{\varrho}^c(-\mathbf{k}) \rangle = \frac{1}{\bar{Q}^2} \sum_{\alpha, \beta=1}^m (Q_\alpha - \bar{Q}) S_{\alpha\beta}(k). \quad (2.105)$$

In addition to the structure factors $S_{NN}(k)$, $S_{CC}(k)$ and $S_{NC}(k)$, known as Bhatia-Thornton structure factors,^[6] it is convenient to introduce a further quantity $S_\chi(k)$, the compressibility structure factor,^[7] which is defined by

$$S_\chi(k) = \frac{|\mathbf{S}(k)|}{\sum_{\alpha, \beta=1}^m x_\alpha x_\beta |\mathbf{S}(k)|_{\alpha\beta}}; \quad (2.106)$$

at $k \rightarrow 0$, the right-hand side coincides with the result given in eqn (2.97) for the isothermal compressibility, so that

$$S_\chi(0) = n k_B T \chi_T. \quad (2.107)$$

The expressions for the various structure factors introduced above for mixtures become rather simple for systems of only two components. In this case the Bhatia-Thornton structure factors are^[8]

$$S_{NN}(k) = S_{11}(k) + 2S_{12}(k) + S_{22}(k), \quad (2.108)$$

$$S_{CC}(k) = \frac{(Q_1 - Q_2)^2}{\bar{Q}^2} [x_2^2 S_{11}(k) - 2x_1 x_2 S_{12}(k) + x_1^2 S_{22}(k)], \quad (2.109)$$

$$S_{NC}(k) = \frac{Q_1 - Q_2}{\bar{Q}} [x_2 S_{11}(k) + (x_2 - x_1) S_{12}(k) - x_1 S_{22}(k)], \quad (2.110)$$

Here, it is evident that the correlations described by $S_{CC}(k)$ and $S_{NC}(k)$ increase with increasing charge asymmetry. The compressibility structure factor can be

expressed as

$$\begin{aligned} S_\chi(k) &= \frac{S_{11}(k)S_{22}(k) - S_{12}^2(k)}{x_1^2S_{22}(k) - 2x_1x_2S_{12}(k) + x_2^2S_{11}(k)} \\ &= \frac{S_{\text{NN}}(k)S_{\text{CC}}(k) - S_{\text{NC}}^2(k)}{S_{\text{CC}}(k)}. \end{aligned} \quad (2.111)$$

The last expression shows that the compressibility cannot be expressed in terms of the number-number structure factor $S_{\text{NN}}(0)$ alone.

2.3 Light scattering

2.3.1 The scattered electromagnetic field

2.3.1.1 General results. Scattering of an electromagnetic wave in a medium arises from variations in the electromagnetic properties. In the case of a colloidal suspension this variation arises from the presence of the colloidal particles, which will have, in general, a dielectric constant (or refractive index) which is different from that of the surrounding solvent. If ϵ_0 denotes the dielectric constant of the solvent, the electric displacement \mathbf{D} is different from $\epsilon_0\mathbf{E}$ inside the suspended particles. To obtain the scattered field one starts from Maxwell's equations in the absence of sources:

$$\nabla \times \mathbf{E} = -\frac{1}{c} \frac{\partial \mathbf{B}}{\partial t}, \quad \nabla \times \mathbf{H} = \frac{1}{c} \frac{\partial \mathbf{D}}{\partial t}, \quad (2.112, 2.113)$$

$$\nabla \cdot \mathbf{B} = 0, \quad \nabla \cdot \mathbf{D} = 0. \quad (2.114, 2.115)$$

The material equations are

$$\mathbf{D} = \epsilon_0\mathbf{E} + 4\pi\mathbf{P} = \boldsymbol{\epsilon}(\mathbf{r}) \cdot \mathbf{E}(\mathbf{r}), \quad (2.116)$$

$$\mathbf{B} = \mu_0\mathbf{H}, \quad (2.117)$$

where \mathbf{P} is the polarization and where magnetic effects are neglected. The dielectric properties of the particles are described by the dielectric tensor $\boldsymbol{\epsilon}(\mathbf{r})$, which depends on the position within the particles. From these equations it is straightforward to obtain a wave equation for \mathbf{D} :

$$\nabla^2 \mathbf{D} - \frac{\epsilon_0 \mu_0}{c^2} \frac{\partial^2 \mathbf{D}}{\partial t^2} = -4\pi \nabla \times \nabla \times \mathbf{P}. \quad (2.118)$$

The right-hand side arises from the presence of the particles and this part disturbs the free propagation of the incoming waves. As can be seen from eqn (2.116), the disturbance depends on \mathbf{D} and therefore, in general, is not known. Assuming a time dependence proportional to $e^{-i\omega t}$ for the unperturbed fields and also for the departures $\mathbf{D} - \epsilon_0\mathbf{E}$, eqn (2.118) becomes

$$(\nabla^2 + k^2)\mathbf{D} = -4\pi \nabla \times \nabla \times \mathbf{P}, \quad (2.119)$$

where $k^2 = \mu_0 \epsilon_0 \omega^2 / c^2$. The wavelength of the light in the solvent is $\lambda = 2\pi/k$.

The solution of eqn (2.119) is of the form

$$\mathbf{D} = \mathbf{D}_i + \mathbf{D}_s, \quad (2.120)$$

where \mathbf{D}_i solves the homogeneous equation, which describes the unperturbed incoming wave. The scattered part, \mathbf{D}_s , is obtained by introducing the Hertz vector $\mathbf{\Pi}$,

$$\mathbf{D}_s = \nabla \times \nabla \times \mathbf{\Pi}, \quad (2.121)$$

which satisfies^[9]

$$(\nabla^2 + k^2)\mathbf{\Pi} = -4\pi\mathbf{P}. \quad (2.122)$$

The solution of this equation is

$$\mathbf{\Pi}(\mathbf{r}) = \int d\mathbf{r}' G(|\mathbf{r} - \mathbf{r}'|)\mathbf{P}(\mathbf{r}'). \quad (2.123)$$

where

$$G(r) = e^{ikr}/r \quad (2.124)$$

is the Green function of the Helmholtz equation for the unbounded space (propagator).

The total electric field is the sum of the incoming and scattered fields:

$$\mathbf{E} = \mathbf{E}_i + \mathbf{E}_s. \quad (2.125)$$

Since one is interested in the scattered field far away from the colloidal particles, where $\mathbf{P} = 0$,

$$\mathbf{E}_s(\mathbf{r}) = \frac{1}{\epsilon_0} \nabla \times \nabla \times \int d\mathbf{r}' \frac{e^{ik|\mathbf{r}-\mathbf{r}'|}}{|\mathbf{r}-\mathbf{r}'|} \mathbf{P}(\mathbf{r}'). \quad (2.126)$$

At a point $\mathbf{r} = \mathbf{R}$ sufficiently outside the scattering volume, which can be considered as the position of the detector, the Green function can be simplified. Since \mathbf{r}' is restricted to positions inside the scattering particles,

$$\begin{aligned} |\mathbf{R} - \mathbf{r}'| &= (R^2 + r'^2 - 2R\mathbf{r}' \cdot \hat{\mathbf{k}}_f)^{1/2} \\ &\simeq R - \mathbf{r}' \cdot \hat{\mathbf{k}}_f. \end{aligned} \quad (2.127)$$

Here $\hat{\mathbf{k}}_f = \mathbf{R}/R$ is the unit vector of the propagation direction towards the detector. With eqn (2.127) the Green function simplifies to

$$\frac{e^{ik|\mathbf{r}-\mathbf{r}'|}}{|\mathbf{r}-\mathbf{r}'|} \simeq \frac{e^{ikR}}{R} e^{-i\mathbf{k}_f \cdot \mathbf{r}'}, \quad (2.128)$$

where $\mathbf{k}_f = k\hat{\mathbf{k}}_f$. Furthermore, in the far field range

$$\nabla \frac{e^{ikR}}{R} \simeq \frac{e^{ikR}}{R} ik\nabla R = \frac{e^{ikR}}{R} i\mathbf{k}_f, \quad (2.129)$$

so that the operator ∇ becomes equivalent to $i\mathbf{k}_f$. Substituting eqns (2.128) and (2.129) in eqn (2.126), one obtains

$$\mathbf{E}_s(\mathbf{R}) = \frac{e^{ikR}}{\epsilon_0 R} \int d\mathbf{r}' \{ -\mathbf{k}_f \times (\mathbf{k}_f \times \mathbf{P}(\mathbf{r}')) \} e^{-i\mathbf{k}_f \cdot \mathbf{r}'} . \quad (2.130)$$

From eqn (2.116) we rewrite the polarization as

$$4\pi\mathbf{P}(\mathbf{r}) = (\epsilon(\mathbf{r}) - \epsilon_0 \mathbf{1}) \cdot \mathbf{E}(\mathbf{r}) = \epsilon_r(\mathbf{r}) \delta\epsilon_r(\mathbf{r}) \cdot \mathbf{E}(\mathbf{r}), \quad (2.131)$$

where $\delta\epsilon_r(\mathbf{r}) = \epsilon_r(\mathbf{r}) - \mathbf{1}$ and $\epsilon_r(\mathbf{r}) = \epsilon(\mathbf{r})/\epsilon_0$ is the dielectric tensor of the suspended particles relative to that of the surrounding solvent. Then the scattered field is given by^[10,11]

$$\mathbf{E}_s(\mathbf{R}) = \frac{e^{ikR}}{R} \frac{k^2}{4\pi} \int d\mathbf{r}' \{ -\hat{\mathbf{k}}_f \times (\hat{\mathbf{k}}_f \times \delta\epsilon_r(\mathbf{r}') \cdot \mathbf{E}(\mathbf{r}')) \} e^{-i\mathbf{k}_f \cdot \mathbf{r}'} . \quad (2.132)$$

The expression represents the scattered field as an outgoing spherical wave e^{ikR}/R , multiplied by a scattering amplitude which depends on the direction of observation $\hat{\mathbf{k}}_f$ and the direction of the field $\mathbf{E}(\mathbf{r}')$. This field is, however, not known without further approximation. Equations (2.125) and (2.132) form an integral equation for the total field $\mathbf{E}(\mathbf{r})$. The field $\mathbf{E}(\mathbf{r}')$ under the integral in (2.132) is the total electric field inside the particles; it consists of the incident field $\mathbf{E}_i(\mathbf{r}')$ and the field coming from other particles and it includes therefore multiple scattering effects.

2.3.1.2 The first Born approximation; Rayleigh–Debye–Gans scattering. The general expression for the scattering amplitude in eqn (2.132) can be used to obtain approximate results. In the spirit of a first iteration of the integral equation for $\mathbf{E}(\mathbf{r})$, one replaces $\mathbf{E}(\mathbf{r}')$ in eqn (2.132) by the incident field

$$\mathbf{E}_i(\mathbf{r}) = E_0 \mathbf{n}_i e^{i\mathbf{k}_i \cdot \mathbf{r}}, \quad (2.133)$$

where E_0 is the magnitude of \mathbf{E}_i , \mathbf{n}_i the polarization direction and \mathbf{k}_i is the wave vector.

This procedure not only restricts the following results to single scattering, but it also assumes that the phase of the wave traversing the scattering particle is the same as it would be if the particle were not present. This assumption is valid when

$$\frac{2\pi\sigma}{\lambda} \left| \frac{n_p}{n_s} - 1 \right| \ll 1,$$

where n_p and n_s are the refractive indices of the particle of diameter σ and the solvent, respectively. The above condition defines the Rayleigh–Debye–Gans approximation; it breaks down for large particles and if the refractive index of the particle is sufficiently larger than that of the solvent.

With these assumptions eqn (2.132) becomes

$$E_s(\mathbf{R}) = E_0 \frac{e^{ikR}}{R} \frac{k^2}{4\pi} \int d\mathbf{r}' \{ -\hat{\mathbf{k}}_f \times (\hat{\mathbf{k}}_f \times \delta\epsilon_r(\mathbf{r}') \cdot \mathbf{n}_i) \} e^{i\mathbf{k}_s \cdot \mathbf{r}'}, \quad (2.134)$$

where $\mathbf{k}_s = \mathbf{k}_i - \mathbf{k}_f$ is the scattering vector. Since we are considering elastic scattering, the magnitude of \mathbf{k}_s is $2k \sin(\vartheta/2)$, where ϑ is the scattering angle.

One is often interested in the component of the scattered field in a direction \mathbf{n}_f ; this is given by

$$E_s(\mathbf{R}) = E_0 \frac{e^{ikR}}{R} \frac{k^2}{4\pi} \int d\mathbf{r}' \delta\epsilon_{if}(\mathbf{r}') e^{i\mathbf{k}_s \cdot \mathbf{r}'}, \quad (2.135)$$

where

$$\delta\epsilon_{if}(\mathbf{r}) = \mathbf{n}_f \cdot \delta\epsilon_r(\mathbf{n}) \cdot \mathbf{n}_i. \quad (2.136)$$

The integral in eqn (2.135) is taken over the volumes of the suspended particles. If there are N particles of m different species such that N_α particles belong to species α ,

$$N = \sum_{\alpha=1}^m N_\alpha \quad (2.137)$$

and if \mathbf{r}_j^α denotes the position of the centre of mass of particle j of species α , eqn (2.135) can be rewritten as

$$E_s(\mathbf{R}) = E_0 \frac{k^2 e^{ikR}}{4\pi R} \sum_{\alpha=1}^m \sum_{j=1}^{N_\alpha} e^{i\mathbf{k}_s \cdot \mathbf{r}_{ja}} \int_{V_j^\alpha} d\mathbf{x} \delta\epsilon_{if}^\alpha(\mathbf{x}) e^{i\mathbf{k}_s \cdot \mathbf{x}}, \quad (2.138)$$

where the integral is over the volume of particle j of type α . This expression can be used to obtain the scattered intensity from a polydisperse suspension of particles of arbitrary shapes and of an arbitrary dependence of $\delta\epsilon_r(\mathbf{r})$ inside the particles; it also allows us to consider polarized and depolarized scattering.

For the simple case of spherical particles, which are homogeneous in their dielectric properties, the integral in eqn (2.138), which is known as the form amplitude, becomes

$$f_\alpha(\mathbf{k}_s) = \delta\epsilon_{if}^\alpha \int_{V_\alpha} d\mathbf{x} e^{i\mathbf{k}_s \cdot \mathbf{x}} = \delta\epsilon_{if}^\alpha V_\alpha \frac{3j_1(k_s \sigma_\alpha / 2)}{k_s \sigma_\alpha / 2} = f_\alpha(k_s) \quad (2.139)$$

where $j_1(x) = (\sin x - x \cos x)/x^2$ is the spherical Bessel function of index 1, σ_α denotes the diameter of a sphere of type α and V_α is its volume. It should be noted that f_α depends in this case only on the magnitude of k_s because of the spherical symmetry of the particles.

The situation is different for non-spherical particles. Considering a thin rod of length L and denoting the direction of the rod by the unit vector \mathbf{u} , one has

$$f_{rod}(\mathbf{k}_s) = \delta\epsilon_{if} \int_{-L/2}^{L/2} ds e^{i\mathbf{k}_s \cdot \mathbf{u}s} = \delta\epsilon_{if} L j_0(\mathbf{k}_s \cdot \mathbf{u}L/2), \quad (2.140)$$

where $j_0(x) = \sin x/x$. There is now a dependence not only on the magnitude of \mathbf{k}_s but also on the angle between \mathbf{k}_s and \mathbf{u} , the direction of the rod. The factor L in eqn (2.140) is the ‘volume’ of the rod.

2.3.1.3 Mie scattering. A proper treatment of the scattering of an incident plane wave from an object with optical constants different from those of the surrounding medium has to take into consideration, besides the incident and the scattered waves, also the wave inside the particle. The three electromagnetic waves have to satisfy the correct electromagnetic boundary conditions at the surface of the particle. The solution of the wave equations for these fields together with the proper boundary conditions is the content of Mie theory. Detailed results for the components of the scattered field are available for spheres.^[11–13] When the incident wave is plane polarized and propagating along the positive z -axis with its electric vector of unit amplitude pointing in the x -direction,

$$\mathbf{E}_i = \hat{\mathbf{x}} e^{ikz}, \quad (2.141)$$

the scattered field components $E_{s,\phi}$ and $E_{s,\theta}$ in polar coordinates can be calculated for a sphere of radius a centred at the origin of the coordinate system. The medium is characterized by the dielectric constant ε_0 and the uniform sphere by $\varepsilon = \varepsilon_r \varepsilon_0 = m^2 \varepsilon_0$. The results are

$$E_{s,\phi} = -\frac{i e^{ikr}}{kr} S_1(\theta) \sin \phi, \quad E_{s,\theta} = \frac{i e^{ikr}}{kr} S_2(\theta) \cos \phi, \quad (2.142, 2.143)$$

where

$$S_1(\theta) = \sum_{n=1}^{\infty} \frac{2n+1}{n(n+1)} \{a_n \pi_n(\cos \theta) + b_n \tau_n(\cos \theta)\}, \quad (2.144)$$

$$S_2(\theta) = \sum_{n=1}^{\infty} \frac{2n+1}{n(n+1)} \{a_n \tau_n(\cos \theta) + b_n \pi_n(\cos \theta)\}. \quad (2.145)$$

The functions π_n and τ_n are given by

$$\pi_n(\cos \theta) = \frac{P_n^{(1)}(\cos \theta)}{\sin \theta}, \quad \tau_n(\cos \theta) = \frac{d}{d\theta} P_n^{(1)}(\cos \theta), \quad (2.146)$$

where

$$P_n^{(1)}(\cos \theta) = -\frac{d P_n(\cos \theta)}{d\theta} \quad (2.147)$$

and $P_n^{(1)}(\cos \theta)$ are the Legendre polynomials. The coefficients a_n and b_n in eqns (2.144) and (2.145) are

$$a_n = \frac{\psi_n(\alpha) \psi'_n(\beta) - m \psi_n(\beta) \psi'_n(\alpha)}{\xi_n(\alpha) \psi'_n(\beta) - m \psi_n(\beta) \xi'_n(\alpha)}, \quad (2.148)$$

$$b_n = \frac{m \psi_n(\alpha) \psi'_n(\beta) - \psi_n(\beta) \psi'_n(\alpha)}{m \xi_n(\alpha) \psi'_n(\beta) - \psi_n(\beta) \xi'_n(\alpha)}, \quad (2.149)$$

where $\alpha = ka$ and $\beta = mka$. The functions $\psi_n(x)$ are related to spherical Bessel functions by $\psi_n(x) = x j_n(x)$, and the functions $\xi_n(x)$ to spherical Hankel functions by $\xi_n(x) = x h_n^{(1)}(x)$.

These results of Mie theory apply to a single spherical particle in an unbounded solvent. The theory does not take into account the presence of other nearby particles, an effect which can become important for concentrated suspensions. It has been shown that in strongly scattering media the transport velocity for the electromagnetic energy may differ by an order of magnitude from the phase velocity.^[14]

2.3.2 The scattered intensity in first Born approximation

2.3.2.1 General results. The scattered intensity at a position sufficiently far from the scattering volume follows from eqn (2.138), obtained in the first Born approximation, as

$$\langle |E_s(\mathbf{R})|^2 \rangle = \frac{E_0^2 k^4}{16\pi^4 R^2} \left\langle \left| \sum_{\alpha=1}^m \sum_{i=1}^{N_\alpha} f_\alpha(\mathbf{k}_s) e^{i\mathbf{k}_s \cdot \mathbf{r}_{iz}} \right|^2 \right\rangle. \quad (2.150)$$

The bracket denotes an ensemble average and the argument of the form amplitude f_α has been written as \mathbf{k}_s in order to include the case of non-spherical particles. The ensemble average is to be performed with the configuration space distribution function, which is essentially the Boltzmann factor of the total potential energy of interaction between the particles. For non-spherical objects the pair interaction does not only depend on the distance between their centres of mass but also on their relative orientation. For the special case of two rods the interaction potential is of the form $v(\mathbf{r}, \mathbf{u}_1, \mathbf{u}_2)$, where \mathbf{r} is the vector connecting the centres of the rods and where \mathbf{u}_1 and \mathbf{u}_2 denote their directions. Therefore, the configurational integral in (2.150) contains the rod orientations both in the amplitude $f_{\alpha, \text{rod}}$ and in the Boltzmann factor, so that a factorization of the ensemble average into an average over the amplitudes and an average over the positions \mathbf{r}_{iz} is not possible.

2.3.2.2 Monodisperse spherical particles. The situation is much simpler for spherical particles, for which $f_\alpha(\mathbf{k}_s)$ is given by eqn (2.139); in that case the ensemble average is only over the phase factors depending on the centres of the spheres. For monodisperse suspensions the index α is irrelevant, so that the scattered intensity, apart from the prefactor in eqn (2.150), becomes

$$I(k) = N f^2(k) S(k). \quad (2.151)$$

Here and in the following, k_s is written as $k = (4\pi/\lambda) \sin(\theta/2)$, where λ is the wavelength of light in the solvent. The (unnormalized) form factor $f^2(k)$ depends on the strength of the scattering; from eqn (2.139) the form amplitude can be written as

$$f(k) = f(0)B(k). \quad (2.152)$$

Expressing $\delta\varepsilon_{if}$ in terms of refractive indices n_p and n_s of the particles and the solvent,

$$f(0) = \frac{\pi}{6} \frac{n_p + n_s}{n_s^2} (n_p - n_s) \sigma^3 \approx \frac{\pi}{3} \frac{n_p - n_s}{n_s} \sigma^3. \quad (2.153)$$

The (normalized) form factor is

$$P(k) = B^2(k) = \left(\frac{3j_1(k\sigma/2)}{k\sigma/2} \right)^2, \quad (2.154)$$

with $P(0) = 1$. The factor $S(k)$ in eqn (2.151) is given by

$$S(k) = \frac{1}{N} \sum_{i,j} \langle e^{ik \cdot (r_i - r_j)} \rangle. \quad (2.155)$$

Apart from a term proportional to $\delta(\mathbf{k})$, which describes scattering in the forward direction and which will therefore be discarded, eqn (2.155) is identical to the static structure factor introduced in eqn (2.52), so that $I(k)$ for a system of N monodisperse spherical particles is

$$\begin{aligned} I(k) &= N f^2(0) P(k) \left\{ 1 + n \int d\mathbf{r} e^{ik \cdot \mathbf{r}} (g(r) - 1) \right\} \\ &= N f^2(0) P(k) \left\{ 1 + \frac{4\pi n}{k} \int_0^\infty dr r (g(r) - 1) \sin kr \right\}. \end{aligned} \quad (2.156)$$

This is the link between the statistical mechanical description of the microstructure as summarized by the pair distribution function $g(r)$ and the static light scattering experiment. In this case the scattered intensity clearly separates into a product of single particle properties, such as the material constants determining $f^2(0)$, the distribution of scattering material inside the particle described by the form factor $P(k)$, and the correlations between the particles as described by $S(k)$ or $g(r)$. This latter property is independent of the quantities which describe the coupling of light to the system ($f^2(0)$) and the geometrical form. This factorization makes the experimental determination of $S(k)$ very easy; one dilutes the sample until all correlations have disappeared, so that for the dilute system of N_0 particles in the scattering volume the structure factor is equal to unity. Denoting the scattered intensity of the dilute sample by $I_0(k)$, the structure factor of the origin system can be obtained from

$$\frac{I(k)}{I_0(k)} = \frac{N}{N_0} S(k). \quad (2.157)$$

2.3.2.3 Mixtures of spherical particles. For m -component mixtures of spherical particles, the scattered intensity—again apart from the prefactor in eqn (2.150)—is

$$I(k) = N \sum_{\alpha, \beta=1}^m f_\alpha(k) f_\beta(k) S_{\alpha\beta}(k), \quad (2.158)$$

where the form amplitude $f_\alpha(k)$ of particles of component α is

$$f_\alpha(k) \approx \frac{\pi}{3} \frac{n_{p,\alpha} - n_s}{n_s} \sigma_\alpha^3 \frac{3j_1(k\sigma_\alpha/2)}{k\sigma_\alpha/2}. \quad (2.159)$$

Here, $n_{p,\alpha}$ is the refractive index of the particles of component α and σ_α is their diameter. The $S_{\alpha\beta}(k)$ in eqn (2.158) are the partial static structure factors, defined in eqn (2.99) as the correlations of the density fluctuations of components α and β .

When there are no correlations, $S_{\alpha\beta}(k) = x_\alpha \delta_{\alpha\beta}$ from eqn (2.100), so that the scattered intensity becomes

$$I_0(k) = N \sum_{\alpha=1}^m x_\alpha f_\alpha^2(k) \equiv N \overline{f^2(k)}. \quad (2.160)$$

This suggests that eqn (2.158) should be rewritten formally as the scattered intensity for monodisperse suspensions, eqn (2.151),

$$I(k) = N \overline{f^2(k)} S^M(k), \quad (2.161)$$

where

$$S^M(k) = \frac{1}{\overline{f^2(k)}} \sum_{\alpha, \beta} f_\alpha(k) f_\beta(k) S_{\alpha\beta}(k) \quad (2.162)$$

is called the measurable structure factor,^[15] since it is this quantity which can be obtained from the experiment. Although eqn (2.161) has the same form as eqn (2.151), it should be noted that the factorization of $I(k)$ into a one-particle property and a genuine statistical mechanical quantity such as $S(k)$, which does not depend on the coupling of the radiation to the system, is no longer possible; $S^M(k)$ depends on the form amplitudes $f_\alpha(k)$. The truly thermodynamic quantities are the partial structure factors $S_{\alpha\beta}(k)$. For $k \rightarrow \infty$, $S^M(k) \rightarrow 1$, because $S_{\alpha\beta}(k \rightarrow \infty) = x_\alpha \delta_{\alpha\beta}$.

Since $f_\alpha \sim \sigma_\alpha^3$ the coupling of the radiation to the mixture will strongly depend on the size of the particles; large particles scatter more strongly at small k than small ones. However, the k -dependent part of $f_\alpha(k)$ is also different for particles of different diameters; for the larger particles of the mixture the form amplitudes decrease faster with increasing k than for the smaller ones. Furthermore, the correlations, described by the partial structure factors, will also depend on which kind of components are considered. This effect can be expected to be particularly important when charge-stabilized mixtures are considered. In this case particles of different sizes will carry different charges, so that the electrostatic repulsions and therefore the correlations between particles will depend on the components to which these particles belong.

2.3.2.4 The substitutional model. If the mixture consists of more than two components it is not possible to express the measured structure factor $S^M(k)$ using the Bhatia–Thornton structure factors. There is, however, one interesting case in which $S^M(k)$ can be further simplified. With eqn (2.100), the measured

structure factor (2.162) can be written as

$$S^M(k) = \frac{1}{f^2(k)} \sum_{\alpha, \beta} f_\alpha(k) f_\beta(k) [x_\alpha \delta_{\alpha\beta} + n x_\alpha x_\beta \tilde{h}_{\alpha\beta}(k)], \quad (2.163)$$

where $\tilde{h}_{\alpha\beta}(k)$ is the Fourier transform of $h_{\alpha\beta}(r) = g_{\alpha\beta}(r) - 1$. For a mixture of particles, which are of identical size and carry identical charges, but differ in their refractive indices, the correlations between all components of the mixture are the same. Therefore, there is only one structure factor $S(k) = 1 + n\tilde{h}(k)$ which characterizes the correlations, and eqn (2.163) simplifies to

$$S^M(k) = R(k) + (1 - R(k))S(k), \quad (2.164)$$

where

$$R(k) = 1 - \frac{\overline{f(k)^2}}{\overline{f^2(k)}}, \quad (2.165)$$

with

$$\overline{f(k)} = \sum_{\alpha=1}^m x_\alpha f_\alpha(k). \quad (2.166)$$

Expression (2.166) shows that the scattered intensity of a mixture of optically different but otherwise identical particles has an incoherent contribution $R(k)$.

This result, which is exact for optical polydispersity, has been used as an approximation for mixtures.^[16,17] When the components of the mixture are not too different one assumes that the correlations among all particles of the mixture are identical, but that the coupling of light to the particles of different diameters is taken properly into account. The approximation consists in replacing $S(k)$ in (2.164) by the structure factor $S^I(k)$ of the idealized monodisperse system. One possibility for defining this system is to introduce an averaged pair potential $v(r)$ using the weighted average of the potentials $v_{\alpha\beta}(r)$ between particles of components α and β ,

$$v(r) = \sum_{\alpha, \beta=1}^m x_\alpha x_\beta v_{\alpha\beta}(r). \quad (2.167)$$

Since $v(r)$ defines just one effective type of interaction, one has only to calculate one effective pair correlation function $g(r)$ from which $S^I(k)$ can be obtained by eqn (2.61). One therefore avoids the much more complicated determination of the partial pair distribution functions $g_{\alpha\beta}(r)$. This approximate scheme to treat a mixture, known as the substitutional model, is appropriate for fairly narrow distributions of diameters of hard spheres. For charged spheres it misses any structural effects which arise from charge-ordering, since the charge-charge structure factor for this model is^[8]

$$S_{CC}(k) = \frac{\bar{Q}^2 - \bar{Q}^2}{\bar{Q}^2} \equiv s_Q^2, \quad (2.168)$$

which is independent of k , and $S_{\text{NC}}(k) = 0$. Therefore, structural effects of charge-polydispersity are not included. Furthermore, in this model $S_{\text{NN}}(k) = S_\chi(k) = S^1(k)$.

2.3.2.5 Binary mixtures. For $Q_1 \neq Q_2$, the measurable structure factor can be represented by the Bhatia-Thornton structure factors as

$$S^M(k) = \frac{1}{f^2(k)} \left\{ \bar{f}(k)^2 S_{\text{NN}}(k) + 2\bar{f}(k)(f_1(k) - f_2(k)) \frac{\bar{Q}S_{\text{NC}}(k)}{Q_1 - Q_2} \right. \\ \left. + (f_1(k) - f_2(k))^2 \frac{\bar{Q}^2 S_{\text{CC}}(k)}{(Q_1 - Q_2)^2} \right\}. \quad (2.169)$$

A considerable simplification arises for binary mixtures of particles of different charge ($Q_1 \neq Q_2$) but identical refractive indices and identical diameters ($f_1(k) = f_2(k)$); in this case

$$S^M(k) = S_{\text{NN}}(k). \quad (2.170)$$

For the case of only optical bidispersity, for which eqn (2.164) applies, the incoherent part $R(k)$ is independent of k :

$$R = \frac{x_1 x_2 (n_{p,1} - n_{p,2})^2}{x_1 (n_{p,1} - n_s)^2 + x_2 (n_{p,2} - n_s)^2}, \quad (2.171)$$

where $n_{p,\alpha}$, $\alpha = 1, 2$, are the refractive indices of the two kinds of particles and n_s is the refractive index of the solvent. If the mixture is strongly correlated, $S(k=0)$ in eqn (2.164) will be rather small, say 0.01, so that $S^M(0) \approx S(0) + R$. Since $S_\chi(k) = S(k)$ for optically bidisperse systems, it follows that the compressibility structure factor at $k=0$ is smaller than that obtained from the scattered intensity in the forward direction. This effect arises from the incoherent scattering, which contributes to S^M but not to S_χ .

2.3.2.6 Rod-like particles. After eqn (2.156) it was stressed that the scattered intensity $I(k)$ for the case of monodisperse spherical particles factorizes into single-particle properties and a structure factor, which is a purely statistical mechanics property. This factorization does not apply to a system of non-spherical particles, such as rods, even when they are monodisperse. Using eqn (2.138) for a monodisperse system and eqn (2.140), the scattered field is

$$E_s \propto \sum_{m=1}^N e^{ik \cdot r_m} j_0(\mathbf{k} \cdot \mathbf{u}_m L/2) \alpha_{if}(\mathbf{u}_m) \quad (2.172)$$

where $\alpha_{if}(\mathbf{u}) = \mathbf{n}_f \cdot \boldsymbol{\alpha}(\mathbf{u}) \cdot \mathbf{n}_i$. Here $\boldsymbol{\alpha}(\mathbf{u})$ is the polarizability tensor of a rod having the direction \mathbf{u} , which can be written as

$$\boldsymbol{\alpha}(\mathbf{u}) = \alpha_{||} \mathbf{u}\mathbf{u} + \alpha_{\perp} (\mathbf{1} - \mathbf{u}\mathbf{u}). \quad (2.173)$$

Then the scattered intensity is proportional to

$$I(k) = \sum_{m,n} \langle e^{ik \cdot (r_m - r_n)} j_0(\mathbf{k} \cdot \mathbf{u}_m L/2) j_0(\mathbf{k} \cdot \mathbf{u}_n L/2) \alpha_{if}(\mathbf{u}_m) \alpha_{if}(\mathbf{u}_n) \rangle. \quad (2.174)$$

Separating the summation into an intramolecular part ($m = n$) and a contribution from intermolecular correlation, eqn (2.174) becomes^[18]

$$I(k) = N[F(k) + \tilde{S}(\mathbf{k})], \quad (2.175)$$

where

$$F(k) = \frac{1}{4\pi} \int d\mathbf{u} j_0^2(\mathbf{k} \cdot \mathbf{u} L/2) \alpha_{if}^2(\mathbf{u}) \quad (2.176)$$

and

$$\begin{aligned} \tilde{S}(\mathbf{k}) = n & \int \frac{d\mathbf{u}_1}{4\pi} \int \frac{d\mathbf{u}_2}{4\pi} j_0(\mathbf{k} \cdot \mathbf{u}_1 L/2) j_0(\mathbf{k} \cdot \mathbf{u}_2 L/2) \alpha_{if}(\mathbf{u}_1) \alpha_{if}(\mathbf{u}_2) \\ & \times \int d\mathbf{r} e^{i\mathbf{k} \cdot \mathbf{r}} (g(\mathbf{r}, \mathbf{u}_1, \mathbf{u}_2) - 1). \end{aligned} \quad (2.177)$$

Here it has been taken into account that the configurational average in eqn (2.174) includes an average over the orientations \mathbf{u} . The function $g(\mathbf{r}, \mathbf{u}_1, \mathbf{u}_2)$ in eqn (2.177) is the generalization of the radial distribution function $g(r)$ appearing in eqn (2.156) to rod-like particles. Whereas $g(r)$ is proportional to the probability of finding the centre of a spherical particle at a distance r from the centre of another particle, $g(\mathbf{r}, \mathbf{u}_1, \mathbf{u}_2)$ is related to the probability of finding a rod with direction \mathbf{u}_2 and centre of mass at \mathbf{r} , given that there is a rod with direction \mathbf{u}_1 with its centre of mass at the origin. The form factor of a rod follows from eqn (2.176), as

$$P(k) = \frac{1}{4\pi} \int d\mathbf{u} j_0^2(\mathbf{k} \cdot \mathbf{u} L/2). \quad (2.178)$$

Setting $\mathbf{k} \cdot \mathbf{u} = k \cos \vartheta = kv$, this can be written as

$$\begin{aligned} P(k) &= \frac{1}{2} \int_{-1}^{+1} dv j_0^2\left(\frac{kLv}{2}\right) \\ &= \frac{2}{kL} \int_0^{kL} dx j_0(x) - j_0^2\left(\frac{kL}{2}\right). \end{aligned} \quad (2.179)$$

The scattered intensity (2.175) can formally be expressed as for spherical particles, as

$$\begin{aligned} I(k) &= NF(k) \left[1 + \frac{\tilde{S}(k)}{F(k)} \right] \\ &\equiv NF(k)\bar{S}(k), \end{aligned} \quad (2.180)$$

but it is obvious that $\bar{S}(k)$ is now not independent of single-particle properties.

A factorization of the centre-of-mass correlations and the average over the orientations in eqn (2.174) is only possible if the interaction potential is dominated by the centre-of-mass distances of the rods. Then the orientations become uncoupled from the separations, so that $g(\mathbf{r}, \mathbf{u}_1, \mathbf{u}_2)$ is independent of \mathbf{u}_1 and \mathbf{u}_2 , and eqn (2.174) can be written as

$$I(k) = N \left[F(k) + \frac{1}{N} \sum'_{m,n} \langle e^{i\mathbf{k} \cdot (\mathbf{r}_m - \mathbf{r}_n)} \rangle f^2(k) \right], \quad (2.181)$$

where

$$f(k) = \frac{1}{4\pi} \int d\mathbf{u} j_0(\mathbf{k} \cdot \mathbf{u} L/2) \alpha_{if}(\mathbf{u}), \quad (2.182)$$

and the ensemble average in eqn (2.181) refers only to the centre-of-mass correlations. Denoting the corresponding structure factor as $S_K(k)$, eqn (2.181) becomes

$$I(k) = NF(k) \left[1 + \frac{f^2(k)}{F(k)} (S_K(k) - 1) \right]. \quad (2.183)$$

2.4 Calculation of the microstructure

2.4.1 The Ornstein–Zernike equation and closure relations

The Ornstein–Zernike (OZ) equation for a homogeneous fluid is a relation between ‘total’ and ‘direct’ two-particle correlation functions. The total correlations are described by $h(r) = g(r) - 1$ for two particles separated by the distance r . In a many-body system these correlations will be the result of a direct correlation between these two particles and of many indirect contributions, which involve chains of direct correlations starting from one of the particles of the pair, going through other particles and ending at the other partner of the pair. This concept leads to the equation

$$h(r) = c(r) + n \int d\mathbf{r}' c(|\mathbf{r} - \mathbf{r}'|) h(\mathbf{r}'), \quad (2.184)$$

which is the OZ equation.^[1] Successive iterations give rise to the chains of direct correlations just mentioned. However, the direct correlation function $c(r)$ is unknown. To make use of the OZ equation for a calculation of $h(r)$, and from its knowledge a calculation of $S(k)$, a further relation for $c(r)$ is needed. Such relations, known as closure relations, introduce approximations.^[1]

To obtain an idea of the direct correlations one may consider the low-density limit of the OZ equation. Neglecting the integral term and using the fact that $g(r) = \exp(-\beta v(r))$ for $n \rightarrow 0$, one obtains

$$c(r) = e^{-\beta v(r)} - 1, \quad (2.185)$$

which becomes

$$c(r) = -\beta v(r) \quad (2.186)$$

if $\beta v(r) \ll 1$. This condition is fulfilled asymptotically for large separations. An approximate closure relation can now be obtained by assuming eqn (2.186) for all separations $r > \sigma$, where σ is the particle diameter, together with $h(r) = -1$ for $r < \sigma$, which applies exactly if the particles are impenetrable hard spheres. With these two relations the OZ equation determines $c(r)$ for $r < \sigma$ and $h(r)$ for $r > \sigma$. This scheme constitutes the mean-spherical approximation (MSA).

Further, more accurate, closure relations have been derived by systematic density expansions of the correlation functions.^[1] These relations, and a more precise meaning of the direct correlations, can also be obtained by functional derivative methods. This procedure is described in Appendix 2.A. There it is shown how one of the most useful closure relations, the hypernetted-chain (HNC) approximation can be established. Equation (2.A.24), which is

$$g(r) = e^{-\beta v(r) + h(r) - c(r)} \quad (\text{HNC}), \quad (2.187)$$

provides the additional relation between the functions appearing in the OZ equation and it contains also the pair potential $v(r)$. Solving eqn (2.187) for $c(r)$ and using the fact that $h(r) \rightarrow 0$ for $r \rightarrow \infty$ shows that the HNC satisfies the asymptotic relation $c(r) = -\beta v(r)$ for $r \rightarrow \infty$, just as eqn (2.186), but without assuming that $n \rightarrow 0$.

Expanding the factor $\exp[h(r) - c(r)]$ in eqn (2.187) to linear order gives

$$g(r) = e^{-\beta v(r)}[g(r) - c(r)] \quad (\text{PY}), \quad (2.188)$$

which is another frequently used closure relation, known as the Percus-Yevick approximation (PY).^[19]

If the potential $v(r)$ can be separated as $v(r) = v_0(r) + w(r)$, where v_0 is a short-range repulsive part and $w(r)$ a weak long-range contribution, a linear expansion of eqn (2.188) in terms of w gives

$$g(r) = e^{-\beta v_0(r)}(1 - \beta w(r))(g(r) - c(r)). \quad (2.189)$$

Since $c(r) \rightarrow 0$ and $g(r) \rightarrow 1$ for $r \gg \sigma$, one may approximate further to obtain

$$g(r) = e^{-\beta v_0(r)}(g(r) - c(r) - \beta w(r)) \quad (\text{SMSA}), \quad (2.190)$$

which is known as the ‘soft’ MSA (SMSA).^[20,21] For particle separations larger than the range of $v_0(r)$ this relation simplifies to

$$c(r) = -\beta w(r). \quad (2.191)$$

When $v_0(r)$ is the hard-core potential,

$$v_0(r) = \begin{cases} \infty, & r < \sigma, \\ 0, & r > \sigma. \end{cases} \quad (2.192)$$

Equation (2.191) applies at $r > \sigma$; this closure is the mean-spherical approximation.

Another useful procedure is to separate $c(r)$ into a contribution $c_0(r)$, which arises from the short-range part $v_0(r)$ of the potential, and a long-range part, which is approximated as in eqn (2.191):

$$c(r) = c_0(r) - \beta w(r). \quad (2.193)$$

Then the short-range part can, for instance, be treated in the PY approximation, whereas the long-range contribution is treated in the spirit of eqn (2.191).

The direct correlation function $c(r)$ is useful for representing various measurable quantities. From eqn (2.61), the static structure factor can be expressed in terms of the Fourier transform $\hat{h}(k)$ of the total correlation function,

$$S(k) = 1 + n\hat{h}(k). \quad (2.194)$$

Taking the Fourier transform of the OZ equation (2.184), $S(k)$ becomes

$$S(k) = \frac{1}{1 - n\hat{c}(k)}. \quad (2.195)$$

Since $S(0)$ is, according to eqn (2.62), related to the isothermal compressibility, one finds that

$$(nk_B T \chi_T)^{-1} = 1 - 4\pi n \int_0^\infty dr r^2 c(r). \quad (2.196)$$

Using the approximation (2.193) for $c(r)$ in eqn (2.195), one obtains

$$\frac{1}{S(k)} = \frac{1}{S_0(k)} + n\beta\hat{w}(k), \quad (2.197)$$

where $S_0(k)$ is the structure factor of the reference system having only the short-range potential $v_0(r)$. The result given in eqn (2.197) is often referred to as the random phase approximation.

When the various closure relations listed above are combined with the OZ equation the resulting equations can be solved analytically only in a few special cases, depending on the closure relation used and the particular pair potential. Analytical solutions exist for the MSA closure for Coulomb^[22] and screened Coulomb^[23] potentials and for the PY closure for a hard sphere potential.^[24,25] In other cases, in particular for the HNC closure, numerical methods have to be used.

The quality of a particular closure relation can be judged by comparing with computer simulation results. As a general rule, the HNC closure reproduces the structure of systems with long-range potentials well, whereas the PY closure works particularly well for short-range potentials. The analytical solution of the MSA for screened Coulomb (Yukawa) potentials has been used for weakly interacting charge-stabilized suspensions of moderate density.^[26] For strongly charged particles at low density the MSA fails; it produces pair distribution functions $g(r)$, which become negative near contact. This failure can, however,

be overcome by a rescaling procedure, introduced by Hansen and Hayter.^[27] The resulting scheme, known as the rescaled MSA (RMSA), has been widely used because of its simplicity. Its major drawback is that it underestimates the structure in $g(r)$, as compared to computer simulations for strongly interacting systems. However, it can be used successfully as a fitting procedure for simulation results if the value of the charge on the particles is sufficiently increased over its value as used in the simulations.^[28]

For strongly correlated systems of repulsively interacting particles, both the HNC and the PY closure deviate systematically from computer simulation results. One finds, for instance, for repulsive Yukawa potentials, that HNC somewhat underestimates the structure of $g(r)$, whereas PY overestimates it. In the case of uncharged hard spheres at relatively high concentrations (volume fraction $\phi \approx 0.4$) the situation is reversed. However, in both cases the ‘true’ result for $g(r)$ lies between those of the two closures. This observation has been used to introduce a further closure scheme which mixes the HNC and PY closures. Following Rogers and Young,^[29] one writes

$$g(r) = e^{-\beta v(r)} \left\{ 1 + \frac{1}{f(r)} [e^{f(r)(h(r) - c(r))} - 1] \right\} \quad (\text{RY}), \quad (2.198)$$

where the mixing function is

$$f(r) = 1 - e^{-\alpha r} \quad (2.199)$$

and α is the mixing parameter. When r and/or α are small, $f(r) \rightarrow 0$ and eqn (2.198) is seen to reduce to the PY closure given in eqn (2.188). In the opposite limit $f(r) \rightarrow 1$ and eqn (2.198) becomes the HNC closure given in eqn (2.187).

The mixing parameter α has to be determined by an additional condition. Because of the approximate character of the closure relations, the results for the thermodynamic quantities, calculated from the approximate pair distribution function $g(r)$ or the direct correlation function $c(r)$, depend on the statistical mechanical routes. Taking the isothermal compressibility χ_T as an example, one can either use the compressibility equation (2.196) or one can obtain χ_T from the derivative of the pressure, eqn (2.46), and use for the pressure the virial equation (2.41). Denoting the result of the first method by χ_T^c and of the second one by χ_T^v , one will find that $\chi_T^c \neq \chi_T^v$; there is a certain inconsistency of the thermodynamics because of the use of approximate results for $g(r)$. If the mixing parameter α of the Rogers–Young (RY) closure relation is chosen by demanding that $\chi_T^c = \chi_T^v$, the thermodynamic inconsistency of the compressibility is removed; other thermodynamic quantities may still depend on the route used. When it is intended to obtain reliable results for structural quantities, such as $S(k)$ and $g(r)$, it is suggested to use the equality of χ_T as the additional condition to fix α , since eqn (2.62) ensures that the value of $S(k)$ at $k = 0$ is calculated precisely. One can therefore expect that the results for $S(k)$ are also reliable for $k \neq 0$. As will be shown later, the RY scheme indeed reproduces computer-simulated results for $g(r)$ rather well.

To also treat in a thermodynamically self-consistent way potentials which have an attractive part, Zerah and Hansen^[30] introduced a new closure by mixing SMSA and HNC. The closure, which is called HMSA, reads

$$g(r) = e^{-\beta v^{\text{rep}}(r)} \left\{ 1 + \frac{1}{f(r)} [e^{f(r)[h(r) - c(r) - v^{\text{att}}(r)]}] - 1 \right\} \quad (\text{HMSA}), \quad (2.200)$$

where $v^{\text{rep}}(r)$ and $v^{\text{att}}(r)$ are, respectively, the repulsive and the attractive parts of the potential as obtained from the Weeks *et al.*^[31] procedure. In this case, as $f(r) \rightarrow 0$ the SMSA closure is recovered and as $f(r) \rightarrow 1$ the HNC closure is recovered. If $v^{\text{att}}(r) = 0$, the HMSA reduces to the RY closure.

2.4.2 Multi-component systems

The microstructure of the m -component mixtures considered in Section 2.2.3 is characterized by the $m(m+1)/2$ partial distribution functions $h_{\alpha\beta}(r) = g_{\alpha\beta}(r) - 1$ and alternatively by the partial structure factors $S_{\alpha\beta}(k)$. The distribution functions are obtained from a set of coupled OZ equations

$$h_{\alpha\beta}(r) = c_{\alpha\beta}(r) + n \sum_{\gamma=1}^m x_{\gamma} \int d\mathbf{r}' c_{\alpha\gamma}(|\mathbf{r} - \mathbf{r}'|) h_{\gamma\beta}(r') \quad (2.201)$$

and closure relations. The latter have the same form as for monodisperse systems, except that the pair of indices $(\alpha\beta)$ has to be attached to $g(r)$, $c(r)$, $v(r)$ and $h(r)$. In the Rogers–Young equation the mixing function can, in principle, be replaced by a set of mixing functions $f_{\alpha\beta}(r)$, which introduce $m(m+1)/2$ mixing parameters. To fix these parameters one needs as many conditions. The simplest approach, however, is to use only one parameter α and to determine it as before by demanding the equality $\chi_T^c = \chi_T^v$ for the compressibilities.

Also in this case, the Fourier transform of the OZ equations has a simple structure. By introducing matrix notation, the relation between the total correlation functions and the direct correlation functions is given by

$$\mathcal{H} = (\mathcal{R} - \mathcal{RCR})^{-1} \mathcal{R}^{-1}, \quad (2.202)$$

where the matrices \mathcal{R} and \mathcal{C} are, respectively, $\mathcal{R}_{\alpha\beta} = \delta_{\alpha\beta} n_{\alpha}$ and $\mathcal{C}_{\alpha\beta} = \tilde{c}_{\alpha\beta}(k)$. This matrix equation will become useful in the next section dealing with methods, especially when the number of components m to be treated is quite large ($m > 3$).

2.5 Solution of integral equations

In this section we select and present solution methods of integral equations. Although exhaustive reviews of solution methods are not yet available, it is not our intention to cover the entire field: such a review lies outside the aims of this contribution. Instead, we will only select and present solution methods which are simple to implement, sufficiently stable and which can easily be

extended to the treatment of multi-component systems. We concentrate only on those integral equations presented in the previous section; that is, on PY, HNC, HMSA and RY. Also in this case, the choice is motivated by simplicity of implementation and, in addition, by accuracy in reproducing simulated and/or experimental data. The reader interested in more specific integral equations, such as the Martynov and Sarkisov equation for additive and non-additive hard-spheres,^[32,33] the modified HNC equation with a properly chosen hard-sphere bridge function^[34–38] or the Mean Spherical Approximation MSA (see ref. 1 and the works listed therein), can refer to the cited literature.

Whereas analytical solutions are known for the ‘linear’ PY integral equation for hard-spheres, there are no known analytical solutions for the ‘non-linear’ HNC and thermodynamically self-consistent integral equations. This class of non-linear equations is solved by using numerical methods. The most efficient and stable solution method originates from the work of Gillan^[39] and Abernethy and Gillan.^[40] It is a combination of the traditional Picard iterative scheme and the Newton–Raphson technique. Later, Zerah^[41] improved the algorithm by better exploiting the Newton method for non-linear equations and by using the conjugate gradient method for the iterative part. Another efficient method is that developed by Labik, Malijevsky and Vonka.^[42]

According to our selection criteria, we will instead present a fast version of a simple iterative Picard method, which is due to Ng.^[43] It is easy to implement, it is as stable as and almost as fast as the Gillan method but, more importantly for our applications, it is easily extendible to the treatment of systems with a large number of components.^[5,44]

The following subsections are devoted to analytical solutions and numerical algorithms that are useful for cases of interest in colloid physics, and for which expressions of the scattered intensity in terms of correlation functions have already been given in Section 2.3.

2.5.1 Solution of PY scheme

2.5.1.1 One-component hard sphere systems. The PY closure for spherical particles of diameter σ with a hard-core interaction potential

$$\begin{aligned} v(r) &= +\infty, & r < \sigma, \\ &= 0, & r > \sigma, \end{aligned} \quad (2.203)$$

reduces to the following conditions

$$\begin{aligned} g(r) &= 0, & r < \sigma & \text{(exact),} \\ c(r) &= 0, & r > \sigma & \text{(approximate).} \end{aligned} \quad (2.204)$$

The solution of the OZ equation with these boundary conditions has been obtained by Wertheim and Thiele^[24,25,45] by using Laplace transform methods. Later Baxter^[46] developed an alternative method which can be extended to

potentials consisting of a hard-core and a ‘soft’ tail. Details of both solution methods can be found in refs. 1 and 3. The final solution for hard spheres is

$$\begin{aligned} c(r) &= A_0 + A_1(r/\sigma) + A_3(r/\sigma)^3, & r < \sigma, \\ &= 0 & r > \sigma, \end{aligned} \quad (2.205)$$

with

$$\begin{aligned} A_0 &= -(1 + 2\phi)^2/(1 - \phi)^4, \\ A_1 &= 6\phi(1 + \frac{1}{2}\phi)^2/(1 - \phi)^4, \\ A_3 &= -\frac{1}{2}\phi(1 + 2\phi)^2/(1 - \phi)^4, \end{aligned} \quad (2.206)$$

where $\phi = \pi n\sigma^3/6$ is the packing or volume fraction.

The Fourier transform $\tilde{c}(k)$ is easily obtained and it reads as follows:

$$\begin{aligned} \tilde{c}(k) &= 4\pi \left[-\frac{2A_1}{(k\sigma)^4} + \frac{24A_3}{(k\sigma)^6} - \frac{\cos(k\sigma)}{(k\sigma)^2} (A_0 + A_1 + A_3) + \frac{\sin(k\sigma)}{(k\sigma)^3} (A_0 + 2A_1 + 4A_3) \right. \\ &\quad \left. + \frac{\cos(k\sigma)}{(k\sigma)^4} (2A_1 + 12A_3) - 24A_3 \frac{\sin(k\sigma)}{(k\sigma)^5} - 24A_3 \frac{\cos(k\sigma)}{(k\sigma)^6} \right]. \end{aligned} \quad (2.207)$$

The structure factor $S(k)$ to be used in the scattering relations follows from eqn (2.195). The pair distribution function $g(r)$ is obtained from an inverse numerical Fourier transform of the function

$$\tilde{\gamma}(k) = \tilde{h}(k) - \tilde{c}(k) = \frac{n\tilde{c}^2(k)}{1 - n\tilde{c}(k)} \quad (2.208)$$

and from the analytical expression of $c(r)$. We obtain

$$\begin{aligned} g(r) &= 0, & r < \sigma, \\ &= \text{FT}^{-1}(\tilde{\gamma}(k)) + c(r) + 1, & r > \sigma. \end{aligned} \quad (2.209)$$

This procedure has to be used since $\gamma(r)$ is always continuous at σ , whereas $c(r)$ and $h(r)$ are not.^[1]

The equation of state of hard-spheres in the PY approximation is obtained by substituting $c(r)$ in the compressibility equation (2.196) and by integrating the result with respect to ϕ :

$$\frac{\beta p^C}{n} = \frac{1 + \phi + \phi^2}{(1 - \phi)^3}. \quad (2.210)$$

Alternatively, the equation of state can also be obtained from the virial equation (2.41) (see, for example, Hansen and McDonald^[11]):

$$\frac{\beta p^V}{n} = \frac{1 + 2\phi + 3\phi^2}{(1 - \phi)^2}. \quad (2.211)$$

These two equations for $\beta p/n$ show the internal thermodynamic inconsistency of the PY scheme, while the comparison with ‘exact’ simulation data shows the inaccuracy of both expressions, particularly at densities close to the freezing density, $\phi = 0.49$.

An empirical equation of state, which fits the simulation data nicely, has been introduced by Carnahan and Starling.^[47] It is an interpolation between the PY virial and compressibility equations of state, and is given by

$$\frac{\beta p}{n} = \frac{\beta}{n} \left(\frac{2}{3} p^C + \frac{1}{3} p^V \right) = \frac{1 + \phi + \phi^2 - \phi^3}{(1 - \phi)^3}. \quad (2.212)$$

A Fortran program **P/1** exists by which all the correlation functions $g(r)$, $c(r)$ and $S(k)$ of hard spheres systems for different volume fractions ϕ can be calculated. In the program, the PY results are improved by using the Verlet–Weis^[48] parameterization which ‘minimizes’ the absolute difference between the calculated and simulated $g(r)$ in an interval $r = [1.6\sigma, 3\sigma]$. The minimization is achieved by solving the PY for a reduced volume fraction ϕ' given by

$$\phi' = \phi - \frac{\phi^2}{16}. \quad (2.213)$$

The contact value of $g(r)$, which further deviates from its exact value due to this parameterization, is re-corrected by adding to the calculated $g(r)$ a short-range contribution

$$\delta g(r) = \frac{A}{r} \cos[\alpha(r - \sigma)] e^{-\alpha(r - \sigma)}. \quad (2.214)$$

The parameters A and α are obtained by requiring, respectively, a contact value, $g(\sigma)$ in agreement with the Carnahan–Starling equation and a full $g(r)$ in agreement with the correct isothermal compressibility. Details of the method can be found in refs. 1 and 48.

2.5.1.2 Polydisperse hard sphere systems. A polydisperse hard sphere system is characterized by a one-parameter distribution function $F(\sigma)$ or, equivalently, by the specification of the complete set of the moments of such a distribution. The system consists of an infinite number of different components, each one with its specific value of σ and $F(\sigma)$. This case represents the generalization of the ‘multi-component mixture’ case, in which there is a finite number of particle species. The correlations in systems having the continuous size distribution $F(\sigma)$ are described by an infinite set of OZ equations

$$h_{\sigma\sigma'}(r) = c_{\sigma\sigma'}(r) + n \int d\sigma'' F(\sigma'') \int d\mathbf{r}' h_{\sigma''\sigma'}(r') c_{\sigma\sigma''}(|\mathbf{r} - \mathbf{r}'|). \quad (2.215)$$

The corresponding PY closure is

$$\begin{aligned} g_{\sigma\sigma'}(r) &= 0, & r < \frac{1}{2}(\sigma + \sigma') & \text{(exact),} \\ c_{\sigma\sigma'}(r) &= 0, & r > \frac{1}{2}(\sigma + \sigma') & \text{(approximate).} \end{aligned} \quad (2.216)$$

Solutions of the closed set of equations (2.215) and (2.216) have been reported by several authors. Blum and Stell^[49] extended the Baxter solution of the PY approximation for hard sphere mixtures with a finite number of components^[50] to the continuous distribution. The solution is given in terms of integrals involving the distribution, $F(\sigma)$, of particle diameters. Griffith, Triolo and Compere^[51,52] gave a fully analytic solution of the PY approximation, with the size polydispersity given in terms of the Schulz (or Gamma) distribution^[53]

$$F(\sigma) = \left(\frac{t+1}{\langle \sigma \rangle} \right)^{t+1} \frac{\sigma^t}{\Gamma(t+1)} \exp\left(-\frac{t+1}{\langle \sigma \rangle} \sigma \right) \quad (t > 0), \quad (2.217)$$

in which $\Gamma(t)$ is the gamma function and t is a parameter describing the width of the distribution. The standard deviation of $F(\sigma)$, which can be used as a measure of the degree of polydispersity, is linked to the parameter t by

$$s = \frac{(\langle \sigma^2 \rangle - \langle \sigma \rangle^2)^{1/2}}{\langle \sigma \rangle} = \frac{\langle \sigma \rangle}{(t+1)^{1/2}}. \quad (2.218)$$

The complete set of equations are, for the sake of completeness, given in Appendix 2.B. The solution of Griffith, Triolo and Compere also represents an improvement of the original method outlined by Vrij,^[54,55] which used a discretized representation of $F(\sigma)$. The results provided by the two methods are identical.

The relevant structural information of polydisperse hard sphere (PHS) systems is contained in the number–number pair distribution function

$$g_{NN}(r) = \int d\sigma \int d\sigma' F(\sigma) F(\sigma') g_{\sigma\sigma'}(r), \quad (2.219)$$

and in the number–number structure factor

$$S_{NN}(k) = \int d\sigma \int d\sigma' F(\sigma) F(\sigma') S_{\sigma\sigma'}(k), \quad (2.220)$$

where

$$S_{\sigma\sigma'}(k) = \frac{\delta_{\sigma\sigma'}}{F(\sigma)} + n \tilde{h}_{\sigma\sigma'}(k) \quad (2.221)$$

are the partial structure factors. The shape variation of such functions with respect to the standard deviation s elucidates the polydispersity effects on the local and global order of the system.

Thermodynamics properties, such as the equation of state, the chemical potential, the isothermal compressibility, etc., have been obtained by Salacuse and Stell,^[56] who extended the thermodynamic approach of Mansoori *et al.*^[57] to PHS, and also derived expressions for the phase equilibrium conditions. The generalization of the Carnahan and Starling^[47] equation of state is

$$\frac{p}{kT} = \frac{6}{\pi} \left\{ \frac{\xi_0}{1-\xi_3} + \frac{3\xi_1\xi_2}{(1-\xi_3)^2} + \frac{3\xi_2^3}{(1-\xi_3)^3} - \frac{\xi_3\xi_2^3}{(1-\xi_3)^3} \right\}, \quad (2.222)$$

where

$$\xi_j = \frac{\pi}{6} n \int d\sigma F(\sigma) \sigma^j \quad (2.223)$$

are the rescaled moments of the size distribution. The isothermal compressibility associated with this equation of state is

$$\chi_T^{-1} = \frac{6 k T}{\pi \xi_0} \left\{ \frac{\xi_0}{(1 - \xi_3)^2} + \frac{6 \xi_1 \xi_2}{(1 - \xi_3)^3} + \frac{9 \xi_2^3}{(1 - \xi_3)^4} - \frac{\xi_3 \xi_2^3 (4 - \xi_3)}{(1 - \xi_3)^4} \right\}. \quad (2.224)$$

It is interesting to note that the thermodynamic properties depend on the size distribution only through its first four moments ξ_0 , ξ_1 , ξ_2 and ξ_3 . In other words, the thermodynamic properties of PHS fluids can always be reduced to those of a specific two-component HS fluid, which is uniquely defined by requiring the equality of the moments ξ_0 , ξ_1 , ξ_2 and ξ_3 of $F(\sigma)$ and of the two-component distribution

$$\int d\sigma F(\sigma) \sigma^j = \sum_{i=1}^2 x_i \sigma_i^j, \quad j = 0, 1, 2, 3, \quad (2.225)$$

where x_1 and x_2 are the number fractions of the two-component system. However, the shapes of the correlation functions of such an effective system are drastically different from the corresponding ones of the true PHS fluid. This is due to the discontinuous nature of the hard sphere interaction potential, and the use of the effective two-component system is not allowed when structural information is of interest.

The derivation of expressions for the light-scattered intensity of PHS systems has also been the subject of intense study. Within the PY scheme, they were first derived by Vrij^[54,55] for different types of discretized distributions. Other expressions were later obtained by Blum and Stell^[49] and by Griffith, Triolo and Compere^[51,52] for the continuous Schulz distribution. The results are given in Appendix 2.C.

All the quantities listed in this section are evaluated in the Fortran program **P/2**, which also contains a subroutine for the determination of the scattered intensity.

2.5.2 Solution of HNC scheme

2.5.2.1 One-component systems. The most often used numerical solution method for a non-linear integral equation is the iterative method. By formally writing the non-linear integral equation as

$$f(x) = A f(x), \quad (2.226)$$

the iterative solution method for solving such an equation is simply

$$f_{n+1}(x) = A f_n(x). \quad (2.227)$$

From an initial input $f_1(x)$, a series of functions $f_2(x), \dots, f_n(x)$ is generated. If such a series converges uniformly, the procedure is stopped when the quantity

$$d_n = \left[\int dx [Af_n(x) - f_n(x)]^2 \right]^{1/2}, \quad (2.228)$$

is less than a given small quantity ε , and the last element of the series is the solution of eqn (2.226).

By following a rapidly convergent Picard procedure introduced by Ng,^[43] which is strictly valid for a linear operator A , the rate of convergence of the series f_n is increased by constructing a new input function, \bar{f}_{n+1} , from a given number of previously obtained output functions (three in the following example, but such a number could be increased)

$$\bar{f}_{n+1} = (1 - c_1 - c_2)Af_n + c_1Af_{n-1} + c_2Af_{n-2}, \quad (2.229)$$

and by determining c_1 and c_2 so that \bar{f}_{n+1} is the best possible solution of eqn (2.226).

This is achieved by introducing the norm

$$\Delta = \|A\bar{f} - \bar{f}\|, \quad (2.230)$$

and by minimizing Δ^2 with respect to c_1 and c_2 . We obtain the system

$$\begin{aligned} (d_{01}, d_{01})c_1 + (d_{01}, d_{02})c_2 &= (d_n, d_{01}), \\ (d_{01}, d_{02})c_1 + (d_{02}, d_{02})c_2 &= (d_n, d_{02}), \end{aligned} \quad (2.231)$$

where

$$d_{0i} = d_n - d_i, \quad (u, v) = \int dx u(x)v(x). \quad (2.232)$$

The values of c_1 and c_2 obtained from the solution of the system of equations (2.231) are then inserted in eqn (2.229) to build the input for the iteration $n + 1$.

To implement this speeding up procedure in the HNC scheme, the HNC closure (2.187) at the n th iteration step is rewritten as

$$c_n(r) = -1 - \gamma_{n-1}(r) + e^{-\beta v(r) + \gamma_{n-1}(r)}, \quad (2.233)$$

where $\gamma(r) = h(r) - c(r)$ and which, together with $c(r)$, are the functions to be determined.

The function $c_n(r)$ is Fourier transformed to $\tilde{c}_n(k)$ through a numerical Fast Fourier Transform (FFT), and it is used to obtain the function $\tilde{\gamma}_n(k)$ via the OZ equation in k -space. This function is inverse Fourier transformed, and the output of the n th iteration step, $\gamma_n(r)$, is obtained.

By using the Ng procedure, and the output $\gamma_n(r)$, $\gamma_{n-1}(r)$ and $\gamma_{n-2}(r)$, the new input $\gamma_{n+1}(r)$ is constructed. The procedure is iterated until convergence, as checked via eqn (2.228), is reached.

Although this rapidly convergent procedure is particularly appealing due to its simplicity, it suffers all the drawbacks of iterative schemes, the technical solution of which is critical for a practical numerical implementation.

The first problem is connected with the choice of the input function. Obviously, an input close to the solution will guarantee fast convergence and good stability throughout the procedure. However, the estimation of such an input is, in general, extremely difficult. In all the mentioned Fortran programs based on the iterative method, this problem is bypassed by including within the iterative loop extra loops in which the density and/or the temperature of the system are changed until they reach the values characteristic of the particular case to be solved. By starting from almost the ideal gas limit, which means from low densities and high temperatures, it is found that an input function, $\gamma_{in}(r)$, identically equal to zero is always a good input.

Other technical problems arise from the presence of discontinuities and of long-range terms in the interaction potential.

The discontinuities in the potential generate discontinuities in all the correlation functions. In turn, the discontinuities in the correlations generate errors in the numerical FFT, and the overall numerical scheme becomes unstable. A simple way of handling a discontinuity at a position r_0 in the function $c(r)$ is to generate a new smooth function

$$c^*(r) = c(r) + \theta(r_0 - r)(a + br), \quad (2.234)$$

where $\theta(r)$ is the step function and a and b are two coefficients to be determined by requiring

$$c^*(r_0^-) = c^*(r_0^+) \quad \text{and} \quad \left. \frac{dc^*(r)}{dr} \right|_{r_0^-} = \left. \frac{dc^*(r)}{dr} \right|_{r_0^+}. \quad (2.235)$$

The smooth function $c^*(r)$ is transformed by using FFT and the needed $\tilde{c}(k)$ is obtained by subtracting from $\tilde{c}^*(k)$ the analytic Fourier transform of the last term on the right-hand side of eqn (2.234):

$$\begin{aligned} \tilde{c}(k) = & \tilde{c}^*(k) - \frac{4\pi}{k^2} \left\{ a \left(\frac{\sin(kr_0)}{k} - r_0 \cos(kr_0) \right) \right. \\ & \left. + b \left[\frac{2}{k} \left(r_0 \sin(kr_0) + \frac{\cos(kr_0) - 1}{k} \right) - r_0^2 \cos(kr_0) \right] \right\}. \end{aligned} \quad (2.236)$$

This treatment reduces the error introduced by the discontinuity to $O((\delta r)^2)$, with δr the step size of the FFT, and it is equivalent to an alternative numerical approach used by Fushiki.^[58] Although the error is not fully eliminated, the procedure is consistent with the trapezoidal rule used in the numerical FFT.

Also, the instabilities introduced in the procedure by the presence of long-range order terms in the interaction potential—such as, for example, Coulombic terms—are derived from the numerics involved in the FFT. If the decay of the functions to be transformed is too slow, the accuracy of the numerical FFT is very low. To eliminate the inaccuracy, many methods have

been developed,^[59–62] all based on a rewriting of the functions to be transformed in such a way as to obtain new functions with a sufficiently fast decay.

In the method which has been extensively used to study electrolytes and molten salts,^[61,62] the direct correlation function is decomposed into short- and long-range parts. The short-range $c^{SR}(r)$ is defined as

$$c^{SR}(r) = c(r) - c^{LR}(r) = c(r) + \beta v(r)(1 - e^{-\alpha r}). \quad (2.237)$$

By using

$$c(r) \xrightarrow{r \rightarrow \infty} -\beta v(r), \quad (2.238)$$

the short-range $c^{SR}(r)$ can be made arbitrarily small outside a given distance interval $[0, r_{max}]$ by a proper choice of the parameter α :

$$e^{-\alpha r} \ll 1 \quad \text{for} \quad r \approx r_{max}. \quad (2.239)$$

The previous definition of $c^{SR}(r)$ is not unique, and other functions with simple analytical FT and with no divergences—such as, for example, $\beta v(r) \operatorname{erf}(\alpha r)$ —can equally well be chosen.

The following relations summarize an iterative HNC step for the most general case in which both a discontinuity at r_0 and a long-range term in the interaction potential are present. The function on which the iteration is performed is $\gamma^{SR}(r) = h(r) - c^{SR}(r)$:

$$c_n^{SR}(r) = -\gamma_{n-1}^{SR}(r) - 1 + \exp[-\beta v(r)e^{-\alpha r} + \gamma_{n-1}^{SR}(r)], \quad (2.240)$$

$$c_n^{*,SR}(r) = \theta(r_0 - r)(a_n + b_n r) + c_n^{SR}(r), \quad (2.241)$$

$$\tilde{c}_n^{SR}(k) = \text{FFT}[c_n^{*,SR}(r)] - \text{FT}[\theta(r_0 - r)(a_n + b_n r)], \quad (2.242)$$

$$\tilde{c}_n(k) = \tilde{c}_n^{SR}(k) - \text{FT}[\beta v(r)(1 - e^{-\alpha r})], \quad (2.243)$$

$$\tilde{\gamma}_n^{SR}(k) = \frac{\tilde{c}_n(k)}{1 - n\tilde{c}_n(k)} - \tilde{c}_n^{SR}(k), \quad (2.244)$$

$$\gamma_n^{SR}(r) = \text{FFT}^{-1}[\tilde{\gamma}_n^{SR}(k)], \quad (2.245)$$

where FT indicates the analytical Fourier transform and the coefficients a_n and b_n are determined from eqn (2.235) at each iteration step.

Since the procedure is based on direct and inverse numerical FFT, the solution of the HNC scheme has to be found on a grid of equally spaced points in real and inverse space, the intervals δr and δk of which are linked by $\delta r \delta k = 2\pi/N$, where N is the number of points used in the numerical transform. Concerning the extension of the grid and the number N of points, more accurate results are expected by using a large number of very closely spaced points. Reasonable numbers of points range from $512 \leq N \leq 2048$, while the spacing in r -space is fixed by requiring at least 40–50 points in the excluded hard core region or in an interval corresponding to the mean interparticle distance $\bar{r} = n^{-1/3}$.

Table 2.1. Available Fortran programs.^a

Systems	Integral equations	Programs
One-component hard spheres	PY	P1
Polydisperse hard spheres (Schulz distribution)	PY	P2
Yukawa spheres		
One-component	HNC, HMSA, RY	P3
Two-components	HNC, HMSA, RY	P4
Multi-component	HNC, HMSA, RY	P5
Square-well spheres	HNC, HMSA	P6

^a All FORTRAN programs are available from the second author (B. D'Aguanno) upon request.

At this point, by supplementing eqns (2.241)–(2.245) with the speeding up procedure of Ng, and by inserting such equations into the loops for the density and/or temperature, we have all the ingredients to construct a working computer program for the solution of the HNC scheme, for a variety of interaction potentials.

However, due to the intrinsic nonlinear nature of the equations and the iterative method, the computer programs cannot be fully automated. The residual instability of the algorithm and the presence, in specific regions of the thermodynamic state diagram, of multiple solutions^[63] require constant interaction with the program output in order to determine the optimal values of the parameters involved, and to check the eventual dependence of the output on the parameters. Unfortunately, there are no rigorous recipes and each case requires its own special case.

All HNC-based programs listed in Table 2.1 are constructed by following the considerations of this section.

2.5.2.2 Multi-component systems. Together with its simplicity, the solution scheme presented in the previous subsection has the advantage of being easily extendible to systems with a large number, m , of components.^[5,44] The iterative HNC step given by eqns (2.241)–(2.245) becomes:

$$c_{n,\alpha\beta}^{SR}(r) = -\gamma_{n-1,\alpha\beta}^{SR}(r) - 1 + \exp[-\beta v_{\alpha\beta}(r)e^{-\lambda r} + \gamma_{n-1,\alpha\beta}^{SR}(r)], \quad (2.246)$$

$$c_{n,\alpha\beta}^{*,SR}(r) = \theta(r_0 - r)(a_{n,\alpha\beta} + b_{n,\alpha\beta}r) + c_{n,\alpha\beta}^{SR}(r), \quad (2.247)$$

$$\tilde{c}_{n,\alpha\beta}^{SR}(k) = \text{FFT}[c_{n,\alpha\beta}^{*,SR}(r)] - \text{FT}[\theta(r_0 - r)(a_{n,\alpha\beta} + b_{n,\alpha\beta}r)], \quad (2.248)$$

$$\tilde{c}_{n,\alpha\beta}(k) = \tilde{c}_{n,\alpha\beta}^{SR}(k) - \text{FT}[\beta v_{\alpha\beta}(r)(1 - e^{-\lambda r})], \quad (2.249)$$

$$\tilde{\gamma}_{n,\alpha\beta}^{SR}(k) = ((\mathcal{R} - \mathcal{B}C_n\mathcal{R})^{-1}\mathcal{R}^{-1})_{\alpha\beta} - \tilde{c}_{n,\alpha\beta}^{SR}(k), \quad (2.250)$$

$$\gamma_{n,\alpha\beta}^{SR}(r) = \text{FFT}^{-1}[\tilde{\gamma}_{n,\alpha\beta}^{SR}(k)], \quad (2.251)$$

where $\alpha = 1, \dots, m$ and $\beta = \alpha, \dots, m$.

For cases without discontinuity and without long-range terms in the potential, the previous set of equations reduces to

$$c_{n,\alpha\beta}(r) = -\gamma_{n-1,\alpha\beta}(r) - 1 + e^{-\beta v_{\alpha\beta}(r) + \gamma_{n-1,\alpha\beta}(r)}, \quad (2.252)$$

$$\tilde{c}_{n,\alpha\beta}(k) = \text{FFT}[c_{n,\alpha\beta}(r)], \quad (2.253)$$

$$\tilde{\gamma}_{n,\alpha\beta}(k) = ((\mathcal{R} - \mathcal{RC}_n\mathcal{R})^{-1}\mathcal{R}^{-1})_{\alpha\beta} - \tilde{c}_{n,\alpha\beta}(k), \quad (2.254)$$

$$\gamma_{n,\alpha\beta}(r) = \text{FFT}^{-1}[\tilde{\gamma}_{n,\alpha\beta}(k)]. \quad (2.255)$$

Equations (2.247) and (2.253) are the HNC closure, while eqns (2.251) and (2.255) are the OZ equations in k -space.

Possible limitations on the number m of components which can be treated derive from the numerical accuracy of the matrix inversion procedure required in the OZ equations, and from the available CPU time: cases with $m = 10$ components have been successfully studied.^[5] However, the first limitations can be partially removed by symbolically inverting the matrices, and by using the explicit expressions for the set of correlations $\tilde{\gamma}_{\alpha\beta}(k)$. The mentioned Fortran programs use such explicit expressions for all cases up to $m = 5$.

2.5.2.3 Solution of thermodynamically self-consistent schemes. There are no substantial differences between the solution algorithm for the HNC scheme and for the thermodynamically self-consistent schemes, either HMSA or RY. The part to be added to the new algorithm concerns the evaluation of the isothermal compressibilities, χ_T^v and χ_T^c , from the virial and the fluctuation route, and the checking of the equality of these two quantities.

Once a mixing parameter α has been chosen (see eqn (2.199)), it is inserted in the RY (or HMSA) equation (2.198), and the corresponding RY (or HMSA) step is executed; the compressibility χ_T^c follows, in a straightforward way, from eqn (2.196). In order to evaluate χ_T^v from eqn (2.46) it is instead necessary to execute the RY (or HMSA) step for different densities (typically for n and $n \pm \Delta n$), and to evaluate the density derivative of the pressure by using finite differences. In this process, the mixing parameter α is kept constant, since it has been found to be a slowly varying function of the density n .^[5,30,64]

The algorithm for the RY (or HMSA) scheme, in the form of a pseudo-code, is stated below, where the mixing parameter α is varied by using a factor v , which is a number close to one, but either lower or higher.

The algorithm for the HMSA/RY solution scheme is as follows:

1. *{Initialize variables}*

Set n_s as the number of approaching steps to the final T_f and n_f

Set the mixing parameter α equal to a positive number

Set $\gamma_{in} = 0$

2. *{Solve HMSA/RY for the given α }*

for $i := 1$ to n_s

$T := T_f n_s / i;$

$n := n_f i / n_s;$

```

repeat
    evaluate  $\gamma_{out}$  from a HMSA/RY step;
    generate a  $\gamma_{in}$  from Ng procedure;
    until (converging criterion is met)
endfor
3. {Solve HMSA/RY for thermodynamic consistency}
repeat
    for  $i := -1, 0, 1$ 
     $n := n + i\Delta n;$ 
    repeat
        evaluate  $\gamma_{out}$  from HMSA/RY step;
        generate a  $\gamma_{in}$  from Ng procedure;
        until (converging criterion is met)
    endfor
    evaluate  $\chi_T^v, \chi_T^c$ 
     $\alpha := v\alpha;$ 
until (thermodynamic self-consistency criterion is met)
Output correlation functions, measured structure factor, and thermodynamic quantities

```

The extension of this RY/HMSA algorithm to multi-component systems is also straightforward. Note that now the mixing parameter α has, in principle, to be replaced by a set of parameters $\alpha_{\alpha\beta}$, and a new problem arises. Although for an uncharged system with m components there are m thermodynamic constraints (in fact, it is possible to define m partial compressibilities), the number of $\alpha_{\alpha\beta}$ is $m(m + 1)/2$. Thus, it is necessary to impose extra conditions on the choice of some of the $\alpha_{\alpha\beta}$ parameters. Many possibilities have already been investigated in the literature,^[30,64,65] but here, for the sake of simplicity, we restrict ourselves to $\alpha_{\alpha\beta} = \alpha$ for all indices, satisfying only the constraint on the total compressibility.

2.6 Applications

2.6.1 Monodisperse hard sphere systems

The hard sphere potential is the simplest interaction model which is useful to interpret scattering data from concentrated dispersions. It describes excluded volume effects due to the finite size of the colloidal particles. In nature, silica particles coated by octadecyl chains in good solvents^[66,67] and sterically stabilized PMMA particles in a decalin/CS₂ solvent mixture are the best realization of the HS model. Strong evidence is provided by the ‘phase diagram’ of the PMMA particles,^[68] which nicely fits the predictions of the density functional theory of freezing, as obtained by using PY correlation functions.^[69]

However, the best test of the accuracy of the integral equation results is given by comparison with exact simulation data. The pair distribution function, $g(r)$, of a HS system with $\phi = 0.4$ is shown in Fig. 2.1. The PY scheme underestimates

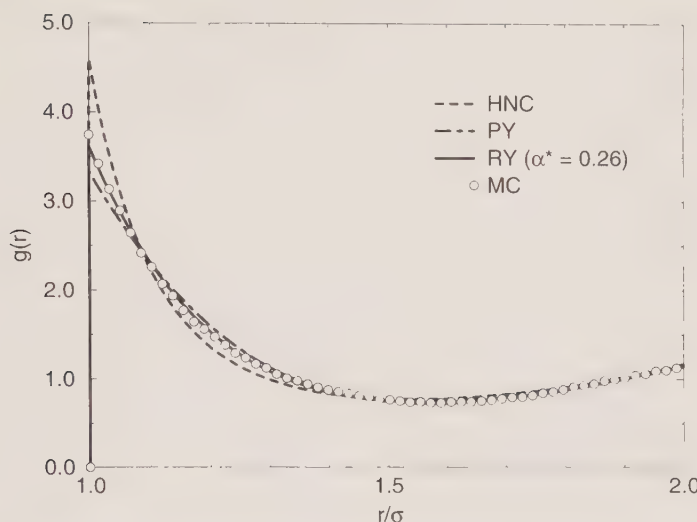


FIG. 2.1. The pair distribution function $g(r)$ for HS at $\phi = 0.4$. The parameter α^* is the RY mixing parameter in units of σ .

the value of $g(r)$ at contact, while this value is overestimated by HNC. For larger distances, the disagreement between the schemes reduces, although oscillations are slightly out of phase and, as for the contact value, the MC data lie between the HNC and PY results. These observations led Rogers and Young^[29] to propose the RY thermodynamically self-consistent scheme, which continuously interpolates between PY and HNC. It turns out that the agreement of the RY results with the MC data of Fig. 2.1 is quantitative, recovering the exact contact value and the phase of oscillations.

The RY results of the structure factor $S(k)$, which in this case is directly linked to the scattered intensity (see eqn (2.151)), are shown in Fig. 2.2 for different densities. At $\phi = 0.5$ (the freezing density of HS), the PY and HNC results are also shown. The peak value of $S(k)$ is overestimated by PY and this is connected with the persistence of oscillations in $g_{PY}(r)$ at large r . In addition, the PY peak value, which is larger than 2.92, violates the empirical Hansen–Verlet rule for freezing localization.^[70] As the density is reduced, the system becomes more disordered and more ‘gas-like’. This information is reflected in the main peak of $S(k)$, which reduces and broadens, in its position which, being proportional to the inverse mean interparticle distance, is shifted to the left, and in the value of $S(0)$ (or compressibilities; see eqn (2.62)), which increases strongly.

The equation of state obtained from RY is also in quantitative agreement with the exact MC data. This is another consequence of the interpolation nature of the RY scheme. In fact, the MC data for the equation of state lie between the HNC and PY results (see Fig. 5.4 of Hansen and McDonald^[11]) according to

$$p_{HNC}^v > p_{PY}^c > p_{MC} > p_{PY}^v > p_{HNC}^c,$$

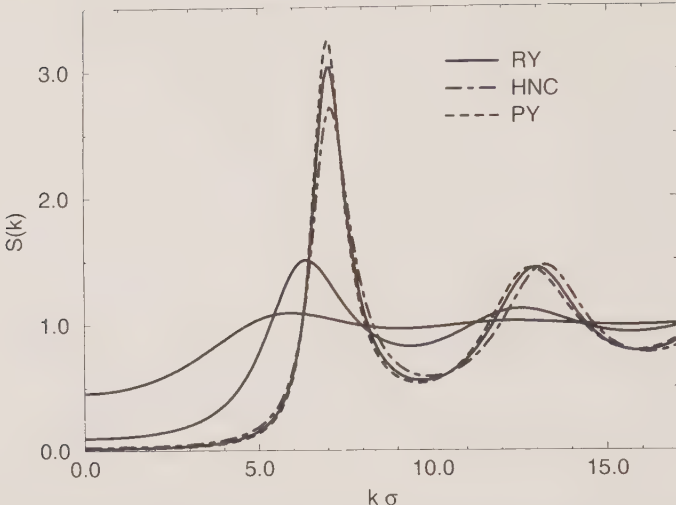


FIG. 2.2. The structure factor $S(k)$ for HS at three different densities. The most structured $S(k)$ corresponds to $\phi = 0.5$, the less structured to $\phi = 0.1$ and the intermediate one to $\phi = 0.3$.

where the superscripts c and v indicate the compressibility and the virial route, respectively.

The Verlet–Weis parameterization for the pair distribution function and the Carnahan–Starling empirical equation for the pressure (see Section 2.5.1.), produce results which are indistinguishable from the RY and, consequently, are in good agreement with MC data. For routine work on monodisperse HS, well inside the liquid phase, these approaches appear to be computationally the most convenient.

2.6.2 Polydisperse hard sphere systems

In this section we present a systematic application of the methods described in Section 2.5.1.2 to HS systems with a varying degree of polydispersity s .

All of the results reported in this section are obtained by using the PY solution method of Griffith, Triolo and Compere^[51,52] presented in Appendices 2.B and 2.C (which utilizes Fortran program P2), and by using the relations and definitions given in Section 2.5.1.2. The particle size distribution is always described by the Schulz distribution of eqn (2.217) and the particles are assumed to be homogeneous scatterers (see eqn (2.159)). The investigated systems are polydisperse HS systems at fixed volume fraction with increasing polydispersity s . Since in polydisperse systems the volume fraction is given by

$$\phi = \frac{\pi}{6} n \langle \sigma^3 \rangle,$$

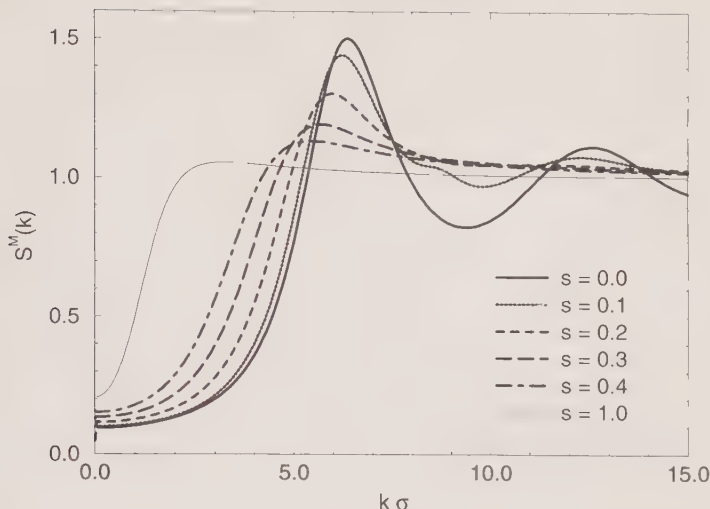


FIG. 2.3. The measured structure factor $S^M(k)$ at a constant volume fraction $\phi = 0.3$ for several standard deviations, s , of the particle diameter distribution. The diameter distribution is the Schulz distribution and the HS are homogeneous scatterers. Results from program **P2**.

with $\langle \sigma^3 \rangle$ the third moment of the particle size distribution function, a constant ϕ with an increasing s (and also $\langle \sigma^3 \rangle$) implies systems with decreasing number density n .

We first analyze the effects of s on the measured structure factor $S^M(k)$ (see eqns (2.162) and (2.C.1)). From Fig. 2.3 we observe several striking modifications of $S^M(k)$ as a function of increasing s : (i) the main peak of $S^M(k)$ is reduced; (ii) it is shifted to lower k -values; (iii) it is broadened; (iv) the oscillations after the main peak are washed out; and (v) the $k = 0$ value of $S^M(k)$ is increased. Equation (2.162) clarifies that the features are a combination of both *intra-* and *interparticle* effects, and then no longer connected to a clear statistical mechanics interpretation.^[5, 71] In particular: (i) the position of the main peak of $S^M(k)$, k_{max} , no longer scales, as in the case of monodisperse systems, with $n^{1/3}$ and, therefore, it is no longer a measure of the mean interparticle distance; (ii) the peak value of $S^M(k)$ can no longer be used as a signature of the microscopic order; and (iii) $S^M(k = 0)$ does not coincide with the normalized isothermal compressibility, $n k_B T \chi_T$, as is the case for monodisperse systems. Thus, to understand the new physics introduced by the polydispersity, it is better to study quantities such as the number number structure factor $S_{NN}(k)$ (see eqn (2.102)), and the isothermal compressibility χ_T (see eqn (2.97)).

In Fig. 2.4 we show $S_{NN}(k)$ for the systems of Fig. 2.3. The reduction of the main peak of $S_{NN}(k)$ for increasing s is now associated with an increase in the microscopic ‘disorder’ of the polydisperse particles. The monodisperse system was at the freezing density and it has, essentially, been ‘melted’ by the

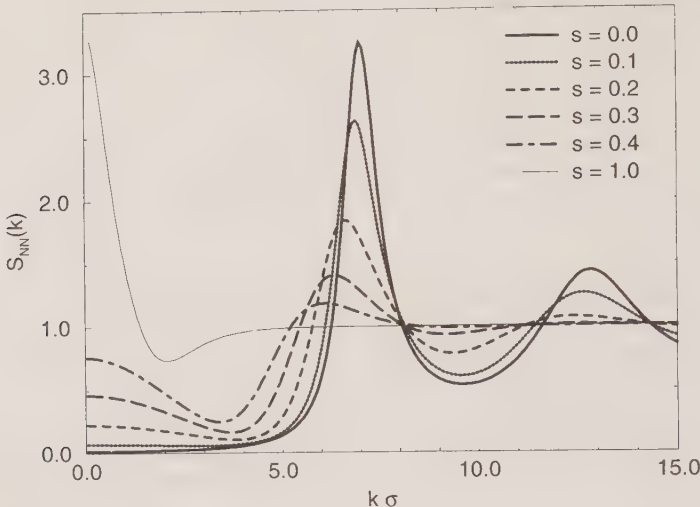


FIG. 2.4. The number–number structure factor $S_{NN}(k)$ at a constant volume fraction $\phi = 0.5$ for several standard deviations of the particle diameter distribution. Other conditions are as in Fig. 2.3. Results from program P2.

polydispersity. The residual shift of the main peak to low k -values is due to the reduction of the total number density n . The behaviour at small k is mostly determined by the strongly fluctuating small particles of the size distribution. With increasing s there is an increasing number of these small particles, which produce the observed increase in $S_{NN}(k)$ for $k \rightarrow 0$. As observed in Fig. 2.3, this latter effect is less drastic for $S^M(k)$. This is due to the form amplitudes $f_\alpha f_\beta \approx \sigma_\alpha^3 \sigma_\beta^3$ in eqn (2.162), which reduce the importance of the strongly fluctuating small particles. Nevertheless, there is a strong effect of polydispersity on the long-wavelength scattered intensity, as shown in Fig. 2.5. A polydispersity of $s = 0.2$ nearly doubles $I(k = 0)$ as compared to the monodisperse case. Thus, an experimentalist might detect such a deviation if trying to fit the experimental results using a monodisperse model.^[72]

The variation of the isothermal compressibility, χ_T , of polydisperse HS systems as a function of s is shown in Fig. 2.6, together with $S^M(0)$ and the rescaled compressibility $\chi_T^* = nk_B T \chi_T$. The systems have a constant volume fraction of $\phi = 0.3$. In this case, the increase in s generates an increase in χ_T (see eqn (2.224)). However, if the calculations are performed at constant n , then χ_T decreases. A more important indicator from this figure is the difference (although not large) between $S^M(0)$ and χ_T^* . It shows that in polydisperse systems the identification of the structure factor at $k = 0$ with the rescaled compressibility, which is the case for monodisperse systems, is no longer valid. This fact has immediate consequences for the interpretation of light scattering experiments and the determination of isothermal compressibility.

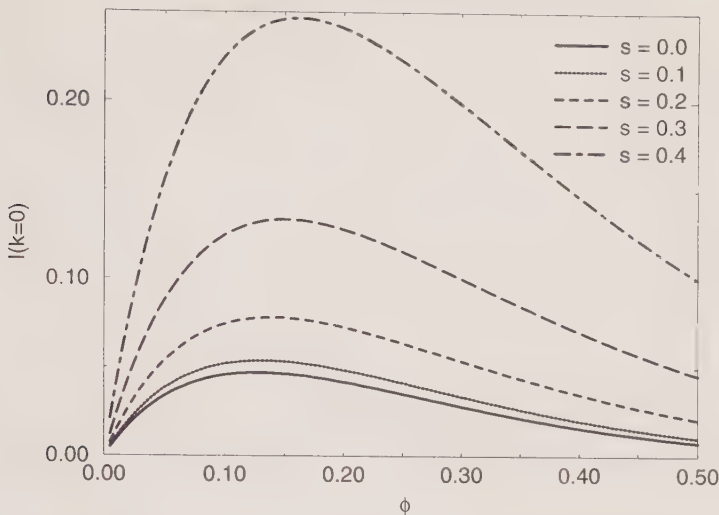


FIG. 2.5. Scattering intensity at $k = 0$ as a function of the volume fraction ϕ for HS suspensions of various degrees of polydispersity. The data are obtained from $I(0) = \xi_2(\xi_6 - 6\xi_4\xi_5/(1 + 2\xi_3) + 9\xi_4^3/(1 + 2\xi_3)^2)$.

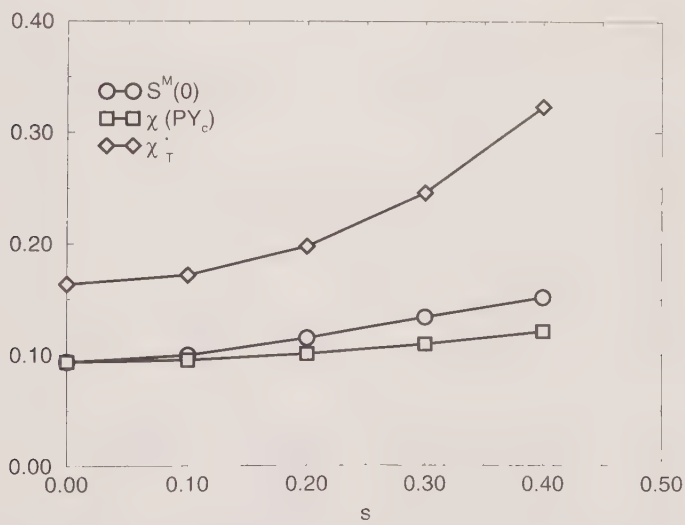


FIG. 2.6. The measured structure factor $S^M(0)$, the rescaled isothermal compressibility χ^* and the isothermal compressibility χ_T for PHS at a constant $\phi = 0.3$ as a function of s .

The effect of the polydispersity on the pressure, as determined from the generalized Carnahan and Starling equation (2.222), is shown in Fig. 2.7. The results from this equation have been compared with MC data^[73] from PHS and from two-component systems chosen according to the requirements of

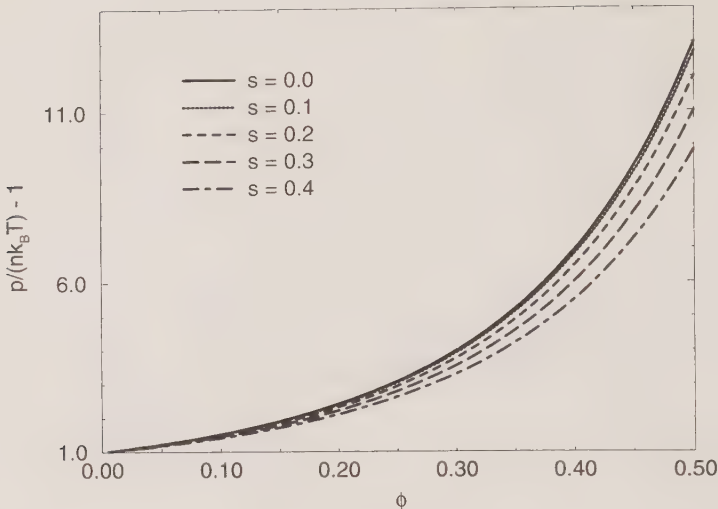


FIG. 2.7. The Carnahan and Starling excess pressure of PHS systems as a function of volume fraction ϕ and for several degrees of polydispersity.

eqn (2.225). It has been found that the two-component systems describe quantitatively the equation of state for all thermodynamic states that are not close to phase transitions.

The results from PY have also been compared with simulation results and experimental data. Frenkel *et al.*^[74] performed MC simulations on a set of polydisperse HS particles described by the log-normal distribution, and for two scattering particle models: the homogeneous and the thin shell scattering models. A good agreement with the PY results, as obtained from the Vrij solution method,^[54,55,75] is found, except for the highest investigated density ($\phi = 0.5$), at which it is already known that for monodisperse systems PY shows perceptible deviations from exact data.

Comparisons of PY results and experimental scattering data have been presented by de Kruif *et al.*^[66] They analyzed the measured structure factor, $S^M(k)$, for concentrated dispersions in cyclohexane of silica particles sterically stabilized by octadecyl chains terminally grafted to the surface, by means of Small Angle Neutron Scattering. Although the authors concluded, from measurements at low densities, that the silica dispersions were properly described by a polydisperse HS model, the fitting of high-concentration data with PY results from such a model was found to be unsatisfactory. However, since the small k region was always accurately described, the disagreement between theory and experiment has to be mainly associated with experimental difficulties in the data statistics at large k , rather than to failure of the theory.

2.6.3 Monodisperse Yukawa sphere systems

The most frequently employed model for the description of suspensions of electrostatically stabilized colloidal particles is the Yukawa sphere model.^[26,27,76–80] It has been used successfully to describe scattering data on real suspensions of polystyrene particles in aqueous solvents.^[5,81–83]

The results that we shall present have been obtained by using the following Yukawa-type interaction potential:

$$\begin{aligned}\beta v(r) &= \infty & r < \sigma, \\ &= \frac{Q^2}{4\pi e\epsilon_0 k_B T} \frac{e^{\kappa\sigma}}{(1 + \kappa\sigma/2)^2} \frac{e^{-\kappa r}}{r}, & r > \sigma,\end{aligned}$$

where Q is the ‘effective’ charge on a particle and $\kappa = (enQ/(\epsilon\epsilon_0 k_B T))^{1/2}$ denotes the inverse Debye–Hückel screening length, with e the electronic charge. The effective charge is introduced in order to write the potential in a DLVO form^[76] and, strictly speaking, it does not have an obvious physical meaning.^[79] This Yukawa potential is then characterized by a hard core part and a repulsive tail. The presence of the tail, and the interplay between the hard core and the tail, generate a different microstructure of the particles as compared, for instance, to the HS of the previous section. For these reasons, we now concentrate on structural functions.

The accuracy of the PY, HNC and RY schemes in describing Yukawa sphere (YS) systems is shown in Fig. 2.8, where the results for the pair distribution function, $g(r)$, are compared with MC data. In contrast to the HS case (see

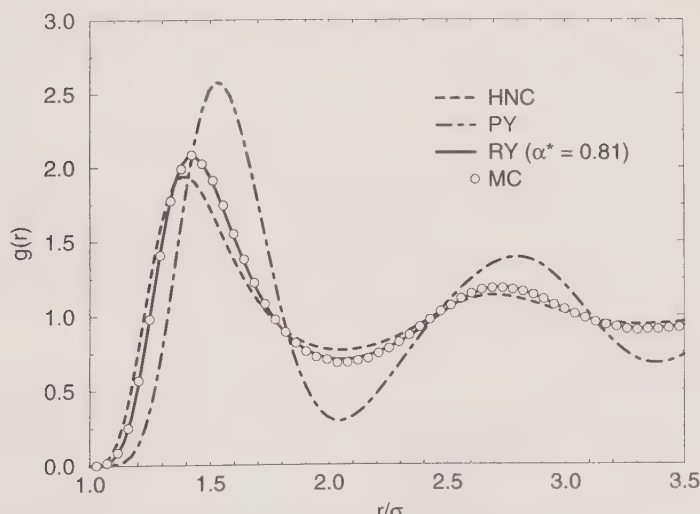


FIG. 2.8. MC, PY, HNC and RY results for $g(r)$ of a monodisperse system of Yukawa particles. The full set of system parameters is given in Méndez-Alcaraz, D’Aguanno and Klein.^[93] HNC and RY results from program P3.

Table 2.2. $P^{ex}/nk_B T$ and $U^{ex}/Nk_B T$ for the monodisperse Yukawa system in Fig. 2.8.^a

	MC	PY	HNC	RY
$P^{ex}/nk_B T$	18.12	16.17 ^v	18.91 ^v	18.13 ^v
$U^{ex}/Nk_B T$	7.64	6.57 ^c	8.08 ^c	7.65 ^c

^a Superscripts *v* and *c* refer to the virial equation and to the compressibility equation, respectively.

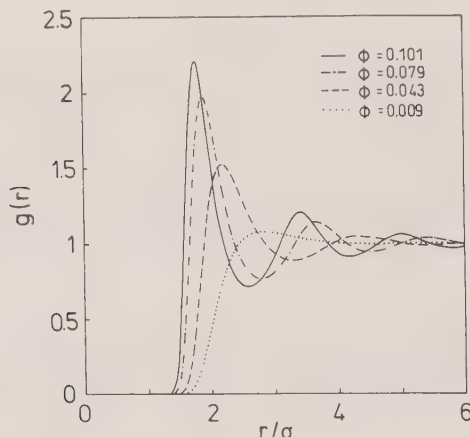


FIG. 2.9. HNC results for $g(r)$ of a monodisperse system of Yukawa particles at different densities. The full set of system parameters is given in Nägele, Kellerbauer, Krause and Klein.^[102] Results from program P3.

Fig. 2.1), the PY results now overestimate and the HNC results underestimate the structure of $g(r)$, although HNC is more accurate than PY. The agreement between the RY results and the MC data is excellent. Thermodynamic consistency ($\chi_T^c = \chi_T^v$) was obtained for the mixing parameter $\alpha = 0.81$, showing the RY scheme to contain more HNC than for HS. Other RY/MC comparisons are given in D'Aguanno and Klein.^[5]

Results for the excess pressure and the internal energy for the system of Fig. 2.8 are given in Table 2.2. In view of the results for the pair distribution function, it is no surprise to observe the very good agreement between RY and MC for the thermodynamics of the system.

The role played by the Yukawa tail (or electrostatic repulsion) is demonstrated in Fig. 2.9, where HNC results for $g(r)$ are shown. The strong electrostatic repulsion keeps the particles apart from each other such that configurations with particles at contact are highly unlikely. For the cases shown in the figure, the main maxima of $g(r)$ are around $\approx 2\sigma$, while for HS they are always at

contact. Also important is the amount of local order which is introduced by the electrostatic repulsion. A well defined first peak is obtained already at low volume fraction, for example at $\phi = 0.079$, where the corresponding HS system has a structureless $g(r)$. A further increase in ϕ produces well defined shells of nearest and next-nearest neighbours, but even at $\phi = 0.1$ there remains a volume around each particle from which other particles are excluded. Although not shown, these kinds of qualitative conclusions are true for RY results.

2.6.4 Polydisperse Yukawa sphere systems

2.6.4.1 The effective mixture. The generalization of the treatment given in the previous section to the description of polydisperse Yukawa sphere systems or, better, of suspensions of polydisperse spherical and charge-stabilized colloidal particles, is by no means trivial. As already observed in Fig. 2.8, the best description of Yukawa systems is achieved by using the RY scheme. We shall show how infinitely-many-component, or continuous polydisperse, systems can be successfully described in the framework of the RY closure, which only has numerical solutions (see Section 2.5.2.3): this point appears to be a serious handicap if one wants to apply the RY scheme to a case with infinite components.

To overcome this difficulty, the continuous distribution $F(\sigma)$, which can describe the distribution of charges, sizes and therefore of interaction strengths, is replaced by a m -component histogram (possibly with a small m). It is then necessary to determine the parameters σ_i , $i = 1, \dots, m$, and the number fractions w_i . They are obtained by requiring the equality of the first $2m$ moments of both the continuous and discretized distributions:^[5,44]

$$\sum_{i=1}^m w_i \sigma_i^p = \int d\sigma F(\sigma) \sigma^p, \quad p = 0, 1, \dots, 2m-1.$$

The continuous polydisperse system is, therefore, replaced by an ‘effective mixture’ of m different species identified by the parameters $\{\sigma\}$ and by the number fractions $\{w\}$. For this effective mixture, the RY scheme can be solved by using the procedure detailed in Sections 2.5.2.2 and 2.5.2.3.

As a consequence of the histogrammatic reduction, quantities such as $g_{NN}(r)$ and $S^M(k)$, which for continuous polydispersities are given as integrals over the variable σ , are now expressed by summations over m :

$$\begin{aligned} g_{NN}(r) &= \int d\sigma \int d\sigma' F(\sigma) F(\sigma') g_{\sigma\sigma'}(r) \simeq \sum_{\sigma=1}^m \sum_{\sigma'=1}^m w_\sigma w_{\sigma'} g_{\sigma\sigma'}(r), \\ S^M(k) &= \frac{\int d\sigma \int d\sigma' F(\sigma) F(\sigma') f_\sigma(k) f_{\sigma'}(k) S_{\sigma\sigma'}(k)}{\int d\sigma F(\sigma) f_\sigma^2(k)} \\ &\cong \frac{\sum_{\sigma=1}^m \sum_{\sigma'=1}^m w_\sigma w_{\sigma'} f_\sigma(k) f_{\sigma'}(k) S_{\sigma\sigma'}(k)}{\int d\sigma F(\sigma) f_\sigma^2(k)}, \end{aligned}$$

The integral in the denominator of the last equation is not rewritten as a sum,

since it can be evaluated analytically. A collection of analytical results for various $F(\sigma)$, and for $f_\sigma(k)$ given in eqn (2.159), has been reported by Sheu.^[84]

On the basis of the observation that the previous transformation from integrals to sums can also be achieved using numerical methods for integral evaluation, it has been shown^[44] that the histogrammatic reduction is equivalent to a reduction obtained by using a p -point Gauss-generalized Laguerre quadrature method, once one tries to evaluate in the most accurate way quantities such as $g_{NN}(r)$ and $S^M(k)$. By this latter approach it turns out that the number m of components of the effective mixture is small ($m \approx 3$). Thus, if some inaccuracy is present in the results it can be mainly traced back to the closure scheme used for the evaluation of the correlation functions, rather than to the proposed histogrammatic reduction.

2.6.4.2 Systematic analysis. The test of the accuracy of the effective mixture model has been performed by comparing RY results obtained from a three-component mixture with MC data from the corresponding continuous polydisperse system.^[44] Here we report the results for $g_{NN}(r)$, as a function of the standard deviation s . The particles interact through the potential

$$\beta v_{\sigma\sigma'}(r) = \infty \quad r < \frac{\sigma + \sigma'}{2},$$

$$= \frac{1}{4\pi\epsilon_0 k_B T} \frac{Q_\sigma e^{\kappa\sigma/2}}{(1 + \kappa\sigma/2)} \frac{Q_{\sigma'} e^{\kappa\sigma'/2}}{(1 + \kappa\sigma'/2)} \frac{e^{-\kappa r}}{r}, \quad r > \frac{\sigma + \sigma'}{2},$$

which generalizes the Yukawa potential of the monodisperse case. In addition, the particles are polydisperse in size with a constant surface charge density. The polydisperse function $F(\sigma)$ is given by the Schulz distribution.

The results are shown in Fig. 2.10 where, for all cases, quantitative agreement is observed, proving that both the RY scheme and the effective mixture model are genuinely good approximations. In the RY calculations, only $m = 3$ components are used.

Once the reliability of the method is established, the effects of polydispersity on structural quantities can be safely analysed. Several cases can be studied in which the polydispersity s is changed by either keeping the number density n or the volume fraction ϕ constant, and by having both charge and size polydispersity or charge polydispersity only.

Figure 2.11 shows the measured structure factor $S^M(k)$ for systems with different values of s , a constant n , and with both charge and size polydispersity. The number of components in the effective mixture ranges from $m = 3$, for $s = 0.1$, to $m = 9$, for the case with $s = 0.4$. Qualitatively, the effects of polydispersity on $S^M(k)$ are similar to those in the PHS (see Section 2.6.2). However, a closer analysis of $S^M(k = 0)$, as compared to $S_\chi(k = 0)$ (see eqns (2.106) and (2.107)), reveals that, in this case, the effects are drastically enhanced. Figure 2.12 shows these two quantities for the systems of Fig. 2.11. While $S_\chi(k = 0)$ is practically unchanged (a slight decrease is actually observed

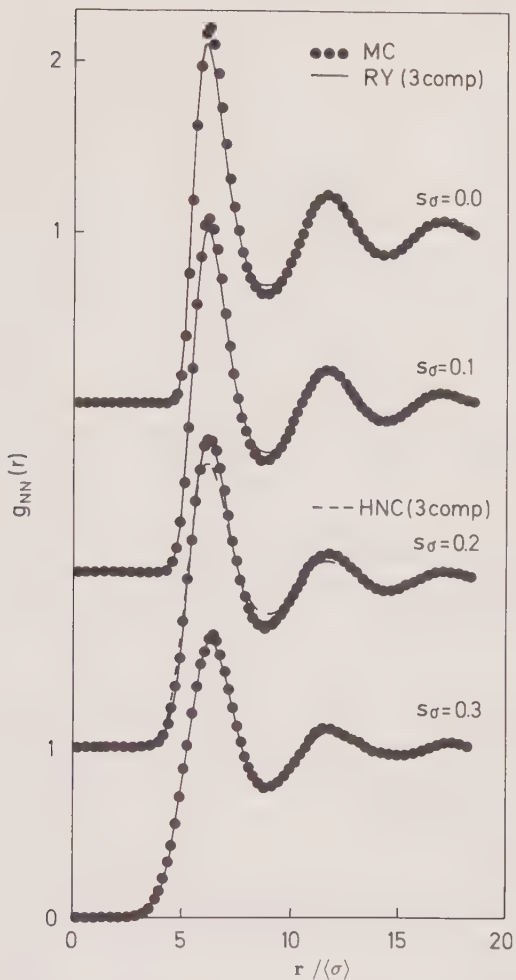


FIG. 2.10. MC and RY results for $g_{NN}(r)$ versus the reduced distance $r^* = r/\langle\sigma\rangle$. Except for the monodisperse case, the RY results are from the $m = 3$ effective mixture model. System parameters are given in ref. 44. RY results from program P5.

as a consequence of the increase in the ‘mean’ electrostatic interaction^[5]), the value of $S^M(k=0)$ increases by roughly two orders of magnitude when s varies from 0 to 0.4. This fact has immediate consequences for the interpretation of light scattering experiments to obtain χ_T . For $s = 0.1$, $S^M(k=0)$ is already larger by a factor of 3 than for the corresponding monodisperse system, whereas the compressibility is practically unchanged.

At a fixed volume fraction ϕ , the shift of the main peak of $S^M(k)$ to a smaller k -value with increasing s is more pronounced, while the effects on the peak height and on the value at $k = 0$ are rather similar, as in the case of constant

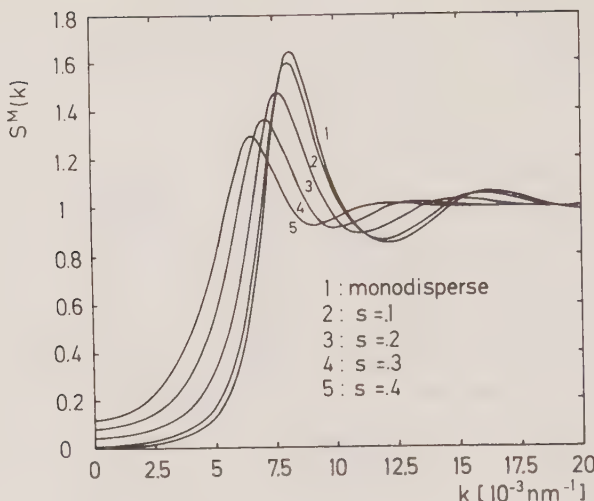


FIG. 2.11. The measured structure factor $S^M(k)$ as determined from the RY scheme (program P5) for several degrees of polydispersity. The full set of system parameters is given in D'Aguanno and Klein.^[5]

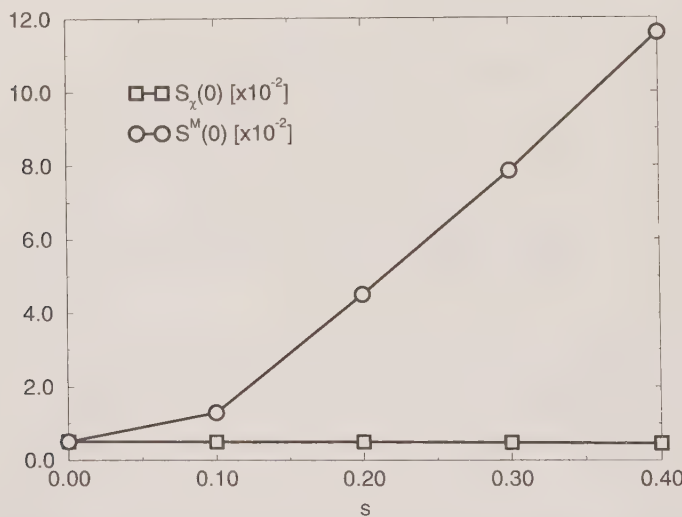


FIG. 2.12. $S^M(k = 0)$ and $S_\chi(k = 0)$ as functions of the standard deviation, s , for the systems of Fig. 2.11. RY results from program P5.

n. However, at constant ϕ we have to distinguish between the behaviour of $S_\chi(k = 0)$ and the isothermal compressibility χ_T . Figure 2.13 shows $S^M(k = 0)$, $S_\chi(k = 0)$ and χ_T . The behaviour of $S^M(k = 0)$ and $S_\chi(k = 0)$ is similar to that of Fig. 2.12, while χ_T increases. A constant ϕ implies a decreasing density

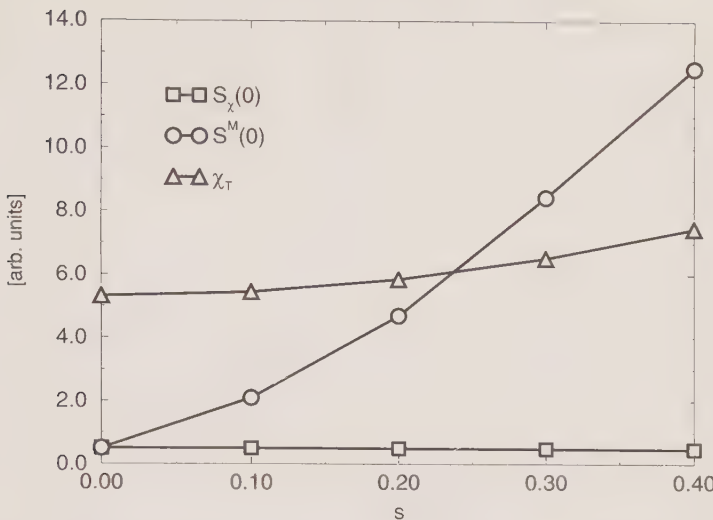


FIG. 2.13. $S^M(k = 0)$, $S_\chi(k = 0)$ and χ_T as functions of the standard deviation, s , for systems at constant ϕ . The full set of system parameters is given in D'Aguanno and Klein.^[5] RY results from program **P5**.

when the polydispersity is increased and, consequently, the system becomes softer, which is just the opposite behaviour to that of the system of Fig. 2.12.

The effects of charge and size polydispersities on the microscopic particle structure are better understood from the viewpoint of the Bhatia Thornton structure factors introduced in Section 2.2.3.2. Here, we only mention that, for the systems of Fig. 2.11, the increase in s destroys the ‘concentration order’, which means the order of particles regardless of their charge, whereas a certain degree of ‘charge order’ starts to develop. For further details, the reader may refer to D'Aguanno and Klein.^[5]

2.6.4.3 Comparison with experiments. All of the efforts expended in the last two sections find their natural and conclusive applications in comparisons with experimental data. Many of these comparisons have been published in the literature,^[5,81–83] and from this body of work we have selected the example shown in Fig. 2.14.

When integral equations are used in connection with experimental data, the charge on the particles is left as a free parameter to be determined from the fitting of the main peak value of the experimentally measured structure factor. The results of this procedure, for both the monodisperse and the effective mixture models, are shown in Fig. 2.14. The monodisperse model can fit the main peak nicely, but it fails to describe the experimental data in the small- k region, where they are systematically too high, and in the region following the first peak, where they are systematically out of phase. Instead, the agreement

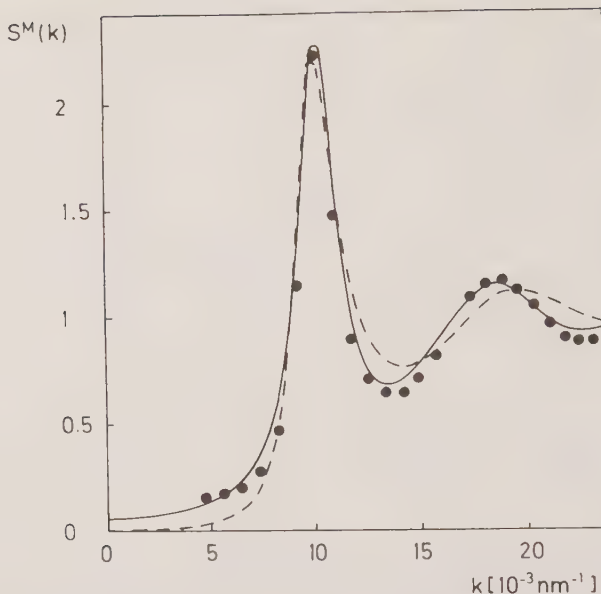


FIG. 2.14. The measured structure factor $S^M(k)$. ●, Experimental data from sample 3 of Krause *et al.*^[103]; —, RY results from the effective mixture model with $s = 0.2$; - - -, RY results from a monodisperse model. The full set of system parameters is given in D'Aguanno and Klein.^[5] RY results from program P5.

between the results from the effective mixture model and the experimental data is quantitative: the real system is polydisperse and must be treated as such. In addition, it turns out that the average value $\langle Q \rangle$ for the charge of the effective mixture model, which is necessary to obtain a good fit to the experimental results, is substantially higher than the value of the charge obtained from the fit of the monodisperse model to the main peak. This fact should be considered when effective charges on colloidal particles or ionic micelles are determined by fitting the measured structure factors.

To close this section, we briefly mention that this treatment of polydispersity can be applied to the *inverse problem*; namely, to the characterization of colloidal particles and suspensions from scattering data. The exact determination of the density of the suspension, of the refractive index of the particles and of the shape and the moments of the size distribution, requires the simultaneous fitting of several experimentally accessible quantities with the results from the effective mixture model. The experimental quantities to be analysed are the measured structure factor, the averaged form factor, and the Porod^[85] and the Guinier and Fournet^[86] plots. A successful application of this methodology to the inverse problem can be found in Wagner *et al.*^[82]

2.6.5 Binary mixtures

2.6.5.1 Mixtures of hard spheres. In contrast to monodisperse systems there are fewer experimental studies of binary mixtures of hard spheres. Cuits, May, Vrij and de Kruif^[87] made small-angle neutron scattering experiments on binary mixtures of silica particles by using the contrast variation technique. However, although the separate pure components interact through a HS potential, the experimental partial structure factors show marked deviations from the HS behaviour.

Theoretical results have been reported by Méndez-Alcaraz^[88] by using the RY scheme with only one mixing parameter α . The author studied the structure factors $S^M(k)$, $S_{NN}(k)$ and $S_\chi(k)$ as a function of the number fraction $x_1 = n_1/n$. The systems are characterized by a size ratio $\sigma_2/\sigma_1 = 2$ and a constant total volume fraction $\phi = 0.4$. All three structure factors change in a non-monotonous way as a function of x_1 . In particular, $S^M(0)$ has a maximum at $x_1 \approx 0.95$ and $S_{NN}(0)$ at $x_1 \approx 0.9$, which almost coincide with the position of the maximum of the standard deviation of the diameter distribution, $x_1 \approx 0.97$. It is concluded that such quantities are strongly controlled by the bidispersity of the system. Instead, the maximum of $S_\chi(0)$ is at $x_1 \approx 0.6$. This behaviour is explained, in a qualitative way, by saying that at $x_1 \approx 0.6$ it is easier to accommodate small particles in the empty space in between the large ones and, therefore, to compress the system.

Theoretical studies have been extended to large size asymmetries by Biben and Hansen.^[89] They studied concentrated mixtures with size ratios going from 0.5 to 0.1. By using the RY scheme, they were able to determine a spinodal decomposition line. Indications of such a phase transition have been found experimentally by van Duijneveldt, Heinen and Lekkerkerker.^[90]

2.6.5.2 Mixtures of Yukawa spheres. Extensive comparisons of static light scattering data with integral equation results have been given in a series of papers.^[81,83,91] In the work of Krause *et al.*^[81] the systems studied were binary mixtures of polystyrene spheres, with both charge and size bidispersity, while in D'Aguanno *et al.*^[83] binary mixtures of polystyrene particles, with equal size but with different charge, were considered. A satisfactory agreement between the experimental data and the HNC and/or RY results has always been found. Structure factors have first been measured for the one-component systems. By using the RY scheme to fit the peak values of $S^M(k)$, the effective charges Q_1 and Q_2 to be used in the interaction potential were obtained. By keeping these values fixed, the structure factors $S^M(k)$ were calculated for all samples with different compositions. However, some discrepancies between theory and experiments remain in the region of small k -values, where the experimental data are above the theoretical results, and at large k , where the oscillations are out of phase. From the experience gained by studying polydisperse systems, the authors repeated the analysis, associating an intrinsic polydispersity to both constituents of the mixtures. By using an intrinsic polydispersity with a standard

deviation of $s = 0.1$, all fine details of $S^M(k)$ were reproduced, and the separate effects of the bidispersity and of the intrinsic polydispersity were clearly identified. In conclusion, it can be stated that all details of the measurable structural properties of binary mixtures of either charge, or charge and size bidisperse mixture, can be reproduced and understood in terms of integral equation theories.

A systematic theoretical analysis of the microscopic structure of binary Yukawa mixtures has been presented by Méndez-Alcaraz, D'Aguanno and Klein.^[8] In this case, the variation of all structural functions is analysed by fully exploiting the molar fraction range from one pure component to the other. In addition, the effects of both charge and size polydispersity are examined separately in order to understand their importance.

At first, a series of three mixtures with a constant number density, an equimolar composition, equal diameters and with increasing charge bidispersity is considered. As the charge asymmetry is increased, $S^M(0)$ increases, whereas the height of the main peak of $S^M(k)$ decreases; note that in the present case $S^M(k) = S_{NN}(k)$ (see Section 2.3.2.5 and eqn (2.170)). The decrease of the peak value of $S_{NN}(k)$ (see eqn (2.108)) arises mainly from the decrease of the total mean charge of the systems, which also results in a decrease of the mean interaction strength. The progressive reduction of the concentration order is accompanied by an increase in the charge order, which is described by $S_{CC}(k)$ (see eqn (2.109)), and in the coupling of charge and concentration fluctuations, as measured by $S_{NC}(k)$ (see eqn (2.110)). Finally, the main peak of the compressibility structure factor, which is defined in eqn (2.111), decreases appreciably, while the compressibility, $S_\chi(0)$, remains practically constant. The behaviour of $S^M(k)$ was also observed in the experimental studies described at the beginning of this section.

The case with size bidispersity only gives rise to practically constant Bhatia–Thornton structure factors, since they do not depend explicitly on the particle size. A weak dependence is, however, expected because the Yukawa potential (see Section 2.6.4.2) contains the particle size. In contrast to this behaviour, the increase in the size bidispersity generates a strong increase in $S^M(0)$, due to the incoherent scattering, and a decrease in the peak value of $S^M(k)$.

2.6.5.3 Mixtures of hard and Yukawa spheres.

Although mixtures of hard and Yukawa particles are of interest for several reasons, they are experimentally even less studied than the systems reviewed in the last two sections. Hanley, Straty and Lindner^[92] performed measurements on binary mixtures of silica and polystyrene spheres using small-angle neutron scattering.

The reasons of interest are twofold: one, which is more technical, is connected with the closure relations; and the other is related to the competition of two different length scales. In Sections 2.5.1.1 and 2.6.1, we have already observed that the relevant length scale in HS systems is given by the HS diameter σ_H . Later (in Section 2.6.3), we saw that in systems of charged colloidal particles

(Yukawa particles) the physical diameter σ_Y is fairly unimportant, since the long-range repulsion keeps the particles apart. The characteristic length scale is, therefore, the mean interparticle distance d , which scales with the number density as $d \propto n^{-1/3}$. Because of these two length scales in the pure systems, interesting effects can be expected when they are mixed in different proportions. Here, we briefly review the effects of mixing on thermodynamic and structural properties. The reader interested in the technical aspects connected with the solution of the RY scheme for such systems is referred to the work of Méndez-Alcaraz, D'Aguanno and Klein.^[93]

RY results for $S^M(k)$ have been reported^[93] for five mixtures with compositions $x_Y = 0, 0.3, 0.6, 0.9$ and 1 , with $\sigma_H = \sigma_Y$ and with a constant total volume fraction. For $x_Y = 0.3$, the main peak of $S^M(k)$ remains at $k\sigma_H \approx 2\pi$, as in monodisperse hard sphere systems; the only visible effect of this change of composition is the appearance of a small shoulder at $k \approx k_{max}/2$. This shoulder grows, and for $s = 0.6$, which corresponds to the replacement of 60% of HS with Yukawa spheres, $S^M(k)$ has a double peak. By further increasing x_Y , the old peak at $k\sigma_H$ disappears, and for $x_Y = 0.9$ the measured structure factor looks much like that of a pure Yukawa system. From these results, which essentially refer to an intermediate (non-thermodynamic) length scale, it is evident that the structural properties of such mixtures are much more sensitive to the replacement of a small amount of charged particles by uncharged particles than to the replacement of the same amount of uncharged by charged ones.

Thermodynamic quantities, which refer to a macroscopic length scale, behave rather differently. In particular, the isothermal compressibility χ^* is already drastically reduced at $x_Y = 0.3$. Further increase in x_Y produces a monotonous slight decrease of χ^* , until the value for the pure Yukawa system is reached at $x_Y = 1$.

Therefore, it is concluded that hard spheres play a dominant role concerning the local order, while for the isothermal compressibility, which is a macroscopic quantity, Yukawa particles are more important.

2.7 Conclusions

In this chapter it has been shown that a rigorous application of the methods of statistical mechanics provides a quantitative description of the results of static scattering experiments performed on model colloidal suspensions. These model systems consist mainly of spherical particles which may be of different sizes and may carry different charges. This aspect of polydispersity is, even for model systems, often unavoidable. As the results for polydisperse hard spheres and polydisperse charged-stabilized (Yukawa) spheres have shown, the quantitative interpretation of scattering experiments on such systems is considerably more complicated than for the corresponding monodisperse suspensions. From the various examples considered it should be obvious that the interpretation of scattering data for polydisperse samples in terms of theoretical

results from monodisperse systems can lead to significant errors. On the other hand, a proper interpretation can provide detailed information about the particles, their interactions and the resulting microstructure.

Besides the two kinds of models for colloidal particles considered here, hard spheres and Yukawa spheres, there are other kinds of models for spherical colloids for which some results on their microstructure are known. Among these there are soft spheres consisting of a hard core with a repulsive tail,^[94,95] which mimic polymerically stabilized colloids (the tail in the potential extends through the region containing the polymer layer), and hard spheres with an attractive square well potential,^[96–99] which describe, for example, silica particles stabilized by octadecyl chains are dispersed in poor solvents.^[100] Furthermore, the microstructure of charge-stabilized rod-like particles, which may serve as a model system for tobacco mosaic virus suspensions, has also been studied.^[101]

Much less is known about the quantitative microstructure of technologically relevant colloids, which may be electrosterically stabilized. However, one may hope that the understanding of the simpler model suspensions, described in this chapter, will form a useful basis for a description of the more complicated colloidal suspensions.

Acknowledgements

The authors would like to thank A. Ferrante, J. Méndez-Alcaraz, G. Nägele, N. Wagner and B. Weyerich for many helpful discussions. Many thanks go to J. Bender, who gave his code for PHS systems. The financial support of the Deutsche Forschungsgemeinschaft (SFB 306) and of the Regione Autonoma della Sardegna is gratefully acknowledged. Part of the manuscript was written during a visit to the Department of Chemical Engineering of the University of Delaware, under the sponsorship of the NATO Collaborative Research Program (CRG-910465), which is also acknowledged.

Appendix 2.A: the Ornstein–Zernike equation and closure relations

The basis of the functional derivative method is to consider an inhomogeneous fluid. The system is under the influence of an external potential $\varphi(\mathbf{r})$, which adds a term

$$\Phi = \sum_{i=1}^N \varphi(\mathbf{r}_i) = \int d\mathbf{r}' \varphi(\mathbf{r}') \hat{\varrho}(\mathbf{r}') \quad (2.A.1)$$

to the Hamiltonian in the expression (2.18) for the grand canonical distribution function and the expression (2.20) for the grand canonical partition function. The latter becomes

$$\begin{aligned} \Xi &= \sum_N \frac{1}{h^{3N} N!} \int d\Gamma e^{-\beta H} \exp \left\{ \beta \int d\mathbf{r}' \mu^*(\mathbf{r}') \hat{\varrho}(\mathbf{r}') \right\} \\ &\equiv \Xi[\mu^*(\mathbf{r})]. \end{aligned} \quad (2.A.2)$$

Here, use has been made of the fact that $N = \int d\mathbf{r}' \hat{\varrho}(\mathbf{r}')$, and

$$\mu^*(\mathbf{r}) = \mu - \varphi(\mathbf{r}), \quad (2.A.3)$$

which is the intrinsic chemical potential, has been introduced.

The notation $\mathcal{E} = \mathcal{E}[\mu^*(\mathbf{r})]$ indicates that \mathcal{E} is considered to be a functional of $\mu^*(\mathbf{r})$. The same applies to the phase space distribution and to the grand potential

$$\Omega[\mu^*(\mathbf{r})] = -k_B T \ln \mathcal{E}[\mu^*(\mathbf{r})]. \quad (2.A.4)$$

It is easily seen that $\Omega[\mu^*(\mathbf{r})]$ is a generating functional of the n -particle distribution functions of the inhomogeneous system. From eqns (2.A.2) and (2.A.4) it follows that

$$\begin{aligned} \frac{\delta \Omega}{\delta \mu^*(\mathbf{r})} &= -k_B T \frac{1}{\mathcal{E}} \frac{\delta \mathcal{E}}{\delta \mu^*(\mathbf{r})} \\ &= -k_B T \frac{1}{\mathcal{E}_N} \sum_N \frac{1}{h^{3N} N!} \int d\Gamma e^{-\beta(H + \Phi - \mu N)} \beta \hat{\rho}(\mathbf{r}) \\ &= -\langle \hat{\rho}(\mathbf{r}) \rangle = -\varrho^{(1)}(\mathbf{r}), \end{aligned} \quad (2.A.5)$$

which is the one-particle density in the inhomogeneous system. It is therefore a functional of $\varphi(\mathbf{r})$ or $\mu^*(\mathbf{r})$, so that a further functional derivative gives

$$\begin{aligned} \frac{\delta \varrho^{(1)}(\mathbf{r})}{\delta \mu^*(\mathbf{r}')} &= -\frac{\delta^2 \Omega}{\delta \mu^*(\mathbf{r}) \delta \mu^*(\mathbf{r}')} \\ &= \beta (\langle \hat{\varrho}(\mathbf{r}) \hat{\varrho}(\mathbf{r}') \rangle - \varrho^{(1)}(\mathbf{r}) \varrho^{(1)}(\mathbf{r}')) \\ &= \beta (\varrho^{(1)}(\mathbf{r}) \varrho^{(1)}(\mathbf{r}') h^{(2)}(\mathbf{r}, \mathbf{r}') + \delta(\mathbf{r} - \mathbf{r}') \varrho^{(1)}(\mathbf{r})). \end{aligned} \quad (2.A.6)$$

In the last step eqns (2.39), (2.28) and $h^{(2)} = g^{(2)} - 1$ have been used.

It can be shown that the external potential $\varphi(\mathbf{r})$ is uniquely determined by $\varrho^{(1)}(\mathbf{r})$. Therefore the equilibrium phase space distribution is also a unique functional of $\varrho^{(1)}(\mathbf{r})$, and because of eqn (2.A.5) it is possible to perform a Legendre transformation from $\Omega[\mu^*]$ to a free energy

$$A[\varrho^{(1)}(\mathbf{r})] = \Omega[\mu^*(\mathbf{r})] + \int d\mathbf{r} \mu^*(\mathbf{r}) \varrho^{(1)}(\mathbf{r}). \quad (2.A.7)$$

Since the functional derivatives of Ω describe correlations, it can also be expected that the derivatives of $A[\varrho^{(1)}]$ are related to particle correlations.

The free energy consists of an ideal part

$$\beta A_{id}[\varrho^{(1)}(\mathbf{r})] = \int d\mathbf{r} \varrho^{(1)}(\mathbf{r}) [\ln(A^3 \varrho^{(1)}(\mathbf{r})) - 1] \quad (2.A.8)$$

and an excess part $A_{ex} = A - A_{id}$. This latter contribution will therefore be related to particle correlations. Accordingly, one defines direct correlation

functions by

$$c^{(1)}(\mathbf{r}) = -\beta \frac{\delta A_{ex}[\varrho^{(1)}(\mathbf{r})]}{\delta \varrho^{(1)}(\mathbf{r})}, \quad (2.A.9)$$

$$c^{(2)}(\mathbf{r}, \mathbf{r}') = \frac{\delta c^{(1)}(\mathbf{r})}{\delta \varrho^{(1)}(\mathbf{r}')}. \quad (2.A.10)$$

It will be seen that the (expected) relation between $c^{(2)}$ and $h^{(2)}$ is just the OZ equation.

Taking the derivative of eqn (2.A.7) with respect to $\varrho^{(1)}(\mathbf{r})$ and using eqn (2.A.5) gives

$$\frac{\delta \beta A[\varrho^{(1)}]}{\delta \varrho^{(1)}(\mathbf{r})} = \beta \mu^*(\mathbf{r}). \quad (2.A.11)$$

On the other hand, differentiation of $A = A_{id} + A_{ex}$, using eqns (2.A.8) and (2.A.9), leads to

$$\frac{\delta \beta A[\varrho^{(1)}]}{\delta \varrho^{(1)}(\mathbf{r})} = \ln(\Lambda^3 \varrho^{(1)}(\mathbf{r})) - c^{(1)}(\mathbf{r}). \quad (2.A.12)$$

From the last two equations

$$c^{(1)}(\mathbf{r}) = -\beta \mu^*(\mathbf{r}) + \ln(\Lambda^3 \varrho^{(1)}(\mathbf{r})). \quad (2.A.13)$$

This result shows how the one-particle density $\varrho^{(1)}(\mathbf{r})$ is determined both by the external field $\varphi(\mathbf{r})$ and the correlations described by the excess part of the free energy, which in turn determines $c^{(1)}$. To illustrate the physical significance of $c^{(1)}$, eqn (2.A.13) can be specialized to an homogeneous system. This is obtained for $\varphi = 0$ and $\varrho^{(1)}(\mathbf{r}) = n$. Then

$$c^{(1)} = -(\beta \mu - \ln(\Lambda^3 n)) = -\beta \mu_{ex}, \quad (2.A.14)$$

where μ_{ex} is the excess part of the chemical potential.

From eqn (2.A.19) and (2.A.13), the two-particle direct correlation function is

$$c^{(2)}(\mathbf{r}, \mathbf{r}') = -\beta \frac{\delta \mu^*(\mathbf{r})}{\delta \varrho^{(1)}(\mathbf{r}')} + \frac{\delta(\mathbf{r} - \mathbf{r}')}{\varrho^{(1)}(\mathbf{r})}. \quad (2.A.15)$$

This expression can now be used to connect $c^{(2)}$ to the total correlation function $h^{(2)}$, since the first term in eqn (2.A.15) is just the inverse of eqn (2.A.6). Multiplying (2.A.15) by $\delta \varrho^{(1)}(\mathbf{r}')/\delta \mu^*(\mathbf{r}'')$, integrating over \mathbf{r}' and rearranging terms gives

$$h^{(2)}(\mathbf{r}, \mathbf{r}') = c^{(2)}(\mathbf{r}, \mathbf{r}') + \int d\mathbf{r}'' c^{(2)}(\mathbf{r}, \mathbf{r}'') \varrho^{(1)}(\mathbf{r}'') h^{(2)}(\mathbf{r}'', \mathbf{r}'). \quad (2.A.16)$$

This is the OZ equation for an inhomogeneous fluid. For homogeneous and isotropic systems the correlation functions depend only on the magnitude of the differences of their arguments; furthermore, $\varrho^{(1)}(\mathbf{r}'') = n$, so that eqn (2.A.16) reduces to the usual form eqn (2.184) of the OZ equation.

Although $c^{(2)}(\mathbf{r}, \mathbf{r}')$ in eqn (2.A.16) is a well-defined function, one has to introduce approximations, since the excess part of the free energy is not known. One procedure to obtain the approximate closure relations is to use perturbation theory. The idea is to represent the correlation functions of the state of interest in terms of those of a reference state. When $\varrho_0^{(1)}(\mathbf{r})$ denotes the one-particle density of the reference state, one defines

$$\begin{aligned}\varrho^{(1)}(\mathbf{r}; \lambda) &= \varrho_0^{(1)}(\mathbf{r}) + \lambda(\varrho^{(1)}(\mathbf{r}; \lambda) - \varrho_0^{(1)}(\mathbf{r})) \\ &= \varrho_0^{(1)}(\mathbf{r}) + \Delta\varrho^{(1)}(\mathbf{r}; \lambda),\end{aligned}\quad (2.A.17)$$

so that $\varrho^{(1)}(\mathbf{r}; \lambda = 1) \equiv \varrho^{(1)}(\mathbf{r})$ describes the state of interest. Integration of eqn (2.A.10) gives

$$c^{(1)}[\mathbf{r}; \varrho^{(1)}] = c^{(1)}[\mathbf{r}; \varrho_0^{(1)}] + \int_0^1 d\lambda \int d\mathbf{r}' \Delta\varrho^{(1)}(\mathbf{r}'; \lambda) c^{(2)}[\mathbf{r}, \mathbf{r}'; \varrho^{(1)}(\lambda)]. \quad (2.A.18)$$

An elegant method to proceed with this equation is due to Percus. One considers an homogeneous fluid consisting of $N + 1$ particles as an inhomogeneous fluid of N particles in the potential of particle $N + 1$. Because of translational invariance of the $(N + 1)$ -particle system, the origin of the coordinate system can be chosen to coincide with the position of particle $N + 1$. Then the remaining N particles experience the external potential

$$\phi(\mathbf{r}) = v(\mathbf{r}, \mathbf{r}' = 0) = v(\mathbf{r}) \quad (2.A.19)$$

due to the particle at the origin, where $v(\mathbf{r}, \mathbf{r}')$ is the pair potential. The one-particle density of the inhomogeneous N -particle system is $\varrho^{(1)}(\mathbf{r}) = ng_0(r)$, where g_0 is the pair correlation function of the homogeneous fluid, and its one-particle direct correlation function follows by eqn (2.A.13) with eqn (2.A.19), as

$$c^{(1)}[\mathbf{r}; \varrho^{(1)}] = \beta v(\mathbf{r}) + \ln\left(\frac{ng_0(r)}{z}\right), \quad (2.A.20)$$

where $z = e^{\beta\mu}/A^3$. The function $c^{(1)}[\mathbf{r}, \varrho_0^{(1)}]$ in eqn (2.A.18) describes the homogeneous $(N + 1)$ -particle system, and it is given by eqn (2.A.14) as

$$c^{(1)}[\mathbf{r}; \varrho_0^{(1)}] = \ln\frac{n}{z}. \quad (2.A.21)$$

Since $\Delta\varrho^{(1)}(\mathbf{r}; \lambda) = ng_0(r) - n = nh_0(r)$, eqn (2.A.18) becomes

$$\ln g_0(r) = -\beta v(r) + n \int_0^1 d\lambda \int d\mathbf{r}' h_0(r') c^{(2)}[\mathbf{r}, \mathbf{r}'; \varrho^{(1)}(\lambda)]. \quad (2.A.22)$$

Now one approximates the two-particle direct correlation function in the integral by replacing $\varrho^{(1)}(\lambda)$ by $\varrho^{(1)}(\lambda = 0) = n$, so that $c^{(2)}[\mathbf{r}, \mathbf{r}'; \varrho^{(1)}(\lambda)]$ is replaced by $c_0(|\mathbf{r} - \mathbf{r}'|)$, the direct correlation function of the homogeneous fluid

of density n . Then eqn (2.A.22) becomes an approximation:

$$\ln g_0(r) = -\beta v(r) + n \int d\mathbf{r}' c_0(|\mathbf{r} - \mathbf{r}'|) h_0(\mathbf{r}'). \quad (2.A.23)$$

Omitting the index and using the OZ equation (2.184) for the last term in eqn (2.A.23) gives the approximate relation

$$g(r) = \exp[-\beta v(r) + h(r) - c(r)], \quad (2.A.24)$$

which is known as the hypernetted-chain approximation (HNC).

Appendix 2.B: the solution of PY for polydisperse HS

In this appendix we report the analytical solution of the PY approximation for polydisperse hard spheres when the distribution of particle diameters, $F(\sigma)$, is the Schulz distribution (see eqn (2.217)): no derivation is given. We closely follow the presentation of Griffith, Triolo and Compere.^[52]

The solution of eqn (2.204) is usually expressed in terms of the Fourier transform of the total correlation functions:^[49]

$$\tilde{h}_{\sigma\sigma'}(k) = -2 \frac{Z_2 Z_3 + Z_1 Z_4}{k^3(X^2 + Y^2)}. \quad (2.B.1)$$

Here

$$Z_1 = Y \sin(kd_{\sigma\sigma'}) - X \cos(kd_{\sigma\sigma'}), \quad (2.B.2)$$

$$Z_2 = X \sin(kd_{\sigma\sigma'}) + Y \cos(kd_{\sigma\sigma'}), \quad (2.B.3)$$

$$Z_3 = Q''_{\sigma\sigma'} - kR_3, \quad Z_4 = kQ'_{\sigma\sigma'} + kR_4. \quad (2.B.4, 2.B.5)$$

The quantities needed to evaluate these equations are as follows:

$$d_{\sigma\sigma'} = \frac{1}{2}(\sigma + \sigma'), \quad Q''_{\sigma\sigma'} = \frac{2\pi}{\Delta} \left(1 + \frac{1}{2\Delta} \xi_3 \pi \right), \quad (2.B.6, 2.B.7)$$

$$Q'_{\sigma\sigma'} = \frac{\pi}{\Delta} \left(\sigma + \sigma' + \frac{1}{2\Delta} \sigma \sigma' \xi_2 \pi \right), \quad (2.B.8)$$

$$\Delta = 1 - \frac{\pi \xi_3}{6}, \quad \xi_i = n \left(\frac{\langle \sigma \rangle^i}{t+1} \right) \frac{\Gamma(t+1+i)}{\Gamma(t+1)}, \quad (2.B.9, 2.B.10)$$

$$R_3 = (\pi/\Delta)^2 n \int_0^\infty d\sigma'' F(\sigma'') (\sigma'' - \sigma)(\sigma'' - \sigma') y_1(\sigma''), \quad (2.B.11)$$

$$R_4 = (\pi/\Delta)^2 n \int_0^\infty d\sigma'' F(\sigma'') (\sigma'' - \sigma)(\sigma'' - \sigma') x_1(\sigma''), \quad (2.B.12)$$

$$\begin{aligned}
X = & 1 - \left(\frac{2\pi}{\Delta} \right) \left(1 + \frac{\pi\xi_3}{2\Delta} \right) n \int_0^\infty d\sigma'' F(\sigma'') x_2(\sigma'') \\
& - \left(\frac{2\pi}{\Delta} \right) n \int_0^\infty d\sigma'' F(\sigma'') \sigma'' x_1(\sigma'') \left(1 + \frac{\pi\xi_2\sigma}{4\Delta} \right) \\
& - \frac{1}{2} \left(\frac{n\pi}{\Delta} \right)^2 \int_0^\infty d\sigma'' F(\sigma'') \int_0^\infty d\sigma F(\sigma) [x_1(\sigma'') x_1(\sigma) \\
& - y_1(\sigma'') y_1(\sigma)] (\sigma'' - \sigma)^2, \tag{2.B.13}
\end{aligned}$$

$$\begin{aligned}
Y = & - \left(\frac{2\pi}{\Delta} \right) \left(1 + \frac{\pi\xi_3}{2\Delta} \right) n \int_0^\infty d\sigma'' F(\sigma'') y_2(\sigma'') \\
& - \left(\frac{2\pi}{\Delta} \right) n \int_0^\infty d\sigma'' F(\sigma'') \sigma'' y_1(\sigma'') \left(1 + \frac{\pi\xi_2\sigma''}{4\Delta} \right) \\
& - \frac{1}{2} \left(\frac{n\pi}{\Delta} \right)^2 \int_0^\infty d\sigma'' F(\sigma'') \int_0^\infty d\sigma F(\sigma) [x_1(\sigma'') y_1(\sigma) \\
& + y_1(\sigma'') x_1(\sigma)] (\sigma'' - \sigma)^2, \tag{2.B.14}
\end{aligned}$$

$$x_1(\sigma) = k^{-2} [\cos(k\sigma) - 1], \quad y_1(\sigma) = k^{-2} [k\sigma - \sin(k\sigma)], \quad (2.B.15, 2.B.16)$$

$$x_2(\sigma) = k^{-3} [k\sigma - \sin(k\sigma)], \tag{2.B.17}$$

$$y_2(\sigma) = -k^{-3} [\cos(k\sigma) + k^2\sigma^2/2 - 1]. \tag{2.B.18}$$

The integrals involving $F(\sigma)$ can be written as

$$\int_0^\infty d\sigma F(\sigma) \sigma^n g(\sigma), \tag{2.B.19}$$

and the list of analytic solutions is given in Table B.1.

From these expressions, and by using eqns (2.220) and (2.221) the number-number structure factor can be determined. The result is as follows:

$$\begin{aligned}
S_{NN}(k) = & 1 - 2n \{ \lambda [\lambda(Y\delta_1 - X\delta_6) + \lambda'(Y\delta_2 - X\delta_4) + \mu(X\delta_1 + Y\delta_6) \\
& + \mu'(X\delta_2 + Y\delta_4)] + \lambda' [\lambda(Y\delta_2 - X\delta_4) + \lambda'(Y\delta_3 - X\delta_5) + \mu(X\delta_2 + Y\delta_4) \\
& + \mu'(X\delta_3 + Y\delta_5)] + \mu [\lambda(X\delta_1 + Y\delta_6) + \lambda'(X\delta_2 + Y\delta_4) + \mu(X\delta_6 - Y\delta_1) \\
& + \mu'(X\delta_4 - Y\delta_2)] + \mu' [\lambda(X\delta_2 + Y\delta_4) + \lambda'(X\delta_3 + Y\delta_5) \\
& + \mu(X\delta_4 - Y\delta_2) + \mu'(X\delta_5 - Y\delta_3)] \} / [k^3(X^2 + Y^2)]. \tag{2.B.20}
\end{aligned}$$

Table B.1. Integral notation.^a

$g(\sigma)$	n	$(b^c \Gamma(c))^{-1} \int_0^\infty d\sigma F(\sigma) \sigma^n g(\sigma)$	Notation
1	0	1	1
1	1	bc	ζ'
1	2	$b^2 c(c+1)$	ζ''
1	3	$b^3 c(c+1)(c+2)$	ζ'''
$\sin(k\sigma)$	0	$v_1^{c/2} \sin[c \tan^{-1}(bk)]$	ψ
$\sin(k\sigma)$	1	$bcv_1^{(c+1)/2} \sin[(c+1) \tan^{-1}(bk)]$	ψ'
$\sin(k\sigma)$	2	$b^2 c(c+1)v_1^{(c+2)/2} \sin[(c+2) \tan^{-1}(bk)]$	ψ''
$\sin(k\sigma/2)$	0	$2^c v_2^{c/2} \sin[c \tan^{-1}(bk/2)]$	μ
$\sin(k\sigma/2)$	1	$2^{c+1} bcv_2^{(c+1)/2} \sin[(c+1) \tan^{-1}(bk/2)]$	μ'
$\cos(k\sigma)$	0	$v_1^{c/2} \cos[c \tan^{-1}(bk)]$	χ
$\cos(k\sigma)$	1	$bcv_1^{(c+1)/2} \cos[(c+1) \tan^{-1}(bk)]$	χ'
$\cos(k\sigma)$	2	$b^2 c(c+1)v_1^{(c+2)/2} \cos[(c+2) \tan^{-1}(bk)]$	χ''
$\cos(k\sigma/2)$	0	$2^c v_2^{c/2} \cos[c \tan^{-1}(bk/2)]$	λ
$\cos(k\sigma/2)$	1	$2^{c+1} bcv_2^{(c+1)/2} \cos[(c+1) \tan^{-1}(bk/2)]$	λ'

^a $c = t + 1$; $b = \langle \sigma \rangle / (t + 1)$; $v_m = (m^2 + b^2 k^2)^{-1}$.

The various quantities appearing in $S_{NN}(k)$ are given by

$$\begin{aligned} X &= 1 - (2\pi/\Delta)(1 + \pi\xi_3/(2\Delta)nk^{-3}(k\zeta' - \psi) - (\pi/\Delta)nk^{-2}[(\chi' - \zeta')] \\ &\quad + \pi\xi_2/(4\Delta)(\chi'' - \zeta'') - (\pi/\Delta)^2(nk^{-2})^2[(\chi - 1)(\chi'' - \zeta'') - (\chi' - \zeta')^2 \\ &\quad - (k\chi' - \psi)(k\chi''' - \psi'') + (k\zeta'' - \psi')^2], \end{aligned} \quad (2.B.21)$$

$$\begin{aligned} Y &= (2\pi/\Delta)(1 + \pi\xi_3/(2\Delta)nk^{-3}(\chi + k^2\zeta''/2 - 1) - (2\pi n/\Delta k^2)[k\zeta'' - \psi' \\ &\quad + \pi\xi_2/(4\Delta)(k\zeta''' - \psi'')] - (\pi/\Delta)^2(nk^{-2})^2[(k\zeta' - \psi)(\chi'' - \zeta'')] \\ &\quad - 2(k\zeta'' - \psi')(\chi' - \zeta') + (k\zeta''' - \psi'')(\chi - 1)], \end{aligned} \quad (2.B.22)$$

and by

$$\delta_1 = (\pi/\Delta)\{2 + (\pi/\Delta)[\xi_3 - (n/k)(k\zeta''' - \psi'')]\}, \quad (2.B.23)$$

$$\delta_2 = (\pi/\Delta)^2(n/k)(k\zeta'' - \psi'), \quad (2.B.24)$$

$$\delta_3 = -(\pi/\Delta)^2(n/k)(k\zeta' - \psi), \quad (2.B.25)$$

$$\delta_4 = (\pi/\Delta)[k - (\pi/\Delta)(n/k)(\chi' - \zeta')], \quad (2.B.26)$$

$$\delta_5 = (\pi/\Delta)^2[(n/k)(\chi - 1) + k\xi_2/2], \quad (2.B.27)$$

$$\delta_6 = (\pi/\Delta)^2(n/k)(\chi'' - \zeta''). \quad (2.B.28)$$

Appendix 2.C: scattering intensity from polydisperse HS in the PY approximation

As in Appendix B, we quote the results of Griffith, Triolo and Compere^[52] without any derivation.

We write the scattered intensity, eqn (2.161), of a polydispersed HS system in the form

$$\begin{aligned} I(k) &= n\overline{f^2(k)}S^M(k) = I_1(k) + I_2(k) \\ &= n \int d\sigma F(\sigma)f_\sigma^2(k) + n \int d\sigma \int d\sigma' F(\sigma)F(\sigma')f_\sigma(k)f_{\sigma'}(k)\tilde{h}_{\sigma\sigma'}(k), \end{aligned} \quad (2.C.1)$$

and we use for $F(\sigma)$ the Schulz distribution and for $f_\sigma(k)$ the expression (2.152). For the two integrals $I_1(k)$ and $I_2(k)$ we obtain

$$I_1(k) = 8\pi^2 np^2 k^{-6} [1 - \chi - k\psi' + k^2(\xi'' + \chi'')/4] \quad (2.C.2)$$

and

$$\begin{aligned} I_2(k) &= -2\{\Gamma[\Gamma(Y\delta_1 - X\delta_6) + \Gamma'(Y\delta_2 - X\delta_4) + M(X\delta_1 + Y\delta_6) + M'(X\delta_2 + Y\delta_4)] \\ &\quad + \Gamma'[\Gamma(Y\delta_2 - X\delta_4) + \Gamma'(Y\delta_3 - X\delta_5) + M(X\delta_2 + Y\delta_4) + M'(X\delta_3 + Y\delta_5)] \\ &\quad + M[\Gamma(X\delta_1 + Y\delta_6) + \Gamma'(X\delta_2 + Y\delta_4) + M(X\delta_6 - Y\delta_1) + M'(X\delta_4 - Y\delta_2)] \\ &\quad + M'[\Gamma(X\delta_2 + Y\delta_4) + \Gamma'(X\delta_3 + Y\delta_5) + M(X\delta_4 - Y\delta_2) \\ &\quad + M'(X\delta_5 - Y\delta_3)]\}/[k^3(X^2 + Y^2)], \end{aligned} \quad (2.C.3)$$

in which

$$p = 2(n_p - n_s)/n_s, \quad (2.C.4)$$

$$\Gamma = 2\pi nk^{-3}[\psi - \frac{1}{2}k(\zeta' + \chi')], \quad (2.C.5)$$

$$\Gamma' = 2\pi nk^{-3}[\psi' - \frac{1}{2}k(\zeta'' + \chi'')], \quad (2.C.6)$$

$$M = 2\pi nk^{-3}(1 - \chi - \frac{1}{2}k\psi'), \quad (2.C.7)$$

$$M' = 2\pi nk^{-3}(\zeta' - \chi' - \frac{1}{2}k\psi''), \quad (2.C.8)$$

and where all the other quantities are given in Appendix B.

References

1. Hansen, J. P., and McDonald, I. R. (1986). *Theory of simple liquids*. Academic Press, London.
2. March, N. H., and Tosi, M. P. (1976). *Atomic dynamics in liquids*. Macmillan, London.
3. Balescu, R. (1975). *Equilibrium and non-equilibrium statistical mechanics*. Wiley Interscience, New York.
4. Hill, T. L. (1956). *Statistical mechanics*. McGraw-Hill, New York.
5. D'Aguanno, B., and Klein, R. (1991). *J. Chem. Soc. Faraday Trans.*, **87**, 379.
6. Bhatia, A. B., and Thornton, D. E. (1970). *Phys. Rev.*, **B2**, 3004.
7. Kusalik, P. G., and Patey, G. N. (1987). *J. Chem. Phys.*, **86**, 5110.
8. Méndez-Alcaraz, J. M., D'Aguanno, B., and Klein, R. (1991). *Physica A*, **178**, 421.

9. Marion, J. B. (1965). *Classical electromagnetic radiation*. Academic Press, New York.
10. Berne, J. B., and Pecora, R. (1976). *Dynamic light scattering*. John Wiley, New York.
11. Ishimaru, A. (1978). *Wave propagation and scattering in random media*. Academic Press, New York.
12. Van de Hulst, H. C. (1957). *Light scattering by small particles*. John Wiley, New York.
13. Kerker, M. (1969). *The scattering of light*. Academic Press, New York.
14. van Albada, M. P., van Tiggelen, B. A., Lagendijk, A., and Tip, A. (1991). *Phys. Rev. Lett.*, **66**, 3131.
15. Pusey, P. N., Fijnaut, H. M., and Vrij, A. (1982). *J. Chem. Phys.*, **77**, 4270.
16. Faber, J. E., and Ziman, J. M. (1965). *Phil. Mag.*, **11**, 153.
17. Tata, B. V. R., Kesavamoorthy, R., and Sood, A. K., (1987). *Mol. Phys.*, **61**, 943.
18. Schneider, J., Karrer, D., Dhont, J. K. G., and Klein, R. (1987). *J. Chem. Phys.*, **87**, 3008.
19. Percus, J. K., and Yevick, G. J. (1958). *Phys. Rev.*, **110**, 1.
20. Chihara, J. (1973). *Prog. Theoret. Phys.*, **50**, 409.
21. Madden, W. G., and Rice, S. A. (1980). *J. Chem. Phys.*, **72**, 4208.
22. Waisman, E., and Lebowitz, J. L. (1972). *J. Chem. Phys.*, **56**, 3086.
23. Waisman, E. (1973). *Mol. Phys.*, **25**, 45.
24. Wertheim, M. S. (1963). *Phys. Rev. Lett.*, **10**, 321.
25. Thiele, E. (1963). *J. Chem. Phys.*, **39**, 474.
26. Hayter, J. B., and Penfold, J. (1981). *Mol. Phys.*, **42**, 109.
27. Hansen, J. P., and Hayter, J. B. (1982). *Mol. Phys.*, **46**, 651.
28. Nägele, G., Medina-Noyola, M., Klein, R., and Arauz-Lara, J. L. (1988). *Physica A*, **149**, 123.
29. Rogers, F. J., and Young, D. A. (1984). *Phys. Rev.*, **30A**, 999.
30. Zerah, G., and Hansen, J. P. (1986). *J. Chem. Phys.*, **84**, 2336.
31. Weeks, J. D., Chandler, D., and Andersen, H. C. (1971). *J. Chem. Phys.*, **54**, 5237.
32. Martynov, G. A., and Sarkisov, G. N. (1983). *Mol. Phys.*, **49**, 1495.
33. Ballone, P., Pastore, G., Galli, G., and Gazzillo, D. (1986). *Mol. Phys.*, **59**, 275.
34. Lado, F. (1973). *Phys. Rev.*, **A8**, 2548.
35. Rosenfeld, Y., and Ashcroft, N. W. (1979). *Phys. Rev.*, **A20**, 1208.
36. Kambayashi, S., and Hiwatari, Y. (1990). *Phys. Rev.*, **A41**, 1990.
37. Kambayashi, S., and Hiwatari, Y. (1990). *Phys. Rev.*, **A42**, 2176.
38. Gazzillo, D. and Della Valle, R. G. (1993). *J. Chem. Phys.*, **99**, 6915.
39. Gillan, M. J. (1979). *Mol. Phys.*, **38**, 1781.
40. Abernethy, G. M., and Gillan, M. J. (1980). *Mol. Phys.*, **39**, 839.
41. Zerah, G. (1985). *J. Comput. Phys.*, **61**, 280.
42. Labik, S., Malijevsky, A., and Vonka, P. (1985). *Mol. Phys.*, **56**, 709.
43. Ng, J. C. (1974). *J. Chem. Phys.*, **61**, 2680.
44. D'Aguanno, B., and Klein, R. (1992). *Phys. Rev.*, **A46**, 7652.
45. Wertheim, M. S. (1964). *J. Math. Phys.*, **5**, 643.
46. Baxter, R. J. (1968). *Austral. J. Phys.*, **21**, 563.
47. Carnahan, N. F., and Starling, K. E. (1969). *J. Chem. Phys.*, **51**, 635.
48. Verlet, L., and Weis, J. J. (1972). *Phys. Rev.*, **A5**, 939.
49. Blum, L., and Stell, G. (1979). *J. Chem. Phys.*, **71**, 42.
50. Baxter, R. J. (1970). *J. Chem. Phys.*, **52**, 4559.
51. Griffith, W. L., Triolo, R., and Compere, A. L. (1986). *Phys. Rev.*, **A33**, 2197.
52. Griffith, W. L., Triolo, R., and Compere, A. L. (1987). *Phys. Rev.*, **A35**, 2200.
53. Schulz, G. V. (1939). *Z. Phys. Chem. Abt. B*, **43**, 25.
54. Vrij, A. (1978). *J. Chem. Phys.*, **69**, 1742.
55. Vrij, A. (1979). *J. Chem. Phys.*, **71**, 3267.

56. Salacuse, J. J., and Stell, G. (1982). *J. Chem. Phys.*, **77**, 3714.
57. Mansoori, G. A., Carnahan, N. F., Starling, K. E., and Leland, T. W. (1971). *J. Chem. Phys.*, **54**, 1523.
58. Fushiki, M. (1988). *J. Chem. Phys.*, **89**, 7445.
59. Watts, R. O. (1973). In *Statistical mechanics*, volume 1. Chemical Society Specialist Periodical Report.
60. Cooper, R. S. (1973). *Phys. Rev.*, **A7**, 1.
61. Larsen, B. (1978). *J. Chem. Phys.*, **68**, 4511.
62. Carley, D. D. (1967). *J. Chem. Phys.*, **46**, 3783.
63. Belloni, L. (1993). *J. Chem. Phys.*, **98**, 8080.
64. Belloni, L. (1988). *J. Chem. Phys.*, **88**, 5143.
65. Bernu, B., Hansen, J. P., Hiwatari, Y., and Pastore, G. (1987). *Phys. Rev.*, **A36**, 4891.
66. de Kruif, C. G., Briels, W. J., May, R. P., and Vrij, A. (1988). *Langmuir*, **4**, 668.
67. Vrij, A., Jansen, J. W., Dhont, J. K. G., Pathmamanoharam, C., Kops-Werkhoven, M. M., and Fijnaut, H. M. (1983). *Faraday Discuss. Chem. Soc.*, **76**, 19.
68. Pusey, P. N., and van Megen, W. (1986). *Nature*, **320**, 340.
69. Haymet, A. D. J. (1983). *J. Chem. Phys.*, **78**, 4641.
70. Hansen, J. P., and Verlet, L. (1969). *Phys. Rev.*, **184**, 151.
71. Salgi, P., and Rajagopalan, R. (1993). *Adv. Colloid Interface Sci.*, **43**, 169.
72. Vrij, A. (1982). *J. Colloid Interface Sci.*, **90**, 110.
73. D'Aguanno, B. (1993). *Physica Scripta*, **T49**, 84.
74. Frenkel, D., Vos, R. J., de Kruif, C. G., and Vrij, A. (1986). *J. Chem. Phys.*, **84**, 4625.
75. van Beurten, P., and Vrij, A. (1981). *J. Chem. Phys.*, **74**, 2744.
76. Verwey, E. J. W., and Overbeek, J. T. G. (1948). *Theory of the stability of lyophobic colloids*. Elsevier, Amsterdam.
77. Medina-Noyola, M., and McQuarrie, D. A. (1980). *J. Chem. Phys.*, **73**, 6279.
78. Beresford-Smith, B., Chan, D. Y. C., and Mitchell, D. J. (1985). *J. Colloid Interface Sci.*, **105**, 216.
79. Belloni, L. (1986). *J. Chem. Phys.*, **85**, 519.
80. Löwen, H., Madden, P. A., and Hansen, J. P. (1992). *Phys. Rev. Lett.*, **68**, 1081.
81. Krause, R., D'Aguanno, B., Méndez-Alcaraz, J. M., Nägele, G., Klein, R., and Weber, R. (1991). *J. Phys.: Condens. Matter*, **3**, 4459.
82. Wagner, N. J., Krause, R., Rennie, A. R., D'Aguanno, B., and Goodwin, J. (1991). *J. Chem. Phys.*, **95**, 494.
83. D'Aguanno, B., Krause, R., Méndez-Alcaraz, J. M., and Klein, R. (1992). *J. Phys.: Condens. Matter*, **4**, 3077.
84. Sheu, E. Y. (1992). *Phys. Rev.*, **A45**, 2428.
85. Porod, G. (1976). *Kolloid Z.*, **124**, 83.
86. Guinier, A., and Fournet, G. (1955). *Small angle scattering of X rays*. John Wiley, New York.
87. Cuits, M. G. H., May, R. P., Vrij, A., and de Kruif, C. G. (1991). *J. Chem. Phys.*, **94**, 4521.
88. Méndez-Alcaraz, J. M. (1993). *Statische Eigenschaften kolloidaler Suspensionen*. PhD thesis, University of Konstanz.
89. Biben, T., and Hansen, J. P. (1991). *Phys. Rev. Lett.*, **66**, 2215.
90. van Duijneveldt, J. S., Heinen, A. W., and Lekkerkerker, H. N. W. (1993). *Europhys. Lett.*, **21**, 369.
91. Härtl, W., Segschneider, C., Versmold, H., and Linse, P. (1991). *Mol. Phys.*, **73**, 541.
92. Hanley, H. J. M., Stratton, G. C., and Lindner, P. (1991). *Physica A*, **174**, 60.
93. Méndez-Alcaraz, J. M., D'Aguanno, B., and Klein, R. (1992). *Langmuir*, **8**, 2913.

94. Mewis, J., Frith, W. J., Strivens, T. A., and Russel, W. B. (1989). *Am. Inst. Chem. Engrs J.*, **35**, 415.
95. Genz, U., D'Aguanno, B., Mewis, J., and Klein, R. (1994). *Langmuir*, **10**, 2206.
96. Bergenholz, J., Wu, P., Wagner, N. J., and D'Aguanno, B. (1996). *Mol. Phys.*, to be published.
97. Smith, W. R., Henderson, D., and Murphy, R. D. (1974). *J. Chem. Phys.*, **61**, 2911.
98. Robertus, C., Philipse, W. H., Joosten, J. G. H., and Levine, Y. K. (1989). *J. Chem. Phys.*, **90**, 4482.
99. Menon, S. V. G., Manohar, C., and Srinivasa Rao, K. (1991). *J. Chem. Phys.*, **95**, 9186.
100. Vrij, A., Penders, H. G. M., Rouw, P. W., de Kruif, C. G., Dhont, J. K. G., Smits, C. S., and Lekkerkerker, H. N. W. (1990). *Faraday Discuss. Chem. Soc.*, **90**, 31.
101. Canessa, E., D'Aguanno, B., Weyerich, B., and Klein, R. (1991). *Mol. Phys.*, **73**, 175.
102. Nägele, G., Kellerbauer, O., Krause, R., and Klein, R. (1993). *Phys. Rev.*, **47**, 2562.
103. Krause, R., Nägele, G., Schneider, J., Klein, R., and Weber, R. (1988). *Physica A*, **153**, 400.

3

The theory of light scattering from rod-like polyelectrolytes

Theo Odijk

3.1 Introduction

A significant class of polyelectrolytes consists of slender, rod-like particles. Important examples include biopolymers such as short double-stranded DNA, helical xanthan, schizophyllan, F-actin, tobacco mosaic virus and fd virus. They may be semi-flexible but if the ratio of the persistence length to the contour length is smaller than unity, it becomes useful to model the polyions by charged rods. Inorganic colloids such as vanadium pentoxide and boehmite form another interesting subclass which may be considered completely rigid rods for most practical purposes. My objective here is to present a virial theory for the scattering by semi-dilute and concentrated isotropic solutions of rod-like polyelectrolytes, albeit under excess salt conditions.

Even this restricted problem has posed considerable difficulties in the past. In effect, let us consider for a moment what basic physical quantities determine the system. They are the (supposedly) uniform linear charge density ev (i.e. ev elementary charges per unit length along the cylindrical polyion axis), the (supposedly) uniform permittivity of the solvent ϵ , the length L and bare diameter d of the polyion rods, the number density ρ_L of polyions and the ionic strength n_s of the excess 1-1 electrolyte solution. A relevant electrostatic scale is the Bjerrum length $Q \equiv e^2/\epsilon k_B T$, in which k_B is Boltzmann's constant and T is the temperature; so there are actually seven length scales in the problem: L , Q , d , v^{-1} , $\rho_L^{-1/3}$, $n_s^{-1/3}$ and the inverse magnitude of the scattering vector q^{-1} . Fortunately we can lump d , Q , v and n_s into one scale, d_{eff} , the effective diameter, to a good approximation. The structure factor may thus be written as $S = S(qL, d_{\text{eff}}/L, A_{2,0}\rho_L)$, where I have introduced the second virial coefficient $A_{2,0} = (\pi/4)L^2d_{\text{eff}}^{[1]}$. Previous work^[2,3] focused on $S(qL, 0, A_{2,0}\rho_L)$ in the second virial approximation, but the structure factor is now evaluated up to and including the third virial term, and will be shown to be a monotonically increasing function of q when it is divided by the structure factor at infinite dilution of polyelectrolyte. Hence the present theory will be of practical use under a wide variety of conditions.

A general and convenient route towards the analytical computation of the structure factor is via Yvon's linear response theorem^[4,5]

$$\delta\hat{\rho}(\mathbf{q}) = -\rho S(\mathbf{q})\hat{\psi}(\mathbf{q}) \quad (3.1)$$

A weak external potential ψ (in units of $k_B T$) which is hypothetical, acts on the fluid, the small ions or the polyions and induces a non-uniform density of the relevant species. In Fourier language the response function is simply $-\rho S(\mathbf{q})/k_B T$, where S is the pertinent structure factor. Equation (3.1) has the following advantages: (1) the structure factor is evaluated via a physical operation so its derivation is transparent; (2) we do not need to calculate the pair correlation function first; (3) approximation methods (say of the virial or self-consistent field type) can be used as directly as possible. I shall first illustrate how eqn (3.1) may be employed to estimate the scattering from non-electroneutral charge fluctuations (which are generally very small under conditions of excess salt) and then compute the scattering by the polyions themselves.

Before focusing on the scattering theory, I first discuss the basis of the Poisson–Boltzmann equation, since it lies at the heart of polyelectrolyte theory and its merits and limitations are often imperfectly understood. Along the way it is straightforward to comprehend charge fluctuations with the aid of eqn (3.1).

3.2 The Poisson–Boltzmann equation and scattering by charge fluctuations

The solution of volume V contains excess 1–1 electrolyte (N^+ ions and N^- ions; electrolyte density $n_s = N/V$). The polyions are temporarily held fixed in the solution and may be viewed as source charges or boundary conditions within the electrolyte fluid. What is the distribution of small ions?

Quite generally, it is possible to set up self-consistent field theories according to the following prescription: (1) formulate an ideal entropy and average energy; (2) use a Hartree approximation—the average of a product is a product of the averages—to obtain the total free energy as a functional of the single particle density; (3) derive a mean-field theory for the sought distribution by minimizing the free energy. Carrying out this recipe for the system at hand, one obtains the following: average Coulomb energy,

$$\begin{aligned} U_c &= \left\langle \frac{1}{2} k_B T \sum_{\pm, i \neq \pm, j} \frac{z_i z_j Q}{|\mathbf{r}_i - \mathbf{r}_j|} \right\rangle \\ &= \frac{1}{2} k_B T Q \int d\mathbf{r} \int d\mathbf{r}' \frac{\langle (\bar{\rho}_+(\mathbf{r}) - \bar{\rho}_-(\mathbf{r}))(\bar{\rho}_+(\mathbf{r}') - \bar{\rho}_-(\mathbf{r}')) \rangle}{|\mathbf{r} - \mathbf{r}'|} \\ &\approx \frac{1}{2} Q \int d\mathbf{r} \int d\mathbf{r}' \frac{(\rho_+(\mathbf{r}) - \rho_-(\mathbf{r}))(\rho_+(\mathbf{r}') - \rho_-(\mathbf{r}'))}{|\mathbf{r} - \mathbf{r}'|} \end{aligned} \quad (3.2)$$

where a short-distance cut-off is implied in the integration and the ion densities are given by

$$\bar{\rho}_{\pm}(\mathbf{r}) \equiv \sum_i \delta(\mathbf{r} - \mathbf{r}_{\pm, i}), \quad (3.3)$$

with $\mathbf{r}_{\pm,i}$ the positions of the respective ions ($i = 1, 2, \dots, N$) and z_i their valencies (± 1). The average ion densities are given by

$$\rho_{\pm}(\mathbf{r}) \equiv \langle \bar{\rho}_{\pm}(\mathbf{r}) \rangle = \left\langle \sum_i \delta(\mathbf{r} - \mathbf{r}_{\pm,i}) \right\rangle \quad (3.4)$$

which are normalized as follows:

$$\int d\mathbf{r} \rho_{\pm}(\mathbf{r}) = N. \quad (3.5)$$

The entropy is ideal:

$$S = -k_B \int d\mathbf{r} \rho_+ \log \rho_+ - k_B \int d\mathbf{r} \rho_- \log \rho_-. \quad (3.6)$$

There are two external terms, one caused by the polyion sources, and the other by a weak hypothetical field chosen to act on the + ions only, for now:

$$U_s = k_B T \int d\mathbf{r} (\rho_+(\mathbf{r}) - \rho_-(\mathbf{r})) \psi_s(\mathbf{r}), \quad (3.7)$$

$$U_+ = k_B T \int d\mathbf{r} \rho_+(\mathbf{r}) \psi_+(\mathbf{r}). \quad (3.8)$$

Next, we minimize $F_{\text{tot}} = U_c - TS + U_s + U_+$ with respect to $\rho_+(\mathbf{r})$ and with respect to $\rho_-(\mathbf{r})$, remembering to take account of eqn (3.5):

$$\log \rho_{\pm}(\mathbf{r}) \pm Q \int d\mathbf{r}' \frac{\rho_+(\mathbf{r}') - \rho_-(\mathbf{r}')}{|\mathbf{r} - \mathbf{r}'|} + \psi_s(\mathbf{r}) + \begin{cases} \psi_+(\mathbf{r}) \\ 0 \end{cases} + \text{constant} = 0. \quad (3.9)$$

3.2.1 The Poisson–Boltzmann equation

We set the hypothetical field ψ_+ equal to zero. Applying the Laplacian operator to eqn (3.9), we obtain

$$\Delta \log \rho_{\pm}(\mathbf{r}) \mp 4\pi Q(\rho_+(\mathbf{r}) - \rho_-(\mathbf{r})) = 0, \quad (3.10)$$

where $\Delta \psi_s$ simply reduces to the source charges on the (presumably negatively charged) polyion cylinders which constitute boundary conditions. Setting $\rho_+ = n_s \exp \varphi$ and $\rho_- = n_s \exp -\varphi$ now yields the Poisson–Boltzmann equation with the boundary condition $\rho_{\pm} \rightarrow n_s$ far away from the polyions in the interstitial region,

$$\Delta \varphi = \kappa^2 \sinh \varphi, \quad (3.11)$$

where the Debye screening length κ^{-1} is given by

$$\kappa^2 = 8\pi Q n_s. \quad (3.12)$$

I have given the above derivation, which differs somewhat from classic treatments,^[6,7] in order to link with other SCF theories (liquid crystals,^[1] polymers,^[8] quantum mechanics,^[9] two-dimensional Euler fluid,^[10-12] random interactions,^[13] etc.).

3.2.2 Scattering by small ions

We do not have to solve the Poisson–Boltzmann equation (3.11) in order to investigate the scattering by the small ions. Assuming that the external field ψ_+ is weak, we write $\rho_{\pm} = \rho_{0,\pm} + \delta\rho_{\pm}$, where $\delta\rho_{\pm}$ are the perturbations in the ion densities, and so deduce linear equations

$$\rho_{0,+}(\mathbf{r})^{-1}\delta\rho_+(\mathbf{r}) + Q \int d\mathbf{r}' \frac{\delta\rho_+(\mathbf{r}') - \delta\rho_-(\mathbf{r}')}{|\mathbf{r} - \mathbf{r}'|} + \psi_+(\mathbf{r}) = 0 \quad (3.13a)$$

and

$$\rho_{0,-}(\mathbf{r})^{-1}\delta\rho_-(\mathbf{r}) + Q \int d\mathbf{r}' \frac{\delta\rho_-(\mathbf{r}') - \delta\rho_+(\mathbf{r}')}{|\mathbf{r} - \mathbf{r}'|} = 0. \quad (3.13b)$$

These expressions clearly exhibit the electric potential caused by the non-electroneutral inhomogeneity $\delta\rho_+ - \delta\rho_-$, which is the origin of electric restoring forces. If the latter were zero (i.e. setting the charge or Bjerrum length Q equal to zero), eqn (3.13a) would reduce to a linearized Boltzmann distribution and $\delta\rho_-$ would vanish altogether since, obviously, the field ψ_+ would not interfere with the negatively charged ions.

Next, we look at ion fluctuations beyond the double layers surrounding the polyions, by setting $\rho_0(\mathbf{r}) \equiv n_s$. The integral equations (3.13) are reduced to ordinary equations by three-dimensional Fourier transformation:

$$\delta\hat{\rho}_+(\mathbf{q}) + \frac{\kappa^2}{2q^2} (\delta\hat{\rho}_+(\mathbf{q}) - \delta\hat{\rho}_-(\mathbf{q})) + n_s\hat{\psi}_+(\mathbf{q}) = 0, \quad (3.14a)$$

$$\delta\hat{\rho}_-(\mathbf{q}) + \frac{\kappa^2}{2q^2} (\delta\hat{\rho}_-(\mathbf{q}) - \delta\hat{\rho}_+(\mathbf{q})) = 0. \quad (3.14b)$$

At short distances (i.e. for large q/κ), the electric restoring forces become negligible, since we need not require strict electroneutrality within volumes substantially less than κ^{-3} . On the other hand, at large distances the ions fluctuate effectively only as electroneutral pairs; the negative ions are completely slaved to the positive ions in the limit $\kappa \ll q$, as can be seen by solving eqn (3.14):

$$\delta\hat{\rho}_+(\mathbf{q}) = -\left(\frac{2q^2 + \kappa^2}{2q^2 + 2\kappa^2}\right)n_s\hat{\psi}_+(\mathbf{q}), \quad (3.15a)$$

$$\delta\hat{\rho}_-(\mathbf{q}) = \frac{\kappa^2}{2q^2 + \kappa^2} \delta\hat{\rho}_+(\mathbf{q}). \quad (3.15b)$$

Accordingly, by Yvon's theorem (eqn (3.1)) we have simply computed the structure factors

$$S_{++} = \frac{2q^2 + \kappa^2}{2q^2 + 2\kappa^2} \quad \text{and} \quad S_{-+} = \frac{\kappa^2}{2q^2 + 2\kappa^2}. \quad (3.16a,b)$$

Therefore, in view of $+/-$ symmetry, we may write for the intensity of light scattered by the electrolyte bulk

$$\begin{aligned} I(\mathbf{q}) &\equiv \sum_i \sum_j a_i a_j S_{ij} n_s \\ &= a_+^2 n_s + a_-^2 n_s - \frac{n_s \kappa^2 (a_+ + a_-)^2}{2(q^2 + \kappa^2)}, \end{aligned} \quad (3.17)$$

where a_+ and a_- are the scattering powers of the $+$ and $-$ ions respectively. This expression was first derived by Hermans^[14] who first solved the Debye–Hückel approximation to φ (eqn (3.11) for $\varphi \ll 1$), and then computed the pair correlation function and inserted this in the usual formal expression for the structure factor (i.e. a Fourier transform of the pair correlation). A similar discussion is presented by Berne and Pecora.^[15] Recently, Jannink and van der Maarel used a random phase approximation to derive the structure factor of electrolytes and also discussed sum rules.^[62] For polyelectrolytes such an approximation neglects orientation–translation coupling, which is addressed in Section 3.4.

Next I consider qualitatively the scattering by the counterions within the double layers around the polyions.^[14] Near a polyion surface the magnitude of the potential φ is substantially greater than unity, so that $\rho_{0,+} \gg n_s$ and $\rho_{0,-} \ll n_s$. Hence, eqns (3.13) reduce to

$$Q \int d\mathbf{r}' \frac{\delta\rho_+(\mathbf{r}')}{|\mathbf{r} - \mathbf{r}'|} + \psi_+(\mathbf{r}) \simeq 0 \quad \text{and} \quad \delta\rho_-(\mathbf{r}) \simeq 0. \quad (3.18a,b)$$

The high electric field is the dominant force restraining the ions against the external field so, by the same token, the scattering must be very low. A complete calculation of the scattering by the small ions is now involved in view of the inhomogeneity of the equilibrium distribution (eqn (3.11)).

3.2.3 Merits and limitations of the Poisson–Boltzmann equation

The Poisson–Boltzmann equation (3.11) in a 1–1 solution works quite well for two reasons. First, at low potentials it can be linearized and reduces to the classic Debye–Hückel theory,^[16] which is known to be an exact limiting law.^[17] Second, in high fields, density fluctuations should become small, the Hartree approximation (eqn (3.2)) is tenable and the free energy minimum (eqn (3.9)) should become sharp. Moreover, the electric potential arising from the source terms swamps the ideal entropy. In fact, corrections to the Poisson–Boltzmann equation analysed within the context of liquid state theory by Fixman^[7] are

indeed small. The potential of average force between charged mica surfaces has been measured by Israelachvili and coworkers and found to compare with solutions of eqn (3.11) fairly well.^[18] Monte Carlo simulations also bear out eqn (3.11).^[19]

For ions that are not univalent eqn (3.11) is quite useless. This was pointed out by Oosawa some time ago.^[20] His reasoning is comprehensible, since the fluctuational corrections should increase as z_+^2 (z_+ = valency of a counterion) whereas the bare Coulomb energy scales as z_+ . There is now a substantial literature—theoretical,^[21–23] computational^[23,24] and experimental^[25]—on the breakdown of the Poisson–Boltzmann equation under these circumstances.

Finally, in many cases of practical importance the polyions are not extremely long, so it is of some concern whether end effects come into play. At low salt the ion distribution has been calculated recently.^[26] The self-consistent potential is virtually constant because of the buffering action by the counterions. The distribution along the rod contour can be approximated by

$$\begin{aligned} v_{\text{eff}}(s) &\simeq \frac{2 \log(2/\kappa d)}{Q \log(4s/\kappa d^2)} \quad \text{for } \frac{1}{2}d \leq s \leq \kappa^{-1} \\ &\simeq 1/Q \quad \text{for } \kappa^{-1} \leq s \leq \frac{1}{2}L, \\ v_{\text{eff}}(L-s) &= v_{\text{eff}}(s). \end{aligned} \tag{3.19}$$

In the midsection, the ion distribution is identical to the usual Oosawa–Manning limit^[6,27] but fewer counterions are condensed at the two ends.

3.2.4 The Poisson–Boltzmann equation beyond the double layer

The solution to eqn (3.11) is a third Painlevé transcendent, which is impossible to express in terms of classical transcendent functions only. A convenient approximation has been developed by Philip and Wooding^[28] and advocated by Stroobants, Lekkerkerker and Odijk for statistical thermodynamic work.^[29]

For a cylindrical polyion in a 1–1 electrolyte, the magnitude of the far field of the dimensionless electric potential is given to sufficient accuracy by

$$\phi = \frac{K_0(\kappa R)}{K_0(\kappa R_*)} \equiv 2v_{\text{eff}} Q K_0(\kappa R) \quad \text{for } R' \equiv \kappa R \geq \kappa R_*, \tag{3.20}$$

where R is the distance from the cylinder axis, K_0 is the zero-order modified Bessel function of the second kind, and κR_* is identical to the parameter R_* introduced by Philip and Wooding.^[28] We have also defined an effective linear charge density v_{eff} : eqn (3.20) is the potential arising from a superposition of Debye–Hückel potentials exerted by a line charge of density v_{eff} (i.e. the solution to the linearized cylindrical version of eqn (3.11)). In practice we often let the polyion cylinder bear a constant surface charge density of σ elementary charges

per unit area. The charge density parameter is then given by

$$\xi \equiv Qv \equiv \pi dQ\sigma. \quad (3.21)$$

The boundary condition at the polyion surface is

$$\left. \frac{d\phi}{dR'} \right|_{R'=\frac{1}{2}\kappa d} = -2\xi \quad (3.22)$$

and enables one to compute R_* with the help of eqn (14) and the second and sixth columns in Table I of ref. 28.

3.3 Interaction between two polyions and virial coefficients

Consider the interaction w between two nearby test polyions (see the configuration shown in Fig 3.1). Configurations with $w/k_B T$ much larger than unity are rare, for they are weighted by a Boltzmann factor $\exp(-w/k_B T)$.^[30] Hence, the distance X between the centre lines is, statistically speaking, more often than not, larger than R_* . Thus it is plausible to employ an effective Debye–Hückel approximation

$$w_{el}/k_B T \simeq Qv_{eff}^2 \int_{-\infty}^{\infty} di \int_{-\infty}^{\infty} dj \frac{e^{-\kappa r_{ij}}}{r_{ij}}, \quad (3.23)$$

where $r_{ij}^2 = i^2 + j^2 + X^2 - 2ij \cos \gamma$ and the end effects^[33] are momentarily neglected. With the help of the substitutions $u = i - j \cos \gamma$, $t = j \sin \gamma$, and the use of polar coordinates, eqn (3.23) is simplified to^[31,32]

$$w_{el}/k_B T = \frac{2\pi Qv_{eff}^2 e^{-\kappa X}}{\kappa \sin \gamma}. \quad (3.24)$$

This form exhibits screening and a twist or torque towards a perpendicular configuration, the latter effect being of some importance in the formation of the nematic or cholesteric phase.^[29]

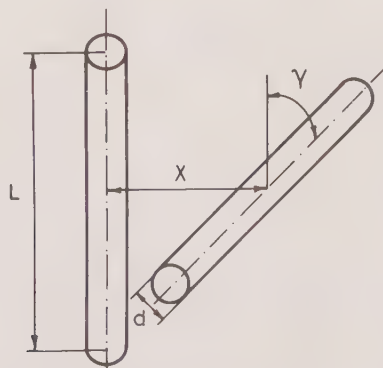


FIG. 3.1. Two skewed polyions.

It is now possible to derive an analytic expression for the second virial coefficient $A_{2,0}$ in terms of the effective diameter:^[31]

$$A_{2,0} = \frac{\pi}{4} L^2 d_{\text{eff}}, \quad (3.25)$$

$$d_{\text{eff}} \simeq \kappa^{-1}(0.7704 + \log(2\pi v_{\text{eff}}^2 Q \kappa^{-1})) \quad (3.26)$$

if $2\pi v_{\text{eff}}^2 Q \kappa^{-1} e^{-\kappa d} \gtrsim 2$.

End effects are often important in practice. A lengthy asymptotic analysis yields^[33]

$$A_2 \simeq A_{2,0} \left(1 + \frac{4d_{\text{eff}}}{L}\right). \quad (3.27)$$

For instance, for mononucleosomal DNA of length 50 nm in a 0.1 M NaCl aqueous buffer, we have $d_{\text{eff}} = 5.6$ nm and the end effect amounts to a substantial 45%.

I have also proposed an approximation for the third virial coefficient^[33] (neglecting end effects):

$$A_3 \simeq \frac{4d_{\text{eff}} A_{2,0}}{L}. \quad (3.28)$$

This scales as the effective diameter to the third power, so A_3 is very sensitive to the ionic strength. For a recent discussion of higher order virials for uncharged spherocylinders, see ref. 34; in order to gauge the effect of charge in an approximate fashion, replace d in that paper by d_{eff} .

Equations (3.25), (3.27) and (3.28) hold true only in the case of excess salt, a condition we can define in a quantitative way as follows. In a rough approximation of the condensation type, the Debye screening length may be written as

$$\begin{aligned} \kappa^2 &\simeq 8\pi Q \left(n_s + \frac{n_c}{2Qv} \right) \\ &\equiv 8\pi Q n_s (1 + \tau) \end{aligned} \quad (3.29)$$

where the equivalent concentration of counterions arising from the polyelectrolyte is given by $n_c = vL\rho_L$ and

$$\tau \equiv \frac{2c}{\pi L d_{\text{eff}} Q n_s}, \quad c \equiv A_{2,0} \rho_L. \quad (3.30, 3.31)$$

The condition of ‘excess salt’ is simply $\tau \ll 1$. From eqn (3.26) we have $d_{\text{eff}} = \mu\kappa^{-1}$ with $\mu = \mathcal{O}(4-10)$ in a typical experiment so that

$$\tau \lesssim \frac{cd_{\text{eff}}}{L}. \quad (3.32)$$

Since c is never greater than $\mathcal{O}(1)$, the excess salt condition $\tau \ll 1$ is easily attainable in practice. Russel has presented an original attempt to discuss the onset of correction terms in the statistical thermodynamics for $\tau \ll 1$.^[35]

3.4 The virial theory of the structure factor

3.4.1 The third virial approximation

Having introduced the electrostatics within the Poisson–Boltzmann approximation, we are now in a position to set up a systematic theory of the structure factor. The essential problem that we have to resolve is the coupling of orientational and translational degrees of freedom of the polyions. I first present an extension of an earlier paper^[3] so as to incorporate the third virial term and then discuss the relation of this theory to previous work.

The generalized coordinates of a rod-like polyion are denoted by $g \equiv (\mathbf{r}, \mathbf{u})$, where \mathbf{r} are the coordinates of the centre of mass of the test polyion and \mathbf{u} is the orientation of its centre-axis. I introduce an inhomogeneous polyion density $f(g)$ normalized to the total number of macromolecules N within volume V :

$$\int dg f = N. \quad (3.33)$$

In the uniform state $f = f_{\text{eq}} = \rho_L/4\pi$, where $\rho_L = N/V$ is the polyion number density. The total free energy of the system of polyions acted upon by an external field $\psi(g)$ can be written as a virial expansion provided that ψ does not vary too strongly:

$$\begin{aligned} F_{\text{tot}}[f]/k_B T &= \int dg_1 f(g_1) \log(4\pi f(g_1)/\rho_L) \\ &+ \frac{1}{2} \iint dg_1 dg_2 f(g_1)f(g_2)W_2(g_1, g_2) \\ &+ \frac{1}{6} \iiint dg_1 dg_2 dg_3 f(g_1)f(g_2)f(g_3)W_3(g_1, g_2, g_3) \\ &+ \int dg_1 f(g_1)\psi(g_1). \end{aligned} \quad (3.34)$$

The first term is an ideal entropy and the second and third virial terms depend on the generalized Mayer function W_2 :

$$W_2(g_1, g_2) = 1 - \exp(-w_{\text{tot}}(g_1, g_2)/k_B T), \quad (3.35)$$

$$W_3(g_1, g_2, g_3) = W_2(g_1, g_2)W_2(g_2, g_3)W_2(g_3, g_1). \quad (3.36)$$

The interaction w_{tot} is the sum of the hard-core and electrostatic interactions between two test polyions with coordinates g_1 and g_2 (the electrostatic

interaction is analogous to eqn (3.23) but now includes end effects). If we were to switch off the external potential ψ , the system would relax to uniform equilibrium $f = f_{\text{eq}}$ and we would regain the classic Onsager form:^[1]

$$\frac{1}{(4\pi)^2} \iint dg_1 dg_2 W_2(g_1, g_2) = 2A_2 V, \quad (3.37)$$

$$\frac{1}{(4\pi)^2} \iiint dg_1 dg_2 dg_3 W_3(g_1, g_2, g_3) = 3A_3 V. \quad (3.38)$$

We obtain the actual inhomogeneous distribution f by minimizing the functional F_{tot} of eqn (3.34) and taking account of the constraint (3.33). In addition, the external field is weak, so we write $f = f_{\text{eq}} + \delta f$ where the perturbation is small, so as to derive the following linear integral equation:

$$\delta f(g_1) + f_{\text{eq}} \int dg_2 W_2(g_1, g_2) \delta f(g_2) + f_{\text{eq}}^2 \int dg_2 \bar{W}_2(g_1, g_2) \delta f(g_2) + f_{\text{eq}} \psi(g_1) = 0, \quad (3.39)$$

with

$$\begin{aligned} \bar{W}_2(g_1, g_2) &\equiv \int dg_3 W_3(g_1, g_2, g_3) \\ &= W_2(g_1, g_2) \int dg_3 W_2(g_2, g_3) W_2(g_3, g_1). \end{aligned} \quad (3.40)$$

At this stage I analyse the function \bar{W}_2 with the help of Fig. 3.2. Polyions 1 and 2 are held fixed, are skewed at an angle typically greater than d_{eff}/L and are separated by a distance at most of order d_{eff} , otherwise eqn (3.40) vanishes. Such a configuration contributing to \bar{W}_2 is shown in Fig. 3.2(a), where rod 3 is within a distance d_{eff} of rods 1 and 2 at the same time. However, the dominant contribution to the integral actually arises from an inner region displayed in Fig. 3.2(b). Rods 1 and 2 form essentially a ‘surface of interaction’ scaling as $d_{\text{eff}}^2 \sin^{-1} \gamma$, where γ is the angle between \mathbf{u}_1 and \mathbf{u}_2 . Thus, the integral over g_3

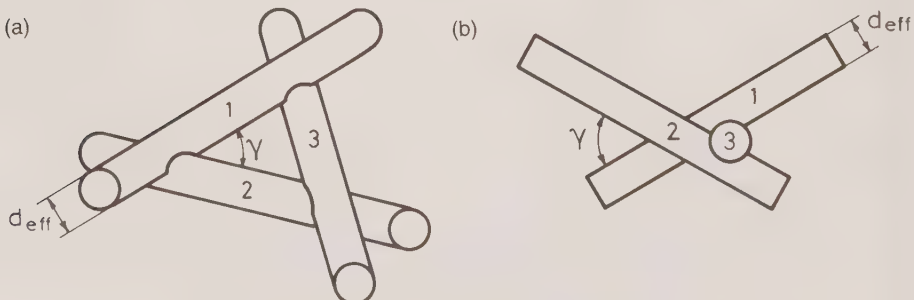


FIG. 3.2. (a) A cluster of three polyions with three pairs of interactions. (b) A schematic view of a typical cluster dominating A_3 .

is proportional to L and $d^2 \sin^{-1} \gamma$ if we neglect end effects, and is independent of the positions \mathbf{r}_1 and \mathbf{r}_2 (note that it is consistent within the same approximation to neglect higher order terms arising from electrostatic twist). Furthermore, by the same argument, the third virial coefficient must scale as $L d_{\text{eff}}^2 A_{2,0}$, as is indeed the case (see eqn (3.28), in conformity with the reasoning for uncharged rods given by Straley^[37] and elaborated in ref. 38. The as yet unspecified constant is readily determined by integrating both sides of eqn (3.40) over g_1 and g_2 and using eqns (3.37) and (3.38):

$$\bar{W}_2(g_1, g_2) \simeq \frac{3\pi^2 A_3 W_2(g_1, g_2)}{2A_2 \sin \gamma}. \quad (3.41)$$

Next, one notes that $W_2(g_1, g_2) = W_2(\mathbf{r}_1 - \mathbf{r}_2, \mathbf{u}_1, \mathbf{u}_2)$ in view of translational invariance, so that a spatial Fourier transform of eqn (3.39) yields (on deleting index 1)

$$\delta \hat{f}(\mathbf{q}, \mathbf{u}) + f_{\text{eq}} \int d\mathbf{u}_2 \left[1 + \frac{3\pi A_3 \rho_L}{8A_2 \sin \gamma} \right] \hat{W}_2(\mathbf{q}, \mathbf{u}, \mathbf{u}_2) \delta \hat{f}(\mathbf{q}, \mathbf{u}_2) + f_{\text{eq}} \psi(\mathbf{q}, \mathbf{u}) = 0. \quad (3.42)$$

Equation (3.42) is a linear integral equation which is impossible to solve exactly and contains the kernel \hat{W}_2 , expressing the coupling of orientational and translational degrees of freedom. We next choose $\psi = -\varepsilon s_{\mathbf{q}}(\mathbf{u})$, with $-\varepsilon$ the field on an infinitesimal segment of a test polyion, \mathbf{q} the scattering vector in the experiment and the rod interference factor $s_{\mathbf{q}}$,

$$s_{\mathbf{q}}(\mathbf{u}) \equiv \frac{\sin \mathbf{K} \cdot \mathbf{u}}{\mathbf{K} \cdot \mathbf{u}}, \quad \mathbf{K} \equiv \mathbf{q}L/2, \quad (3.43, 3.44)$$

because this choice results in the correct structure factor for a single rod at zero concentration, as it should. The fluctuation in the segment concentration is now given by eqn (3.1) on the one hand,

$$\delta \hat{\rho}(\mathbf{u}) = \rho_L S(\mathbf{u}) \varepsilon, \quad (3.45)$$

and by

$$\delta \rho(\mathbf{r}) \equiv \int d\mathbf{r}' \int d\mathbf{u} L^{-1} \int_{-L/2}^{L/2} ds \delta(\mathbf{r} - \mathbf{r}' - \mathbf{u}s) \delta \hat{f}(\mathbf{r}', \mathbf{u})$$

or

$$\delta \hat{\rho}(\mathbf{q}) = \int d\mathbf{u} s_{\mathbf{q}}(\mathbf{u}) \delta \hat{f}(\mathbf{q}, \mathbf{u}) \quad (3.46)$$

on the other. If we define the unknown function $y \equiv \delta f / \varepsilon f_{\text{eq}}$ in the limit $\varepsilon \rightarrow 0$, the structure factor and eqn (3.42) may be rewritten as

$$S(\mathbf{q}) = \langle s_{\mathbf{q}}(\mathbf{u}) y(\mathbf{q}, \mathbf{u}) \rangle, \quad (3.47)$$

$$y(\mathbf{q}, \mathbf{u}) + \rho_L \left\langle \left[1 + \frac{3\pi A_3 \rho_L}{8A_2 \sin \gamma} \right] \hat{W}_2(\mathbf{q}, \mathbf{u}, \mathbf{u}') y(\mathbf{q}, \mathbf{u}') \right\rangle' = s_{\mathbf{q}}(\mathbf{u}), \quad (3.48)$$

where the orientational average $(4\pi)^{-1} \int d\mathbf{u}$ is conveniently denoted by $\langle \rangle$ (with an analogous prescription for the primed average). For double layers that are not too thick (i.e. whenever $qd_{\text{eff}} < 1$ and two effects (charge fluctuations; interference within the double-layer interaction) are negligible), it is straightforward to calculate \hat{W}_2 : one replaces $L^2 d \sin \gamma$ in eqn (A4) of ref. 39 by eqn (2) of ref. 3:

$$\hat{W}_2 \simeq 2A_2(\sin \gamma)s_q(\mathbf{u})s_q(\mathbf{u}'), \quad (3.49)$$

$$A_2(\sin \gamma) \simeq L^2 \kappa^{-1} \sin \gamma [\log(2\pi v_{\text{eff}}^2 Q \kappa^{-1}) + 0.5722 - \log \sin \gamma]. \quad (3.50)$$

Finally, we apply the variational principle explained in Appendix 3.A to eqns (3.47) and (3.48) by choosing $Z = s_q(\mathbf{u})$ and using the addition theorem:^[40]

$$S(K) \simeq \frac{F^2}{F + 2A_2\rho_L F^2 + 3A_3\rho_L^2 F^2 - \frac{5}{4}A_2\rho_L G^2 - \frac{9}{32}A_2\rho_L H^2}, \quad (3.51)$$

where the single-rod structure factor is given by

$$F(K) \equiv \langle s_q^2(\mathbf{u}) \rangle = K^{-1} \text{Si}(2K) - \left(\frac{\sin K}{K} \right)^2, \quad (3.52)$$

with

$$\text{Si}(2K) \equiv \int_0^{2K} dx \frac{\sin x}{x}. \quad (3.53)$$

The functions G and H are rather complicated:

$$G \equiv \frac{3}{4}K^{-2} \left(1 - \frac{\sin 2K}{2K} \right) - \frac{1}{2}F(K), \quad (3.54)$$

$$H \equiv \frac{3}{8}F - \frac{55}{48K^2} - \frac{5 \sin 2K}{32K^3} - \frac{35 \cos 2K}{32K^4} + \frac{35 \sin 2K}{64K^5}. \quad (3.55)$$

Note that it is consistent to include end effects in A_2 in eqn (3.51). Also, eqn (3.51) has the right compressibility limit as K tends to zero. It is important to stress that the structure factor does not exhibit oscillations at the level of the third virial approximation.

3.4.2 Relation to previous work

An early attempt^[41] which neglects orientation–translation coupling is regained by setting A_3 , H and G equal to zero and expanding the resulting form to linear order in the small quantity $A_2\rho_L$. This theory^[41] is clearly invalid in the important regime $A_2\rho_L = \mathcal{O}(1)$. Another attempt^[42] is legitimate only in the Debye–Hückel approximation when the polyions are very weakly charged, and so is obviously at odds with the non-linear theory presented here. Klein *et al.*^[43–45] tried to improve on their first paper.^[42] Unfortunately, the device of lumping together many elementary charges into effective segments is a rather

severe approximation for strictly quantitative work on polyions which are, for all practical purposes, uniformly charged rods (meanwhile, the interaction between finite polyions has become established^[133]). Shimada *et al.*^[46] first derived an Yvon equation similar to eqn (3.48) for uncharged rods in the second virial approximation. They tried to solve their integral equation by a perturbation scheme, but in general this approach to integral equations is known to cause potentially serious problems. In point of fact, the higher order terms in the expansion of Shimada *et al.*^[46] diverge at $\rho_L A_{2,0} = 4$. For instance, their structure factor at small scattering vectors is given by

$$S^{-1} = 1 + 2A_{2,0}\rho_L + \frac{1}{9}K^2 + \frac{7}{2025} \left[1 - \frac{5A_{2,0}\rho_L}{7(1 - \frac{1}{4}A_{2,0}\rho_L)} \right] K^4, \quad (3.56)$$

which should be compared with the analogous expansion of eqn (3.51),

$$S^{-1} = 1 + 2A_2\rho_L + 3A_3\rho_L^2 + \frac{1}{9}K^2 + \frac{7}{2025}[1 - 0.732A_2\rho_L]K^4, \quad (3.57)$$

which is free from the divergence, as it should be. In order to avoid this type of spurious divergence, Van der Schoot and Odijk attempted a global solution to the structure factor via a variational method^[40] (as in Appendix 3.A) which agrees rather well with Maeda's numerical work,^[47] showing no anomalies at $\rho_L A_{2,0} = 4$. Maeda^[2] and Odijk^[3] extended the variational procedure^[40] to the case of charged rods; again, the theory is in very good agreement with numerical computations.^[2] Equation (3.51) now incorporates the third virial coefficient, which is of some importance in a quantitative comparison with experiments on polyions that are not too long or in concentrated solution.

3.4.3 High K limit

It is possible to derive the asymptotic $K \rightarrow \infty$ limit of the structure factor exactly. In this limit y must approach $s_q(\mathbf{u})$ exactly, as can be seen from eqns (3.48) and (3.49). Moreover, we have the following relation:

$$\begin{aligned} \frac{1}{2} \int_{-1}^1 dx \left(\frac{\sin Kx}{Kx} \right) f(x) &= \frac{1}{2K} \int_{-K}^K du \left(\frac{\sin u}{u} \right)^2 f\left(\frac{u}{K}\right) \\ &\sim \frac{\pi f(0)}{2K}, \end{aligned} \quad (3.58)$$

where $x \equiv \cos \theta \rightarrow 0$ is the region weighted heavily as $K \rightarrow \infty$. Hence, likewise, we have

$$\begin{aligned} \langle\langle s_q^2(\mathbf{u}) \sin y s_q^2(\mathbf{u}') \rangle\rangle' &\sim \frac{\pi^2}{4K^2} \langle\langle \sin|\phi_1 - \phi_2| \rangle\rangle' \\ &\sim \frac{\pi}{2K^2}. \end{aligned} \quad (3.59)$$

Finally, we end up with

$$S^{-1} \sim \frac{2K}{\pi} + \frac{2}{\pi^2} + \frac{16A_2\rho_L}{\pi^2} + 3A_3\rho_L^2 + \mathcal{O}(K^{-1}). \quad (3.60)$$

3.4.4 Comparison with experiment

Unfortunately, very few systematic scattering experiments have been performed on rod-like polyions in the semi-dilute and concentrated regimes. One recent experiment on 50 nm long DNA^[48] is in good accord with eqn (3.51) except when the DNA aggregates at high concentrations. Schulz *et al.*^[49–51] carried out light scattering experiments, both static and dynamic, on fd virus suspensions under a wide variety of conditions. One of their curves allows us to test eqn (3.51). The fd virus particle bears ten elementary charges per nm contour, is 6.6 nm thick and is 880 nm long; it is very stiff since the persistence length is 2200 nm.^[52] Sample 3 of ref. 51 is dissolved in a 0.6 mM Na-citrate buffer yielding a Debye length of $\kappa^{-1} = 12.4$ nm (the Bjerrum length $Q = 0.714$ nm). The effective diameter $d_{\text{eff}} = 80.4$ nm is calculated with the aid of the solution to the Poisson–Boltzmann equation^[28] and eqn (3.26). At a polyion concentration of $\rho_L L^3 = 9.25$,^[51] we have $A_2\rho_L = 0.907$ from eqn (3.27) and $A_3\rho_L^2 = 0.161$ from eqn (3.28); hence the contribution from the third virial is appreciable in this case. As can be seen in Fig. 3.3, the experimental data^[51] are in fairly good agreement with the structure factor calculated with the help of eqn (3.51) if one considers that no adjustable parameters have been used.

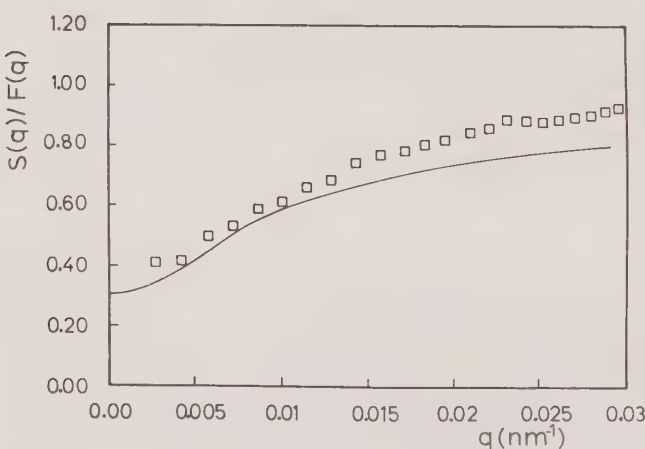


FIG. 3.3. A light scattering experiment (□) on an fd virus by Schulz *et al.*^[51] compared with theory (eqn (3.51); curved line).

3.5 Concluding remarks

The theory surveyed here is of course of rather restricted validity. Topics not addressed include the following. Corrections due to semi-flexibility have been analysed in depth at zero concentration.^[53–55] Shimada *et al.*^[46] computed the low q form of the structure factor for semi-flexible uncharged chains in a semi-dilute solution using the second virial and random phase approximations (the latter is equivalent to setting G and H equal to zero in eqn (3.51)). Their expression can be obtained heuristically by replacing the length L in the low q form of the structure factor of uncharged rigid rods by $\sqrt{12R_g}$, where R_g is the radius of gyration of the worm-like chain. Hence, one semi-empirical form of the structure factor for semi-flexible polyelectrolytes valid for all scattering factors, a form that may prove useful in interpreting experiments, is obtained by a similar substitution in $F(K)$, $G(K)$ and $H(K)$ of eqn (3.51) and letting A_2 and A_3 be experimentally determined virial coefficients. At high q (i.e. $q > \kappa$), ion fluctuations that are not electroneutral have to be accounted for, at least in principle (see eqn (3.18a)), as also do interference contributions within the excluded-volume effect itself (disregarded in eqn (3.49)). Polyelectrolytes without salt are still imperfectly understood, in part, because we have not come to terms with the strong coupling between the polyions and the small ion distribution. As yet, we have no mathematical method of describing the way in which small-ion screening depends on the configurational statistics of the polyions. This coupling problem shows up in the structure factor of salt-free rod-like polyelectrolytes, which is an oscillatory function of the scattering vector.^[49–51,56] The reader is referred to the contributions by Klein and D’Aguanno (Chapter 2) and Sedlák (Chapter 4), who discuss some of these problems.

Appendix 3.A: the variational principle for the structure factor

We wish to compute the quantity

$$S = \langle s(u) y(u) \rangle \quad (3.A.1)$$

by solving the integral equation

$$y(u) + \langle K(u, u') y(u') \rangle = s(u), \quad (3.A.2)$$

where the kernel K is symmetric but non-definite. Schwinger was the first to invent variational principles of the kind to be discussed, for linear definite operators.^[59,60] Rowlands and Selengut extended the principle to non-definite operators.^[61] Consider the functional

$$J[z] \equiv 2\langle sz \rangle - \langle z^2 \rangle - \langle\langle z(u)K(u, u')z(u') \rangle\rangle' \quad (3.A.3)$$

and expand it in the supposedly small fluctuation δz ($z(u) = y(u) + \delta z(u)$) using eqn (3.62):

$$J \equiv S - \langle \delta z^2 \rangle - \langle\langle \delta z(u)K(u, u')\delta z(u') \rangle\rangle' + \mathcal{O}(\delta z^3). \quad (3.A.4)$$

Hence, J deviates from S to second order only, but it may be bounded from below or from above. Next, we can find the optimal amplitude of z by inserting $z(u) = hZ(u)$ in eqn (3.A.3) and extremalizing J with respect to the variational parameter h :

$$J = \frac{\langle sZ \rangle^2}{\langle Z^2 \rangle + \langle \langle Z(u)K(u, u')Z(u') \rangle \rangle'}. \quad (3.A.5)$$

We may optimize this expression with respect to Z , but it only yields an extremum.^[61] Clearly, if Z is chosen shrewdly we will attain an excellent estimate for S . Note that the trial function Z need not depend on an adjustable parameter.

References

1. Onsager, L. (1949). *Ann. N.Y. Acad. Sci.*, **51**, 627.
2. Maeda, T. (1991). *Macromolecules*, **24**, 2740.
3. Odijk, T. (1992). In *Laser light scattering in biochemistry* (eds S. E. Harding, D. B. Satelle and V. A. Bloomfield). Royal Society of London.
4. Yvon, J. (1958). *Suppl. Nuovo Cimento*, **9**, 144.
5. Hansen, J. P. and McDonald, I. R. (1976). *Theory of simple liquids*. Academic, London.
6. Oosawa, F. (1971). *Polyelectrolytes*. Marcel Dekker, New York.
7. Fixman, M. (1979). *J. Chem. Phys.*, **70**, 4995.
8. Lifshitz, I. M., Grosberg, A. Yu. and Khokhlov, A. R. (1978). *Rev. Mod. Phys.*, **50**, 683.
9. Landau, L. D. and Lifshitz, E. M. (1975). *Quantum mechanics*, Pergamon, Oxford.
10. Montgomery, D. and Joyce, G. (1974). *Phys. Fluids*, **17**, 1139.
11. Pointin, Y. B. and Lundgren, T. S. (1976). *Phys. Fluids*, **19**, 1459.
12. Miller, J., Weichman, P. B., and Cross, M. C. (1992). *Phys. Rev.*, **A45**, 2328.
13. Odijk, T. (1990). *Macromolecules*, **23**, 1875.
14. Hermans, J. J. (1949). *Rec. Trav. Chim.*, **68**, 859.
15. Berne, B. J. and Pecora, R. (1976). *Dynamic light scattering*. John Wiley, New York.
16. Debye, P. and Hückel, E. (1923). *Phys. Z.*, **24**, 185.
17. Mayer, J. (1950). *J. Chem. Phys.*, **18**, 1426.
18. Israelachvili, J. (1985). *Intermolecular and surface forces*. Academic Press, London.
19. Jönsson, B., Wennerström, H., and Halle, B. (1980). *J. Chem. Phys.*, **84**, 2179.
20. Oosawa, F. (1968). *Biopolymers*, **6**, 1633.
21. Mitchell, D. J. and Ninham, B. W. (1978). *Chem. Phys. Lett.*, **53**, 397.
22. Kjellander, R. and Marçelja, S. (1984). *Chem. Phys. Lett.*, **112**, 49.
23. Kjellander, R., Åkesson, T., Jönsson, B., and Marçelja, S. (1992). *J. Chem. Phys.*, **97**, 1424.
24. Guldbrand, L., Jönsson, B., Wennerström, H., and Linse, P. (1984). *J. Chem. Phys.*, **80**, 2221.
25. Kekicheff, P. and Ninham, B. W. (1990). *Europhys. Lett.*, **12**, 471.
26. Odijk, T. (1991). *Physica A*, **176**, 201.
27. Manning, G. S. (1969). *J. Chem. Phys.*, **51**, 924.
28. Philip, J. R. and Wooring, R. A. (1970). *J. Chem. Phys.*, **52**, 953.
29. Stroobants, A., Lekkerkerker, H. N. W., and Odijk, T. (1986). *Macromolecules*, **19**, 2232.

30. Brenner, S. L. and Paresgian, V. A. (1974). *Biophys. J.*, **14**, 327.
31. Stigter, D. (1977). *Biopolymers*, **16**, 1435.
32. Fixman, M. and Skolnick, J. (1978). *Macromolecules*, **11**, 863.
33. Odijk, T. (1990). *J. Chem. Phys.*, **93**, 5172.
34. Frenkel, D. (1987). *J. Phys. Chem.*, **91**, 4912.
35. Russel, W. B. (1982). *J. Polym. Sci., Polym. Phys. Ed.*, **29**, 1233.
36. Onsanger, L. (1949). *Phys. Rev.*, **10**, 3.
37. Straley, J. P. (1973). *Mol. Cryst. Liq. Cryst.*, **24**, 7.
38. Odijk, T. (1986). *Macromolecules*, **19**, 2313.
39. Doi, M., Shimada, T., and Okano, K. (1988). *J. Chem. Phys.*, **88**, 4070.
40. Van der Schoot, P. and Odijk, T. (1990). *Macromolecules*, **23**, 4181.
41. Benmouna, M., Weill, G., Benoît, H., and Akcasu, Z. (1982). *J. Phys., France*, **43**, 1679.
42. Schneider, J., Hess, W., and Klein, R. (1985). *J. Phys. A*, **18**, 1221.
43. Schneider, J., Karrer, D., Dhont, J. K. G., and Klein, R. (1987). *J. Chem. Phys.*, **87**, 3008.
44. Weyerich, B., D'Aguanno, B., Canessa, E., and Klein, R. (1990). *Faraday Discuss. Chem. Soc.*, **90**, 245.
45. Canessa, E., D'Aguanno, B., Weyerich, B., and Klein, R. (1991). *Mol. Phys.*, **73**, 175.
46. Shimada, T., Doi, M., and Okano, K. (1988). *J. Chem. Phys.*, **88**, 2815.
47. Maeda, T. (1989). *Macromolecules*, **22**, 1881.
48. Wissenburg, P., Odijk, T., Cirkel, P., and Mandel, M. (1995). *Macromolecules*, **28**, 2315.
49. Maier, E. E., Schulz, S. F., and Weber, R. (1988). *Macromolecules*, **21**, 1544.
50. Schulz, S. F., Maier, E., and Weber, R. (1989). *J. Chem. Phys.*, **90**, 7.
51. Schulz, S. F., Maier, E. E., Krause, R., Hagenbüchle, M., Deggelman, M., and Weber, R. (1990). *J. Chem. Phys.*, **92**, 7087.
52. Fraden, S. (1995). In *Observation, prediction and simulation of phase transitions in complex fluids* (eds M. Baus, L. F. Rull and J. P. Ryckaert). Kluwer, Dordrecht, The Netherlands.
53. des Cloiseaux, J. (1973). *Macromolecules*, **6**, 403.
54. Norisuye, T., Murakama, H., and Fujita, H. (1978). *Macromolecules*, **11**, 966.
55. Yoshizaki, T. and Yamakawa, H. (1980). *Macromolecules*, **13**, 1518.
56. Maier, E. E., Krause, R., Deggelman, M., Hagenbüchle, M., Weber, R., and Fraden, S. (1992). *Macromolecules*, **25**, 1125.
57. Van der Maarel, J. R. C., Groot, L. C. A., Mandel, M., Jesse, W., Jannink, G., and Rodriguez, V. (1992). *J. Phys. II, France*, **2**, 109.
58. Van der Maarel, J. R. C., Mandel, M., and Jannink, G. (1992). *Europhys. Lett.*, **20**, 607.
59. Levine, H. and Schwinger, J. (1948). *Phys. Rev.*, **74**, 958.
60. Levine, H. and Schwinger, J. (1949). *Phys. Rev.*, **75**, 1423.
61. Tait, J. H. (1964). *Neutron transport theory*. Longman, London.
62. Jannink, G. and van der Maarel, J. R. C. (1991). *Biophys. Chem.*, **41**, 15.

Polyelectrolytes in solution

Marián Sedlák

4.1 Polyelectrolytes: definition and classification

Polyelectrolytes can be defined as compounds which are macromolecules or supramolecular entities carrying a large number of ionizable groups. These groups dissociate in solution under certain conditions. As a result, the macromolecule becomes highly charged and is referred to as a polyion. The dissociation of each group on the polyion results in the creation of one counterion of opposite charge with respect to the polyion. If the polyion charge is $Q = Ze$ (e being the electron charge), then each polyion is ‘accompanied’ by Z counterions. Figure 4.1 shows schematically the situation in a polyelectrolyte solution.

From the point of view of dissociation in aqueous media, polyelectrolytes are classified as weak or strong. Ionizable groups on strong polyelectrolytes are fully dissociated upon dissolution in water, whereas those on weak polyelectrolytes are dissociated only upon neutralization (pH change). A typical example of a strong polyelectrolyte is sodium poly(styrenesulphonate) (Fig. 4.2). A typical example of a weak polyelectrolyte is poly(methacrylic acid) (Fig. 4.3). Figure 4.3 also shows the process of neutralization (ionization) of the polyacid.

Polyelectrolytes are of both biological and artificial origin. From the point of view of the polyion architecture, polyelectrolytes can be classified as follows:

- (1) linear flexible polyelectrolytes, such as sodium poly(styrenesulphonate) (Fig. 4.2), poly(methylacrylic acid) (Fig. 4.3), poly(acrylic acid), the polybases poly(2-vinylpyridine) and poly(4-vinylpyridine), the polypeptides poly(L-lysine) and poly(L-aspartic acid), etc.;
- (2) worm-like semi-rigid polyelectrolytes, such as DNA;
- (3) rod-like rigid polyelectrolytes, e.g. TMV (tobacco mosaic virus);
- (4) globular charged macromolecules with a tertiary structure very little influenced by the presence of charges, e.g. proteins; and
- (5) spherical polyelectrolytes such as latex particles, dendrimers, micelles, mineral colloids, etc.

We will deal mainly with groups (1)–(4) in this chapter. Attention will be paid especially to the most complex system—linear flexible polyelectrolytes.

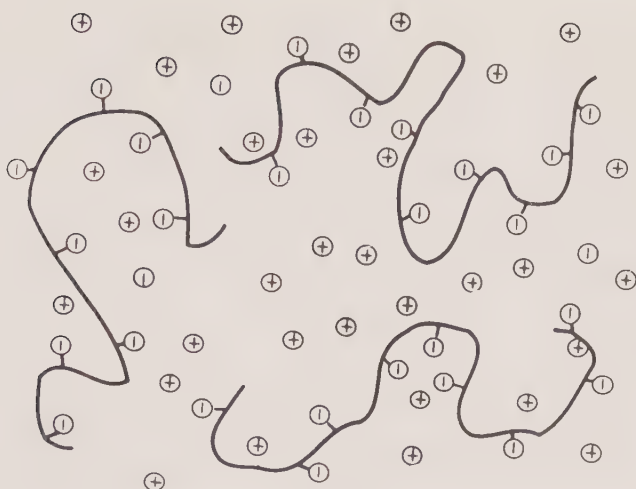


FIG. 4.1. A schematic illustration of a polyelectrolyte solution.

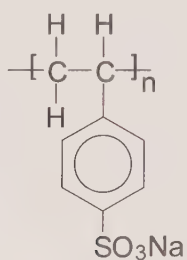


FIG. 4.2. A typical example of a linear flexible polyelectrolyte: sodium poly(styrene-sulphonate).

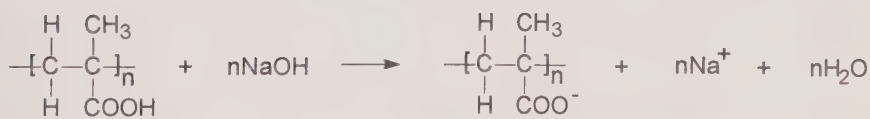


FIG. 4.3. The ionization of poly(methacrylic acid) by neutralization with sodium hydroxide.

4.2 General problems of polyelectrolyte physics: definition of basic quantities for the characterization of polyelectrolytes

The traditional procedure in light scattering methodology is: (1) creation of a model that is as close as possible to the investigated system; (2) derivation of scattering equations for the accepted model; and (3) system characterization, based on fitting of experimental data by theoretical dependencies derived from

scattering equations. The general problem in light scattering from polyelectrolytes is that an adequate model is still absent. This holds mainly for polyelectrolyte solutions in the limit of low ionic strength where electrostatic interactions are weakly screened. Nevertheless, light scattering is a very useful tool for the investigation of polyelectrolyte solutions because the wavelength of visible light (which serves as a probe) is comparable with the range of electrostatic interactions. Although not trivially interpretable, the effects of electrostatic interactions are reflected in light scattering data. In this section I would like to summarize the general problems of polyelectrolyte physics and to define basic quantities for the characterization of polyelectrolyte solutions which will be used throughout this chapter.

From the point of view of static light scattering, several problems can be outlined. The first one is the single-chain conformation, determined by intramolecular interactions in dilute solutions, and both intra- and intermolecular interactions at moderate concentrations. The second problem concerns the intermolecular correlations (correlations between positions of individual polyions). The third problem, important in light scattering experiments, is the osmotic compressibility of polyelectrolyte solutions. Another issue is the presence of small ions in solution. The scattering power of a small ion in solution can in most cases be neglected compared to the scattering power of a polyion. Nevertheless, small ions influence light scattering from polyelectrolyte solutions indirectly by their influence on electrostatic interactions.

The common denominator of the most of the above outlined questions is the issue of electrostatic interactions between charged particles in solution. Even the nature of these interactions (repulsive vs. attractive) is currently the subject of discussion.^[1,2]

4.2.1 *The nature of electrostatic interactions*

In 1938 Langmuir^[3] treated a solution of charged micelles. He considered counterions as a part of the interaction energy and, as a result, he obtained an excess of attractive force just as in the sodium chloride crystal. To achieve equilibrium, some kind of an additional repulsive force was required.

The currently most widely accepted DLVO (Derjaguin–Landau–Overbeek) theory considers oppositely screened Coulomb repulsion between charges. The additional attractive force is the van der Waals force, which becomes significant at relatively close distances (less than 2 nm). The long-range interaction is purely repulsive. The repulsive part of the DLVO potential of interaction between two colloidal particles with radius R_p and charge Q is

$$U(r) = \left(\frac{e^{\kappa R_p}}{1 + \kappa R_p} \right)^2 \frac{Q^2}{\varepsilon} \frac{e^{-\kappa r}}{r} = X_{\text{DLVO}}^2 \frac{Q^2}{\varepsilon} \frac{e^{-\kappa r}}{r}, \quad (4.1)$$

where ε is the solution dielectric permittivity, r is the distance between particles, and κ^{-1} is a parameter called the Debye–Hückel screening length. The DLVO

potential was able to explain many phenomena in colloid science, although the apparent charges required to fit the data were always smaller than structural (chemical) charges. This was explained by charge renormalization concepts or by redefining the 'particle unit' as the macroion and *tightly* associated counterions.

However, Ise and co-workers^[2] reported in recent years numerous experimental results which are not consistent with the DLVO theory. They have emphasized that these experimental results require some form of long-range attractive interaction and they have proposed interaction potentials with a minimum at finite separation distances of the order of several hundred nanometers, as experimentally observed.^[4,5] The potential given by Sogami in ref. 5 is based on the assumption of a two-state electrolyte ion distribution in solution. While region I covers the macroion with an associated ion cloud, region II covers the space between two 'macroion units'. The resulting potential can be expressed as

$$U(r) = X_s^2 \frac{Q^2 e^{-\kappa_{II} r}}{\varepsilon r}, \quad (4.2)$$

where κ_{II}^{-1} is the screening length in region II and X_s^2 is the model-specific term which defines the minimum in $U(r)$ by multiplying the rest of the formula (Yukawa part). The presence of the minimum is due to the difference between the concentrations of counterions and coions in region II. If these concentrations are set equal, then the Sogami potential reduces to the same form as the DLVO potential (minimum at infinity). While we will not proceed in the discussion of the 'repulsion vs. attraction problem' at this point, we will focus briefly on the importance of the definition of the screening parameter.

4.2.2 Screening parameter

As already indicated, electrostatic interactions between charged particles are screened by the presence of other charged species in solution. The screened interaction potential can be expressed in general as $U(r) = (A/r) \exp(-\kappa r)$, where κ is the so-called screening parameter and κ^{-1} is referred to as the screening length.

In the case of simple electrolytes, the Debye–Hückel theory yields the well known expression for the screening length (called the Debye–Hückel screening length, κ_{DH}^{-1})

$$\kappa_{DH}^2 = 8\pi l_B i, \quad (4.3)$$

where l_B is the Bjerrum length, $l_B = e^2/\varepsilon k_B T$, and i is the ionic strength, $i = \frac{1}{2} \sum_{j=1}^m c_j Z_j^2$. The meaning of the other symbols is as follows: e is the electron charge, ε is the dielectric permittivity, k_B is Boltzmann's constant, T is temperature, m is the number of different ionic species in solution, and c_j and Z_j are the molar concentration and the charge of the j th ionic species, respectively. All ionic species present in solution are taken into account, as

only one ion is considered as the test ion. In the treatment of solutions of macroions, several definitions of the screening parameter are possible: in the DLVO theory, macroions and associated counterions are not taken into account; in the coupled mode theory^[6] all ions (i.e. macroions, counterions, and added-salt small ions) are considered; and also an ‘intermediate’ definition of the screening length is used by taking into account only added-salt small ions and counterions.^[7,8] Another important issue regarding the definition of the screening length is the problem of its ‘global vs. local character’. In all of the above-mentioned definitions of the screening length, the concentration of ions is considered uniform throughout the solution. However, this is not always true. Counterions are more concentrated in the vicinity of the macroion, while coions are repelled from the macroion environment. This effect is pronounced at high charge densities on macroions. Therefore, in other theoretical approaches^[9–11] the space around a macroion is divided into inner and outer regions with different screening lengths of a local character. The same idea was used also in the theory of Sogami^[4,5].

It was also noted^[1] that correlations between mobile particles in calculating screened electrical interactions are neglected, while the usual screened potentials are *mean* potentials and it is required that fluctuations in the potential are small. This condition may not be sufficiently fulfilled for highly asymmetrical systems of macroions and small ions.^[1]

4.2.3 Counterion condensation

Depending on its chemical structure, the macroion is capable of carrying a certain number of charges that originate by separation of counterions from the surface of the macroion. However, this number cannot be obtained in some cases. If the charge density exceeds some limit, further counterions condense onto the surface of the polyion to reduce the total charge. The fraction of condensed counterions depends on the macroion geometry. For a rod-like, infinitely long polyion, the Oosawa–Manning theory^[12,13] yields the critical parameter

$$\xi = l_B/A, \quad (4.4)$$

where A is the average spacing between charges on the polyion. The meaning of the parameter ξ is that if $\xi > 1$, then the average spacing A is reduced by counterion condensation until $\xi = 1$. Then, of course, $A = l_B$. The minimum accessible charge spacing is equal to the Bjerrum length. The Oosawa–Manning theory^[12,13] must be employed with great caution for linear polyions with finite length and thickness, other macroion geometries, and site-specific binding. There is no clear consensus on the status of condensed counterions (locally bound, territorially bound, or just ‘trapped’ in the ion cloud surrounding the macroion). The onset of counterion condensation is experimentally evidenced mostly just as a reduction of the effective polyion charge.

The polyion charge can in practice be adjusted within the limits of counterion condensation by changing the solution pH. The commonly used quantity for the characterization of polyion charge is the degree of ionization, α . It is defined as the fraction of ionized groups on the polyion (i.e. the ratio of the number of ionized groups to the total number of ionizable groups). The degree of neutralization, α' , is used mainly to characterize ionization of polyacids by neutralization, and is defined as the ratio of the molar concentration of added hydroxide to the monomer molar concentration of the polyacid. In the case of weak polyacids with negligible natural ionization in aqueous solutions, $\alpha \cong \alpha'$.

4.2.4 Persistence length

The single-chain conformation problem is mainly important in the case of linear flexible polyions where electrostatic interactions have appreciable influence. The common quantity for the characterization of the polymer chain conformation is the persistence length L_p , which is proportional to the smallest accessible radius of curvature of the chain. It is defined by the formula

$$\langle \cos \beta \rangle = \exp(-L_c/L_p) \quad (4.5)$$

where β is the angle between end segments separated by the contour distance L_c . To characterize the conformation of a linear polyion, the notion of electrostatic persistence length was introduced.^[14-16] The total persistence length is then defined as the sum of the intrinsic persistence length of the chain without charges and the electrostatic persistence length $L_{p,e}$:

$$L_{p,e} = \frac{l_B}{4A^2\kappa^2} h(\kappa L_c), \quad (4.6)$$

where $h(\kappa L_c)$ is the finite chain length correction factor. Other calculations of $L_{p,e}$ with slightly different results were made by taking into account the finite thickness of the polyion^[17] and the effect of fluctuations in the chain configuration.^[18] Exact numerical calculations of the electrostatic persistence length were performed using a screened Coulomb pairwise interaction for a continuously bent rod.^[11]

4.2.5 The semi-dilute regime

The onset of an entangled network can be visualized as in the case of neutral polymers, with the exception that there are no actual contacts between chains because of electrostatic repulsions. The existence of the critical concentration of this transition, C^* , was confirmed in excess of added low molecular weight salt.^[19] In the absence of added salt, the situation is less clear. The value of the C^* concentration can be considerably different compared to the equivalent neutral polymer. This is because of a different single-chain conformation in the vicinity of C^* , which is not sufficiently understood at the

moment. In addition, the calculation of C^* in a classical way, as $C^* \approx M_w/(4/3)\pi N_A R^3$, where N_A is Avogadro's number, and M_w and R are the molecular weight and the radius of the polyion, respectively, is based on an assumption of a homogeneous structure throughout the solution. This is questionable in the case of low-salt polyelectrolyte solutions.

4.3 The application of static light scattering to polyelectrolyte solutions

4.3.1 Theoretical considerations

In order to discuss specific aspects of light scattering from rather complex systems—polyelectrolyte solutions—we will first investigate the limits of applicability of the classical light scattering formulae, which are frequently, and in most cases successfully, used for uncharged scattering media.

According to fluctuation theory, the scattering intensity from a volume V of the scattering medium at zero angle is given by^[20]

$$I(0) = \frac{4\pi^2 \bar{n}^2 V(\Delta n)^2}{\lambda_0^4}, \quad (4.7)$$

where $\Delta n = n - \bar{n}$, n and \bar{n} are the refractive index and the mean refractive index, respectively, and λ_0 is the wavelength in vacuum. The intensity $I(0)$ is normalized with respect to the incident light intensity I_0 and the distance r from the scattering volume. In the case of a vertically polarized incident light, it is defined as $I(0) = r^2 I_s(0)/I_0(0)$, where $I_s(0)$ is the actual scattering intensity at the distance r . (The scattering intensity normalized in this way is commonly referred to as the Rayleigh ratio.)

Equation (4.7) was derived on the assumption that the volume V can be divided into small volume elements ΔV such that:

- (1) they are small enough with respect to the wavelength of the light used and hence phase differences between light rays scattered from different places of the volume element are negligible; and
- (2) they are large enough to make concentration fluctuations in neighbouring volume elements independent.

If both of these conditions are satisfied, then the volume elements may be considered as radiating dipoles with independently fluctuating amplitudes and the total scattering from volume V can be calculated as the sum of contributions from small volume elements ΔV yielding eqn (4.7). If the scattering volume is divided into slices of thickness d , than the first condition is satisfied when the maximum phase difference from the given slice $2d \sin(\theta/2)/\lambda \ll 1$, and the second condition is satisfied when the size of particles or intermolecular forces $R \ll d$. Fluctuation theory can therefore be applied if the scattering volume can be divided into small volume elements with thickness d such that $R \ll d \ll \lambda/2 \sin(\theta/2)$.

Fluctuation theory applied to a two-component system (particles and solvent), where particles and interparticle forces are reasonably small, yields for polarized light the well known relation^[21]

$$\frac{KC}{I(0)} = \frac{1}{RT} \frac{\partial\pi}{\partial C}, \quad (4.8)$$

where π is the osmotic pressure against the solvent, C is the solute concentration in g/L, R is the gas constant, T is the absolute temperature, and the constant K is defined as

$$K = \frac{4\pi^2 n^2 (\mathrm{d}n/\mathrm{d}C)^2}{\lambda_0^4 N_A}, \quad (4.9)$$

where N_A is Avogadro's number and $\mathrm{d}n/\mathrm{d}C$ is referred to as the refractive index increment. $I(0)$ in eqn (4.8) represents here the excess light scattering by particles, i.e. $I(0) = r^2(I_s(0) - I_{s,\text{solvent}}(0))/I_0(0)$. (It may be noted here that when unpolarized light is used the factor of 4 in eqn (4.9) is replaced by 2 and the factor $(1 + \cos^2 \theta)$ is introduced into the denominator of the expression for the Rayleigh ratio.) As can be seen from eqn (4.7), the light scattering is proportional to fluctuations in refractive index of the scattering medium. These fluctuations in a two-component system are due to density and concentration fluctuations. The former are determined by the isothermal compressibility $RT(\partial\rho/\partial p)$, and the latter by the osmotic compressibility $RT(\partial C/\partial\pi)$. For moderate concentrations (up to 20%), the density fluctuations in solution can be assumed to be equal to density fluctuations in the pure solvent. Hence, if the solvent scattering is subtracted, only concentration fluctuations given by osmotic compressibility are taken into account in eqn (4.8). The inverse quantity $(1/RT)(\partial\pi/\partial C)$ is referred to as the osmotic modulus.

The intensity $I(\theta)$ scattered at a non-zero angle θ is, in general, decreased by interference effects:

$$\frac{KC}{I(\theta)} = \frac{1}{RT} \frac{1}{p(\theta)} \frac{\partial\pi}{\partial C}, \quad (4.10)$$

where $p(\theta)$ is defined as $p(\theta) = I(\theta)/I(0) \leq 1$. $p(\theta)$ governs both the intra- and interparticle interference. The former is due to the interference of light rays scattered from different segments of the same particle, while the latter is due to the interference of light rays scattered from segments belonging to different particles. In the case of homogeneous spheres, $p(\theta)$ can be factored as

$$p(\theta) = P(\theta)S(\theta), \quad (4.11)$$

where $P(\theta)$ is the so-called single particle form factor, reflecting only the intraparticle interference, and $S(\theta)$ is referred to as the solution structure factor, reflecting only the interparticle interference. Equation (4.11) does not hold in general for other particle architectures and is certainly not valid for rigid rods.^[22] Nevertheless, it can be considered as a good approximation in most cases. $p(\theta)$ functions can be calculated for different particle architectures:

however, theoretical expressions for $S(\theta)$ are in most cases still absent. The effect of $S(\theta)$ can be eliminated by extrapolation to infinite dilution. At non-zero concentrations interparticle correlations are important and depend on interparticle interactions. These are generally concentration-dependent and therefore eqn (4.10) should be written more exactly as

$$\frac{KC}{I(\theta)} = \frac{1}{RT} \frac{1}{p(\theta, C)} \frac{\partial \pi}{\partial C}. \quad (4.12)$$

The unknown concentration dependence of $p(\theta, C)$ can be eliminated only at $\theta = 0$, where scattering is given only by thermodynamics (osmotic compressibility). For $\theta = 0$, theoretical calculations of the concentration dependence of $p(\theta, C)$ can be done realistically for various systems. Conversely, at $C \rightarrow 0$, $p(\theta, C) = P(\theta)$ and the angular dependence of light scattering can be calculated satisfactorily. It can be done even for large particles where the requirement of fluctuation theory $R \ll \lambda/2 \sin(\theta/2)$ does not hold. In this case, of course, absolute intensities and the concentration dependence cannot be given by fluctuation theory, and usually only information on the particle size and shape can be obtained from the angular dependence of light scattering.

If the particles and the range of interparticle interactions are small enough to satisfy the requirement of fluctuation theory, and interparticle interactions are also weak enough for neglect of interparticle correlations, eqn (4.12) can be written in the form

$$\frac{KC}{I(\theta)} = \frac{1}{RT} \frac{1}{P(\theta)} \frac{\partial \pi}{\partial C} \quad (4.13)$$

and, after inserting a virial expansion of solution osmotic pressure,

$$\frac{KC}{I(\theta)} = \frac{1}{P(\theta)} \left(\frac{1}{M_w} + 2A_2 C + \dots \right) \quad (4.14)$$

where M_w is the weight average of the particle molecular weight and A_2 is the second virial coefficient. Equation (4.14) was simplified further by Zimm^[23] on the assumption that particles (polymers) interact with each other through only one segment of each particle at a time, which is better fulfilled the lower the concentration:

$$\frac{KC}{I(\theta)} = \frac{1}{M_w P(\theta)} + 2A_2 C. \quad (4.15)$$

As regards light scattering, polyelectrolyte solutions are complex systems and theoretical considerations are complicated by several factors:

- (1) Polyelectrolyte solutions are multi-component systems consisting of solvent, polyions, counterions, and coions. Equations for two-component systems in the previous paragraph thus do not automatically hold.
- (2) Electrostatic interactions are long-range interactions. If the ionic strength of the solution is very small (usually $< 10^{-3}$ M), the range of these

interactions becomes comparable with the wavelength of visible light, the relation $R \ll \lambda/2 \sin(\theta/2)$ does not hold, and fluctuation theory cannot be used in its usual form, unless $\theta = 0$.

- (3) Even at $\theta = 0$, when interference effects are eliminated and light scattering is given only by thermodynamics, problems arise due to the fact that calculations of osmotic pressure in polyelectrolyte solutions are not trivial.
- (4) When focusing only on angular dependencies $p(\theta, C)$ instead of complete expressions for scattering intensity, light scattering theory still encounters difficulties (many-body problems with long-range interactions).

The multi-component nature of polyelectrolyte solutions was treated by Vrij and Overbeek.^[24] Their theory was restricted to the zero-angle scattering limit where the problem of the long-range nature of electrostatic forces is eliminated, as indicated in (2). In this case eqn (4.7) retains its validity. Another restriction is that non-electroneutral fluctuations are neglected as compared to neutral fluctuations. Neglect of non-electroneutral fluctuations means that the polyion, together with the surrounding atmosphere consisting of small ions, is considered as the scattering unit. In other words, the atmosphere is carried along with the polyion. This approximation is valid in volume elements the linear dimensions of which are larger than the Debye–Hückel screening length κ^{-1} . The condition $\kappa^{-1} \ll d \ll \lambda/2 \sin(\theta/2)$ then implies that

$$\frac{2 \sin(\theta/2)}{\lambda \kappa} \ll 1 \quad (4.16)$$

or $\kappa^{-1} \ll q^{-1}$, where q is the commonly used scattering vector, defined as $q = (4\pi/\lambda) \sin(\theta/2)$. It means that at length scales given by q^{-1} the non-electroneutral fluctuations not persisting over distances of a few κ^{-1} can be neglected. It has been shown^[25] that to keep deviations from the assumption of purely electroneutral fluctuations below 1% at all scattering angles, the left-hand side of eqn (4.16) must be $\ll 0.05$. This corresponds to $\kappa^{-1} < 10 \text{ nm}$ or, in aqueous solutions of 1:1 electrolyte, to the ionic strength $i > 10^{-3} \text{ M}$.

With these conditions, Vrij and Overbeek^[24] applied a more general treatment developed for multi-component systems^[20,26] to a three-component polyelectrolyte solution. The mean square of the fluctuation in the refractive index of the scattering medium, $(\Delta n)^2$ in eqn (4.7), in this treatment is expressed in terms of fluctuations in concentrations of the components and partial refractive index increments. When applied to a three-component polyelectrolyte system, it appeared that the total scattering can be split into three contributions: concentration fluctuations of polyions moving with a surrounding small-ion atmosphere, concentration fluctuations of small ions, and density fluctuations mainly due to the solvent. The last two contributions were shown to be equal to the scattering from a salt solution (solvent with small ions) which is in Donnan equilibrium with the polyelectrolyte solution. The excess light scattering of the polyelectrolyte over the scattering of a simple salt solution, which is in Donnan equilibrium with the polyelectrolyte solution, is then equal to the

contribution from concentration fluctuations of polyions moving together with a surrounding small-ion atmosphere, and can be expressed as

$$\frac{K^*C}{I(0)} = \frac{1}{RT} \left(\frac{\partial \pi}{\partial C} \right)_{\mu_s}, \quad (4.17)$$

where the index μ_s means that the chemical potentials of all the solutes except that used in differentiation are constant, and K^* is given by

$$K^* = 4\pi^2 n^2 \left[\sum_{i=1}^m \left(\frac{\partial n}{\partial C_i} \right)_{P, C_j} \left(\frac{\partial C_i}{\partial C} \right)_{\mu_s} \right]^2 / \lambda_0^4 N_A, \quad (4.18)$$

where P is the pressure, and the index $i = 0$ is assigned to solvent (water), $i = 1$ to polyion, and $i = 2$ to the added low molecular weight salt. If different salts are added, the summation can be performed over $i = 3, \dots, m$. Terms $(\partial C_i / \partial C)_{\mu_s}$ are the adsorption of components i on the polyion and can be estimated in a Donnan membrane equilibrium experiment or calculated in special cases. Refractive index increments $(\partial n / \partial C_i)_{P, C_j}$ can be measured at normal pressure. However, it has been shown^[27,28] that the sum in eqn (4.18) can be well approximated as $(\partial n / \partial C)_{\mu_s}$. Thus the constant K^* can be expressed simply as

$$K^* = \frac{4\pi^2 n^2 (\partial n / \partial C)_{\mu_s}^2}{\lambda_0^4 N_A}, \quad (4.19)$$

which is formally equivalent to eqn (4.9) for neutral two-component systems. The only difference is that the refractive index increment is at a constant chemical potential of salt rather than at the constant concentration of salt. Details concerning measurements of refractive index increments at a constant chemical potential of salt will be given in Section 4.3.2.

The Donnan osmotic pressure in eqn (4.17) can be expanded in the virial form

$$\pi = RT \left(\frac{C}{M_w} + (A_2)_{\mu_s} C^2 + (A_3)_{\mu_s} C^3 + \dots \right), \quad (4.20)$$

where M_w is the polyelectrolyte molecular weight and $(A_i)_{\mu_s}$ are virial coefficients at the Donnan pressure. Equation (4.17) can be then written in the form

$$\frac{K^*C}{I(0)} = \frac{1}{M_w} + 2(A_2)_{\mu_s} C + \dots, \quad (4.21)$$

which is again formally equivalent to the formula commonly used for neutral two-component systems, with the exception that experiments must be done at a constant chemical potential of salt (Donnan equilibrium pressure). If polyelectrolyte solutions are not equilibrated (dialysed against the low molecular weight salt solution) before measurements, only apparent molecular weights and apparent second virial coefficients can be obtained from eqn (4.21). The differences between apparent and true molecular weights and second virial coefficients will be discussed in Section 4.3.3.

The angular dependence of the scattering intensity is not influenced by the choice of the constant K . The influence of K on the scattered intensity cancels in the factor $p(\theta) = I(\theta)/I(0)$ (see eqn (4.20)). At higher salt concentrations ($C_s > 10^{-3}$ M) and upon extrapolation to $C \rightarrow 0$, $p(\theta)$ equals the single-particle form factor $P(\theta)$, which can be expressed as

$$P(\theta)^{-1} = 1 + \frac{1}{3} \langle R_g^2 \rangle_z q^2 + \dots, \quad (4.22)$$

where $\langle R_g^2 \rangle_z$ is the z -average of the square of the radius of gyration of the polyion. The polyion size can be thus obtained from the angular dependence of scattering intensity. What is actually measured in such a light scattering experiment is the radius of gyration of a complex of the polyion with adsorbed small ions. Although there is no strong theoretical or experimental evidence, it is assumed that the scattering power of counterions is negligible compared to the scattering power of the polyion and therefore the radius of the complex is very close to the radius of the polyion.

While the fluctuation theory can be expanded to non-zero scattering angles at higher salt concentrations ($C_s > 10^{-3}$ M), the situation is more complicated in the case of salt-free polyelectrolyte solutions. There is no rigorous, general theory describing such a complex problem at the moment. Only qualitative considerations can be made.

If the scattering angle is kept zero, the validity of the basic equation (4.7) derived from fluctuation theory is maintained as discussed before. If we neglect scattering due to counterions, eqn (4.8) for a two-component system may be used with caution. The osmotic pressure of a salt-free solution can be expressed as $\pi = g\pi_{id}$, where π_{id} is the ideal osmotic pressure and g is the so-called osmotic coefficient reflecting the degree of non-ideality. π_{id} can be written as

$$\pi_{id} = RT \frac{C}{M_m} \left(\frac{1}{N} + \alpha \right), \quad (4.23)$$

where M_m is the monomer molecular weight, N is the degree of polymerization and α is the degree of ionization. After the substitution from eqn (4.23) into eqn (4.18) we obtain

$$\frac{KC}{I(0)} = \frac{1}{M_m} \left(\frac{1 + \alpha N}{N} \right) \left(g + C \frac{dg}{dC} \right). \quad (4.24)$$

If we assume that the term dg/dC is small and that $\alpha N \gg 1$, the right-hand side of eqn (4.24) can be expressed as $\alpha g/M_m$, and the following conclusions can be drawn. (1) The scattering from salt-free polyelectrolyte solutions is not proportional to the molecular weight as compared to the high-salt limit or neutral polymers. (2) It decreases upon charging the chains because the product αg increases upon increasing α . (3) Scattering from charged polymers should be substantially weaker compared to neutral polymers if N is large and the difference in dn/dc is not substantial.

If the scattering angle $\theta > 0$, fluctuation theory becomes a too crude approximation for salt-free solutions. Absolute scattered intensities and their

concentration dependencies cannot be rigorously predicted. However, angular dependencies of scattered intensity $p(\theta, C) = I(\theta, C)/I(0, C)$ containing information on the particle architecture and the solution structure can be calculated. As already mentioned before, $p(\theta, C)$ can in some cases be factored according to eqn (4.11) into the single-particle form factor $P(\theta)$ and the solution structure factor $S(\theta)$. $S(\theta)$ can be calculated as^[29]

$$S(\theta) = S(q) = 1 + 4\pi\rho_n \int_0^\infty [g(r) - 1][\sin(qr)/qr]r^2 dr, \quad (4.25)$$

where ρ_n is the number density of the particles and $g(r)$ is the radial distribution function of the particles, reflecting the probability of finding a particle at distance r from another particle. If the dimensions and the shape of the particle are known, then $P(\theta)$ can be calculated theoretically and $S(\theta)$ can be obtained from experiment. Experimental $S(\theta)$ can then be compared with calculations based on eqn (4.25) and various models for $g(r)$. This is, for instance, the case for charged spherical polyions. If $P(\theta)$ varies with experimental conditions, as in the case of linear flexible polyions, the interpretation of $p(\theta, C)$ is less straightforward.

4.3.2 Experimental procedures and special polyelectrolyte sample preparations

The experimental technique and the methodology of static light scattering from polyelectrolyte solutions is in many aspects identical or similar to the case of static light scattering from neutral polymers (particles). A traditional complication is the fact that scattering is much weaker compared to neutral systems, especially in the case of low ionic strength polyelectrolyte solutions, where electrostatic interactions are weakly screened. This requires longer repeated photon counting at each scattering angle and a more careful elimination of dust particles from the solution. Another complication arises from the fact that most polyelectrolyte solutions are aqueous solutions and there is a large difference between the refractive index increments of water and glass. This causes much stronger laser beam reflections at the interface between water and the glass sample cell. A remarkable difference is, however, in measurements of refractive index increments.

As discussed in detail in Sections 4.3.1 and 4.3.3, a specific feature of measurements of refractive index increments in polyelectrolyte solutions is the fact that the measurement must be performed between a polyelectrolyte solution and solvent which are in osmotic equilibrium. The solution and solvent are brought into equilibrium by dialysis against each other. Two types of set-up can be used for this purpose: osmometer-like dialysis cells and dialysis bags. In osmometer-like dialysis cells the solution and solvent are in two compartments of equal or comparable volume, which are separated by a semi-permeable membrane. Dialysis bags are filled with solution and immersed in beakers with an excess of solvent. The use of dialysis bags is very simple and convenient.

The disadvantage is that the solution volume may change during dialysis and consequently influence solution concentration. Both dialysis bags and membranes must be checked for the molecular weight cut-off to avoid the permeation of polymer through the membrane. Especially at low molecular weights, it is recommended to check (e.g. spectroscopically) for a change in polymer concentration after dialysis. The composition of solvent on both sides of the membrane should be similar to avoid high initial osmotic pressure differences which could cause leaking in the set-up or even destruction of the membrane. The time needed to establish osmotic equilibrium depends on the permeability of the membrane, the viscosity of the solvent, and the ratio of membrane area to liquid volume. 24 hours of dialysis is a convenient routine time. It is also necessary to realize that the solvent composition changes during dialysis according to the polymer concentration on the other side of the dialysis membrane. Therefore, strictly speaking, the dialysate should be used for both refractive index increment measurements and scattered intensity measurements when calculating the excess scattering (solvent subtraction). To avoid this problem and to use the same solvent for different polymer concentrations, the dialysis can be performed in such a way that the solvent volume on one side of the membrane is considerably higher than the solution volume on the other side. The solvent composition change during dialysis can be neglected in this case.

The dialysis technique is used in polyelectrolyte sample preparations not only in connection with the refractive index increment measurements, but also as a way of adjusting the concentration of added salt (ionic strength) in the investigated solution. Because the dialysis step is quite time-consuming, an alternative method is used in which the dry, salt-free polymeric material is dissolved directly in a solution of a known ionic strength. This procedure requires elimination of all salt residuals from the polymeric material. Two alternative methods can be employed:

- (1) Material is exhaustively dialysed against a large volume of deionized water. The usual duration of dialysis is 2–3 days with 3–4 exchanges of deionized water per day. It is recommended to perform dialysis in large beakers (typically 2–5 l).
- (2) Material is purified by ion exchange. The most advantageous procedure is to use a mixed-bed ion exchange resin which exchanges both cations and anions in solution. Dissolved polyelectrolyte material is passed through a column filled with ion exchange resin or the resin is added directly to the solution and stirred gently for approximately 30 minutes. Then the solution is filtered through an appropriate filter to remove resin particles, and is freeze-dried.

The purification procedure is important because some (even dialysed-grade) commercial samples contain as much as several percent of salt residuals as an impurity. Results from purified and non-purified samples can differ appreciably.^[30]

4.3.3 Experimental results in the limit of high ionic strength

As discussed in Section 4.2, electrostatic interactions between charges on polymer chains are screened in the presence of an excess of low molecular weight salt and the behaviour of polyelectrolyte solutions more or less resembles that of solutions of neutral polymers. At low ionic strengths, the behaviour of polyelectrolyte solutions is qualitatively different. This is also reflected in light scattering experiments and therefore the discussion of experimental results is divided into the two following subsections: results in the limit of high and low ionic strengths, respectively. Section 4.3.5 is then devoted to the transition between the high and low ionic strength limits.

Figure 4.4 shows a typical example of a Zimm plot for a polyelectrolyte solution at the high ionic strength limit. The main features of the plot are the same as for neutral polymers,^[31] where on combining eqns (4.15) and (4.22) it is possible to obtain the molecular weight of the polymer from the intercept on the ordinate, the second virial coefficient from the slope of the ' $\theta = 0^\circ$ extrapolated line' and the radius of gyration from the slope of the ' $C = 0$ ' extrapolated line'.

4.3.3.1 Molecular weight. Taking into account the multi-component nature of polyelectrolyte solutions, equations (4.17) and (4.21) should be employed. They are valid at the Donnan equilibrium pressure (constant chemical potential of the diffusible low molecular weight salt). This means that the investigated polyelectrolyte solution should be dialysed against the solvent with the low molecular weight salt (hereafter referred to only as 'solvent') until equilibrium is reached. Then the excess scattering intensity of the dialysed polyelectrolyte

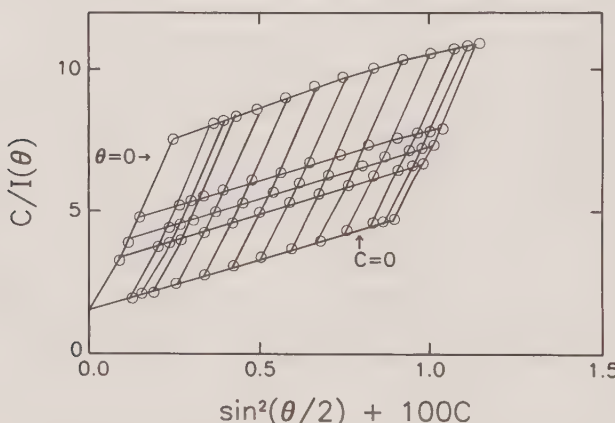


FIG. 4.4. An example of the Zimm plot for polyelectrolyte solution with an excess of added salt: sodium poly(styrenesulphonate) ($M_w = 155\,000$) in 0.1 M NaCl. (From Nagasawa, M. and Takahashi, A. (1972). In *Light scattering from polymer solutions* (ed. M. B. Huglin), pp. 671–723. Academic Press, London.)

solution over the dialysed solvent should be entered as $I(0)$ in eqn (4.17). However, the difference between the excess scattering with and without previous dialysis can in most cases be neglected. What cannot be neglected are differences between the constants K and K^* (differences between refractive index increments measured at a constant salt concentration and constant chemical potential of the salt). If samples are not dialysed and refractive index increments are measured only at constant salt concentration, then apparent rather than true molecular weights and second virial coefficients are measured (while radii of gyration are unaffected by the K constant). According to eqns (4.9), (4.18), and (4.21), the apparent molecular weight M'_w is related to the true molecular weight M_w as follows:

$$M'_w = M_w \frac{K}{K^*} = M_w \left[1 + \frac{(\partial n / \partial C_s)_C}{(\partial n / \partial C)_{C_s}} (\partial C_s / \partial C)_{\mu_s} \right]^2. \quad (4.26)$$

Similarly, the apparent second virial coefficient A'_2 is related to the true second virial coefficient A_2 as follows:

$$A'_2 = A_2 \frac{K^*}{K} = A_2 \left[1 + \frac{(\partial n / \partial C_s)_C}{(\partial n / \partial C)_{C_s}} (\partial C_s / \partial C)_{\mu_s} \right]^2, \quad (4.27)$$

where K^* is obtained from eqn (4.18) by assigning indices $i = 1$ to polymer ($C_1 = C$) and $i = 2$ to salt ($C_2 = C_s$). The term $(\partial C_s / \partial C)_{\mu_s}$ corresponds to the adsorption of salt on the polyion and the most obvious contribution is from the formation of the electrical double layer (excess of counterions and deficit of coions in the vicinity of the polyion). $(\partial C_s / \partial C)_{\mu_s}$ can be estimated from the theory of Donnan membrane equilibrium or from solving the Poisson–Boltzmann equation to calculate the concentration of counterions and coions in the vicinity of the polyion. It can be expressed as^[22]

$$(\partial C_s / \partial C)_{\mu_s} = - \frac{M_s}{M_w} \left(\frac{\partial c_s}{\partial c} \right)_{\mu_s} = - \frac{M_s}{M_w} Za, \quad (4.28)$$

where c_s and c are molar concentrations, M_s and M_w are molecular weights of the low molecular weight salt and the polyion, respectively, Z is the polyion valency and the factor $a = 0.5$ for low Z and $a < 0.5$ for high Z . The quantity $(\partial c_s / \partial c)_{\mu_s}$ is the adsorption of salt on the polyion in molar concentrations, i.e. the number of salt molecules on one polyion. The electrical double layer around the polyion is a result of the excess of counterions and the deficit of coions in the polyion environment. At low surface charge (low Z), the deficit of coions and the excess of counterions increases symmetrically when approaching the polyion surface. The number of counterions per polyion is given by Z (to compensate the charge) and the number of coions is also given by Z . Then the adsorption of salt given by the deficit of coions is equal to $Z/2$ salt molecules per particle. At high surface charge (high Z), the excess of counterions rises much faster than the deficit of coions and the adsorption of salt is less than $Z/2$ salt molecules per particle. It should be emphasized that it is a *negative*

Table 4.1. Refractive index increments of salt and of PMA at 20°C.

Solvent	$M_s(\partial n/\partial C_s)_{C=0}$ (ml/mole)	$(\partial n/\partial C)_{C_s}$ (ml/g)	$(\partial n/\partial C)_{\mu_s}$ (ml/g)
0.045 M HCl	—	0.156	0.162
0.1 M NaF	5.5	0.229	0.219
0.1 M NaCl	10.2	—	0.213
0.1 M NaBr	13.4	0.234	0.209
0.1 M NaI	21.2	—	0.197
0.1 M Na_2SO_4	21.3	—	0.210
0.01 M $(\text{NH}_4)_6\text{Mo}_7\text{O}_{24}$	—	0.227	0.169

The polymer in the salt solutions is half neutralized; concentrations C are expressed in gram PMA (acid form) per millilitre.

adsorption because the salt is expelled from the polyion surroundings. Therefore there is a minus charge in eqn (4.28). After substituting eqn (4.28) into eqn (4.26), the following relationship between M'_w and M_w is obtained:

$$\sqrt{M'_w} = \sqrt{M_w} \left[1 - \frac{(\partial n/\partial C_s)_C}{(\partial n/\partial C)_{C_s}} \frac{M_s}{M_w} Za \right] = \sqrt{M_w} \left[1 - \text{const } M_s \left(\frac{\partial n}{\partial C_s} \right)_C \right]. \quad (4.29)$$

Equation (4.29) was verified experimentally by Vrij and Overbeek.^[24] Poly(methacrylic acid) neutralized to the degree of neutralization $\alpha' = 0.5$ by NaOH was investigated in 0.1 M solutions of various salts. The cation was always Na^+ , and the anion was varied (NaCl, NaF, NaBr, etc.). Refractive index increments were measured both at constant salt concentration (0.1 M) and at constant chemical potential (after dialysis against 0.1 M salt solution). The results are reported in Table 4.1, together with refractive index increments of low molecular weight salt solutions. On the basis of these values, apparent molecular weights were calculated according to eqn (4.29) and are plotted in Fig. 4.5. A straight line was obtained, as predicted by eqn (4.29). The intercept gives the true molecular weight and the negative salt adsorption can be calculated from the slope of this line. We refer the reader to the original paper^[24] for values of true vs. apparent second virial coefficients and more detail.

Here we will simply make some notes on the multi-component nature of polyelectrolyte solutions and the related necessity to dialyse them to obtain correct physical parameters. The low molecular weight salt solution can be considered to be a mixed solvent, and parallels may be drawn between light scattering from polyelectrolyte solutions and light scattering from polymer solutions in mixed solvents. In both cases there is a preferential sorption of one solvent component to the polymer. Then the entities responsible for light scattering are not the polymers themselves, but complexes of these particles with the preferentially sorbed component. Equations describing light scattering from polymer solutions in one-component solvents also hold in mixed solvents,

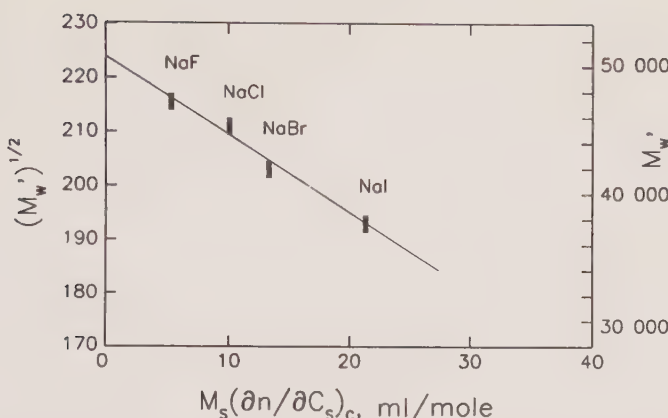


FIG. 4.5. The dependence of the apparent molecular weight M'_w on the molar refractive index increment of salt. Poly(methacrylic acid), half neutralized by NaOH, in solutions of various salts. (From Vrij, A. and Overbeek, J. Th. G. (1962). *J. Colloid. Sci.*, **17**, 570–588.)

provided that the molar mass, the refractive index increment, and the concentration of the polymer are expressed in terms of the complex of the polymer with the selectively sorbed component. Then, of course, the apparent molecular weight obtained from a light scattering experiment in a classical way corresponds to the molecular weight of the complex. As there is a negative sorption of coions to the polyanion in polyelectrolyte solutions, the apparent molecular weights are lower than true values. The difference is greater the heavier the coion is (see Fig. 4.5).

The necessity for dialysing samples before measurements of the refractive index increment is clear from the following consideration. $\Delta n / \Delta C$ expresses the change of the refractive index with concentration fluctuations (the contrast of the polymer with respect to the solvent). $\Delta n / \Delta C$ is usually approximated as $\Delta n / \Delta C$, where Δn is a difference in refractive index between two solutions with polymer concentrations C_a and C_b ($\Delta C = C_b - C_a$). Because of the negative preferential sorption of the salt, there will be a lower concentration of salt around the polyanions and a higher concentration of salt in the bulk solvent (the rest of the solution). If $C_b > C_a$, then the salt concentration in the bulk solvent will also be higher in the solution having polymer concentration C_b . The measured Δn then reflects not only the change in the polymer concentration, but also the change in the salt concentration in the bulk solvent. This can be avoided if the two solutions with C_a and C_b are dialysed against each other or against an infinitely large volume of the low molecular weight salt solution. The differences in the composition of the bulk solvent in the two solutions disappear during the dialysis due to the migration of diffusible small ions through the semi-permeable membrane. Then, as required, Δn simply reflects the change in the polymer concentration in the otherwise identical bulk solvent.

4.3.3.2 Second virial coefficient. The dependence of the second virial coefficient on basic quantities such as the solution ionic strength or the polymer molecular weight is usually of greater scientific interest compared to the knowledge of exact vs. apparent values. Therefore the time-consuming dialysis step is usually omitted and consequently apparent rather than true values of the second virial coefficient are frequently reported in papers dealing with the behaviour of the second virial coefficient.

Figure 4.6 shows the dependence of $C/I(0)$ on C for sodium poly(styrene-sulphonate) (NaPSS) in aqueous NaCl solutions of different molarity.^[32] It is evident that the initial slope of the dependence increases upon decreasing the low molecular weight salt content. Because the initial slope is, according to eqns (4.14) or (4.21), determined by the second virial coefficient, it can be concluded that the second virial coefficient increases upon decreasing the low molecular weight salt content. Qualitatively this is expected, because electrostatic interactions between charges on polyions are less and less screened upon decreasing the solution ionic strength. The theta conditions for NaPSS were reported as 4.17 M aqueous NaCl solution at 25 °C.^[33] Data for NaCl concentrations lower than 0.005 M are not reported here, because the virial expansion of osmotic pressure is not justified at these conditions (see Section 4.3.4).

The exact form of the dependence of the second virial coefficient on the added salt concentration C_s is of appreciable interest. Figure 4.7 shows a log-log plot of the second virial coefficient vs. C_s for NaPSS in aqueous NaCl solutions obtained by different authors.^[34,35] Values obtained by osmometry are also shown for comparison.^[34] The general trend is that the dependence is stronger

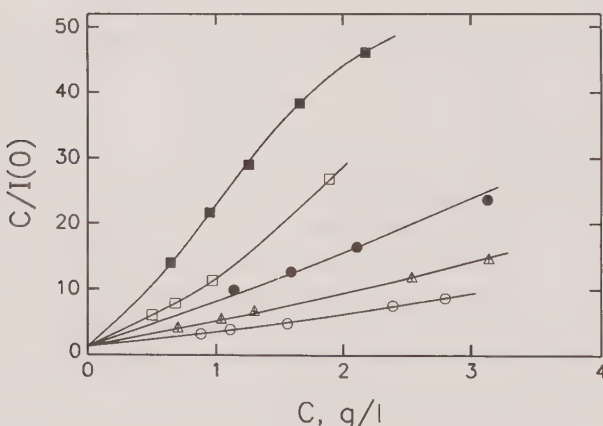


FIG. 4.6. Examples of plots of $C/I(0)$ against C for sodium poly(styrene-sulphonate) ($M_w = 155\,000$) in NaCl solutions. Concentrations of NaCl: ■, 0.005 M; □, 0.01 M; ●, 0.02 M; △, 0.05 M; ○, 0.1 M. (From Takahashi, A., Kato, T., and Nagasawa, M. (1967). *J. Phys. Chem.*, **71**, 2001–2010. [Errata: *idem*, **72**, 4724 (1968)].)

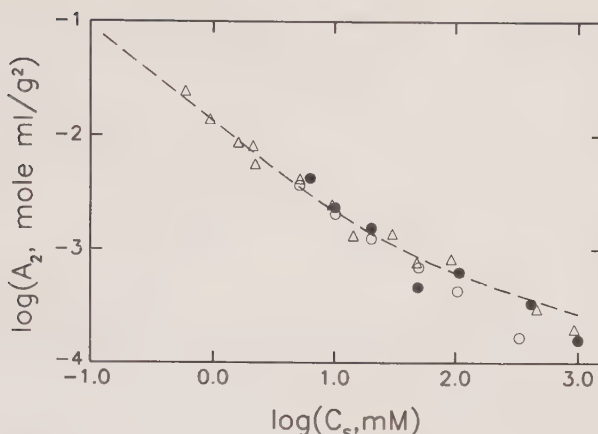


FIG. 4.7. The dependence of the second virial coefficient on added-salt concentration: sodium poly(styrenesulphonate) in NaCl solutions. Results by light scattering (Δ , Peitzsch, R. M., Burt, M. J., and Reed, W. F. (1992). *Macromolecules*, **25**, 806; ●, Takahashi, A., Kato, T., and Nagasawa, M. (1970). *J. Phys. Chem.*, **74**, 944–946) and by osmometry (\circ , Takahashi, A., Kato, T., and Nagasawa, M. (1970). *J. Phys. Chem.*, **74**, 944–946). The dashed line shows the calculation of the second virial coefficient by incorporating electrostatic excluded volume effects (Peitzsch, R. M., Burt, M. J., and Reed, W. F. (1992). *Macromolecules*, **25**, 806).

at lower C_s and weaker at higher C_s . It was proposed that $A_2 \sim C_s^{-1}$ in the former case and that $A_2 \sim C_s^{-1/2}$ in the latter.^[34] The dashed line represents calculated values of A_2 according to Yamakawa's theory.^[35,36] A qualitatively similar dependence of A_2 on C_s was found in solutions of poly(methacrylic acid)^[37] and biological polyelectrolytes.^[38,39]

The second virial coefficient of polyelectrolytes is treated either by applying the theory for spherical colloidal electrolyte solutions with a correction for the chain character of the polyion or as an extension of the theory of the second virial coefficient for non-ionic linear polymers. We note that the ideal 'Donnan' second virial coefficient calculated from the electroneutrality condition at the Donnan membrane equilibrium between a low molecular weight 1:1 valency salt solution and a thermodynamically ideal polyelectrolyte solution with uniformly distributed point-like polyions, having $-Z$ charges and molecular weight M_w , is^[40]

$$A_2^0 = 10^3 Z^2 / 4M_w^2 C_s. \quad (4.30)$$

The experimentally measured second virial coefficients are as much as 100 times lower than A_2^0 , exhibiting a high degree of non-ideality. Therefore correction factors taking into account electrostatic interactions between the ions (Γ_1) and the chain character of the polyion (Γ_2) are used to calculate A_2 , as $A_2 = A_2^0 \Gamma_1 \Gamma_2$.^[41–44] The C_s -dependence of A_2 (the deviation from $A_2 \sim C_s^{-1}$) is influenced by the C_s dependence of Γ_2 , which is more pronounced at higher C_s .^[41–44]

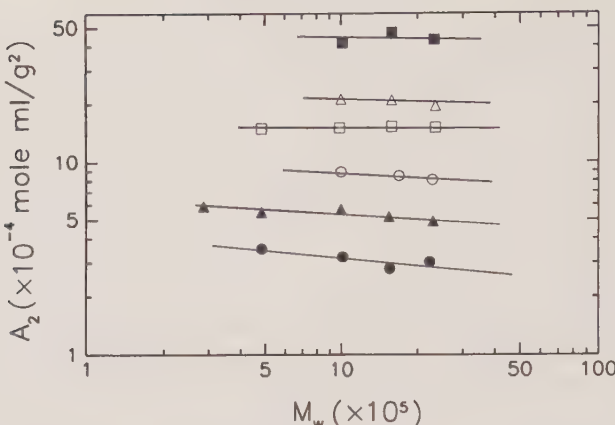


FIG. 4.8. The dependence of the second virial coefficient on molecular weight: sodium poly(styrenesulphonate) in NaCl solution. Concentration of NaCl: ■, 0.005 M; △, 0.01 M; □, 0.02 M; ○, 0.05 M; ▲, 0.1 M; ●, 0.3 M. (From Takahashi, A., Kato, T., and Nagasawa, M. (1967). *J. Phys. Chem.*, **71**, 2001–2010. [Errata: *idem*, **72**, 4724 (1968)].)

An example of an extension of the theory of the second virial coefficient for non-ionic linear polymers to polyelectrolytes is Yamakawa's approach of using perturbation theory of the excluded volume to express A_2 .^[35] A satisfactory agreement between experiment data and theoretically predicted values of A_2 (see the dashed line in Fig. 4.7) was reached by using Yamakawa's expression for A_2 .^[35]

The molecular weight dependence of A_2 is much weaker compared to solutions of neutral polymers. Figure 4.8 shows data on NaPSS in aqueous NaCl solutions.^[32] A_2 is almost independent of M_w at lower C_s and only weakly dependent on M_w at higher C_s . This is consistent with the fact that both A_2^0 and Γ_1 are independent of M_w : Γ_2 is almost constant at high expansion (low C_s), and changes with M_w only near the theta point.^[32]

4.3.3.3 Radius of gyration. As indicated above, radii of gyration of polyions can be evaluated from the data extrapolated to zero polymer concentration (Fig. 4.4). Measurements of the radius of gyration are especially attractive in the case of linear flexible polyelectrolytes. The chain conformation is determined by the interaction between neighbouring segments and the interaction between distant segments along a polymer which, via chain flexibility, are located in each other's vicinity. The former effect results in an increased local chain stiffness. The latter is referred to as the excluded volume effect. Both types of interaction can be of electrostatic or non-electrostatic origin.

In the absence of excluded volume effects (flexible polyions in a theta state or semi-rigid polyions), the radius of gyration is referred to as 'unperturbed' (R_{g0}). The local stiffening of the chain is expressed in terms of the persistence

length L_p consisting of an intrinsic and an electrostatic part (see Section 4.2). R_{g0}^2 can be expressed in three different ways: (1) $R_{g0}^2 = L_c^2/12$ in the rod limit where $L_p \gg L_c$ (L_c being the contour length); (2) $R_{g0}^2 = L_c L_p/3$ in the random coil limit where $L_p \ll L_c$; and (3) in the worm-like chain limit, which represents a transition between cases (1) and (2):

$$R_{g0}^2 = L_p^2 \left[\frac{b}{3} - 1 + \frac{2}{b^2} (b - 1 + e^{-b}) \right], \quad (4.31)$$

where $b = L_c/L_p$.

In the presence of excluded volume effects the 'perturbed' radius of gyration R_g is usually expressed as $R_g^2 = \alpha_r R_{g0}^2$. The expansion factor α_r is influenced both by the local stiffening (persistence length effect) and the excluded volume effect. α_r has been the subject of intense theoretical investigation and several formulas have been suggested.^[45-52] To evaluate the persistence length from R_g values, the excluded volume effect must be known. If it is neglected ($R_g^2 \cong R_{g0}^2$), then only an apparent persistence length can be calculated.

The most discussed aspect concerning the conformation of polyions is its dependence on the concentration of low molecular weight salt C_s . A typical result obtained by static light scattering is shown in Fig. 4.9 (NaPSS in aqueous NaCl solutions). The radius of gyration of the chain increases with a decrease in the salt content. Qualitatively, the same results were obtained on other systems: carboxymethyl cellulose in NaCl solutions,^[53,54] partially and fully neutralized poly(acrylic acid) in NaCl solutions,^[37] and poly(vinylsulphonate) in KCl solutions.^[55] The swelling of polyions upon lowering the added salt content is expected due to repulsive interactions between charges along the chain, which are screened by the presence of the low molecular weight salt

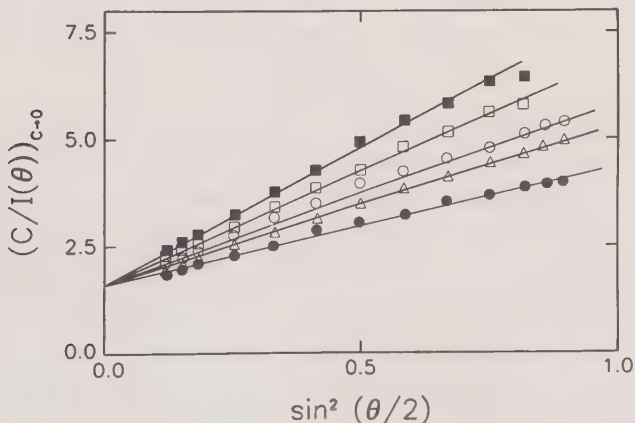


FIG. 4.9. Examples of plots of $(C/I(\theta))_{c=0}$ against $\sin^2(\theta/2)$ for sodium poly(styrene-sulphonate) ($M_w = 155\,000$) in NaCl solutions. The concentration of NaCl increases from the upper to the lower curves. (From Takahashi, A., Kato, T., and Nagasawa, M. (1967). *J. Phys. Chem.*, **71**, 2001–2010. [Errata: *idem*, **72**, 4724 (1968)].)

in the solution. The same effect (an increase) is expected regarding the local stiffness of the chain as well as the excluded volume.

The approximate relation $R_g^2 \sim C_s^{-1/2}$ was found for various polyelectrolytes.^[35,56,57] Then, the apparent persistence length in the coil limit is: $L_{p,e} \sim R_g^2 \sim C_s^{-1/2}$. This is in disagreement with the original prediction for the electrostatic persistence length $L_e \sim C_s^{-1}$.^[14-16] However, lower exponents were obtained by a refinement of the original theory by taking into account the toroidal geometry of the polyion with a non-conducting surface,^[17] the effect of fluctuations in the chain configuration in the calculation of the electrostatic persistence length,^[18] or by exact numerical calculations for a continuously bent rod using the concept of 'local' screening.^[11] A satisfactory agreement between experimental data and the $L_{p,e} \sim C_s^{-1}$ original prediction^[14-16] for the electrostatic persistence length was found by taking electrostatic excluded volume effects into account.^[58] First the unperturbed radius of gyration was calculated using the original expression for the persistence length.^[14-16] Then the perturbed radius of gyration was calculated using the Gupta–Forsman^[59] relation between the expansion factor α_r and the perturbation parameter (the excluded volume between rod-like segments^[60]). On the basis of the deviations of theoretical predictions from experimental data, it was concluded that the electrostatic excluded volume effect is dominant over the electrostatic persistence length effect at higher ionic strengths ($C_s \sim 0.001\text{ M}$ to 1 M).

It should be noted that the radii of gyration reported in refs 35, 56 and 57 were obtained from single concentration data (without extrapolation to $C = 0$). This approximation was reported^[56] as appropriate when the scatterers resemble ideal Gaussian scatterers to a first approximation, the polydisperse population is such that $R_g^2 q^2 > 3$ for the majority of the weight fraction, and the slope of $KC/I(q)$ is independent of C upon isoionic dilution.

In the case of rigid polyions, the measurement of R_g by static light scattering is a routine procedure for system characterization (problems of sample purity, dimerization and aggregation phenomena, etc.).

4.3.3.4 Light scattering from semi-dilute polyelectrolyte solutions. Experimental data in the range of semi-dilute polyelectrolyte concentrations are sparse. Light scattering is mostly used to investigate the dilute solution behaviour (to study the isolated macromolecule at infinite dilution).

It appears that light scattering from semi-dilute (entangled) polyelectrolyte solutions at higher ionic strengths displays the same qualitative behaviour as light scattering from solutions of neutral polymers. Figure 4.10 shows the dependence of the excess scattered intensity at a scattering angle of $\theta = 90^\circ$ on polymer concentration for sodium salt of poly(acrylic acid) ($M_w = 500\,000$) in 0.01 M NaCl . While the intensity increases with C at low concentrations, it levels off and even decreases slightly at higher concentrations. The commonly used plot of C/I vs. C (see the closed circles and the right-hand side axis in Fig. 4.10) shows that the dependence is linear at low C , as in classical Zimm plots, with the slope determined by the second virial coefficient, and a clear

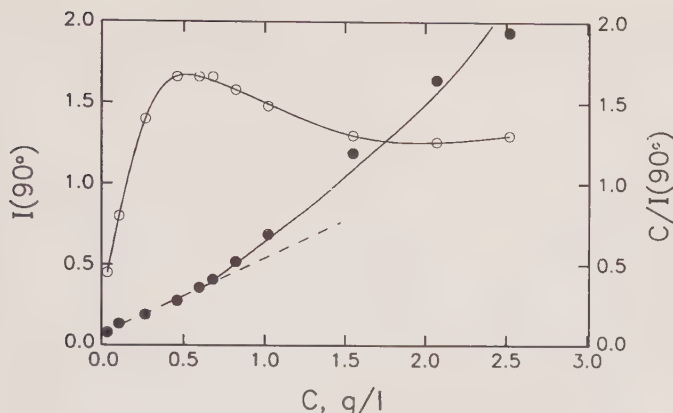


FIG. 4.10. The concentration dependence of the scattered intensity for sodium poly(acrylate) ($M_w = 500\,000$) in 0.01 M NaCl at 25 °C. Scattering intensities at $\theta = 90^\circ$ are expressed in arbitrary units. (From Hara, M. and Nakajima, A. (1980). *Polym. J.*, **12**, 711–718.)

departure from a linear dependence at higher concentrations. The beginning of the departure from the linear dependence is related to the position of maximum intensity. The log-log plot of C/I vs. C for concentrations above the maximum (not shown here) yields a straight line with a slope of 1.22, which means that the concentration dependence of the scattered intensity can be expressed as $C/I \sim C^{1.22}$. This behaviour is qualitatively similar to the situation in solutions of neutral polymers. The concentration scaling of osmotic pressure in neutral semi-dilute solutions $\pi \sim C^{9/4}$ ^[61] determines $C/I \sim C^{5/4}$ according to eqn (4.8). This relation was experimentally verified for neutral polymers by Noda.^[62] The position of the maximum in the plot of I vs. C (the departure from the linear dependence in the plot of C/I vs. C) is related to the crossover concentration C^* .

Scattered intensities should be extrapolated to zero scattering angle as required by eqn (4.8). This is impossible in the case of the data in Fig. 4.10, because of the curvature in the angular dependency at lower angles. The curvature is more pronounced the higher the concentration. Similar effects were not observed in the experiments of Noda,^[62] but they were observed in other neutral polymer solutions.^[63–65] They were explained as a result of a solution inhomogeneity in the vicinity of and slightly above C^* . Upon increasing the concentration, polymer chains were assumed to interpenetrate each other and form ‘clusters’ before creating a uniform interpenetrated matrix.^[66] The formation of clusters resulted in curvature at low scattering angles. The effect of the curvature at lower angles was observed to weaken upon more intensive centrifugation, which may homogenize the solution.^[65] An alternative explanation of the curvature in the case of polyelectrolyte solutions (Fig. 4.10) is that ‘polyelectrolyte domains’ are already present in 0.01 M NaCl. It will be shown in the next sections that at lower ionic strengths (usually

0.001 M and less), the formation of multi-chain domains is observed, accompanied by strong angular dependencies over the whole range of scattering angles.

4.3.4 Experimental results in the limit of low ionic strength

As discussed in Section 4.3.1, there is currently no exact light scattering theory for polyelectrolyte solutions in the limit of low ionic strength. We will therefore present here experimental results accompanied by a qualitative discussion (interpretation) rather than a direct comparison with theoretical formulas. We stress that most features of light scattering in the limit of low ionic strength are typical for polyelectrolytes as a group of polymeric materials and are only slightly dependent on the detailed chemical composition or structure. However, the physical parameters, such as charge density, molecular weight, concentration, etc., are important.

Figure 4.11 shows a concentration molecular weight regime diagram of salt-free solutions of NaPSS as observed by light scattering.^[30] The diagram is constructed on the basis of both static light scattering (SLS) and dynamic light scattering (DLS) results. DLS results will be mentioned briefly here as an important complement to SLS (the basic principles of DLS from polyelectrolyte solutions can be found in specialized monographs^[67–69]).

Regime III (very low polymer concentrations) is quite difficult to reach experimentally because the scattering signal is very weak. The excess scattering intensity is lower than the solvent scattering. Consequently, light scattering data

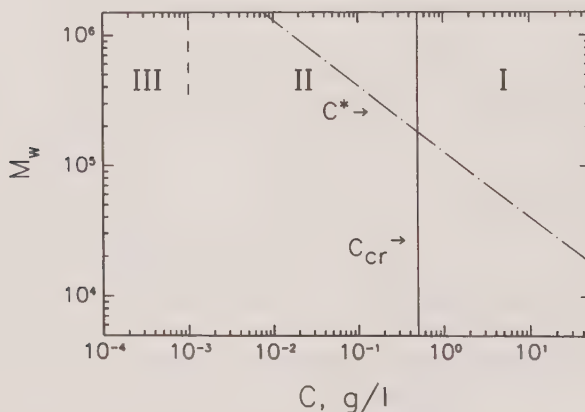


FIG. 4.11. The concentration and molecular weight regime diagram for salt-free aqueous solutions of sodium poly(styrenesulphonate) (NaPSS) as determined by light scattering. Three regimes are recognized on the basis of measurements of the angular and concentration dependencies of scattering intensity, and on the measurements of the diffusion coefficients. The dotted-dashed line represents the theoretical transition from a dilute to a semi-dilute regime (see text for details). (From Sedláček, M. and Amis, E. J. (1992). *J. Chem. Phys.*, **96**, 826.)

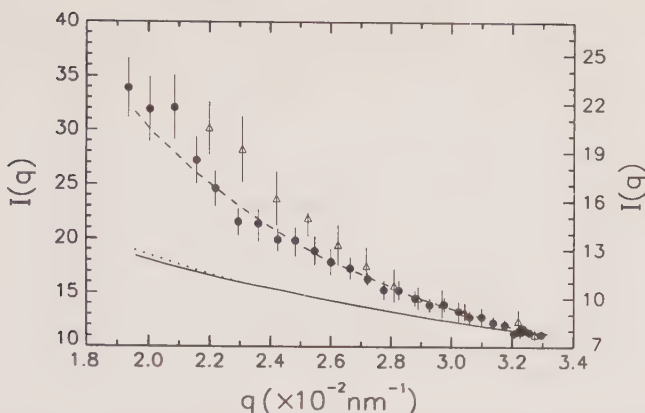


FIG. 4.12. Angular dependencies of excess scattered intensity for highly diluted solutions of NaPSS: ●, $M_{w1} = 354\,000$, $C = 2.7 \times 10^{-4}$ g/l; △, $M_{w2} = 1\,060\,000$, $C = 3.46 \times 10^{-4}$ g/l). The left ordinate corresponds to M_{w1} , and the right ordinate corresponds to M_{w2} . Intensities are expressed in arbitrary units. The data are compared to the calculated rod form factor of both contour lengths (—, ·····) and a coil-like form factor (----), respectively. (From Krause, R., Maier, E. E., Deggelmann, M., Hagenbüchle, M., Schultz, S. F., and Weber, R. (1989). *Physica A*, **160**, 135.)

in this concentration range are sparse. Krause *et al.*^[70] reported SLS measurements at concentrations as low as $C = 2.7 \times 10^{-4}$ g/l (Fig. 4.12). The angular dependencies can be well-fitted by a single-chain form factor assuming a coil-like chain conformation. The data are also compared to the calculated rod form factor. It is evident from Fig. 4.12 that the chains are quite far from the fully extended conformation. It appears that at these low concentrations the intermolecular interactions are rather small due to the large separation between polyions. Contributions from independent individual chains are measured by SLS (scattering is dominated by the form factor).

Regime II is characterized by the presence of peaks in the angular dependencies of the scattered intensity. Figure 4.13 shows results^[70] for the same sample as in Fig. 4.12 (NaPSS, $M_w = 354\,000$) in the concentration range $C = 5.5 \times 10^{-3}$ g/l to 2.8×10^{-2} g/l. The position of the peak maximum q_m changes as $q_m \sim C^{0.36}$. The same concentration scaling was measured for another sample ($M_w = 1\,060\,000$).^[70] Similar angular maxima were reported also by Drifford and Dalbiez^[71] for NaPSS with $M_w = 780\,000$ in the range $C = 1.0 \times 10^{-2}$ g/l to 3.98×10^{-2} g/l. Because the peaks occur approximately at $C \cong 2 \times 10^{-2}$ g/l, and the single-particle form factor is obtained at $C \cong 2.7 \times 10^{-4}$ g/l, the transition from regime III to regime II is taken as approximately $C \cong 10^{-3}$ g/l. The data are limited to higher molecular weights, and therefore the dashed line separating regimes III and II in the regime diagram does not continue below $M_w = 300\,000$.

The presence of angular maxima shows unequivocally that intermolecular interactions are important in regime II. Before discussing various interpretations

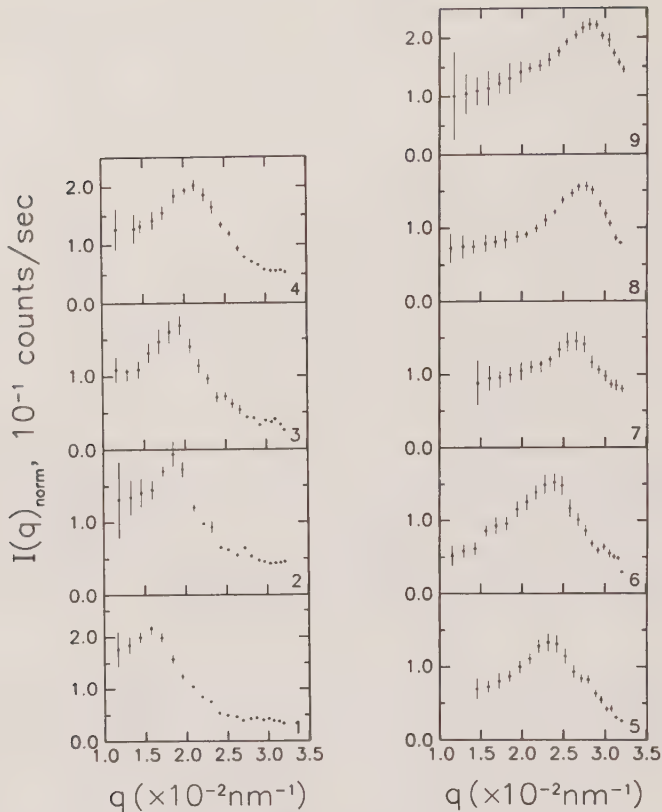


FIG. 4.13. Normalized excess scattered intensities of nine solutions of NaPSS ($M_w = 354\,000$) in salt-free water at concentrations (in g/l): (1) 0.00553, (2) 0.00829, (3) 0.01106, (4) 0.01383, (5) 0.01660, (6) 0.01936, (7) 0.02213, (8) 0.02490, (9) 0.02766. (From Krause, R., Maier, E. E., Deggelmann, M., Hagenbüchle, M., Schultz, S. F., and Weber, R. (1989). *Physica A*, **160**, 135.)

of these maxima, we recall that angular maxima were also obtained by SLS on other polyelectrolytes with different conformations (architectures): semi-flexible proteoglycan monomers^[57] ($q_m \sim C^{1/3}$), semi-rigid succinoglycan polysaccharide^[39] ($q_m \sim C^{0.45}$), and rigid TMV particles^[72] ($q_m \sim C^{1/3}$). Angular maxima were also obtained by small-angle X-ray scattering (SAXS) and small-angle neutron scattering (SANS) on various polyelectrolytes^[2,73] at high polymer concentrations, for which these techniques are limited because of weak scattering signals.

The existence of the maxima was explained by several concepts. The correlation hole concept^[74-76] is based on the assumption that each polyelectrolyte chain is surrounded by a correlation tube (hole) from which other chains are expelled. The radius of the tube, ξ_c , is proportional to the screening length κ^{-1} . Expressions for the static structure factor $S(q)$ derived on the basis

of the correlation hole concept.^[74,77] are continuously increasing functions of q , which tend to an asymptotic value at high q . After combining with the continuously decreasing form factor $P(q)$, a maximum in $I(q) = P(q)S(q)$ is obtained at $q_m \cong \xi_c^{-1}$. The correlation hole concept was disproved by the finding that $S(q)$ extracted from $I(q)$ by a proper modelling of $P(q)$ itself gives a peak.^[57,70-72] For instance, $S(q)$ extracted from scattering intensities in Fig. 4.13 displays a peak in both marginal cases when $P(q)$ is calculated for rods and Gaussian chains, respectively. Another proof of the existence of a maximum in $S(q)$ follows from the fact that the apparent diffusion coefficient measured by DLS^[39,57,71] exhibits a minimum at the same q_m at which $I(q)$ reaches a maximum, according to the classical relation for interacting Brownian particles,^[78] $D_{app}(q) \cong D_0/S(q)$, where D_0 is the free-particle diffusion coefficient.

The peak in $S(q)$ suggests that the maxima result from correlations between polyion positions. In general, maxima in $S(q)$ arise when the mean interparticle spacing is comparable to the wavelength of the scattered radiation. Strong interparticle interactions in solutions of charged particles can result in a long-range order on length scales exceeding many interparticle spacings. This is, for instance, the case for charged latex particles which are large enough to be photographed.^[79] While long-range order is not excluded, the existence of peaks in solutions of charged macromolecules can also be explained by simple liquid-like correlations between particles.^[39,57,70,72] The presence of only one, fairly broad peak suggests the nearest-neighbour correlations. Sometimes feeble secondary or tertiary maxima indicating weak correlations between second and third neighbours appear, but they are mostly within experimental uncertainty (see, e.g., Fig. 4.13, the lowest concentration). In dilute solutions ($C \ll C^*$), the scatterers can be considered as point-like charges and q_m should scale as $q_m \sim C^{1/3}$. Particle liquid-like correlations between anisotropic scatterers at $C \geq C^*$ yield $q_m \sim C^{1/2}$. The transition from a $C^{1/3}$ -dependence to a $C^{1/2}$ -dependence upon crossing C^* was observed for TMV particles^[72] and other rigid polyions.^[80] An exponent between 1/3 and 1/2 is thus expected for linear polyelectrolytes in regime II, depending on the chain stiffness and molecular weight (C^*).

Figure 4.14 shows angular dependencies of the scattered intensity at the transition from regime II to regime I. The angular dependence in regime II disappears upon approaching the critical concentration of the transition C_{cr} . For $C > C_{cr}$ (regime I), the reciprocal scattered intensity exhibits an increasingly pronounced angular dependence, which is linear when plotted vs. $\sin^2(\theta/2)$. The existence of this angular dependence is closely related to results from dynamic light scattering, namely the presence of a slow diffusive mode in the spectra of relaxation times. Figure 4.15 shows the angular dependence of the integral scattered intensity obtained by SLS and the A_f/A_s ratio of the scattering amplitudes of the fast and slow modes, respectively, obtained by DLS. Because A_f is independent of the angle, it is evident that the angular dependence of the integral scattering intensity is fully determined by the angular dependence of A_s . In addition, the slow diffusion coefficient D_s also exhibits a linear dependence on $\sin^2(\theta/2)$.

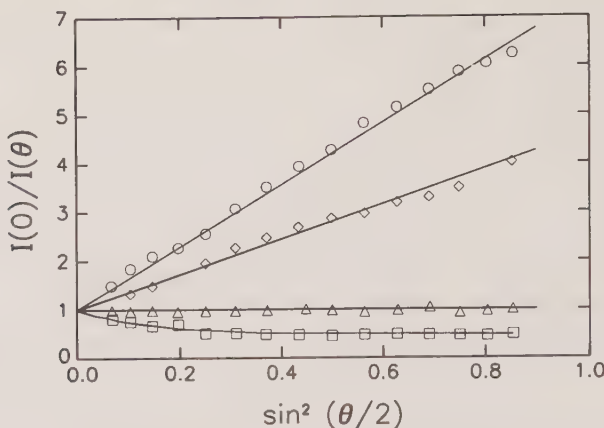


FIG. 4.14. The dependence of the reciprocal of the excess scattered intensity on scattering angle for salt-free solutions of NaPSS ($M_w = 1\,200\,000$) at the following concentrations: \circ , 45.6 g/l; \diamond , 11.6 g/l; \triangle , 0.4 g/l; \square , 0.01 g/l. (From Sedlák, M. and Amis, E. J. (1992). *J. Chem. Phys.*, **96**, 826.)

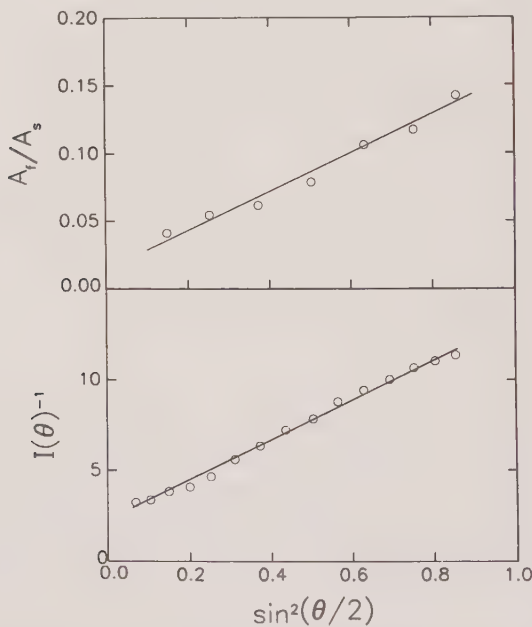


FIG. 4.15. The dependence of the fast- and slow-mode scattered intensity ratio, A_f/A_s , and the integral excess scattered intensity $I(\theta)$, on scattering angle θ for salt-free solutions of NaPSS ($M_w = 1\,200\,000$) at $C = 45.6$ g/l. Intensities are in arbitrary units. A_f/A_s ratios are obtained from DLS experiments. (From Sedlák, M. and Amis, E. J. (1992). *J. Chem. Phys.*, **96**, 826.)

The slow diffusive mode has been observed in a wide variety of biological and synthetic polymers: poly(L-lysine),^[6] t-RNA,^[81] DNA,^[82,83] BSA, latex particles, polynucleosomes,^[84] poly(adenylic acid),^[85] poly(acrylic acid),^[86,87] poly(methacrylic acid),^[88] NaPSS,^[30,89,90] quaternized poly(vinylpyridine),^[91,92] and poly(ethyleneimine).^[92] The most acceptable interpretation of the slow mode is that it appears to be the result of the formation of multi-chain domains (clusters, aggregates) in solution,^[84,88-91] although other interpretations were given as well.^[93,94]

The angular dependencies of D_s and I have been observed for polyions with molecular weights as low as $M_w = 5000$, which definitely cannot be due to intraparticle interference effects manifested in the single-particle form factor.^[89] The apparent dimensions of the multi-chain domains were estimated from both static scattering intensity angular dependencies $p(\theta) = I(\theta)/I(0)$ and slow diffusion coefficient angular dependencies.^[88,89] Equation (4.22) was used in the former case on the assumption that $p(\theta)$ can be considered as a form factor of the domain (aggregate). In the latter case, the apparent radius of gyration was calculated according to the formula^[95] for the angular dependence of the diffusion coefficient in a dilute solution of scatterers with dimensions comparable to q^{-1} . Because of quite crude approximations, the measured apparent radii of gyration of the domains should be considered as semi-quantitative estimates rather than exact values. Nevertheless, they are useful in making qualitative conclusions and evaluating relative changes in the dimensions of the domains. Values of $R_{g,app}$ calculated from SLS and DLS results are in a relatively good agreement (Table 4.2). As can be seen, $R_{g,app}$ is independent of M_w . It follows that the number of chains per domain varies from a couple of chains (high M_w) to several hundreds of chains, or more (low M_w). We also recall that $R_{g,app}$ is dependent on the concentration (Fig. 4.14).

Domains arise in solution as a result of electrostatic interactions. This was demonstrated in salt-free solutions of poly(methacrylic acid) and poly(acrylic acid), which were ionized to various degrees of ionization α by neutralization.^[87,88] With increasing α , an angular dependence of the integral scattering intensity gradually developed, accompanied by a slow diffusive mode. A similar effect was observed upon decreasing the salt content (ionic strength) in solutions of strong polyelectrolytes, and this will be discussed in more detail in the next section. It has been shown^[96] that the formation of domains (aggregation) is not caused by hydrophobic interactions, although polyion backbones are highly incompatible with the polar water medium and may cause microphase separation in solutions of weakly charged polyelectrolytes.^[97-99] The exact nature of domains still remains a puzzle. There are no predictions for such a phenomenon on the grounds of classical polyelectrolyte theory. Schmitz^[84] qualitatively explained the existence of 'temporal aggregates' as the result of fluctuating forces created by counterion dynamics. The instantaneous distribution of counterions around the charged chain is asymmetric and leads to long-range attractive dipolar interactions.^[84] A frequently discussed and controversial attractive interaction between charged particles through the mediation of

Table 4.2. Values of apparent radius of gyration of domains for NaPSS samples with different molecular weights. No added salt, $C = 45.6 \text{ g/l}$.

$M_w (10^3 \text{ g mol}^{-1})$	$R_{G,\text{app}}^a (\text{nm})$	$R_{G,\text{app}}^b (\text{nm})$	
		$C = 0.2$	$C = 0.098$
5	62	35	57
5.4	67	31	52
8	57	39	65
17.4	68	35	58
38.2	56	37	61
47.3	69	31	52
100	85	40	67
200	84	32	54
400	70	46	77
780	91	54	90
1200	135	65	109

^a Determined from static light scattering.

^b Calculated from the q dependence of D_s from dynamic light scattering for two values of constant C corresponding to limiting cases of various particle architectures.

counterions was proposed by Ise^[2] on the basis of extensive experimental work on charged latex particles and colloids. The author suggested that the same mechanism might also apply to linear polyelectrolytes, where individual chains have a compact conformation due to intramolecular attractive interactions and the system resembles a solution of charged spheres. However, no exact theoretical explanation of the ‘domain phenomenon’ in solutions of linear polyelectrolytes has yet been given.

In addition to the influence of the degree of ionization, the ionic strength, the polymer concentration, and the molecular weight, the effect of domain formation was recently investigated as a function of other physical parameters, such as temperature^[96,100] and the dielectric permittivity of the solvent.^[96,101,102] The effect was also observed in polyelectrolyte binary mixtures.^[103] While a detailed discussion of these results is beyond the scope of this chapter, we may conclude that domains are regions of a different refractive index with respect to the rest of the solution. This is a condition of ‘visibility’ in light scattering. The difference in refractive index can be caused by a different density and/or a different order inside the domains. While at lower concentrations and molecular weights, polyions are not shared between domains, the overlap of individual chains and formation of an inhomogeneous network is possible at higher concentrations and molecular weights. Domains are probably rather loose arrangements, because the formation of dense aggregates is usually accompanied by a pronounced increase in the scattered intensity, which is not the case in polyelectrolyte solutions.

Regime I can be characterized as a regime dominated by the formation of multi-chain domains (aggregates) with a strong coupling of the polyion and counterion dynamics. The critical concentration C_{cr} for the transition from regime II to regime I (see Fig. 4.11) was defined as the concentration at which the angular dependence of the scattering intensity disappears. Other characteristics of this transition are a break in the concentration dependence of the fast diffusion coefficient (coupled diffusion due to polyions and counterions) and a minimum in the reduced scattered intensity $I(0)/C$ (see ref. 30 and the next section on the concentration dependence of the scattered intensity). The transition is independent of molecular weight. It has been suggested that it may be related to a critical concentration of counterions in solution. Counterions seem appreciably to influence the solution structure and dynamics at higher polymer concentrations, where their role is probably more than just a passive screening of the Coulombic repulsion. Neither SLS nor DLS results reflect the theoretical crossover concentration C^* (see the dotted dashed line in Fig. 4.11).

4.3.4.1 Concentration dependence of the scattered intensity. Figure 4.16 shows the concentration dependence of the total scattered intensity I_t , the excess scattered intensity I (after subtraction of the solvent scattering) and the reduced scattered intensity I/C of NaPSS ($M_w = 1\,200\,000$) in salt-free water.^[30] Intensities are extrapolated to a zero scattering angle and normalized by the scattered intensity of a benzene standard. As is apparent from the figure, the concentration

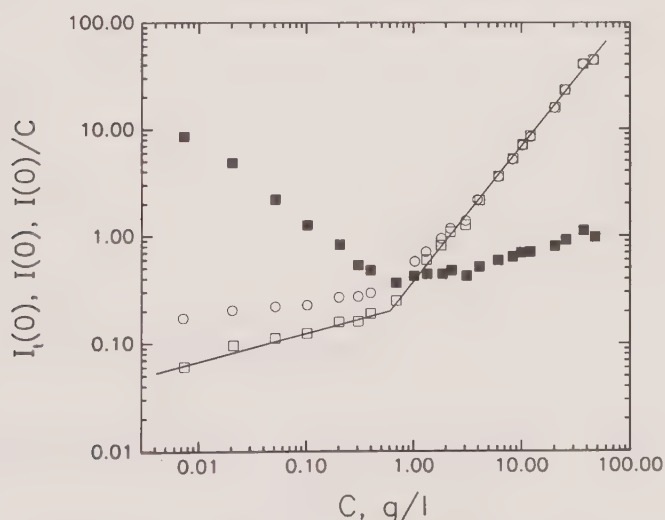


FIG. 4.16. The concentration dependence of the total scattered intensity $I_t(0)$ (○), the excess scattered intensity $I(0)$ (□) (after subtraction of solvent scattering), and the reduced intensity $I(0)/C$ (■) for salt-free solutions of NaPSS ($M_w = 1\,200\,000$). Intensities are normalized by the scattered intensity of a benzene standard. (From Sedlák, M. and Amis, E. J. (1992). *J. Chem. Phys.*, **96**, 826.)

dependence can be well-approximated by power laws. In terms of the exponents in the relation $I \sim C^a$, for $C > 0.5 \text{ g/l}$, $a = 1.26$, and for $C < 0.5 \text{ g/l}$, $a = 0.26$. The discontinuity at $C = 0.5 \text{ g/l}$ is mainly evident in the I/C plot, which shows that while the reduced scattering decreases below 0.5 g/l , it increases above 0.5 g/l . The discontinuity in the scattered intensity is consistent with discontinuities in other quantities and is related to the transition from regime II to regime I in the regime diagram (Fig. 4.11). The exponents a are weakly dependent on molecular weight for $C > C_{\text{cr}}$ ($a = 1.15$ for $M_w = 100\,000$ and $a = 1.18$ for $M_w = 5000$) and more strongly dependent on molecular weight for $C < C_{\text{cr}}$ ($a = 0.45$ for $M_w = 100\,000$ and $a = 0.57$ for $M_w = 5000$).

As indicated in Section 4.3.1, eqn (4.8) can be used for salt-free polyelectrolyte solutions. If we further assume that dn/dC is fairly independent of concentration in the interval investigated, the concentration dependence of the scattered intensity can be transformed into the concentration dependence of osmotic pressure $\pi \sim C^{1.74}$ for $C < C_{\text{cr}}$ and $\pi \sim C^{0.74}$ for $C > C_{\text{cr}}$. The relatively high exponent for $C < C_{\text{cr}}$ can be ascribed to strong Coulombic repulsions between polyions, which dominate the intermolecular interactions. The interpretation of the concentration dependence of osmotic pressure (scattered intensity) for $C > C_{\text{cr}}$ is less straightforward. Most of the scattering in this concentration range corresponds to the slow diffusive mode (domains). The dimensions of the domains increase upon increasing C . The apparent molecular weight of the domain is also expected to increase, although it is not known by how much. The increase in the apparent molecular weight of the domain is expected to influence the osmotic pressure. Therefore direct conclusions about the nature of intermolecular interactions cannot be made.

Data from Fig. 4.16 are replotted in Fig. 4.17 in a more common format, where KC/I or C/I is plotted against C on arithmetic axes. While data at zero scattering angle go through a maximum at C_{cr} , the data at 90° exhibit a characteristic curvature with a very strong dependence at low C , which gradually weakens upon increasing C . The 'characteristic curvature dependence' was also observed on other salt-free systems (bovine serum albumin,^[104] poly-(methacrylic acid),^[105,106] and lightly sulphonated polystyrene in DMF^[107]). These data were usually taken over too narrow an interval in concentration to perform an analysis over several decades on log-log plots. Doty and Steiner^[104] explained the KC/I vs. C dependence using a model which treats the macroions as if they are neutral but have an effective size. This effective size defines an effective volume around a polyion from which other polyions are expelled due to repulsive interactions. Using eqn (4.25) with an adequately defined radial distribution function, and combining this with eqns (4.10) and (4.11), the following formula was obtained:^[104]

$$\frac{KC}{I(\theta)} = \frac{1}{M_w P(\theta)} \left[1 + 2 \frac{B'}{M_w} C \Phi(qD) \right], \quad (4.32)$$

where $\Phi(x) = (3/x^3)(\sin x - x \cos x)$, and $B' = \frac{2}{3}\pi D^3 N_A$, D being the effective

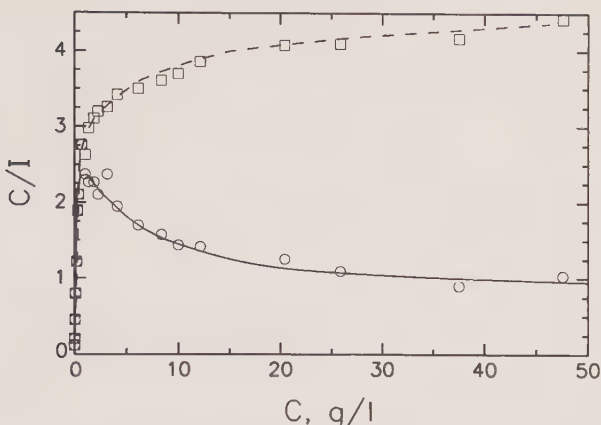


FIG. 4.17. The concentration dependence of the excess scattered intensity for salt-free solutions of NaPSS ($M_w = 1\ 200\ 000$). Data from Fig. 4.16 are replotted in a different format. Intensities are normalized by the scattered intensity of a benzene standard and correspond to scattering angles $\theta = 90^\circ$ (□) and $\theta = 0^\circ$ (○).

diameter proportional to $C^{1/3}$. This equation was used to explain the ‘characteristic curvature dependence’ at $\theta = 90^\circ$. A semi-quantitative agreement between the data on BSA^[104] and the theoretical prediction given by eqn (4.32) was achieved. Similar results were obtained upon using exponential or electrostatic repulsion potentials for the radial distribution function instead of the hard sphere potential.

Equation (4.32), however, fails to explain data at zero scattering angle where $\Phi(x) = 1$, and $P(\theta) = 1$, namely the decrease of $C/I(0)$ at higher concentrations (Fig. 4.17). When B' is positive, $KC/I(0)$ should increase with C according to eqn (4.32). We note that $B' = A_2 M_w^2$ and that the positive B' corresponds to a positive second virial coefficient. The notion of a simple repulsion between polyions having an effective volume is not sufficient to explain the data at higher concentrations. It is to be noted that the NaPSS sample with $M_w = 1\ 200\ 000$ (data in Fig. 2.17) may be entangled at higher concentrations. However, qualitatively the same results were also obtained on the sample with $M_w = 5000$, which cannot be entangled at the concentrations used.

4.3.4.2 Molecular weight dependence of scattered intensity. Figure 4.18 shows the molecular weight dependence of the scattered intensity and the ratio of the scattering amplitudes of the slow and fast diffusive modes, respectively. The scattered intensities are extrapolated to zero angle and normalized to the scattering of a benzene standard. The striking feature of Fig. 4.18 is that the zero-angle scattering from salt-free polyelectrolyte solutions is not proportional to the molecular weight, as opposed to the high-salt limit or neutral polymers. This is consistent with conclusions resulting from eqn (4.24) (see Section 4.3.1) and also with the notion of domains, where it is assumed that almost all of the

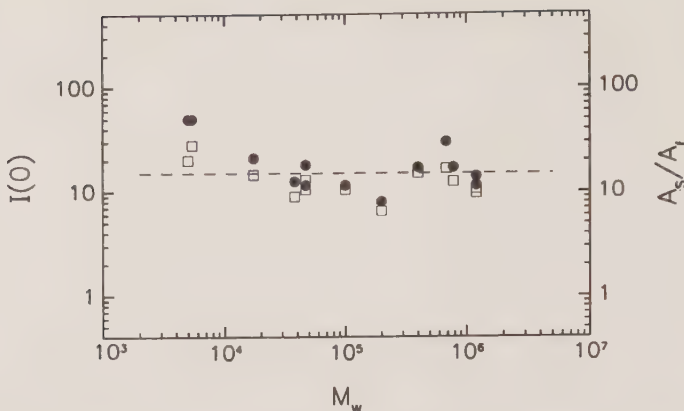


FIG. 4.18. The molecular weight dependence of the excess scattered intensity $I(0)$ (\square) and of the slow- and fast-mode scattered intensity ratio A_s/A_f (\bullet) for NaPSS samples in deionized water at concentration $C = 45.6$ g/l. Intensities are normalized by the scattered intensity of a benzene standard. A_s/A_f ratios are obtained from DLS experiments. (Sedláček, M., unpublished results.)

scattering derives from domains of constant (molecular weight independent) size rather than from individual polyions. Although the scattered intensity is almost independent of molecular weight, the scatter in measured values is quite large. It is evident that the scattering in the data for $I(0)$ and A_s/A_f ‘is correlated’. Positive or negative deviations from the average scattered intensity for particular molecular weights are caused by correspondingly higher or lower values of A_s/A_f . Those can be influenced, for instance, by different sulphonation of particular samples. It should also be noted that *absolute* values of the excess scattering intensity corresponding to the fast mode are independent of molecular weight, too (not shown here).

4.3.5 The transition between low and high ionic strength regimes

We divide the discussion into three parts, according to the three concentration regimes defined in the previous section.

(1) Data from regime III, which would cover a whole range of accessible added-salt concentration, C_s , are still unavailable.

(2) The influence of increasing C_s on the angular maxima in scattered intensity, which are typical for regime II, is reflected mainly in the diminished peak height, while the position of the peak does not change.^[39,57] A slight shift towards higher q values has been reported for the position of the maximum in the static structure factor $S(q)$ (Fig. 4.19).^[72] The reduction of the peak height is interpreted as a result of decreased correlations between particle positions due to an increased screening of electrostatic interactions by the presence of added-salt small ions.^[39,57] The shift in the maximum in $S(q)$ is explained in terms of the radial pair distribution function $g(r)$.^[72] When the weakening of

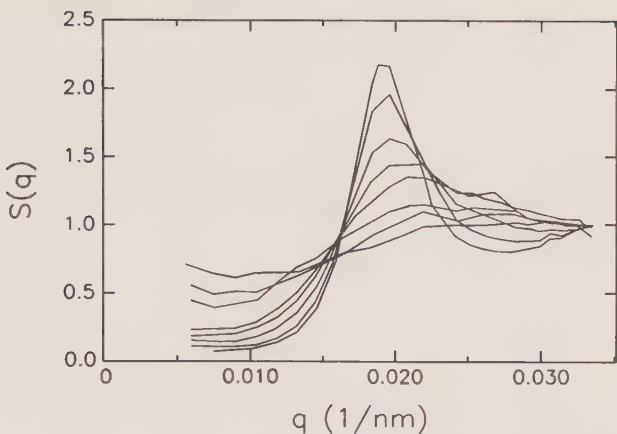


FIG. 4.19. The static structure factor $S(q)$ obtained by SLS from an aqueous TMV (tobacco mosaic virus) sample of $C = 0.53C^*$ as a function of the measured conductivity of the solution. The conductivity is proportional to the salt concentration. The maximum value of $S(q)$ decreases with increasing conductivity. (From Maier, E. E., Krause, R., Deggelmann, M., Hagenbuchle, M., Weber, R., and Fraden, S. (1992). *Macromolecules*, **25**, 1125.)

Coulombic repulsion allows the particles to penetrate into previously excluded interparticle space, the distance between neighbouring particles, r_{\max} , decreases. The change in r_{\max} is then reflected in the change in q_m .

Upon further increase of C_s , the angular dependence of the scattered intensity in regime II changes from peak-type dependence into single-chain form factor dependence. Data at higher C_s , showing deswelling of individual polyions, are discussed in Section 4.3.3.

(3) The transition from high to low C_s conditions in regime I is usually referred to as the ordinary-extraordinary transition. Figure 4.20 shows how the angular dependence of the scattered intensity weakens upon increasing C_s . The change in the angular dependence probably corresponds to a gradual dissolution of domains (aggregates) upon increasing C_s . This effect is accompanied in the DLS spectra of relaxation times by a decrease in the relative amplitude of the slow diffusive mode. While the slow mode usually dominates the spectrum of relaxation times at low C_s (almost all of the scattering comes from the slow mode), the spectrum is dominated by the fast diffusive mode at high C_s . The relevant quantity determining this transition is the ratio C_s/C_p , not simply C_s .^[108,109]

Let us now discuss the dependence of the scattered intensity on the salt concentration C_s . In general, the scattered intensity increases with C_s (see Fig. 4.21, data for univalent salt (open circles)). The increase in the scattered intensity over the whole range of accessible values of C_s is proportional to the molecular weight of the sample: the lower the molecular weight, the smaller the decrease. This is demonstrated in Table 4.3, which shows data for

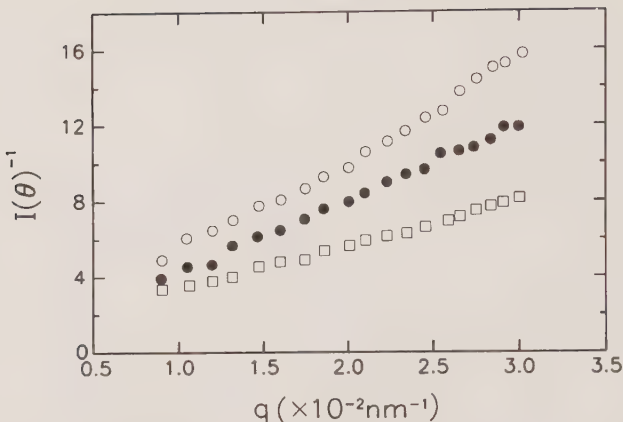


FIG. 4.20. Angular dependencies of reciprocal of the total scattered intensity from polynucleosome solutions with various concentrations of added salt: \square , 10 mM; \bullet , 1.0 mM; \circ , 0.1 mM. (From Schmitz, K. S., Lu, M., and Gauntt, J. (1983). *J. Chem. Phys.*, **78**, 5059.)

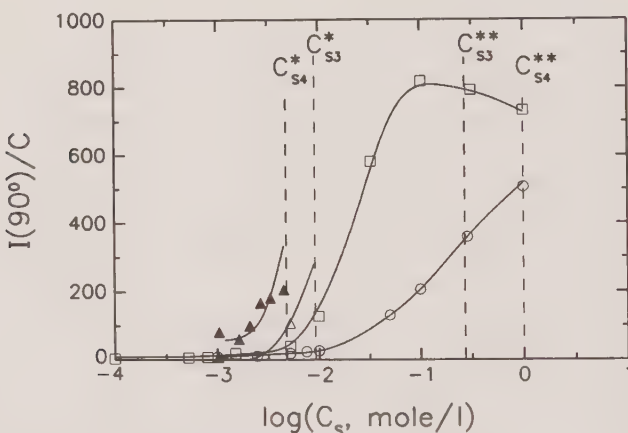


FIG. 4.21. The dependence of the reduced scattered intensity from NaPSS solutions ($M_w = 780\,000$, $C = 7 \text{ g/l}$) on the concentration of added salt with cations of various valence: \circ , NaCl; \square , CaCl₂; \triangle , LaCl₃; \blacktriangle , Th(NO₃)₄. Vertical dashed lines represent the boundaries of the two phases region for cations of valency $Z \geq 3$. A phase separation appears when $C_{sZ}^* \leq C_s \leq C_{sZ}^{**}$. (From Delsanti, M., Dalbiez, J. P., Spalla, O., Belloni, L., and Drifford, M. (1994). In *ACS Symposium Series 548* (ed. K. S. Schmitz), pp. 381–394. American Chemical Society, Washington, DC.)

NaPSS in aqueous NaCl solutions.^[109] The molecular weight dependence is understandable if we recall that the scattered intensity at zero added-salt conditions is molecular weight independent (Fig. 4.18) and in the high-salt limit, of course, molecular weight dependent.

Table 4.3. The ratio of total scattered intensities measured in 1 M NaCl and zero added-salt NaPSS solutions at $\theta = 90^\circ$ and $C = 5 \text{ g/l}$.

$M_w (\text{g mol}^{-1})$	$I(1 \text{ M})/I(0 \text{ M})$
5 000	1.1
47 000	7.1
1 200 000	39.0

If we restrict to $\theta = 0^\circ$ and extrapolate data to zero scattering angle, we may proceed with the discussion of the general trend of increasing scattered intensity by using eqns (4.17) and (4.24). It follows that the scattered intensity can be mainly influenced by two factors: the change in the refractive index increment and the osmotic compressibility, respectively. However, experiments on NaPSS^[109] show that the refractive index increment is independent of C_s in the range $5 \times 10^{-6} \text{ M}$ to 3 M. Therefore the increase in the scattered intensity is caused only by an increase in the osmotic compressibility of the solution due to an increased screening of electrostatic interactions.

A similar trend in the scattered intensity is observed in salt-free solutions of weak polyacids (PMA, PAA) as a function of the degree of ionization. The scattered intensity decreases with an increase in the degree of ionization. This derives only from the decrease in the osmotic compressibility, because the refractive index increment increases with the degree of ionization.^[110,111]

According to eqn (4.24), the reciprocal scattered intensity in salt-free conditions can be expressed by means of the product αg , where g is the osmotic coefficient and α is the degree of ionization. It has been shown experimentally^[112] that αg increases with α , in agreement with the fact that the scattered intensity decreases with α .

An increase in the salt concentration results finally (at very high C_s) in a macroscopic solution decomposition. For instance, theta conditions for NaPSS were reported in 4.17 M aqueous NaCl solution at 25 °C.^[33] The approach to the theta conditions is reflected in a great increase in the scattered intensity followed by visible turbidity. The effect of multivalent counterions^[113] (using salts such as CaCl₂, LaCl₃ or Th(NO₃)₄) is shown in Fig. 4.21. The increase in scattered intensity begins at lower C_s and is more pronounced the higher the valency of the counterion. In addition, in the case of trivalent and tetravalent counterions, a salt concentration region exists between C_s^* and C_s^{**} in which the solutions phase separate. Figures 4.22 and 4.23 show phase diagrams for NaPSS in aqueous LaCl₃ solutions as a function of the salt concentration C_s , the polymer concentration C , and the polymer molecular weight M_w .^[113] While C_s^* is dependent on C and independent of M_w , C_s^{**} is, conversely, independent of C and dependent on M_w . An understanding of these phase diagrams on a

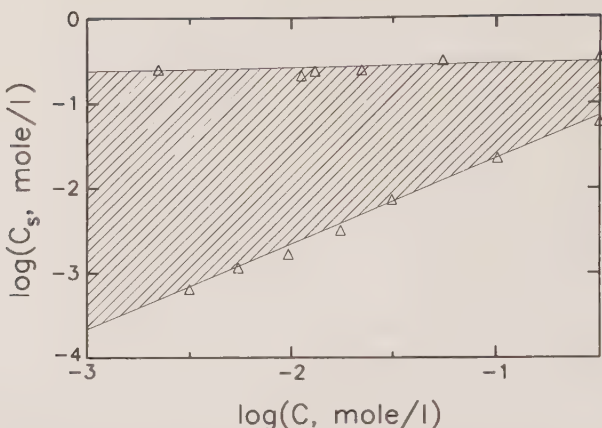


FIG. 4.22. The phase diagram of solutions of NaPSS ($M_w = 780\,000$) with added LaCl_3 . The hatched region represents the two-phase region. (From Delsanti, M., Dalbiez, J. P., Spalla, O., Belloni, L., and Drifford, M. (1994). In *ACS Symposium Series 548* (ed. K. Schmitz), pp. 381–394. American Chemical Society, Washington, DC.)

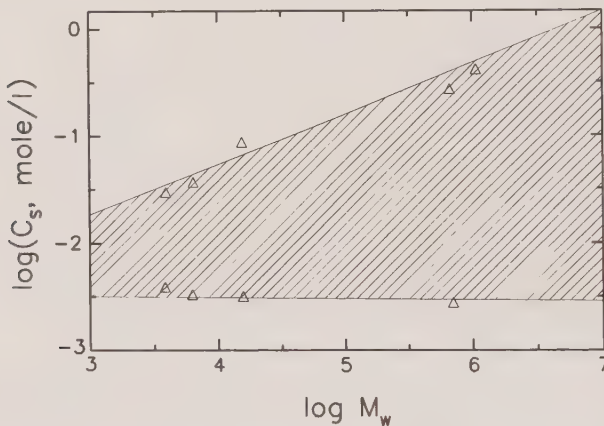


FIG. 4.23. The phase diagram of solutions of NaPSS ($C = 2 \text{ g/l}$) with added LaCl_3 . The hatched region represents the two-phase region. (From Delsanti, M., Dalbiez, J. P., Spalla, O., Belloni, L., and Drifford, M. (1994). In *ACS Symposium Series 548* (ed. K. S. Schmitz), pp. 381–394. American Chemical Society, Washington, DC.)

molecular level is still absent. The existence of C_s^* cannot be explained by the simple counterion condensation theory of multivalent counterions. The molecular weight dependence of C_s^{**} suggests that the effect of the C_s^{**} concentration is probably a ‘polymer effect’ rather than an electrostatic effect. Electrostatic interactions are expected to be appreciably screened at such high C_s .^[113]

4.3.6 Determination of osmotic pressure from light scattering measurements

As the excess light scattering is given by the osmotic compressibility of the scattering medium, information about osmotic pressure can be obtained from light scattering measurements. If the osmotic pressure of a salt-free polyelectrolyte solution is expressed as $\pi = g\pi_{id}$, where π_{id} is the ideal osmotic pressure and g is the so-called osmotic coefficient reflecting the degree of non-ideality, then g can be obtained from light scattering data according to eqn (4.24). Alexandrowicz^[110] determined the osmotic coefficient in salt-free solutions of poly(acrylic acid), poly(methacrylic acid) and BSA (bovine serum albumin) in the concentration range $C \cong 2\text{--}40\text{ g/l}$ by both light scattering and direct osmotic methods. Scattered intensities were measured at 90° and no correction for angular dependencies was made. To calculate g from the scattered intensity according to eqn (4.24), the concentration dependencies of g were determined by direct osmotic methods and the experimental dg/dC values were inserted into eqn (4.24). The terms $C dg/dC$ were small in the case of polyacids and even below the experimental resolution in the case of BSA (for instance, g scaled as $C^{0.15}$ and $C^{0.20}$ for polyacids with degrees of neutralization 0.5 and 0.8, respectively, which means that the term $(g + C dg/dC)$ in eqn (4.24), amounted to $1.15g$ and $1.20g$, respectively). The agreement between the osmotic coefficients determined by the different methods was quite satisfactory. Figure 4.24 shows results for polyacids at various concentrations and degrees of ionization.^[110]

Klooster *et al.*^[111] similarly determined osmotic coefficients in methanolic solutions of poly(acrylic acid) neutralized by lithium methoxide to different degrees of ionization at polymer concentrations of $c = 0.017\text{ M}$ and $c = 0.087\text{ M}$. Scattered intensities were measured at an angle of 5° . The concentration dependence of g was again very weak and the term $C dg/dC$ in eqn (4.24) was neglected. The agreement between osmotic coefficients determined by light scattering and osmometry was very good.

While the concentration dependence of osmotic pressure (osmotic coefficient) in the above-mentioned experiments was determined by direct osmotic methods, it can also be obtained from light scattering data. According to eqn (4.8), the osmotic pressure can be calculated as

$$\pi = RT \int_0^c \frac{KC}{I(0)} dC. \quad (4.33)$$

The calculation of the osmotic pressure in this way requires data over a rather broad interval of C to perform numerical integration. However, whenever the concentration C is sufficiently high, the numerical integration of the portion of the C/I curve in the region of low concentrations ($C \rightarrow 0$) will contribute relatively little to the total numerical integration. Equation (4.33) can be applied to data on salt-free solutions of NaPSS ($M_w = 1\,200\,000$) covering 3.5 decades in C (Fig. 4.16). Because the concentration dependence of K (or dn/dc) was

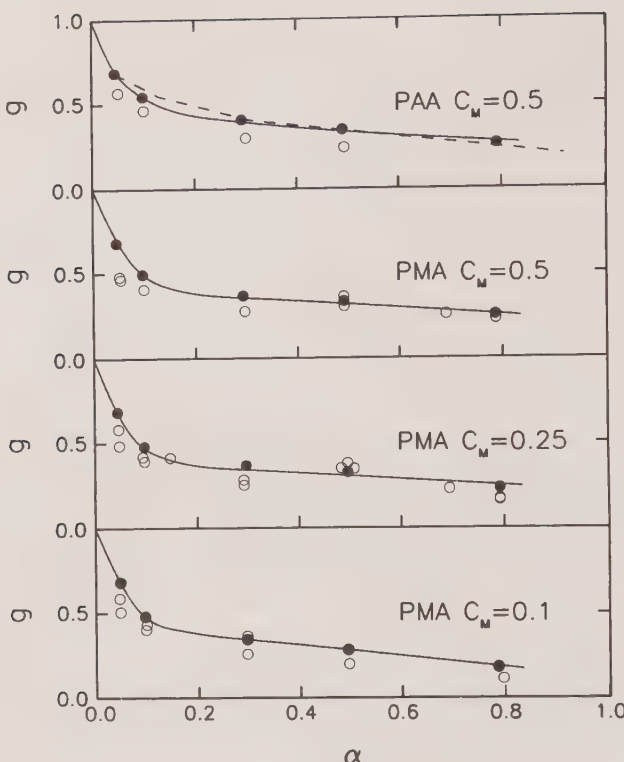


FIG. 4.24. Osmotic coefficients in solutions of poly(acrylic acid) and poly(methacrylic acid) ionized to various degrees of ionization α by NaOH. Values were determined by light scattering (\circ) and by osmometry (\bullet). Polymer concentrations C_M are expressed in mole/l. (From Alexandrowicz, Z. (1959). *J. Polym. Sci.*, **40**, 91.) The dashed line denotes the data from Kern, W. (1937). *Z. Phys. Chem.*, **A184**, 197.

not measured, we assume it to be constant and omit numerical coefficients in eqn (4.33). The concentration dependence of osmotic pressure (in arbitrary units) calculated from the data in Fig. 4.16 according to eqn (4.33) is shown in Fig. 4.25. While at lower concentration $\pi \sim C^{1.75}$, at higher concentrations $\pi \sim C^{0.75}$. The concentration scaling at higher concentrations can be compared to the concentration dependence of osmotic pressure determined by direct osmotic measurements^[114] for salt-free NaPSS solutions with different molecular weights $\pi \sim C^{1.125}$. The difference between the exponents from light scattering and direct osmotic methods may be due to the fact that the constant K is concentration-dependent at higher concentrations and/or that eqn (4.8) is not strictly valid.

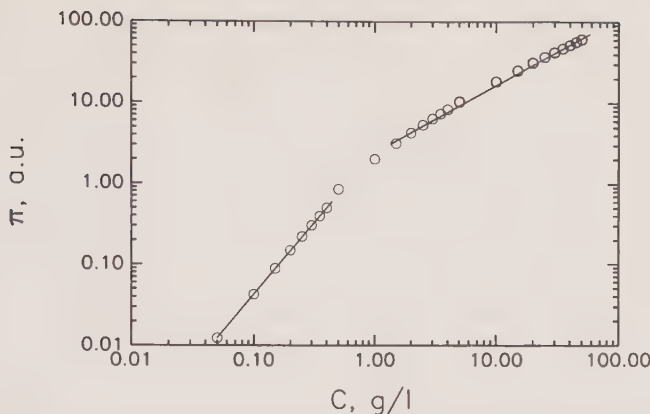


FIG. 4.25. The concentration dependence of osmotic pressure in salt-free solutions of NaPSS ($M_w = 1\,200\,000$). Osmotic pressure was calculated from light scattering data in Fig. 4.16 and is expressed in arbitrary units (see text for details).

4.3.7 Light scattering from ionomers

Ionomers can be defined as flexible polymers containing small numbers of ionizable groups. The content of ionizable groups is typically up to 5 mol% (in this nomenclature, 5 mol% means that on average five out of every 100 repeat units carries an ionizable group). A typical example is, for instance, lightly sulphonated polystyrene. Because of a low content of ionizable groups, ionomers are insoluble in water. Interest in these materials derives from industrial applications in the bulk and in organic solvent solutions. The purely scientific interest in ionomers follows from this rather unusual behaviour due to a complicated balance of forces, including electrostatic repulsion, van der Waals interactions, the entropic driving force for mixing, and chain elasticity.

The ionizable groups on ionomers do not dissociate in solvents of low dielectric permittivity. In this case, dipole–dipole attractive interactions between ion pairs result in association behaviour^[115–120] (the ‘ion pair’ is understood here as the charged group with its counterion). In organic solvents of higher dielectric permittivity (DMF, DMSO), however, the dissociation is strong enough to result in a ‘polyelectrolyte effect’. Typical polyelectrolyte behaviour has been observed by viscosity^[115,118,121] and also by light scattering.^[115,121–123] Figure 4.26 shows low-angle light scattering data ($\theta = 6\text{--}7^\circ$) showing $KC/I(\theta)$ as a function of polymer concentration for a series of monodisperse sodium-neutralized lightly sulphonated polystyrenes in dimethylformamide (upper part) and tetrahydrofuran (lower part). In tetrahydrofuran, which is a non-ionizing solvent, the concentration dependence of the scattered intensity reflects a decrease in the second virial coefficient upon increasing the sulphonation level. In the ionizing solvent (dimethylformamide), the concentration dependence of the scattered intensity exhibits a curvature, which is typical for polyelectrolyte solutions (see Section 4.3.4). The effect is stronger the higher the sulphonation level.

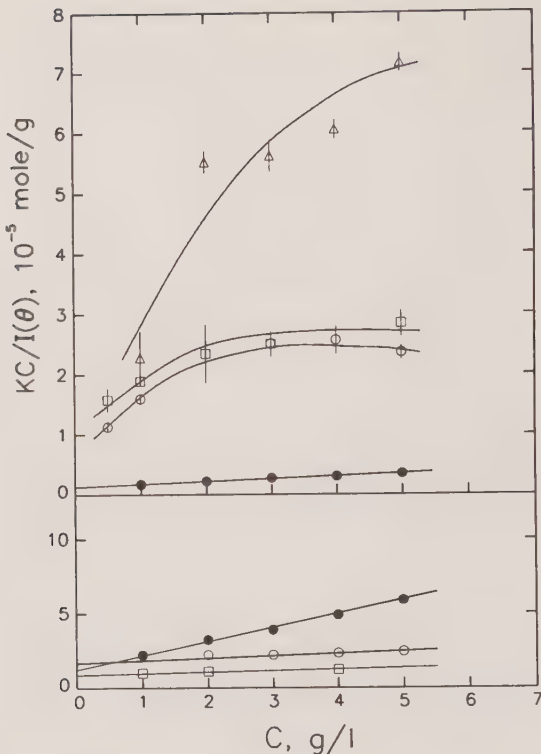


FIG. 4.26. Low-angle light scattering data ($\theta = 6\text{--}7^\circ$) showing $KC/I(\theta)$ as a function of polymer concentration for a series of monodisperse sodium-neutralized sulphonate ionomers in dimethylformamide (upper part) and tetrahydrofuran (lower part). The sulphonation levels were as follows: ●, 0%; ○, 0.5%; □, 1.72%; △, 3.2%. (From Lantman, C. W., MacKnight, W. J., Peiffer, D. G., Sinha, S. K., and Lundberg, R. D. (1987). *Macromolecules*, **20**, 1096.)

References

1. Schmitz, K. S. (1994). In *ACS Symposium Series 548* (ed. K. S. Schmitz), pp. 1–24. American Chemical Society, Washington, DC.
2. Ise, N. (1986). *Angew. Chem.*, **25**, 323.
3. Langmuir, I. (1938). *J. Chem. Phys.*, **6**, 873.
4. Sogami, I. (1984). *J. Chem. Phys.*, **81**, 6320.
5. Sogami, I. In *Ordering and organisation in ionic solutions* (eds N. Ise and I. Sogami), pp. 624–634. World Scientific, Teaneck, NJ.
6. Lin, S. C., Lee, W. I., and Schurr, J. M. (1978). *Biopolymers*, **17**, 1041.
7. Beresford-Smith, B., Chan, D. Y. C., and Mitchell, D. J. (1985). *J. Colloid Interface Sci.*, **105**, 216.
8. Belloni, L. (1986). *J. Chem. Phys.*, **85**, 519.
9. Alexandrowicz, Z. and Katchalsky, A. (1963). *J. Polym. Sci. Part A*, **1**, 3231.
10. Russel, W. B. (1982). *J. Polym. Sci.*, **29**, 1233–1247.
11. Schmitz, K. S. (1990). *Polymer*, **31**, 1823.

12. Oosawa, F. (1971). *Polyelectrolytes*. Marcel Dekker, New York.
13. Manning, G. S. (1978). *Q. Rev. Biophys.*, **11**, 179.
14. Odijk, T. (1977). *J. Polym. Sci., Polym. Phys. Ed.*, **15**, 477.
15. Odijk, T. and Houwaart, A. C. (1978). *J. Polym. Sci., Polym. Phys. Ed.*, **16**, 628.
16. Skolnick, J. and Fixman, M. (1977). *Macromolecules*, **10**, 944.
17. Le Bret, M. (1982). *J. Chem. Phys.*, **76**, 6243.
18. Barrat, J. L. and Joanny, J. F. (1993). *Europhys. Lett.*, **24**, 333.
19. Koene, R. S. and Mandel, M. (1983). *Macromolecules*, **16**, 220–236.
20. Brinkman, H. C. and Hermans, J. J. (1949). *J. Chem. Phys.*, **17**, 574.
21. Debye, P. (1947). *J. Phys. Colloid Chem.*, **51**, 18.
22. Schneider, J., Hess, W., and Klein, R. (1986). *Macromolecules*, **19**, 1729.
23. Zimm, B. H. (1948). *J. Chem. Phys.*, **16**, 1093.
24. Vrij, A. and Overbeek, J. Th. G. (1962). *J. Colloid. Sci.*, **17**, 570.
25. (a) Hermans, J. J. (1949). *Rec. Trav. Chim.*, **68**, 859. (b) *Ibid.* (1950). *Proc. Intern. Colloq. Macromolecules, Amsterdam*, p. 238.
26. Zernike, F. (1918). *Arch. Neerl. Sci.*, **IIIA**, 74; dissertation, Amsterdam (1915).
27. Casassa, E. F. and Eisenberg, H. (1960). *J. Phys. Chem.*, **64**, 753.
28. Ooi, T. (1958). *J. Polym. Sci.*, **28**, 459.
29. Zernike, F. and Pins, J. A. (1927). *Z. Phys.*, **41**, 184.
30. Sedláč, M. and Amis, E. J. (1992). *J. Chem. Phys.*, **96**, 826.
31. Kratochvíl, P. (1987). *Classical light scattering from polymer solutions*. Elsevier, Amsterdam.
32. Takahashi, A., Kato, T., and Nagasawa, M. (1967). *J. Phys. Chem.*, **71**, 2001. Errata: *idem*, **72**, 4724 (1968).
33. Brandrup, J. and Immergut, E. H. (1989). *Polymer handbook*. John Wiley, New York.
34. Takahashi, A., Kato, T., and Nagasawa, M. (1970). *J. Phys. Chem.*, **74**, 944.
35. Peitzsch, R. M., Burt, M. J., and Reed, W. F. (1992). *Macromolecules*, **25**, 806.
36. Yamakawa, H. (1972). *Modern theory of polymer solutions*. Harper & Row, New York.
37. Hara, M. and Nakajima, A. (1980). *Polym. J.*, **12**, 701.
38. Ghosh, S., Li, X., Reed, C. E., and Reed, W. F. (1990). *Biopolymers*, **30**, 1101.
39. Morfin, I., Reed, W. F., Rinaudo, M., and Borsali, R. (1994). *J. Phys. II*, **4**, 1001.
40. Donnan, F. G. and Guggenheim, E. A. (1932). *Z. Phys. Chem.*, **162**, 360.
41. Orofino, T. A. and Flory, P. J. (1957). *J. Chem. Phys.*, **26**, 1067.
42. Orofino, T. A. and Flory, P. J. (1959). *J. Phys. Chem.*, **63**, 283.
43. Nagasawa, M., Takahashi, A., Izumi, M., and Kagawa, I. (1959). *J. Polym. Sci.*, **38**, 213.
44. Alexandrowicz, Z. (1960). *J. Polym. Sci.*, **43**, 325–336, 337–349.
45. Katchalsky, A. and Lifson, S. (1953). *J. Polym. Sci.*, **11**, 409.
46. Ptitsyn, O. B. (1961). *Vysokomol. Soedin.*, **3**, 1084.
47. Fixman, M. (1964). *J. Chem. Phys.*, **41**, 3772.
48. Kurata, M. (1966). *J. Polym. Sci.*, **15**, 347.
49. Ptitsyn, O. B. (1961). *Vysokomol. Soedin.*, **3**, 1251.
50. Alexandrowicz, Z. (1967). *J. Chem. Phys.*, **47**, 4377.
51. Flory, P. J. (1953). *J. Chem. Phys.*, **21**, 162.
52. Hermans, J. J. and Overbeek, J. Th. G. (1948). *Rec. Trav. Chim.*, **67**, 761.
53. Schneider, N. S. and Doty, P. M. (1954). *J. Phys. Chem.*, **58**, 762.
54. Trap, H. J. L. and Hermans, J. J. (1954). *J. Phys. Chem.*, **58**, 757.
55. Eisenberg, H. (1966). *J. Phys. Chem.*, **44**, 137.
56. Ghosh, S., Li, X., Reed, C. E., and Reed, W. F. (1990). *Biopolymers*, **28**, 1101.
57. Li, X. and Reed, W. F. (1991). *J. Chem. Phys.*, **94**, 4568.

58. Reed, W. F. (1994). In *ACS Symposium Series 548* (ed. K. S. Schmitz), pp. 297–314. American Chemical Society, Washington, DC.
59. Gupta, S. K. and Forsman, W. C. (1972). *Macromolecules*, **5**, 779.
60. Fixman, M. and Skolnick, J. (1978). *Macromolecules*, **11**, 8638.
61. des Cloizeaux, J. (1975). *J. Phys. (Paris)*, **36**, 281.
62. Noda, I., Kato, N., Kitano, T., and Nagasawa, M. (1981). *Macromolecules*, **14**, 668.
63. Hyde, A. J. and Taylor, R. B. (1963). *Makromol. Chem.*, **62**, 204.
64. Benoît, H. and Picot, C. (1966). *Pure Appl. Chem.*, **12**, 545.
65. Dautzenberg, H. (1972). *J. Polym. Sci.*, **C39**, 123.
66. Hara, M. and Nakajima, A. (1980). *Polym. J.*, **12**, 711.
67. Schmitz, K. S. (1990). *An introduction to dynamic light scattering by macromolecules*. Academic Press, San Diego, CA.
68. Mandel, M. (1993). In *Dynamic light scattering: The method and some applications* (ed. W. Brown). Oxford Science Publications, Oxford.
69. Schmitz, K. S. (1993). *Macroions in solution and colloidal suspension*. VCH Publishers, New York.
70. Krause, R., Maier, E. E., Deggelmann, M., Hagenbuchle, M., Schultz, S. F., and Weber, R. (1989). *Physica A*, **160**, 135.
71. Drifford, M. and Dalbiez, J. P. (1984). *J. Phys. Chem.*, **88**, 5368.
72. Maier, E. E., Krause, R., Deggelmann, M., Hagenbüchle, M., Weber, R., and Fraden, S. (1992). *Macromolecules*, **25**, 1125.
73. Jannink, G. (1986). *Makromol. Chem., Macromol. Symp.*, **1**, 67.
74. Hayter, J., Jannink, G., Brochard, F., and de Gennes, P. G. (1980). *J. Phys. Lett. (Paris)*, **41**, L-451.
75. de Gennes, P. G., Pincus, P., Velasco, R. M., and Brochard, F. (1976). *J. Phys. (Paris)*, **37**, 1461.
76. Benmouna, M., Weill, G., Benoît, H., and Akcasu, A. Z. (1982). *J. Phys. (Paris)*, **43**, 1679.
77. Koyama, R. (1983). *Physica (B)*, **120**, 418.
78. Ackerson, B. (1976). *J. Chem. Phys.*, **64**, 242.
79. Ise, N., Okubo, T., Sugimura, M., Ito, K., and Nolte, H. J. (1983). *J. Chem. Phys.*, **78**(1), 536.
80. Wang, L. and Bloomfield, V. A. (1991). *Macromolecules*, **24**, 5791.
81. Patkowski, A., Gulari, E., and Chu, B. (1980). *J. Chem. Phys.*, **73**(9), 4178.
82. Fulmer, A. W., Benbasat, J. A., and Bloomfield, V. A. (1981). *Biopolymers*, **20**, 1147.
83. Newman, J., Tracy, J., and Pecora, R. (1994). *Macromolecules*, **27**, 6808.
84. Schmitz, K. S., Lu, M., and Gauntt, J. (1983). *J. Chem. Phys.*, **78**, 5059.
85. Mathiez, P., Mouttet, C., and Weisbuch, G. (1981). *Biopolymers*, **20**, 2381.
86. Schmitz, K. S. and Yu, J. (1988). *Macromolecules*, **21**, 484.
87. Sedlák, M. PhD Thesis.
88. Sedlák, M., Koňák, Č., Štěpánek, P., and Jakeš, J. (1987). *Polymer*, **28**, 873.
89. Sedlák, M. and Amis, E. J. (1992). *J. Chem. Phys.*, **96**, 817.
90. Drifford, M. and Dalbiez, J. P. (1985). *Biopolymers*, **24**, 1501.
91. Förster, S., Schmid, M., and Antonietti, M. (1990). *Polymer*, **31**, 781.
92. Smits, R. G., Kuil, M. E., and Mandel, M. (1994). *Macromolecules*, **27**, 5599.
93. Ghosh, S., Peitzsch, R. M., and Reed, W. F. (1992). *Biopolymers*, **32**, 1105.
94. Koene, R. S. and Mandel, M. (1993). *Macromolecules*, **16**, 973.
95. Burchard, W. (1983). *Adv. Polym. Sci.*, **48**, 1.
96. Sedlák, M. (1994). *J. Chem. Phys.*, **101**, 10140.
97. Borue, V. and Erukhimovich, I. (1988). *Macromolecules*, **21**, 3240.
98. Joanny, J. F. and Leibler, L. J. (1990). *J. Phys. (France)*, **51**, 545.

99. Khokhlov, A. R. and Nyrkova, I. A. (1992). *Macromolecules*, **25**, 1493.
100. Sedlák, M., Koňák, Č., Štěpánek, P., and Jakeš, J. (1990). *Polymer*, **31**, 253.
101. Sedlák, M., Koňák, Č., and Labský, J. (1991). *Polymer*, **32**, 1688.
102. Sedlák, M. and Amis, E. J., unpublished results.
103. Sedlák, M. (1994). In *ACS Symposium Series 548* (ed. K. Schmitz), pp. 337–349. American Chemical Society, Washington, DC.
104. Doty, P. and Steiner, R. F. (1952). *J. Chem. Phys.*, **20**, 85.
105. Alexander, P. and Stacey, K. A. (1955). *Trans. Faraday Soc.*, **51**, 307.
106. Sedlák, M., unpublished results.
107. Hara, M. and Wu, J. (1986). *Macromolecules*, **19**, 2887.
108. Drifford, M. and Dalbiez, J. P. (1985). *J. Phys. Lett.*, **46**, L-311.
109. Sedlák, M., unpublished results.
110. Alexandrowicz, Z. (1959). *J. Polym. Sci.*, **40**, 91.
111. Klooster, N. Th. M., van der Touw, F., and Mandel, M. (1984). *Macromolecules*, **17**, 2070.
112. Klooster, N. Th. M., van der Touw, F., and Mandel, M. (1984). *Macromolecules*, **17**, 2078. See Fig. 3.
113. Delsanti, M., Dalbiez, J. P., Spalla, O., Belloni, L., and Drifford, M. (1994). In *ACS Symposium Series 548* (ed. K. Schmitz), pp. 381–394. American Chemical Society, Washington, DC.
114. Wang, L. and Bloomfield, V. A. (1990). *Macromolecules*, **23**, 804.
115. Lantman, C. W., MacKnight, W. J., Peiffer, D. G., Sinha, S. K., and Lundberg, R. D. (1987). *Macromolecules*, **20**, 1096.
116. Lantman, C. W., MacKnight, W. J., Higgins, J. S., Peiffer, D. G., Sinha, S. K., and Lundberg, R. D. (1988). *Macromolecules*, **21**, 1339.
117. Lantman, C. W., MacKnight, W. J., Sinha, S. K., Peiffer, D. G., Lundberg, R. D., and Wignall, G. D. (1988). *Macromolecules*, **21**, 1344.
118. Lundberg, R. D. and Phillips, R. R. (1982). *J. Polym. Sci., Polym. Phys. Ed.*, **20**, 1143.
119. Pedley, A. M., Higgins, J. S., Peiffer, D. G., and Burchard, W. (1990). *Macromolecules*, **23**, 1434.
120. Gabrys, B., Higgins, J. S., Lantman, C. W., MacKnight, W. J., Pedley, A. M., Peiffer, D. G., and Rennie, A. R. (1989). *Macromolecules*, **22**, 3746.
121. Wu, J., Wang, Y., Hara, M., Granville, M., and Jerome, R. J. (1994). *Macromolecules*, **27**, 1195.
122. Hara, M. and Wu, J. (1986). *Macromolecules*, **19**, 2887.
123. Hara, M. and Bodycomb, J. (1994). *Macromolecules*, **27**, 7369.

Scattering from concentrated polymer solutions

Taco Nicolai and Wyn Brown

5.1 Introduction

Following the development of scaling theories by de Gennes and coworkers,^[1,2] a main focus of interest in polymer–solvent systems has been the so-called semi-dilute regime. Semi-dilute solutions are those having a very low polymer volume fraction and at the same time a strong overlap of the polymer coils. The overlap concentration may be defined as $C^* \cong 3M/N_A 4\pi R_g^3$, where M is the molar mass of the polymers, R_g is the radius of gyration and N_A is Avogadro's number. It is clear that in order to satisfy both conditions very high molar masses are required. The concentration regime in which semi-dilute theories can be properly applied is not well defined. Generally, investigations are rather arbitrarily limited to volume fractions less than 10%. Taking this upper limit and assuming a lower limit of $3C^*$, the molar mass of, for example, polystyrene in a good solvent such as toluene must be larger than 7×10^4 g/mol and in a theta solvent such as cyclohexane at 35 °C larger than 5×10^5 g/mol. One of the appealing features of semi-dilute systems is that many of the scattering properties are general for flexible linear polymers and independent of the chemical nature of the solvents provided that they have the same solvent quality.

Semi-dilute solution theories are usually presented in terms of static, ξ_s , and dynamic, ξ_h , screening lengths. The first represents the distance beyond which excluded volume interactions are screened and the second the distance beyond which hydrodynamic interactions are screened. Experimentally, an apparent radius of gyration, R_g^a , is determined from the initial scattering wave vector dependence of the time-averaged scattered intensity (see eqn (5.11)). From dynamic light scattering an apparent hydrodynamic radius, R_h^a , can be determined using the Stokes–Einstein relation for the cooperative diffusion coefficient (see eqn (5.27)). For semi-dilute solutions $R_g^a \propto \xi_s$ and $R_h^a \propto \xi_h$ are proportional with a factor of order unity. At higher concentrations, however, the relationship between the theoretical lengths ξ_s and ξ_h and the experimentally observed R_g^a and R_h^a is less direct. It therefore becomes necessary to distinguish clearly between the experimental and the theoretical parameters. In much of the literature on semi-dilute solutions this distinction is not made, and R_g^a has been equated with $\sqrt{3}\xi_s$ and R_h^a with ξ_h . The reason for the factor of $\sqrt{3}$ between R_g^a and ξ_s will become clear in the following section.

In recent years a number of scattering studies on concentrated solutions has been reported. In this chapter we will review the main findings of these investigations. It may seem surprising that, in the past, few scattering studies have been made on more concentrated solutions. This lack may be explained on the one hand by the experimental difficulty of preparing optically clean polymer solutions at high concentrations and, on the other hand, by the fact that scattering properties become system-dependent at high concentrations. Investigations on concentrated systems are not only important for their own sake, but also make more explicit features that in some cases are also important in semi-dilute solutions. Two examples are the chain stiffness in the case of polymers with large persistence lengths and the solvent mobility close to the glass transition temperature. By discussing the scattering properties of linear flexible polymers over the whole concentration regime we hope to elucidate in what sense the tripartition into dilute, semi-dilute and concentrated solutions is valid and where this separation breaks down. We will focus on the scattering due to concentration fluctuations, as in most cases this is the dominant contribution to the scattered intensity.

5.2 Time-averaged scattered intensity

The time-averaged intensity of light scattered by a binary solution of polymers is generally dominated by the contribution from concentration fluctuations. The contribution from density fluctuations is significant only if the contrast between the polymers and the solvent is small or at very low or very high concentrations. In the latter case the scattering due to concentration fluctuations is obtained by subtraction of the scattering by the pure solvent or pure polymer, respectively. The scattered intensity due to isotropic concentration fluctuations about the average concentration C of scattering units, $\delta C(r) = C(r) - C$, is proportional to the spatial Fourier transform of the autocorrelation function of the concentration fluctuations:^[3,4]

$$I = K \int_V \langle \delta C(0) \delta C(r) \rangle 4\pi r^2 \frac{\sin(qr)}{qr} dr, \quad (5.1)$$

where the integral is taken over the scattering volume, V . Here K is a constant which depends on the set-up and the contrast between the polymers and the solvent, or between labelled polymers and the solutions, and q is the scattering wave vector.

In the case of light scattering with vertically polarized incident light of intensity I_0 and wavelength λ , K becomes

$$K = \frac{VI_0 4\pi^2 n^2 (\partial n / \partial C)^2}{R^2 N_A \lambda^4} \quad (5.2)$$

and $q = (4\pi n / \lambda) \sin(\theta/2)$. Here n is the refractive index of the solution, $\partial n / \partial C$ is the refractive index increment at constant chemical potential, R is the distance

between the scattering volume, V , and the detector, and θ is the angle of observation. If all scattering units are identical, the q dependence of I can be expressed as the product of the structure factor of the centre of mass distribution of the scattering units, $S(q)$, and the form factor of the scattering units, $P(q)$:

$$I = KCP(q)S(q). \quad (5.3)$$

$S(q)$ is related to the pair correlation function of the scattering units, $g(r)$, by

$$S(q) = 1 + \int_V (g(r) - C) 4\pi r^2 \frac{\sin(qr)}{qr} dr, \quad (5.4)$$

with $\int_V (g(r) - C) 4\pi r^2 dr = N - 1$, where N is the number of scattering units in the scattering volume; $g(r)$ is the number concentration of scattering units at distance r given that there is a scatterer at the origin.

If C is the concentration in weight per unit volume, $P(q)$ has to be normalized to give the molar mass of the scattering units at small q : $P(q \rightarrow 0) = M_0$. If $N \gg 1$, we can ignore the influence of the self term in eqn (5.4). In very dilute monodisperse polymer solutions the positions of different polymer molecules are not correlated, so that $S(q)$ is equal to the structure factor of the individual chains, which has the same form as eqn (5.4), but with $g(r)$ as the pair correlation function of the individual polymers and N as the number of scattering units per polymer chain. For unperturbed linear flexible polymers the distribution of the scattering units is Gaussian and $S(q)$ is given by the so-called Debye function for wave vectors much smaller than the distance between the scattering units, r_0 :^[5]

$$S(q) = N \frac{2}{q^4} (\exp(-q^2) - 1 + q^2), \quad qr_0 \ll 1 \text{ and } N \gg 1. \quad (5.5)$$

The corresponding pair correlation function may be written as^[6,7]

$$g(r) = \frac{d_f}{4\pi r_0^{d_f}} r^{d_f-3} f(r/\xi), \quad r \ll r_0, \quad (5.6)$$

where $d_f = 2$ is the fractal dimension of the polymers and $f(r/\xi)$ is a cut-off function at correlation length ξ . A stretched exponential cut-off $f(r/\xi) = \exp[-(r/\xi)^{1.2}]$ is a good approximation (see ref. 7). The radius of gyration, R_g , can be calculated from $g(r)$ as

$$R_g^2 = \frac{\int g(r) 4\pi r^4 dr}{2N}. \quad (5.7)$$

Inserting eqn (5.6) into eqn (5.7), one obtains

$$R_g = r_0 N^{1/d_f}, \quad N \gg 1. \quad (5.8)$$

Generally, the radius of gyration of a Gaussian chain is written in terms of the so-called Kuhn length, l_k , which equals twice the persistence length, l_p , of the

polymer: $R_g^2 = Nl_k^2/6$. Comparing this expression with eqn (5.8), it follows that $r_0 = \sqrt{(2/3)}l_p$.

The Gaussian chain model describes well the main features of dilute polymer solutions in theta solvents at larger distances, i.e. $r \gg r_0$ and $N \gg 1$. At smaller distances down to the monomer size, $S(q)$ and R_g are well described by the so-called helical worm-like chain model.^[8]

In good solvents we have to include the effect of excluded volume interactions, which swell the chains and reduce the fractal dimension. When calculated using renormalization group theory the fractal dimension is expected to become 1.70,^[9] in good agreement with the experimentally observed fractal dimension of linear flexible polymers in athermal solvents. Excluded volume interactions become effective only over larger distances due to the intrinsic stiffness of polymers, i.e. short chains do not swell even in good solvents. Experimentally, the onset of excluded volume interactions in athermal solvents is found to occur at $N \approx 50$ for a number of polymers with very different persistence lengths.^[10] The static structure factor is very similar to the Debye function for $qR_g < 3$, but at large q the dependence is $S(q) \propto q^{-1.7}$ instead of $S(q) \propto q^{-2.0}$ for Gaussian coils.^[11] The pair correlation can again be described by eqn (5.6) with $d_f = 1.70$.

When the concentration exceeds the overlap concentration, the correlation between segments belonging to the same chain is screened by excluded volume interactions with segments of other chains.^[1,6] For Gaussian coils it can be shown that, if $C \gg C^*$,

$$S(q) = \frac{N}{(\xi_s^2 q^2 + 1)}, \quad qr_0 \ll 1. \quad (5.9)$$

The concentration dependence of the screening length, ξ_s , can be written in terms of binary, B_1 , and ternary, B_2 , interaction terms: $\xi_s^{-2} = B_1 C + B_2 C^2$.^[12] The corresponding pair correlation function is given by

$$g(r) - C = \frac{1}{2\pi r_0^2} r^{-1} \exp(-r/\xi_s), \quad r \gg r_0. \quad (5.10)$$

For $r < \xi_s$ the pair correlation function is the same as that for dilute chains. For $r > \xi_s$, $g(r)$ becomes equal to the average concentration. Equations (5.9) and (5.10) are equivalent to expressions for a dilute solution of non-interacting polymers with $N = 2(\xi_s/r_0)^2$ segments and $R_g = \sqrt{3}\xi_s$. This approach is valid when the excluded volume interactions are very weak and do not swell the polymers significantly. In good solvents, however, the chains are still swollen at distances smaller than ξ_s and have a fractal dimension $d_f = 1.70$. Scaling arguments give $\xi_s \propto C^{-1/(3-d_f)}$, i.e. $\xi_s \propto C^{-0.77}$.^[2] Again, the system is equivalent to that of a dilute solution of non-interacting polymers with $N \propto (\xi_s/r_0)^{1.70}$ and $R_g \propto \xi_s$. The multiplying terms in these relations are of order unity, but depend on the shape of the cut-off function of $g(r)$ at large r .

It is possible to label only a few chains, so that the contrast is not between the polymers and the solvent but between a dilute solution of labelled chains and the unlabelled chains.^[13] The scattered intensity is then proportional to the static structure factor of individual chains. At distances $r < \xi$ the chains are swollen due to excluded volume interactions, but at large distances these interactions are screened. The polymer can be visualized as a Gaussian chain of m segments with size ξ and with radius of gyration $R_g \propto \xi_s m^{0.5}$. As $m \propto (\xi_s/r_0)^{-1.70}$ and $\xi_s \propto C^{-0.77}$ it follows that the radius of gyration decreases for $C \gg C^*$ as $R_g \propto C^{-0.12}$.^[12] In the melt all excluded volume interactions are screened and the chain dimension is unperturbed.

Muthukumar and Edwards^[14] have included the effect of correlation of connected segments in the Flory–Huggins mean-field theory. They derive an expression for ξ_s in terms of the expansion factor of the chain due to excluded volume interactions. For $C \gg C^*$ the same concentration dependencies of ξ_s and R_g are obtained in the limits of dominating binary or ternary interactions.

5.2.1 Comparison with experiments

Scattering experiments on polymer solutions above the overlap concentration are mostly limited to the so-called Guinier regime, in which one measures an apparent molar mass (M_{ap}) and radius of gyration (R_g^a):

$$\frac{KC}{I} = \frac{1}{M_{ap}} \left(1 + \frac{(qR_g^a)^2}{3} \right), \quad qR_g^a < 1, \quad (5.11)$$

with

$$M_{ap}/M_0 = \int (g(r) - C) 4\pi r^2 dr \quad (5.12)$$

and

$$(R_g^a)^2 = \frac{\int (g(r) - C) 4\pi r^4 dr}{2M_{ap}}. \quad (5.13)$$

In dilute solutions M_{ap} is equal to the weight-average molar mass of the polymers and R_g^a is the z-average radius of gyration. If $g(r)$ has the general form given by eqn (5.6), R_g^a is proportional to the screening length with a proportionality constant of order unity which depends on the shape of the cut-off function. If $f(r/\xi_s)$ is a single exponential $R_g^a = \sqrt{3}\xi_s$.^[17] Above the overlap concentration ξ_s , and consequently M_{ap} and R_g^a , decrease due to excluded volume interactions. It is clear that, as far as the scattering properties are concerned, polymer solutions above the overlap concentration can be modelled as dilute solutions of polymers with molar mass and radius determined by the screening length. The only difference is that the cut-off function of the pair correlation function is not the same, which means that the proportionality factor between ξ_s and R_g^a may be different. The apparent molar mass becomes independent of the molar mass of the particles if $R_g^a < R_g$. Inserting eqn (5.6)

into eqn (5.13), we obtain

$$R_g^a = a M_{ap}^{1/d_f}, \quad R_g^a \gg r_0, \quad (5.14)$$

with $d_f = 1.70$ in athermal solvents and $d_f = 2.0$ if the polymer dimensions are unperturbed. In the latter case we can express the multiplying term a in terms of the persistence length and the molar mass per unit length M_l : $a = (0.5l_p/M_l)^{0.5}$ (see above).

On the other hand, the scattered intensity due to concentration fluctuations at $q \rightarrow 0$ is related to the osmotic compressibility (see, e.g., refs 3, 4, and 14):

$$I(q \rightarrow 0) = K C R T (\partial \pi / \partial C)^{-1}, \quad (5.15)$$

where R is the gas constant and T is the absolute temperature. The inverse osmotic compressibility is thus inversely proportional to the apparent molar mass:

$$(\partial \pi / \partial C) = R T / M_{ap}. \quad (5.16)$$

Using $M_{ap} \propto \zeta_s^{d_f}$ we obtain directly the concentration dependence of the osmotic pressure from the concentration dependence of ζ_s : $\pi \propto C^{2.3}$ in good solvents and $\pi \propto C^{3.0}$ in theta solvents.

The most systematically studied polymer is polystyrene, for which experimental values of M_{ap} and R_g^a are available over a wide concentration regime, both in good solvents and in theta solvents. In Figs. 5.1 and 5.2, M_{ap} and R_g^a have been plotted as functions of C with $C \gg C^*$. At low concentrations both

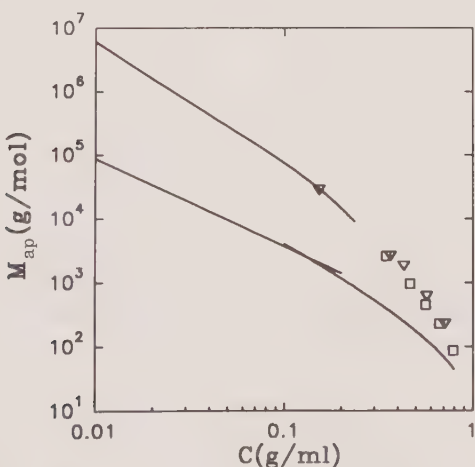


FIG. 5.1. A double logarithmic representation of the apparent molar mass as a function of the polymer concentration for polystyrene in toluene (good solvent) at 25 °C (lower curve) and cyclohexane (theta solvent) at 25 °C (upper curve). The good solvent curve is constructed from the data from ref. 15 for $C < 0.2$ g/ml and from ref. 16 for $C > 0.1$ g/ml (solid lines). The theta solvent results are taken from ref. 17 for $C < 0.2$ g/ml and for the high concentration from ref. 17 (∇) and ref. 18 (\square).

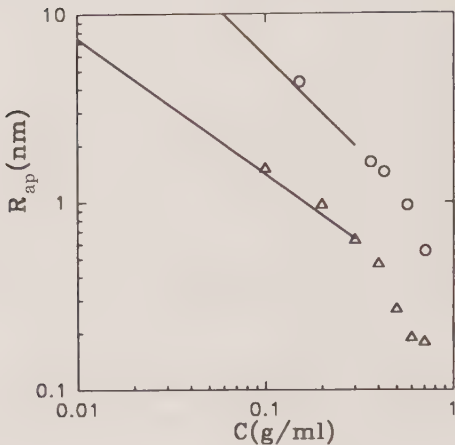


FIG. 5.2. A double logarithmic representation of the apparent radius of gyration as a function of the polymer concentration for polystyrene in several good solvents (lower curve) and cyclohexane at 35 °C (upper curve). The good solvent results are taken from ref. 19 for $C < 0.2$ g/ml (solid line) and from ref. 20 for $C > 0.1$ g/ml (Δ). The theta solvent results are taken from ref. 19 for $C < 0.2$ g/ml (solid line) and from ref. 21 for $C > 0.1$ g/ml (\circ).

M_{ap} and R_g^a have a power-law dependence on the concentration in good solvents, given by

$$M_{ap} = 1.55 \times 10^2 C^{-1.38} \text{ g/mol}, \quad R_g^a = 0.5C^{-0.72} \text{ nm} \quad (5.17)$$

and in theta solvents by

$$M_{ap} = 7.1 \times 10^2 C^{-2.0} \text{ g/mol}, \quad R_g^a = 1.0C^{-1.0} \text{ nm}. \quad (5.18)$$

Here C is expressed in g/ml. In good solvents the concentration exponent of M_{ap} is slightly larger than the theoretical value of 1.31 and the concentration exponent of R_g^a is slightly smaller than the theoretical value of 0.77. Various semi-dilute good solvent data reported in the literature are in close agreement, while the results of different authors in theta solvents show a considerable spread, probably owing to the strong influence of temperature. Combining these results gives the following relationship between R_g^a and M_{ap} in good solvents:

$$R_g^a = 3.6 \times 10^{-2} M_{ap}^{0.52} \text{ nm}, \quad (5.19)$$

and in theta solvents

$$R_g^a = 3.9 \times 10^{-2} M_{ap}^{0.5} \text{ nm}. \quad (5.20)$$

These relationships can be compared with those in dilute solutions; $R_g = 1.1 \times 10^{-2} M^{0.595}$ nm in good solvents and $R_g = 2.7 \times 10^{-2} M^{0.5}$ nm in theta solvents. If the cut-off function of the pair correlation function is the same in dilute and semi-dilute solutions, the relationship between R_g^a and M_{ap} should

be identical to the relationship between R_g and M in dilute solutions. In fact, the cut-off function of the pair correlation function for flexible chains is less gradual than an exponential decay, so that a somewhat smaller prefactor is expected in the dilute samples. The mean-field result is $R_g^a = 3.9 \times 10^{-2} M_{ap}^{0.5}$ nm, using $l_p = 1.1$ nm and $M_l = 367$ g/nm,^[22] in good agreement with the observed relationship in theta solvents. The power-law exponent of M_{ap} in good solvents, however, is significantly smaller than expected theoretically and observed in dilute solutions.

Deviations from the power-law dependence are clearly visible for $C > 0.3$ g/l in the case of good solvents and at somewhat higher concentrations in theta solvents. The deviations occur at values of R_g^a and M_{ap} , where the intrinsic stiffness of the polymers influences the relation between R_g and M . Similar observations were made for PDMS in octane and PVAc in toluene, both of which are good solvents.^[21] As shown in Fig. 5.3, to a certain extent R_g^a vs. M_{ap} mirrors R_g vs. M . At distances smaller than the polymer thickness $d \approx 1.0$ nm, the concentration dependences of R_g^a and M_{ap} are determined by the detailed structure of the polymer. The applicability of the theories outlined above to the more concentrated regime depends on the persistence length and the thickness of the polymer, which define the size of the elementary scattering unit. As yet, no theory has been developed that gives the concentration dependence of ξ_s for $\xi_s < l_p$.

It is clearly established that the polymer chain dimensions in the melt are those of a Gaussian chain (see, e.g., ref. 24). The concentration dependence of R_g is less well established. Two reports of the concentration dependence of the radius of gyration of polystyrene in good solvents describe contradictory results.^[2,25] A power-law dependence of R_g on the concentration was observed in both cases over the whole concentration regime above C^* , but with a different exponent. However, one would expect R_g to decrease only at lower concentrations where ξ_s is large enough for the chains to be locally swollen and to remain constant at higher concentrations.

5.3 Dynamic light scattering

Using the dynamic light scattering technique one measures the normalized intensity autocorrelation function, $g_2(t) = \langle I(0)I(t) \rangle / I^2$.^[3] If the statistics of the scattered light are Gaussian, $g_2(t)$ is related to the normalized electric field autocorrelation function, $g_1(t)$:

$$g_2(t) = B(1 + \beta|g_1(t)|^2), \quad (5.21)$$

with β a constant between 0 and 1, which depends on the experimental set-up, and where B is a baseline term. Considering again only concentration fluctuations, $g_1(t)$ is related to the time-correlation function of concentration fluctuations:

$$g_1(t) = \int_V \frac{\langle \partial C(0, 0) \partial C(r, t) \rangle}{\langle \partial C(0) \partial C(r) \rangle} 4\pi r^2 \frac{\sin(qr)}{qr} dr. \quad (5.22)$$

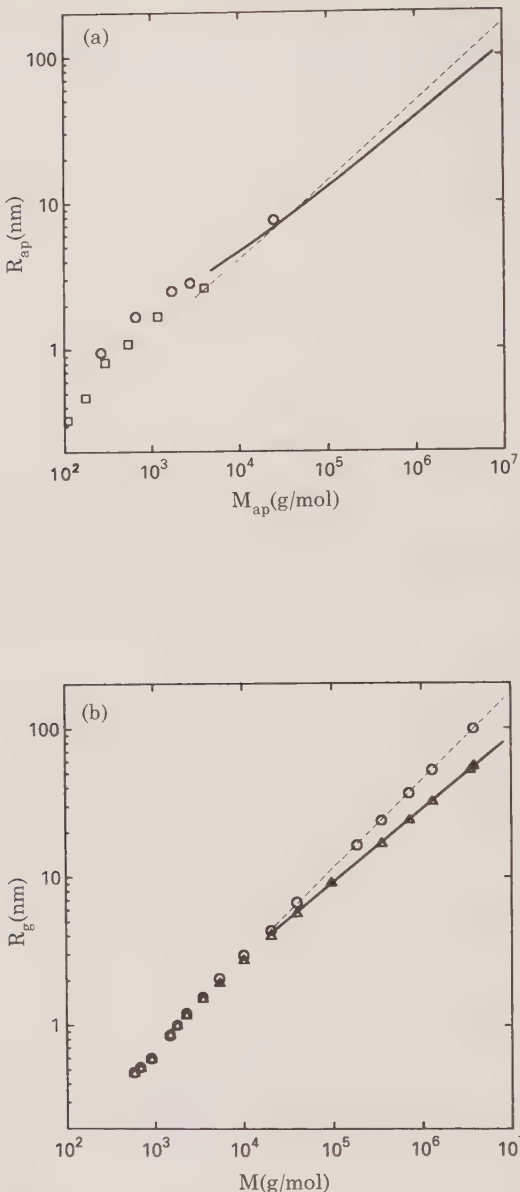


FIG. 5.3. A double logarithmic representation of the apparent radius of gyration as a function of the apparent mass at the same concentration interpolated from Fig. 5.1. Symbols are the same as in Fig. 5.2. The dashed and solid lines represent the limiting power law dependences in toluene and cyclohexane, respectively. (b) A double logarithmic representation of the radius of gyration at infinite dilution of polystyrene as a function of the molar mass in toluene at 25 °C (\circ) and in cyclohexane at 35 °C (\triangle), reproduced from ref. 23. The dashed and solid lines represent the limiting power-law dependences in toluene and cyclohexane, respectively.

For small values of q , the concentration fluctuations relax by diffusion and

$$g_1(t) = \exp(-D_c q^2 t). \quad (5.23)$$

Here D_c is the cooperative diffusion coefficient in the laboratory-fixed coordinate frame. For $q > \xi_s$ one has to take into account relaxation through internal dynamics of the flexible polymer chain. D_c can be written in terms of the osmotic compressibility and the friction coefficient, f , between a polymer chain and the solvent and φ is the polymer volume fraction:

$$D_c = (1 - \varphi)^2 \frac{M}{N_A f} \left(\frac{\partial \pi}{\partial C} \right). \quad (5.24)$$

Alternatively we can write D_c in terms of the apparent molar mass utilizing eqn (5.16):

$$D_c = (1 - \varphi)^2 \frac{k_B T}{f} \frac{M}{M_{ap}}, \quad (5.25)$$

where k_B is Boltzmann's constant and T is the absolute temperature. f should not be confused with the friction coefficient of an individual polymer chain moving with respect to the solution, which determines the self-diffusion coefficient of the polymers, D_p . Only at infinite dilution are the two friction coefficients the same and D_c equals D_p . In this case $M_{ap} = M$ and $f = 6\pi\eta_s R_h$, so that eqn (5.25) reduces to the so-called Stokes-Einstein relationship:

$$D_0 = k_B T / 6\pi\eta_s R_h, \quad (5.26)$$

with η_s the solvent viscosity R_h the hydrodynamic radius, i.e. the radius of an impenetrable sphere with the same friction coefficient as that of the polymer chain. Experimentally, it is observed that R_h is proportional to R_g in theta solvents which shows that the polymer coils are essentially non-draining.^[26] In good solvents the molar mass dependence of R_h is slightly weaker than that of R_g , which has been attributed to a slower approach to R_h to the limiting power law dependence.^[27]

If the concentration is increased above the overlap concentration, the hydrodynamic interactions between segments of the same chain are screened by the presence of segments of other chains. One can introduce a hydrodynamic screening length, ξ_h , such that segments further apart than ξ_h do not interact, while segments at shorter distances retain full hydrodynamic interactions.^[17] The friction coefficient per polymer chain is then $f = (M/M_b)^* f_b$, where M_b is the molar mass of the part of the polymer chain with size ξ_h that is non-draining and f_b is its friction coefficient. With increasing concentration f_b increases from that for a fully non-draining (Zimm type) chain, $f = 6\pi\eta_s R_h$, to that for a fully draining (Rouse type) chain, $f = (M/M_0)^* f_0$, where f_0 is the segmental friction coefficient. If we assume that the solvent mobility is not modified by the presence of other polymers we can write f_b in terms of an effective hydrodynamic radius, R_{hb} , proportional to ξ_h , so that $f = (M/M_b) \times 6\pi\eta_s R_{hb}$. Inserting this expression

for f in eqn (5.25) we obtain

$$D_c = (1 - \varphi)^2 \frac{k_B T}{6\pi\eta_s R_h^a}, \quad (5.27)$$

with an apparent hydrodynamic radius

$$R_h^a = R_{hb}(M_{ap}/M_b). \quad (5.28)$$

In semi-dilute solutions ζ_s and ζ_h have the same concentration dependence both in good and theta solvents, which means that $M_b \propto M_{ap}$, so that $R_h^a \propto R_g^a$. Experimentally, R_h^a is found to be proportional to R_g^a for semi-dilute solutions in good solvents ($R_g^a/R_h^a = 0.9$).^[19] In theta solvents one needs to take into account the contribution of the elastic modulus; see below. After correction R_h^a is again found to be proportional to R_g^a for semi-dilute solutions ($R_g^a/R_h^a = 0.5$).^[19]

In this treatment the influence of viscoelastic interactions is ignored. This is permissible only if the time-dependent elastic longitudinal modulus, $M_{el}(t)$, at $t = \tau_c = 1/(D_c q^2)$, is much smaller than the osmotic modulus $K_{os} = C(\partial\pi/\partial C)$. Earlier studies^[19, 28] on semi-dilute polymer solutions showed that the relaxation of concentration fluctuations occurs mainly through a local swelling/deswelling of the transient (gel) network formed by the entangled polymer chains. Part of the concentration fluctuations, however, relax through structural relaxation of the transient network. The longest relaxation time characterizing these latter processes is q -independent and has a value close to the final relaxation time ($G(t)$) obtained in dynamic mechanical measurements. This situation has been discussed in some detail in ref. 29.

Typical correlation curves are shown in Fig. 5.4 for several different theta systems.^[30, 31] Temperature-shifting on the delay time axis brings the correlograms into coincidence, showing that the relative amplitudes of the fast and slow parts are system-independent. The relative amplitude of the q -independent part of the relaxation spectrum decreases strongly when the osmotic compressibility of the solution increases and is thus highly sensitive to the quality of the solvent. For this reason, the q -independent structural relaxation spectrum is only observable with a significant amplitude, and has only been extensively studied close to theta conditions.

A reasonable postulate is that the slow modes in semi-dilute solutions are related to the viscoelastic properties of the transient network, the seat of which is the topological constraints which come into play above a certain minimum concentration and molecular weight necessary to produce entanglements. (It is emphasized that these q -independent modes are distinguished from the slow modes due to the diffusion of 'dynamic clusters' in some concentrated polymer solutions as well as viscoelastic liquids such as o-terphenyl; these will be briefly discussed below). On a time scale shorter than the characteristic lifetime of the entanglements, the system will behave as a crosslinked network. Thus there will be contributions to the longitudinal modulus both from the osmotic modulus and the elastic modulus of the transient network. In the low frequency

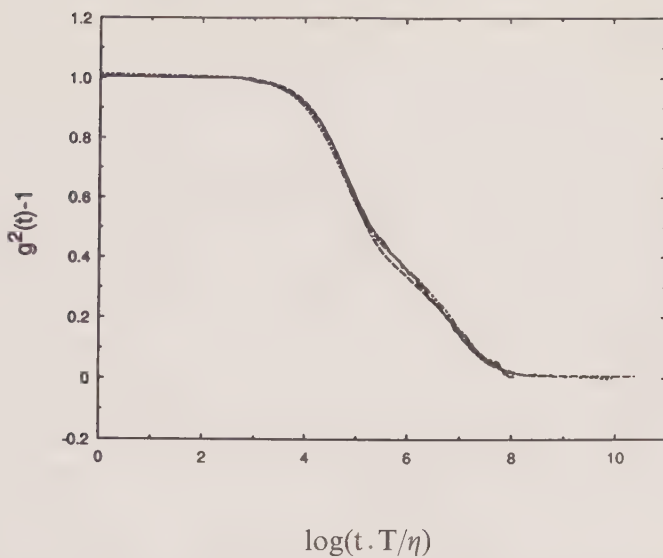


FIG. 5.4. Normalized second-order correlation functions for polystyrene solutions measured in four solvents at the respective theta temperatures: bis(2-ethylhexyl)phthalate; diethyl oxalate; diethylmalonate; cyclohexane. The delay time axis is multiplied by (T/η) to bring the correlograms into coincidence (reproduced from ref. 31).

limit, the chains can disentangle and the concentration fluctuations will then relax as in a viscous solvent.

The cooperative diffusion coefficient is related to the total longitudinal modulus by^[1,32,33]

$$D_c = (1 - \phi)^2 (K_{os} + M_{el}) M / N_A C f \quad (5.29)$$

The term $M/N_A C$ is included because f is the friction per polymer chain and not per unit volume as is usual in this context. It is important to note that the relevant elastic modulus for cooperative diffusion is that of the transient network, and that this is not related to the overall compressibility of the solution, which is orders of magnitude larger than M_{el} . This view is contested by Wang,^[34] who introduced a coupling parameter, β , proportional to the difference in densities of polymer and solvent and through which the concentration and viscoelastic relaxations were considered to be coupled in semi-dilute solutions. Subsequent developments include an experimental study of the role played by the parameter β .^[31] For several different theta systems, it was established that the relative amplitude of the viscoelastic modes is unrelated to the parameter β in semi-dilute solutions (see Fig. 5.4, for example, for which systems the β parameter varies substantially). More importantly, in contradiction to the theoretical prediction, a substantial amplitude of the viscoelastic component was observed under conditions selected so that $\beta = 0$.^[31] However, the theoretical development is still controversial.^[35]

M_{el} contains contributions from the bulk and shear elastic modulus: $M_{el}(t) = K_{el}(t) + 4G(t)/3$.^[36] (If the crosslinks are permanent,

$$K_{os} + K_{el} = C(\partial\omega/\partial C),$$

where ω is the osmotic swelling pressure.^[37] If $M_{el}(t)$ cannot be neglected compared to K_{os} , the intensity correlation function contains a contribution from the viscoelastic relaxation. In the simplest case, in which the viscoelastic relaxation is characterized by a single-exponential decay with relaxation time $\tau_v \gg \tau_c$, $M_{el}(t) = M_0 \exp(-t/\tau_v)$, and $g_1(t)$ is a double-exponential decay. The relatively fast decay is q^2 -dependent and results from the cooperative diffusion, while the slow decay is q -independent with relaxation time $\tau_v(1 + M_0/K_{os})$. The relative amplitude of the slow decay is given by $A_s = M_0/(K_{os} + M_0)$. In reality, of course, $M_{el}(t)$ is characterized by a distribution of relaxation times and in principle the time-dependence of $M_{el}(t)$ for $t > \tau_c$ can be obtained from $g_1(t)$ if $M_{el}(t)$ is not much smaller than K_{os} .

When the polymer volume fraction becomes large, the solvent mobility will be modified by the presence of polymer chains, and application of eqn (5.27) leads to values of R_h^a which are no longer proportional to R_g^a . An alternative approach is to use the fact that for $C > C^*$ the self-diffusion coefficient of the polymer, D_p , is much smaller than that of the solvent, D_s .^[38,39] In this case D_c can be expressed in terms of D_s :

$$D_c = \frac{D_s}{A} \frac{(1 - \phi)M_s V_s}{RTV_p} \left(\frac{\partial \pi}{\partial C} \right) \quad (5.30)$$

with

$$A = \left(\frac{M_s V_s D_s}{M V_p D_p} \right)_{C \rightarrow 0} (1 - \phi)^2 + 3\phi - 2\phi^2. \quad (5.31)$$

Here V_s and V_p are the partial specific volumes of the solvent and the polymer, respectively, and M_s is the molar mass of the solvent. The first term of the factor A was chosen by Vrentas *et al.* to give $D_c = D_p$ for $\phi \ll 1$. This choice leads to wrong values for D_c in semi-dilute solutions, where the screening effect of hydrodynamic interactions is important. If ϕ is not very small this term becomes negligible with respect to the other terms. In the other limit of $(1 - \phi) \ll 1$, eqn (5.30) gives $D_c = D_s$. Equation (5.30) is observed experimentally to work well down to low concentrations for low molar mass polystyrene in toluene, where semi-dilute conditions do not apply. For high molar mass polystyrene the agreement is good at higher concentration; see below.

The self-diffusion coefficient can be expressed in terms of free volume parameters:

$$D_s = D_\infty \exp\left(-\frac{E}{RT}\right) \exp\left[-\frac{\gamma(\omega_s V_s^* + \omega_p \zeta V_p^*)}{V_{FH}}\right], \quad (5.32)$$

where V_{FH} is the hole free volume, given by

$$V_{FH} = \omega_s k_s(T - T_{0s}) + \omega_p k_p(T - T_{0p}). \quad (5.33)$$

Here, ω is the mass fraction, V^* is the specific hole free volume required for a jump of either a solvent or a polymer jumping unit, and ζ is the ratio of the critical molar volume of the solvent jumping unit to that of the polymer jumping unit. T_0 is the temperature at which V_{FH} becomes zero. E is the energy per mole that a molecule needs to overcome the attractive forces which hold it to its neighbours. When the temperature and concentration dependencies of the energy term are weak compared to the effect of the free volume, the energy term can be incorporated in the multiplying term D_∞ . This is the case at temperatures not too far from the glass transition temperature, T_g . γ is an overlap factor introduced to account for the fact that the same free volume is available to more than one jumping unit, and k is a free-volume parameter related to the thermal expansion coefficient. The indices p and s denote polymer and solvent parameters, respectively. We can rewrite eqn (5.32) in the form of the so-called Vogel–Fulcher–Hesse–Tamman (VFHT) equation:

$$D_s = D_\infty \exp\left(-\frac{B}{T - T_0}\right), \quad (5.34)$$

with

$$T_0 = \frac{k_s \omega_s T_{0s} + k_p \omega_p T_{0p}}{k_s \omega_s + k_p \omega_p}, \quad (5.35)$$

$$B = (\omega_s V_s^* + \omega_p \zeta V_p^*) \left/ \left(\omega_s \frac{k_s}{\gamma} + \omega_p \frac{k_p}{\gamma} \right) \right. \quad (5.36)$$

T_0 is the temperature at which the friction coefficient becomes infinite and is about 50 °C below T_g .^[36] Alternatively, we can write D_s in terms of an effective local viscosity, η_{eff} , and the hydrodynamic radius of the solvent molecules, R_{hs} :

$$D_s = k_B T / 6\pi \eta_{eff} R_{hs}, \quad (5.37)$$

with

$$\eta_{eff} = \eta_0 \exp\left(\frac{B}{T - T_0}\right). \quad (5.38)$$

R_{hs} is not expected to have a strong temperature or concentration dependence. At very low polymer concentrations η_{eff} reduces to η_s . Utilizing eqns (5.37) and (5.34) in eqn (5.30), we can express D_c in terms of η_{eff} :

$$D_c = (1 - \varphi)^2 \frac{k_B T}{6\pi \eta_{eff} R_h^a}, \quad (5.39)$$

with

$$R_h^a = R_{hs} = \frac{M_{ap} V_p (3\varphi - 2\varphi^2)(1 - \varphi)}{M_s V_s}, \quad (5.40)$$

where we have assumed that the first term in the factor A can be neglected.

Equation (5.39) can be used over the whole concentration range since R_h^a contains contributions from both excluded volume and hydrodynamic interactions. In highly dilute solutions R_h^a is equal to the hydrodynamic radius, while in semi-dilute solutions R_h^a is proportional to ζ_h . In both cases, η_{eff} is close to η_s . In highly concentrated solutions most hydrodynamic interactions are screened and eqn (5.40) gives $R_h^a \propto M_{ap}$. The concentration regime in which we can neglect the difference between η_{eff} and η_s depends on the temperature. Close to T_g , η_{eff} will differ significantly from η_s even at low concentrations. In general, T_g of the polymer is higher than that of the solvent, so that T_0 and therefore η_{eff} at fixed temperature increase with increasing polymer concentration at fixed temperature. If D_c is measured as a function of the polymer concentration at a temperature intermediate between the T_g of the solvent, T_{gs} , and of the polymer, T_{gp} , D_c will decrease dramatically when the glass transition temperature of the solution is close to the measurement temperature.

5.4 Dynamic properties: comparison with experiments

In bulk polymer systems, it is well-established that the primary α -relaxation dominates the dynamic light scattering correlation function, which consequently displays a very broad non-exponential decay. The α -relaxation is due to localized main-chain motions and is therefore insensitive to the chain molecular weight. The characteristic relaxation time, τ , is typified by a non-Arrhenius temperature dependence, which is well-described by the VFHT equation having the form:

$$\tau = \tau_0 \exp[B/(T - T_0)]. \quad (5.41)$$

It has been found for several polymer-solvent systems in the concentration range 0.7–0.9 g/ml that both τ_0 and B are constant while T_0 increases with increasing concentration. In the presence of the solvent, the dynamics are more complicated than in the melt, since concentration fluctuations are then present in addition to the longitudinal density and local anisotropy fluctuations and contribute to the polarized (VV) correlation function. In the depolarized (VH) DLS experiment, only the anisotropy fluctuations due to segmental reorientational relaxation are observed. The density and reorientational relaxation rates are independent of the scattering vector, since they reflect local motions and not diffusional processes. Only at very high (or very low) concentrations, when the contribution from the concentration fluctuations is small, is it possible clearly to distinguish the contribution of the density fluctuations in the polarized (VH) DLS experiment. Concentration fluctuations in the concentrated solution, on the other hand, relax by cooperative diffusion, which involves local swelling and deswelling of the highly entangled transient network. The characteristic relaxation time is q^2 -dependent except in the proximity of the glass point; see below.

The earlier studies^[40] on polystyrene in good solvents showed that D_c decreases dramatically when the measurement temperature is close to the glass transition

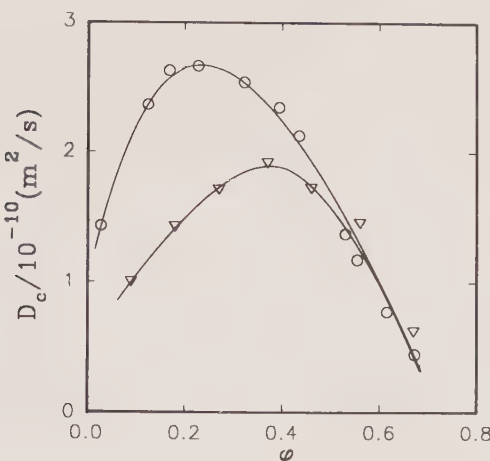


FIG. 5.5. A double logarithmic representation of the cooperative diffusion coefficient of polystyrene in toluene as a function of the volume fraction. Direct measurements from DLS are represented by ∇ and values calculated via eqn (5.30) using experimental values of $(\partial\pi/\partial C)$ and D_s are represented by \circ .

for a given concentration. This is illustrated in Fig. 5.5 with data from the polystyrene/toluene system at 25 °C. At low concentrations, D_c increases strongly due to the increase of the osmotic compressibility, which dominates over the initially weak increase of the friction coefficient. At higher concentrations, however, the increase in the friction coefficient becomes dominant so that D_c becomes small. Included in the plot are values of D_c calculated via eqn (5.30) using experimental osmotic compressibility data from ref. 15 and self-diffusion coefficients from ref. 41, but neglecting the first term in A . The good agreement at the higher concentrations shows that the effect of hydrodynamic screening has become small and that D_c is mainly determined by the solvent mobility and the osmotic compressibility; i.e. M_{ap} .

A system which has recently been investigated in considerable detail is mixtures of polystyrene (PS) in the highly viscous solvent bis-2-ethylhexylphthalate (DOP). Results from this system are summarized below in order to illustrate how different scattering methods have contributed to a deeper understanding of the dynamical behaviour. Figure 5.6(a) presents characteristic depolarized (VH) relaxation times as a function of temperature for bulk PS and three concentrations in DOP.^[42] These data can be temperature-shifted with respect to bulk PS to give a master curve as shown in Fig. 5.6(b).

In highly concentrated solutions of polymers, it is possible to determine both the concentration fluctuation relaxation time, τ_c , and the orientational relaxation time, τ_{or} , by making polarized and depolarized DLS measurements. In this way it was shown that τ_{or} has a stronger temperature dependence than τ_c if $T_{gp} > T_{gs}$.^[42,43] With present autocorrelators, τ_{or} can be determined only in a small temperature range close to T_g . At other temperatures, τ_{or} lies

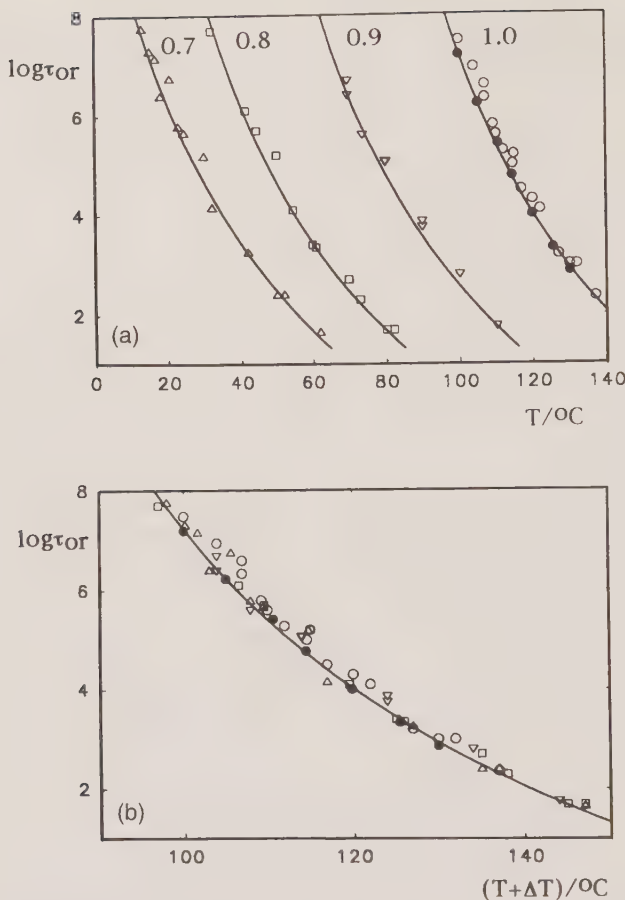


FIG. 5.6. (a) Characteristic relaxation times from depolarized (VH) DLS measurements, plotted as a function of temperature for bulk polystyrene and three concentrations in diethylphthalate as shown. Filled points are from ref. 62. Solid lines are guides to the eye. (b) The same data temperature-shifted with respect to data for bulk polystyrene to give a master curve (reproduced from ref. 42).

outside of the correlator window ($10^{-6} < t < 10$ s). Figure 5.7(a) shows a comparison between depolarized and polarized correlation functions for a PS solution in DOP (0.9 g/ml) at 90 °C. The ILT result in Fig. 5.7(b) corresponds to the polarized (VV) correlogram. The slower mode is q^2 -dependent, indicating a translational process, while the broader fast mode is q -independent and was found to have the same relaxation time as that evaluated in the depolarized measurement.

Figure 5.8(a) shows characteristic relaxation times from polarized (τ_c) and depolarized (τ_{or}) measurements on PS in DOP as a function of temperature. Figure 5.8(b) shows the data in Fig. 5.8(a) which have been temperature-shifted

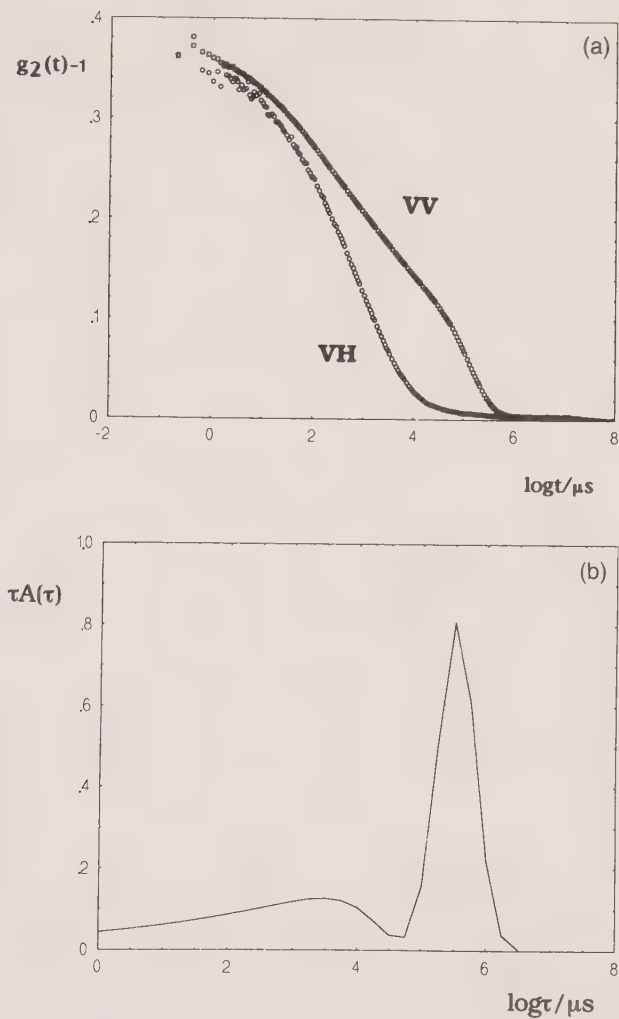


FIG. 5.7. (a) A comparison of depolarized (left) and polarized (right) correlation functions on the same solution of polystyrene in diethylphthalate ($C = 0.9$ g/ml) and $\theta = 90^\circ$. (b) The relaxation time distribution corresponding to the polarized (VV) correlation function in Fig. 5.7(a) (reproduced from ref. 42).

with respect to the data for bulk polystyrene using the same shift factors for both modes to give the master curves. At $T \gg T_g$, τ_{or} is much shorter than τ_c but, due to their different temperature dependences, τ_{or} becomes equal to τ_c at a temperature close to T_g . At lower temperatures, the relaxation of the concentration fluctuations is strongly coupled to the density fluctuations and $\tau_c \approx \tau_{or}$. As a result, close to the glass transition temperature (T_g) the relaxation rate is found to become independent of q over the experimentally accessible range of the scattering vector.^[42] It was shown in ref. 42 that the concentration

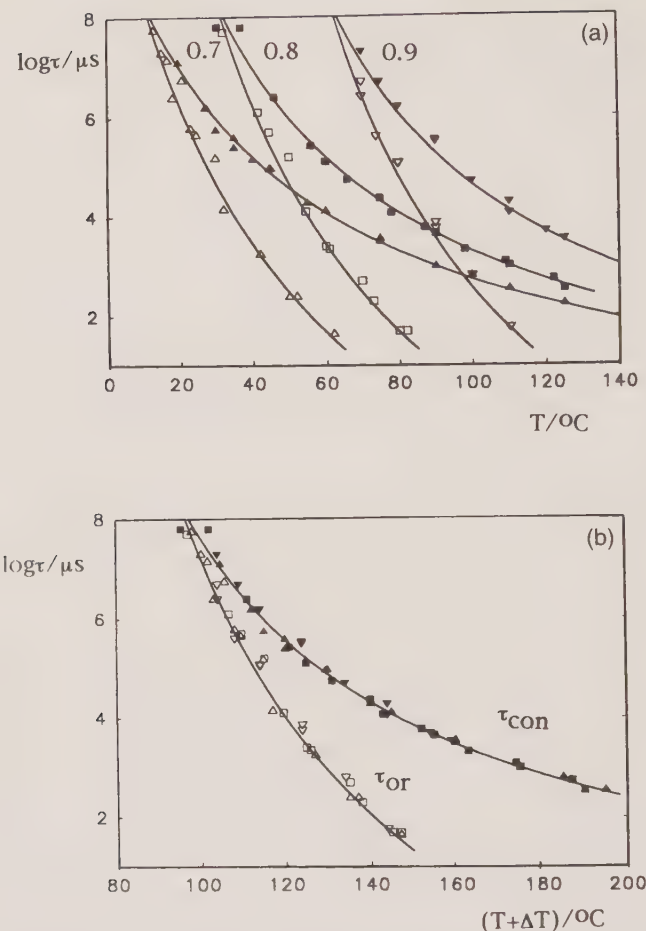


FIG. 5.8. (a) Characteristic relaxation times from polarized (τ_c —filled points) and depolarized (τ_{or} —open points) data plotted as a function of temperature for three concentrations of polystyrene in DOP as shown at $\theta = 90^\circ$. Solid lines are guides to the eye. (b) The data in Fig. 5.8(a) which have been temperature-shifted with respect to the data for bulk polystyrene using the same shift factors for τ_c and τ_{or} to form master curves (reproduced from ref. 42).

fluctuations in fact relax by cooperative diffusion until their relaxation rate closely approaches that of the density fluctuations (usually the so-called α -relaxation). At this point, the relaxation rate of the concentration fluctuations becomes q -independent over a range of q and the relaxation rate is determined by the mobility of the chain backbone, i.e. the reorientational relaxation rate. This phenomenon is demonstrated in Fig. 5.9, where data for the q -dependence of the relaxation rate of the concentration fluctuations (τ_c) are presented for the PS/DOP sample with $c = 0.7$ g/ml and for which the contribution of concen-

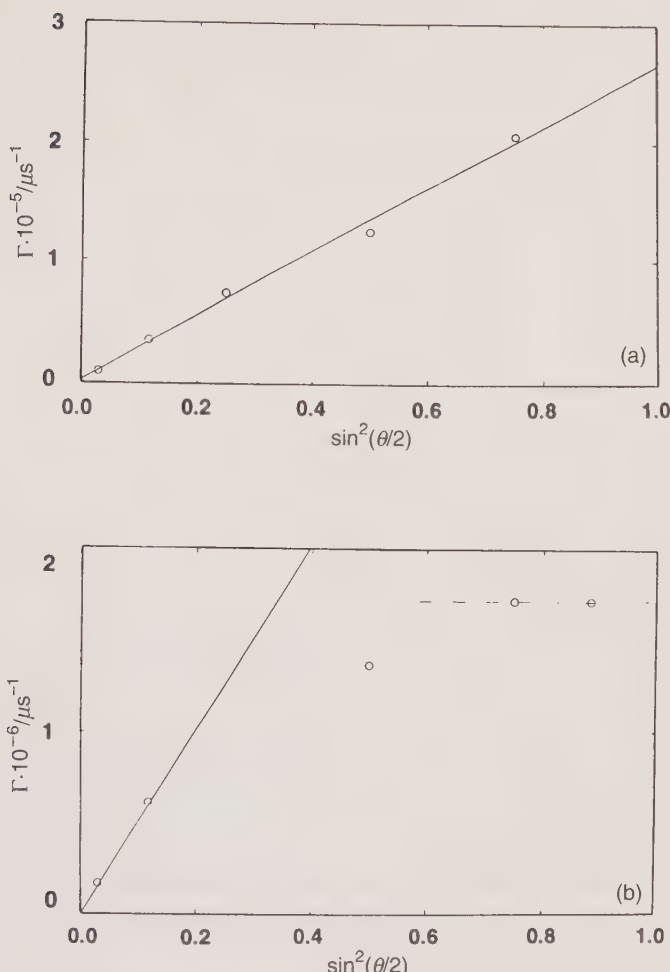


FIG. 5.9. Plots of relaxation rate ($\Gamma = 1/\tau_c$) vs. $\sin^2(\theta/2)$ for polystyrene in DOP at $C = 0.7 \text{ g/ml}$ in the polarized mode at (a) 45°C and (b) 35°C . The slopes of the solid lines correspond to the diffusion coefficient (reproduced from ref. 42).

tration fluctuations to the polarized scattering is dominant. At 45°C , τ_c is q^2 -dependent over the accessible q -range (Fig. 5.9(a)). At 35°C , however, τ_c is q^2 -dependent at lower q -values but becomes q -independent at higher q -values, where $\tau_c \approx \tau_{or}$ (Fig. 5.9(b)). Similar observations have been made by Koch *et al.*^[44] This situation has been described theoretically by Jäckle *et al.*^[45] and is also the subject of ref. 46. The reason for the change from a q^2 -dependence of the concentration fluctuations relaxation to a q -independent relaxation is thus the coupling to the density fluctuations.

For the PS/DOP system, the effect of the concentration on the temperature dependence of both τ_c and τ_{or} is, within experimental error, due only to the

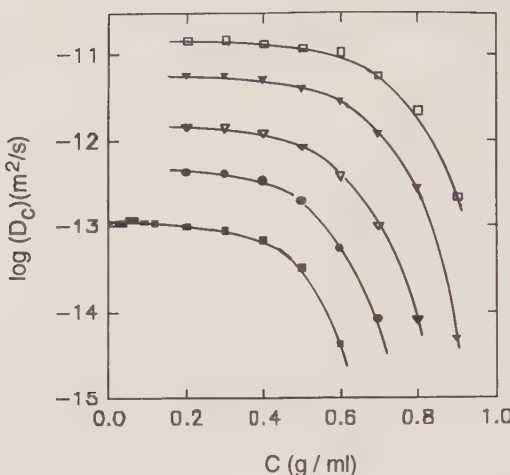


FIG. 5.10. The dependence of the cooperative diffusion coefficient for polystyrene in DOP on polymer concentration at the temperatures from bottom to top of 22, 40, 60, 90 and 120°C (from ref. 47).

increase of T_0 in eqn (5.41) with increasing concentration. The concentration dependence of D_c is shown in Fig. 5.10 at five temperatures. As anticipated, the strong decrease in D_c occurs at a higher concentration when the temperature is higher. Solvent self-diffusion coefficients were calculated from eqn (5.30) using osmotic compressibility data obtained from static light scattering measurements. The data could be fitted to eqn (5.34) using the same value for B and D_∞ over the entire investigated concentration range (0.2–0.9 g/ml). In Fig. 5.11 values of T_0 are plotted versus concentration, together with results from VFHT fits to τ_{or} . Included in this plot are the T_0 values from VFHT fits to the temperature dependence of the shear modulus from dynamic mechanical measurements.^[48] The T_0 values obtained by the three different approaches are close, as one would expect, since T_0 is the temperature at which all polymer segmental motion ceases, and this temperature should be the same whichever dynamic process is probed, as long as it reflects the segmental motion of the polymer.

5.5 Solvent relaxation in concentrated solutions

The reorientational relaxation of the solvent DOP is slowed down and broadened by the presence of the PS and part of the relaxational spectrum of DOP then becomes visible in the time window of the autocorrelator. This behaviour is clearly shown in Fig. 5.12(a). In Fig. 5.12(b), the corresponding ILT result is illustrated.

Figure 5.13 shows results for 0.7 g/ml PS in DOP,^[49] together with DLS data for pure PS and dielectric relaxation (DS) data for pure DOP.^[50] There is good agreement between the relaxation times determined from depolarized scattering and dielectric measurements, and also between the results from

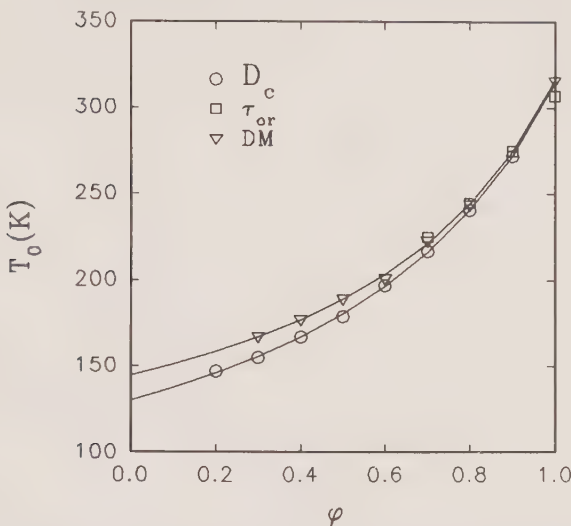


FIG. 5.11. The volume fraction dependence of the parameter T_0 in the VFHT equation characterizing the temperature dependence of co-operative diffusion (\circ), the α -relaxation (\square) and the shear modulus from dynamic mechanical (DM) measurements.^[48] The solid line is a fit to eqn (5.35) (reproduced from ref. 47).

dynamic light scattering and depolarized Rayleigh scattering. However, since the DOP relaxation is only partly seen in the time window, the scatter of the fast relaxation times for the solvent is greater than those for the polymer.

The very different reorientational dynamics of polymer and solvent are clearly shown in typical depolarized spectra for the solvent DOP and for the 0.1 and 0.3 g/ml PS/DOP solutions^[49] shown in Fig. 5.14. The difference in the integrated intensities of the narrow and broad peaks is due to the difference in concentration and optical anisotropies of solute and solvent.

Two distinct time scales thus exist in the (macroscopically homogeneous) PS/DOP concentrated solutions, which are associated with the modified-solvent and the modified-polymer relaxations. Although lying outside of the scope of this chapter, we note that the relaxation times obtained from the linewidth maximum in Rayleigh-Brillouin experiments^[49] reveal the existence of an additional faster process, which is probably associated with a localized motion of the phenyl group of the DOP molecule when present in concentrated solutions with polystyrene.

The size of the solvent molecule is thus a critical factor. When toluene is present instead of the relatively large DOP molecule, a small part of the concentration fluctuations is able to relax more rapidly within the available free volume than can the reorientational fluctuations in the 'frozen' network below T_g . This is shown in Fig. 5.15 for the PS/toluene system,^[42] in which there is a low-amplitude q^2 -dependent mode having a shorter relaxation time

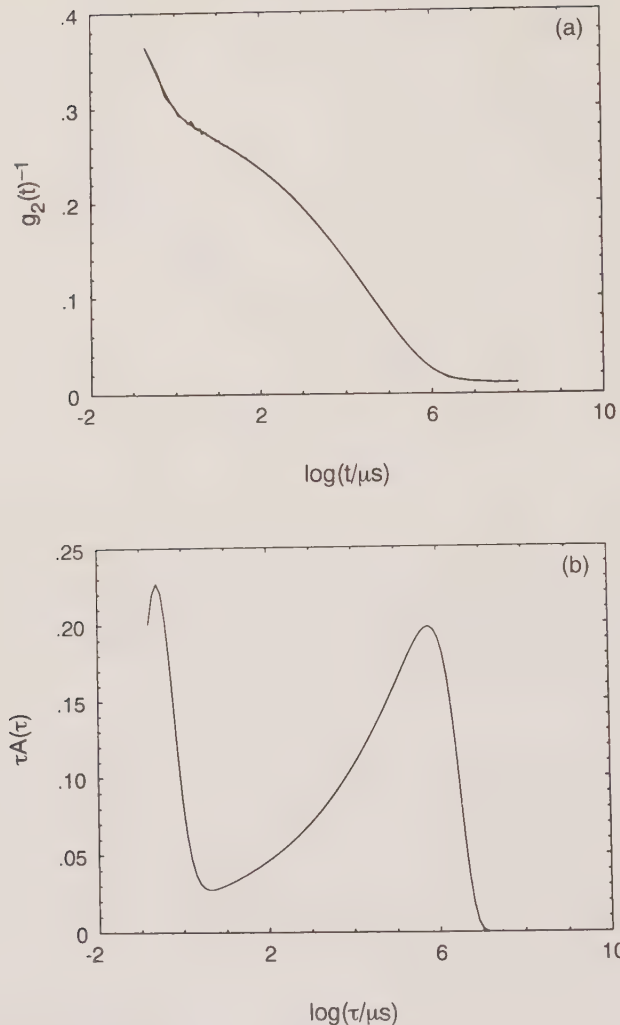


FIG. 5.12. (a) The depolarized intensity correlation function for the polystyrene/DOP solution; $C = 0.7 \text{ g/ml}$ at 290 K and $\theta = 140^\circ$. (b) The inverse Laplace transform (ILT) of the correlogram in Fig. 5.12(a) (reproduced from ref. 49).

than the q -independent mode. This relaxation mode is not seen in DOP solutions of PS. It may be noted that a fast diffusive relaxation together with a slow viscoelastic mode has also been reported for the PMMA/toluene system.^[51]

Well above T_{gp} , on the other hand, the diffusional mode will always relax more slowly than the reorientational mode, as in the case of PS in DOP (i.e. τ_c is always much longer than τ_{or}) and then D_c can be determined over the entire concentration range. This is shown in Fig. 5.16 for the ‘soft’ polymer poly(*n*-laurylmethacrylate) ($T_g \approx 208 \text{ K}$)^[52] in ethyl acetate at 25°C .^[53]

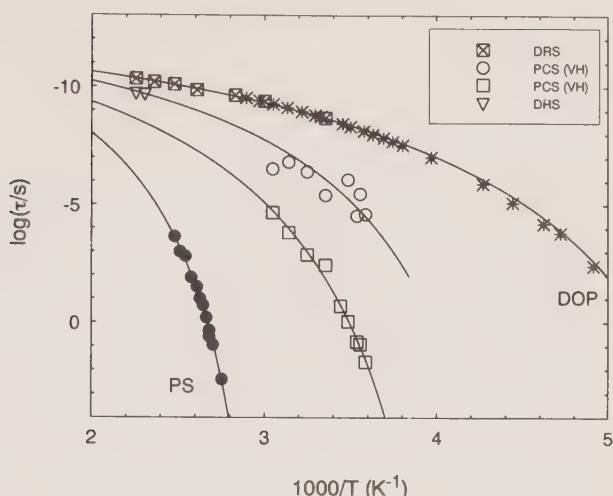


FIG. 5.13. The temperature dependence of the fast (DOP) and slow (polystyrene) relaxation processes in the $C = 0.7 \text{ g/ml}$ solution.^[49] The open circles are for the fast depolarized mode (DOP in the solution) and the squares for the slow (polystyrene in the solution). Depolarized Rayleigh scattering data are included for the solution state DOP and for pure DOP. Dielectric spectroscopy data of Floudas *et al.*^[50] for DOP are included.

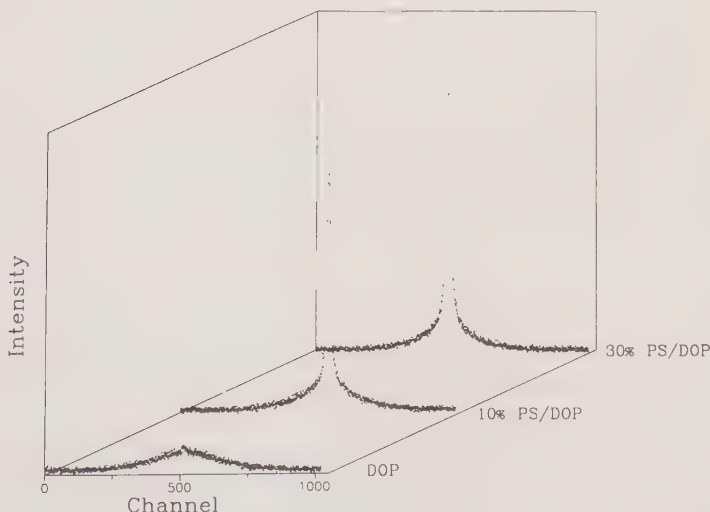


FIG. 5.14. Depolarized Rayleigh spectra for pure DOP and the 0.1 and 0.3 g/ml solutions at 363 K: Fabry-Perot (FSR 22, 12.8 and 5.9) (reproduced from ref. 49).

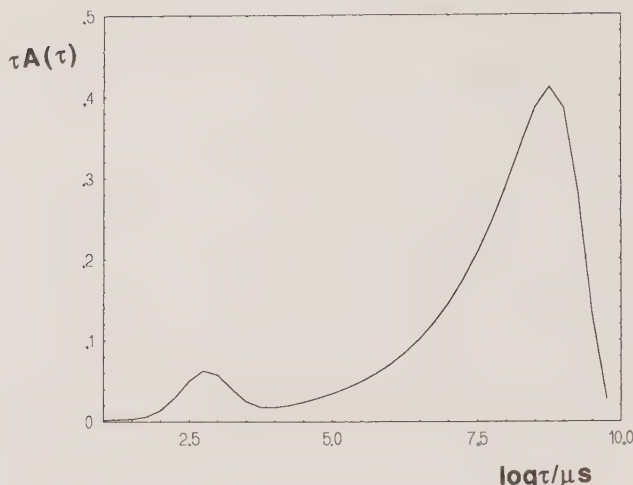


FIG. 5.15. The relaxation time distribution (Gauss-GEX analysis) for polystyrene in toluene below the glass transition ($C = 0.9$ g/ml) at 30°C and $\theta = 90^\circ$. A narrow q^2 -dependent mode precedes the broad q -independent mode (τ_{or}) when the solvent can diffuse through the free volume in the 'frozen' network (reproduced from ref. 42).

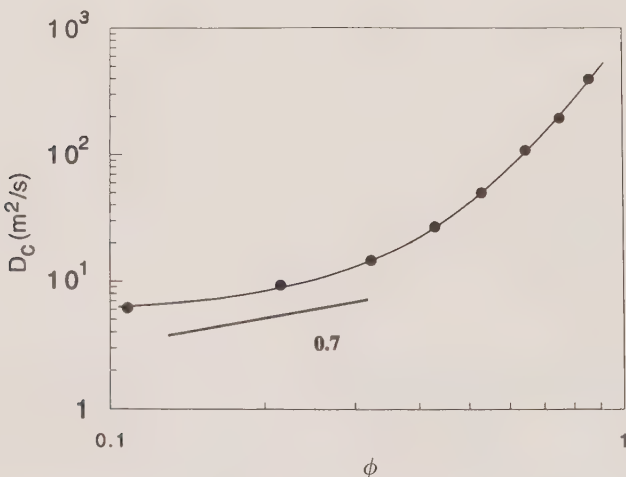


FIG. 5.16. The cooperative diffusion coefficient for poly(*n*-laurylmethacrylate) in ethyl acetate at 25°C versus the polymer volume fraction (from ref. 53).

Other light scattering methods, such as depolarized Rayleigh scattering, may be utilized to follow in more detail the solvent relaxation in the concentrated (up to $C = 0.6$ g/ml) polymer solutions. Floudas *et al.*^[45] examined the toluene mobility in concentrated solutions of polystyrene using depolarized light

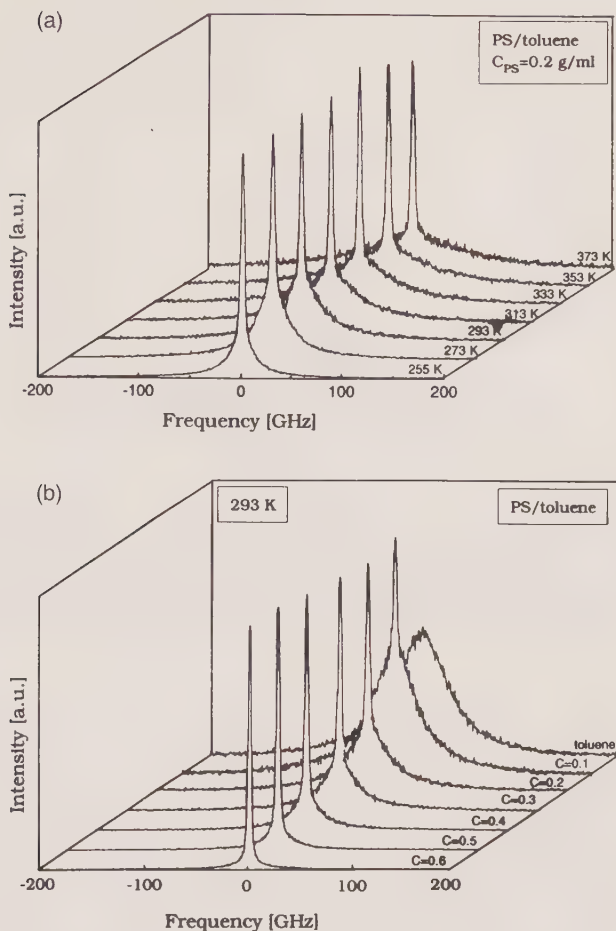


FIG. 5.17. (a) Depolarized Rayleigh spectra for a polystyrene/toluene solution ($C = 0.2 \text{ g/ml}$) as a function of temperature, taken up using a tandem Fabry-Perot ($\text{FSR} = 220 \text{ GHz}$). (b) Depolarized Rayleigh spectra of toluene and six polystyrene/toluene solutions at the concentrations shown and 293 K (reproduced from ref. 54).

scattering (as well as dielectric spectroscopy). Depolarized Rayleigh spectra were taken up with different spectrometers in order to achieve separation of the fast solvent relaxation (in the ps range) from the slow polymer dynamics (on the ns time scale). Figure 5.17(a) shows depolarized spectra assembled by means of a tandem Fabry-Perot interferometer ($\text{FSR} = 220 \text{ GHz}$) as a function of temperature for a PS/toluene solution of 0.2 g/ml . Figure 5.17(b) presents analogous spectra at six concentrations at 293 K. While the pure toluene spectrum can be fitted to a single Lorentzian, a fit to a double Lorentzian is required for the solutions.

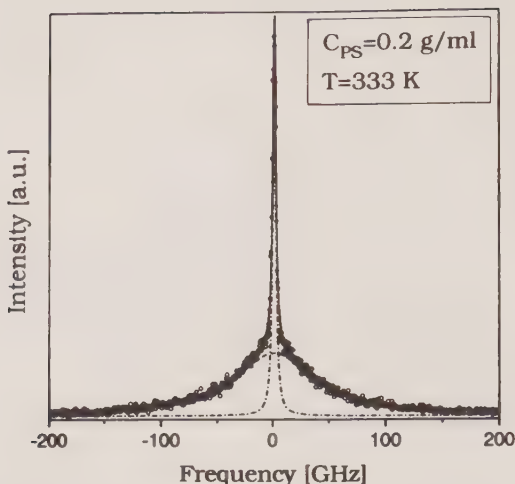


FIG. 5.18. The depolarized Rayleigh spectrum of a polystyrene/toluene solution of $C = 0.2 \text{ g/ml}$ at 333 K (FSR 220). Narrow and broad Lorentzians are shown by the dash-dot line and the dashed lines and correspond to the two primary α -relaxations reflecting the polymer and solvent dynamics in the solution (reproduced from ref. 54).

A typical fit is shown in Fig. 5.18 for the solution of $C = 0.2 \text{ g/ml}$ at 333 K. The solid line denotes the contributions of the narrow (dash-dot line) and broad (dashed line) Lorentzian components. The broader Lorentzian is due to the fast reorientational motion of the toluene and the narrower component has a half-width at half-height that cannot be distinguished from the instrumental width and which mostly reflects the slow reorientational dynamics of the PS chains. The narrow component can, however, be resolved using a confocal Fabry–Perot (FSR = 20 GHz), as shown in Fig. 5.19. The fast process is now too rapid for resolution in the spectral range of this interferometer and contributes only to the baseline, but with the slow component resolved.

Figure 5.20 shows the relationship between $\log(\tau/\tau_0)$ and concentration of PS at different temperatures, where τ is the reorientational relaxation time for toluene in the solution normalized by the pure toluene value, τ_0 . The ratio τ/τ_0 reflects the average local friction that the solvent molecule experiences in the vicinity of the polymer. It shows an exponential dependence on polymer concentration up to 0.6 g/ml in agreement with viscoelastic measurements in several other systems. Similar findings were made earlier for the PMMA/toluene system.^[55] It was concluded that the reorientational time of the toluene is sensitive only to the local free volume, and that it is the local viscosity which determines the solvent dynamics, even for highly concentrated solutions.

Combining depolarized light scattering data with dielectric data thus allows resolution of two processes with distinct time scales, and both have a VHFT behaviour rather than Arrhenius, i.e. they are both α -processes. The two time

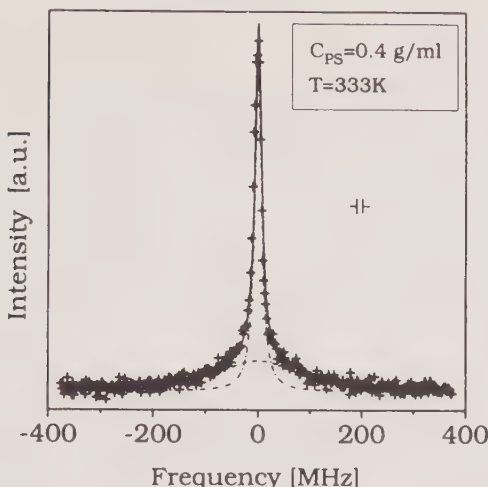


FIG. 5.19. The depolarized Rayleigh spectrum for a polystyrene/toluene solution ($C = 0.4$ g/ml) at 333 K taken up with a confocal Fabry–Perot (FSR = 750 GHz). The fit is for a delta function (broadened by instrumental resolution) with a broad Lorentzian (instrumental half-width as indicated by $\dagger\dagger$) (reproduced from ref. 54).

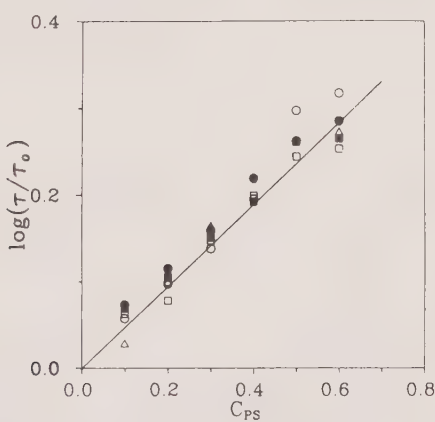


FIG. 5.20. Reduced solvent relaxation times as a function of polystyrene concentration in toluene at five temperatures: \square , 293 K; \bullet , 313 K; \circ , 333 K; \blacksquare , 353 K; \triangle , 373 K. The reorientation of small molecules is sensitive only to the locally available free volume in the polymer solution (reproduced from ref. 54).

scales (as was also observed in the PS/DOP^[56] and the PMMA/toluene^[55] systems) were interpreted as demonstrating the presence of concentration heterogeneities in the macroscopically homogeneous solutions: i.e. PS-rich and toluene-rich domains. These data disprove the earlier assumption of a single time scale in the mixed glass given by a unique T_g for the mixture.

5.5.1 Cluster formation

The presence of 'dynamic clusters' (long-range density fluctuations) has been the subject of intensive investigation, particularly for low molecular weight polymeric glass-forming liquids such as o-terphenyl close to T_g .^[57,58] In o-terphenyl, their presence or absence was shown to be dependent on the thermal history of the sample. Deep-quenching from a high-temperature, cluster-free, state allowed examination of the system free of clusters, but clusters again slowly re-form. The relaxation times from depolarized Rayleigh spectroscopy follow an Arrhenius behaviour, diverging from the relaxation times of the primary α -process. The cluster contribution to the measured correlation function in the polarized geometry is a single exponential function allowing characterization in terms of a translational diffusion coefficient/dynamic length.

In concentrated polymer solutions we conclude that cluster formation is highly system-dependent. In the investigated solutions of PS/DOP and PS/toluene, which are close to T_g , no such slow diffusive mode (i.e. a q^2 -dependent mode slower by some orders of magnitude than the usual density fluctuations), has been observed^[42] over the entire concentration range (0.1–0.9 g/ml) investigated; i.e. the correlation functions decay to the theoretical baseline, and the solutions are ergodic over extended periods (at least up to more than one year). This is not the case, however, for the higher concentrations of solutions of poly(*n*-laurylmethylacrylate) in ethyl acetate^[53] which are far above T_g . As shown with typical data in Fig. 5.21, for concentrations of 0.6 g/ml and higher

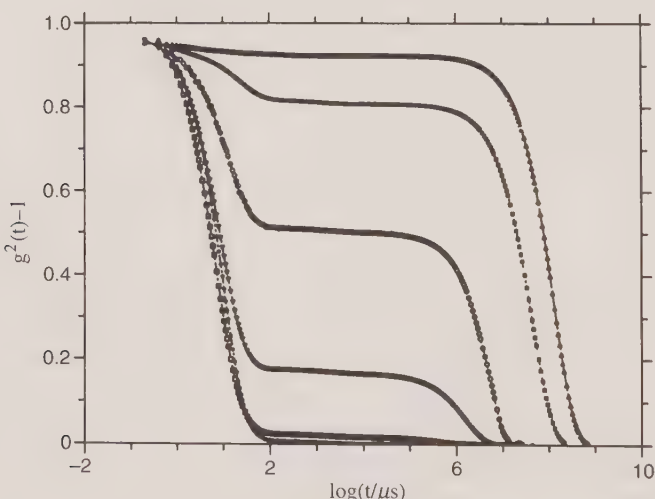


FIG. 5.21. Time correlation functions for concentrated (laurylmethylacrylate) in ethyl acetate at various concentrations and in the melt. Angle 90° and temperature 298 K (reproduced from ref. 53). From bottom to top: 0.5, 0.6, 0.7, 0.8, 0.9 g/ml and melt.

there is a substantial contribution from a slow diffusive mode. This may be interpreted as representing an analogous phenomenon to that investigated, primarily in low MW glass-forming liquids. It would appear that, in the presence of a polar solvent such as ethyl acetate, the non-polar segments of the polymer are constrained to locally aggregate at high concentration. A slow diffusive mode has, however, previously been noted in polystyrene solutions in ethyl acetate.^[59] One may conclude that the formation of clusters reflects the properties of the particular polymer-solvent system, rather than being ubiquitous behaviour of concentrated polymeric mixtures.

5.5.2 Melt dynamics

The dynamics of polystyrene melts are relatively simple and reflect only the α -relaxation for the segmental dynamics. Generally, density fluctuations only give rise to a low scattering intensity, which is difficult to study using DLS. As mentioned above, density fluctuations in concentrated solutions and polymer melts may be measured directly using depolarized dynamic light scattering. This aspect has been dealt with in some detail in refs 60 and 61. Figure 5.22 shows a depolarized (VH) master correlogram (circles) together with a polarized (VV) master correlogram (squares) for bulk PS. Each correlogram consists of a composite of data at five temperatures (104, 107, 112, 127 and 137 °C) which

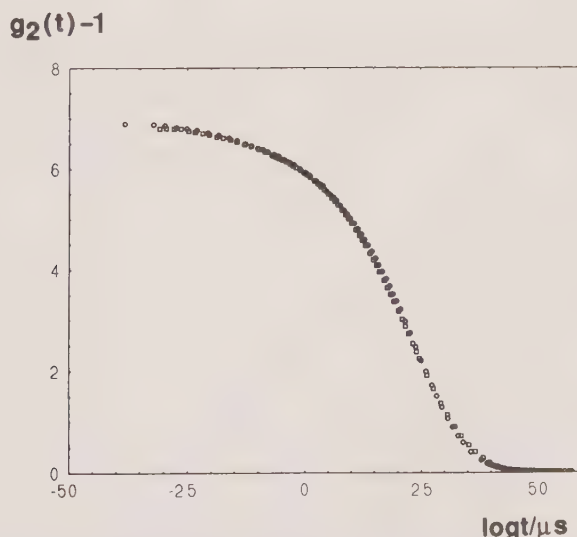


FIG. 5.22. The depolarized master correlogram and the polarized master correlogram for bulk polystyrene measured at $\theta = 90^\circ$. Each of these correlograms is a composite of measured correlograms at five temperatures (104, 107, 112, 127 and 137 °C) which have been time-shifted relative to the respective correlation function at 127 °C. The differences between the master correlograms in the VV and VH geometries are insignificant (reproduced from ref. 42).

have been time-shifted relative to the data at 127 °C as described in ref. 42. This procedure, which resembles the temperature–frequency shifts familiar to rheologists, yields a master correlogram covering a significantly wider time range than the individual correlograms. The VV and VH correlograms are practically indistinguishable. Earlier work by Lindsey *et al.*^[62] reported a slightly broader relaxation time distribution in the VV geometry compared to the VH. The temperature dependence of the characteristic relaxation time is, however, the same for the two investigations.

In other polymers, such as the methacrylates, β - and γ -relaxations, which reflect the relaxational motions of the side-groups, may also be present in addition to the α -relaxation. Some recent experiments^[63] will be described here on poly(*n*-laurylmethacrylate) melts to complement the overall picture obtained in polystyrene solutions and to illustrate the limits of the scattering technique and the necessity of using several methods to probe the dynamics in highly concentrated systems. Depolarized light intensity correlation functions ($g^2(t)_{VH} - 1$) are shown in Fig. 5.23 at different temperatures (limited at the low-temperature end by crystallization). The broad correlation functions clearly show two relaxation processes, although the faster is less well-determined, since it still appears only partially in the time window at –28.8 °C. The polarized correlation function for the melt has a large contribution from the cluster component; see Fig. 5.21. The ILT results are depicted in Fig. 5.24(a), while Fig. 5.24(b) shows data at three measurement angles.

The slower mode is a mixed α,β -relaxation: this has a considerably stronger temperature dependence than the faster model, which is termed a fast β -relaxation. The latter is a new feature of methacrylate polymers with longer

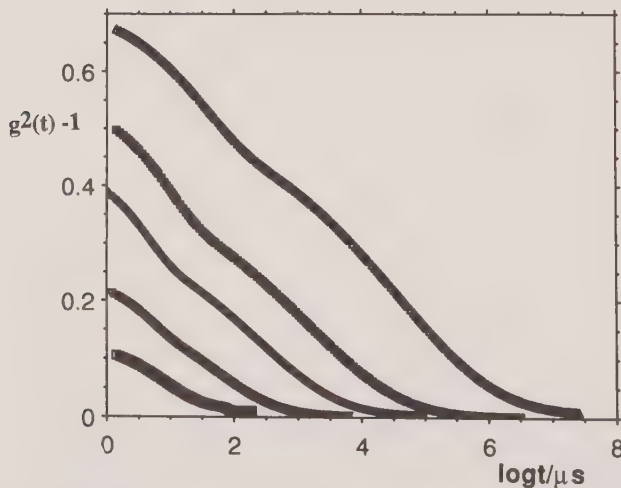


FIG. 5.23. Depolarized (VH) dynamic light scattering spectra: intensity–intensity correlation functions for poly(*n*-laurylmethacrylate) in the melt. Temperatures (top to bottom): –28.8, –19.6, –8.2, +2.6 and +19.9 °C. Angle 90° (reproduced from ref. 63).

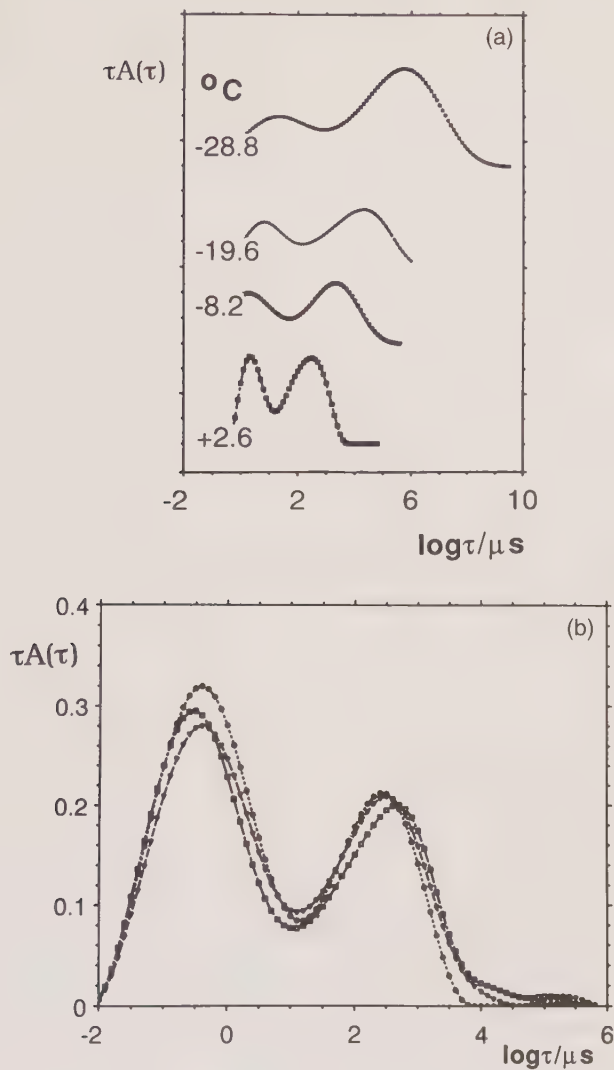


FIG. 5.24. (a) ILT results for the VH correlograms in Fig. 5.27 at the temperatures shown (reproduced from ref. 63). (b) ILT results on poly(*n*-laurylmethacrylate) melts at $2.6^\circ C$ at angles of 60 , 90 and 140° (reproduced from ref. 63).

($n = 10, 12$) polyethylene-like alkyl chains. A recent discussion is provided in ref. 64. The correlation functions in Fig. 5.23 have been fitted using a Kohlrausch-Williams-Watts (KWW) model:

$$g^2(t)_{VH} = [A \exp(-t/\tau)^\beta + B]^2, \quad (5.42)$$

where β ($0 < \beta < 1$) is a fitting parameter describing the shape of the distribution

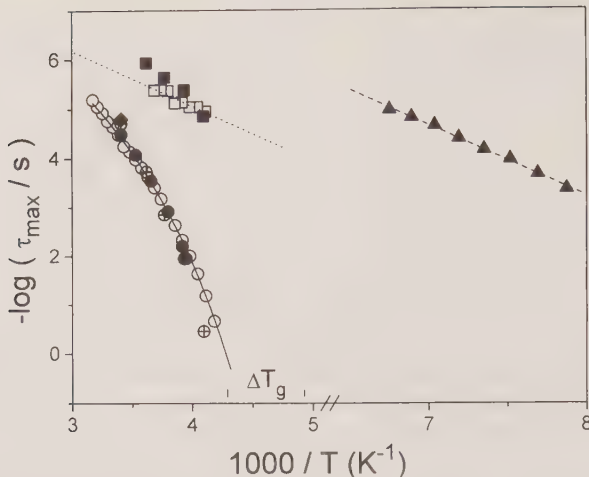


FIG. 5.25. The temperature dependence of relaxation times (τ_{max}) in poly(*n*-laurylmethacrylate) melts obtained using dynamic light scattering (depolarized) and dielectric spectroscopy (DS). ○, τ_α light; ■, τ_β light; ○, τ_α DS; □, τ_β DS; ●, τ_α Williams; ▲, τ_γ DS (reproduced from ref. 63).

and τ is an average relaxation time. Double KWW functions are clearly required for the correlation functions.

The temperature dependencies of τ are illustrated in Fig. 5.25, which brings together data from different techniques. The curve for the α -relaxation follows a VFHT equation while the fast β -relaxation corresponds to an Arrhenius fit. Included in the diagram are dielectric spectroscopy (DS) data, since with this technique one is able to probe the fast relaxations with higher precision than scattering methods in the short decay time range. A fit to the first 11 DS points gives $\log \tau_0 = -8.3$, $B = 439$ K and $T_0 = 181.5$. The light scattering times for the β -relaxation are systematically faster than those from the dielectric measurements, a discrepancy which arises due to the limitation of the PCS time window only allowing approximate localization of the β -relaxation times.

The DS measurements also provide relaxation times for the γ -relaxation shown at low temperatures. The activation energy is 6.6 kcal/mol with a corresponding intercept $\tau_0 = 1.6 \times 10^{-15}$ s (in $\tau = \tau_0 \exp(-E/RT)$). This process may correspond to the mechanical relaxation found in poly(*n*-alkylmethacrylates) with $n > 3$, having an activation energy of ≈ 5.5 kcal/mol. ($T_{max} \approx 90$ K at $\omega = 0.5$ Hz), which has been assigned to the rotation of the ethyl end group.^[65] The range of T_g obtained using DSC is included.

References

1. de Gennes, P.-G. (1979). *Scaling concepts in polymer physics*. Cornell University Press, London.

2. Daoud, D., Cotton, J. P., Farnoux, B., Jannink, G., Sarma, G., Benoît, J., Duplessix, C., Picot, C., and de Gennes, P.-G. (1975). *Macromolecules*, **8**, 804.
3. Berne, B. and Pecora, R. (1976). *Dynamic light scattering*. John Wiley, New York.
4. Yamakawa, H. (1971). *Modern theory of polymer solutions*. Harper & Row, New York.
5. Debye, P. (1946). *J. Chem. Phys.*, **55**, 572.
6. Doi, M. and Edwards, S. F. (1986). *The theory of polymer dynamics*. Clarendon Press, Oxford.
7. Chapter 6 of this book, section 6.2.1.
8. Fujita, H. (1990). *Polymer solutions*. Elsevier, Amsterdam.
9. Le Guillou, J. C. and Zinn-Justin, J. (1977). *Phys. Rev. Lett.*, **39**, 95.
10. Norisuye, T. and Fujita, H. (1982). *Polym. J.*, **14**, 143.
11. Kirste, R. G. and Oberthur, R. C. (1982). In *Small angle X-ray scattering* (eds O. Glatter and O. Kratky), Academic Press, London; Chapter 12.
12. Moore, M. A. J. (1977). *J. Phys.*, **38**, 265.
13. Higgins, J. S. and Benoît, H. C. (1994). *Polymers and neutron scattering*. Oxford University Press, Oxford.
14. (a) Muthukumar, M. and Edwards, S. F. (1982). *J. Chem. Phys.*, **76**, 2720.
(b) Muthukumar, M. (1986). *J. Chem. Phys.*, **85**, 4722.
15. Amirzadeh, J. and McDonell, M. E. (1982). *Macromolecules*, **15**, 927.
16. Noda, I., Kato, N., Kitano, T. and Nagasawa, M. (1981). *Macromolecules*, **14**, 668.
17. Scholte, Th. G. (1970). *J. Polym. Sci. A2*, **8**, 841; (19971). *J. Polym. Sci. A2*, **9**, 1553.
18. Geissler, E., Mallam, S., Hecht, A.-M., Rennie, A. R. and Horkay, F. (1990). *Macromolecules*, **23**, 5270.
19. Brown, W. and Nicolai, T. (1990). *Colloid. Polym. Sci.*, **268**, 977.
20. Brown, W., Mortensen, K., and Floudas, G. (1992). *Macromolecules*, **25**, 6904.
21. Horkay, F., Hecht, A.-M., Stanley, H. B., and Geissler, E. (1994). *Eur. Polym. J.*, **30**, 215.
22. Konishi, T., Yoshizaki, T., Toshiya, S., Einaga, Y., and Yamakawa, H. (1990). *Macromolecules*, **23**, 290.
23. Abe, F., Einaga, Y., Yoshizaki, T., and Yamakawa, H. (1993). *Macromolecules*, **26**, 1884.
24. Cotton, J. P., Decker, D., Benoît, H., Farnoux, B., Higgins, J., Jannink, G., Ober, R., Picot, C., and des Cloizeux, J. (1974). *Macromolecules*, **7**, 863.
25. King, J. S., Boyer, W., Wignall, G. D., and Ullman, R. (1985). *Macromolecules*, **18**, 709.
26. Schmidt, M. and Burchard, W. (1981). *Macromolecules*, **14**, 210.
27. Nyström, B. and Roots, J. (1992). *Prog. Polym. Sci.*, **8**, 333.
28. Nicolai, T., Brown, W., Johnsen, R. M., and Štěpánek, P. (1990). *Macromolecules*, **23**, 1165.
29. Nicolai, T., Brown, W., Hvidt, S., and Heller, K. (1990). *Macromolecules*, **23**, 5088.
30. Brown, W. and Štěpánek, P. (1993). *Macromolecules*, **26**, 6884.
31. Brown, W. and Štěpánek, P. (1994). *Macromolecules*, **27**, 4842.
32. Doi, M. and Onuki, A. (1992). *J. Phys. II Fr.*, **2**, 1631.
33. Genz, U. (1994). *Macromolecules*, **27**, 5691.
34. Wang, C. H. (1993). In *Dynamic light scattering* (ed. W. Brown). Oxford University Press, Oxford; Chapter 5.
35. Akcasu, Z., Klein, R., and Wang, C. H. (1994). *Macromolecules*, **27**, 2736.
36. Ferry, J. D. (1970). *Viscoelastic properties of polymers*, 2nd edn. John Wiley, New York.

37. Geissler, E. (1993). In *Dynamic light scattering* (ed. W. Brown). Oxford University Press, Oxford; Chapter 5.
38. Vrentas, J. S. and Duda, J. L. (1977). *J. Polym. Sci.*, **15**, 403.
39. Vrentas, J. S. and Vrentas, C. M. (1993). *Macromolecules*, **26**, 6129.
40. Brown, W., Johnsen, R. M., Koňák, Č., and Dvoranek, L. (1991). *J. Chem. Phys.*, **95**, 8568.
41. Pickup, S. and Blum, F. D. (1989). *Macromolecules*, **22**, 3961.
42. Brown, W. and Nicolai, T. (1994). *Macromolecules*, **27**, 2470.
43. Fytas, G., Floudas, G., and Ngai, K. L. (1990). *Macromolecules*, **23**, 1104.
44. Koch, T., Strobl, G., and Stuhn, B. (1992). *Macromolecules*, **25**, 6255.
45. (a) Jäckle, J. and Frisch, H. L. (1985). *J. Polym. Sci.*, **23**, 675.
(b) Jäckle, J. and Pieroth, M. (1990). *J. Phys. Condens. Matter.*, **2**, 4963.
46. Koňák, Č. and Brown, W. (1993). *J. Chem. Phys.*, **98**, 1014.
47. Nicolai, T. and Brown, W., *Macromolecules* (in press).
48. Pakula, T., Brown, W., and Nicolai, T. (to be published).
49. Rizos, K., Brown, W., Johnsen, R. M., and Ngai, K. L. (1995). *Macromolecules*, **28**, 5450.
50. Floudas, G., Higgins, J. S., and Fytas, G. (1992). *J. Chem. Phys.*, **96**, 7672.
51. Gapinski, J., Fytas, G., and Floudas, G. (1992). *J. Chem. Phys.*, **96**, 6311.
52. Rogers, S. R. and Mandelkern, L. (1957). *J. Phys. Chem.*, **61**, 685.
53. Brown, W. and Štěpánek, P., *J. Polym. Sci.* (submitted).
54. Floudas, G., Steffen, W., Fischer, E. W., and Brown, W. (1993). *J. Chem. Phys.*, **99**, 695.
55. Floudas, G., Fytas, G., and Brown, W. (1992). *J. Chem. Phys.*, **96**, 2164.
56. Floudas, G., Steffen, W., Giebel, L., and Fytas, G. (1993). *Progr. Colloid Polym. Sci.*, **91**, 124.
57. Gerharz, B., Meier, G., and Fischer, E. W. (1990). *J. Chem. Phys.*, **92**, 7110.
58. Fischer, E. W., Meier, G., Rabenau, T., Steffen, W., and Thöennes, W. (1991). *J. Non-Crystalline Solids*, **131–133**, 134.
59. Brown, W., and Štěpánek, P. (1988). *Macromolecules*, **21**, 1791.
60. Fytas, G., and Meier, G. (1993). In *Dynamic light scattering* (ed. W. Brown). Oxford University Press, Oxford; Chapter 9.
61. Fytas, G., and Patkowski, A. (1993). In *Dynamic light scattering* (ed. W. Brown). Oxford University Press, Oxford; Chapter 10.
62. Lindsey, C. P., Patterson, G. D., and Stevens, J. R. (1979). *J. Polym. Sci.*, **17**, 1547.
63. Floudas, G., Placke, P., Štěpánek, P., Brown, W., Fytas, G., and Ngai, K. L. (1995). *Macromolecules*, **28**, 6799.
64. Floudas, G., Rizos, A., Brown, W., and Ngai, K. L. (1994). *Macromolecules*, **27**, 2719.
65. Heigboer, J., Pineri, M. (1982). In *Non-metallic materials and composites at low temperatures* (eds G. Hartwig and D. Evens). Plenum Press.

Scattering properties and modelling of aggregating and gelling systems

*Taco Nicolai, Dominique Durand, and
Jean-Christophe Gimel*

6.1 Introduction

In physics, chemistry, biology and geology, there are many random processes in which small particles come together to form large complex structures called aggregates, clusters or flocs. In some cases aggregating systems eventually form a gel which can be described in terms of percolation^[1,2] and gives new properties to the system, e.g. conductivity or elasticity. Study of these phenomena raises interest both from theoretical and practical points of view. Very often, the resulting structures are highly disordered but self-similar and can therefore be described in terms of fractal geometry.^[3] In addition, the gel formation may involve a connectivity transition.

A number of theoretical approaches have been developed to model the kinetics, the resulting structure and the sol–gel transition of such systems, but none is able to take into account all aspects of the aggregation and gelation process.

Scattering techniques can probe the system at different length and time scales and are thus suitable to reveal self-similar properties in terms of static and dynamic structure factors.

In this chapter we will describe the scattering properties of dilute solutions of fractal aggregates. We will first discuss the influence of the fractal dimension and the polydispersity, but we do not treat the effect of interactions, which is dealt with in Chapter 2. As concerns dynamic light scattering (DLS), we will only consider translational diffusion and show how parameters that characterize the aggregation number distribution can be obtained from DLS.

In the second section we will discuss the process of aggregation and gelation. The aggregation process of dilute particles is already described extensively in the literature, as is the growth of the aggregates close to the gel point. Here we will focus on the less well known features of the transition between these two limiting cases.^[4]

In the last section we will review selected experimental studies to illustrate some of the features discussed in the previous sections.

6.2 Light scattering theory applied to aggregating systems

6.2.1 Static structure factor of monodisperse aggregates

Consider a very dilute solution of monodisperse non-interacting aggregates built up from m identical units or monomers. If the scattering volume contains N aggregates, the excess intensity of radiation scattered by this volume, $I(q)$, is a function of the scattering wave vector q and is related to the static structure factor, $S_m(q)$, given in terms of the centre of mass positions of the monomers in an individual aggregate and their form factor $P(q)$ by

$$I(q) \propto Nm^2 S_m(q) P(q), \quad (6.1)$$

with $S_m(q \rightarrow 0) = P(q \rightarrow 0) = 1$ and $S_m(\infty) = 1/m$. $Nm = N_0$ is the number of monomers in the scattering volume. Using the number concentration of monomers, C , we have

$$I(q) = KCmS_m(q)P(q), \quad I(q \rightarrow 0)/KC = m, \quad (6.2)$$

where K is a constant depending on the apparatus set-up and the scattering contrast between solvent and aggregates. For light, neutron and X-ray scattering the latter depends on the difference in the refractive index, the neutron scattering length and the electron density respectively.^[5,6]

For isotropic systems in three dimensions, $S_m(q)$ is related to the pair correlation function ($g_m(r)$) of the centres of mass of a single aggregate:^[7]

$$S_m(q) = \frac{1}{m} \left(1 + \int_0^\infty g_m(r) 4\pi r^2 \frac{\sin(qr)}{qr} dr \right), \quad (6.3)$$

with

$$\int_0^\infty g_m(r) 4\pi r^2 dr = m - 1. \quad (6.4)$$

The contribution of the self term has been neglected in eqn (6.4). Consider a cluster, where $g_m(r)$ is the average number density of centres of mass at a distance r from any other arbitrary centre. It is also called the pair correlation function of connectivity, to emphasize the fact that the two centres of mass belong to the same cluster. For fractal aggregates the average number of monomers $m(r)$ included in a sphere of radius r centred on the aggregate scales as:^[7]

$$m(r) = (r/r_0)^{d_f}, \quad r_0 \ll r \ll \xi, \quad (6.5)$$

leading to

$$dm(r) = \frac{d_f}{r_0^{d_f}} r^{d_f-1} dr, \quad r_0 \ll r \ll \xi, \quad (6.6)$$

where d_f is the fractal dimension of the object, $2r_0$ is the distance between the two nearest neighbour centres of mass and ξ is the characteristic size of the

aggregate. On the other hand, $dm(r)$ represents the number of monomers included in the shell of radius r with thickness dr :

$$dm(r) = 4\pi r^2 g_m(r) dr. \quad (6.7)$$

Identifying relations (6.6) and (6.7) we obtain

$$g_m(r) = \frac{d_f}{4\pi r_0^{d_f}} r^{d_f - 3}, \quad r_0 \ll r \ll \xi. \quad (6.8)$$

We still have to define the internal and external cut-off of the pair correlation function. One can introduce an external cut-off function $f(x)$ to take into account the finite characteristic size, ξ , of the aggregate:

$$g_m(r) = \frac{d_f}{4\pi r_0^{d_f}} r^{d_f - 3} f(r/\xi), \quad r_0 \ll r. \quad (6.9)$$

$f(r/\xi)$ is close to unity for $r \ll \xi$ and decreases faster than any power law to zero for $r > \xi$. We will assume a stretched exponential form, $f(r/\xi) = \exp(-(r/\xi)^\gamma)$ with $\gamma > 0$, so that by varying this exponent we can take into account the influence of the sharpness of the cut-off.

As regards the internal cut-off, we emphasize that we only deal with the centres of mass of the monomers. $g_m(r)$ can also be defined using the distribution function $h(r)$ of all the distances between centres of mass in the aggregate. $h(r)$ represents the number of couples at distances between r and $r + \Delta r$. Considering the $m(m - 1)/2$ couples, we have

$$g_m(r) = \lim_{\Delta r \rightarrow 0} \left[\frac{2h(r)}{4\pi mr^2 \Delta r} \right]. \quad (6.10)$$

Assuming that all monomers are identical and that z_1 represents the average number of contacts per monomer, there are a total of mz_1 contacts in the aggregate and $mz_1/2$ distances equal to $2r_0$. Considering eqn (6.10), $g_m(r)$ presents a Dirac peak at $r = 2r_0$ and is zero for r smaller than $2r_0$ due to excluded volume effects:

$$g_m(r) = \frac{z_1}{4\pi(2r_0)^2} \delta(r - 2r_0), \quad 0 \leq r \leq 2r_0, \quad (6.11)$$

The additional Dirac peak at $r = 0$ related to the self contribution has been omitted. The primary shell gives a divergence of $g_m(r)$ at $r = 2r_0$ and it has been shown by computer simulations^[8,9] that the secondary shell containing z_2 monomers gives a discontinuity at $r = 4r_0$ (cf. Fig. 6.1). For distances larger than $4r_0$, the fractal regime is reached.^[8,10]

If we only consider large aggregates ($m \gg z_1 + z_2$), then it follows from eqn (6.9) that

$$m = \frac{d_f \Gamma(d_f/\gamma)}{\gamma} \left(\frac{\xi}{r_0} \right)^{d_f}, \quad m \gg 1. \quad (6.12)$$

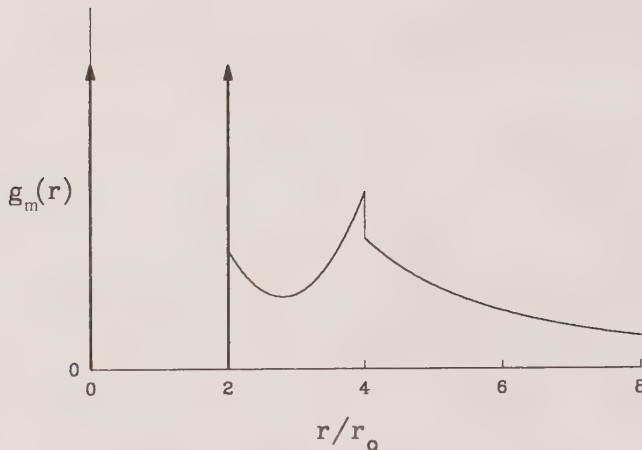


FIG. 6.1. A schematic representation of the pair correlation function of an aggregate.

The squared radius of gyration, $[R_g(m)]^2$, of the aggregates is equal to

$$[R_g(m)]^2 = \frac{1}{2m} \int_0^\infty 4\pi r^4 g_m(r) dr, \quad m \gg 1. \quad (6.13)$$

Using eqns (6.9) and (6.12) in eqn (6.13) gives

$$[R_g(m)]^2 = \frac{\Gamma((d_f + 2)/\gamma)}{2\Gamma(d_f/\gamma)} \xi^2, \quad R_g(m) \gg r_0. \quad (6.14)$$

$R_g(m)$ can be obtained directly from scattering experiments by a series development of $S_m(q)$:

$$S_m(q) = 1 - \frac{1}{2}q^2 [R_g(m)]^2 + \dots, \quad qR_g(m) \ll 1. \quad (6.15)$$

Combining eqns (6.12) and (6.14), we obtain

$$m = a[R_g(m)]^{d_f}, \quad (6.16)$$

with

$$a = \left(\frac{2\Gamma(d_f/\gamma)}{\Gamma((d_f + 2)/\gamma)} \right)^{d_f/2} \frac{d_f \Gamma(d_f/\gamma)}{\gamma r_0^{d_f}}. \quad (6.17)$$

Substituting eqn (6.9) and eqn (6.3), and for $qr_0 \ll 1$, one obtains:

$$S_m(q) = \frac{1}{m} \left(1 + \frac{d_f}{r_0^{d_f}} \int_0^\infty r^{d_f-1} \exp(-(r/\xi)^\gamma) \frac{\sin(qr)}{qr} dr \right), \quad qr_0 \ll 1. \quad (6.18)$$

The limiting case $q\xi \ll 1$ can be written in terms of ξ using eqns (6.14) and (6.15). The opposite limit of large $q\xi \gg 1$, but still with $qr_0 \ll 1$, is given by

$$S_m(q) = \frac{b}{m} q^{-d_f}, \quad qr_0 \ll 1 \ll q\xi, \quad (6.19)$$

with

$$b = r_0^{-d_f} d_f \Gamma(d_f - 1) \sin\left(\frac{\pi}{2}(d_f - 1)\right). \quad (6.20)$$

b does not depend on ξ and γ and therefore $I(q)/(KC)$ is independent of the overall size of aggregates for $qr_0 \ll 1 \ll q\xi$.

In the special case when $\gamma = 1$, eqn (6.18) can be solved analytically^[7] for $\xi \gg r_0$:

$$S_m(q) = \frac{1}{m} \left[1 + \frac{d_f \Gamma(d_f - 1) \sin((d_f - 1) \arctan(q\xi))}{(qr_0)^{d_f} \left(1 + \frac{1}{q^2 \xi^2}\right)^{(d_f - 1)/2}} \right], \quad \gamma = 1, \quad qr_0 \gg 1. \quad (6.21)$$

If $d_f = 2$, eqn (6.21) can be simplified even further to give

$$S_m(q) = \frac{1}{m} + \frac{1}{(1 + q^2 \xi^2)}, \quad \gamma = 1, \quad d_f = 2, \quad qr_0 \gg 1. \quad (6.22)$$

For aggregates with the same values of d_f and γ , $S_m(q)$ is only a function of $qR_g(m)$. Combining eqns (6.16) and (6.19), the limiting power-law dependence becomes

$$S_m(q) = \frac{b}{a} (qR_g(m))^{-d_f}, \quad qr_0 \ll 1 \ll qR_g(m), \quad (6.23)$$

with a and b given by eqns (6.17) and (6.20), respectively. The term b/a is independent of the local structure of the aggregate, i.e. r_0 . In Fig. 6.2, $S_m(q)$ is shown as a function of $qR_g(m)$ for various values of d_f while keeping $\gamma = 1$. When d_f approaches 3 closely, the initial slope of $\log(S_m(q))$ vs. $\log(qR_g(m))$ is 4 as expected for dense objects and only reaches d_f at larger $qR_g(m)$. If $d_f = 3$ the slope remains 4. The influence of γ is illustrated in Fig. 6.3, keeping $d_f = 2$. For large values of γ undulations appear due to the sharpening of the interface. The effect of the undulations is already important for $\gamma = 2$, where the slope reaches a maximum value of 2.37 at $qR_g(m) = 4$. For comparison, we have included the so-called Debye function^[11] which describes $S_m(q)$ if the distance between monomers has a Gaussian distribution, e.g. linear polymer chains without excluded volume interactions:

$$S_m(q) = \frac{2}{(qR_g(m))^4} (\exp(-(qR_g(m))^2) - 1 + (qR_g(m))^2). \quad (6.24)$$

The Debye function can be well approximated by eqn (6.18) with $d_f = 2$ and $\gamma \approx 1.2$.

In order to have a simple analytical expression for $S_m(q)$, the following empirical equation has been proposed:^[12]

$$S_m(q) = \left[1 + \sum_{i=1}^n c_i (qR_g(m))^{2i} \right]^{-d_f/2n}. \quad (6.25)$$

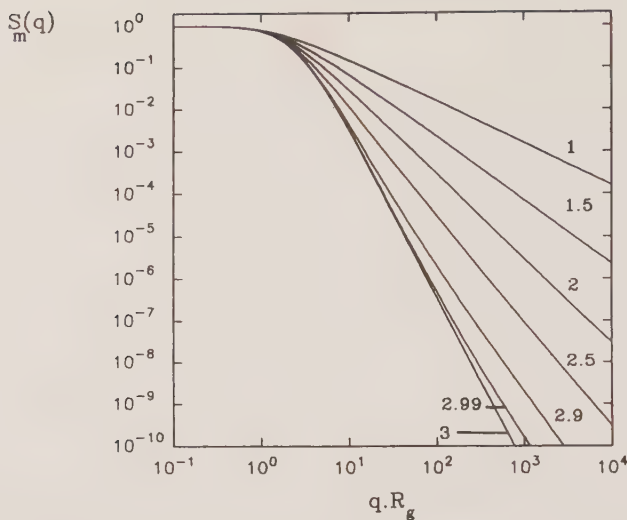


FIG. 6.2. A double logarithmic plot of $S_m(q)$ vs. $qR_g(m)$ with $\gamma = 1$ for different values of the fractal dimension d_f , as indicated on the graph. From ref. 14.

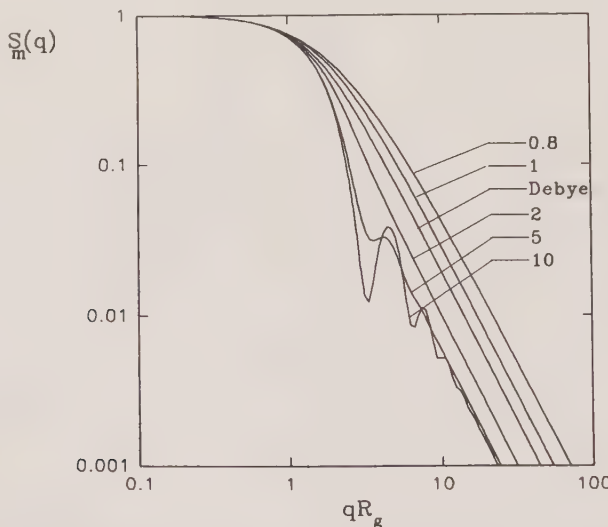


FIG. 6.3. A double logarithmic plot of $S_m(q)$ vs. $qR_g(m)$ with $d_f = 2$ for different values of the exponent γ , as indicated on the graph. From ref. 14.

The correct limiting behaviours at small and large $qR_g(m)$ are retained if $c_1 = (2n)/(3d_f)$ and $(c_n)^{-d_f/(2n)} = b/a$. If the cut-off function of $g(r)$ is gradual (i.e. small values of γ) only a few terms are needed to describe $S_m(q)$. In the case of a sharper cut-off, more terms are necessary for a correct description.

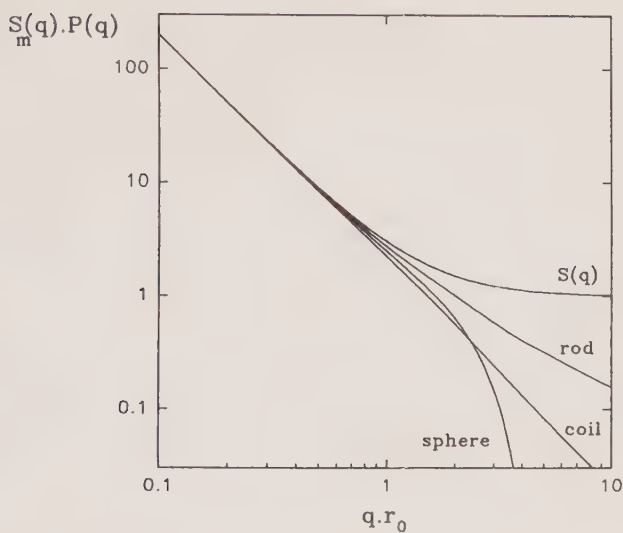


FIG. 6.4. A double logarithmic plot of $S_m(q)$ vs. qr_0 , with $d_f = 2$, $\gamma = 1$ for different form factors ($P(q)$) of the elementary unit. From ref. 14.

Sometimes only one term has been used (the so-called Fisher–Burford function^[13]), but it is easy to see that this can only give a correct description if $b/a = (2/(3d_f))^{-d_f/2}$.

In Figs. 6.2 and 6.3, we have taken $qr_0 \ll 1$. The influence of the monomer structure on $S_m(q)$ is illustrated in Fig. 6.4 for aggregates with $d_f = 2$ and $\gamma = 1$ and with monomers that are point scatterers, rods with length $2r_0$, coils with $R_g = r_0$, or spheres with radius r_0 . In these plots the local excluded volume effects that determine the detailed shape of $S_m(q)$ around $qr_0 = 1$ are ignored.^[18]

6.2.2 Static structure factor of polydisperse aggregates

Under the same very dilute conditions, the excess intensity of radiation scattered by a polydisperse solution, with $N(m)$ the number of aggregates having an aggregation number m and a static structure factor $S_m(q)$ in the scattering volume, is

$$I(q) \propto \sum_{m=1}^{\infty} m^2 N(m) S_m(q) P(q), \quad (6.26)$$

leading to

$$I(q) \propto N_0 m_w S_z(q) P(q), \quad (6.27)$$

with

$$N_0 = \sum_{m=1}^{\infty} m N(m), \quad (6.28)$$

$$m_w = \left[\sum_{m=1}^{\infty} m^2 N(m) \right] / \left[\sum_{m=1}^{\infty} m N(m) \right], \quad (6.29)$$

$$S_z(q) = \left[\sum_{m=1}^{\infty} m^2 N(m) S_m(q) \right] / \left[\sum_{m=1}^{\infty} m^2 N(m) \right]. \quad (6.30)$$

N_0 is the number of monomers in the scattering volume, and is directly proportional to the concentration C , m_w is the weight average aggregation number and $S_z(q)$ the z-average structure factor. Now we have:

$$I(q) = KC m_w S_z(q) P(q), \quad I(q \rightarrow 0)/KC = m_w. \quad (6.31)$$

$S_z(q)$ can also be seen as the Fourier transform of $g_w(r) = (\sum m N(m) g_m(r)) / (\sum m N(m))$, the weight-average pair correlation function of the clusters in the system:

$$S_z(q) = \frac{1}{m_w} \left(1 + \int_0^\infty 4\pi r^2 g_w(r) \frac{\sin(qr)}{qr} dr \right). \quad (6.32)$$

A series expansion of $S_z(q)$ at small q values leads to an equation similar to eqn (6.15), but involving the z-average radius of gyration, R_{gz} :

$$S_z(q) = 1 - \frac{1}{3} q^2 R_{gz}^2 + \dots, \quad qR_{gz} \ll 1, \quad (6.33)$$

with

$$R_{gz}^2 = \left[\sum_{m=1}^{\infty} m^2 N(m) [R_g(m)]^2 \right] / \left[\sum_{m=1}^{\infty} m^2 N(m) \right]. \quad (6.34)$$

In many processes in which fractal aggregates are formed, the number $N(m)$ decreases as a power-law function of m : $N(m) \propto m^{-\tau}$ (see below). The distribution is cut off at a characteristic mass, m^* , which increases during the aggregation process. Often the cut-off function is a single exponential decay, but more or less gradual cut-offs may be allowed by taking a stretched exponential decay. Thus the aggregation number distribution is characterized by two parameters:

$$N(m) \propto m^{-\tau} \exp(-(m/m^*)^\beta), \quad m^* \gg 1. \quad (6.35)$$

Combination of eqns (6.29), (6.34) and (6.35) gives

$$m_w = a_z R g_z^{d_f}, \quad (6.36)$$

with

$$a_z = a \left(\frac{\Gamma((3-\tau)/\beta)}{\Gamma((3+2/d_f-\tau)/\beta)} \right)^{d_f/2} \frac{\Gamma((3-\tau)/\beta)}{\Gamma((2-\tau)/\beta)}, \quad \tau < 2, \quad (6.37)$$

$$a_z = a \left(\frac{\Gamma((3-\tau)/\beta)}{\Gamma((3+2/d_f-\tau)/\beta)} \right)^{d_f/2} \frac{(\tau-2)}{\beta} \frac{\Gamma((3-\tau)/\beta)}{\Gamma((2-\tau)/\beta)}, \quad 2 < \tau < \min(2+\beta, 3), \quad (6.38)$$

The apparent fractal dimension d_f^* is related to the true fractal dimension and τ :

$$\left. \begin{aligned} d_f^* &= d_f, & \tau < 2, \\ d_f^* &= d_f(3 - \tau), & 2 < \tau < \min(2 + \beta, 3). \end{aligned} \right\} \quad (6.39)$$

Inserting eqns (6.35) and (6.18) in eqn (6.30), it follows that at large values of qR_{gz} , $S_z(q)$ will again decrease as a power-law function of q :

$$S_z(q) = \frac{b}{m_w} q^{-d_f^*}, \quad I(q)/KC = bq^{-d_f^*}, \quad qr_0 \ll 1 \ll qR_{gz}, \quad (6.40)$$

with b given by eqn (6.20). $\tau = 2$ represents a special case in which the power-law relations (6.36) and (6.40) are only reached asymptotically.^[14] As the term b is independent of the overall size of the aggregates, it is not influenced by polydispersity. However, $S_z(q)$ is influenced by polydispersity, but remains independent of the local structure of the aggregates:

$$S_z(q) = \frac{b}{a_z} (qR_{gz})^{-d_f^*}, \quad qr_0 \ll 1 \ll qR_{gz}, \quad (6.41)$$

with a_z given by eqns (6.37) or (6.38) and b by eqn (6.20). The term b/a_z is a complicated function of the four parameters in our model (d_f , γ , τ , β), but is of order unity in most realistic cases. Different combinations of d_f , γ , τ and β can lead to the same value of b/a_z and d_f^* , so that caution is required when interpreting the same limiting behaviour as a sign that the aggregates have the same structure. The influence of the polydispersity on $S_z(q)$ is illustrated in Fig. 6.5 for different τ with $d_f = 2$, $\gamma = 1$ and $\beta = 1$. d_f^* can be obtained directly

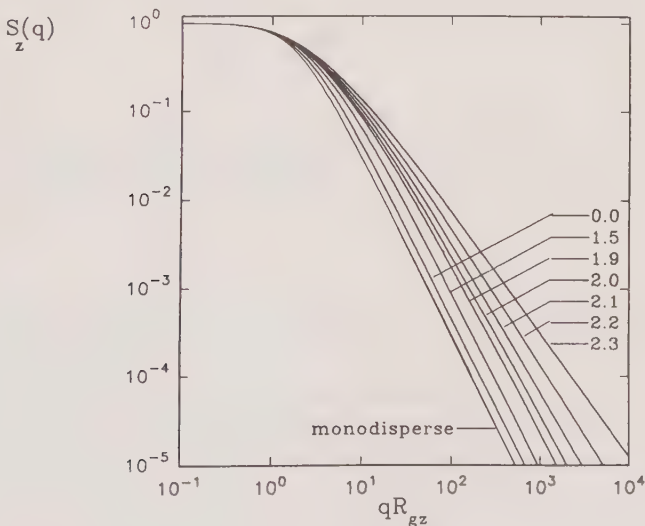


FIG. 6.5. A double logarithmic plot of $S_z(q)$ vs. qR_{gz} with $d_f = 2$, $\gamma = 1$, $\beta = 1$ at different values of the polydispersity exponent τ , as indicated on the graph. From ref. 14.

by measuring the limiting slope of $\log(S_z(q))$ vs. $\log(qR_{gz})$ provided that $r_0 \ll q^{-1} \ll R_{gz}$. However, systematic calculations of $S_z(q)$ ^[14] show that for values of τ close to two, the limiting slope is approached very slowly and, in practice, is difficult to determine accurately.

6.2.3 Investigation of polydispersity using dynamic light scattering

The dynamic light scattering (DLS) technique^[15] measures the autocorrelation function of the scattered light intensity: $g_2(t) = \langle I(0)I(t) \rangle / \langle I \rangle^2$, where the brackets indicate a time average. The normalized electric field autocorrelation function, $g_1(t)$, is determined from $g_2(t)$ through the Siegert relation: $g_2(t) = 1 + |g_1(t)|^2$. Here we will only consider $g_1(t)$ for very dilute solutions at $qR_{gz} \ll 1$ and assume that the relaxation of the solvent scattering is outside the time window of the autocorrelator, as is generally the case.

For monodisperse aggregates, $g_1(t)$ is a single exponential decay:

$$g_1(t) = \exp(-t/\tau_r), \quad (6.42)$$

with a relaxation time determined by the diffusion coefficient of the aggregates $\tau_r = (q^2 D)^{-1}$. The diffusion coefficient can be related to the hydrodynamic radius, R_h , using the Stokes–Einstein relation:

$$D = k_B T / 6\pi\eta_s R_h, \quad (6.43)$$

where η_s is the solvent viscosity. In the non-draining limit, $R_h \propto R_g \propto m^{1/d_f}$. Proportionality between R_g and R_h is generally observed, with a proportionality constant that depends on the structure of the aggregates.

For polydisperse aggregates, $g_1(t)$ is a weighted sum of exponentials:

$$g_1(t) = \left[\sum_{m=1}^{\infty} m^2 N(m) \exp(-t/\tau_m) \right] / \left[\sum_{m=1}^{\infty} m^2 N(m) \right], \quad (6.44)$$

where τ_m is determined by the hydrodynamic radius of aggregates with aggregation number m . $g_1(t)$ is thus characterized by a distribution of relaxation times, $A(\tau_r)$:

$$g_1(t) = \int_0^{\infty} A(\tau_r) \exp(-t/\tau_r) d\tau_r, \quad (6.45)$$

where we have replaced the sum by an integral and taken $\int A(\tau_r) d\tau_r = 1$. Two different average relaxation times are readily obtained: the arithmetic average,

$$\tau_a = \int_0^{\infty} \tau_r A(\tau_r) \exp(-t/\tau_r) d\tau_r, \quad (6.46)$$

by taking the area under $g_1(t)$, and the harmonic average,

$$\tau_h = \left(\int_0^{\infty} 1/\tau_r A(\tau_r) \exp(-t/\tau_r) d\tau_r \right)^{-1}, \quad (6.47)$$

by taking the initial slope of $\ln(g_1(t))$ vs. t . Generally, the harmonic average is used to calculate the z -average hydrodynamic radius, although using the arithmetic average would give values closer to R_{gz} . The ratio τ_a/τ_h increases with increasing polydispersity. If R_h is proportional to R_g , τ_m in eqn (6.44) can be written as

$$\tau_m = \tau_0 m^{1/d_f}, \quad (6.48)$$

where τ_0 is the relaxation time associated with $m = 1$. Utilizing eqn (6.48) in eqn (6.44) and taking the continuous limit, we obtain

$$g_1(t) \propto \int_0^\infty \frac{m^3 N(m)}{\tau_m} \exp(-t/\tau_m) d\tau_m. \quad (6.49)$$

Comparing eqn (6.49) with eqn (6.46), we can relate the relaxation time distribution to $N(m)$:

$$\tau_r A(\tau_r) \propto m^3 N(m). \quad (6.50)$$

If we assume that $N(m)$ is given by eqn (6.35), we find that

$$A(\tau_r) \propto \tau_r^{p-1} \exp(-(\tau_r/\tau_g)^s), \quad (6.51)$$

with

$$p = d_f(3 - \tau), \quad s = d_f \beta, \quad \tau_g = \tau_{m^*}. \quad (6.52)$$

Equation (6.51) expresses the so-called generalized exponential (GEX) distribution. The properties and some applications of this function will be reported elsewhere.^[16] For $p > 1$ the two average relaxation times τ_a and τ_h can be expressed in terms of p , s and τ_g :

$$\tau_a = \tau_g \frac{\Gamma((p+1)/s)}{\Gamma(p/s)}, \quad p > 0 \quad . \quad (6.53)$$

and

$$\tau_h = \tau_g \frac{\Gamma((p-1)/s)}{\Gamma(p/s)}, \quad p > 1. \quad (6.54)$$

For real systems the condition $p > 1$ is generally satisfied. For smaller values of p , τ_a and τ_h depend on τ_0 .^[16]

6.3 Aggregation and gelation

6.3.1 The growth process

Two main conceptual theoretical frameworks are used to describe aggregation and gelation processes: on the one hand, the kinetic approach initially proposed by Smoluchowski^[17,18] and on the other equilibrium theories, e.g. the classical Flory–Stockmayer approach^[19–21] and percolation theory.^[2,3] The kinetic approach gives a mean field description of aggregation processes when the positions of the aggregates are not correlated. This assumption is only reasonable in the case of very dilute solutions. Following Jullien and Botet^[22]

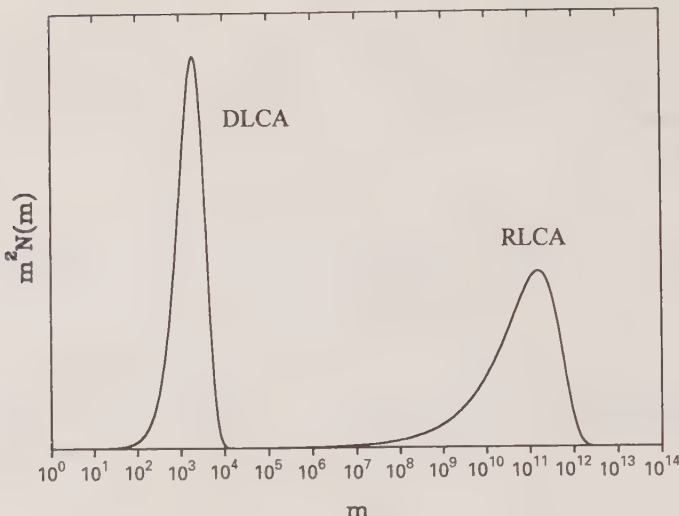


FIG. 6.6. A comparison of the mass distribution function ($m^2 N(m)$) on a logarithmic scale for m) between a DLCA and a RLCA population, having the same initial number of particles (N_0) and the same number $N(1)$ of clusters with $m = 1$. Under these conditions, the general relation between the two cut-off aggregation numbers is $m_{\text{RLCA}}^* \propto (m_{\text{DLCA}}^*)^4$.

we will call this kind of aggregation flocculation. This theory can describe many different growth processes because of the infinite number of possible reaction kernels involved in the rate equations and the possibility of including fragmentation processes. Two well studied limiting cases are reaction limited cluster aggregation (RLCA), where the sticking probability between particles tends to zero, and diffusion limited cluster aggregation (DLCA), where the sticking probability equals unity. The cluster distributions for these processes are given by eqn (6.29) with $\tau = 0$, $\beta = 1$ for DLCA^[23] and $\tau = 1.5$, $\beta = 1$ for RLCA.^[24] Figure 6.6 clearly shows that the polydispersity is much larger for the RLCA process. The kinetic approach is unable to predict the cluster geometry which is, however, obtained by computer simulations.^[25-28] The static structure factor is well described by eqn (6.16) with $d_f = 1.8$, $\gamma = 2$ for DLCA and $d_f = 2.1$, $\gamma = 2$ for RLCA.^[14] As the theory can only meaningfully be applied to very dilute solutions, it cannot describe the gelation process.^[29]

When the gel point is approached, there is a strong overlap between the aggregates and the fundamental underlying assumption of the kinetic theory is no longer valid. The growth close to the gel point is better described in terms of bond percolation models which give the increase in connectivity between close-packed particles. The number distribution of aggregates formed by a percolation process is again given by eqn (6.29) with $\tau = 2.2$ and $\beta \cong 0.9$.^[30,31] The fractal dimension is 2.5 and the cut-off function of the pair correlation function is well described by a stretched exponential with $\gamma = 2$.^[4] These random bonding models are only valid in ‘congested’ systems and cannot

describe the evolution of spatial correlations occurring during the initial stage of the aggregation when the aggregates are not close-packed.^[29]

Between these two limiting situations, the very dilute and the ‘congested’ states, exists a smooth cross-over due to gradual interpenetration of aggregates which cannot be described by any presently available theory. Recent computer simulations^[4] give insight into this gradual cross-over. To quantify the evolution of the interpenetration we need to introduce two different volume fractions: the cumulative, V_{cum} , and the effective, V_{eff} , volume fractions. If $V(m)$ is the volume fraction occupied by one cluster of mass m , we have

$$V_{cum} = \sum_{m=1}^{\infty} N(m)V(m), \quad V_{eff} = \bigcup_{m=1}^{\infty} \bigcup_{i=1}^{N(m)} V(m). \quad (6.55, 6.56)$$

The difference between V_{cum} and V_{eff} indicates the amount of interpenetration. If $V_{cum} = V_{eff}$, all clusters are separated from each other. When $V_{eff} = V_{cum} \ll 1$ the positions of the aggregates are uncorrelated and they grow by a flocculation process. In the opposite limit, when $V_{cum} \gg 1$, the system is highly congested and the aggregates grow through a percolation process. At the gel point V_{cum} diverges and V_{eff} is unity. For macroscopic systems V_{eff} reaches exactly unity only at the gel point when an infinite aggregate spans the whole space. Below the gel point there is always a finite chance for a volume element not to be occupied by any aggregate. Figure 6.7 gives the evolution of V_{cum} and V_{eff} as a function of time reduced by the gelation time (t_g) for the DLCA process.

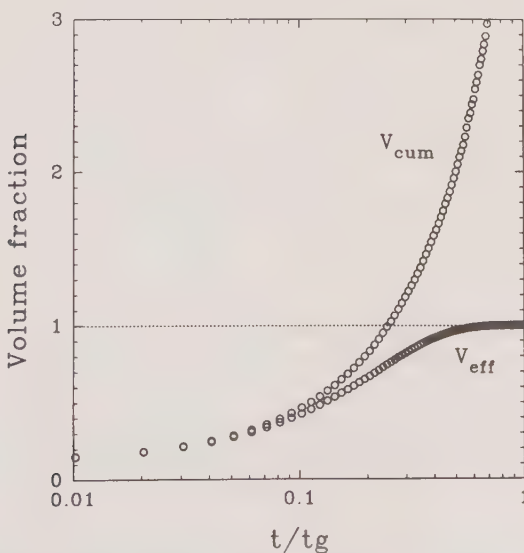


FIG. 6.7. The evolution of V_{cum} and V_{eff} as a function of the reduced time (t/t_g) for a DLCA process.

The aggregation number m^+ that characterizes the transition between these two types of growth is defined as

$$\sum_{m=1}^{m^+} N(m)V(m) = 1. \quad (6.57)$$

Due to their branched structure, clusters of similar size (on a logarithmic scale) do not significantly interpenetrate and, due to their fractal nature, large clusters are nearly transparent to small ones. If we consider a cluster with aggregation number i , the excluded volume generated by this cluster with respect to another, V_{ij} , depends strongly on the aggregation number j of the other cluster. In good solvents V_{ij} will be of the order $(i/j)V(j)$. For i close to j the excluded volume is close to $V(i)$, while for $i \gg j$ it will be relatively small. The mechanisms governing the local bond formation (e.g. DLCA) determine the structure and the distribution of all the clusters only for $V_{cum} \ll 1$. At later stages very small clusters with $m \ll m^+$ will still be well separated and will continue to grow via a flocculation process because they are insensitive to the presence of very large clusters. Very large clusters with $m \gg m^+$ will be close-packed and grow through a percolation process. These clusters grow mainly by fusion between aggregates of similar size, again because of the insensitivity of small clusters to the presence of large ones. Clusters with $m \ll m^+$ do not share a common volume and their positions are uncorrelated. Clusters with $m \gg m^+$ share common volume with many other clusters and are hierarchically interpenetrated^[32,33] (cf. the 'Russian doll model', Fig. 6.8). R_g^+ is the radius of gyration of the cluster with aggregation number m^+ , where m^+ depends on the monomer volume fraction, ϕ_0 , and the values of d_f , γ , τ and β generated by the flocculation process.

Between these two limiting regimes there is a large crossover where τ and d_f change gradually from the flocculation values to the percolation values. The width of the cross-over depends on the polydispersity created by the flocculation process. There is a sharp transition between flocculation and percolation only if the aggregation process leads to exactly monodisperse aggregates up to m^+ . However, such a growth process is not realistic. Figure 6.9 shows the extent of the cross-over between the DLCA process and percolation. For the RLCA process an even larger cross-over is expected. The cross-over will be reflected both in the structure and the distribution of the clusters. Small aggregates ($R_g \ll R_g^+$) and large aggregates at small distances will have a fractal dimension characteristic of the flocculation process, while large aggregates will have a fractal dimension $d_f = 2.5$ at large distances. Similarly, $N(m)$ will be described by eqn (6.29), with τ given by the flocculation process for $m \ll m^+$ and $\tau = 2.2$ for $m \gg m^+$. Figure 6.10(a) shows a schematic cluster distribution with its characteristics.

If the monomer volume fraction ϕ_0 is smaller, a larger m_w is needed to reach the same V_{cum} , which means that m^+ increases with decreasing ϕ_0 . It has been shown elsewhere^[4] that in the case of a DLCA process for any given V_{cum}

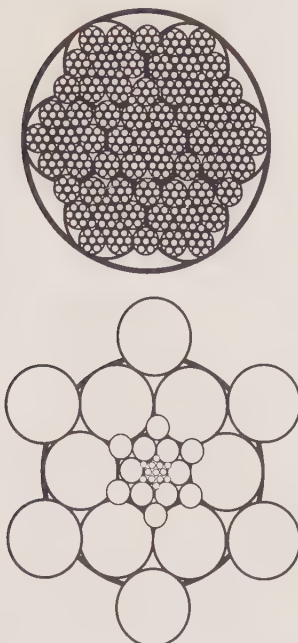


FIG. 6.8. A schematic representation of the Russian doll model.

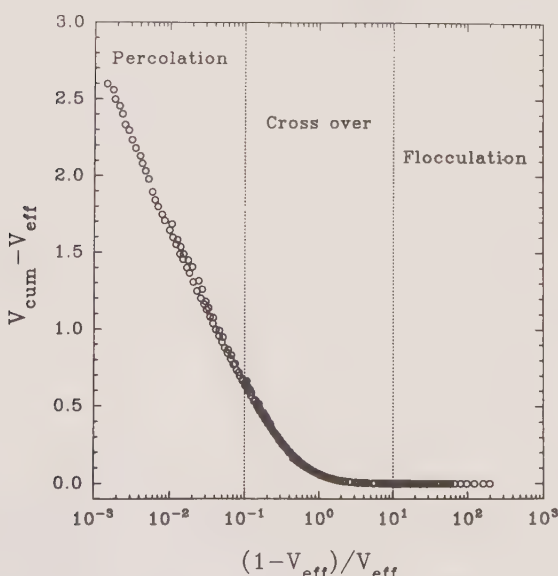


FIG. 6.9. The cross-over between flocculation and percolation for a DLCA process. In the flocculation regime, $V_{cum} - V_{eff} = 0$. In the percolation regime V_{eff} is very close to 1 and $V_{cum} \propto -\log(1 - V_{eff})$.

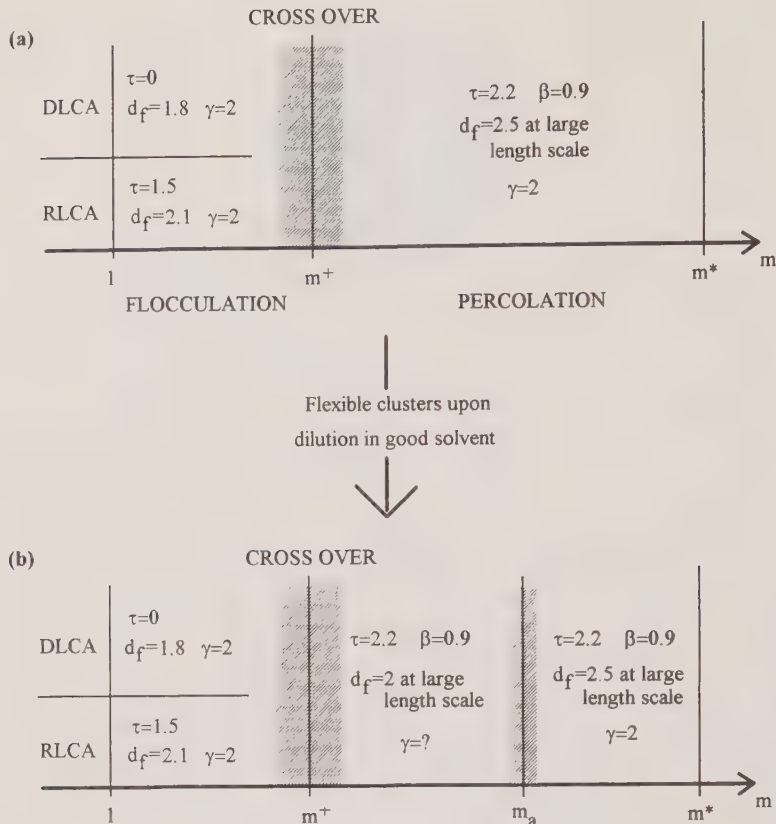


FIG. 6.10. The schematic evolution of the cluster distribution.

we have the relation

$$m_w \phi_0^{1.3} = A, \quad (6.58)$$

where A is a constant independent of m_w and ϕ_0 . Figure 6.11 shows this universal behaviour.

6.3.2 Static light scattering during aggregation

As long as $V_{cum} \ll 1$, we may consider the system to be infinitely dilute, so that the scattered intensity will be given by eqn (6.32), with $S_z(q)$ determined by the values of d_f , γ , τ and β generated by the flocculation process. With increasing V_{cum} , we can no longer consider the centre of mass positions of the larger aggregates as uncorrelated. At small values of V_{cum} this effect can be treated as a perturbation in terms of a virial expansion.^[34]

At larger values of V_{cum} , one also needs to take into account correlation between monomers belonging to different aggregates, and we have to consider

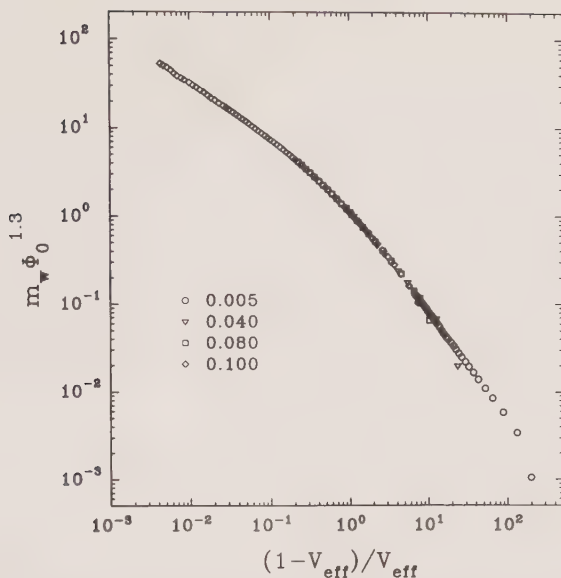


FIG. 6.11. The universal behaviour of $m_w \phi_0^{1.3}$ as a function of $(1 - V_{eff})/V_{eff}$ for different values of ϕ_0 , as indicated on the graph. From ref. 4.

the pair correlation function of the whole system, $g(r)$.^[35] It is no longer equal to the weight average pair correlation function of connectivity, $g(r)$ measures the average monomer number concentration at a distance r from another arbitrary monomer, whether or not they belong to the same cluster. At distances much smaller than the average distance between monomers of different aggregates $g(r)$ is not influenced by the presence of other aggregates and $g(r) = g_w(r)$. At much larger distances the system becomes homogeneous and $g(r)$ approaches the average concentration, C . The cross-over between these two regimes can be very complex, and is not necessarily a continuously decreasing function. The expression for $I(q)$ is

$$I(q) = KCm_a S(q)P(q), \quad (6.59)$$

with

$$S(q) = \frac{1}{m_a} \left(1 + \int_0^\infty 4\pi r^2 (g(r) - C) \frac{\sin(qr)}{qr} dr \right) \quad (6.60)$$

and

$$\int_0^\infty 4\pi r^2 (g(r) - C) dr = m_a - 1, \quad (6.61)$$

where m_a is an apparent aggregation number. $S(q \rightarrow 0) = 1$ and $S(\infty) = 1/m_a$. Equation (6.59) reduces to eqn (6.31) when C tends to zero.

If the aggregates are monodisperse and have a net repulsive interaction, they will tend to be situated at the maximum separation distance, d_m . For spherical

monodisperse aggregates $d_m \propto C^{-0.33}$ and for rod-like monodisperse aggregates $d_m \propto C^{-0.5}$. In this case $g(r)$ peaks at d_m and $S(q)$ is modulated by a sinusoidal oscillation with the first maximum at $q \propto 1/d_m$ and secondary maxima at $q \propto i/d_m$, with $i = 2, 3, \dots$. In fact, even if there is no preferred distance, a maximum can occur merely due to excluded volume interactions, which create a so-called correlation hole. The amplitude of these maxima depends on the strength of the interactions. Polydispersity reduces the amplitude as d_m will be less well defined. This is the reason why a maximum is observed for DLCA, but not for RLCA.^[36,37]

In the case of very polydisperse flexible aggregates, small aggregates can penetrate larger ones and screen the excluded volume interaction at distances larger than the screening length ξ_s in a way analogous to the case of linear polymer solutions, and therefore

$$g(r) = \frac{d_f}{4\pi r_0^{d_f}} r^{d_f-3} f(r/\xi_s) + C, \quad r_0 \ll r. \quad (6.62)$$

If $V_{cum} \ll 1$, $\xi_s = \xi$ and eqn (6.62) reduces to eqn (6.9). With increasing V_{cum} , ξ_s decreases and is independent of the overall size when V_{cum} is larger than unity.

From the initial q -dependence of $I(q)$ one obtains an apparent molar mass, m_a , and a radius of gyration, R_{ga} , using a series expansion of $S(q)$ at small q :

$$I(q)/KC = m_a(1 - \frac{1}{3}q^2 R_{ga}^2 + \dots), \quad qR_{ga} < 1. \quad (6.63)$$

The squared radius, R_{ga}^2 , is defined as

$$R_{ga}^2 = \frac{1}{2m_a} \int_0^\infty 4\pi r^4 (g(r) - C) dr. \quad (6.64)$$

From the discussion in the previous section it is clear that $R_{ga} \approx R_g^+$ and $m_a \approx m^+$. During the aggregation process the apparent aggregation number, m_a , and radius of gyration, R_{ga} , determined via eqn (6.63) grow until they reach approximately m^+ and R_g^+ , respectively (cf. Fig. 6.12). A weak variation still occurs due to the growth of aggregates with $m < m^+$, but the scattering is dominated by that of particles with m close to m^+ .

6.3.3 Static light scattering upon dilution of quenched systems

If further growth can be stopped, we can study the structure and cluster distribution at different stages of aggregation by diluting the system. Upon dilution the interaction between the aggregates decreases and m_a and R_{ga} increase from about m^+ and R_g^+ in the undiluted state to m_w and R_{gz} at infinite dilution. As discussed above, at infinite dilution the intensity may be compared with predictions of the various models for aggregation and DLS can be used to measure the cluster distribution. For $V_{cum} \gg 1$ the excluded volume interactions of the larger aggregates with $m \gg m^+$ are screened by the presence

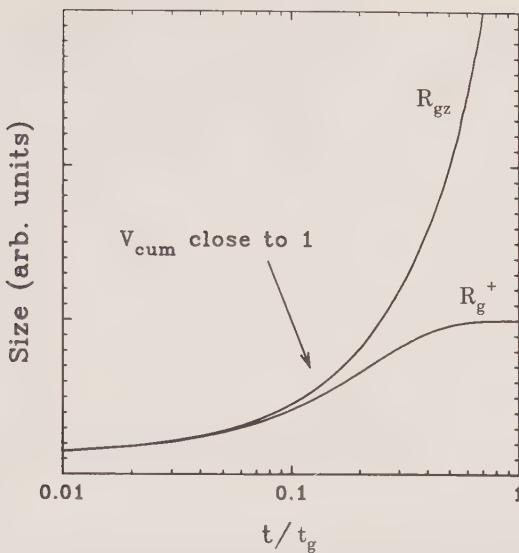


FIG. 6.12. The schematic evolution of R_{gz} and R_g^+ as a function of the reduced time t/t_g .

of smaller aggregates. However, at infinite dilution in a good solvent the excluded volume interactions are no longer screened, so that flexible aggregates will swell. This effect decreases the fractal dimension of flexible percolating cluster from $d_{fb} = 2.5$ ('bulk') to $d_{fs} = 2$ ('swollen').^[38] Figure 6.10(b) gives a schematic description of the evolution of the cluster distribution upon dilution in a good solvent.

It is difficult to predict, in general, the dependence of m_a and R_{ga} on dilution, i.e. on the concentration. Daoud and Leibler^[38] have used scaling theory to derive the concentration dependence of m_a and R_{ga} for flexible aggregates in good solvents:

$$m_a \propto C^{[1 - d_{fs}(3 - \tau)]/[3(1 - d_{fs}/d_{fb})]} \propto C^{-8/3}, \quad C \gg C^*, \quad (6.65)$$

$$R_{ga} \propto C^{-1/[3(1 - d_{fs}/d_{fb})]} \propto C^{-5/3}, \quad C \gg C^*, \quad (6.66)$$

$$m_a \propto R_{ga}^{d_{fs}(3 - \tau)}. \quad (6.67)$$

To derive these relations it was assumed that $m_a \propto m_w$ and $R_{ga} \propto R_{gz}$ at $C = C^*$, and that m_a/m_w and R_{ga}/R_{gz} scale with C/C^* , where

$$C^* = \left[\sum_{m=1}^{\infty} m N(m) \right] / \left[\sum_{m=1}^{\infty} \frac{4}{3} \pi [R_g(m)]^3 N(m) \right] \propto m_w^{(3/d_{fb} - 3/d_{fs})/(3 - \tau)}, \quad (6.68)$$

with $N(m)$ and $R_g(m)$ for swollen percolating clusters. $C = C^*$ corresponds to $V_{cum} = 1$. The only other assumption is that m_a and R_{ga} are independent of m_w and R_{gz} for $C > C^*$. Even if we can neglect the contribution of aggregates with $m < m^+$ to the occupied volume, this approach completely ignores the effect of

interpenetration at $V_{cum} < 1$ and assumes that $V_{eff} = V_{cum}$ until $V_{cum} = 1$. The large cross-over present in real systems, and shown by simulation,^[4] probably limits the domain in which these scaling relations can be applied. Interestingly, if we apply the same reasoning to non-swelling percolating clusters, no scaling relation can be derived (see eqn 6.69). In this case C^* has a logarithmic dependence on m_w :

$$C^* \propto \left(\int_1^\infty m^{3/d_f - \tau} \exp(-(m/m^*)^\beta) \right)^{-1} \propto (\ln(m^*))^{-1} \propto (\ln(m_w))^{-1}. \quad (6.69)$$

This situation occurs for rigid aggregates or on dilution in a theta solvent.

6.4 Applications to real systems

6.4.1 Branched aggregates of a globular protein formed and studies in the dilute state

Polydisperse aggregates formed upon heat-induced denaturation of β -lactoglobulin have been studied by static and dynamic scattering.^[39] Figure 6.13 shows the evolution of $I(q)/(KC)$ as a function of q for samples made at different heating times and then diluted. It is clear that both m_w and R_{gz} increase with the heating time. For the larger populations of aggregates, the internal structure is probed and all data fall on the same curve, as expected from eqn (6.40).

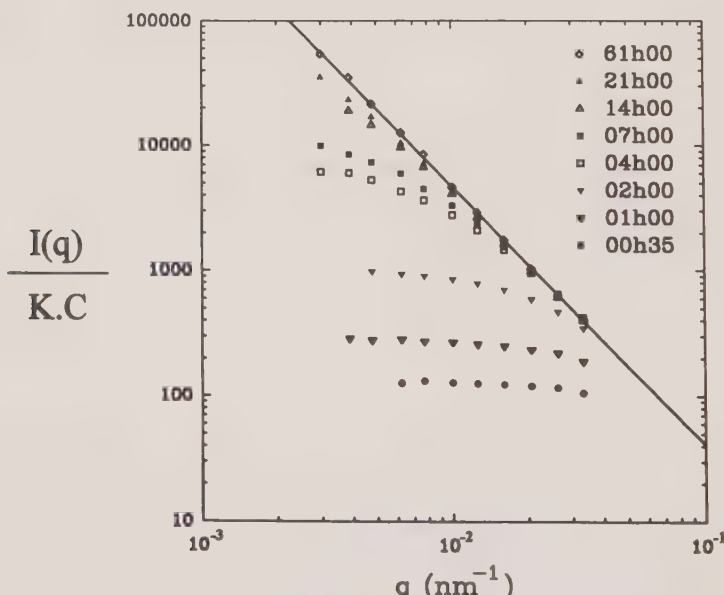


FIG. 6.13. $I(q)/(KC)$ as a function of q for aqueous solutions of β -lactoglobulin (pH 7, 0.1 M salt) at various heating times at 76 °C. The solid line has a slope -2.02 ± 0.02 . From ref. 39.

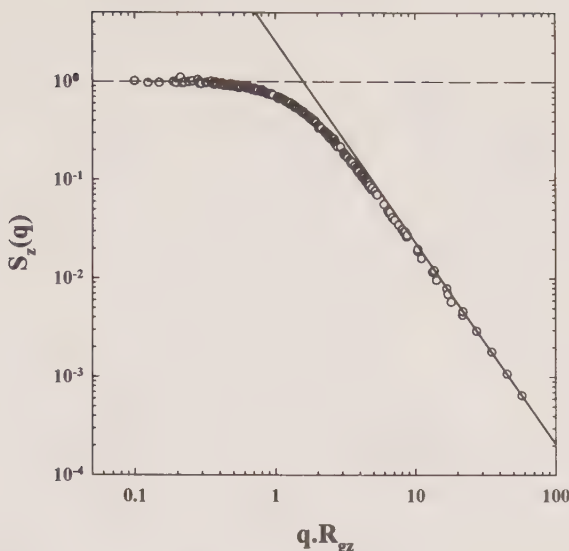


FIG. 6.14. The evolution of $S_z(q)$ as a function of qR_{gz} for aggregates of β -lactoglobulin (pH 7, 0.1 M salt). From ref. 39.

d_f^* is 2.02 ± 0.02 . All the experimental data for different initial concentrations, heating times, and heating temperatures can be superimposed on a master curve $S_z(q)$ as a function of qR_{gz} , showing the self-similarity of the structure and the distribution (cf. Fig. 6.14). The analysis of the cluster distribution obtained by Steric Exclusion Chromatography (SEC) (cf. Fig. 6.15(a)) shows that the maximum of this distribution moves with the aggregation extent, which means that $\tau < 2$ and $d_f = d_f^* = 2.02 \pm 0.02$ (it is assumed that the elution volume is proportional to $\log(m)$ plus a constant over the relevant volume range). In addition, GEX analysis of DLS data (Fig. 6.16) in the range $qR_{gz} \ll 1$ gives $p = 4.1$ and $s = 2.1$. According to eqns (6.51) and (6.52), $\tau \approx 1$ and $\beta \approx 1$. From Fig. 6.14, we find that b/a_z is close to 2.2 (cf. eqn (6.41)), which leads to $\gamma \approx 2$ (cf. eqns (6.37) and (6.20)). $S_z(q)$ could also be well-fitted to the Debye function (eqn (6.24)), which shows that we cannot determine all four parameters (τ , β , d_f) unambiguously purely on the basis of $S_z(q)$. Independent knowledge of some of these parameters, e.g. from DLS or SEC, is necessary. SANS experiments (Fig. 6.17) show clearly the internal cut-off of the fractal domain around 10 nm and give the local structure factor ($P(q)$) of the aggregates.^[39]

This aggregation process does not follow the DLCA mechanism because (a) the aggregation rate is too slow, (b) the fractal dimension is too high and (c) the polydispersity is too large. Neither is it an RLCA process, because the growth is not exponential and the polydispersity is too small. The growth process is mainly driven by reaction between large and small clusters,^[40] which leads to a value of τ intermediate between DLCA (where large-large reactions are totally negligible) and RLCA (where no kind of reaction is dominant).^[41,42]

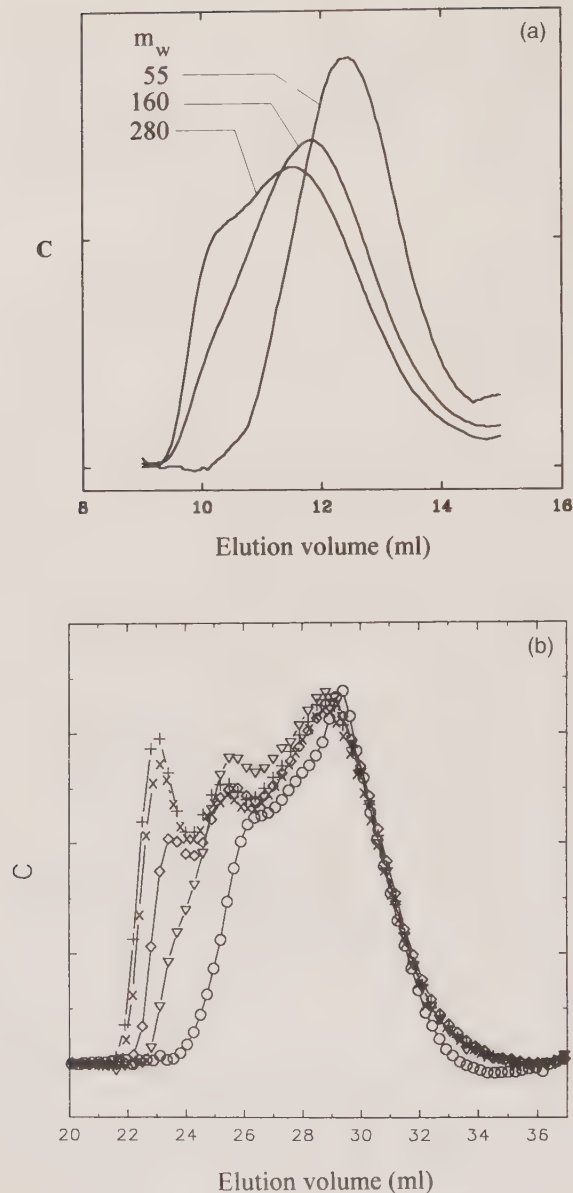


FIG. 6.15. The cluster distribution obtained by SEC analysis: (a) for β -lactoglobulin aggregates at various aggregation extents; (b) for PMMA branched aggregates at increasing reaction extents (\circ , ∇ , \diamond , \times , $+$).

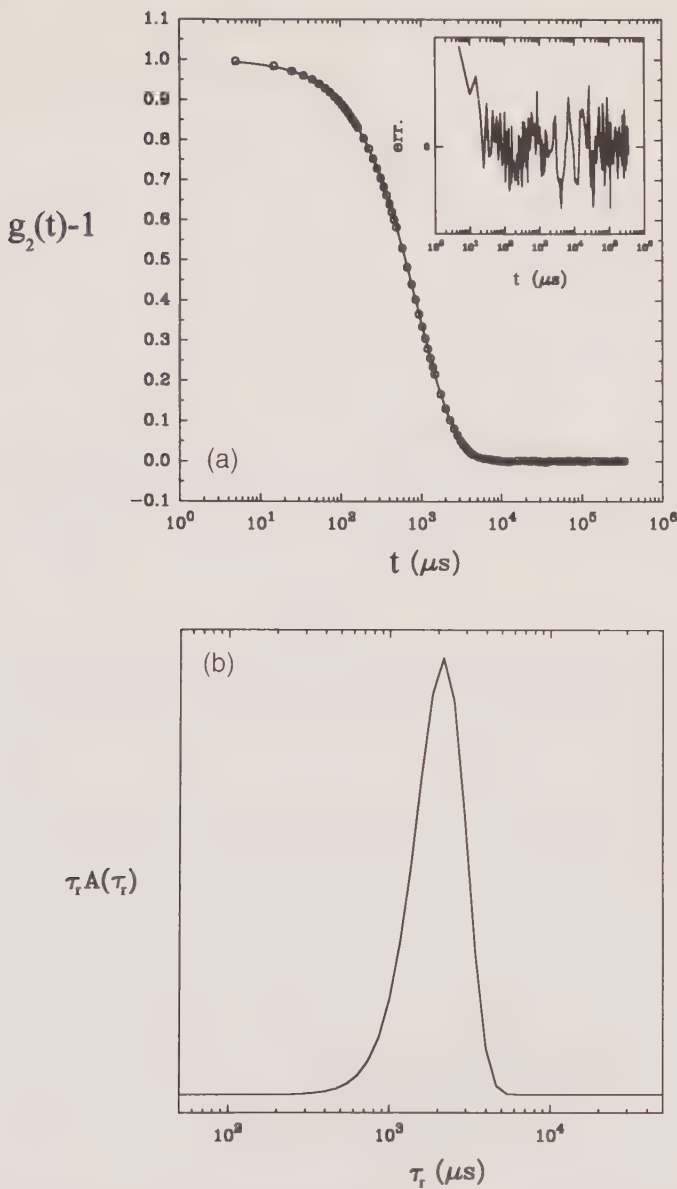


FIG. 6.16. (a) $g_2(t) - 1$ vs. t for β -lactoglobulin aggregates with $qR_{gz} \ll 1$. The solid line shows the data fit with a GEX function, giving $p = 4.1$ and $s = 2.1$. The inset shows the residues. (b) The time relaxation spectrum of the same data.

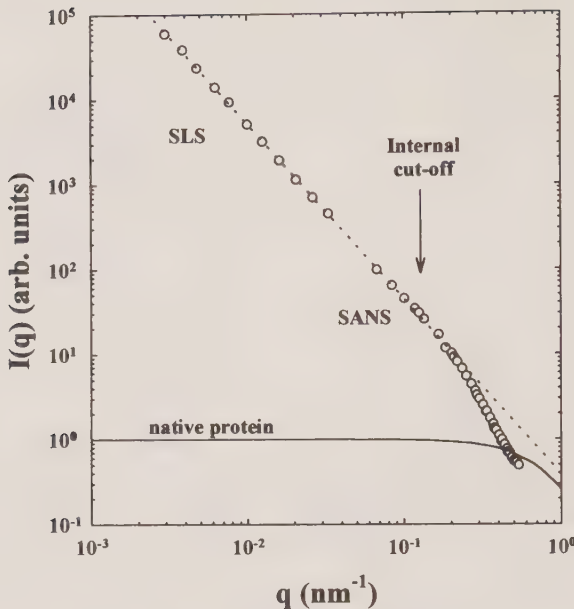


FIG. 6.17. The local structure factor of β -lactoglobulin aggregates (\circ) at pH 7, 0.1 M salt, combining SLS and SANS data. The solid line represents the scattering data for the native protein. The dotted line is a fit through SLS data. From ref. 39.

6.4.2 Branched poly(methylmethacrylate) (PMMA) in the highly dilute state

Copolymerization of methyl methacrylate (MMA) and ethylene glycol methacrylate (EGDMA) in solution leads to the formation of polydisperse branched PMMA. At low reaction extent mostly linear PMMA is formed with $M_w \cong 7 \times 10^4$ g/mol and $M_w/M_n \cong 2$, where M_w and M_n are the weight and number average molar mass, respectively. Only when the concentration of the linear PMMA is close to C^* does the branching become important and does the polydispersity increase. For sufficiently high initial concentrations of MMA and EGDMA the system eventually forms a gel. Figure 6.15(b) shows the mass distributions at different reaction extents obtained by SEC. Contrary to the case of β -lactoglobulin, the maximum in the distribution does not move with increasing reaction extent, which implies that $\tau > 2$. The distribution shows undulations which have also been observed for other highly polydisperse branched polymer solutions. The origin of these undulations is as yet unknown. The overall shape of the distribution can be described using a power-law dependence with τ between 2.1 and 2.2.

Master plots of the static structure factor are shown in Fig. 6.18 for the polydisperse system and for the monodisperse system. The latter curve was obtained using on-line light scattering detection of the SEC chromatogram.

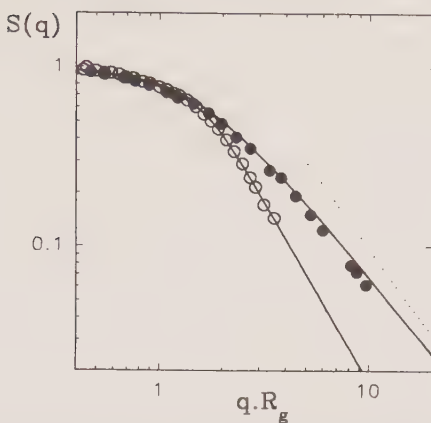


FIG. 6.18. Static structure factors for monodisperse and polydisperse branched aggregates of PMMA. The solid line through the open circles represents a fit to eqn (6.25), with $d_f = 2$ and $n = 4$. The solid line through the filled circles represents eqn (6.30) with $N(m)$ given by eqn (6.35) and $\tau = 2.2$. The dotted line has a slope of -1.6 . From ref. 43.

Unfortunately, due to limited column resolution, the qR_g range is not very large and the limiting slope cannot be obtained with high precision, but it is close to 2. The limiting slope of the polydisperse system was found to be 1.6. The difference is due to the effect of polydispersity (see eqn (6.39)). These results are expected for percolating clusters. As mentioned earlier, the initially linear PMMA chains essentially only form larger branched clusters for $C > C^*$ so that one would, indeed, expect the structure and cluster distribution to be close to that of percolation. The solid line through the monodisperse structure factor is a non-linear least squares fit to eqn (6.24) with $d_f = 2$. The results were used to calculate the corresponding polydisperse structure factor using $\tau = 2.2$. For more details, see ref. 43.

Figure 6.19 shows the effect of dilution on the apparent molar mass M_a .^[44] The data are compatible with the power-law dependence expected by the scaling theory outlined above. The solid line is the result of a linear least squares fit, which gives $M_a \propto C^{-2.7}$, and is close to the predicted exponent of $-8/3$.

6.4.3 Branched aggregates of polyurethanes formed in bulk, studied in the semi-dilute state

Different studies have shown that the growth of randomly branched polyurethanes made in bulk is described by a percolation process.^[45-48] The fractal dimension (d_f) and the apparent fractal dimension (d_f^*) of the aggregates are 2.5 and 2.0, respectively, in the bulk and 2.0 and 1.6, respectively, in dilute good solvent solutions, which implies $\tau = 2.2$ (see eqn (6.39)). As the branched polyurethanes are flexible, the effect of dilution in a good solvent of the

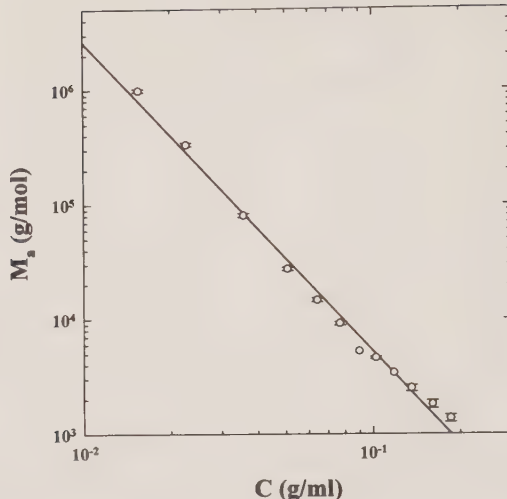


FIG. 6.19. The evolution of M_a as a function of C , for branched aggregates of PMMA. The solid line is the result of a linear least squares fit giving a slope of -2.7 ± 0.1 . From ref. 44.

system quenched close to the gel point can be compared to the theory of Daoud and Leibler described above.

The evolution of the scattered intensity at a given q as a function of the concentration, $I_q(C)$, exhibits a maximum value at a characteristic concentration C_q^* . From eqns (6.40) and (6.63) it follows that

$$I_q(C) = KCbq^{-d_f}, \quad qR_{ga} \gg 1 \quad (6.70)$$

and

$$I_q(C) = KCm_a \propto C^{-5/3}, \quad qR_{ga} \ll 1. \quad (6.71)$$

At $C = C_q^*$, R_{ga} is close to q^{-1} , so that using eqn (6.66) the q -dependence of C_q^* is given by

$$C_q^* \propto q^{3/5}, \quad qR_{gz} \gg 1. \quad (6.72)$$

Figure 6.20 shows the evolution of C_q^* as a function of q . We can clearly see the power-law behaviour predicted by eqn (6.72). At q tending to zero, C_q^* tends to C^* , as expected.

Renormalizing the experimental set of curves $I_q(C)$ by $I_q(C_q^*)$ and plotting them as a function of C/C_q^* , a master curve is obtained (cf. Fig. 6.21).^[49] For the lowest concentrations ($C/C_q^* \ll 1$), the asymptotic regime has a power-law dependence,

$$I_q(C)/I_q(C_q^*) \propto (C/C_q^*)^{0.98 \pm 0.03}, \quad (6.73)$$

in agreement with eqn (6.70).

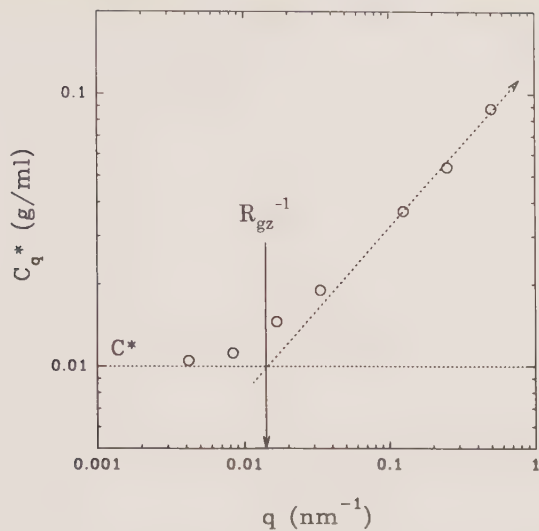


FIG. 6.20. The evolution of C_q^* as a function of q , for branched polyurethane.

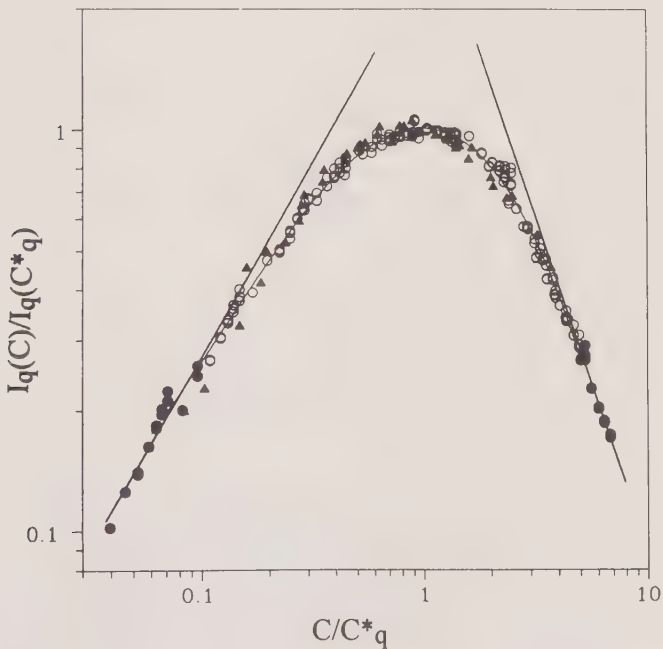


FIG. 6.21. The evolution of the reduced intensity $I_q(C)/I_q(C_q^*)$ as a function of the reduced concentration of C/C_q^* , for branched polyurethane. From ref. 49.

For the highest concentrations ($C/C_q^* \gg 1$), the asymptotic regime again has a power-law dependence:

$$I_q(C)/I_q(C_q^*) \propto (C/C_q^*)^{-1.68 \pm 0.05}, \quad (6.74)$$

in agreement with eqn (6.71).

6.5 Conclusions

Scattering techniques are very useful for the characterization of aggregates. At infinite dilution the structure can be obtained from the q -dependence of the time-averaged intensity, while the flexibility and the size distribution can be estimated from DLS. For the special case of self-similar aggregates and size distribution treated in this chapter, the structure can be obtained over a wide range of distance scales by the combination of measurements on aggregates at different stages of the growth process. At finite concentration, scattering techniques can give information on the interaction and the extent of inter-penetration of the aggregates. Monte Carlo type simulation of model aggregation processes are very helpful for the interpretation of experimentally observed structure factors. They give new insight into the gradual change of the structure and the size distribution of the clusters which is directly related to the increase of the space filling during the aggregation process.

Appendix 6.A: list of symbols

$A(\tau_r)$	relaxation time distribution
β	exponent of the stretched exponential cut-off of the cluster distribution
C	number concentration of monomers in the scattering volume
C^*	number concentration of monomer $V_{cum} = 1$. Also called the overlap concentration
$\delta(r)$	Dirac function
d_f	fractal dimension of clusters
d_f^*	apparent fractal dimension
d_{fb}	fractal dimension of percolating clusters in bulk
d_{fs}	fractal dimension of swollen percolating clusters
ϕ_0	monomer volume fraction
$f(r/\xi)$	cut-off function of $g_m(r)$
γ	exponent of the stretched exponential cut-off of $g_m(r)$
$\Gamma(x)$	gamma function
$g(r)$	pair correlation function of the whole system
$g_1(t)$	autocorrelation function of the scattered electric field
$g_2(t)$	autocorrelation function of the scattered light intensity
$g_m(r)$	pair correlation function of a cluster; also called pair correlation function of connectivity
$g_w(r)$	weight-averaged pair correlation function of clusters in the system

η_s	viscosity of the solvent
$h(r)$	distribution function of distances inside an aggregate
$I(q)$	excess light scattered by aggregates in the scattering volume
k_B	Boltzmann constant
K	constant depending on the apparatus and the polymer studied
m	aggregation number
m_a	apparent aggregation number measured in concentrated systems
m_w	weight-averaged aggregation number
m^+	characteristic aggregation number such that the cumulative volume fraction of all clusters with $m < m^+$ is equal to one
m^*	characteristic cut-off aggregation number in $N(m)$
M_a	apparent molar mass
M_n	number-averaged molar mass
M_w	weight-averaged molar mass
$N(m)$ or N	number of clusters with aggregation number m in the scattering volume
p	exponent of the power-law distribution of the relaxation time
$P(q)$	form factor of the monomer
q	scattering wave vector
r	distances in Euclidean space
r_0	radius of a monomer
$R_g(m)$	radius of gyration of a cluster with aggregation number m
R_{ga}	apparent radius of gyration measured in the concentrated system
R_{gz}	z -average radius of gyration of the cluster distribution
R_g^+	radius of gyration of aggregates with $m = m^+$
R_h	hydrodynamic radius of a cluster
s	exponent of the stretched exponential cut-off of the relaxation time distribution
$S(q)$	static structure factor of the whole system
$S_m(q)$	static structure factor of the centres of mass of an aggregate
$S_z(q)$	z -average static structure factor of the cluster distribution
τ	exponent of the power-law distribution of clusters
τ_0	arithmetic average of the relaxation time distribution
τ_g	characteristic cut-off relaxation time in $A(\tau)$
τ_h	relaxation time of a cluster with aggregation number m
τ_r	relaxation time
t	time
V_{cum}	cumulative volume fraction occupied by aggregates in the system
V_{eff}	effective volume fraction occupied by aggregates in the system
$V_{i,j}$	excluded volume generated by a cluster with an aggregation number i with respect to another cluster with aggregation number j
$V(m)$	volume fraction occupied by a cluster with an aggregation number m
ξ	characteristic cut-off size in $g_m(r)$
ξ_s	characteristic cut-off size in $g(r)$

- z_1 average number of contacts per monomer in a cluster; it is also the average number of monomers located in the primary shell of another monomer
- z_2 average number of monomers located in the secondary shell of another monomer

References

1. Stauffer, D. (1985). *Introduction to percolation theory*. Taylor and Francis, London.
2. de Gennes, P. G. (1979). *Scaling concepts in polymer chemistry*. Cornell University Press, London.
3. Mandelbrot, B. (1982). *The fractal geometry of nature*. W. H. Freeman, New York.
4. Gimel, J. C., Durand, D. and Nicolai, T. (1995). *Phys. Rev. B*, **51**, 11348.
5. Cotton, J. P. (1991). In *Neutron, X-ray and light scattering* (eds P. Linder and Th. Zemb), p. 3. North-Holland Delta Series, Elsevier, Amsterdam.
6. Schmitz, K. S. (1990). *Dynamic light scattering by macromolecules*, p. 11. Academic Press, London.
7. Teixeira, J. (1986). In *On growth and form* (eds H. E. Stanley and N. Ostrowsky), p. 145. Martinus Nijhoff, Dordrecht.
8. Hasmy, A., Foret, M., Pelous, J., and Jullien, R. (1993). *Phys. Rev. B*, **48**, 9345.
9. Bennett, C. H. (1972). *J. Appl. Phys.*, **43**, 2727.
10. Dimon, P., Sinha, S. K., Weitz, D. A., Safinya, C. R., Smith, G. S., Varady, W. A., and Lindsay, H. M. (1986). *Phys. Rev. Lett.*, **57**, 595.
11. Debye, P. (1947). *J. Phys. Colloid Chem.*, **51**, 18.
12. Klein, R., Weitz, D. A., Lin, M. Y., Lindsay, H. M., Ball, R. C., and Meakin, P. (1990). *Progr. Colloid Polym. Sci.*, **81**, 161.
13. Fisher, M. E. and Burford, R. J. (1967). *Phys. Rev.*, **156**, 583.
14. Nicolai, T., Durand, D., and Gimel, J. C. (1994). *Phys. Rev. B*, **50**, 16357.
15. Berne, B. J. and Pecora, R. (1976). *Dynamic light scattering with application to chemistry, biology and physics*. John Wiley, New York.
16. Nicolai, T., Gimel, J. C., and Johnsen, R., *J. Phys. II France*, accepted.
17. von Smoluchowski, M. (1916). *Phys. Z.*, **17**, 585.
18. von Smoluchowski, M. (1917). *Z. Phys. Chem.*, **92**, 129.
19. Flory, P. J. (1953). *Principles of polymer chemistry*. Cornell University Press, New York.
20. Stockmayer, W. H. (1943). *J. Chem. Phys.*, **11**, 45.
21. Stockmayer, W. H. (1944). *J. Chem. Phys.*, **12**, 125.
22. Jullien, R. and Botet, R. (1987). *Aggregation and fractal aggregates*. World Scientific, Singapore.
23. Cohen, R. J. and Benedeck, G. B. (1982). *J. Chem. Phys.*, **86**, 3696.
24. Ball, R. C., Weitz, D. A., Witten, T. A., and Leyvraz, F. (1987). *Phys. Rev. Lett.*, **58**, 274.
25. Meakin, P. (1983). *Phys. Rev. Lett.*, **51**, 1119.
26. Kolb, M., Botet, R., and Jullien, R. (1983). *Phys. Rev. Lett.*, **51**, 1123.
27. Vicsek, T. (1989). *Fractal growth phenomena*. World Scientific, London.
28. Meakin, P. (1993). *Physica Scripta*, **46**, 295.
29. Durand, D. (1986). In *Polymer yearbook*, p. 229. Harwood Academic Publishers, 3.
30. Stauffer, D. (1986). In *On growth and form* (eds H. E. Stanley and N. Ostrowsky), p. 79. Martinus Nijhoff, Dordrecht.

31. Leath, P. L. (1976). *Phys. Rev. B*, **14**, 5046.
32. Daoud, M. (1989). *Prog. Reaction Kinetics*, **15**, 1.
33. Daoud, M. and Martin, J. E. (1989). In *The fractal approach to heterogeneous chemistry: surfaces, colloids, polymers* (ed. D. Avnir), p. 109. John Wiley, New York.
34. Morawetz, H. (1975). *Macromolecules in solution*. Robert E. Krieger, Malabar, second edition.
35. Higgins, J. S. and Benoît, H. C. (1994). *Polymers and neutron scattering*. Oxford University Press, Oxford.
36. Carpineti, M. and Goglio, M. (1992). *Phys. Rev. Lett.*, **68**, 3327.
37. Carpineti, M. and Goglio, M. (1993). *Phys. Rev. Lett.*, **70**, 3828.
38. Daoud, M. and Leibler, L. (1988). *Macromolecules*, **21**, 1497.
39. Gimel, J. C., Durand, D., and Nicolai, T. (1994). *Macromolecules*, **27**, 583.
40. Gimel, J. C. (1993). Thesis, ENSIA, Massy, France.
41. Leyvraz, F. (1986). In *On growth and form* (eds H. E. Stanley and N. Ostrowsky), p. 136. Martinus Nijhoff, Dordrecht.
42. van Dongen, P. G. J., and Ernst, M. H. (1985). *J. Phys. A: Math. Gen.*, **18**, 2779.
43. Degoulet, C., Nicolai, T., Busnel, J. P., and Durand, D. (1995). *Macromolecules*, **28**, 6819.
44. Lesturgeon, V., Nicolai, T., Durand, D., submitted to *Europhys. Lett.*
45. Adam, M., Delsanti, M., Munch, J. P., and Durand, D. (1987). *J. Phys. France*, **48**, 1809.
46. Bouchaud, E., Delsanti, M., Adam, M., Daoud, M., and Durand, D. (1986). *J. Phys. France*, **47**, 1273.
47. Adam, M., Lairez, D., Boué, F., Busnel, J. P., Durand, D., and Nicolai, T. (1991). *Phys. Rev. Lett.*, **67**, 3456.
48. Durand, D., Adam, M., Delsanti, M., and Munch, J. P. (1988). In *Universalities in condensed matter physics* (eds R. Jullien, L. Peleti, R. Rammal and N. Boccara), p. 27. Springer Proceedings in Physics, Springer-Verlag, **32**.
49. Munch, J. P., Delsanti, M., and Durand, D. (1992). *Europhys. Lett.*, **18**, 577.

Polymer–polymer interactions in dilute solution

Jim Selser

7.1 Introduction and background

This chapter deals with interactions between polymers in dilute solution. The chapter does not present a summary either of the results of an extensive search of the relevant literature to date or of a consideration of the behaviours of all possible kinds of polymers under all possible circumstances. Instead, it deals primarily with light scattering studies of interactions in binary systems between non-electrolytic polymer coils, carried out by the author and his coworkers. Two themes emphasized throughout this chapter are: (1) the benefits of using static light scattering ('SLS') and the dynamic light scattering technique of photon correlation spectroscopy ('DLS') together to investigate polymer–polymer interactions in dilute solution (see Chapter 8 of ref. 6 and Chapter 13 of this volume), and (2) the interplay between intra-polymer and inter-polymer behaviour in dilute solution. Special attention is given to the recent development and use of a particularly powerful experimental method in which both SLS and DLS are employed to 'map out' the behaviour of coil–coil interactions in binary solutions over a wide range of solution solvent quality.^[1–3]

In general, polymer–polymer interactions, even in dilute solution and even for non-electrolytic polymers, are complex. For example, it is well known that linear, flexible non-electrolytic polymers swell in good solvents and coil–coil interactions in solution are stronger as a result of the increase in coil size.^[4,5(a)] For linear, flexible polyelectrolytes in aqueous solution, the situation is even more complex (ref. 7, Chapter 7 in ref. 6 and Chapter 4 this volume). In addition to the behaviour described above, other important interactions occur. Examples of interactions which can play critical roles both in intra-polymer and inter-polymer behaviour include long-range charge–charge interactions, shorter-range dipole–dipole interactions, and salt–ion concentration fluctuations which couple to polymer motions.

In the rich aqueous milieu of biopolymers, the diversity of such situations is particularly great.^[8,9] There is extensive variety in the sizes, shapes and functions of such macromolecules which typically coexist in concentrated multicomponent media. Typical environments include proteins, viruses, cell organelles, salts, and so on. Important interactions in these surroundings include hydrogen bonding and the hydrophobic effect, both of which are critical to the formation and stabilization of the structure of DNA in solution, for

example.^[19] The application of SLS to the study of biopolymer interactions is treated in refs 8 and 10, while that of DLS is treated in refs. 11 and 12 and in Chapter 15 of ref. 6.

A variety of tools is routinely used for studying the physical properties of macromolecular solutions. Especially difficult problems necessitate attack using an arsenal of experimental methods, including light scattering. Of these methods, light scattering is especially useful and powerful as it provides a non-invasive method for studying both the sizes, conformations and equilibrium interactions of these macromolecules, using static light scattering, along with studies of macromolecular dynamic behaviour using dynamic light scattering. For macromolecules, the DLS technique of photon correlation spectroscopy has proven especially useful for investigating polymer translational motions, intra-polymer motions, and interactions between polymers.^[6,11–18]

7.2 Macromolecular behaviour in dilute solutions

7.2.1 Equilibrium behaviour

The effect at equilibrium of interactions between non-electrolytic macromolecules in a binary solution may be described by an expression of the same form as that describing interactions between the molecules comprising a dilute gas. For dilute solutions of non-electrolytes, McMillan and Mayer^[19] showed that the solution osmotic pressure, π , can be expressed as a polynomial expansion in the solute concentration, c , which has the same form as the virial expansion for non-ideal gases,

$$\pi = RT \left(\frac{1}{M} c + A_2 c^2 + A_3 c^3 + \dots \right), \quad (7.1)$$

with M the solute molar mass, the A_n the virial coefficient, the gas constant $R = N_A k_B$, and N_A and k_B the Avogadro and Boltzmann constants, respectively. When the A_n vanish, ideal solution behaviour obtains. For sufficiently dilute solutions, as for gases at low density, pairwise interactions dominate and the expansion may be truncated after the second term on the right-hand side. Thus the osmotic second virial coefficient, A_2 , is an important parameter describing equilibrium behaviour associated with polymer–polymer interactions in dilute solution. In general, dilute solution physical properties may be treated using analogous virial expansions in the solute molecule concentration.

7.2.1.1 Static light scattering. It is possible to characterize the medium fluctuations associated with static light scattering in a variety of ways. A particularly useful characterization for SLS measurements from binary polymer solutions is in terms of thermally activated osmotic pressure fluctuations associated with polymer concentration fluctuations. In this characterization, the link between the thermodynamic behaviour of the scattering system and the intensity of the associated scattered light itself is particularly evident.

For dilute binary solutions, osmotic pressure fluctuations associated with polymer concentration fluctuations, $\partial\pi/\partial c$, may be expanded in the polymer concentration, c , as

$$\frac{\partial\pi}{\partial c} = RT \left(\frac{1}{M} + 2A_2c + 3A_3c^2 + \dots \right). \quad (7.2)$$

For stationary processes, $I_s(q)$ is used to represent the time-averaged, ‘excess’ scattering intensity due to polymer solution concentration fluctuations—above that due to solvent density fluctuations—which is directly proportional to the associated dimensionless *scattering function*, $S(q)$: $I_s(q) \sim S(q)$. In turn, $S(q) \sim \partial\pi/\partial c$.

For the *isolated* macromolecule with n scattering segments

$$S(q) = \frac{1}{n^2} \sum_{j,k} e^{i\vec{q} \cdot \vec{r}_{jk}} \quad (7.3)$$

with $\vec{r}_{j,k}$ the displacement vector connecting polymer segment pairs comprising the macromolecule, indexed by j and k . The magnitude of the scattering wavevector, \vec{q} , $q = (4\pi n/\lambda_0) \sin(\theta/2)$, with n the solvent refractive index, λ_0 the vacuum wavelength of the incident light and θ the scattering angle. Since the size of the fluctuation probed varies inversely as q , fluctuations of small spatial extent, i.e. ‘local’ structure, is probed for large q while fluctuations of large extent, or ‘global’ structure, is probed for small q .

For dilute solutions of macromolecules, as $q \rightarrow 0$, the relationship between the scattering function and the fluctuations in the solution osmotic pressure with polymer concentration, $\partial\pi/\partial c$, takes the explicit form:^[5(a)]

$$S(0) = \frac{RT}{M(\partial\pi/\partial c)}. \quad (7.4)$$

Combining eqns (7.2) and (7.4),

$$S(0) = (1 + 2A_2Mc + 3A_3Mc^2 + \dots)^{-1}, \quad (7.5)$$

so that as $c \rightarrow 0$, $S(0) \rightarrow 1$, the isolated polymer result.

As $c \rightarrow 0$, i.e. for the isolated polymer and for sufficiently small but non-zero q , intrapolymer interference contributes to $I_s(q)$ and, for macromolecules of any shape, $S(q)$ is given by

$$S(q) = 1 - q^2 R_G^2 / 3 + O(q^4 R_G^4), \quad (7.6)$$

with R_G the radius of gyration of the molecule. Now as $q \rightarrow 0$, the light scattering probe length becomes large compared to the dimensions of the macromolecule and the distances to, and phases of the scattered light, at the detector from each scattering segment within the macromolecule are essentially the same. Then, $S(0) = 1$ (see eqn (7.3)).

The *spatial* behaviour of $I_s(q)$ is reflected in its dependence on the scattering wavevector, \vec{q} , with differing \vec{q} values corresponding to scattering at differing

scattering angles from differing Fourier components of the polymer concentration fluctuation in solution. Because at finite polymer concentrations as $q \rightarrow 0$ the length probed in a light scattering measurement becomes large, the entire scattering volume containing many macromolecules is sampled. As a result, the measurement records the effects of macromolecular interactions in the solution, as seen by the appearance of the virial coefficients in eqn (7.5).

The method used to analyse the results of the SLS studies discussed below will be described here only briefly, since it is a standard method, described in detail in ref. 10, for example. In this method, as with other SLS methods, it is the reciprocal of $I_s(q)$ rather than $I_s(q)$ itself which is used in the analysis. As is conventional, the dependencies of the parameter Kc/R_θ on polymer concentration and on q^2 are employed in the analysis. K is the conventional, experimentally determined optical constant for binary solutions and $I_s(q)$ is proportional to the Rayleigh 'ratio', R_θ .^[5(a), 10]

From eqn (7.5), it is seen that the reciprocal of $S(q)$, as $q \rightarrow 0$, depends linearly on the polymer concentration, c . Thus in the limit $q \rightarrow 0$, the slope of $S(0)$ versus c is proportional to the equilibrium pairwise polymer-polymer interaction parameter, A_2 .

In SLS measurements of polydisperse dilute polymer solutions,^[5(a)] the concentration and q dependencies of Kc/R_θ when measured at sufficiently small q may be written as

$$Kc/R_\theta = \frac{1}{P(q)M_w} + 2A_2c + \dots \quad (7.7a)$$

and as $q \rightarrow 0$, $P(q) \rightarrow 1 - q^2 R_G^2/3$, so that

$$Kc/R_\theta = \frac{1}{M_w} (1 + q^2 R_G^2/3) + 2A_2c, \quad (7.7b)$$

with M_w the polymer weight-averaged molar mass and $P(q)$ the macromolecule form factor accounting for the interference of light scattered from different segments of the same polymer chain. Note that $P(q) \sim S(q)$. For scattering angles sufficiently small that the second term in the parentheses of eqn (7.7b) is negligible (see Chapter 12 in this volume, 'Low angle light scattering and its applications'), M_w and A_2 are then determined from the intercept and slope, respectively, of linear fits to the concentration dependence of Kc/R_θ . Alternatively, R_G and M_w may be determined from the slope and intercept, respectively, of linear fits to the q^2 dependence of Kc/R_θ in the limit $c \rightarrow 0$.

Estimates of M_w and A_2 from determinations of the concentration dependence of Kc/R_θ made at small scattering angles may be improved, particularly for large polymers, by fits to 'square-root' plots,^[20] i.e. by fits to

$$\left(\frac{Kc}{R_\theta}\right)^{1/2} = \left(\frac{1}{M_w}\right)^{1/2} [1 + A_2 M_w c]. \quad (7.7c)$$

Using a low angle laser light scattering photometer,^[3] this approach was used to both measure M_w values and to extract A_2 values for nine well characterized poly(α -methylstyrene) (P α MS) samples for good, marginal, theta and sub-theta solvent quality conditions. A_2 values were then combined with P α MS diffusion coefficient results from DLS measurements, as described below, to 'map out' dilute solution P α MS-P α MS interactive behaviour across this wide range of solvent quality.

Using 'Zimm plot' analyses,^[5(a),21] both $q \rightarrow 0$ and $c \rightarrow 0$ limiting behaviour from studies of the angular and concentration dependencies of the light scattered from dilute macromolecular solutions provides R_G , A_2 and M_w values for the polymer in solution. Zimm plot analyses, along with the results of DLS and viscosity measurements, were used in the study of polymer-polymer interactions for polyethylene oxide in aqueous solutions, as discussed below.

7.2.2 Dynamic behaviour

While the equilibrium behaviour of dilute polymer solutions has been reasonably comprehensively understood for some time, principally in terms of the 'two parameter' theory (see refs 4 and 5, for example), more recent developments^[22-24] have stimulated renewed interest in polymer solution behaviour generally, and in the issue of polymer dynamics in solution in particular.

In this regard, the work of Akcasu and Akcasu and Han and coworkers^[1,2] is especially relevant here as it deals specifically with the interplay between polymer dynamic and equilibrium behaviour, and its results and predictions are cast expressly in terms of parameters determined by static and dynamic light scattering measurements on dilute polymer solutions. This work provides the framework for the interpretation of SLS and DLS studies of the interactions of linear, flexible coils in dilute solution such as the P α MS-P α MS interaction study described in some detail below.

7.2.2.1 Dynamic light scattering. The intensity autocorrelation function of light scattered from a polymer solution expressed in terms of instantaneous intensities, and intensities time shifted by t , $\langle I(q, t)I(q, 0) \rangle$, can be measured in the DLS technique of photon correlation spectroscopy (see ref. 11, for example). After normalization by the baseline, the resulting dimensionless intensity autocorrelation function, $g_2(q, t)$, is

$$g_2(q, t) = \frac{\langle I(q, t)I(q, 0) \rangle}{\langle I^2(q, 0) \rangle}. \quad (7.8)$$

Then, it is usually the associated field autocorrelation function, $|g_1(q, t)|$, that is analysed, with

$$g_2(q, t) = 1 + \beta|g_1(q, t)|^2. \quad (7.9)$$

β , an experimental constant, is determined primarily by the collection efficiency of the detection apparatus. The relationship between $|g_1(q, t)|$ and the dynamic

scattering function, $S(q, t)$, is given by

$$|g_1(q, t)| = S(q, t)/S(q, 0). \quad (7.10)$$

For $q \rightarrow 0$, macromolecules appear ‘point-like’ so that $S(q, t)$ becomes insensitive to polymer orientational and internal motions and consequently only the effect of centre-of-mass (CM) translational motions appear in $S(q, t)$. Then

$$S(q, t) = S_{CM}(q, t) = S(0) e^{-Dq^2 t}, \quad (7.11)$$

with D the concentration-dependent polymer mutual diffusion coefficient. The measurement of D as $q \rightarrow 0$ for dilute solutions reflects the detection of relative motions between macromolecule centres of mass, mutual diffusion, i.e. in the scattering volume. These relative motions give rise to phase fluctuations in the scattered light electric field, and thereby to the scattered light intensity fluctuations that the detector responds to. Scattering from fluctuations resulting from the movement of molecules into and out of the scattering volume contributes negligibly to measured autocorrelation functions in these experiments. As a practical matter, it is usually found that reliable measurements of D do not require the extrapolation to $q = 0$ of multiple $D(q)$ measurements, but can instead be made at a single, experimentally accessible scattering angle, and incident light wavelength, for ‘sufficiently small’ values of q .

Experimentally, D is found to exhibit concentration dependence of the form

$$D(c) = D_0(1 + k_D c + \dots) \quad (7.12)$$

with D_0 the isolated polymer diffusion coefficient.

The nature of the dependence of D on solution concentration is seen through^[5(b)]

$$D(c) = \frac{M(1 - \bar{v}c)^2}{N_A f(c)} \left(\frac{\partial \pi}{\partial c} \right), \quad (7.13)$$

with \bar{v} the polymer partial specific volume in solution. With $\partial \pi / \partial c$ as in eqn (7.2) and the polymer friction coefficient concentration dependence given by^[5]

$$f(c) = f_0(1 + k_s c + \dots), \quad (7.14)$$

and retaining terms in eqn (7.13) up to order c , the diffusion virial coefficient, k_D , is

$$k_D = 2A_2 M - k_s - 2\bar{v}. \quad (7.15)$$

Thus, k_D , a ‘dynamic’ interaction parameter, incorporates the effect both of polymer–polymer equilibrium interactions, manifested in A_2 , and the effects of polymer–polymer hydrodynamic interactions, manifested in k_s .

Assigning a volume $V_H = 4\pi R_H^3/3$ to each macromolecule in solution, k_D is expressed in volume fraction units as

$$k_D^\phi = \frac{M}{N_A V_H} k_D, \quad (7.16)$$

with R_H the hydrodynamic radius of the isolated macromolecule:

$$R_H = k_B T / 6\pi\eta_0 D_0. \quad (7.17)$$

Then

$$D(\phi) = D_0(1 + k_D^\phi\phi), \quad (7.18)$$

with $\phi = \bar{v}c$ the polymer volume fraction in solution. To study polymer-polymer interactions in solution, attention is then focused on the behaviour of the diffusion virial coefficient, k_D^ϕ .

7.3 k_D^ϕ versus X ‘maps’

In the Akcasu-Benmouna (A-B) treatment, it is shown that this behaviour may be studied via SLS and DLS by tracking experimentally determined values of k_D^ϕ as solution solvent quality progresses from that corresponding to the theta condition, through that for poor and intermediate qualities, to that ultimately corresponding to the good solvent system. Light scattering determinations of k_D^ϕ are then plotted as a function of the reduced interaction length $X = \bar{S}/R_H$, i.e. in terms of the interaction length X expressed in units of the macromolecule size. X , like k_D^ϕ , reflects both equilibrium and dynamic behaviour and includes the effects both of polymer molecular weight and system temperature. \bar{S} , which is obtained from A_2 , is an equilibrium interaction length corresponding to the effective radius of a hypothetical, equivalent hard sphere used to represent polymer coils in solution:^[5(a)]

$$\bar{S} = (3M^2 A_2 / 16\pi N_A)^{1/3}. \quad (7.19)$$

These k_D^ϕ versus X plots, or maps, are then used to assess theoretical treatments predicting k_D^ϕ behaviour. Different treatments differ mainly in the choice of model used to characterize the polymer-polymer interaction potential in solution. Thus far, the A-B approach has been confined to investigations of the interactive behaviour of synthetic, linear, flexible polymers—‘coils’—in solution. As stated at the outset, macromolecular coils in dilute solution are the focus of attention here.

In volume fraction units and in terms of the reduced length, X ,

$$k_D^\phi = 8X^3 - k_s^\phi, \quad (7.20)$$

with the polymer partial specific volume ignored as it contributes negligibly to k_D^ϕ for larger polymers. In the original A-B treatment^[1(a)]

$$k_D^\phi = X^2(8X - 6) \quad (7.21)$$

with

$$X^3 = \frac{3}{8R_H^3} \int_0^\infty R^2[1 - g(R)] dR \quad (7.22)$$

and $g(R)$ the pair correlation function for coils having a centre-of-mass separation, R .

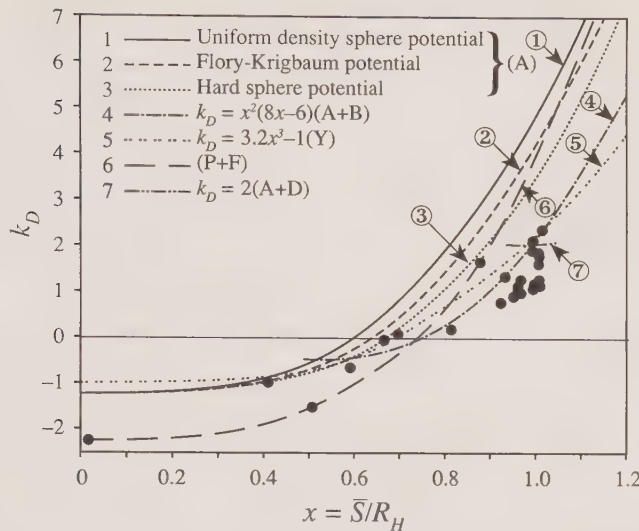


FIG. 7.1. A k_D^ϕ versus X map for polystyrene and poly(α -methylstyrene) along with theoretical predictions. A + B, Akcasu and Benmouna; Y, Yamakawa; P + F, Pyun and Fixman; A + D, Altenburger and Deutsch (from ref. 2(a), with permission).

The initial application of the A-B approach to the light scattering study of polymer-polymer interactions in dilute solution is summarized in Fig. 7.1, which is taken from ref. 2(a). In this study, A_2 and k_D^ϕ results for two narrow molecular weight distribution, high molecular weight polystyrene samples were combined with earlier polystyrene and P α MS data to yield the 22 data points presented on the plot. These data represent a solvent quality, ranging from theta through intermediate to good. From these results, it was concluded that while the Yamakawa^[5(a)] and A-B treatments adequately described good and intermediate solvent quality behaviour, and the Pyun-Fixman (P-F) treatment^[25] provided a better description of poor and theta solvent behaviour, no treatment adequately explained the observed behaviour over the entire solvent quality range. These results demonstrated that more quantitative comparisons between experiment and theory would require additional theoretical and computational effort—along with additional measurements, since excessive scatter in the data precludes adequate quantitative comparison with more sophisticated theoretical treatments, anyway.

The second use of the A-B map to characterize coil-coil interactions in dilute solution is that cited as ref. 2(b). In this study, earlier results for SLS and DLS measurements of a single, high molecular weight poly(2-vinyl pyridine) sample in tetrahydrofuran made in intermediate and good solvent quality systems were combined with earlier polystyrene and P α MS data from several workers. The conclusions from this work were essentially those presented in ref. 2(a). Again, there was considerable scatter in the data (Fig. 7.2), and thus the need for

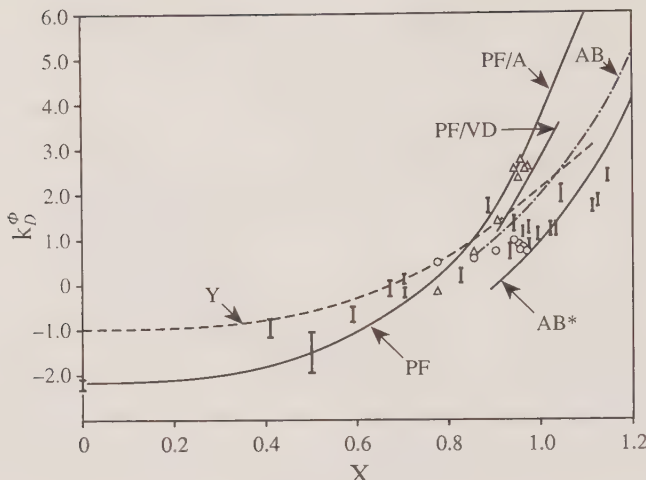


FIG. 7.2. A k_D^ϕ versus X map with the data from Fig. 7.1 (vertical bars) and poly(2-vinyl pyridine)/tetrahydrofuran data (open circles, triangles) along with theoretical predictions: PF, PF/A, PF/VD, 'pure' Pyun and Fixman and two variations: AB, AB*, Akcasu and Benmouna and an AB variation (from ref. 2(b), with permission).

'tighter' measurements to allow a more quantitative test of theory versus experiment was even more apparent.

Given the need for better k_D^ϕ versus X maps for the reasons cited above, SLS and DLS were used to study the interaction behaviour of one set of nine well characterized, narrow molecular weight distribution P α MS samples.^[3] These samples ranged in molecular weight from 6300 to 2 900 000, and were studied for sub-theta, theta, poor, marginal and good solvent quality conditions.

The theta through good solvent quality results for the nine P α MS samples are summarized in the k_D^ϕ versus X map presented as Fig. 7.3. The indicated error bars notwithstanding (these were very conservatively estimated, and the small scatter in the data suggests they were exaggerated), the data in Fig. 7.3 are sufficient in number and quality to provide a meaningful test, via k_D^ϕ versus X maps, of theories describing coil-coil interactions in dilute solution across the solvent quality range from theta to good. As for the earlier studies presented in refs 2(a) and 2(b), the Yamakawa and original A-B theories provided a reasonable description of the data for good and intermediate solvent qualities, while the P-F treatment described the theta and poor solvent behaviour reasonably well. Neither treatment described the data adequately over the entire solvent quality range.

Differences in theoretical treatments of coil interpenetration and consequent coil segment redistribution during binary encounters are thought to be mostly responsible for differences in the way in which different treatments describe the k_D^ϕ versus X data.^[11] For example, the original A-B treatment^[1(a),(b); 2(b)] replaced the distance between segment pairs on different polymers by the separation

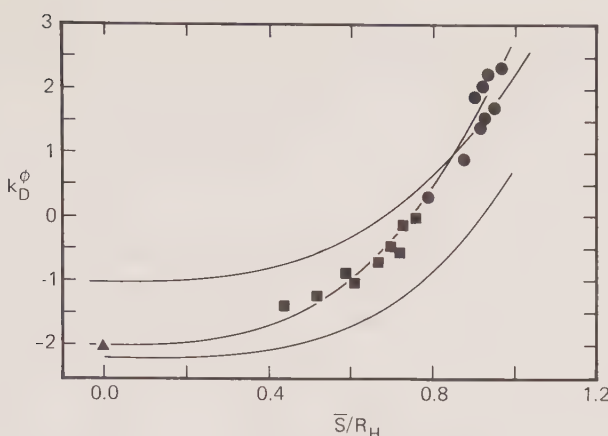


FIG. 7.3. A k_D^ϕ versus X map for poly(α -methylstyrene). Upper curve: Yamakawa treatment, Lower curve: treatment of Pyun and Fixman, Fit curve: semi-empirical fit based on treatment of Akcasu and Benmouna (from ref. 3, with permission).

distances of their respective centres of mass, an assumption justified in intermediate and good solvent systems in which polymer interpenetration and associated coil segment redistribution is relatively insignificant—but inadequate to treat interactive behaviour in theta and poor solvent systems. By contrast, Pyun and Fixman accounted for shape changes in polymer coils that were spherically symmetric before interpenetration by assuming that during a binary encounter, coils maintain their spherical shapes and segment distributions even though the interpenetrating pair take on an ellipsoidal shape—an attractively simple approach which provided a reasonably realistic account of interpenetration behaviour in poor and theta solvents. However, judging from the k_D^ϕ versus X plots from this and earlier studies, the P-F treatment did not adequately account for a reduction in the effects due to interpenetration as solvent quality improved.

Since publication of the results of the first two k_D^ϕ versus X studies, Akcasu modified the original A-B treatment describing coil-coil interactions in dilute solution.^[1(c)] Specifically, k_s^ϕ was modified to $k_s^\phi = 6Y^2$, so that

$$k_D^\phi = 8X^2 - 6Y^2 \quad (7.23)$$

with

$$Y^2 = \frac{1}{2R_H^2} \int_0^\infty R[1 - g(R)] dR. \quad (7.24)$$

Since Y^2 is positive and X may be positive, zero or negative, eqn (7.23) can qualitatively reproduce k_D^ϕ data behaviour over the entire solvent quality range from sub-theta to good. Note also that in good solvents $Y \cong X$ and the original A-B treatment result for k_s^ϕ is retained. Thus, eqn (7.23) should provide a better

description of polymer–polymer interactions in poor and theta solvent systems than its predecessor, eqn (7.20) (see ref. 1(b) and Chapter 1 of ref. 6). However, as yet there is no satisfactory general theoretical description for Y . Currently, the effects of interpenetration on polymer segment distributions during binary encounters are studied primarily via computational treatments of coil–coil interactions (ref. 23 in ref. 1(b)).

With limited theoretical or computational results available to provide $Y(X)$, a semi-empirical approach to its characterization was taken in ref. 3. Making use of the proportionality, $Y^2(X) \sim X^3$, a polynomial least-squares fit to the data of Fig. 7.3 for $X \geq 0$ provided a good description of P α MS–P α MS interactions over the solvent quality range from theta to good, viz.:

$$Y(X) = (0.33 + 0.53X^3)^{1/2}. \quad (7.25)$$

Then

$$k_s^\phi(X) = 3.2X^3 + 2.0 \quad (7.26)$$

and

$$k_D^\phi(X) = 4.8X^3 - 2.0. \quad (7.27)$$

Equation (7.25) provides reliable Y values determined directly from light scattering measurements across the solvent quality range corresponding to $0 \leq X \leq 1$, which can be used to test theoretical and computational predictions.

An important result of this analysis is that the interactive behaviour of P α MS coils in dilute solution, as manifested in the behaviour of the interactive parameter k_D^ϕ , may be described expressly in terms of X^3 , a term proportional to the coil volume (eqn (7.27)). In this respect, this result is reminiscent of the earlier Yamakawa result for coils in solution,^[5] $k_D^\phi = 3.2X^3 - 1$.

A particularly striking result of this study is illustrated in Fig. 7.4. Having

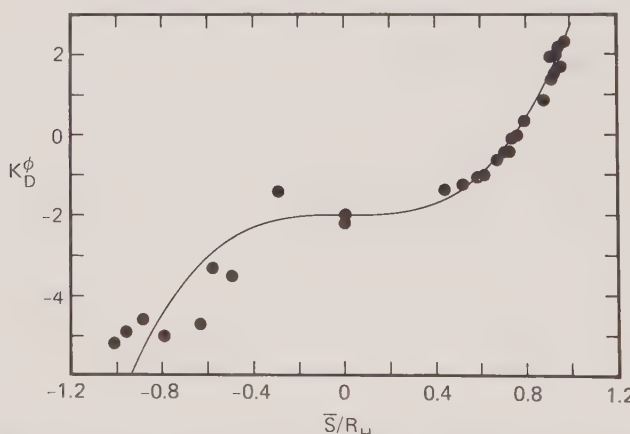


FIG. 7.4. A k_D^ϕ versus X for poly(α -methylstyrene) including sub-theta results with extension of the solvent quality range $-1 \leq X \leq 1$. The fit curve was made for data over the solvent quality range theta to good, $0 \leq X \leq 1$ presented in Fig. 7.3 (from ref. 3, with permission).

established earlier that P α MS solutions well below theta were stable,^[26] it was appreciated that the investigation of P α MS-P α MS interactions for sub-theta systems was possible. Figure 7.4 shows P α MS behaviour over the extended range $-1 \leq X \leq 1$. The fit in Fig. 7.4 throughout the range $-1 \leq X \leq 1$ is to eqn (7.27), based solely on the data for $X \geq 0$ (Fig. 7.3). Despite the scatter in the sub-theta results, the odd symmetry of the k_D^ϕ behaviour with X is evident. Equation (7.23) clearly admits k_D^ϕ behaviour below theta, and these P α MS results extend the range for which meaningful comparisons can be made between light scattering data and predictions of Y from eqn (7.23) into the sub-theta range of solvent quality. Such comparisons invite investigation of the physical nature of coil-coil binary encounters when X is negative. In this regard it is interesting to note that while X is an excluded volume parameter (eqn (7.22)), Y may be considered to be an excluded surface parameter (eqn (7.24)). Indeed, a recent treatment^[27] modelling A_2 for ellipsoidal polymeric globules formed from interpenetrating spheroidal coils, and dealing expressly with sub-theta behaviour, was developed based on the assumption that the interpolymer attraction between coils is driven by surface forces. This assumption is consistent with the role of Y in eqn (7.23) in determining the behaviour of coils experiencing binary encounters for sub-theta systems.

7.4 Polyethylene oxide studies

Polyethylene oxide (PEO), the only amphipathic member in the homologous series of linear polyethers, is a very interesting and very useful polymer (see refs 29–30 and references therein). PEO is sterically thin and very flexible and probably comes closer than any synthetic or biological polymer to behaving as the idealized linear, flexible ‘chain’ that theorists employ in their calculations. Having established that it is possible to prepare stable, aggregate-free aqueous solutions of PEO,^[28] the behaviour of seven well characterized, narrow molecular weight distribution PEO samples in water at 30 °C was studied using static and dynamic light scattering and viscometry.^[29,30] These samples ranged in molar mass from 86 000 to 996 000.

Zimm plot analyses (see Fig. 7.5) of SLS measurements on aqueous solutions of PEO provided M_W , A_2 and R_G results for each sample, while complementary DLS measurements on the same samples under the same conditions provided corresponding $D(c)$ and k_D^ϕ results.^[29] In addition, intrinsic viscosities were determined for the seven PEO samples in water under the same experimental conditions as those used for light scattering.^[30]

The molar mass dependencies of A_2 , R_G , R_H and k_D^ϕ ^[29] for PEO exhibited asymptotic good solvent behaviour in water at 30 °C, even for relatively small values of PEO molar mass (the smallest M_W value in this study was 86 000, but good solvating behaviour consistent with that reported in ref. 29 has since been reported for PEO having a molar mass as low as 8000^[31]). Specifically, it was

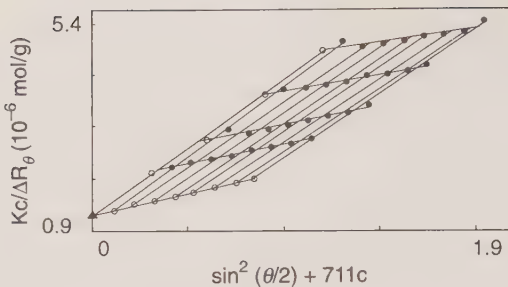


FIG. 7.5. A Zimm plot for 838 000 molar mass PEO in water at 30 °C (from ref. 29, with permission).

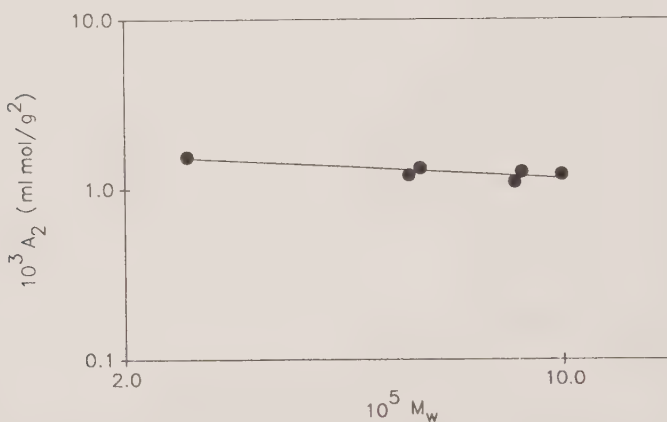


FIG. 7.6. A_2 results from SLS measurements of PEO in water at 30 °C. These results illustrate the asymptotic good solvent behaviour of PEO and the unusually large magnitude of these A_2 values (from ref. 29, with permission).

determined that

$$R_G \sim M_w^{0.583}, \quad (7.28)$$

$$R_H \sim M_w^{0.571} \quad (7.29)$$

and

$$A_2 \sim M_w^{-0.20}. \quad (7.30)$$

It was also discovered that the magnitudes of R_G and R_H values for PEO were large compared to those for other linear, flexible chains of comparable molar mass in good solvents. PEO A_2 values were especially large (Fig. 7.6). Ordinarily, polymer coils in good solvents exhibit hard-sphere behaviour with an interaction length \bar{S} approximately equal to the coil hydrodynamic radius^[3] so that $X = \bar{S}/R_H \approx 1$. By comparison, and although PEO exhibited 'hard-sphere' k_D^ϕ values, $k_D^\phi \approx 2$ (Fig. 7.7), it is noted that $X \cong 1.3$, which is

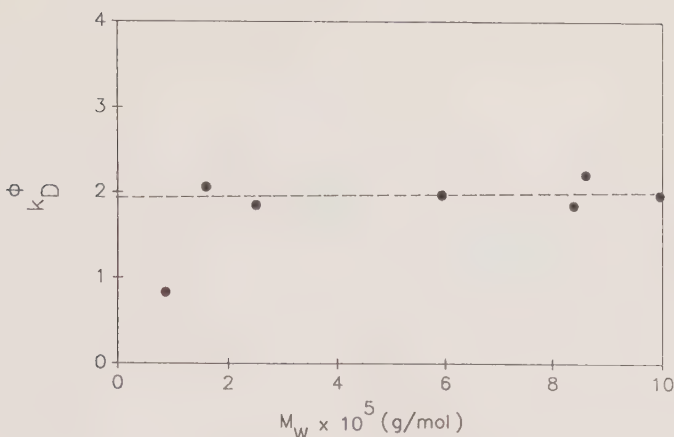


FIG. 7.7. The diffusion virial coefficient dependence on molar mass for PEO in water at 30°C. $k_D^\phi \approx 2$ is consistent with hard-sphere interactions in solution (from ref. 29, with permission).

unusually large compared to typical values^[3] of $X \approx 1$. It was concluded that long-range PEO-PEO interactions, particularly evident in the unusually large A_2 values, were responsible for the observed behaviour.

The conclusion that PEO-PEO interactions in water are long-range was supported by subsequent viscosity measurements.^[30] The viscosity study was carried out using the same PEO samples as used in the light scattering study for the same experimental conditions. As for A_2 , R_G and R_H in the light scattering studies, the PEO intrinsic viscosity, $[\eta]$, exhibited asymptotic good solvent behaviour:

$$[\eta] \sim M_W^{0.791}. \quad (7.31)$$

Combining the PEO light scattering and viscosity studies results was especially illuminating. The light scattering study^[29] yielded high values for the dimensionless ratios $X = \bar{S}/R_H$ and $\rho = R_G/R_H$. These high values provided evidence for PEO coil draining in solution since draining, particularly through coil outer portions, is consistent with relatively small coil hydrodynamic radii and relatively large \bar{S} and R_G . The viscosity study then revealed extraordinarily large values for the ratios $\Pi = M A_2/[\eta]$ and $k_s/[\eta]$. Π is a dimensionless parameter used to assess the interplay between coil draining and excluded volume effects, and $k_s/[\eta]$ were ‘mixed’ parameters expressible as ratios with numerators containing equilibrium variables such as A_2 and R_G and denominators containing hydrodynamic variables such as $[\eta]$ and R_H . While both equilibrium and dynamic factors, such as A_2 and R_H , were large, the unusually large magnitudes of the equilibrium factors – principally A_2 – were considered to be primarily responsible for the unusually large ratios. For example, Π may be expressed as the ratio of two molecular volumes:

$$\Pi = M A_2/[\eta] = V_{A_2}/V_\eta, \quad (7.32)$$

with

$$V_{A_2} = M^2 A_2 / N_A \quad (7.33)$$

and

$$V_\eta = M[\eta] / N_A. \quad (7.34)$$

A_2 in the numerator in eqn (7.32) is an unusually large equilibrium variable, while the denominator contains a combination of large, but not anomalously large, equilibrium and dynamic variables, $[\eta] \sim R_H R_G^2$. Moreover, A_2 is an equilibrium variable, while R_H is a hydrodynamic variable. Evidently, A_2 in the numerator is mostly responsible for the unusually large magnitude of Π .

By comparison, the interpenetration function, Ψ , determined from SLS measurements of A_2 and R_G and often used to assess the extent of interpenetration of polymers in binary encounters, was not usually large. Ψ may also be expressed as a ratio of molecular volumes:

$$\Psi = A_2 M^2 / 4\pi^{3/2} N_A R_G^3 \quad (7.36)$$

$$= 0.188 V_{A_2} / V_{R_G}, \quad (7.37)$$

with

$$V_{R_G} = 4\pi R_G^3 / 3. \quad (7.38)$$

Like X (actually X^3), Ψ is a dimensionless, equilibrium measure of the interaction (excluded) volume of the polymer in solution, but it is expressed in units of the volume associated with R_G rather than that associated with R_H . Unlike Π , Ψ is a ratio containing two purely equilibrium parameters, A_2 and R_G . The associated volume in the denominator of Π , V_{R_G} , does not reflect coil hydrodynamic behaviour and the ratio is therefore presumably unaffected by draining. Moreover, although each volume increased markedly as a result of excluded volume swelling, it did so keeping the value of Ψ in the ‘normal’ range. By contrast, the behaviour of Π underscores the connection between excluded volume behaviour and PEO intracoil hydrodynamic behaviour. It reflects the increase in coil draining with increasing excluded volume. However, even in the asymptotic good solvent limit with the coil exhibiting hard-sphere interactions,^[5] it is calculated that $\Pi = 1.6$, only. In fact, for PEO in water at 30 °C, the average value of Π was found to be 1.9, a value almost double that for typical coils in organic and solvents.^[30] The fact that this unusually large value for Π is distinctly larger than the hard-sphere value provides additional support for the contention that PEO–PEO interactions extend beyond the range of the equivalent hard sphere, and are thus long-range. Considering the special relationship PEO appears to have with water, it seems likely that the influence of PEO on water structure and behaviour plays a role in the long-range character of these interactions.

Unusually large $k_s/[\eta]$ ratios are also consistent with the picture of PEO–PEO interactions presented above. Neither k_s nor $[\eta]$ is a pure parameter, since both contain equilibrium and dynamic terms. Unusually large PEO $k_s/[\eta]$ values are due to the combined effects of A_2 in k_s and R_H in $[\eta]$. Again, since k_D values were of typical magnitude for this good solvent system, A_2 was mostly

responsible:

$$k_s = 2A_2M - k_D - 2\bar{v}. \quad (7.39)$$

7.5 Intra-coil behaviour and coil-coil interactions

Intra-polymer and inter-polymer behaviour are inextricably interrelated. For example, polymer coils swell as the solvent quality changes from poor to good, and both the equilibrium interaction parameter A_2 and the dynamic interaction parameter k_D increase. Coils in solution in particular exhibit many modes of diffusive motion as polymer segment concentration fluctuations form and dissipate. Associated with intra-coil relaxations is the translational diffusive movement of the coil as a whole. These two types of coil motion—*intra-coil* and *translational*—are effectively uncoupled (see, e.g., refs 2–5 in ref. 32(b)), and this decoupling allows for considerable simplification in the interpretation of scattered light autocorrelation functions from dilute solutions of polymer coils. For example, the scattering function may be factored so that

$$S(q, t) = e^{-\Gamma_0 t} S'(q, t), \quad (7.40)$$

with $\Gamma_0 = Dq^2$ corresponding to the translational CM motion of the coil as a whole. Note, however, that although the decay of the translational mode has been factored out of $S(q, t)$ in eqn (7.40), the *amplitude* of this mode remains in $S'(q, t)$.

The role that intra-polymer behaviour plays in polymer-polymer interactions is clearly delineated in the Akcasu-Benmouna treatment discussed above. In particular, the interaction parameter Y (eqn (7.23)) in k_D^ϕ ,

$$k_D^\phi = 8X^3 - 6Y^2, \quad (7.23)$$

reflects the redistribution of segments within polymer coils occurring during binary encounters. However, DLS measurements of k_D^ϕ in binary systems do not ‘look’ directly at coil internal motions, but measure instead the concentration-dependent coil translational diffusion coefficient, $D(c)$.

Recently, several approaches have been developed which use DLS to detect and characterize polymer coil internal motions directly. These developments have, for the most part, been summarized recently in Chapter 6 of ref. 6. Here, an alternative approach for investigating intra-coil dynamic behaviour is presented. This approach, developed expressly to study polymer coil internal dynamic behaviour, has been used thus far in two studies of intra-coil dynamic behaviour^[32(a),(b)] and the results of these studies relevant to coil coil interactions are discussed here.

In the study presented in ref. 32(a), the intra-coil behaviour of a very large, well characterized, narrow molecular weight distribution polystyrene (PS) standard was investigated using DLS in both good and theta solvents. It was found that for both solvents, and over a wide range of the parameter $x = q^2 R_G^2$, the mode structure of $|g_1(q, t)|$ changed from one narrow mode at very small x to two modes for small to intermediate x , and then reverted

back to a single, relatively broad mode for large x . At very small x , the PS coil translational mode was isolated experimentally from intra-coil modes because intra-coil mode amplitudes were negligible in magnitude in comparison to that of the translational mode. Thus for very small x , the electric field autocorrelation function, $|G_1(q, t)|$, was interpreted in terms of the coil CM translational diffusion in the usual way:

$$|G_1(q, t)| = I_{cm}(x) e^{-\Gamma_0 t}, \quad (7.41)$$

with I_{cm} the amplitude (intensity) of the CM mode and the autocorrelation functions related through $|G_1(q, t)|^2 = \beta B |g_1(q, t)|^2$, with B the intensity autocorrelation function baseline (see eqns (7.8) and (7.9)). Of the multitude of coil relaxation modes, only the translational mode in $|G_1(q, t)|$ could be directly separated and then isolated from the others, and this was accomplished experimentally via DLS measurements at very small x (eqn (7.41)).

For larger values of x , $|G_1(q, t)|$ was found to be somewhat more complicated,

$$|G_1(q, t)| = I_{cm}(x) e^{-\Gamma_0 t} + I_{int}(x) e^{-\bar{\Gamma} t}, \quad (7.42)$$

with coil internal mode relaxations lumped together in the second term describing $|G_1(q, t)|$. The intensity of the second relaxation, $I_{int}(x)$, represents the combined contributions of a number of intra-coil modes and its decay constant, $\bar{\Gamma}$, includes both Γ_0 and a decay constant $\Delta\bar{\Gamma}$ representing an averaged or 'collective decay' of a narrow band of detected intra-coil relaxations:

$$\bar{\Gamma} = \Gamma_0 + \Delta\bar{\Gamma}. \quad (7.43)$$

Again, the CM decay, $e^{-\Gamma_0 t}$, can be factored out of the rightmost term in eqn (7.42). At this stage, it was not possible to further separate out or isolate individual intra-coil relaxation modes in $|G_1(q, t)|$. However, as described below, a method was then developed for extracting the characteristic frequency (decay constant) of the slowest, overall intra-coil relaxation mode which was labelled $\Delta\bar{\Gamma}_1$.

Determinations of $\Delta\bar{\Gamma}$ from analyses of measured $|G_1(q, t)|$ were made by first making accurate determinations of Γ_0 at very small x and then factoring the CM decay, $e^{-\Gamma_0 t}$, out of both terms in eqn (7.42). However, even after this factorization, the CM mode amplitude, $I_{cm}(x)$, remained. Because $I_{cm}(x)$ might well be large in comparison to $I_{int}(x)$, accurate estimation of $\Delta\bar{\Gamma}$ could suffer. Therefore, to eliminate $I_{cm}(x)$ and thereby the contribution of the CM mode to $|G_1(q, t)|$ altogether, the product $e^{-\Gamma_0 t}|G_1(q, t)|$ was subtracted, for each point in each autocorrelation function measured, from the autocorrelation function intercepts, $|G_1(q, 0)|$. The resulting modified autocorrelation function, $H(q, t)$, then has the form

$$H(q, t) = |G_1(q, 0)| - e^{-\Gamma_0 t}|G_1(q, t)| \quad (7.44)$$

$$= I_{int}(1 - e^{-\Delta\bar{\Gamma} t}), \quad (7.45)$$

a function with only two fit parameters, $I_{int}(x)$ and $\Delta\bar{\Gamma}$, representing coil internal motions solely.

In the first application of this method,^[32(a)] a parallel study of the q dependence of $\Delta\Gamma$ for PS in good and theta solvents, particularly for large x , exhibited a distinct difference between the two systems. This difference revealed the following about the intra-coil behaviour of PS in dilute solutions: PS coils experienced relatively strong hydrodynamic interactions ('non-draining' behaviour) when excluded volume effects were minimal for the compact coil at the theta condition. However, when excluded volume effects were manifest in the swollen coil in good solvent, only weak hydrodynamic interactions ('partial draining') are experienced.

In the second application of the method,^[32(b)] the interplay between inter-polymer and intra-polymer behaviour for coils in dilute solution was studied by investigating the concentration dependence of the overall intra-coil relaxation, $\Delta\Gamma_1$. The same polystyrene standard employed in the first study described above was also used in this study. A method was then developed for the experimental determination of $\Delta\Gamma_1$ values (Fig. 7.8): $\Delta\Gamma(q)$ exhibited a smooth transition from power-law behaviour at large q to a region at small q in which $\Delta\Gamma$ became independent of q . As q decreased from large to small values, increasingly greater lengths, including those larger than PS coils (i.e. larger than R_G) were probed. Unchanging $\Delta\Gamma(q)$ values for small to intermediate x defined a flat and terminal, or 'plateau' region of the data curve for small q . Measurement for this q region corresponded to the probing of the 'least local' intra-coil relaxation detected in such a light scattering measurement, i.e. to the overall intra-coil relaxation. The decay constant for this mode is $\Delta\Gamma_1$. In the inset to Fig. 7.8, it is seen that for polystyrene in a good solvent, plateau behaviour begins around a q of $1.5 \times 10^5 \text{ cm}^{-1}$. The fact that this q value corresponds to a coil size comparable to R_G for the isolated PS coil supports the contention that it is the overall intra-coil relaxation that is being probed for plateau $\Delta\Gamma$ values.

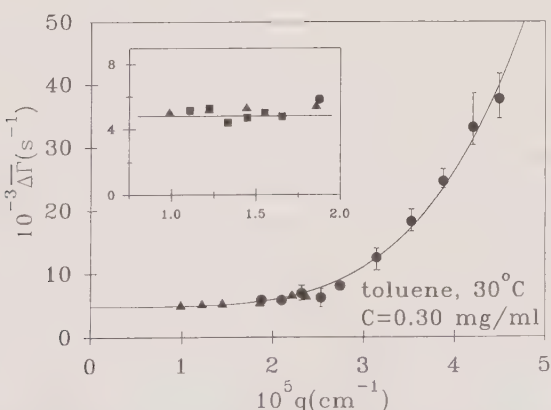


FIG. 7.8. A plot illustrating the wavevector dependence of the collective decay constant, $\Delta\Gamma$. Plateau $\Delta\Gamma_1$ values, including earlier data, are illustrated in the inset. The fit is to eqn (7) pf ref. 32(b) (from ref. 32(b), with permission).

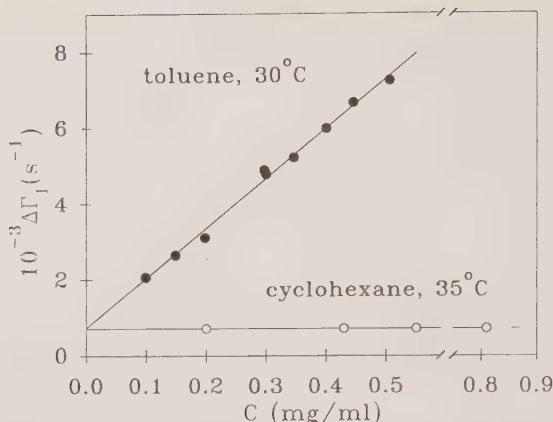


FIG. 7.9. A plot illustrating the contrast between the strong and weak concentration dependencies of $\Delta \Gamma_1$ in good and theta solvents, respectively. The fit lines are primarily to guide the eye (from ref. 32(b), with permission).

The concentration dependences of $\Delta \Gamma_1$ in good and theta solvents are illustrated in Fig. 7.9. The striking difference in the behaviour of the polymer in the two systems was interpreted as follows.

7.5.1 Coil behaviour in good solvent

In a good solvent, coils experience strong, repulsive interactions, i.e. ‘collisions’, and the frequency of these encounters increases with increasing coil concentration. Two causes are thought to be principally responsible for the observed $\Delta \Gamma_1$ concentration behaviour.

First, because $\Delta \Gamma_1$ depends strongly on coil size,

$$\Delta \Gamma_1 \sim D/R_G^2, \quad (7.46)$$

the increase in $\Delta \Gamma_1$ with increasing concentration results from a corresponding shrinkage of these coils. However, the contention that coils in good solvent shrink as coil concentration increases in dilute solutions is disputed.

Theoretical support for coil shrinkage in dilute, good solvent binary solutions is provided in earlier work (ref. 5(a) and references cited therein), but more recently, attention has been focused on shrinkage in more concentrated solutions (ref. 33 and references therein), where it is assumed that shrinkage in dilute solution is insignificant.

Experimental support for shrinkage in dilute, good solvent, binary solutions with increasing polymer concentration is provided by a recent neutron scattering study of aqueous solutions of PEO.^[34] However, earlier neutron scattering studies of dilute, good solvent polystyrene solutions reported little or no coil shrinkage.^[35(a), (b)]

In light scattering studies of ternary solutions (see Chapters 6 and 7 of ref. 6 and Chapters 5 and 9 in this volume) there are also conflicting results. Little or no probe coil shrinkage was reported in refs 33, 36(a) and 36(b), while probe coils reportedly exhibited distinct shrinkage in the studies conducted in refs 37(a) and 37(b). Interpretation of light scattering measurements from ternary systems is complicated by issues such as probe polymer/matrix polymer compatibility, differences in solvent quality between the probe and matrix polymers, screening of probe-probe interactions by the matrix, and small but significant refractive index mismatches between the solvent and matrix polymer. At present, an uncontested resolution to the dispute concerning coil shrinkage in dilute good solvent solutions has not been reached.

In ref. 32(b), it is suggested that coil shrinkage is not the only reason for the marked concentration dependence of $\Delta\Gamma_1$. The second cause is the interruption of overall coil relaxations by coil-coil collisions, the frequency of which increases with increasing polymer concentration in solution. The plausibility of this suggestion was strengthened by a calculation showing that coil-coil collision frequencies and $\Delta\Gamma_1$ values are of comparable magnitude for the range of concentrations studied. Thus, even if coil shrinkage is not significant, the observed $\Delta\Gamma_1$ concentration dependence can be explained by the interruption of intra-coil relaxations due to coil-coil collisions.

7.5.2 Coil behaviour in a theta solvent

In a theta solvent, in contrast to the behaviour of coils in good solvents, $\Delta\Gamma_1$ exhibited little if any concentration dependence (Fig. 7.9). This result is consistent with very weak coil-coil interactions and therefore with the absence both of coil shrinkage and of the interruption of intra-coil relaxation with increasing coil concentration. Moreover, at least in comparison with strongly interacting coils in a good solvent, proximate coils in theta solvent interpenetrate readily without colliding.

These good solvent and theta solvent results illustrate the important role played by coil-coil interactions, especially strong interactions or 'collisions', in determining overall intra-coil dynamic behaviour. As pointed out in ref. 32(b), the marked contrast between the good and theta system behaviour highlights the important role that thermodynamics plays in coil-coil collisions and thus in the concentration dependence of overall intra-coil relaxations for both systems.

7.6 Summary

While much is known and understood about macromolecular behaviour in dilute, binary solutions, important issues remain unresolved. For example, the behaviour of polymer coils during binary encounters is only superficially understood. While earlier treatments provided a good account of such behaviour for coils either in poor or in good solvents, they are unable to describe

coil–coil encounters for solvents of intermediate quality or for sub-theta behaviour. In addition to providing a good account of coil behaviour in good solvent, the treatment of Akcasu and Benmouna separates out and highlights the important role of coil segment redistribution during binary encounters. As a result, the A–B treatment provides a basis for a semi-empirical description of coil–coil interactions across the range of solvent quality from sub-theta to good, as presented in Section 7.3, above. Moreover, fits to k_D^ϕ versus X data from SLS and DLS measurements provide the intra-coil segment distribution parameter, $Y(X)$, over this wide solvent quality range. It should then be possible to test alternative theories describing the redistribution of coils segments against $Y(X)$ determined from light scattering measurements and assess, for example, the effect of this redistribution on $Y(X)$ for differing macromolecular chain architectures.

As shown in ref. 3, light scattering may be used to investigate the sub-theta behaviour of linear, flexible chains in solution. For example, high molecular weight P α MS forms stable solutions well below theta conditions. Studies of such stable—and metastable—solutions should provide new insights into the mechanisms of the phase separation of macromolecular coils in solution. Another important question which needs answering is as follows: How do we understand the odd symmetry around the theta point exhibited by k_D^ϕ in Fig. 7.4?

The dominant influence of thermodynamics (solvent quality) in coil–coil interactions, including such dynamic interactions as collisions, is seen clearly in a comparison of the $\Delta\Gamma_1$ concentration behaviours of polystyrene coils in good and theta solvents (Fig. 7.9). It is important to recognize that this influence occurs for ‘typical’ dilute solutions. Since the CM translational results are consistent with other DLS studies, including those for distinctly lower PS concentrations,^[38] apparently on the characteristic time scales for translational motion, coil–coil collisions are indiscernible from solvent jostling of coils. Moreover, the strong concentration dependence of $\Delta\Gamma_1$ in a good solvent is associated with the fact that $\Delta\Gamma_1$ and coil–coil collision frequencies in solution are comparable. If this is so, the concentration dependence of $\Delta\Gamma_1$ for polymer concentrations well below the smallest of those employed in ref. 32(b) should be relatively weaker. Thus a comparison of the results of a study at lower concentration with the earlier results may allow the separation in $\Delta\Gamma_1$ of effects due to coil shrinkage and those due to the interruption of overall relaxations by collisions.

References

1. (a) Akcasu, A. Z. and Benmouna, M. (1978). *Macromolecules*, **11**, 1193.
 (b) Akcasu, A. Z. (1981). *Polymer*, **22**, 1169.
 (c) Akcasu, A. Z., Hammouda, B., Lodge, T. P., and Han, C. C. (1984). *Macromolecules*, **17**, 759.

2. (a) Han, C. C. and Akcasu, A. Z. (1981). *Polymer*, **22**, 1165.
(b) van den Berg, H. and Jamieson, A. M. (1983). *J. Polym. Sci. A, Polym. Phys. Ed.*, **21**, 2311.
(c) Huber, K., Burchard, W., and Akcasu, A. Z. (1985). *Macromolecules*, **18**, 2743.
3. Cotts, P. M. and Selser, J. C. (1990). *Macromolecules*, **23**, 2050.
4. Flory, P. J. (1963). *Principles of polymer chemistry*. Cornell University Press, Ithaca, New York.
5. (a) Yamakawa, H. (1971). *Modern theory of polymer solutions*. Harper & Row, New York.
(b) Vink, H. (1985). *J. Chem. Soc., Faraday Trans. 1*, **81**, 1725.
6. Brown, W., ed. (1993). *Dynamic light scattering: the method and some applications*. Clarendon Press, Oxford.
7. Schmitz, K. S., ed. (1994). *Macro-ion characterization from dilute solutions to complex fluids*. ACS Symposium Series 548. ACS Press, Washington, DC.
8. Tanford, C. (1961). *Physical chemistry of macromolecules*. John Wiley, New York.
9. Tanford, C. (1973). *The hydrophobic effect: formation of micelles and biological membranes*. John Wiley, New York.
10. Huglin, M. B., ed. (1972). *Light scattering from polymer solutions*. Academic Press, New York.
11. Berne, B. J. and Pecora, R. (1976). *Dynamic light scattering with applications to chemistry, biology and physics*. John Wiley, New York.
12. Schmitz, K. S. (1990). *An introduction to dynamic light scattering by macromolecules*. Academic Press, New York.
13. Chu, B. (1974). *Laser light scattering: basic principles and practice*. Academic Press, New York.
14. Chu, B. (1991). *Laser light scattering: basic principles and practice*, second edition. Academic Press, New York.
15. Pecora, R., ed. (1985). *Dynamic light scattering: applications of photon correlation spectroscopy*. Plenum Press, New York.
16. Cummins, H. Z. and Pike, E. R., eds. (1973). *Photon correlation and light beating spectroscopy*. Nato Advanced Institute series, Series B: Physics, Plenum Press, New York.
17. Chen, S. H., Chu, B., and Nossal, R., eds. (1981). *Scattering techniques applied to supramolecular and nonequilibrium systems*. Nato Advanced Study Institute series, Series B: Physics, Plenum Press, New York.
18. Chu, B., ed. (1990). *Selected papers on quasielastic light scattering by macromolecular, supramolecular and fluid systems*. SPIE Proceedings, Vol. MS 12.
19. McMillan, W. G. and Mayer, J. E. (1945). *J. Chem. Phys.*, **13**, 276.
20. Berry, G. C. (1966). *J. Chem. Phys.*, **44**, 3440.
21. Zimm, B. (1948). *J. Chem. Phys.*, **16**, 1099.
22. de Gennes, P. G. (1984). *Scaling concepts in polymer physics*, second edition. Cornell University Press, Ithaca, New York.
23. de Gennes, P. G. (1990). *Introduction to polymer dynamics*. Cambridge University Press.
24. Doi, M. and Edwards, S. F. (1986). *The theory of polymer dynamics*. Clarendon Press, Oxford.
25. Pyun, C. W. and Fixman, M. J. (1964). *J. Chem. Phys.*, **41**, 935.
26. (a) Selser, J. C. (1985). *Macromolecules*, **18**, 585.
(b) Mays, J. W., Hadjichristidis, N., Graessley, W. W., and Fetters, L. J. (1986). *J. Polym. Sci. B, Polym. Phys. Ed.*, **24**, 2533.
27. Rabin, Y. (1983). *J. Chem. Phys.*, **79**, 3988.

28. Devanand, K. and Selser, J. C. (1990). *Nature*, **343**, 739.
29. Devanand, K. and Selser, J. C. (1991). *Macromolecules*, **24**, 5943.
30. Woodley, D. M., et al. (1992). *Macromolecules*, **25**, 5283.
31. DeLong, L. M., *private communication*.
32. (a) Ellis, A. R., Schaller, J. K., McKiernan, M. L., and Selser, J. C. (1990). *J. Chem. Phys.*, **92**, 5731.
(b) Schaller, J. K., Devanand, K., and Selser, J. C. (1993). *J. Chem. Phys.*, **98**, 1597.
33. Kent, M. S., Tirrell, M., Lodge, T. P. (1991). *Polymer*, **32**, 314.
34. Thiagarajan, P., Chaiko, D. J., and Hjelm, R. P. Jr. (1996). *Macromolecules*, in press.
35. (a) Daoud, M., Cotton, J. P., Farnoux, B., Jannink, G., Sarma, G., Benoît, H., Duplessix, R., Picot, C., de Gennes, P. G. (1975). *Macromolecules*, **8**, 804.
(b) King, J. S., Boyer, W., Wignall, G. D., and Ullman, R. (1985). *Macromolecules*, **18**, 709.
36. (a) Hyde, A. J. and Tanner, A. G. (1968). *J. Colloid Interface Sci.*, **28**, 179.
(b) Brown, W. and Zhou, P. (1991). *Macromolecules*, **24**, 1820.
37. (a) Kuhn, R. and Cantow, H. J. (1969). *Makromol. Chem.*, **122**, 65.
(b) Brown, W. and Zhou, P. (1990). *Macromolecules*, **23**, 5097.
38. Fetters, L. J., Hadjichristidis, N., Lindner, J. S., and Mays, J. W. (1994). *J. Phys. Chem. Ref. Data*, **23**, 619.

Scattering properties of ternary polymer solutions

Redouane Borsali

8.1 Introduction

To achieve a better understanding of polymer mixture properties, considerable effort has been made, over the past decade, on the static and the dynamic behaviours both in solution and in the bulk, from theoretical and experimental points of view. The aim of this chapter is to discuss the scattering properties of these systems on the basis of recent developments and to emphasize how one extracts important parameters such as the mobility of the chains (diffusion process) and the interaction parameter (compatibility) which control the dynamics and the thermodynamics. Using linear response theory and the random phase approximation (RPA), it has been shown that two relaxation modes describe the dynamic behaviour of incompressible polymer/polymer/solvent systems. The first mode characterizes the total polymer concentration fluctuations and reflects the collective motion of all the polymer chains with respect to the solvent (excluded volume effect). The second mode describes the motion of one component with respect to the other and is generated by the composition fluctuations in the mixture; it is related to the interdiffusion process. The identification of these two relaxational modes has been made possible by a combination of methods: dynamic light scattering (DLS), neutron spin echo (NSE), forced Rayleigh scattering (FRS), pulsed-field-gradient NMR (PFG-NMR) and fluorescence recovery after photobleaching (FRAP). All the reported experiments have dealt with homogeneous systems far from the ‘cloud point’ or (micro) phase separation (spinodal decomposition). The results of the experiments presented in this chapter have been analysed in the framework of recent models developed during the past decade by Akcasu, Benoît and Benmouna. The variations of the two relaxation modes as a function of physico-chemical parameters have been found to be in good agreement with theoretical predictions. Particular attention is given in this chapter to the scattering properties of homopolymer mixtures and diblock copolymer (linear) systems in solution. Recent developments and results on the ring diblock copolymer case are included and reveal that substantial differences with respect to the linear case are obtained. We also discuss the scattering behaviour of the melt systems (mixtures of two homopolymers or diblock copolymers) and show that the melt limit can be recovered from the solution case in which the

dynamics are characterized by a single relaxational mode: the so-called interdiffusion process.

8.2 Historical sketch

Ternary polymer systems treated in this chapter deal either with mixtures of two homopolymers (A and B) or diblock copolymer chains (A-B, linear or cyclic) in a solvent. Polyelectrolytes in solution may be also considered as a ternary case consisting of polyion/counter-ions/water but this is beyond the scope of this work (see Chapters 3 and 4). It is generally recognized that two different polymers are thermodynamically incompatible if the specific interactions between both species do not lead to a negative heat of mixing. The phase separation of two polymers (A and B) in organic solvents is relatively well understood and is usually due to repulsive interactions between chains of species A and B. On the other hand, polymer/polymer behaviour in aqueous solution is less well understood, although phase separated polymer solutions have been widely studied and used, for instance, to separate biological materials, as described by Albertson.^[1] In this respect, the mixing of polymers is important and deserves particular attention for several reasons.

Besides the fundamental aspects and the practical importance of understanding and controlling phase separation in polymer mixtures, the knowledge of some parameters such as the mobility of the chains (diffusion process) and the interaction parameter (compatibility) is of great interest for testing the relations between the thermodynamics and the relaxation behaviour in many industrial applications (processing, cosmetics, foods, etc.).

As far as the dynamic properties are concerned when using DLS in solution, the solvent is often chosen to be isorefractive with one of the polymers (i.e. the solvent and the polymer have the same refractive index). The idea is that the dynamics are controlled by the 'visible' polymer (the probe) and therefore the interpretation of the results is simplified. At very low concentrations of the probe, one observes the self-diffusion coefficient of the visible component at a finite concentration of the 'invisible' polymer (matrix). In the past decade, several types of mixtures have been considered in the framework of this idea. In 1983 Cotts,^[2] Hanley *et al.*^[3] and Lodge,^[4] in 1984 Martin^[5] and in 1987 Wheeler *et al.*^[6] studied polystyrene/poly(vinylmethylether) (PS/PVME) in toluene or in o-fluorotoluene (o-FT) because of the high degree of compatibility of these two polymers. With such compatible systems, a wide range of molecular weights and concentrations have been explored, and some scaling laws for the self-diffusion coefficient have been deduced. Other polymer mixtures such as PS/PMMA (polymethylmethacrylate) and a solvent were considered in the framework of similar studies by Hadgraft *et al.*^[7] in 1979, Nemoto *et al.*^[8] in 1986, Chu *et al.*^[9,10] in 1986 and 1987 and Brown and Rymdén^[11] in 1988, but only a limited range of molecular weights and concentrations has been investigated because of the incompatibility of these polymers. The ternary mixture PS₁/PS₂/solvent, where the two polymers differ only in their molecular

weights, was also investigated by Kim *et al.*^[12] in 1986 over reasonable ranges of molecular weights and concentrations because of the compatibility of this system. All the reported experiments dealt with systems far from the 'cloud point' or phase separation (spinodal decomposition). The common point of those studies was the use of a small composition (less than 1%) of the 'visible' polymer in a matrix. Most of the results showed a mono-exponential behaviour of the scattered autocorrelation function as measured using DLS except for a few cases in which two modes were reported by Chu and Wu^[9] with no definitive interpretation of the second relaxation mode. The aim of those studies was to verify if the only observed mode, which decreases with the concentration, could be interpreted in terms of the reptative motion introduced by de Gennes^[13] in 1979 and Doi and Edwards^[14] in 1986, or if an alternative sophisticated dynamic processes, as described by Hess^[15] in 1986, must be taken into account. In spite of the great experimental effort expended, most of the reported results were still the subject of controversy, in terms of reptation or not, up to 1984. This controversy has attracted many researchers from different laboratories and from both sides; theoreticians and experimentalists.

On the theoretical side, a model was developed by Pusey *et al.*^[16] in 1982 for mixtures of hard spheres in solution having different sizes, and the general theory of multicomponent polymeric systems was formulated by Akcasu *et al.*^[17-22] in 1984 and Benmouna *et al.*^[23-26] in 1987 using linear response theory and RPA. Later work was done by Foley and Cohen^[27] in 1987 using the Flory Huggins model; by Borsali and Vilgis^[28] in 1990 using the Edwards Hamiltonian description; by Roby and Joanny^[29] in 1992 using the Rouse-Zimm model and reptation scaling laws; and by Hammouda^[30] in 1993 using a similar method—linear response theory and RPA—by introducing the hydrodynamic interactions. In this chapter we will focus on the model proposed originally by Akcasu *et al.*^[17-23] and Benmouna *et al.*^[23-26] since it has explained most of the experimental results obtained by many authors from different laboratories. The first experimental results using DLS, based on the optical conditions to observe simultaneously the two relaxation modes in a two homopolymers/solvent system (see the discussion later), were obtained by Borsali *et al.*^[31-35] in 1987-1989, followed by Chu and Wu^[10] in 1987, Brown *et al.*^[11,36,37] in 1989 and 1990, Aven and Cohen^[38] in 1990, Daivis *et al.*^[39] in 1992 and Koňák *et al.*^[40-42] in 1990-1993.

The purpose of this chapter is not to produce an extensive survey of theoretical and experimental results obtained on the scattering behaviour of ternary polymer mixtures but rather, to update recent theoretical and experimental results. In the next section, a brief survey of the Akcasu-Benoît-Benmouna model is given, followed by few important and recent experimental contributions. A section of this chapter is devoted to the case of linear diblock copolymer chains in solution, where recent experimental results obtained by Lodge *et al.*^[43-45] and Fytas *et al.*^[46-52] are analysed in the framework of the present model combined with that developed more recently by Semenov *et al.*^[53] We shall also show that, starting from well-known relations that describe the

dynamical behaviour of linear diblocks, the ring diblock properties can be deduced simply by introducing the adequate form factors, as has recently been shown by Benmouna *et al.*^[54] and Borsali and Benmouna.^[55] To conclude, we shall demonstrate that the melt limit of the static and the dynamic behaviours can be simply recovered from the properties of solution when the excluded volume $v = v_0(1/\Phi_s - 2\chi)$ goes to infinity (i.e. the solvent volume fraction $\Phi_s = 0$, χ being the Flory interaction parameter) and where the dynamics are characterized by one relaxation mode: the interdiffusion process.^[56–63]

8.3 General formalism

Using linear response theory, RPA and DLS experiments, it has been shown by Akcasu *et al.*^[17–22] Benmouna *et al.*^[23–26] and Borsali *et al.*^[31–35] that in incompressible ternary mixture consisting of two polymers and a solvent in the semi-dilute range, the total dynamic structure factor $S_T(q, t)$ is a sum of two exponentials:

$$S_T(q, t) = A_1(q) e^{-\Gamma_1(q)t} + A_2(q) e^{-\Gamma_2(q)t}, \quad (8.1)$$

where $q = (4\pi/\lambda)n \sin(\theta/2)$, λ is the wavelength of the incident radiation, θ is the scattering angle, n is the refractive index of the medium, and t is the time. $A_1(q)$ and $A_2(q)$ are the amplitudes of the normal modes having frequencies $\Gamma_1(q)$ and $\Gamma_2(q)$. Under certain conditions they are the so-called cooperative and interdiffusive modes as described by Akcasu *et al.*^[19–22] The general expressions for these two frequencies or normal modes are given by

$$\Gamma_{1,2}(q) = \Omega_{av}(q) \pm [\Omega_{av}^2(q) - \Delta(\Omega)]^{1/2}, \quad (8.2a)$$

where

$$\Omega_{av}(q) = \frac{\Omega_{aa}(q) + \Omega_{bb}(q)}{2}, \quad (8.2b)$$

$$\Delta(\Omega) = \Omega_{aa}(q)\Omega_{bb}(q) - \Omega_{ab}(q)\Omega_{ba}(q). \quad (8.2c)$$

The quantities $\Omega_{ij}(q)$ are the first cumulant matrix elements and are expressed as:^[17,20]

$$\boldsymbol{\Omega}(q) = q^2 k_B T \mathbf{M}(q) \mathbf{S}^{-1}(q), \quad (8.3)$$

where T is the absolute temperature and k_B is the Boltzmann constant. $\mathbf{M}(q)$ and $\mathbf{S}(q)$ are the mobility and static structure factor matrices, respectively. Knowledge of these two quantities, the structure factor $\mathbf{S}(q)$ and the mobility $\mathbf{M}(q)$, allows us to write down the general expressions for the amplitudes and the frequencies which describe the dynamics of any ternary system.

8.3.1 Partial static structure factors

There are different methods for calculating the partial structure factors. Among these, the Random Phase Approximation (RPA), introduced by de Gennes,^[13] when applied to polymers is successful in explaining many scattering results.

For this reason and because of its simplicity, it has been used to calculate the elements of the structure factor matrix $S(q)$ in terms of the 'bare' or intramolecular structure factor $S^0(q)$ of a single chain (i.e. without intermolecular interaction).

8.3.1.1 Diblock copolymer/solvent case. In the case of diblock copolymer systems these relations have been already calculated and are given by^[21,23,32]

$$S_{aa}(q) = \frac{S_{aa}^0(q) + v_{bb}\Delta S^0(q)}{D}, \quad (8.4)$$

$$S_{ab}(q) = S_{ba}(q) = \frac{S_{ab}^0(q) - v_{ab}\Delta S^0(q)}{D}, \quad (8.5)$$

where

$$D = 1 + v_{aa}S_{aa}^0(q) + v_{bb}S_{bb}^0(q) + 2v_{ab}S_{ab}^0(q) + (v_{aa}v_{bb} - v_{ab}^2)\Delta S^0(q) \quad (8.6)$$

and

$$\Delta S^0(q) = S_{aa}^0(q)S_{bb}^0(q) - S_{ab}^{0,2}(q). \quad (8.7)$$

v_{ij} ($i, j = a, b$) is the excluded volume between monomers of type a and type b . $S_{bb}(q)$ is deduced from $S_{aa}(q)$ by simply interchanging the indices. The 'bare' structure factors $S_{ij}^0(q)$ ($i, j = a, b$) for the diblock copolymer A–B with N_a and N_b monomers (degrees of polymerization) at the total polymer volume fraction $\Phi_T = n(N_a + N_b) = nN_T$ (n = total number of chains with a degree of polymerization N_T) may be written according to Leibler^[64] as follows:

$$S_{aa}^0(q) = \Phi_T(N_a + N_b)P_a(x, q), \quad (8.8a)$$

$$S_{bb}^0(q) = \Phi_T(N_a + N_b)P_b(1 - x, q), \quad (8.8b)$$

$$S_{ab}^0(q) = S_{ba}^0(q) = \Phi_T(N_a + N_b)P_{ab}(x, q), \quad (8.8c)$$

where $P_a(x, q)$, $P_b(1 - x, q)$ and $P_{ab}(x, q)$ are, respectively the intramolecular form factors for blocks A and B and the intramolecular interference form factor between blocks A and B. For an ideal copolymer chain, these form factors can be represented by the modified Debye function, namely:

$$P_a(x, q) = 2(e^{-xu} + xu - 1)/u^2, \quad (8.9a)$$

$$P_b(1 - x, q) = 2[e^{-(1-x)u} + (1-x)u - 1]/u^2, \quad (8.9b)$$

$$P_{ab}(x, q) = (1/2)[P_a(1, q) - P_a(x, q) - P_b(1 - x, q)], \quad (8.9c)$$

where x is the composition of species A within the A–B copolymer chain and $u = (qR_{gr})^2$; R_{gr} is the radius of gyration of the whole diblock copolymer chain.

8.3.1.2 *Two homopolymers in solvent.* The expressions for $S_{ij}(q)$ ($i, j = a, b$) in this case can be deduced from the above equations by setting $S_{ab}^0(q) = 0$ which is a direct consequence for the decoupling of intramolecular interactions within the single diblock copolymer chain:

$$S_{aa}(q) = \frac{S_{aa}^0(q)[1 + v_{bb}S_{bb}^0(q)]}{D'}, \quad (8.10)$$

$$S_{ab}(q) = S_{ba}(q) = -\frac{v_{ab}S_{aa}^0(q)S_{bb}^0(q)}{D'}, \quad (8.11)$$

where

$$D' = 1 + v_{aa}S_{aa}^0(q) + v_{bb}S_{bb}^0(q) + (v_{aa}v_{bb} - v_{ab}^2)S_{aa}^0(q)S_{bb}^0(q) \quad (8.12)$$

with the ‘bare’ structure factors $S_{ij}^0(q)$:

$$S_{aa}^0(q) = x\Phi_T N_a P_a(q), \quad S_{bb}^0(q) = (1-x)\Phi_T N_b P_b(q), \quad (8.13a,b)$$

where x in this case is the composition of component A in the (A + B) mixture, $P_a(q)$ and $P_b(q)$ are the intramolecular form factors for homopolymers A and B. For an ideal chain these form factors can be approximated by the Debye function, namely:

$$P_i(q) = 2(e^{-u_i} + u_i - 1)/u_i^2. \quad (8.14)$$

$u_i = (qR_{gi})^2$; and R_{gi} is the radius of gyration of the chain i ($i = a, b$).

8.3.2 First cumulant matrix elements (Rouse model)

In order to proceed further we must specify the mobility matrix $\mathbf{M}(q)$ elements in relation (8.3). In the Rouse model, the most appropriate in the semi-dilute and concentrated regimes ($c > c^*$, where c^* is the overlap concentration), the cross-term mobilities $M_{ab}(q) = M_{ba}(q) = 0$. This implies the assumption that the Zimm-type hydrodynamic interactions are screened out in the semi-dilute and concentrated regimes. This picture of the hydrodynamic screening interactions allows us to simplify the problem. The diagonal mobility elements are q -independent in the Rouse model and, according to Yamakawa,^[65] de Gennes,^[13] Doi and Edwards,^[14] and Akcasu,^[21] may be written simply as:

$$M_{ii}(q) = M_{ii}^0(q) = M_{ii}^0 = \Phi_i/f_i(c) \quad (i = a, b), \quad (8.15)$$

where Φ_i is the volume fraction of the i -species and $f_i(c)$ is the friction coefficient per monomer of type i , which is generally concentration-dependent. One notes that the introduction of the hydrodynamic interactions can be taken into account in this model by the cross-term mobilities $M_{ab}(q)$ and $M_{ba}(q)$, which may be obtained using, for instance, the Oseen tensor description as described by Yamakawa.^[65] The effects of such hydrodynamic interactions have been already discussed elsewhere by Akcasu and Tombakoglu,^[19] Vilgis and

Benmouna,^[66] and Hammouda,^[30] as well as the screening of hydrodynamic interactions by Borsali *et al.*^[67]

At this point, we should mention that the introduction of the hydrodynamic interactions in the framework of this model is possible but is very complicated in the general case. In the section describing the dynamics of linear and cyclic diblock copolymer chain in solution, we shall show in a particular and simple case (i.e. the symmetrical system—same molecular weight and same composition), how such interactions can be introduced and how these modify substantially the results, especially in the dilute range of concentration.

Let us assume that the solvent has the same quality for both components (i.e. the excluded volumes $v_{aa} = v_{bb} = v$) and a small interaction between the monomers of species a and b is taken into account by the parameter $\chi = v_{ab} - v$. Under such considerations, the elements of the first cumulant matrix can be written as:

$$\Omega_{ii}(q) = q^2 \frac{D_i^0}{P_i(q)} \left[\frac{S_{ii}^0(q)S_{jj}^0(q)}{\Delta S^0(q)} + vS_{ii}^0(q) \right] \quad (i = a, b), \quad (8.16a)$$

$$\Omega_{ij}(q) = -q^2 \frac{D_i^0}{P_i(q)} \left[\frac{S_{ij}^0(q)S_{ii}^0(q)}{\Delta S^0(q)} - S_{ii}^0(q)(v + \chi) \right] \quad (i \neq j, a, b) \quad (8.16b)$$

in the diblock copolymer/solvent case and

$$\Omega_{ii}(q) = q^2 \frac{D_i^0}{P_i(q)} [1 + vS_{ii}^0(q)] \quad (i = a, b), \quad (8.17a)$$

$$\Omega_{ij}(q) = q^2 \frac{D_i^0}{P_i(q)} S_{ii}^0(q)[v + \chi] \quad (i \neq j, a, b) \quad (8.17b)$$

in the case of two homopolymer mixtures in solution simply by setting $S_{ab}^0(q) = 0$. One notes that $D_i^0 = kT/N_i f_i(c)$ ($i = a, b$) is the diffusion coefficient of single labelled chain i in a matrix j at concentration c .

8.3.3 Relaxation modes

After straightforward algebraic calculations, the expressions for the relaxation modes in the diblock copolymer systems given by eqns (8.2) are written as follows:

$$\Gamma_1(q) = q^2 \left\{ \left[\frac{D_a^0}{P_a(q)} + \frac{D_b^0}{P_b(q)} \right] \frac{S_{aa}^0(q)S_{bb}^0(q)}{\Delta S^0(q)} + v \left[D_a^0 \frac{S_{aa}^0(q)}{P_a(q)} + D_b^0 \frac{S_{bb}^0(q)}{P_b(q)} \right] - \frac{\mathcal{N}(q)}{\mathcal{D}(q)} \right\} \quad (8.18)$$

$$\Gamma_2(q) = q^2 \frac{\mathcal{N}(q)}{\mathcal{D}(q)}, \quad (8.19)$$

where

$$\begin{aligned} \mathcal{N}(q) = & \frac{D_a^0 D_b^0}{P_a(q) P_b(q)} \left[\frac{S_{aa}^0(q) S_{bb}^0(q)}{\Delta S^0(q)} [1 + 2\chi S_{ab}^0(q) - \chi^2 \Delta S^0(q)] \right. \\ & \left. + v S_{aa}^0(q) S_{bb}^0(q) \left[\frac{S_T^0(q)}{\Delta S^0(q)} - 2\chi \right] \right] \end{aligned} \quad (8.20)$$

and

$$\mathcal{D}(q) = \left[\frac{D_a^0}{P_a(q)} - \frac{D_b^0}{P_b(q)} \right] \frac{S_{aa}^0(q) S_{bb}^0(q)}{\Delta S^0(q)} + v \left[D_a^0 \frac{S_{aa}^0(q)}{P_a(q)} + D_b^0 \frac{S_{bb}^0(q)}{P_b(q)} \right] \quad (8.21)$$

with $S_T^0(q) = S_{aa}^0(q) + S_{bb}^0(q) + 2S_{ab}^0(q)$ and $\Delta S^0(q)$ given by eqn (8.7).

For a two homopolymers and solvent system the expressions for the frequencies can be deduced from eqns (8.18)-(8.21) by setting $S_{ab}^0(q) = 0$ and there is no need to reproduce them here.

8.4 Experimental evidence

In the preceding section, we have briefly described the general dynamic multicomponent formalism of Akcasu and Benmouna. In this section we report some experimental results which establish the validity of this model. Although this model uses some approximations, it has the merit of providing a new description of the general behaviour of ternary polymer mixtures in solution (which was missing before 1984) and the experimental results obtained after the development of this model seem to agree, at least qualitatively.

For the sake of simplicity, most of the reported experimental results were obtained on mixtures of two homopolymers or a linear diblock copolymer in solution having the same molecular weight. To be more general, and since we shall also discuss later the dynamics of asymmetric cases, let us consider a system in which the two polymers have different degrees of polymerization ($N_A \neq N_B$), different excluded volume parameters v_{ij} ($i, j = a, b$) and are slightly incompatible ($\chi \neq 0$). In this case the expressions for the diffusion coefficients (normal modes), D_F (fast) and D_S (slow), after straightforward manipulations of the above dynamic equations, can be expressed as follows:^[32, 63, 68]

$$D_{F,S}(q) = D_{av}(q) \pm [D_{av}^2(q) - \Delta(D)]^{1/2}, \quad (8.22a)$$

where

$$D_{av}(q) = \frac{D_{11}(q) + D_{22}(q)}{2}, \quad (8.22b)$$

$$\Delta(D) = D_{11}(q)D_{22}(q) - D_{12}(q)D_{21}(q) \quad (8.22c)$$

and

$$D_{11} = D_a^0 \frac{1}{P_a(q)} [1 + 2x C_T A_{2,a} M_{w,a} P_a(q)], \quad (8.22d)$$

$$D_{22} = D_b^0 \frac{1}{P_b(q)} [1 + 2(1-x)C_T A_{2,b} M_{w,b} P_b(q)], \quad (8.22e)$$

$$D_{12} = 2D_a^{0x} C_T A_{2,ab} M_{w,a} \frac{m_b}{m_a}, \quad (8.22f)$$

$$D_{21} = 2D_b^0 (1-x) C_T A_{2,ab} M_{w,b} \frac{m_a}{m_b}, \quad (8.22g)$$

where $x = c_1/c_T$ and $P_i(q)$ is the form factor of polymer species i , defined in relation (8.14). The second virial coefficients $A_{2,ij}$ ($i, j = a, b$) have been introduced via the excluded volume parameters v_{ij} , such as

$$v_{ij} = 2A_{2,ij} \frac{m_i m_j}{N_{av}} \quad (i, j = a, b). \quad (8.23)$$

Here m_i are the monomer molecular weights and N_{av} is Avogadro's number. In terms of Flory's interaction parameters $\chi_{i,s}$ (the interaction between the solvent and monomer of species i ; $i = a$ or b) the Flory-Huggins theory^[69] yields

$$A_{2,ii} = \frac{v_i^2}{2v_s} [1/\Phi_s - 2\chi_{i,s}] \quad (i = a, b), \quad (8.24a)$$

$$A_{2,ab} = \frac{v_a v_b}{2v_s} [1/\Phi_s - \chi_{a,s} - \chi_{b,s} + \chi], \quad (8.24b)$$

where $\Phi_s = 1 - \Phi_T$ is the volume fraction of the solvent. v_a and v_b are the specific volumes of both polymers and v_s is the molar volume of the solvent. From eqns (8.22)–(8.24), one observes that the only unknown parameters are the single chain diffusion coefficients $D_i^0(c)$ ($i = a, b$) and the interaction parameter χ . Consequently, studies of the variations of the two modes as a function of the concentration and the composition provide access to those parameters. The identification of these two relaxation modes was made by the use of the DLS and NSE techniques. The next section describes sample preparation and data treatment when DLS is used to scan the dynamics of such systems.

8.4.1 Sample preparation, equipment and data analysis

Generally, a solvent is chosen to be isorefractive for one of the polymers and to have approximately the same thermodynamic quality for both components (good solvent). The molecular weight M_w , the radius of gyration R_g and the second virial coefficient A_2 are usually obtained via static light scattering experiments. This is done by measuring the scattering intensities for four or five binary concentrations in the dilute regime at different scattering angles. The use of a Zimm plot allows determination of $M_{w,i}$, $R_{g,i}$ and $A_{2,i}$ for both components. The model described above is valid in the semi-dilute range

of concentration ($c > c^*$). Assuming that the polymer chains are flexible and in a good solvent the overlap concentration can be estimated as, $c^* = M_w/(N_A 4\pi R_g^3/3)$. The solutions prepared at concentrations above c^* are allowed to mix for several days. They are then filtered or centrifuged to remove dust or ‘aggregates’ and allowed to equilibrate for a few days prior to measurements.

The full homodyne correlation function of the scattered intensity defined over a certain number of channels (generally 256) is obtained by using an auto-correlator. The scattered light of a vertically polarized laser is measured at several angles (generally between 20° and 150°). The total intermediate scattering function $S_T(q, t)$ is related to the measured homodyne intensity autocorrelation function $G^{(2)}(q, t)$ by the Siegert relation:^[70]

$$G^{(2)}(q, t) = B[1 + \beta|S_T(q, t)|^2], \quad (8.25)$$

where B is the baseline and β is the spatial coherence factor depending upon the geometry of the detection. The constrained regularization method (CONTIN) developed by Provencher^[71] may be used to obtain the distribution $A(t)$ of decay times and a statistical parameter ‘probability to reject’ (P) is calculated for each solution; the suggested one is for P closest to 0.5:

$$\left[\frac{G^{(2)}(q, t)}{B} - 1 \right]^{1/2} = \int_0^\infty A(\tau) e^{-(t/\tau)} d\tau = S_T(q, t). \quad (8.26)$$

This method or similar ones^[72] are now routinely used to analyse the DLS data for polymer systems and allows the determination of the relaxation modes which characterize the dynamics of these systems. To have more confidence in the results, when the dynamics are described by one or two relaxation modes, an independent mono or double exponential fit procedure should be used in order to confirm the fit.

8.4.2 Some results and discussion

8.4.2.1 Homopolymer mixtures. The relations obtained in this model are very useful for estimating the optimal experimental conditions necessary to observe simultaneously these two processes. Namely, these ideal conditions correspond to:^[25,32] (i) a total polymer concentration such that $c^* < c_T < c_{SP}$ (i.e. semi-dilute solution and in a one-phase region), where c^* and c_{SP} are the overlap and spinodal concentrations, respectively—in this case the ratio D_F/D_S (it increases with the concentration) is large and the two frequencies can be easily separated; (ii) a relatively high value of the composition x of the probe or ‘visible’ polymer in order to have the amplitudes of these processes in the same order of magnitude as has been already described.^[23–25,31,34]

The first observation of these two relaxation modes was reported by Borsali *et al.*^[31–34] on PS/PMMA/toluene and, unlike other authors, the composition was chosen to be ‘large’ ($x = 0.92$). Indeed, the choice of the composition is

very important and is even one of the crucial parameters. A typical intensity autocorrelation function as revealed by DLS on the ternary polymer mixture PMMA/PDMS/THF^[73] (THF is isorefractive with PDMS) is displayed in Fig. 8.1(a). The dots represent the experimental data and the solid line a monoexponential fit. It is clear from the distribution of residuals, plotted at the top of this figure, that the monoexponential fit is not satisfactory. Because of this unsatisfactory monoexponential fit, the data were analysed with two exponential functions according to relation (8.1) and a satisfactory description is achieved, as shown in Fig. 8.1(b). Without going into further detail, and according to theoretical predictions, it has been shown in these studies that the corresponding diffusion coefficients $D_{F,S}$ = initial slopes of the frequencies $\Gamma_{F,S}(q)$ versus q^2 increase with the concentration for the fast mode (cooperative) and decrease for the slow relaxation (interdiffusive).

Other detailed studies on the same system by Borsali *et al.*^[74] and Giebel *et al.*^[75,76] confirmed the effect of composition x of the probe polymer on the dynamic properties, in which it has been shown how the second process emerges when the composition x of the probe varies from zero to unity. In this respect, Fig. 8.2 shows the variations of the two processes, represented by the two peaks as detected by CONTIN analysis, at a fixed scattering angle as a function of the composition of the 'visible' polymer PMMA in the ternary PMMA/PDMS/THF system. It can be seen from this representation that the amplitude of the fast process increases with x , whereas at the same time one observes a decrease in the amplitude of the slow mode. At small compositions, namely for $x < 0.1$, only the slow process is observable.

We mention by way of comparison that these first results^[31, 35, 73–76] also explain why the earlier experimental works of Cotts,^[2] Hanley *et al.*,^[3] Lodge *et al.*,^[4,77–79] Martin,^[5] Wheeler *et al.*^[6] and Hadgraft *et al.*^[7] on ternary mixtures show the existence of only one relaxation mode: the interdiffusion. Since the composition x of the probe was always very small, less than 1%, this mode is identified as being the self or single diffusion coefficient, which is in perfect agreement with the model; i.e. the limit of $D_I(c)$ when $x \rightarrow 0$ is $D_S(c)$.

Similar studies have been carried out by Brown *et al.*^[36,37] on mixtures of two polyisobutylenes (PIB) in chloroform having different molecular weights. Chu and Wu^[10] investigated a mixture of two polystyrenes in toluene. They found two relaxation modes and their results are qualitatively in good agreement with theoretical predictions as far as the variations with the concentration of both modes are concerned. Another work by Daivis *et al.*^[39] showed that combining DLS and PFG-NMR experiments on ternary mixtures of PS/PVME/toluene allows an accurate determination of the self-diffusion coefficient. The analysis of their data has been done in the framework of the model described above.

There is an interesting case in which the average scattering length (neutrons) or index of refraction (light) of the two components exactly matches that of the solvent. In a symmetrical system (same molecular weight), this condition has been called the 'optical theta condition' (OTC) or 'Zero Average Contrast'

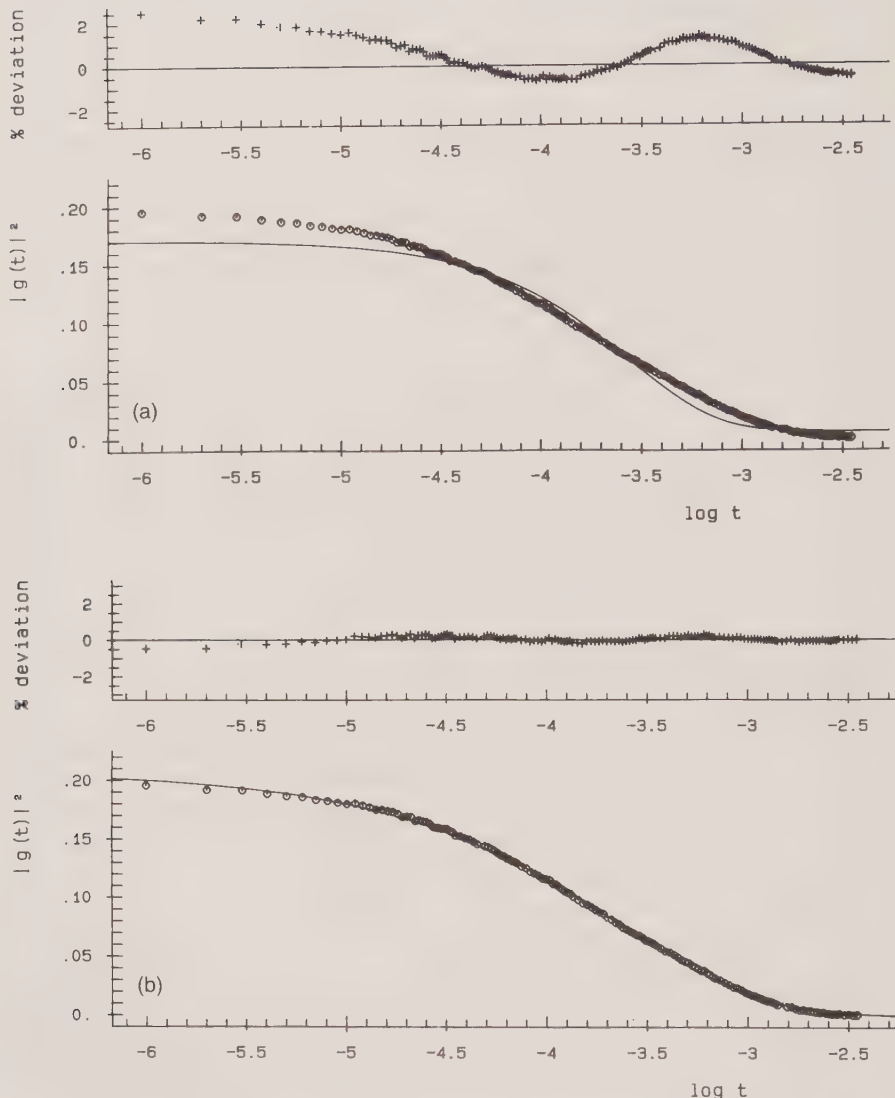


FIG. 8.1. (a) A typical autocorrelation function as measured by DLS on the system PDMS/PMMA/THF at $t = 30^\circ\text{C}$, $\theta = 50^\circ$, $x = 0.90$ and $c_T = 1.33 \times 10^{-2} \text{ g/cm}^3$. The dots represent the experimental data and the solid line a monoexponential fit. (b) The same system with a double exponential fit according to eqn (8.1). From ref. 73. (Reprinted with permission from *Macromolecules*. Copyright 1990 American Chemical Society.)

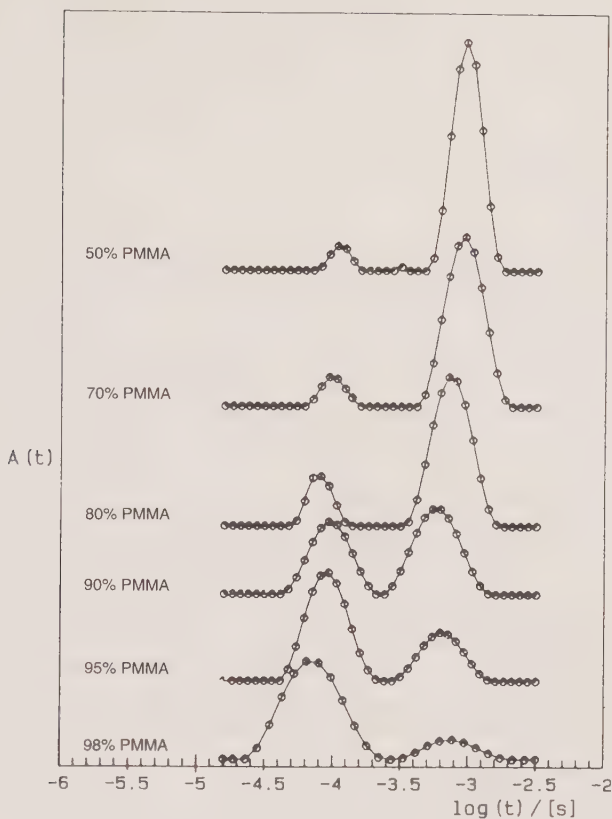


FIG. 8.2. The relaxation-time distribution obtained from CONTIN analysis for the system PDMS/PMMA/THF at $t = 30^\circ\text{C}$, $\theta = 50^\circ$ and $c_T = 1.33 \times 10^{-2} \text{ g/cm}^3$ at the composition shown. From ref. 73. (Reprinted with permission from *Macromolecules*. Copyright 1990 American Chemical Society.)

(ZAC) and obeys the relation

$$[\partial n/\partial c]_1 = -[\partial n/\partial c]_2 \quad \text{for } x = 0.5. \quad (8.27)$$

If a system satisfies this optical condition, only one mode survives: the interdiffusion relaxation. This is also the unique mode which exists in the melted state. Indeed, the measured scattering intensity $I(q, t)$ is, in general, expressed as follows:

$$\begin{aligned} I(q, t) &= [\partial n/\partial c]_1^2 S_{11}(q, t) + [\partial n/\partial c]_2^2 S_{22}(q, t) \\ &\quad + [\partial n/\partial c]_1 [\partial n/\partial c]_2 [S_{12}(q, t) + S_{21}(q, t)], \end{aligned} \quad (8.28)$$

where $S_{ij}(q, t)$ are the partial dynamic structure factors and $(\partial n/\partial c)_i$ is the increment of refractive index of polymer i . It is common in DLS experiments on ternary systems to choose a solvent which is isorefractive with one of the

polymers; i.e. $(\partial n/\partial c)_j = 0$ and then $I(q, t) = (\partial n/\partial c)_i S_{ii}(q, t)$ and we are left with the same procedure to analyse the data as described above. To come back to our particular case, if a symmetrical system satisfies relation (8.27), relation (8.28) reduces to:

$$I(q, t) = [\partial n/\partial c]_1^2 [S_{11}(q, t) + S_{22}(q, t) - S_{12}(q, t) - S_{21}(q, t)]. \quad (8.29)$$

For an arbitrary composition x , it shows that $I(q, t)$ is still a superposition of two exponential decay modes. However, for $x = 1/2$, the amplitude of the cooperative relaxation frequency is identically zero and consequently the total dynamic scattering function $I(q, t)$ is identically described by a single exponential function corresponding to the interdiffusion mode. From an experimental point of view, this case corresponds, for instance, to the system PDMS/PMMA in chloroform. To show this behaviour DLS experiments have been performed on PDMS/PMMA mixtures in three different solvents: (i) THF, isorefractive with PDMS; (ii) toluene, isorefractive with PMMA; and (iii) chloroform, having a refractive index intermediate between those of PDMS and PMMA. The experiments were made at a total polymer concentration, c_T , in the semi-dilute range ($c_T > c^*$) and with the molecular weights of PMMA and PDMS chosen to be approximately the same (about 7.2×10^5). Two relaxation modes were found in toluene over the whole investigated range of compositions $x = c_{\text{PMMA}}/c_T$ ($0 < x < 1$), as in the case of THF (see Figs 8.1 and 8.2). In chloroform, however, the effect of the composition shows two different behaviours depending on the value of x . For x about 0.5, a single relaxation is observed, whereas for values of x different from 0.5, two exponential relaxations are recovered. This behaviour is illustrated in Figs 8.3 and 8.4. Figure 8.3 collects all the data for the diffusion coefficients D_C and D_I as a function of composition x in the three different solvents. One notes that the small differences in the data are due to the fact that the thermodynamic quality of the three solvents is not exactly the same.

Figure 8.4 illustrates the variations of the relative amplitude of the fast cooperative mode in the three solvents. The general observation from these results is that the agreement with the theory is quite satisfactory for arbitrary compositions. Here we would like to focus more on the case of chloroform corresponding to 'ZAC' conditions. For $0.4 < x < 0.6$, the amplitude of the cooperative mode is vanishingly small and therefore the dynamics are described by the interdiffusion mode.

For x outside of this range, two relaxation modes characterize the auto-correlation functions of the mixture. The solid and dashed lines represent the best fit according to the model described above and where the interaction parameter χ has been deduced. One notes that Anasagasti *et al.*^[80] performed static light scattering experiments on the same polymer blend in chloroform and obtained, to within experimental error, the same value for the interaction parameter χ . This is, to the best of our knowledge, the first time that χ has been measured using DLS.

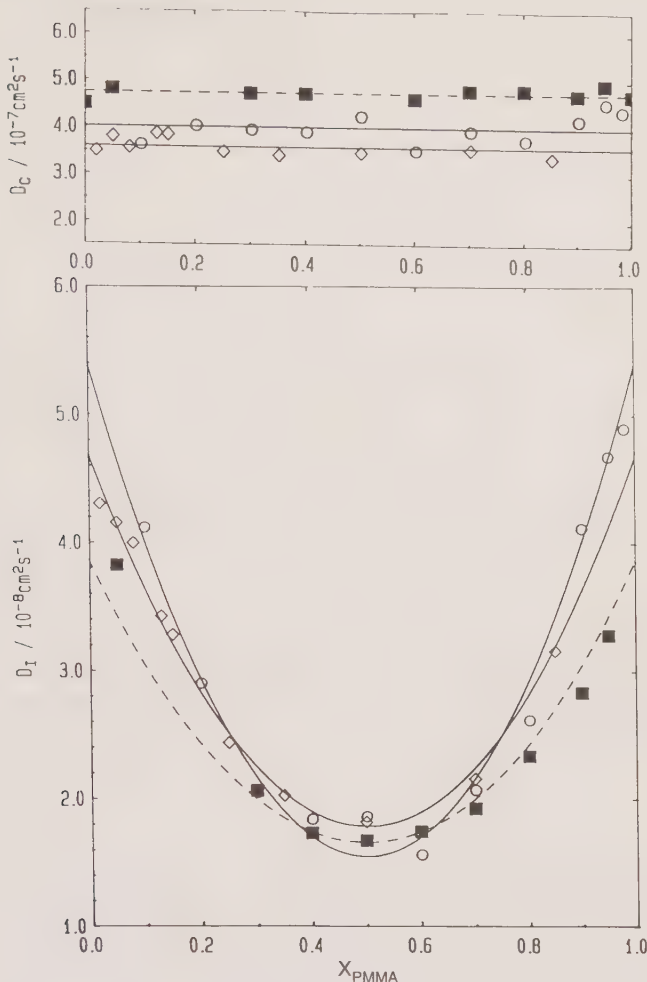


FIG. 8.3. Diffusion coefficients as a function of the composition $x = c_{\text{PMMA}}/c_T$ for different systems: \blacksquare , PDMS/PMMA/CHCl₃; \circ , PDMS/PMMA/THF; \diamond , PS/PDMS/THF. The continuous lines correspond to the best fit according to the model. This figure shows that the cooperative diffusion D_c is independent of x and that the interdiffusion coefficients D_l follow the predicted parabolic behaviour $x(1 - x)$. From ref. 75. (Reprinted with permission from *Macromolecules*. Copyright 1992 American Chemical Society.)

To close the homopolymer mixtures/solution discussion, it is important to note that it is possible to have direct access to the concentration dependencies of the χ parameter, as shown by Benmouna and Borsali,^[25] and that of the single or self-diffusion coefficient D_s by combining dynamic light scattering^[81] and any labelling technique; for instance, fluorescence recovery after photo-bleaching^[82] (FRAP) experiments.

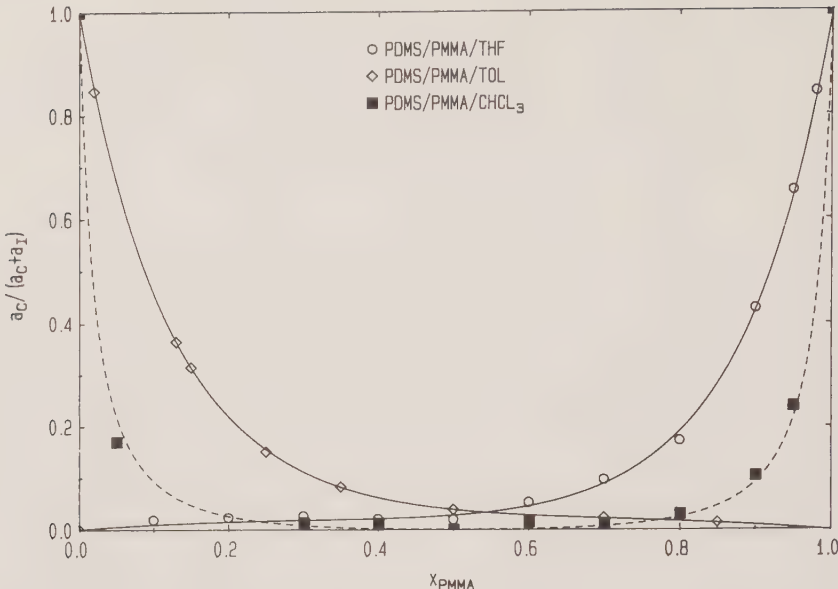


FIG. 8.4. The relative amplitude of the cooperative mode $a_c/(a_c + a_l)$ as a function of the composition $x = c_{\text{PMMA}}/c_T$ for the three different mixtures indicated in Fig. 8.3 and using the same symbols. The continuous lines also correspond to the best fit according to the model. From ref. 75. (Reprinted with permission from *Macromolecules*. Copyright 1992 American Chemical Society.)

Indeed, DLS and FRAP experiments have been performed on dextran/polyvinylpyrrolidone (PVP) mixtures in water at several total polymer concentrations, c_T , from the dilute to the semi-dilute range of concentration ($0.1c^*$ to $10c^*$) in the homogeneous and disordered states. As expected, the dynamics of this system as revealed by DLS experiments show two relaxation modes (see Figs 8.5(a) and 8.5(b)).

From the two relaxation modes it is possible, following the model, to extract as a function of the polymer concentration the values of the interaction parameter χ and those of the single-chain diffusion coefficients for both components. The results of the fits are shown in Figs. 8.6(a) and 8.6(b).

As far as FRAP^[82] is concerned, and as expected, only one relaxation mode is required to describe the dynamics and is identified with the self-diffusion coefficient of the labelled dextran, since the composition of the labelled dextran chain is very small. The value of the self-diffusion coefficients measured directly using this technique (FRAP) has been compared to that deduced from DLS experiments.^[81] The agreement is found to be good in the semi-dilute range, confirming the validity of the Rouse model used to extract the self-diffusion coefficient from DLS experiments. However, as the concentration is decreased, the agreement becomes less satisfactory, revealing that the deduced value of

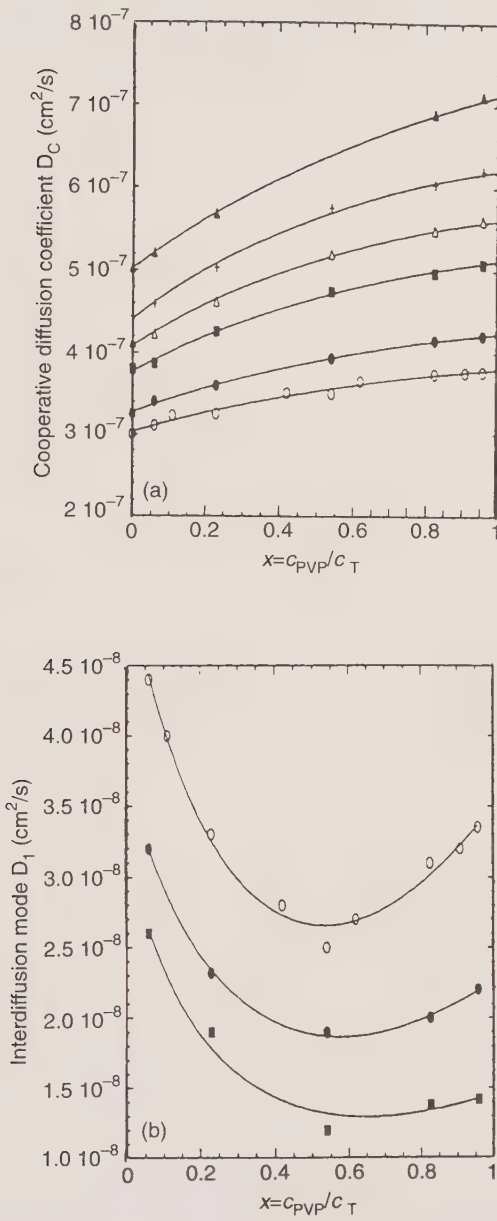


FIG. 8.5. The variation of the fast D_F (a) and slow D_S (b) diffusion modes measured in the ternary polymer mixture PVP/dextran/water using DLS as a function of the composition $x = c_{PVP}/c_T$, for different concentrations: \circ , 2.33×10^{-2} g/cm³; \bullet , 3.0×10^{-2} g/cm³; \blacksquare , 4.0×10^{-2} g/cm³; \triangle , 5.0×10^{-2} g/cm³; $+$, 6.0×10^{-2} g/cm³; \blacktriangle , 8.0×10^{-2} g/cm³. The symbols represent the experimental data and the solid lines the best fits according to eqns (8.22)–(8.24). From ref. 81. (Reprinted with permission from *Macromolecules*. Copyright 1993 American Chemical Society.)

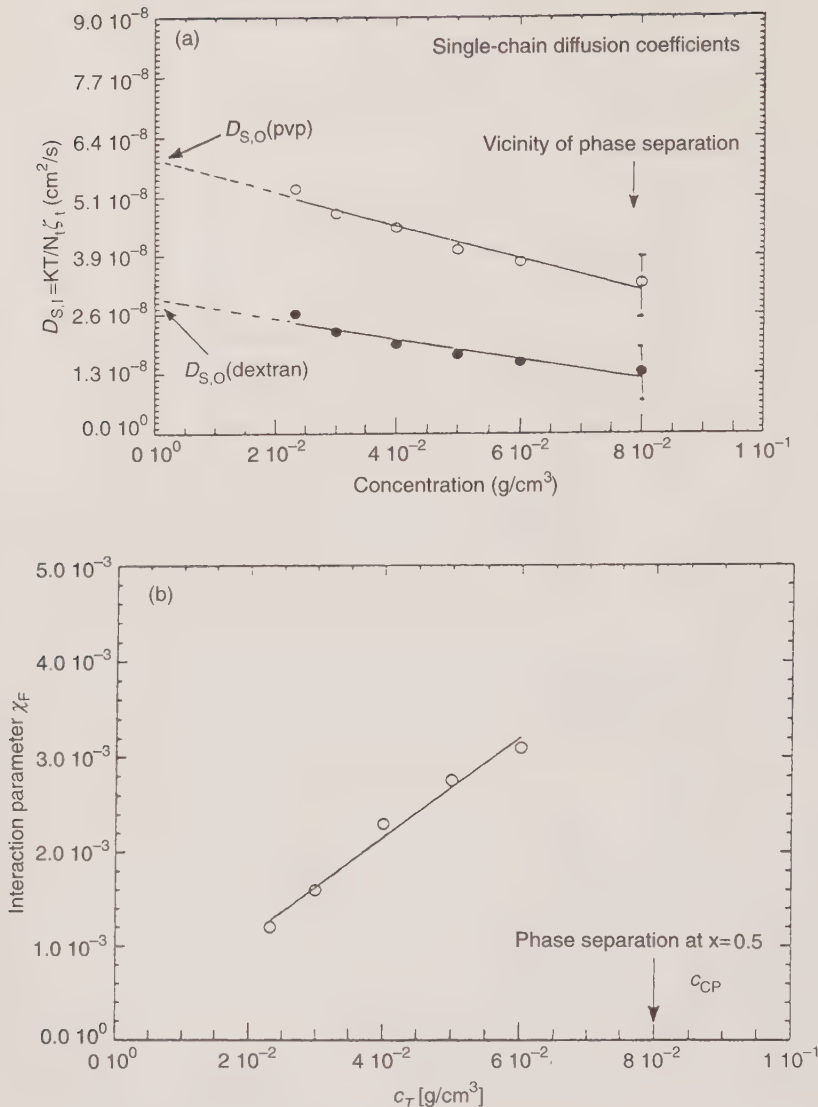


FIG. 8.6. (a) Variation of the single-chain diffusion coefficients $D_{S,i}$ of (○) PVP and (●) dextran as function of the concentration. (b) Variation of the interaction parameter χ in the ternary mixture PVP and dextran in water as function of the concentration. From ref. 81. (Reprinted with permission from *Macromolecules*. Copyright 1993 American Chemical Society.)

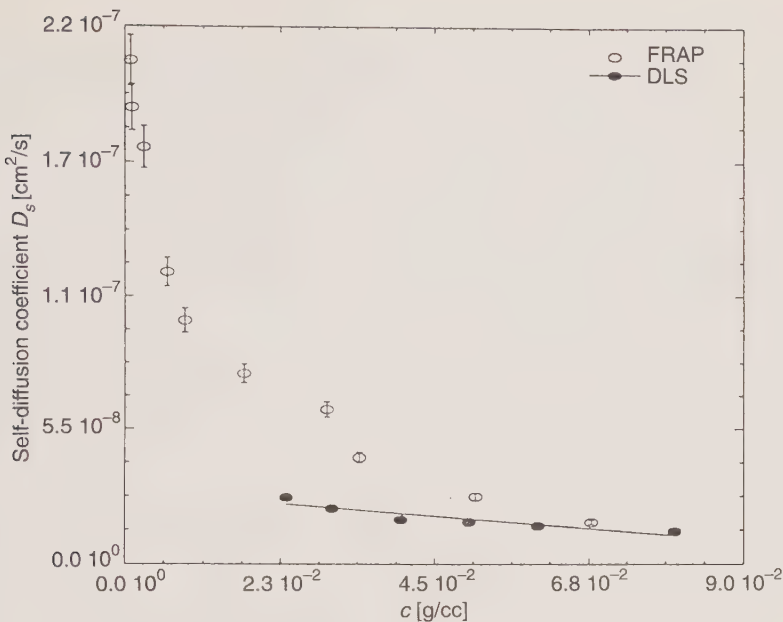


FIG. 8.7. The ternary system dextran/PVP/water: a comparison between the single-chain diffusion coefficients D_s of dextran as a function of the total polymer concentration measured directly using FRAP (\circ) and extracted from DLS (\bullet) using the Rouse model. From ref. 82. (Reprinted with permission from *Macromolecules*. Copyright 1994 American Chemical Society.)

the self-diffusion coefficient in the dilute system on extrapolation to infinite dilution ($c_T \rightarrow 0$) is wrong (see Fig. 8.7). In fact, for $c < c^*$, hydrodynamic interactions are important and have to be taken into account. Re-analysing^[83] the data obtained from the DLS experiments^[81] by introducing hydrodynamic interactions (the Zimm version of the model) shows that the deduced self-diffusion coefficients agree with the values of the self-diffusion coefficient measured directly using FRAP.^[82]

So far the interaction parameter has always been ‘measured’ using static light scattering under particular conditions, namely by choosing an optical theta solvent^[80,84–87] in order to have good accuracy in the determination of χ . According to the results presented in this work, we would like to stress that the interaction parameter and the single chain diffusion coefficient can be directly ‘measured’ *at any composition* (not necessarily a very low concentration as usually done in labelling techniques) and *at any concentration* using DLS if the correct model is used to extract these quantities (Rouse or Zimm) depending on the concentration domain as described above. This conclusion is also valid *in any good solvent* (whatever the refractive index) since the frequencies do not depend on the optical properties of the system.

8.4.2.2 Diblock copolymers. As far as diblock copolymer chains in solution are concerned, the dynamics are also expected to be described by two relaxation modes within the framework of the model, but with a different physical meaning. The first mode (cooperative) reflects the fluctuation of the total copolymer concentration and the second, the so-called internal mode, describes the relative motion of one block with respect to the other. The first experimental results performed on a linear diblock copolymer PS(H)-PS(D)/solvent under 'ZAC' using NSE, and showing the existence of the internal motion within the single chain, were reported by Borsali *et al.*^[35] in 1989. The internal mode shows peculiar behaviour in the small q range: its frequency becomes constant as q approaches zero as predicted by the model and, indeed, as observed experimentally when using NSE. Figure 8.8(a) shows the variation of the normalized frequency $\Gamma_I(q)/q^2$ for the diblock copolymer and the corresponding mixture for comparison. This behaviour is also shown in Fig. 8.8(b), where $\Gamma_I(q)$ is plotted as a function of q and one sees clearly that, for $q \rightarrow 0$, $\Gamma_I(q)$ goes to a constant in the case of the diblock copolymer and, as expected, $\Gamma_I(q)$ goes to zero in the case of the corresponding homopolymer mixture. These experiments have been performed at a single polymer concentration and, as we shall see later, the effect of concentration is not yet completely understood.

To observe simultaneously both of the expected relaxations in diblock copolymer systems, DLS is an adequate tool. However, even studies of nearly symmetric systems (for the sake of simplicity), have shown that the situation is not so obvious as regards the interpretation of the results and contradictory

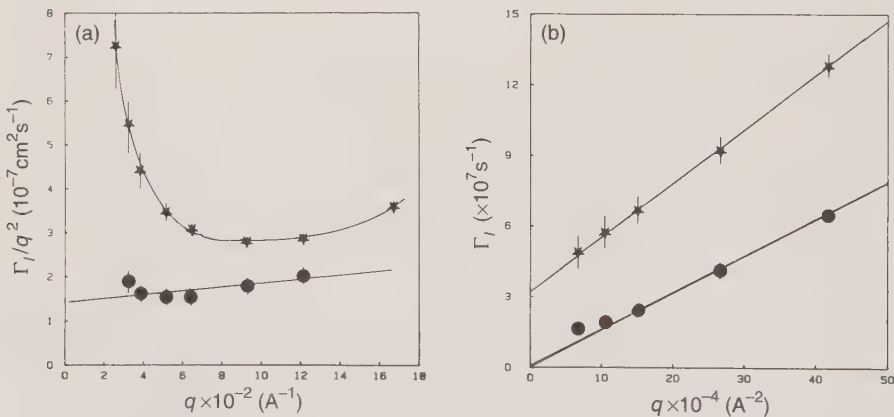


FIG. 8.8. (a) The variation of the normalized frequency $\Gamma_I(q)/q^2$ of the internal mode as a function of q measured using the neutron spin echo technique for two systems: *, diblock copolymer PSD-PSH/(benzene H + benzene D); ●, mixture of homopolymers PSD/PSH/(benzene H + benzene D) at $c = 0.34 \text{ g/cm}^3$. (b) The variation of the frequency $\Gamma_I(q)$ of the internal mode as a function of q measured for the same system as in (a). From ref. 35. (Reprinted with permission from *Macromolecules*. Copyright 1989 American Chemical Society.)

conclusions have been drawn. Indeed, over the past few years, more than ten papers have been published giving different interpretations. The first paper using DLS was published by Borsali *et al.*^[88] in 1991 on the PS-PMMA/toluene system at a single concentration. It was concluded that cooperative and internal modes are observed: the first relaxation has q^2 behaviour and the second shows a frequency that becomes constant as q approaches zero, as predicted by the theory. These results were analysed in the framework of the Akcasu-Benmouna-Benoit model and good agreement was found at least qualitatively (see Fig. 8.9). The same authors examined the effects of concentration change, but no definitive conclusion was satisfactory.^[89] Other papers by Haida *et al.*^[90] and Duval *et al.*^[91] studied the same system, Koňák and Podesva^[41] investigated PS-PI in diphenylethylene and Tsunashima and Kuwamata^[92] studied PS-PMMA/benzene. Depending on the investigated range of concentration, three or four relaxation modes were variously reported by these authors.

Other systems in which more than two relaxational modes have been observed include the dynamics of diblock copolymers near the ordered/disordered transition, reported by Fytas and co-workers^[46-52] and Lodge and co-workers.^[43-45, 93-99] Are these new modes real or is it inhomogeneities (aggregates) in the system which are the source of these observations? Theoretically it is clear that a third mode and *a fortiori* a fourth mode cannot be explained on the basis of the available models described in this chapter. Because of the unclear and sometimes contradictory conclusions and interpretations, there has been a revival and a growing interest in the dynamics of diblock

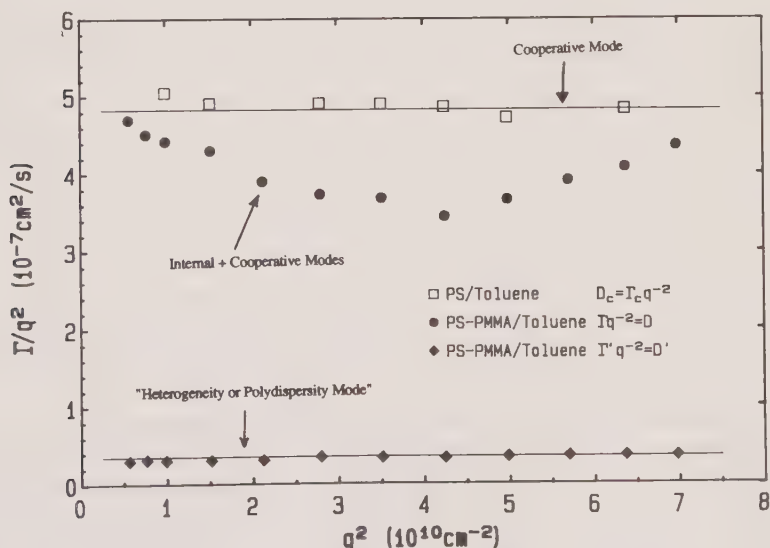


FIG. 8.9. The variation of the normalized frequencies $\Gamma(q)/q^2$ measured on the diblock copolymer system PS-PMMA in toluene and on the corresponding binary system PS/toluene using DLS.

copolymer systems during the past few years which has generated experimental results reported by Lodge and co-workers^[43,44,93] and Fytas and co-workers^[46–52] see Chapter 11.

The current situation has been reviewed in an interesting contribution by Lodge and co-workers^[44,93] in which a comparison between the results obtained by different authors and laboratories is made. Their reported results and interpretation are based on an earlier model of Benmouna *et al.*^[23–26] and recent theoretical results by Semenov.^[53] According to this recent model,^[53] and in addition to the two relaxation modes described in this paper, a third mode observed in the diblock copolymer solution could be explained on the basis of fluctuations in the polydispersity of the composition and governed by the translational diffusion of the diblock chain (the so-called heterogeneity mode). According to both Lodge and Fytas, the experimental results show that the variation of the amplitude and the frequency of this third mode is in good agreement with Semenov's model. Complementary experimental results obtained using pulsed-field-gradient NMR (PFG-NMR) by Balsara *et al.*^[42] confirm the interpretation of the third mode as being governed by the translational diffusion, and therefore it is due to the fluctuation in the polydispersity composition. Figure 8.10 shows the concentration dependence of D_C (the cooperative mode) and D_H (the polydispersity or heterogeneity mode) obtained by DLS, and D_s (single chain diffusion mode) obtained by NMR, for the system polystyrene–polyisoprene in toluene.^[44] In the latter case,^[44] the internal mode, however, could not be resolved over this range of concentration since its amplitude was very low and its frequency was close to D_C . Subsequently, the situation has improved, and other experimental observations by Lodge *et al.*^[93] under Zero Average Contrast (ZAC) have confirmed the actual situation on the dynamics of diblock copolymer chain. Only minor results are still controversial, such as the interpretation of the fourth mode. It may be a 'non-equilibrium state' as suggested by Lodge *et al.*^[43–45,93–99] or it may correspond to 'long-range density fluctuations' as pointed out by Fytas *et al.*^[46–52] The situation is reviewed by P. Štěpánek and T. P. Lodge in Chapter 11 of this volume.

In conclusion, the recent experimental and theoretical work on the dynamic properties of diblock copolymer systems represent considerable efforts made by many authors from different laboratories, and can be summarized as follows. In addition to the existence of the fourth mode, which is still under discussion and investigation, two important relaxational modes describe the intrinsic nature of the copolymer chain. The first one, having q^2 behaviour, is the so-called cooperative mode describing the motion of all the chains with respect to the solvent. It is identical to the cooperative mode measured in the corresponding ternary or binary system. The second mode, the so-called internal mode, reflects the relative motion of one block with respect to the other and is therefore not diffusive: its frequency becomes constant as q approaches zero. A third process, called the heterogeneity mode, is generated by fluctuations in the polydispersity of the composition (i.e. due to the chemistry effect which is not intrinsic to the

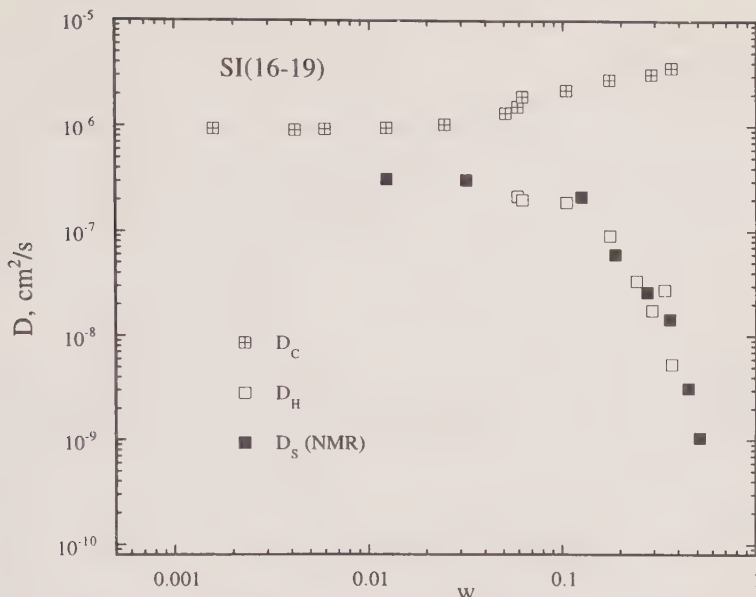


FIG. 8.10. The concentration dependence of D_c and D_h obtained by DLS, and D_s obtained by NMR, for the diblock copolymer polystyrene polyisoprene system in toluene. From 44. (Reprinted with permission from *Macromolecules*. Copyright 1994 American Chemical Society, and by courtesy of T. Lodge.)

copolymer nature). In this respect, for perfectly monodisperse block copolymer chains, the third mode does not exist! However, for a non-monodisperse system in composition (real case), the fluctuations about the mean finite value should lead to the existence of the third mode, as suggested by Semenov,^[53] which is governed by the translational diffusion of the diblock chain (also q^2 behaviour), and has been observed experimentally by Lodge *et al.*^[43-45, 93-99] and Fytas *et al.*^[46-52] Other theoretical work on this subject by Benmouna^[100] will be presented in a forthcoming communication; see also Chapter 1 of this volume.

8.5 The ring diblock copolymer case

Although the properties of linear diblock copolymer systems are still the subject of experimental and theoretical advances, in this section we would like to present and discuss some new results obtained on the static and dynamic properties of ring diblock copolymer chains. What are the expected effects on the scattering properties if both extremities of linear diblock are linked to form a cyclic diblock copolymer chain? Before proceeding with the analysis, and according to the last section, the formalism that we shall use applies to the perfectly monodisperse (length and composition) ring diblock chain and therefore a heterogeneity contribution is not included in the following description.

Cyclic polymers such as the DNA ring described by Weil and Vingrad^[101] in 1965 are important because of their potential applications and their role in the organization of living cells. If A and B polymers in (A–B)_{*l*} diblock polymer chain have different cohesive energy densities, they tend to microphase separate in the segregation limit $(\chi\Phi N) > (\chi\Phi N)_c$. When the two extremities of both species A and B are joined to form a cyclic structure or ring (A–B)_{*r*}, there will be sensitive changes in the static and dynamic scattering properties of the system with respect to those for a linear diblock copolymer chain. The aim of this section is to discuss these changes on a molecular scale, far removed from microphase separation, i.e. in the homogeneous and disordered state.

Special behaviour is found in cyclic chains as compared to the linear counterparts. For instance, Hadzioannou *et al.*^[102] have shown, using small angle neutron scattering in dilute solutions of ring polystyrene in cyclohexane, that the form factor can be well represented by the so-called Cassasa function $P_r(q)$:^[103]

$$P_r(q) = \frac{2}{\sqrt{u}} e^{-(u/4)} \int_0^{\sqrt{u}/2} dx e^{x^2}. \quad (8.30)$$

Here $u = q^2 Na^2/6$, where N is the degree of polymerization and a is the length of the statistical segment. Neutron scattering experiments carried out in dilute solutions of linear chains under the same conditions reveal that the form factor satisfies the Debye function. The radii of gyration extracted from these data are found to satisfy the relationship:

$$R_{gl} = \sqrt{2} R_{gr} \quad (8.31)$$

where the subscripts *l* and *r* refer to linear and ring polymers, respectively. The description that we present here is valid for any cyclic diblock copolymer chain (and any composition). However, for the sake of simplicity, we shall focus on the symmetrical case in which the effects are found to be more pronounced.

8.5.1 Elastic scattering

Consider a cyclic diblock copolymer where the two blocks A and B have the same degree of polymerization ($N_A = N_B = N/2$), the same radius of gyration $R_{gA} = R_{gB} = R_g$, the same excluded volume parameter $v_{AA} = v_{BB} = v$ and a slight incompatibility ($\chi \neq 0$) introduced via the interaction parameter $\chi = v_{12} - v$. The static and dynamic scattering properties of linear diblock copolymers in solution were derived using the framework of linear response theory and RPA, and the results were found to be in reasonable agreement with the neutron scattering data of Borsali *et al.*^[35] To the best of our knowledge, Benoît *et al.*^[104] were the first to study the scattering properties of cyclic copolymer systems during transesterification reactions. Here we show how the results obtained for linear diblocks can be extended to closed chains. The elastic scattering at the polymer volume fraction ϕ for such systems is

given by:^[54]

$$\begin{aligned} \frac{I(q)}{\phi N} = & \left(\frac{a_0 - b_0}{2} \right)^2 \frac{[P_{r1/2}(q) - P_r(q)]}{1 - \frac{\chi}{2} \Phi N [P_{r1/2}(q) - P_r(q)]} \\ & + \left(\frac{a_0 + b_0}{2} - s \right)^2 \frac{P_r(q)}{1 + \left(v + \frac{\chi}{2} \right) \Phi N P_r(q)}, \end{aligned} \quad (8.32)$$

where a_0 , b_0 , and s , depending on the type of radiation to be used (neutrons or light), are the scattering lengths or, equivalently, the indices of refraction for both monomers and the solvent, respectively. The essential difference between this result and that obtained for linear chains is inherent in the form factors $P_r(q)$ and $P_{r1/2}(q)$. These quantities are sensitive to the chain architecture and reflect the entropic interactions of its monomers. The main assumption made in their calculation is to write the average square distance between two monomers i and j separated by the chemical distance $n = |i - j|$ as

$$\langle r_n^2 \rangle = n \left(1 - \frac{n}{N} \right) a^2, \quad (8.33)$$

where the symbol $\langle \dots \rangle$ denotes the thermal average. The second term on the RHS of this equation is due to the fact that one can go from i to j monomers following two different paths along the chain. Using this assumption in the definition of the total form factor, one obtains

$$P_r(q) = \int_0^1 dx e^{-ux(1-x)}, \quad (8.34)$$

which yields the Cassasa function in eqn (8.30). The calculation of $P_{r1/2}(q)$ can be made in a similar way, but the n values should be limited to the range from 1 to $N/2$. One obtains the following simple result:

$$P_{r1/2}(q) = \frac{[1 - e^{-(u/4)}]}{(u/4)}. \quad (8.35)$$

An interesting property of eqn (8.32) is that the two terms carry different physical meanings. The scattering due to the local composition fluctuations is completely decoupled from the scattering due to the total concentration fluctuations of the polymer in the solvent. Furthermore, one can have direct access to each of these terms by choosing the scattering lengths a_0 , b_0 , and s properly. Obviously, the composition fluctuations are more relevant and they can be evaluated unambiguously in so-called ZAC, as demonstrated by Borsali *et al.*,^[35] Giebel *et al.*,^[73-76] Duval *et al.*^[105] and Csiba *et al.*^[106] This means

that $(a_0 + b_0)/2 = s$ and eqn (8.32) becomes

$$\frac{I(q)}{\Phi N} = \left(\frac{a_0 - b_0}{2} \right)^2 \frac{[P_{r1/2}(q) - P_r(q)]}{1 - (\chi/2)\Phi N[P_{r1/2}(q) - P_r(q)]}. \quad (8.36)$$

This result can also be obtained directly from the expressions of the partial structure factors $S_{ij}(q)$ due to interferences between AA, BB, and AB molecules. In the symmetrical case, these are given by

$$\frac{S_{aa}(q)}{\Phi N} = \frac{S_{bb}(q)}{\Phi N} = \frac{S(q)}{\Phi N} = \frac{P_{r1/2}(q) + v\Phi N P_r(q)[P_{r1/2}(q) - P_r(q)]}{4 \mathcal{D}_{en}(q)}, \quad (8.37a)$$

$$\frac{S_{ab}(q)}{\Phi N} = \frac{S_{ba}(q)}{\Phi N} = \frac{S'(q)}{\Phi N} = \frac{P_{r1/2}(q) - (v + \chi)\Phi N P_r(q)[P_{r1/2}(q) - P_r(q)]}{4 \mathcal{D}_{en}(q)}, \quad (8.37b)$$

where

$$\mathcal{D}_{en}(q) = [1 - (\chi/2)\Phi N(P_{r1/2}(q) - P_r(q))][1 + (v + \chi/2)\Phi N P_r(q)]. \quad (8.37c)$$

Here the scattering intensity $I(q)$ should be written as

$$\frac{I(q)}{\Phi N} = (a_0 - b_0)^2 S_I(q), \quad (8.38)$$

where

$$S_I(q) = \frac{S_{aa}(q)}{x^2} + \frac{S_{bb}(q)}{(1-x)^2} - \frac{2S_{ab}(q)}{x(1-x)} \quad (8.39)$$

and, indeed, combination of eqns (8.37)–(8.39) yields the same expression for the scattered intensity given in relation (8.36).

Let us now discuss the changes in the scattering properties for linear and closed diblock copolymer chains. In Fig. 8.11(a), we have plotted the normalized scattered intensity $4I(q)/[(a_0 - b_0)^2 \Phi N]$ as a function of q for linear (curve a) and cyclic (curve b) copolymers made up of monomers of practically the same chemical nature with zero interaction parameter (i.e. $\chi = 0$). It is relevant that the normalized intensity $4I(q)/[(a_0 - b_0)^2 \Phi N]$ is equal to $P_{r1/2}(q) - P_r(q)$, independent of the polymer concentration. Similar behaviour was observed^[35,105] in the neutron scattering data for half-deuterated polystyrene linear chains in a symmetrical mixture of ordinary and deuterated benzene above the overlap concentration c^* . It would be interesting to check whether a similar observation could be made for cyclic copolymers. The position of the maximum is practically unmodified by χ or Φ_T , but its height increases substantially with increasing χ or Φ_T . In fact, if the quantity $\chi\Phi N$ reaches the critical value $2/(P_{1/2rm} - P_{rm})$, the scattered intensity $I(q)$ diverges and the system undergoes a MST. At $\chi\Phi_T N = 10.5$, the linear diblock copolymer chain system microphase separates, whereas the intensity for cyclic copolymers remains finite and comparatively small (see Fig. 8.11(b)). This enhancement of compatibility is an essential property of mixtures involving cyclic polymers, as was first shown by Cates and Deutch^[107] in 1986. It is interesting to note that microphase transition

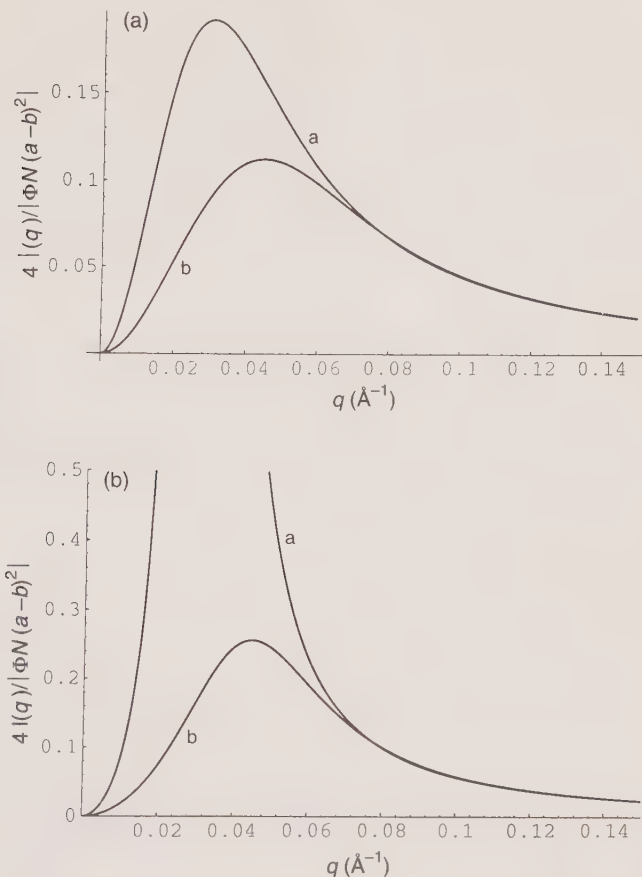


FIG. 8.11. (a) The variation of the normalized scattered intensity as a function of the wavevector q for diblock copolymers made of compatible monomers (i.e. $\chi = 0$) in the zero average contrast condition. Curve a, linear symmetric diblock; curve b, cyclic symmetric diblock. (b) The variation of the normalized scattered intensity as a function of the wavevector q for diblock copolymers made of interacting monomers in the vicinity of the MST for linear diblocks ($\chi\Phi N = 10$) in the zero average contrast condition. Curve a, linear symmetric diblock; curve b, cyclic symmetric diblock with $N = 1000$, $a = 5 \text{\AA}$. From ref. 54. (Reprinted with permission from *J. Phys. II, France*. Copyright 1993, Les Editions de Physiques.)

takes place in the ring system at the critical parameter χ_{mr} such that $\chi_{mr}\Phi N = 18$, which is about 80% higher than the corresponding value in the system of linear chains. These observations can be tested by neutron or light scattering techniques using a proper choice of the mixture to satisfy the so-called optical theta condition or ZAC. In neutron scattering, one can use diblock copolymers made of ordinary and deuterated monomers in a mixture of ordinary and deuterated good solvents. The drawback of this system is that it shows a very

small χ -parameter. In light scattering several systems fulfill the above condition and some have already been studied in the case of linear chains. Finally, one observes in Figs 8.11(a) and 8.11(b) that the position of the maximum, q_m , shifts to higher values with respect to the linear case, indicating a shorter scale for the microstructure in the case of the ring copolymers. Similar conclusions were reported by Marko^[108] and in another work presented by Huber^[109] for the apparent conformational properties in a non-interacting ring diblock copolymer ($\chi = 0$).

8.5.2 Dynamic structure factors (Zimm model)

As in the case of linear diblock copolymers, the intermediate scattering function $S(q, t)$ can be expressed as a sum of two exponential decays. The relevant quantities of interest which can be determined experimentally by the use of dynamic light scattering and/or neutron spin echo are the cooperative relaxation frequency,

$$\Gamma_1(q) = \Gamma_C(q) = q^2 k_B T \frac{M(q) + M'(q)}{S(q) + S'(q)}, \quad (8.40)$$

and the internal mode,

$$\Gamma_2(q) = \Gamma_I(q) = q^2 k_B T \frac{M(q) - M'(q)}{S(q) - S'(q)}, \quad (8.41)$$

where k_B is the Boltzmann constant and T is the absolute temperature. At a 50:50 composition, the partial structure factors for a cyclic diblock copolymer system are

$$S(q) = \frac{(\Phi N/4)\{P_{r1/2}(q) + v\Phi NP_r(q)[P_{r1/2}(q) - P_r(q)]\}}{\{1 + (v + \chi/2)\Phi NP_r(q)\}\{1 - \chi\Phi N[P_{r1/2}(q) - P_r(q)]/2\}}, \quad (8.42)$$

$$S'(q) = \frac{(\Phi N/4)\{2P_r(q) - P_{r1/2}(q) - (v + \chi)\Phi NP_r(q)[P_{r1/2}(q) - P_r(q)]\}}{\{1 + (v + \chi/2)\Phi NP_r(q)\}\{1 - \chi\Phi N[P_{r1/2}(q) - P_r(q)]/2\}}. \quad (8.43)$$

The mobility matrix is symmetric and $M(q)$ and $M'(q)$ represents its elements. They can be written including both the Rouse and the hydrodynamic terms as follows:^[13, 14, 21, 65]

$$M(q) = \frac{\Phi}{2f} + \frac{1}{(2\pi)^2 \eta_0} \int_0^\infty dk F\left(\frac{k}{q}\right) S(k), \quad (8.44)$$

$$M'(q) = \frac{1}{(2\pi)^2 \eta_0} \int_0^\infty dk F\left(\frac{k}{q}\right) S'(k), \quad (8.45)$$

where Φ , f and η_0 are the polymer volume fraction, the friction coefficient per monomer (assumed to be the same for both monomers) and the viscosity of

the solvent, respectively. The function $F(w)$ is given by

$$F(w) = w^2 \left\{ \frac{w^2 + 1}{2w} \log \left| \frac{w + 1}{w - 1} \right| - 1 \right\}, \quad (8.46)$$

with $w = (k/q)$. This description of the hydrodynamic interaction is based on the classical Oseen tensor. There are, of course, other models which can be used depending on the system under consideration. Introducing the expressions of the partial structure factors and those of the mobilities in relations (8.40) and (8.41) yields

$$\begin{aligned} \Gamma_C(q) &= q^2 \left[\frac{k_B T}{Nf} \right] \frac{1}{P_r(q)} [1 + (v + \chi/2)\Phi N P_r(q)] \\ &\times \underbrace{\left\{ 1 + \frac{Na}{(2\pi)^2} \left(\frac{f}{a\eta_0} \right) \int_0^\infty dk F\left(\frac{k}{q}\right) \frac{P_r(k)}{1 + (v + \chi/2)\Phi N P_r(k)} \right\}}_{\text{Zimm term}}, \end{aligned} \quad (8.47)$$

$$\begin{aligned} \Gamma_I(q) &= q^2 \left[\frac{k_B T}{Nf} \right] \left[\frac{1}{P_{r1/2}(q) - P_r(q)} - \frac{\chi\Phi N}{2} \right] \\ &\times \underbrace{\left\{ 1 + \frac{Na}{(2\pi)^2} \left(\frac{f}{a\eta_0} \right) \int_0^\infty dk F\left(\frac{k}{q}\right) \frac{P_{r1/2}(k) - P_r(k)}{1 - \chi\Phi N [P_{r1/2}(k) - P_r(k)]/2} \right\}}_{\text{Zimm term}}. \end{aligned} \quad (8.48)$$

The same expressions hold for linear diblock copolymer in solution, where the subscript r is replaced by l and where the form factors $P_l(q)$ and $P_{l1/2}(q)$ are the standard Debye functions for total and half chains respectively, assuming Gaussian statistics. Interesting results are obtained in the cyclic case and are discussed below.

(i) In the concentration range above the overlap limit c^* , the hydrodynamic interactions are essentially screened and the Rouse model is more likely to describe the dynamical behaviour of the system. In this model the variation of the cooperative mode $\Gamma_C(q)$ versus q for linear and cyclic polymers shows no specific dynamical features which help to distinguish the open and closed polymer chains, except perhaps in the high q range where the dynamics reflect the internal form factors $P_r(q)$ and $P_l(q)$. In this respect, investigation of the cooperative mode is not relevant in the concentration range far above c^* . The interdiffusion mode, however, plays a crucial role. To illustrate these new results, we have plotted in Fig. 8.12 the variation of $\Gamma_I(q)/[q^2(k_B T/Nf)]$ as a function of q for $\chi\Phi N = 1$ and 10. First, regardless of whether or not the system is linear or cyclic, one observes the expected peculiar behaviour of the diblock copolymer character in the small q range, namely a frequency that goes to a finite value as q approaches zero. Moreover, for $\chi\Phi N = 10$, the normalized frequency $\Gamma_I(q)/[q^2(k_B T/Nf)]$ is practically zero at q_m for linear diblock

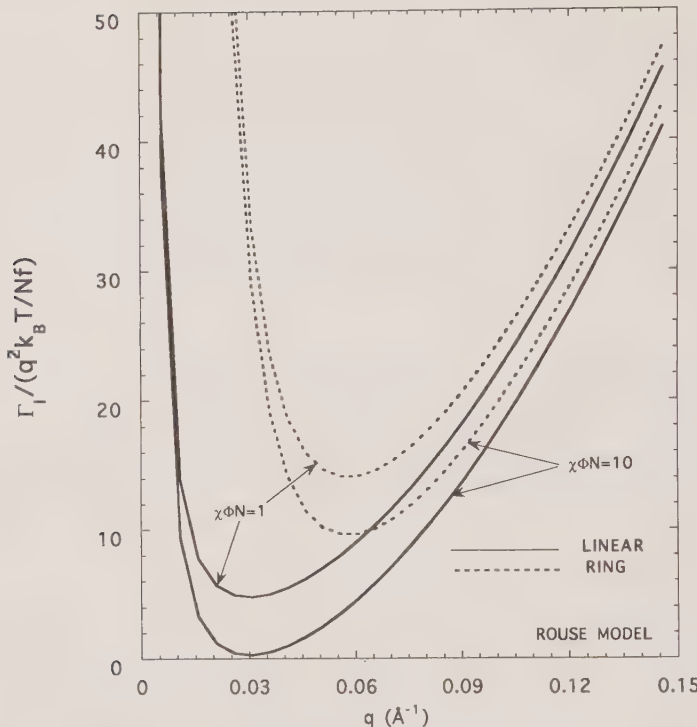


FIG. 8.12. The variation of the normalized frequency $\Gamma_l(q)/[q^2(k_B T/Nf)]$ as function of q at $\chi\Phi N = 1$ and 10 in the Rouse model for cyclic (----) and linear (—) diblock copolymers. From ref. 55. (Reprinted with permission from *Europ. Lett.* Copyright 1993, Les Editions de Physiques.)

copolymers, whereas it remains positive and quite high for diblock cyclic ones. In fact, in the latter system, the normalized frequency $\Gamma_l(q)/[q^2(k_B T/Nf)]$ goes to zero at q_m for $\chi\Phi N = 18$, as has already been pointed out for the static properties. One also observes that the minimum position q_m is shifted significantly towards higher values for cyclic copolymers, indicating that the kinetics at the characteristic size of the microphase structure ($1/q_m$) appear to be much smaller for rings. These observations show that there are substantial differences between the linear and cyclic behaviours, which should be detectable using either static or dynamic experiments.

(ii) Below the overlap concentration c^* , in the dilute regime, the effects of hydrodynamic interaction become important. Here both the cooperative and interdiffusive modes are relevant and also show substantial differences between linear and cyclic copolymers. For example, Fig. 8.13 shows the variation of $\Gamma_C(q)/[q^2(k_B T/Nf)]$ as a function of q for $\chi\Phi N = 1$ and 10 in both systems. In the small q range this plot shows that the diffusion coefficients $D_C(\text{cyclic}) > D_C(\text{linear})$. This result is consistent with the experimental observations obtained

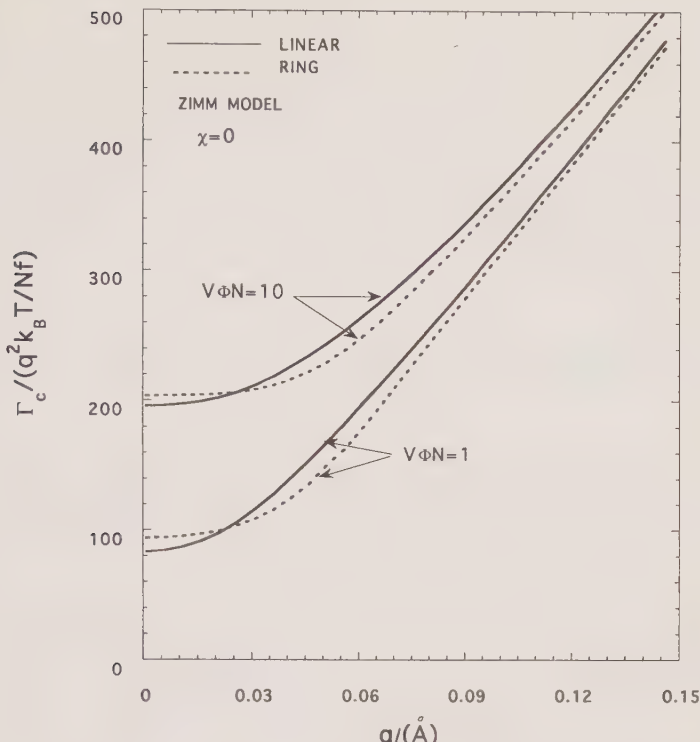


FIG. 8.13. The variation of the normalized frequency for the cooperative mode $\Gamma_c(q)/[q^2(k_B T/Nf)]$ as function of q at $v\Phi N = 1$ and $\chi = 0$ in the Zimm model for cyclic (----) and linear (—) diblock copolymers. $N = 1000$, $a = 52 \text{ \AA}$, $R_g = 65 \text{ \AA}$ and the draining parameter $(f/a\eta_0) = 3\pi$ (a being the monomer diameter). From ref. 55. (Reprinted with permission from *Europhys. Lett.* Copyright 1993, Les Editions de Physiques.)

by Hadzioannou *et al.*^[102] In the q range near $qR_g = 2$ the behaviour is reversed. Above this wavevector, the dynamics of the internal modes are slower for ring copolymers.

To the best of our knowledge, no experimental work has been carried out in this direction, probably because of the difficulty of synthesizing such polymers. However, recent experimental observations combining static and DLS have been carried out by Amis and co-workers^[110,111] on dilute solutions of ring diblock and triblock copolymers (low molecular weights), and show very interesting and promising results.

8.6 Extrapolation to the bulk state

In the melt system only one relaxational mode^[56–63] is required to describe the dynamical behaviour, whereas in solution there are two, as has been shown in the first part of this chapter. The aim of this section is to show that one

of the two relaxational modes ($A_2(q)$ and $\Gamma_2(q)$) which exist in solution is identical to the unique mode in the melt. To illustrate this point we consider two cases (namely two homopolymers/solvent and a diblock copolymer solution) for which the amplitudes and the frequencies can easily be calculated under general conditions. Indeed, starting from the well-known relations that describe the dynamical behaviour of such systems using the Rouse model (see eqns (8.2)–(8.21)), when the excluded volume $v = v_0(1/\Phi_s - 2\chi)$ goes to infinity (i.e. the solvent volume fraction $\Phi_s = 0$ and therefore $\Phi_T = 1$: the melt case), the general expression for the unique relaxation mode is

$$\Gamma_2(q) = q^2 \left(\frac{D_a^0 D_b^0}{P_a(q) P_b(q)} S_{aa}^0(q) S_{bb}^0(q) \left[\frac{S_T^0(q)}{\Delta S^0(q)} - 2\chi \right] \right) / \left(D_a^0 \frac{S_{aa}^0(q)}{P_a(q)} + D_b^0 \frac{S_{bb}^0(q)}{P_b(q)} \right). \quad (8.49)$$

The second mode, characterized by $A_1(q)$ and $\Gamma_1(q)$, disappears when $v \rightarrow \infty$. Its frequency $\Gamma_1(q)$ goes to infinity (eqn (8.18)) and its amplitude vanishes. In fact, the expressions for the amplitudes $A_1(q)$ and $A_2(q)$ are very complicated in the general case. In order to show that $A_1(q)$ goes to zero when $v \rightarrow \infty$, let us consider a simple case: a diblock copolymer system in which the solvent is isorefractive (light) or has the same scattering length (neutrons) as one of the components. In this case the amplitudes are given by^[23,32]

$$A_1(q) = \frac{[\Gamma_1(q) - \Omega_{bb}(q)] S_{aa}(q) + \Omega_{ab}(q) S_{ba}(q)}{\Gamma_1(q) - \Gamma_2(q)}, \quad (8.50)$$

$$A_2(q) = \frac{[\Gamma_2(q) - \Omega_{bb}(q)] S_{aa}(q) + \Omega_{ab}(q) S_{ba}(q)}{\Gamma_2(q) - \Gamma_1(q)}, \quad (8.51)$$

which reduce to

$$A_1(q) = \frac{\Phi N P_T(q) [1 - \chi \Phi N [P_{1/2}(q) - P_T(q)]]}{2 \mathcal{D}_{eno}}, \quad (8.52)$$

$$A_2(q) = \frac{\Phi N [P_{1/2}(q) - P_T(q)] [1 - \Phi N P_T(q)(2v + \chi)]}{2 \mathcal{D}_{eno}}, \quad (8.53)$$

with

$$\begin{aligned} \mathcal{D}_{eno} &= 1 + v[2\Phi N P_T(q) - 2\chi\Phi^2 N^2 P_T(q)[P_{1/2}(q) - P_T(q)]] \\ &\quad + \chi\Phi N [2P_T(q) - P_{1/2}(q)] - \chi^2\Phi^2 N^2 P_T(q)[P_{1/2}(q) - P_T(q)] \end{aligned} \quad (8.54)$$

for the 50:50 diblock copolymer chain. In these relations it is straightforward to see that when $v \rightarrow \infty$, $A_1(q) = 0$ and

$$A_2(q) = \left[\frac{2}{\Phi N [P_{1/2}(q) - P_T(q)]} - 2\chi \right]^{-1}, \quad (8.55)$$

where $P_{1/2}(q)$ and $P_T(q)$ are the intramolecular form factors for one block and

the whole chain, respectively. This relation is identical to Leibler's^[64] result,

$$S(q) = \left[\frac{S_T^0(q)}{\Delta S^0(q)} - 2\chi \right]^{-1}, \quad (8.56)$$

for a symmetrical diblock copolymer. Finally, we deduce from this analysis the dynamic structure factor describing the properties in the melt (subscript *m*) state:

$$S_T(q, t) = S_m(q) e^{-\Gamma_m t}, \quad (8.57)$$

where

$$\Gamma_m(q) = q^2 \left(\frac{D_a^0 D_b^0}{P_a(q) P_b(q)} S_{aa}^0(q) S_{bb}^0(q) \left[\frac{S_T^0(q)}{\Delta S^0(q)} - 2\chi \right] \right) / \left(D_a^0 \frac{S_{aa}^0(q)}{P_a(q)} + D_b^0 \frac{S_{bb}^0(q)}{P_b(q)} \right) \quad (8.58)$$

is identified as the interdiffusion (blend of two homopolymers) or the internal (diblock copolymer melt) relaxation frequency and

$$S_m(q) = \left[\frac{S_T^0(q)}{\Delta S^0(q)} - 2\chi \right]^{-1}, \quad (8.59)$$

where $S_T^0(q) = S_{aa}^0(q) + S_{bb}^0(q) + 2S_{ab}^0(q)$ and $\Delta S^0(q) = S_{aa}^0(q)S_{bb}^0(q) - S_{ab}^{02}(q)$ for the diblock copolymer melt and $S_T^0(q) = S_{aa}^0(q) + S_{bb}^0(q)$; $\Delta S^0(q) = S_{aa}^0(q)S_{bb}^0(q)$ for the binary homopolymer mixture. This result, eqns (8.57)–(8.59), includes all the static and dynamic features of diblock copolymer systems as well as mixtures of two homopolymers in the bulk state. We have shown that all the results obtained, for instance, by Brochard *et al.*,^[57,58] Akcasu *et al.*^[62] and Binder,^[59] directly treating the systems in the bulk state, can be deduced from those for the solution.

8.7 Conclusions

In this chapter we present and discuss the static and dynamic scattering properties of ternary polymer mixtures, containing either two homopolymers or diblock copolymer chains (linear or cyclic), in solution. Using linear response theory and the random phase approximation (RPA), it has been shown that two relaxational modes describe the dynamic behaviour of such systems in solution. In the case of homopolymer mixtures in solution, these two normal modes (q^2 behaviour) can under certain conditions be identified as follows. The first mode characterizes the total polymer concentration fluctuations and is called cooperative. It reflects the relaxation frequency of the mesh size of the pseudo-network formed by all the chains of both species with respect to the solvent. It depends on the excluded volume and increases with increasing concentration. The second one characterizes the composition fluctuations and is called interdiffusion. It depends on the interaction parameter between both components, it decreases with increasing concentration and it reflects to some extent the degree of compatibility of the system. The identification of these

two relaxational modes was made possible using dynamic light scattering and neutron spin echo techniques. Without going into detail, the experimental results obtained by the different authors and laboratories have been found to be in good agreement with the theoretical predictions. As far as the diblock copolymer systems in solution are concerned, the first mode is identical to that measured in the case of ternary or binary homopolymers in a solvent (the so-called cooperative mode), while a different physical meaning is attributed to the second relaxation. This is termed the internal mode and describes the relative motion of one block with respect to the other. It has unusual behaviour in the low q range: its frequency becomes constant as q approaches zero. This mode has been observed using NSE and DLS. Very recently, using DLS, a third mode (the so-called heterogeneity relaxation) has been observed above a certain concentration. This result, based on recent theoretical developments, is explained on the basis of fluctuations in the polydispersity of the composition and its relaxation is governed by the translational diffusion of the diblock chain. Some works have also reported the existence of a fourth relaxation, which is still under investigation and discussion and, according to the authors, may be interpreted as a consequence of a 'non-equilibrium state' or 'long-range density fluctuations'.

The static and dynamic scattering properties of ring diblock copolymers are also presented within the framework of linear response theory and RPA formalism. Among the results it is found that the maximum position, q_m , of the scattered intensity is shifted significantly towards higher values for cyclic copolymers, indicating that the microphase structure will appear on a short scale compared to the linear case. This microphase separation occurs at $(\chi\Phi N)_c \approx 18$ for cyclic diblock copolymers, whereas it is known to be at 10.5 for the corresponding linear diblock copolymers, showing that the ring system is more compatible than the corresponding linear one. We have also examined the relaxation of the modes related to collective and composition fluctuations. In the concentration range above the overlap limit c^* , where the hydrodynamic interactions are screened out and the Rouse model is more likely to describe the dynamical behaviour of the system, the variation of the cooperative mode $\Gamma_c(q)$ versus q shows no specific dynamical features which could help to distinguish the open and closed polymer chains, except perhaps in the high q range where the dynamics reflect the internal form factors $P_r(q)$ and $P_l(q)$. The internal mode however, displays an important difference between linear and cyclic diblock copolymer chains. It is practically zero at q_m for linear diblock copolymers, whereas it remains positive and quite high for diblock cyclic ones. These observations show that there are substantial differences between the dynamical behaviours that are detectable using either static or dynamic scattering experiments. Finally, the synthesis of diblock rings of high enough molecular weight and the use of dynamic light scattering and neutron spin echo techniques is required in order to check these theoretical predictions. We have also shown that the properties of the melt state can be obtained from those of the solutions when the excluded volume parameter $N \rightarrow \infty$.

Acknowledgements

The author expresses his gratitude to Professors H. Benoît, M. Benmouna, A. Z. Akcasu, G. Jannink, E. W. Fischer, T. P. Lodge, G. Fytas and W. Brown for fruitful discussions and valuable comments on this work. T.P.L. and G.F. are gratefully acknowledged for providing preprints of refs 44, 52 and 93 prior to publication.

References

1. Albertson, P. A. (1971). *Partition of cell particles and macromolecules*, 2nd edn. Wiley Interscience, New York.
2. Cotts, D. B. (1983). *J. Polym. Sci., Polym. Phys. Ed.*, **21**, 1381.
3. Hanley, B., Balloge, S., and Tirrell, M. (1983). *Chem. Engng Communs*, **24**, 93.
4. Lodge, T. P. (1983). *Macromolecules*, **16**, 1393.
5. Martin, J. E. (1984). *Macromolecules*, **17**, 1279.
6. Wheeler, L. M., Lodge, T. P., Hanley, B., and Tirrell, M. (1987). *Macromolecules*, **20**, 1120.
7. Hadgraft, J., Hyde, A. J., and Richard, R. W. (1979). *J. Chem. Soc. Faraday Trans. II*, **75**, 507.
8. Nemoto, N., Inoue, T., Makita, K., Tsunashima, Y., and Kurata, M. (1986). *Macromolecules*, **19**, 2305.
9. Chu, B., Wu, D.-Q., and Liang, G.-M. (1986). *Macromolecules*, **19**, 2665.
10. Chu, B. and Wu, D.-Q. (1987). *Macromolecules*, **20**, 1606.
11. Brown, W. and Rymdén, R. (1988). *Macromolecules*, **21**, 840.
12. Kim, H., Chang, T., Yohanan, J. M., Wang, L., and Yu, H. (1986). *Macromolecules*, **19**, 2737.
13. de Gennes, P. G. (1979). *Scaling concepts in polymer physics*. Cornell University Press, Ithaca, New York.
14. Doi, M. and Edwards, S. F. (1986). *The theory of polymer dynamics*. Oxford University Press, Oxford.
15. Hess, W. (1986). *Macromolecules*, **19**, 1395.
16. Pusey, P. N., Fijnaut, H. M., and Vrij, A. (1982). *J. Chem. Phys.*, **77**, 4270.
17. Akcasu, A. Z., Hammouda, B., Lodge, T. P., and Han, C. C. (1984). *Macromolecules*, **17**, 759.
18. Akcasu, A. Z., Benmouna, M., and Benoît, H. (1986). *Polymer*, **27**, 1935.
19. Akcasu, A. Z. and Tombakoglu, M. (1990). *Macromolecules*, **23**, 607.
20. Akcasu, A. Z., Nägele, G., and Klein, R. (1991). *Macromolecules*, **24**, 4408.
21. Akcasu, A. Z. (1993). In *Dynamic light scattering: the method and some applications* (ed. W. Brown). Oxford University Press, Oxford (Chapter 1).
22. Akcasu, A. Z., Klein, R., and Hammouda, B. (1993). *Macromolecules*, **26**, 4136.
23. Benmouna, M., Benoît, H., Borsali, R., and Duval, M. (1987). *Macromolecules*, **20**, 2620.
24. Benmouna, M., Duval, M., and Borsali, R. (1987). *J. Polym. Sci., Polym. Phys. Ed.*, **25**, 1839.
25. Benmouna, M., Benoît, H., Duval, M., and Akcasu, A. Z. (1987). *Macromolecules*, **20**, 1107.
26. Benmouna, M. and Borsali, R. (1992). *C.R. Acad. Sci. (Paris) t-314, Série II*, 759.
27. Foley, G. and Cohen, C. (1987). *Macromolecules*, **20**, 1891.
28. Borsali, R. and Vilgis, T. A. (1990). *J. Chem. Phys.*, **93**, 3610.

29. Roby, F. and Joanny, J. F. (1992). *25*, 4612.
30. Hammouda, B. (1993). *Macromolecules*, **26**, 4800.
31. Borsali, R., Duval, M., Benoît, H., and Benmouna, M. (1987). *Macromolecules*, **20**, 1112.
32. Borsali, R. (1988) PhD Thesis. Louis Pasteur University, Strasbourg.
33. Borsali, R., Duval, M., and Benmouna, M. (1989). *Polymer*, **30**, 610.
34. Borsali, R., Duval, M., and Benmouna, M. (1989). *Macromolecules*, **22**, 816.
35. Borsali, R., Benoît, H., Legrand, J. F., Duval, M., Picot, C., Benmouna, M., and Farago, B. (1989). *Macromolecules*, **22**, 4119.
36. Brown, W. and Zhou, P. (1989). *Macromolecules*, **22**, 3508; *ibid.* **22**, 4031.
37. Brown, W., Koňák, Č., Johnsen, R. M., and Zhou, P. (1990). *Macromolecules*, **23**, 901.
38. Aven, M. R. and Cohen, C. (1990). *Macromolecules*, **23**, 476.
39. Davis, P. J., Pinder, D. N., and Callaghan, P. T. (1992). *Macromolecules*, **25**, 170.
40. Koňák, Č., Tuzar, Z., and Jakes, J. (1990). *Polymer*, **31**, 1866.
41. Koňák, Č. and Podesva, J. (1991). *Macromolecules*, **24**, 6502.
42. Koňák, Č., Vlcek, P., and Bansil, R. (1993). *Macromolecules*, **26**, 3717.
43. Balsara, N. P., Štěpánek, P., Lodge, T. P., and Tirell, M. (1991). *Macromolecules*, **24**, 6227.
44. Pan, C., Maurer, W., Liu, Z., Lodge, T. P., Štěpánek, P., von Meerwall, E. D., and Watanabe, H. (1994). *Macromolecules*, **28**, 1643.
45. Kent, M. S., Tirrell, M., and Lodge, T. P. (1994). *J. Polym. Sci., Polym. Phys. Ed.*, **32**, 1927.
46. Anastasiadis, S. H., Fytas, G., Vogt, S., and Fischer, E. W. (1991). *Phys. Rev. Lett.*, **70**, 2415.
47. Jian, T., Anastasiadis, S. H., Fytas, G., Adachi, K., and Kotaka, T. (1993). *Macromolecules*, **26**, 4706.
48. Jian, T., Anastasiadis, S. H., Semenov, A. N., Fytas, G., Adachi, K., and Kotaka, T. (1993). *Macromolecules*, **27**, 4762.
49. Fytas, G., Anastasiadis, S. H., and Semenov, A. N. (1994). *Macromol. Symp.*, **79**, 117.
50. Vogt, S., Anastasiadis, S. H., Fytas, G., and Fischer, E. W. (1994). *Macromolecules*, **27**, 4335.
51. Anastasiadis, S. H., Fytas, G., Vogt, S., Gerharz, B., Fischer, E. W. (1994). *Europhys. Lett.*, **22**, 619.
52. Jian, T., Anastasiadis, S. H., Semenov, A. N., Fytas, G., Fleischer, G., and Vilessov, A. D. (1994). *Macromolecules*, **28**, 2439–49.
53. Semenov, A. N., Fytas, G., and Anastasiadis, S. H. (1994). *Polym. Prep. (Am. Chem. Soc., Div. Polym. Chem.)* **35**(1), 618.
54. Benmouna, M., Borsali, R., and Benoît, H. (1993). *J. Phys. II (France)*, **3**, 1041.
55. Borsali, R. and Benmouna, M. (1993). *Europhys. Lett.*, **23**(4), 263.
56. Jannink, G. and de Gennes, P. G. (1968). *J. Chem. Phys.*, **48**, 2260.
57. Brochard, F. and de Gennes, P. G. (1983). *Physica*, **118A**, 2260.
58. Brochard, F., Jouffroy, J., and Lovinson, P. (1983). *Macromolecules*, **16**, 1638.
59. Binder, K. (1983). *J. Chem. Phys.*, **79**, 6387.
60. Kramer, E., Green, P., and Palmstrom, C. (1984). *Polymer*, **25**, 473.
61. Sillescu, H. (1984). *Makromol. Chem.*, **18**, 501.
62. Akcasu, A. Z., Benmouna, M., and Benoît, H. (1986). *Polymer*, **27**, 1935.
63. Borsali, R. (1994). In *Advances in polymer blends and alloys technology* (ed. K. Finlayson). Technomic, Lancaster, PA, Vol. 5, Chapter 2, p. 22.
64. Leibler, L. (1980). *Macromolecules*, **13**, 1602.
65. Yamakawa, H. (1971). *Modern theory of polymer solutions*. Harper and Row, New York.

66. Vilgis, T. A. and Benmouna, M. (1991). *J. Chem. Phys.*, **93**, 3610.
67. Borsali, R., Vilgis, T. A., and Benmouna, M. (1993). *J. Phys. II (France)*, **3**, 625.
68. Borsali, R. (1994). In *Trends in macromolecular research, India* (ed. J. Menon), **1**, 49.
69. Flory, P. (1965). *Introduction to polymer chemistry*. Cornell University Press, Ithaca, New York.
70. Siegert, A. J. F. (1943). *MIT Rad. Lab. Rep.* No. **465**.
71. (a) Provencher, S. W., Hendrix, J., De Maeyer, L., and Paulussen, N. J. (1978). *J. Chem. Phys.*, **69**, 4273.
 (b) Provencher, S. W. (1979). *Makromol. Chem.*, **180**, 201.
 (c) Provencher, S. W. (1982) *Comput. Phys. Commun.*, **27**, 213.
 (d) Provencher, S. W. (1988). *Comput. Phys. Commun.*, **21**, 214.
72. Štěpánek, P. (1993). In *Dynamic light scattering: the method and some applications* (ed. W. Brown). Oxford University Press, Oxford (Chapter 4).
73. Giebel, L., Borsali, R., Fischer, E. W., and Meier, G. (1990). *Macromolecules*, **23**, 4054.
74. Borsali, R., Giebel, L., Fischer, E. W., and Meier, G. (1991). *J. Non-Crystalline Solids (North-Holland)*, **131–133**, 816.
75. Giebel, L., Borsali, R., Fischer, E. W., and Benmouna, M. (1992). *Macromolecules*, **25**, 4378.
76. Giebel, L., Benmouna, M., Borsali, R., and Fischer, E. W. (1993). *Macromolecules*, **26**, 2433.
77. Lodge, T. P. and Wheeler, L. M. (1986). *Macromolecules*, **19**, 2983.
78. Lodge, T. P. and Markland, P. (1987). *Polymer*, **28**, 1377.
79. Chang, T., Han, C. C., Wheeler, L. M., and Lodge, T. P. (1988). *Macromolecules*, **21**, 1870.
80. Anasagasti, M., Katime, I., and Strazielle, C. (1987). *Makromol. Chem.*, **188**, 201.
81. Desbrières, J., Borsali, R., Rinaudo, M., and Milas, M. (1993). *Macromolecules*, **26**, 2592.
82. Tinland, B. and Borsali, R. (1994). *Macromolecules*, **27**, 2141.
83. Borsali, R. (unpublished results).
84. Fukuda, T., Nagata, M., and Inagaki, H. (1986). *Macromolecules*, **19**, 1411.
85. Fukuda, T., Nagata, M., and Inagaki, H. (1987). *Macromolecules*, **20**, 654.
86. Fukuda, T., Nagata, M., and Inagaki, H. (1987). *Macromolecules*, **20**, 2173.
87. Ould-Kaddour, L. and Strazielle, Cl. (1987). *Polymer*, **28**, 459.
88. Borsali, R., Fischer, E. W., and Benmouna, M. (1991). *Phys. Rev. A*, **43**, 5732.
89. Borsali, R., Giebel, L., Benmouna, M., Fischer, E. W. (unpublished results).
90. Haida, H., Lingelser, J. P., Gallot, Y., and Duval, M. (1991). *Makromol. Chem.*, **192**, 2701.
91. Duval, M., Haida, H., Lingelser, J. P., and Gallot, Y. (1991). *Macromolecules*, **24**, 6867.
92. Tsunashima, Y., Kuwamata, Y. (1993). *Macromolecules*, **26**, 4899.
93. Liu, Z., Pan, C., Lodge, T. P., and Štěpánek, P. (1995). *Macromolecules*, **28**, 3221–9.
94. Daivi, M. C. and Lodge, T. P. (1993). *Macromolecules*, **26**, 859.
95. Daivi, M. C., Eastman, C. E., and Lodge, T. P. (1993). *Phys. Rev. Lett.*, **71**(16), 2591.
96. Eastman, C. E. and Lodge, T. P. (1994). *Macromolecules*, **27**, 5591.
97. Lodge, T. P. (1994). *Mikrochimica Acta*, **116**, 1.
98. Lodge, T. P., Xu, X., Jin, X., and Daivi, M. C. (1994). *Macromol. Symp.*, **79**, 87.
99. Daivi, M. C. and Lodge, T. P. (1994). *Macromolecules*, **27**, 3487.
100. Benmouna, M. (private communication).
101. Weil, R. and Vingrad, J. (1965). *Proc. Natl Acad Sci. (USA)*, **50**, 730.

102. Hadzioannou, G., Cotts, P. M., Brinke, G. ten, Han, C. C., Lutz, P., Strazielle, Cl., Rempp, P., and Kovacs, A. J. (1987). *Macromolecules*, **20**, 493.
103. Casassa, E. F. (1965). *J. Polym. Sci., Part A*, **3**, 605.
104. Benoît, H., Fischer, E. W., and Zachmann, H. G. (1989). *Polymer*, **30**, 379.
105. Duval, M., Picot, Cl., Benmouna, M., and Benoît, H. (1988). *J. Phys. (France)*, **49**, 1963.
106. Csiba, T., Jannink, G., Durand, D., Papoular, R., Lapp, A., Auvrey, L., Boué, F., Cotton, J. P., and Borsali, R. (1991). *J. Phys. (France) II*, **1**, 381.
107. Cates, M. E. and Deutch, J. M. (1986). *J. Phys.*, **47**, 2121.
108. Marko, J. F. (1993). *Macromolecules*, **26**, 1442.
109. Huber, K. (1987). *Macromolecules*, **21**, 1305.
110. Amis, E. J., Hodgson, D. F., and Wu, W. (1993). *J. Polym. Sci., Polym. Phys. Ed.*, **31**, 2049.
111. Amis, E. J. and Wu, W. (1994). *Polym. Preprint*, **35**, 632.

Light scattering in complex micellar systems

Peter Schurtenberger

9.1 Introduction

Surfactants in solution exhibit a complex aggregation behaviour as a result of a delicate balance of opposing forces.^[1] Micellar solutions and microemulsions represent thermodynamically stable liquid dispersions containing surfactant aggregates, which can often be found in a large region of the phase diagram of two- or multi-component surfactant systems.^[2-4] In micellar dispersions, the aggregates are formed by self-assembly of surfactant monomers. While micelles are frequently spherical, they can also exhibit a sphere-to-rod transition and even grow to giant flexible and polymer-like aggregates. This micellar growth can be induced by a reduction in the so-called spontaneous curvature H_0 due to a change in a ‘control parameter’ such as temperature (in non-ionic surfactant systems), ionic strength (in ionic surfactant systems) or cosurfactant concentration, which subsequently results in a characteristic transition in the particle morphology from spheres to cylinders to lamellae.^[5-7]

Microemulsions are formed in three- or multicomponent systems. The microemulsion aggregates have a liquid core (oil in oil-in-water (o/w), water in water-in-oil (w/o) microemulsions) which is surrounded and stabilized by a surfactant monolayer. They frequently possess a droplet-like structure, but they can also grow into large tubular or sponge-like and multi-connected structures.^[2,6] In addition to micellar and microemulsion phases, a number of liquid crystalline phases such as the lamellar (L_α), hexagonal (H) or cubic (I) phases or the so-called ‘sponge’ phase (L_3) can be found. A typical example for the phase behaviour of a ternary system with a non-ionic surfactant of the ethylene oxide type is shown in Fig. 9.1. The surfactant-to-oil ratio is kept constant, and the temperature and the composition (characterized by the weight fraction of surfactant and oil) is allowed to vary, i.e. the system corresponds to a section through the phase prism as illustrated in Fig. 9.1(a). Three separate phases can be identified in the phase diagram shown in Fig. 9.1(b): a microemulsion phase, L; a lamellar liquid crystalline phase; L_α ; and a second liquid phase, the so-called sponge or L_3 phase.^[8]

The relation between microstructure and phase equilibria is an important aspect of surfactant systems. Several theoretical concepts based either on packing considerations of the surfactants in the aggregates or on the role of the bending elastic energy of the surfactant monolayer have provided us with a

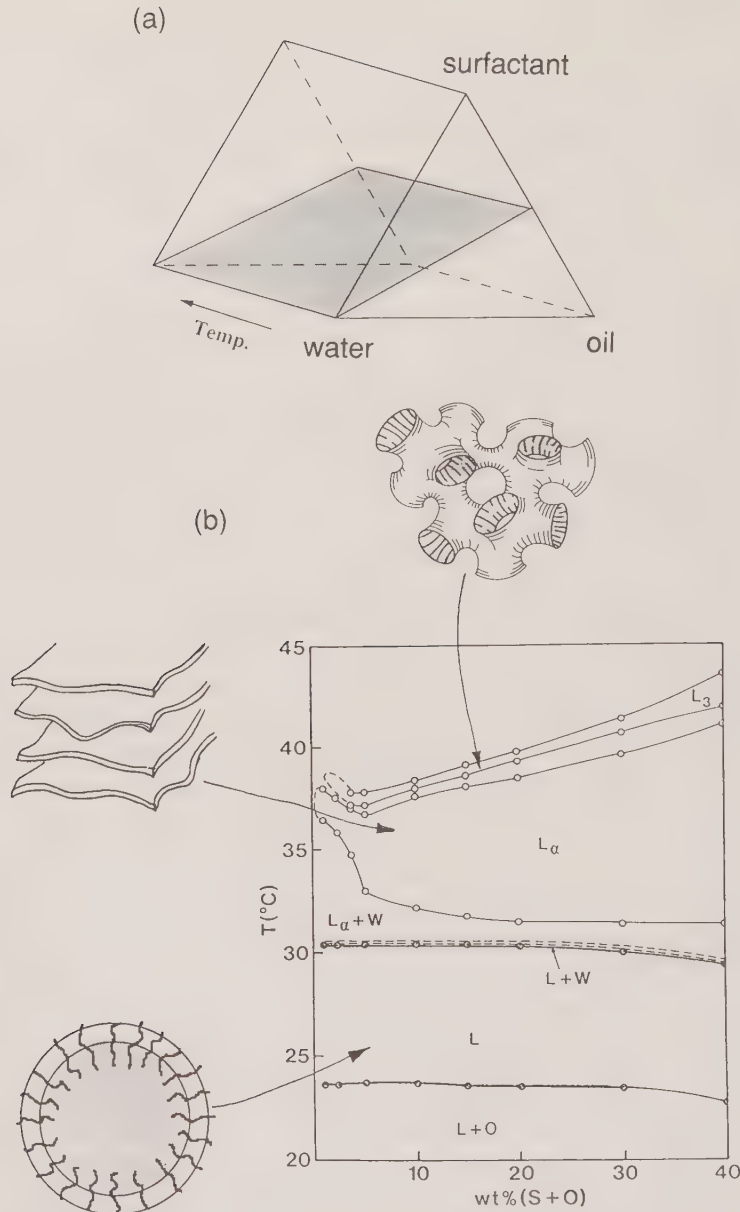


FIG. 9.1. (a) An illustration of the phase prism of a ternary surfactant–water–oil system. The shaded region represents a plane through the phase prism defined by a constant surfactant-to-oil ratio (51.9/48.1 by weight). (b) The phase diagram of the $C_{12}E_5\text{-}D_2O\text{-}$ decane system for a constant surfactant-to-oil ratio of 51.9/48.1 (see (a)), where temperature is plotted versus the total weight fraction of surfactant and oil. L denotes a liquid microemulsion phase, L_a is a lamellar liquid crystalline phase, and L_3 is an isotropic liquid phase, often referred to as the ‘sponge phase’ (adapted from ref. 8).

theoretical framework for a better understanding of these systems.^[1,6,9,10] The sequence of phase transitions shown in Fig. 9.1(b) is, for example, in good agreement with the predictions of the flexible surface model.^[6,8] The phase transitions follow the trend of a decreasing mean curvature of the surfactant film with increasing temperature, i.e. are consistent with the strong temperature-induced variation of the spontaneous curvature for non-ionic surfactants.^[11] This temperature-induced variation of H_0 not only results in the appearance of phase transitions. It also causes variations of the microemulsion structure in the L-phase from almost monodisperse droplets at the lower phase boundary (the so-called emulsification failure^[6]) to anisotropic and possibly multiply-connected particles at the upper phase boundary.^[8,12,13]

It is this particular feature of micelles and microemulsions that makes light scattering investigations of these systems so challenging. The micellar shape, the size distribution and the intermicellar interactions may depend strongly upon solution composition (e.g. surfactant concentration and ionic strength) and temperature, in contrast to other classical macromolecular systems such as polymers, biopolymers or lyophobic colloids. Therefore single particle properties such as the weight average molar mass M_w or the z-average mean square radius of gyration $\langle R_g^2 \rangle_z$ cannot be determined unambiguously from an extrapolation of the scattering data to infinite dilution. The neglect of this inherent property of surfactant systems and the various attempts to decouple micellar growth and intermicellar interactions have led to a number of controversies. This chapter will thus mainly focus on this issue and try to show how contributions from the micellar size distribution and intermicellar interactions to the time-average light scattering intensity can be combined in a self-consistent way for various surfactant systems.

The strong composition and temperature dependence of micellar systems not only represents a serious obstacle in the theoretical interpretation of the light scattering data; it is also complicates the life of the experimentalist. Some classical sample preparation procedures such as filtration of solutions prior to static light scattering measurements should be avoided, since this may result in possible changes in solution composition due to adsorption of the surfactant (or possible cosurfactants) to the filter membrane. Instead, one should subject the samples to centrifugation directly in the scattering cells, while carefully maintaining the required temperature especially in the vicinity of phase boundaries. Additional difficulties can be caused by the sometimes very narrow one-phase regions (see, e.g., the L₃-phase in Fig. 9.1(b)) and the frequently notoriously slow equilibration times found for phase transitions in dilute microemulsion systems, which may lead to ambiguous results if the temperature or dilution line has not been carefully chosen.^[14] Last but not least, the delicate balance of forces that leads to an equilibrium also means that these systems may be strongly influenced by the presence of trace amounts of impurities or minor chemical decomposition such as hydrolysis. This has, for example, stirred a long-lasting controversy on the interpretation of light scattering results in the vicinity of the critical point for non-ionic micellar solutions.^[15–17]

9.2 Spherical micelles and microemulsions: hard and soft spheres

9.2.1 Hard sphere models applied to microemulsions

For a quantitative analysis of a static light scattering experiment, a reduced intensity at a given scattering angle θ , the so-called excess Rayleigh ratio, ΔR_θ (i.e. the differential cross-section of the scattering process), is generally used.^[18,19] For identical micellar particles, ΔR_θ can then be written as

$$\Delta R_\theta = K(C - CMC)MP(q)S(q), \quad (9.1)$$

where $K = 4\pi^2 n^2(dn/dC)^2/(N_A \lambda_0^4)$, dn/dC is the refractive index increment, C is the surfactant concentration (mass/volume), CMC is the critical micellar concentration, and M is the molar mass of the micelles. $P(q)$ is the particle form factor, $S(q)$ is the time-averaged structure factor, and the magnitude of the scattering vector is given by $q = (4\pi n/\lambda_0) \sin(\theta/2)$. Spherical micelles and microemulsions generally have dimensions which are much smaller than the spatial resolution of a light scattering experiment ($\sim 1/q$), and we can set $P(q) = 1$. In the case of a polydisperse micellar solution, we then have to replace M and $S(q)$ with the corresponding effective weighted averages M_w and $S^M(0)$,

$$\lim_{q \rightarrow 0} \Delta R_0 = \Delta R_\theta = K(C - CMC)M_w S^M(0), \quad (9.2)$$

where $S^M(0)$ is given by^[20]

$$S^M(0) = \lim_{q \rightarrow 0} S^M(q) = \lim_{q \rightarrow 0} \frac{1}{Nf^2} \left\langle \sum_j \sum_k f_j f_k \exp[i\mathbf{q}(\mathbf{r}_j - \mathbf{r}_k)] \right\rangle. \quad (9.3)$$

N is the number of micelles in the scattering volume, and f_j and \mathbf{r}_j are the scattering (field) amplitude and position of micelle j , respectively. Equations (9.2) and (9.3) will be the key to the interpretation of data from static light scattering experiments with solutions of spherical micelles and microemulsions. One should keep in mind that the distribution of scattering powers (f_j) is in general coupled to the distribution of aggregate sizes, which will be very important in the interpretation of light scattering data from w/o microemulsions in the vicinity of their optical match point.^[21,22]

We can now try to illustrate the application of static light scattering to micelles and microemulsions with several examples. First we shall take a closer look at a light scattering study of the system $C_{12}E_5$ -D₂O-decane at constant surfactant-to-oil ratio (51.9/48.1 by weight) presented in Fig. 9.1.^[8] The results from the light scattering experiments at 23.6 °C are shown in Fig. 9.2, where the excess Rayleigh ratio at $\theta = 0$, ΔR_0 , is plotted as a function of the total (surfactant and oil) volume fraction ϕ . The low temperature phase boundary of the microemulsion phase at ≈ 23.5 °C can be identified with the emulsification failure, discussed by Safran and co-workers. The flexible surface model predicts spherical oil-swollen micelles on and near this phase boundary.^[6] NMR self-diffusion experiments performed in the vicinity of this emulsification failure

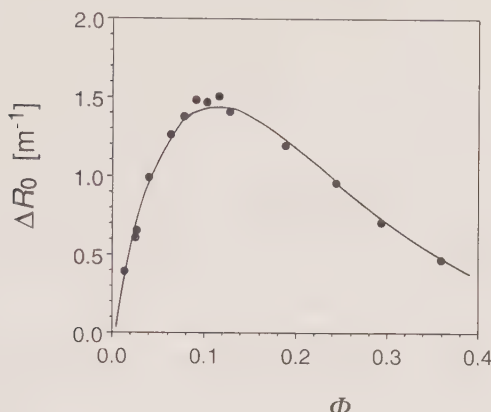


FIG. 9.2. The dependence of the excess Rayleigh ratio ΔR_0 on the total volume fraction ϕ of surfactant and oil. The solid line is the result of a two-parameter fit of eqn (9.7) to the data (see ref. 8 for details).

line indeed clearly demonstrate the existence of discrete, oil-swollen micelles with the same average composition over the whole concentration range investigated.^[8] Furthermore, recent SANS^[23] and ²H-NMR relaxation time^[12] measurements in the same system were consistent with the presence of spherical oil-swollen micelles with a concentration-independent radius under the same conditions. The SANS experiments were interpreted with a structural model of spherical micelles, consisting of a hydrocarbon core with radius $R_{hc} = 80 \pm 5 \text{ \AA}$ coated by the ethylene oxide chains of the non-ionic surfactant, i.e. the structure closely resembles a colloidal particle sterically stabilized by short end-grafted polymer chains. This picture is consistent with simple geometrical considerations for spherical oil-swollen micelles, which predict^[8]

$$R_{hc} = \frac{3(\phi_0 + \phi_s/2)\delta}{\phi_s} \quad (9.4)$$

where ϕ_0 and ϕ_s are the volume fractions of oil and surfactant, respectively, $\delta = v_s/a_s$ is the surfactant length, v_s is the molecular volume of the surfactant, and a_s is the area per surfactant molecule at the polar-apolar interface separating the hydrocarbon from the ethylene oxide chain. For $R_{hc} = 80 \pm 5 \text{ \AA}$, eqn (9.4) leads to $\delta = 15.4 \pm 0.9 \text{ \AA}$, which is in good agreement with the values of δ found for C₁₂E₅ in different liquid crystalline phases.^[24-26]

Based on the close analogy with sterically stabilized colloidal particles, the concentration dependence of the time-averaged light scattering intensity shown in Fig. 9.2 was analysed using a classical hard sphere model. For hard spheres, an application of modern concepts from liquid state theory has yielded good approximations for $S(0)$. The basis for this analysis is the connection between the scattered intensity and the osmotic compressibility. In the limit of $q \rightarrow 0$,

$(\partial\pi/\partial C)^{-1}$ is related to the static structure factor $S(q)$ by the relation^[27]

$$S(0) = \frac{N_A}{M} k_B T \left(\frac{\partial\pi}{\partial C} \right)^{-1}. \quad (9.5)$$

In particular, the semi-empirical extension of the Percus–Yevick theory derived by Carnahan and Starling^[28] provides us with a very accurate analytical expression for the osmotic pressure of a monodisperse hard sphere suspension, which leads to

$$S(0) = \frac{(1 - \phi_{hs})^4}{1 + 4\phi_{hs} + 4\phi_{hs}^2 - 4\phi_{hs}^3 + \phi_{hs}^4}, \quad (9.6)$$

where ϕ_{hs} is the hard sphere volume fraction. Using eqn (9.6) and volume fractions instead of weight concentrations, we can then rewrite eqn (9.1) as

$$\Delta R_0 = \frac{4\pi n^2}{\lambda_0^4} \left(\frac{dn}{d\phi_{hs}} \right)^2 V_{hs} \frac{\phi_{hs}(1 - \phi_{hs})^4}{1 + 4\phi_{hs} + 4\phi_{hs}^2 - 4\phi_{hs}^3 + \phi_{hs}^4}, \quad (9.7)$$

where $V_{hs} = 4\pi R_{hs}^3/3$. As for the case of sterically stabilized colloidal particles, we can expect that $\phi_{hs} > \phi$. Olsson and Schurtenberger therefore used R_{hc} and ϕ_{hs}/ϕ as the two adjustable parameters in their attempt to analyse their data. The result of a non-linear least-squares fit of eqn (9.7) to the data is shown as the solid line in Fig. 9.2. The fit leads to $R_{hc} = 76.1 \pm 0.6 \text{ \AA}$ and $\phi_{hs}/\phi = 1.14 \pm 0.02$, which correspond to $R_{hs} = 86 \pm 1 \text{ \AA}$ and $\delta = 14.7 \pm 0.2 \text{ \AA}$.^[8] These values are in close agreement with those previously found by SANS. The difference $R_{hs} - R_{hc} = 10 \text{ \AA}$ corresponds to approximately half of the contour length of the penta(ethylene oxide) block, which is in good agreement with the calculations for the potential profile and the dimensions of the grafted layer for interacting hydrophobic surfaces with terminally attached poly(ethylene oxide) chains in water by Björling.^[29] Having determined the relation between ϕ_{hs} and ϕ from the static light scattering data, Olsson and Schurtenberger were then able to reproduce the concentration dependence of the collective (D_c) and self-diffusion (D_s) coefficients of the micelles determined by dynamic light scattering and NMR self-diffusion experiments with no adjustable parameters by taking into account the corresponding theoretical relations for hard spheres with hydrodynamic interactions.^[8,30–32] This showed that for droplet-like o/w microemulsions formed by non-ionic surfactants, hard sphere models allow a self-consistent interpretation of static and dynamic light scattering experiments. However, it is clear that such an approach is only valid close to the emulsification failure boundary, where almost monodisperse spherical micelles are formed.

Hard sphere models have often been applied in the interpretation of static light scattering data from water-in-oil microemulsions. In these systems, the microemulsion particles are frequently modelled as water droplets surrounded by a monolayer formed by the surfactant and (if present) part of the cosolvent.

In a pioneering study, Vrij and co-workers measured the scattered intensity of a four-component w/o microemulsion water-potassium oleate-hexanol-benzene (or toluene) over a large range of volume fraction.^[33,34] While they observed that the hard sphere repulsion formed the major contribution to the osmotic compressibility, they had to allow for an attractive perturbation term in eqn (9.6) in order to obtain satisfactory agreement between experiment and theory over the entire range of concentration. This was done by including a semi-empirical van der Waals type attractive term $\pi_A = k_B T A' \phi_{hs}^2 / 2V_{hs}$ in the osmotic pressure π which, together with eqns (9.5) and (9.6), leads to

$$S(0) = \left(\frac{1 + 4\phi_{hs} + 4\phi_{hs}^2 - 4\phi_{hs}^3 + \phi_{hs}^4}{(1 - \phi_{hs})^4} + A'\phi_{hs} \right)^{-1}. \quad (9.8)$$

The same approach has been used by several authors for a number of different systems.^[35-38]

Several attempts have been made to improve the analysis of static scattering data from w/o microemulsions by including polydispersity and/or using other types of interaction potentials. For polydisperse solutions, one should in principle use eqn (9.3) and calculate the partial structure factors. However, depending upon the interaction potential, this can be rather complex. One therefore frequently assumes that the particle sizes and positions are uncorrelated. Kotlarchyk and Chen, for example, used this decoupling approximation in conjunction with the Percus-Yevick hard sphere solution for $S(q)$ in the analysis of SANS data from AOT w/o microemulsions.^[39] However, while this approximation can be quite useful for charged systems with long-range repulsive forces, it leads to a very poor description of $S^M(q)$ for short-range potentials such as in hard sphere systems with or without attraction even at low polydispersities, $\sigma \leq 0.1$.^[20] Furthermore, when interpreting the q -dependence of $I(q)$ from SANS in terms of polydispersity, one has to take into account the fact that shape fluctuations in microemulsion droplets contribute considerably, and that these contributions are easily misinterpreted as due to size (volume) polydispersity.^[22,40,41] Instead of using eqn (9.8) for microemulsion droplets with short-range attractive forces, they can also be described with the so-called sticky hard sphere potential first introduced by Baxter.^[42,43] A multicomponent version of the Baxter model within the Percus-Yevick approximation has, for example, been used to interpret small angle X-ray data from AOT w/o microemulsion.^[44,45]

9.2.2 Optically inhomogeneous particles: the optical match point

However, one has to be extremely careful when applying expressions for $S^M(0)$ derived for homogeneous hard (or sticky) spheres in the analysis of light scattering data from w/o microemulsion systems. This has to do with the phenomenon of the so-called optical match point of microemulsion droplets. The total average intensity ΔR_0 for a polydisperse solution of microemulsion

particles is given by

$$\Delta R_0 \sim \frac{\langle \alpha^2 \rangle \phi}{\lambda^4 \langle V \rangle} \quad \text{and} \quad \langle \alpha^2 \rangle = \int n(R) \alpha^2(R) dR \quad (9.9, 9.10)$$

where $\langle V \rangle$ is the average volume, $\langle \alpha^2 \rangle$ is the mean square excess polarizability and $n(R)$ the explicitly chosen size distribution of the microemulsion droplets, respectively. Due to the layered structure of the microemulsion droplets, their optical polarizability does not obey a simple R^3 law as found for homogeneous colloids. This is illustrated in Fig. 9.3, where the polarizability of a w/o microemulsion droplet is shown as a function of the water core radius R for two different solvents which differ in their index of refraction. We see that $\alpha(R)$ reaches a maximum after an initial increase and then decreases and even crosses zero at the optical match point, at which the droplets become invisible in a light scattering experiment. These special optical properties of w/o microemulsions have important practical consequences when performing static and dynamic light scattering experiments. As we shall see, they permit an extremely accurate determination of the size polydispersity, and they provide us with an option to perform contrast variation experiments usually only accessible in neutron scattering. However, they also invalidate common approaches to interpret the measured structure factors.

As we see from Fig. 9.3, the polarizability of a microemulsion droplet vanishes at a specific value of the water core radius, and size polydispersity thus results in a considerable residual scattered intensity. This has first been recognized by Zulauf and Eicke, who analysed the dependence of the scattered intensity on the water-to-surfactant molar ratio w_0 for AOT–water–isoctane microemulsions in terms of a simple shell model.^[46] For monodisperse w/o microemulsion particles, the water core radius R is related to w_0 by

$$R = 3w_0 v_w / a_s, \quad (9.11)$$

where v_w is the molecular volume of water. In the simple shell or coated sphere model, the polarizability of a droplet is given by^[22]

$$\alpha = 4\pi\epsilon_0 \left[\frac{\epsilon_w - \epsilon_0}{\epsilon_w + 2\epsilon_0} R^3 + \frac{\epsilon_s - \epsilon_0}{\epsilon_s + 2\epsilon_0} 3\delta R^2 \right], \quad (9.12)$$

where ϵ_s , ϵ_w and ϵ_0 are the optical dielectric constants of surfactant, water and oil, respectively, and $\delta = v_s/a_s$ corresponds to the surfactant layer thickness at large values of R . Equation (9.12) corresponds to a simple linear mixing approximation which, however, is quite accurate for the range of values encountered in the experimental studies. Since $\epsilon_w < \epsilon_0$ and $\epsilon_s > \epsilon_0$, we immediately see from eqns (9.11) and (9.12) that α should vanish for a given value of w_0 . However, as shown in Fig. 9.4(a), one experimentally observes that the intensity vs. w_0 curve shows a well defined minimum whose position and depth depends for example on the solvent used.^[22,46–48] This discrepancy between the simple shell model and the experimental results has already been pointed out by Zulauf and Eicke, who correctly attributed it to the polydispersity of the microemulsion

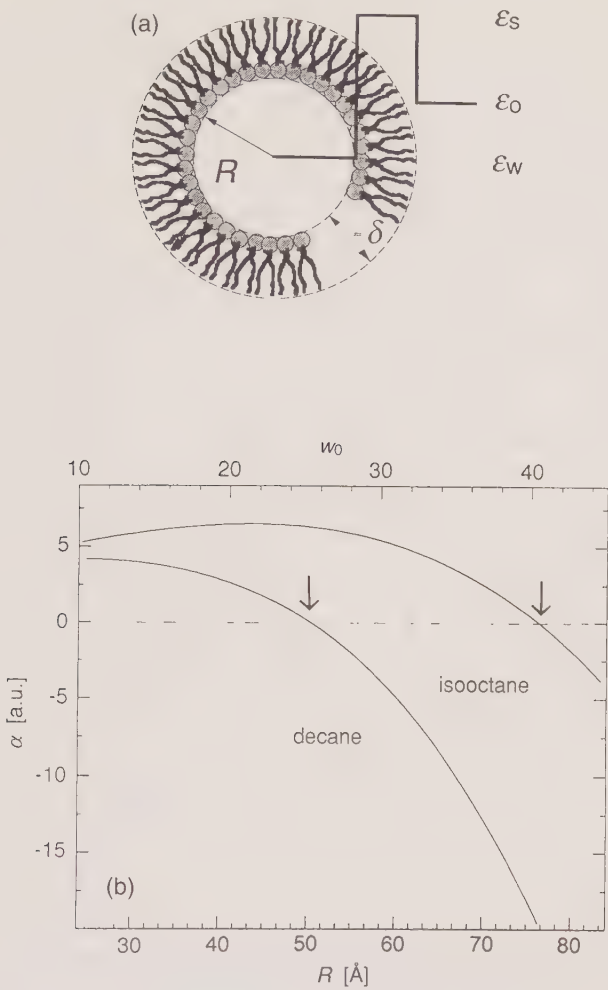


FIG. 9.3. (a) The dielectric constant profile for an AOT reverse micelle, modelled as a layered dielectrical sphere (see text for details). (b) The dependence of the optical excess polarizability $\alpha(R)$ of an AOT reverse micelle on the water core radius R in the systems AOT water isooctane and AOT–water–decane, respectively (see ref. 48 for details).

droplets.^[46] More recently, Ricka *et al.* were able to quantitatively interpret this in the context of a polydisperse layered sphere model.^[22] The effect of polydispersity is illustrated in Fig. 9.4(b). We see that both the position and depth of the intensity minimum are extremely sensitive to the width of the size distribution, and that this allows an accurate determination of microemulsion droplet polydispersity.^[22,48]

The existence of an optical match point in w/o microemulsions cannot only be used for a very precise determination of the size polydispersity of the

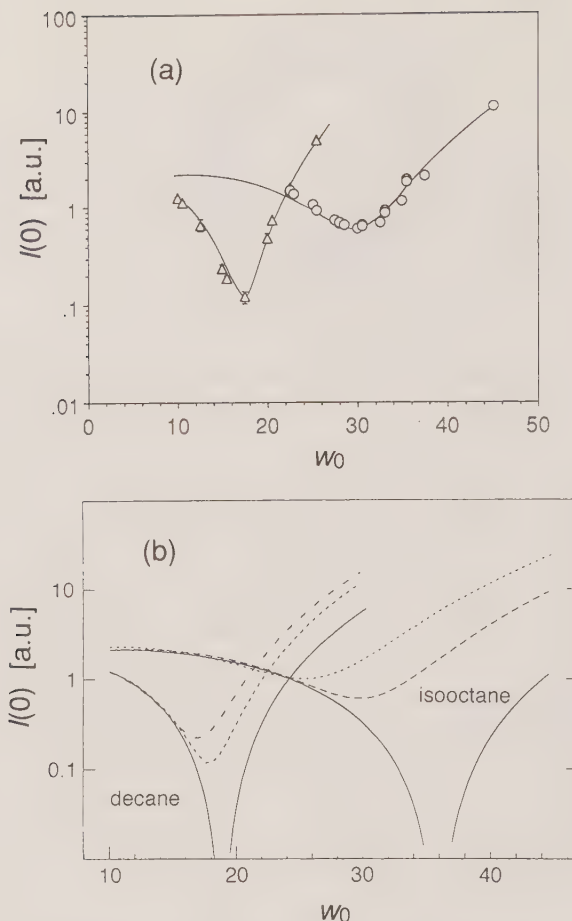


FIG. 9.4. (a) The normalized intensity $I(0)$ as a function of the water content w_0 for the systems AOT water decane (\triangle) and AOT water isoctane (\circ). Also shown are the theoretical curves for a model of polydisperse layered spheres using a Schulz distribution with a polydispersity $\gamma = (\langle R^2 \rangle - \langle R \rangle^2)/\langle R \rangle^2$, where $\gamma = 0.01$ for decane and $\gamma = 0.035$ for isoctane (see ref. 48 for details). (b) The calculated normalized intensity $I(0)$ as a function of the water content w_0 for monodisperse (—) and polydisperse microemulsion droplets in decane and isoctane. The shape of the curves is completely given by the value of the polydispersity index γ . In decane: ·····, $\gamma = 0.01$; ——, $\gamma = 0.02$. In isoctane: ·····, $\gamma = 0.035$; ——, $\gamma = 0.07$ (see ref. 48 for details).

microemulsion droplets, but it also provides us with the interesting possibility to perform optical contrast variation experiments. This can, for example, be used in an investigation of the changes in size and structure that accompany the solubilization of polymers or proteins in microemulsions. The size difference between the empty reverse micelles and the average size measured in a protein-containing solution is often very small, so that the size distribution changes

induced by the presence of biopolymers cannot be determined unambiguously by normal light scattering experiments. However, it has been demonstrated that one can overcome this problem by suppressing the scattering contributions from the empty reverse micelles close to the optical match point of the microemulsion droplets.^[48] The insertion of an enzyme in the microemulsion droplet dramatically alters its polarizability (and thus its scattering cross-section), particularly with small droplet radii. Thus it is possible to perform contrast variation experiments in which either empty or filled microemulsion particles dominate the scattering intensity similarly to neutron scattering measurements,^[18] where large differences in the scattering cross-section can be obtained by choosing a suitable distribution of hydrogen and deuterium atoms. While the resulting differences in droplet radii between the protein-containing and non-protein-containing reverse micelles are too small to be determined unambiguously with DLS measurements directly, we can therefore use SLS and DLS measurements at w_0 values close to the optical match point in order to suppress considerably the scattering contributions from the empty micelles.

An important aspect of optically inhomogeneous particles such as w/o microemulsion droplets is the fact that, close to the optical match point, the measured structure factor $S^M(0)$ does not only reflect the thermodynamic quantity $(\partial\pi/\partial C)^{-1}$ as given in eqn (9.5), but also strongly depends upon the optical contrast. This is based on the fact that for such particles, optical (i.e. polarizability α) and size polydispersity are competely coupled, which has to be taken into account in any attempt to estimate $S^M(0)$ from eqn (9.3). This was first pointed out by Ricka and co-workers, who showed that the apparent 'virial' coefficient k_1^M as determined from an expansion of the initial slope of the concentration dependence of $S^M(0)$,

$$S^M(0) \approx 1 - k_1^M \phi, \quad (9.13)$$

vanishes in the vicinity of the optical match point.^[49] A more refined calculation of $S^M(0)$ for w/o microemulsion droplets was given by Yan and Clarke, who calculated $S^M(0)$ for a core and shell model of polydisperse particles interacting through a hard sphere potential.^[21] Based on the Percus-Yevick approximation, they were able to derive the corresponding equations for the general case with complete coupling between scattering power and size polydispersity. The result of their calculations is shown in Fig. 9.5, which illustrates the striking effect of the variation of the optical contrast on $S^M(0)$ for a given volume fraction. We clearly see from Fig. 9.5 that $S^M(0)$ is strongly enhanced in the vicinity of the optical match point. This contrasts with a system with polydisperse but optically homogeneous hard spheres, where $S^M(0)$ will be independent of the optical contrast and depend on the volume fraction only. Figure 9.5 thus immediately demonstrates why approximations for $S^M(0)$ derived for homogeneous particles should not be used for w/o microemulsions, especially near the optical match point. An application of expressions such as eqns (9.7) and (9.8) may thus lead to a serious misinterpretation of the actual interaction potential, since deviations from the hard sphere result, e.g. too high a value of $S^M(0)$ as observed

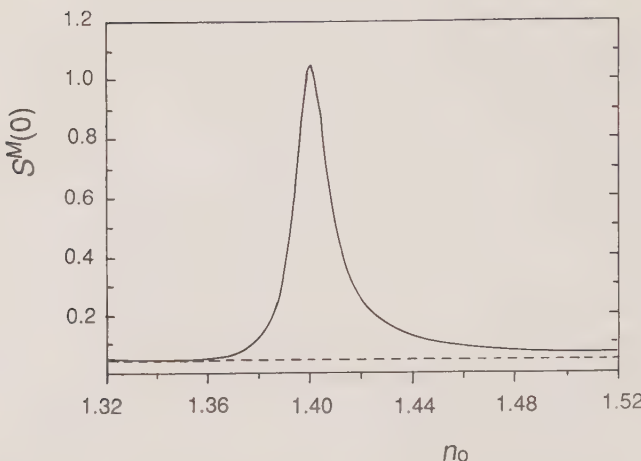


FIG. 9.5. The dependence of the 'measured' static structure factor $S^M(0)$ on the index of refraction of the solvent n_0 for polydisperse core-shell (solid line) and homogeneous (dashed line) hard spheres with a volume fraction $\phi = 0.2$ (see ref. 21 for details).

close to the optical match point, would then necessitate a considerable attractive contribution.

9.2.3 Charged spherical micelles: soft spheres

An even more complicated situation arises with aqueous solutions of ionic surfactants. In such systems there are additional contributions from screened Coulomb interactions with the added possibility of concentration and salt-dependent micellar growth combined with a concomitant change of the micellar morphology (i.e. a sphere-to-rod transition). Furthermore, a crucial parameter in the calculation of the electrostatic contribution to interparticle interactions is the effective charge z (or, equivalently, the surface potential), i.e. the degree of ionization (or counterion binding) of the ionic head groups. While the use of static light scattering to determine the micellar charge was proposed long ago by Prins and Hermans,^[50] it is based on a number of assumptions with quite limited applicability. A detailed investigation of the influence of intermicellar interactions has been presented by Corti and Degiorgio for sodium dodecyl sulphate (SDS) micelles in aqueous NaCl solutions.^[51] In their pioneering work, they presented a thorough study of the apparent molar mass $M_{app} = MS^M(0)$ and the collective diffusion coefficient of the SDS micelles as a function of surfactant and NaCl concentration. The results from their static light scattering experiments are summarized in Fig. 9.6. We see from Fig. 9.6 that $1/M_{app}$ exhibits a linear concentration dependence, and that relatively small variations in salt concentration cause quite large changes in the dependence of $1/M_{app}$ on SDS concentration. Based on the assumption that the observed concentration dependence is due to micellar interactions rather than growth,

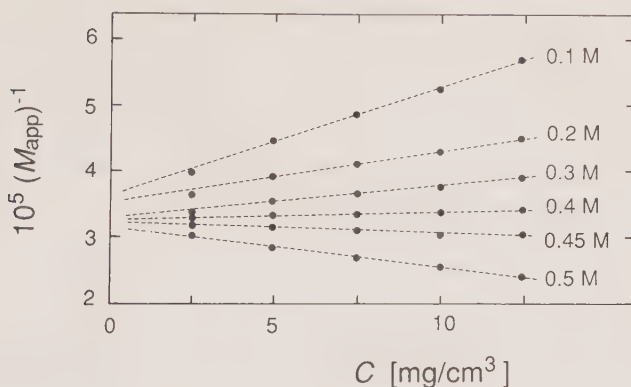


FIG. 9.6. The concentration dependence of $1/M_{\text{app}}$ for SDS micelles at different NaCl concentrations at $T = 25^\circ\text{C}$. Also shown are linear fits of eqn (9.17) to the data (adapted from ref. 51).

Corti and Degiorgio then analysed their results using DLVO theory, where the effective interaction potential $V(r)$ was taken as a sum of a repulsive hard sphere, a repulsive screened Coulomb and an attractive van der Waals term. The starting point in their analysis was

$$S^M(0) = 1 - 4\pi\rho \int_0^\infty (1 - g(r))r^2 \, dr = 1 - \frac{3\phi}{R^3} \int_0^\infty (1 - g(r))r^2 \, dr = 1 - k_i^M \phi, \quad (9.14)$$

where $\rho = N_A(C - CMC)/M$ is the number density of the micelles, R is the micellar radius and the apparent ‘virial’ coefficient, k_i^M , is defined as

$$k_i^M := \frac{3}{R^3} \int_0^\infty (1 - g(r))r^2 \, dr. \quad (9.15)$$

The pair distribution function $g(r)$ characterizes the probability of finding a particle at a distance r from the centre of a given particle and is determined by the interparticle potential. Equation (9.15) was evaluated numerically by Corti and Degiorgio using the so-called dilute gas approximation,^[27] which yields $g(r)$ as the first term of an expansion in powers of the number density. It takes into account only direct two-particle interactions and neglects higher order correlations. Application of the Boltzmann distribution then yields for the pair distribution function:^[27, 51, 52]

$$g(r) \approx e^{-V(r)/k_B T}. \quad (9.16)$$

Neglecting higher order terms results in an interaction potential which overestimates the effect of repulsive interparticle interactions and leads to too small values for $S^M(0)$ (eqn (9.14)). This is partly compensated in the linear approximation used by Corti and Degiorgio by the additional approximation

$1 - x \approx (1 + x)^{-1}$, which leads to

$$\frac{1}{M_{\text{app}}} = \frac{1}{M(1 - k_l^M \phi)} \approx \frac{1}{M} (1 + k_l^M \phi). \quad (9.17)$$

For spherical micelles and in terms of a dimensionless separation parameter $x = (r - 2R)/2R$ one obtains, for k_l^M ,

$$k_l^M = 8 + 24 \int_0^\infty (1 - e^{-V(x)/(k_B T)}) (1 + x)^2 dx, \quad (9.18)$$

where the ‘8’ is the hard sphere contribution. For the van der Waals term, Corti and Degiorgio used an expression derived by Hamaker for the case of two spheres^[53]

$$V_A(x) = -\frac{A}{12} \left(\frac{1}{x^2 + 2x} + \frac{1}{x^2 + 2x + 1} + 2 \ln \frac{x^2 + 2x}{x^2 + 2x + 1} \right) \quad (9.19)$$

and a screened Coulomb term of the form

$$V_R = \frac{\varepsilon R \Psi_0^2}{2} \ln(1 + e^{-2\kappa Rx}), \quad (9.20)$$

where ε is the dielectric constant of the suspending medium, κ is the Debye–Hückel screening parameter^[54] and Ψ_0 is the surface potential which is related to the charge x and the ionic strength.^[51,54] Equation (9.20) represents a limiting case for $\kappa R \gg 1$. An additionally difficulty arises because the Hamaker expression $V_A(x)$ diverges at $x = 0$ (eqn (9.19)). A lower cut-off $x_L > 0$ has thus to be imposed in the integral in eqn (9.18), which can be interpreted as a result of the fact that two particles cannot approach closer than the Stern layer thickness.

From the slope of the experimental data shown in Fig. 9.6, Corti and Degiorgio determined experimental values for k_l^M and the aggregation number N_{agg} as a function of NaCl concentration C_s (see Table 9.1). Based on eqns (9.18)–(9.20), they then calculated theoretical values for k_l^M using best fit values of $z = 37$ and $A = 11.3k_B T$, i.e. they assumed that both the Hamaker constant A as well as the effective charge z are both independent of the salt concentration. As shown in Table 9.1, the agreement between the theoretical and experimental values of k_l^M is moderately good, and the absolute magnitude of k_l^M is generally too small. Part of the discrepancy between experimental and theoretical values possibly arises because the micellar size was assumed to be concentration independent. It has been reported in a number of other studies^[55–60] that the average micellar size increases with surfactant concentration for a given value of C_s , which could of course lower the slope of the straight lines in Fig. 9.6. This would also explain in part the very high value of A obtained by Corti and Degiorgio, which is considerably higher than the values estimated for hydrocarbon droplets in water ($0.5 - 2k_B T$).^[61,62]

Table 9.1. Light scattering data for SDS solutions at 25 °C as a function of NaCl concentration C_s (from ref. 51).

C_s (M)	N_{agg}	k_l^M (cm ³ /g)	
		Experimental	Theoretical
0.10	94	40.2 ± 4.5	29.3
0.20	97	21.1 ± 2.1	14.3
0.30	104	13.7 ± 1.4	8.2
0.40	106	3.0 ± 1.0	3.9
0.45	108	-5.1 ± 1.0	2.5
0.50	110	-19.5 ± 2.0	0.7

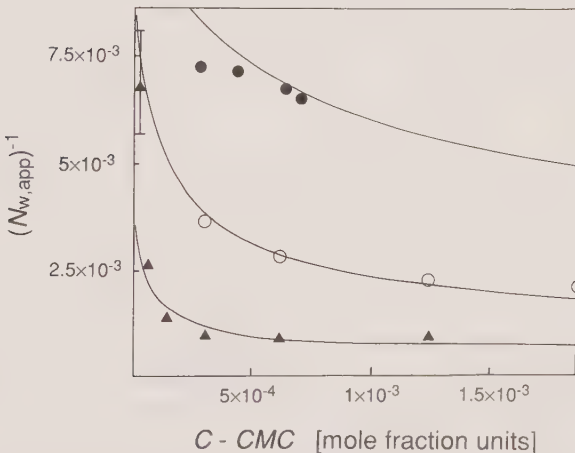


FIG. 9.7. The concentration dependence of the inverse apparent weight-average aggregation number $1/N_{w,app}$ of SDS micelles in aqueous NaCl solutions at $T = 25^\circ\text{C}$: ●, 0.5 M NaCl; ○, 0.6 M NaCl; ▲, 0.8 M NaCl. The solid lines are calculations based on the 'ladder model' for cylindrical micellar growth (adapted from ref. 56).

It is in fact quite illustrative to mention that Benedek and co-workers were able to interpret the data from static and dynamic light scattering experiments with aqueous SDS solutions at NaCl concentrations $C_s \geq 0.5$ M with the so-called 'ladder model' for anisotropic (cylindrical) micellar growth without including any contributions from electrostatic or van der Waals interactions (see Fig. 9.7).^[56] Figures 9.6 and 9.7 and Table 9.1 demonstrate that two very different structural models both allow a self-consistent interpretation of a quite extensive set of light scattering data on an absolute scale. A major difficulty

clearly arises from the limited spatial resolution ($\sim 1/q$) of the static light scattering experiment, which therefore only allows measurement of M_{app} and does not provide any details of the micellar structure for micelles with a mean aggregation number which is not considerably larger than that of the minimum sphere. It is quite obvious that a less ambiguous data interpretation requires absolute values of $I(q)$ over a much more extended q range which can only be obtained from a combination of light and small angle neutron (or X-ray) scattering.

It is also important to point out that the approximations used by Corti and Degiorgio (dilute gas/linear approximation) break down at low electrolyte and high surfactant concentrations. A more profound understanding of the structural properties of strongly interacting charged micelles or microemulsion particles can then only be achieved from a solution of the Ornstein-Zernike equation by closure relations such as hypernetted chain (HNC) or Rogers-Young as, for example, was successfully done for classical colloidal systems such as highly charged polystyrene spheres.^[20,63-67] Such an approach has for example been applied to cetyltrimethylammonium chloride (CTAC) micelles at low-to-moderate ionic strength ($0 \leq C_s \leq 0.1 \text{ M NaCl}$), where Ortega and co-workers were able to obtain quite good agreement between the experimentally determined $S^M(0)$ and calculations based on the HNC approximation.^[68]

9.3 Surfactant systems with extended micellar growth

9.3.1 *The sphere-to-rod transition*

Numerous reports have demonstrated that considerable micellar growth occurs from the minimum sphere to very large anisotropic micelles in aqueous surfactant solutions at high salt concentrations.^[5,37,56-59,69-85] An example for the remarkable changes in the micellar size distribution upon an increase of the surfactant concentration is given in Fig. 9.8 for cetylpyridinium chloride micelles in 0.1 M NaClO₃.^[86] With increasing surfactant concentration the scattered intensity increases and a very strong angular dependence develops. The micellar size is now large enough to produce a measurable particle form factor, which permits, for example, determination of an apparent radius of gyration $R_{g,\text{app}}$. A qualitative explanation of this phenomenon can be given based on the salt dependence of the so-called ‘spontaneous curvature’^[6] or the ‘packing parameter’^[1] of the surfactant molecule. For $C > CMC$, one generally expects that the micelles become larger with increasing C due to mass-action effects. For surfactants with a preference for spherical packing this growth is of course very limited. However, at higher salt concentrations, at which (intramicellar) repulsive interactions between the head groups are screened, the surfactants now have a preference for locally cylindrical packing, which provides them with a possibility for almost unlimited uniaxial growth.^[1] Several simple thermodynamic models have been proposed in order to account for this sphere-to-rod transition in aqueous micellar solutions.^[5,9,55,56,87] A common

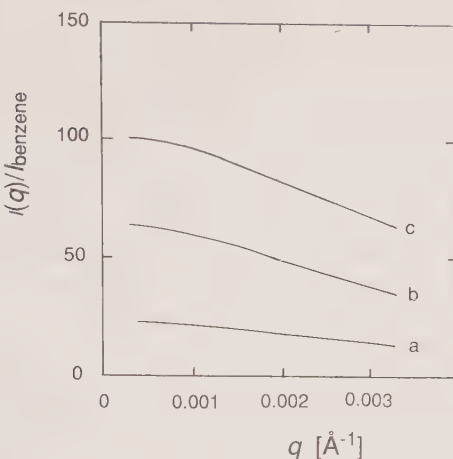


FIG. 9.8. The angular dependence of the normalized intensity $I(q)/I_{\text{benzene}}$ from aqueous solutions of CPClO_3 in 0.1 M NaClO_3 at different surfactant concentrations: (a) 0.001 g/g; (b) 0.0025 g/g; (c) 0.005 g/g (adapted from ref. 86).

feature of these models is the prediction of a power-law concentration dependence of the weight-average aggregation number $N_{\text{agg},w} \sim C^\alpha$ for $C \gg CMC$, with an exponent $0.5 \leq \alpha \leq 0.7$.

Several attempts have been made to demonstrate the existence of cylindrical micelles and to verify the proposed growth law. Benedek and co-workers presented evidence for different alkylsulfate surfactants mainly from a comparison of the apparent hydrodynamic radius $R_{h,\text{app}}$ and M_{app} .^[56,58,69,71] They showed that, in a plot of the normalized scattered intensity versus the corresponding hydrodynamic radius, the data were in good agreement with the theoretical curve for spherocylinders, but in clear disagreement with the corresponding curves for disks and spheres. Furthermore, as already shown in Fig. 9.7, the data were in quantitative agreement with predictions from the ladder model. However, neither intermicellar interactions, polydispersity nor flexibility of the rod-like micelles were taken into account. Evidence for a flexible rod-like structure was given by Ikeda *et al.* in their light scattering study of dodecyldimethylammonium chloride (DDAC) solutions at high salt concentrations.^[73] A detailed study of the flexibility of cetylpyridinium bromide (CPBr) micelles at high ionic strength was then conducted by Porte *et al.*, who combined DLS, magnetic birefringence and NMR measurements. Their results supported a model of semi-flexible cylindrical micelles with a persistence length $l \approx 10\text{--}20\text{ nm}$.^[72,75,76] They were subsequently able to verify this number from a more direct measurement at high q values using SANS.^[84]

Several other groups have estimated values of the persistence length for other surfactants using, for example, a combination of SLS and DLS, i.e. by comparing R_g and R_h or M_{app} and R_g .^[73,85,88,89] However, it is important to point out that in such an attempt one has to take into account micellar

polydispersity and interactions. The effect of polydispersity on R_g and R_h has for example been considered by Schmidt for worm-like chains, who obtained an analytical expression for R_g and numerical results for R_h based on a Schulz-Zimm distribution.^[90] Neglecting polydispersity in model calculations for semi-flexible particles will lead to an overestimation of l due to the characteristic intensity weighting (M_w , $\langle R_g^2 \rangle_z^{1/2}$ and $\langle 1/R_h \rangle_z^{-1}$, where the subscript w stands for weight-average and z for z-average, respectively) of the experimental quantities determined in static and dynamic light scattering experiments.^[91,92] It is clear that a more precise determination of l can be achieved, for example, with SANS or SAXS experiments, where the much smaller wavelength leads to an enhanced structural resolution, even down to the length scale of the cross-sectional radius of the micelle. The characteristic crossover in the q -dependence of the scattering intensity from a scattering pattern typical for rigid rods to one typical for flexible coils then becomes accessible and permits a precise measurement of l that will be weakly affected by polydispersity only.^[84,93–95] Furthermore, the experimental quantities M_{app} , $R_{g,app}$ and $R_{h,app}$ exhibit quite different dependences on intermicellar interactions, which will also result in an incorrect value of the persistence length if not considered correctly.^[92]

In general, while there appears to be unanimous agreement on the existence of a sphere-to-rod transition and the presence of semiflexible cylindrical micelles at high salt content, none of the investigators have presented a quantitative evaluation of M_{app} , R_g (and R_h) with a full account of flexibility, polydispersity and intermicellar interactions that would be required for a decisive test of the various micellar growth models.

9.3.2 Formation of giant flexible micelles: analogies and differences compared to polymers

In the previous section we have seen that an analysis of the detailed structure and size distribution of anisotropic micelles is severely hampered by the difficult task of distinguishing between the contributions from intermicellar interactions and concentration dependent micellar growth to the scattering data. This can be illustrated by the concentration dependence of the scattered intensity $I(0)$ and the apparent diffusion coefficient D_c obtained for CTAB in aqueous solutions of 0.1 M KBr, shown in Fig. 9.9.^[37] After a first initial increase which clearly reflects pronounced micellar growth, the intensity then reaches a maximum and decreases upon a further increase of the surfactant volume fraction ϕ . Analogous behaviour is observed for D_c , which first decreases, reaches a minimum and then increases upon further increase of ϕ . A similar observation for hexadecylpyridinium salicylate by Hoffmann and co-workers was first interpreted in terms of rod-like micelles growing until they overlap at a concentration C^* , where upon their size was then assumed to decline with further increase of concentration such that the overlap was just maintained.^[78,96] A different interpretation was then provided by Candau and co-workers, who

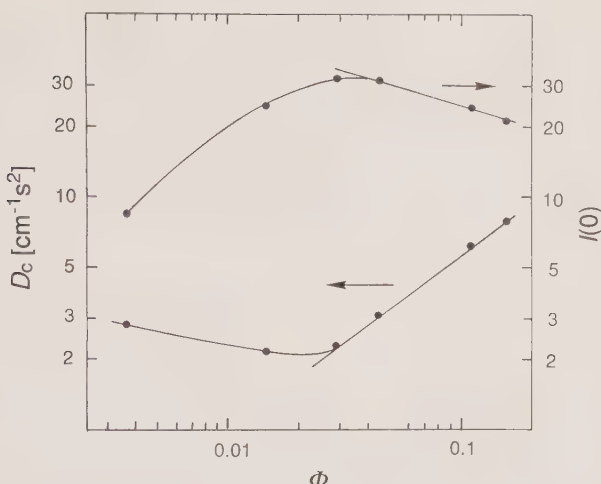


FIG. 9.9. The apparent diffusion coefficient D_c and the scattered intensity $I(0)$ as a function of the surfactant volume fraction for aqueous solutions of CTAB in 0.1 M KBr (adapted from ref. 37).

were the first to realize that the decrease of the scattered intensity could be interpreted based on an analogy to semi-dilute polymer solutions.^[37] They obtained clear evidence that the CTAB micelles present in aqueous solutions at high ionic strength grow with increasing surfactant concentration into long, flexible and cylindrical aggregates. They concluded that at high surfactant concentrations these large and presumably flexible micelles should overlap and form a transient network similar to an entangled polymer solution, which would also explain the viscoelastic behaviour observed in these solutions. Candau *et al.* were subsequently able to show that the results from static and dynamic light scattering and rheological measurements performed on viscoelastic surfactant solutions could be successfully interpreted in terms of theories originally used to describe the behaviour of semi-dilute polymer solutions.^[5,37,81,83]

The theoretical basis for such an interpretation can be summarized as follows. In general, we can recast eqn (9.1) at low values of q and describe the q -dependence of the scattered intensity by a Lorentzian scattering law of the form

$$\frac{K(C - CMC)}{\Delta R_\theta} = \frac{1}{M_{app}} [1 + q^2 \xi_s^2], \quad (9.21)$$

where ξ_s is the so-called static correlation length. Equation (9.21) can be used irrespective of the surfactant concentration provided that the criterion $q\xi_s < 1$ is fulfilled. However, the interpretation of the quantities M_{app} and ξ_s depends strongly on the concentration regime. At low concentrations, the light scattering data primarily reflect the C -dependence of the micellar size distribution which, however, becomes increasingly masked by intermicellar interaction effects. Under these conditions, we can estimate the apparent radius of gyration

through the relationship $\xi_s = R_g/\sqrt{3}$, where $R_g := \langle R_g^2 \rangle_z^{1/2}$ and $\langle R_g^2 \rangle_z$ is the z-average mean square radius of gyration of the micelles. The apparent molar mass, M_{app} , is the result of a combination of both micellar size (M_w) and intermicellar interactions ($S(0)$) which can be expressed at low concentrations and not too large micellar sizes (i.e. at $C \ll C^*$) by a virial expansion of the form of eqn (9.13), where k_1^M is given by $2A_2 M_w$.^[97] For flexible coils, quite reliable expressions exist for the second virial coefficient A_2 , and we can use, for example,^[98]

$$A_2 \approx 4\pi^{3/2} N_A \frac{\langle R_g^2 \rangle_z^{3/2}}{M_w^2} \Psi, \quad (9.22)$$

where Ψ is the degree of interpenetration in dilute solution, i.e. it describes the influence of the solvent quality. Explicit values of the penetration function $\Psi(L/l)$ for semi-flexible polymers can for example be found in Fig. 4 of ref. 99 as a function of the ratio of contour length L to persistence length l . Equation (9.22) has been shown to provide a quantitative description of the concentration dependence of ΔR_0 in dilute solutions of polymer-like micelles when combined with an appropriate description of the micellar growth law and the use of the so-called worm-like chain model (see below) as a link between M_w and $\langle R_g^2 \rangle_z$.^[97]

Once the micellar size and concentration is large enough, the polymer-like structures overlap and start to entangle. At even higher concentrations, the micelles can form an entanglement network, and the solution becomes viscoelastic. The overlap threshold C^* , where the transition from the dilute to the semi-dilute regime occurs, is in reality not a sharp boundary but rather a concentration range which starts when the coils touch and ends when the coils are completely entangled.^[100,101] The situation becomes more complicated for polymer-like micelles due to the quite broad size distribution and its evolution with increasing concentration. Based on this analogy to classical polymer solutions, the quantities determined in a light scattering experiment take a very different meaning. For $C > C^*$, the light scattering experiments are no longer sensitive to individual micellar properties, but probe collective features of the entanglement network which are independent of the micellar size distribution or local chemistry.^[37,101–103] The angular dependence of the scattered intensity is now generally well described by eqn (9.21) over the entire q range, and the correlation length ξ_s corresponds to a screening length for excluded volume interactions in the network, i.e. it can be linked to the ‘mesh size’ of the network. According to scaling theory for semi-dilute polymer solutions, ξ_s should be independent of M and be related to the concentration according to a power law of the form $\xi_s \sim C^{-z}$, where $z = 0.77$. Such a power-law behaviour was indeed found for flexible polymers, with values of approximately 0.72 for the exponent.^[103] Similarly, the scattered intensity at $q = 0$, ΔR_0 , no longer reflects the micellar size and follows a universal scaling law of the form^[101,104]

$$\frac{1}{N_A k_B T} \frac{\Delta R_0}{KC} = \left(\frac{\partial \pi}{\partial C} \right)^{-1} \sim C^{-1.31}. \quad (9.23)$$

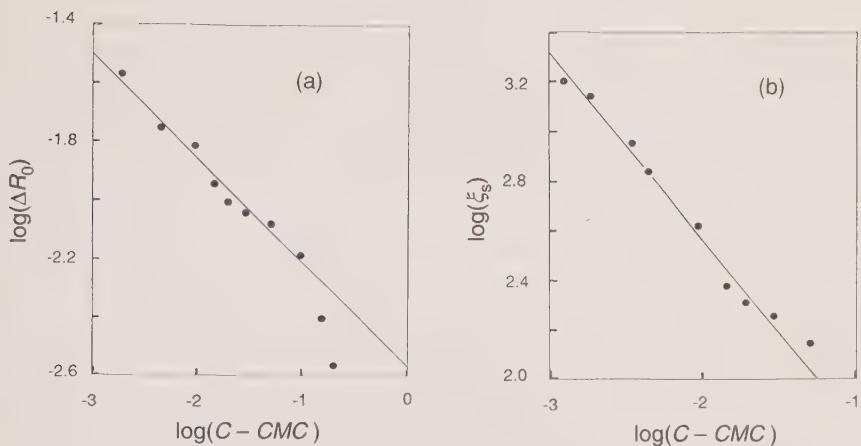


FIG. 9.10. (a) The dependence of the excess Rayleigh ratio ΔR_0 on surfactant concentration for CPClO_3 in 1 M NaClO_3 . Also shown is a scaling relation of the form $\Delta R_0 \sim (C - CMC)^{-0.35}$ (adapted from ref. 108). (b) The dependence of the static correlation length ξ_s on surfactant concentration for CPClO_3 in 1 M NaClO_3 . Also shown is a scaling relation of the form $\xi_s \sim (C - CMC)^{-0.75}$ (adapted from ref. 108).

Several light scattering studies report a transition from dilute to semi-dilute solutions in surfactant solutions followed by a power-law dependence for $(\partial\pi/\partial C)^{-1}$ at $C > C^*$.^[5,73,81,83,86,92,105-110] The data on the concentration dependence of ξ_s is much more limited due to the small values of ξ_s at high values of C and the limited accessible q range of a static light scattering experiment.^[86,92,108,110] The close agreement between the theoretical predictions based on polymer theory and the experimental data for viscoelastic surfactant solutions is demonstrated in Fig. 9.10 with data from cetylpyridinium chloride (CPClO_3) in 1 M sodium chloride solutions.^[108] The close analogy between the structural and dynamic properties of giant micelles and classical polymers provides us with a powerful theoretical framework to quantitatively interpret light scattering data from surfactant systems with extended micellar growth. We are thus confronted with a situation which at first seems counter-intuitive: while an analysis of micellar properties (size, shape) for solutions with limited micellar growth only based on light scattering data is extremely difficult because no rigorous theory exists for interactions between polydisperse anisotropic charged particles, the problem becomes manageable for systems with very pronounced growth, despite the fact that the micelles are so large that they experience strong intermicellar (excluded volume) interactions even close to the CMC . In the next sections we shall see how detailed information on the micellar size, shape and interactions can be obtained by applying corresponding concepts and theoretical expressions used in polymer physics.

9.3.3 Formation of giant polymer-like reverse micelles

While numerous aqueous surfactant systems are known to exhibit polymer-like properties, there are only few reports on polymer-like surfactant aggregates in organic solvents.^[111–113] In contrast to aqueous micellar systems, reverse micelles or water-in-oil microemulsions at moderately high values of surfactant concentration and low values of the molar ratio of water to surfactant, w_0 , are generally believed to have either a droplet-like structure or only a small degree of anisotropy. A notable exception is the system lecithin/organic solvent/water, in which the formation of gel-like, viscoelastic, reverse micellar solutions can be observed.^[114] Their unusual polymer-like properties have been explained by a water-induced one-dimensional micellar growth into long and flexible cylindrical reverse micelles, i.e. a characteristic sphere-to-flexible cylinder transition normally observed in aqueous solutions only.^[47, 94, 110, 115–118] The formation of giant tubular and polymer-like reverse micelles has been demonstrated with a combination of light scattering and small angle neutron scattering at low surfactant concentrations, which allowed verification of the locally cylindrical structure of these reverse micelles and an estimate of the persistence length and overall dimensions.^[118, 119]

The formation of giant polymer-like aggregates upon an addition of trace amounts of water to lecithin reverse micelles is illustrated in Fig. 9.11, where ξ_s is plotted as a function of the volume fraction of the dispersed phase ϕ for different values of the water to surfactant molar ratio w_0 . We observe two characteristic concentration regimes which exhibit a very different dependence of ξ_s on w_0 and ϕ . At low volume fractions $\phi \leq 6 \times 10^{-3}$ the dramatic increase of ξ_s with increasing w_0 primarily reflects the pronounced water-induced growth from relatively small reverse micelles with $\xi_s \approx 7.5$ nm at $w_0 = 4.0$ to giant worm-like particles with $\xi_s \approx 68$ nm at $w_0 = 14.0$. In addition to the clear manifestation of the water-induced micellar growth for $\phi \leq 6 \times 10^{-3}$, we observe an increase in ξ_s with increasing concentration, indicating a ϕ -dependence of the average micellar size which is particularly visible at low values of w_0 , i.e. under conditions where the resulting aggregates are relatively small and $\phi \ll \phi^*$. At $w_0 \geq 10$, the micro-emulsion particles are extremely large even for the lowest values of ϕ investigated: ϕ^* is thus shifted to quite low values and the ϕ -dependence of ξ_s is already masked by strong intermicellar interaction effects. At volume fractions $\phi \geq 6 \times 10^{-3}$, ξ_s first reaches a maximum and becomes increasingly independent of w_0 . At even higher values of $\phi > \phi^*$, ξ_s then decreases with increasing ϕ , and the ϕ -dependence can now be described by a power law of the form $\xi_s \sim \phi^{-z}$, where $z = 0.7 \pm 0.1$ for all values of w_0 . Such a power-law dependence for ξ_s is in quite good agreement with the proposed analogy with classical polymer solutions. The crossover to the power-law dependence provides us with an estimate of the entanglement threshold ϕ^* as a function of w_0 , and we see from Fig. 9.11 that ϕ^* decreases with increasing w_0 , in agreement with the proposed water-induced reverse micellar growth. Analogous behaviour has

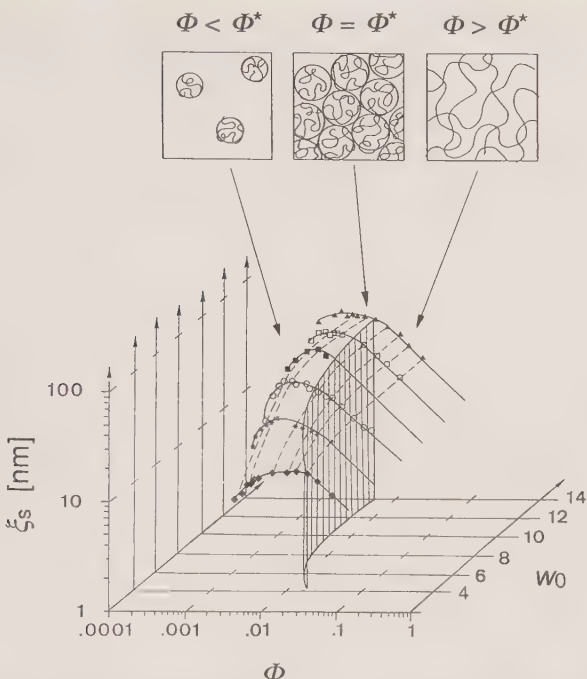


FIG. 9.11. The static correlation length, ξ_s , as a function of volume fraction, ϕ , and the water-to-lecithin molar ratio, w_0 , for lecithin reverse micelles in cyclohexane: \blacklozenge , $w_0 = 4.0$; $*$, $w_0 = 6.0$; \circ , $w_0 = 8.0$; \blacksquare , $w_0 = 10.0$; \square , $w_0 = 12.0$; \blacktriangle , $w_0 = 14.0$. Data sets for $\phi = \text{const.}$ and $w_0 = \text{const.}$ are connected by dashed and solid lines, respectively. The surface marked as Φ^* indicates the crossover from the dilute to the semi-dilute regime (see ref. 92 for details).

been found for the hydrodynamic correlation length ξ_h and the intensity at $q = 0$, ΔR_0 .^[92,120]

9.3.4 The static structure factor of polymer-like micelles and microemulsions

In the previous sections we have seen that for low surfactant concentrations we can describe the q -dependence of the scattered intensity by a Lorentzian scattering law (eqn (9.21)) provided that $q\xi_s < 1$, i.e. we are able to obtain information on the micellar size through the quantities $M_{w,\text{app}}$ and $R_{g,\text{app}}$. However, for systems with pronounced micellar growth we can now apply the polymer analogy and go much beyond an analysis of the initial slope of $I(q)$. The polymer-like micelles are large enough so that we can perform measurements at $q\xi_s \geq 1$ even in light scattering experiments, i.e. we can probe the interior of the micelles and the static light scattering experiment thus provides us with information on the chain conformation. For $q\xi_s \gg 1$ and $ql \ll 1$, $I(q)$ should reach an asymptotic power law of the form $I(q) \sim q^{-2}$ for Gaussian chains

and $I(q) \sim q^{-5/3}$ for ‘perturbed’ chains with excluded volume effects. While the asymptotic limit cannot be reached with light scattering for most systems due to the restricted q range (a notable exception is the CPCIO_3 system studied by Appell and Porte^[108]), evidence for these asymptotic power laws have been found with SANS.^[84, 94] Furthermore, polymer theory allows prediction of the full q -dependence of the scattered intensity. The single particle form factor $P(q)$ of a polymer of N segments can be calculated using the function

$$P(q) = \frac{I(q)}{I(0)} = \frac{2}{N^2} \int_0^N dn(N-n) \int_0^\infty dr P_n(r) \frac{\sin(qr)}{qr}, \quad (9.24)$$

where $P_n(r)$ is the probability density that elements separated by n segments along the chain contour are separated by a distance r .^[121] Equation (9.24) assumes that $P_n(r)$ is a function of n alone. The exact distribution function $P_n(r)$ is unknown, but several approximations have been thoroughly discussed in the literature.

For ideal random flight chains, the resulting form factor is given by the so-called Debye equation

$$P(q) = \frac{2(e^{-x}) + x - 1}{x^2}, \quad (9.25)$$

where $x = \langle R_g^2 \rangle q^2$. We see from eqn (9.25) that $P(q)$ is a function of the product $\langle R_g^2 \rangle q^2$ only. If we apply the worm-like chain model which is commonly used to describe the chain conformation of ‘realistic’ polymer chains, we then obtain the following relation between the mean square radius of gyration $\langle R_g^2 \rangle$, the contour length L and the persistence length l required in any attempt to relate the form factor to the actual dimension of the micelles:^[98]

$$\langle R_g(L)^2 \rangle = l^2 \left(\frac{L}{3l} - 1 + \frac{2l}{L} - \frac{2l^2}{L^2} [1 - e^{-L/l}] \right). \quad (9.26)$$

It has been demonstrated that eqn (9.25) yields a good description of the q -dependence of $I(q)$ for polymer-like micelles, provided that the micelles are not too large.^[97] The Debye equation is valid for small values of qR_g and ql only, which immediately sets limits to its applicability to light and neutron scattering studies of giant polymer-like micelles. Several extensions of eqn (9.25) have been proposed which are valid up to much higher values of ql .^[93, 122-127]¹ In particular, the scattering function for the worm-like chain model derived by Yoshizaki and Yamakawa^[127] provides us with an analytical expression for the form factor of polymer-like micelles capable of quantitatively reproducing the experimental features over an extended range of scattering vectors as, for example, obtained in a combination of light and small angle neutron scattering measurements.^[95] This represents a major improvement compared to the

¹ Note a misprint in ref. 123 in eqn (5) and a missing coefficient of 2, which is also missing in ref. 122, to normalize $P(0) = 1$.

previous characterization of semi-flexible cylindrical micelles by small angle scattering methods, where the analysis primarily relied on an individual interpretation of different q -regimes based on asymptotic expressions such as a Guinier approximation or the Debye equation for the low- q part, the use of simple crossover relations for the incorporation of flexibility in the intermediate q range, and a cross-sectional Guinier approximation for the high- q part.^[84, 94, 110, 128, 129]

However, for large contour-to-persistence length ratios (i.e. a high number of polymer segments) $L/l \geq 100$ in good solvents, the worm-like chain model no longer yields a correct description of the chain statistics, and excluded volume effects have to be taken into account.^[130, 131] This is illustrated in Fig. 9.12, where two examples of the q -dependence of $I(q)$ obtained for giant polymer-like lecithin reverse micelles at $C < C^*$ and $C > C^*$ are shown.^[131, 132] At high concentrations, $C \gg C^*$, $I(q)$ is well described by eqn (9.21) over the entire q range accessible in the light scattering experiment ($4.8 \times 10^{-3} \text{ nm}^{-1} \leq q \leq 3.5 \times 10^{-2} \text{ nm}^{-1}$), as expected for an entanglement network with a relatively small correlation length $\xi_s = 21 \text{ nm}$. However, at $C < C^*$ the giant size of the reverse micelles results in a pronounced angular dependence of the intensity, and deviations from a simple Lorentzian scattering law (eqn (9.21), given by the dotted line) or the corresponding form factor for polydisperse worm-like

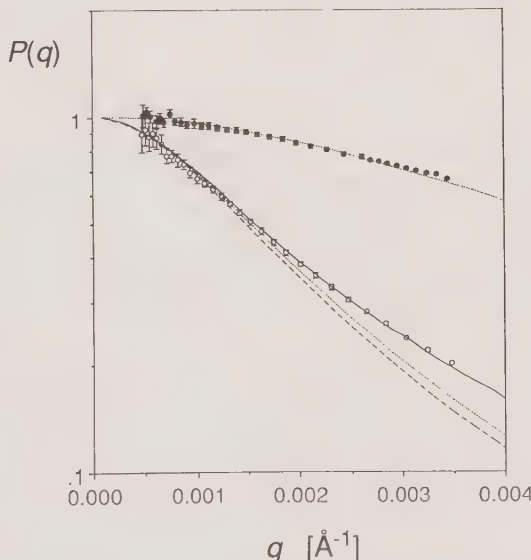


FIG. 9.12. The form factor $P(q)$ as a function of q for lecithin/cyclohexane reverse micelles at $w_0 = 14$, $c = 5.11 \text{ mg/ml}$ (○) and $c = 30.7 \text{ mg/ml}$ (●). Also shown are theoretical curves for a Lorentzian scattering law $P(q) = 1/[1 + q^2 \xi_s^2]$ (eqn (9.21)) (dotted line), polydisperse worm-like chains with $l = 11 \text{ nm}$ (dashed line) and polydisperse semi-flexible chains with excluded volume interactions (solid line). See refs 131 and 132 for details.

chains (dashed line) are clearly visible at higher values of q . Analysis of the low- q part of the intensity data shown in Fig. 9.12 yields $\xi_s = 62.5$ nm, which in turn results in $R_g = 108.3$ nm. This value of R_g is much larger than the value of the persistence length $l = 11.0 \pm 3$ nm previously measured with small angle neutron scattering,^[194] and deviations from the worm-like chain behaviour due to excluded volume effects can thus be expected. As shown in Fig. 9.12, the data at $C < C^*$ is indeed in quantitative agreement with theoretical calculations based on polymer chain statistics appropriate for excluded volume effects (solid line).^[121,131,133] In these calculations, an approximate form of the distribution function $P_n(r)$ proposed by Domb, Gillis and Wilmers on the basis of direct enumeration data^[134] has been inserted into eqn (9.24), which then results in^[121,131]

$$P(q) = 2 \sum_{i=0}^{\infty} (-l^i) \left(\frac{(6 + 5\varepsilon + \varepsilon^2) \Gamma[(3 - \varepsilon)/2]}{\Gamma[(5 - 3\varepsilon)/2]} \right)^i \times \frac{\Gamma\{[3 + 2i - (2i + 1)\varepsilon]/2\} x^i}{\Gamma[(3 - \varepsilon)/2][(1 + \varepsilon)i + 1][(1 + \varepsilon)i + 2]\Gamma(2i + 2)}, \quad (9.27)$$

where $\varepsilon = 0.176$ is the excluded volume exponent describing the influence of excluded volume effects on the molecular weight dependence of the mean square radius of gyration $\langle R_g^2 \rangle \sim N^{1+\varepsilon}$ of a coil with N segments, and where $\langle R_g^2 \rangle$ in $x = \langle R_g^2 \rangle q^2$ is now given by^[133,135,136]

$$\langle R_g^2 \rangle = \frac{(2l)^2 (L/2l)^{1+\varepsilon}}{6 + 5\varepsilon + \varepsilon^2}. \quad (9.28)$$

Equation (9.27) is useful for numerical evaluation of $P(q)$ up to $x \leq 10$. At higher values of x , one can apply an approximation in the form of an inverse power series of x given in eqn (20) of ref. 121. In order to compare the experimental data and the theoretical calculations, we finally have to account for the polydispersity of the micelles. For polydisperse solutions, the experimentally determined values of $\langle P(q) \rangle$ correspond to a z-average given by

$$\langle P(q) \rangle = \left(\int_0^\infty w(L) L P_L(q) dL \right) / \left(\int_0^\infty w(L) L dL \right), \quad (9.29)$$

where $w(L)$ is the weight-fraction distribution and $P_L(q)$ the particle form factor of a polymer chain of contour length L given by eqn (9.27). We have to chose an explicit form for the micellar size distribution. Based on multiple chemical equilibrium models or scaling arguments, an exponential size distribution of the form $n(L) \sim \exp(-L/L_w)$ which results in $L_w/L_n \approx 2$, where L_n is the number-average and L_w is the weight-average contour length, has been predicted for micelles.^[5] Therefore, polydispersity has been included in the calculations for the theoretical curves in Fig. 9.12 using a Schulz–Flory ‘most probable distribution’, for which $L_w/L_n = 2.0$.^[137] Figure 9.12 demonstrates that a theoretical treatment of the form factor, which includes polydispersity

and chain statistics appropriate for excluded volume interactions, yields a quantitative description of the q -dependence of the scattered intensity $I(q)$ for giant polymer-like micelles and microemulsions. It also shows that the use of the worm-like chain model underestimates the dependence of the radius of gyration on the molar mass, and leads to additional errors in the determination of the persistence length from a combination of static and dynamic light scattering if the model is applied to data from samples with pronounced micellar growth.^[131]

As we have seen in the previous section, an application of concepts from polymer theory readily allows interpretation of the light scattering data in the dilute regime ($P(q)$, $M_{w,\text{app}}$) and in the fully entangled state (universal scaling laws for ξ_s and $(\partial\pi/\partial C)^{-1}$). However, it is possible to go beyond a simple virial treatment or application of scaling laws and obtain a quantitative description of the static structure factor of polymer-like micelles and microemulsions based on conformation space renormalization group theory originally developed for semi-dilute polymer solutions. This can be illustrated with data from a recent light scattering study of the formation of giant reverse micelles in lecithin water-in-oil microemulsions, i.e. with the system already introduced in Fig. 9.11.^[92,132] The basis for this analysis was again the connection between the scattered intensity and the osmotic compressibility (eqns (9.1) and (9.5)). For polymers, $S(0)$ can be written as a function of a reduced concentration $X = a(C/C^*) \sim CA_2M_w$, where a is a constant and A_2 is the (weight-average) osmotic second virial coefficient, which results in^[138]

$$\frac{\Delta R_0}{K(C - CMC)} = M_w S(0) = M_w f(X). \quad (9.30)$$

An explicit functional form for $S(0) = f(X)$ has, for example, been calculated by Ohta *et al.* using the renormalization group method,^[139]

$$S(0)^{-1} = 1 + \frac{1}{8} \left(9X - 2 + \frac{2 \ln(1 + X)}{X} \right) \exp \left(\frac{1}{4} \left[\frac{1}{X} + \left(1 - \frac{1}{X^2} \right) \ln(1 + X) \right] \right) \quad (9.31)$$

and good agreement between theory and light scattering data was found for classical polymers with different values of M_w for an extended range of concentrations $10^{-2} < X < 10^2$, where X is given for polydisperse polymers by

$$X = A_2 CM_w / [\frac{9}{16} - \frac{1}{8} \ln(M_w/M_n)]. \quad (9.32)$$

A major problem in a direct application of polymer theory to micellar systems arises from the concentration (and w_0) dependence of the micellar size distribution. Since both A_2 and C^* thus depend on C (and w_0), one has to incorporate a power law of the form

$$M_w = B_1 C^\alpha \quad (9.33)$$

for the C -dependence of the average particle size and a scaling law of the form $R_g \sim M^v$ in the relations for A_2 , given by eqn (9.22), and C^* , which can be approximated by

$$C^* \approx \frac{3M}{4\pi N_A R_g^3}. \quad (9.34)$$

This leads to $A_2 \sim C^{\alpha(3v-2)}$, and the reduced concentration X is then given by

$$X = 2.10 B_1^{(3v-1)} B_2 C^{[\alpha(3v-1)+1]}. \quad (9.35)$$

Equations (9.33) and (9.35) allow explicit description of the micellar features of an equilibrium size distribution in the renormalization group treatment of $S(0)$ given by eqn (9.31).^[120]

As shown in Fig. 9.13(a), it is indeed possible to construct a universal curve $1/S(0)$ vs. X from the experimentally determined values of $\Delta R_0/KC$ if a power law of the form of eqn (9.33) is used for the C -dependence of the average particle size, despite the fact that the raw data from the static light scattering experiments exhibits a pronounced w_0 - and C -dependence (see Fig. 9.11).^[120] Moreover, the agreement between polymer theory and the microemulsion data is very good, thus supporting the attempt to apply polymer renormalization group theory to 'equilibrium polymers' such as worm-like micelles. While the exponents $v = 0.57 \pm 0.03$ and $\alpha = 1.2 \pm 0.3$ and the parameter B_2 were found to be independent of w_0 , the values of B_1 clearly reflect the pronounced water-induced micellar growth in this system. When compared to the theoretical predictions from mean-field models ($\alpha = 0.5$) and scaling arguments ($\alpha = 0.6$), $\alpha = 1.2$ appears to be very large.^[5] However, preliminary results from Kerr effect measurements^[140] with lecithin/cyclohexane w/o microemulsions also indicate a power-law dependence of the particle size on concentration with an exponent which is of the same order as obtained in the previous light scattering study. Moreover, the application of eqns (9.30)–(9.35) is not restricted to polymer-like reverse micelles, as is demonstrated with data from aqueous solutions of the non-ionic surfactant $C_{16}E_6$, which also forms giant polymer-like micelles.^[141] Equation (9.30) in conjunction with a micellar growth law of the form of eqn (9.33) permits quantitative reproduction of the concentration dependence of ΔR_0 , and we see in Fig. 9.13(a) that the data from this system falls perfectly on the same universal master curve as do the data from the lecithin reverse micelles. It is interesting to note that for this system we also obtain a high growth law exponent $\alpha = 1.1 \pm 0.1$, in disagreement with the commonly used mean-field models for micellar growth.

Based on the complete description of the w_0 - and C -dependence of M_w and X , the authors then tried to use this information and test if a self-consistent interpretation of the SLS results shown in Fig. 9.11 is possible within this theoretical framework. The theoretical basis for this is the dependence of $\xi_s/R_{g,o}$ on the overlap parameter X for polymers in good solvents, which can be written as

$$\xi_s/R_{g,o} = F_s(X) \quad (9.36)$$

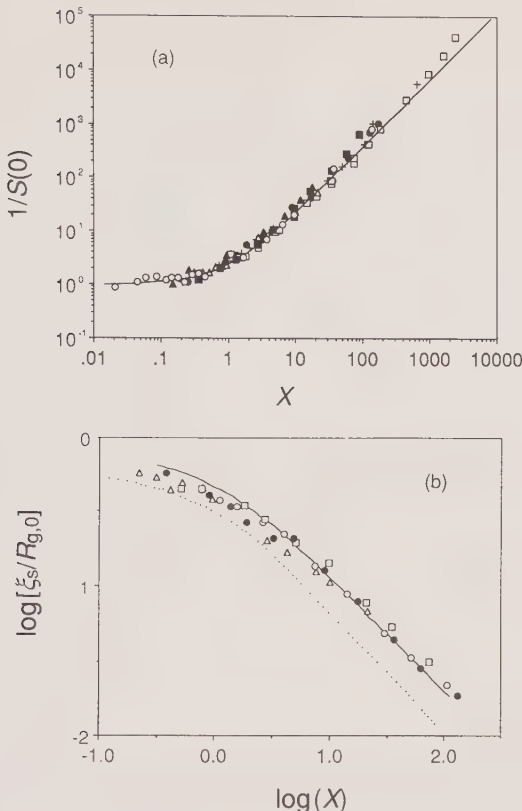


FIG. 9.13. (a) $S(0)^{-1}$ ($= [KC/\Delta R_0]C^\alpha B_1$) as a function of the reduced concentration X (eqn (9.35)) for lecithin/cyclohexane reverse micelles at different values of w_0 : \blacktriangle , $w_0 = 2.0$; \blacksquare , $w_0 = 4.0$; \triangle , $w_0 = 6.0$; \square , $w_0 = 8.0$; $+$, $w_0 = 12.0$; \bullet , $w_0 = 14.0$. Also shown are data for aqueous solutions of the non-ionic surfactant $C_{16}E_6$ in D_2O (\circ) and the theoretical curve $S(0)^{-1}$ vs. X for classical polymers from renormalization group theory (eqn (9.31)) as the solid line (see ref. 120 for details). (b) $\xi_s/R_{g,o}$ as a function of the reduced concentration X for lecithin/cyclohexane reverse micelles at different values of w_0 : \triangle , $w_0 = 6.0$; \square , $w_0 = 8.0$; \circ , $w_0 = 12.0$; \bullet , $w_0 = 14.0$ (see ref. 132 for details). Also shown is the theoretical curve $\xi_s/R_{g,o} = F_s(X)$ vs. X from renormalization group theory as the dotted line, and the experimentally observed $\xi_s/R_{g,o} = F_{s,\exp}(X)$ vs. X for 'classical' polymers as the solid line.^[103]

where $R_{g,o}$ is the radius of gyration which the polymer would have in the limit $C \rightarrow 0$. An explicit functional form for $F_s(X)$ has been calculated with renormalization group methods by Nakanishi and Ohta.^[142] Experimentally, one indeed finds a universal curve $F_{s,\exp}(X)$ for synthetic polymers, which shows no systematic dependence on the molecular weight or the solvent. Based on the known local structure of the lecithin reverse micelles (mass per unit length M_L , persistence length l) previously determined from SANS, and using eqns (9.28),

(9.33) and (9.35), the theoretical values of $R_{g,o}(w_0, C)$ can then be calculated for all values of w_0 and C investigated, and one can obtain the corresponding ratios of $\xi_s/R_{g,o}$ for all the measured values of $\xi_s(w_0, C)$ shown in Fig. 9.11. These ratios are plotted as a function of $X(w_0, C)$ in Fig. 9.13(b), and we see at once that the different individual data sets in Fig. 9.11, which exhibit a very pronounced w_0 - and C -dependence, collapse onto a single ‘universal’ master curve. The values of $\xi_s/R_{g,o}$ closely follow the function $F_{s,\exp}(X)$ previously found for synthetic polymers except for the lowest values of X , where the polymer data also exhibits the largest scatter.

Figure 9.13 shows that we can achieve a self-consistent interpretation of the measured osmotic compressibility from polymer-like micelles, in which we combine intermicellar interactions based on renormalization group theory for flexible polymers, polydispersity and a concentration- (and w_0 -) dependent micellar size distribution. It also shows that this approach can even be extended to a quantitative description of the full scattering curve $I(q)$. Figure 9.13(b) clearly demonstrates that the concentration dependence of the initial q -dependence of the intensity $I(q)$, which can be described by a correlation length ξ_s , is in quantitative agreement with the behaviour found for synthetic polymers such as polystyrene over the entire range of concentrations studied.

9.4 Conclusions

We have seen that the interpretation of static light scattering experiments with micelles and microemulsions is often ambiguous due to the combination of effects from size and shape changes, polydispersity and intermicellar interactions. However, it also demonstrates that in many cases one can find a self-consistent interpretation by applying theoretical concepts from colloid and polymer physics to these systems. When attempting to use static light scattering for a characterization of surfactant systems it is vital to keep in mind the limitations of the technique, and to try to combine measurements on an absolute scale with additional data from complementary techniques such as small angle neutron or X-ray scattering, which provide an extension of the structural resolution to much smaller length scales. In particular, the combination of static and dynamic light scattering is often very powerful in assessing the structural and dynamic properties of surfactant solutions.

Acknowledgements

This chapter has greatly benefited from contributions made by Carolina Cavaco, Sylvie Christ, Stefan Egelhaaf, Götz Jerke, Jan Skov Pedersen and Ulf Olsson, and I am most grateful to Hans Christian Öttinger for helpful discussions on the application of renormalization group theory.

References

1. Israelachvili, J. N. (1992). *Intermolecular and surface forces*. Academic Press, London.
2. Langevin, D. (1992). *Ann. Rev. Phys. Chem.*, **43**, 341.
3. Olsson, U. and Wennerström, H. (1994). *Adv. Colloid Interface Sci.*, **49**, 113.
4. Evans, D. F., Mitchell, D. J., and Ninham, B. W. (1986). *J. Phys. Chem.*, **90**, 2817.
5. Cates, M. E. and Candau, S. J. (1990). *J. Phys.: Condens. Matter*, **2**, 6869.
6. Safran, S. A. (1992). In *Structure and dynamics of strongly interacting colloids and supramolecular aggregates in solution* (eds S. H. Chen, J. S. Huang and P. Tartaglia), Vol. 369, p. 237. Kluwer Academic, Dordrecht.
7. Porte, G., Marignan, J., Bassereau, P., and May, R. (1988). *J. Phys. France*, **49**, 511.
8. Olsson, U. and Schurtenberger, P. (1993). *Langmuir*, **9**, 3389.
9. Israelachvili, J. N., Mitchell, D. J., and Ninham, B. W. (1976). *J. Chem. Soc. Faraday Trans. II*, **72**, 1525.
10. Lindman, B., Olsson, U., Wennerström, H., and Stilbs, P. (1993). *Langmuir*, **9**, 625.
11. Anderson, D., Wennerström, H., and Olsson, U. (1989). *J. Phys. Chem.*, **93**, 4243.
12. Leaver, M. S., Olsson, U., Wennerström, H., and Strey, R. (1994). *J. Phys. II*, **4**, 515.
13. Leaver, M. and Olsson, U. (1994). *Langmuir*, **10**, 3449.
14. Daicic, J., Olsson, U., Wennerström, H., Jerke, G., and Schurtenberger, P. (1995). *J. Phys. II*, **5**, 199.
15. Corti, M. and Degiorgio, V. (1985). *Phys. Rev. Lett.*, **55**, 2005.
16. Dietler, G. and Cannell, D. S. (1988). *Phys. Rev. Lett.*, **60**, 1852.
17. Wilcoxon, J. P., Schaefer, C. W., and Kaler, E. W. (1989). *J. Chem. Phys.*, **90**, 1909.
18. van Holde, K. E. (1985). *Physical biochemistry*. Prentice-Hall, Englewood Cliffs, NJ.
19. Schurtenberger, P. and Newman, M. E. (1993). In *Environmental particles* (eds J. Buffle and H. P. van Leeuwen), Vol. 2, p. 37. Lewis Publishers, Boca Raton.
20. Salgi, P. and Rajagopalan, R. (1993). *Adv. Colloid Interface Sci.*, **43**, 169.
21. Yan, Y. D. and Clarke, J. H. R. (1990). *J. Chem. Phys.*, **93**, 4501.
22. Ricka, J., Borkovec, M., and Hofmeier, U. (1991). *J. Chem. Phys.*, **94**, 8503.
23. Bagger-Jørgensen, H., Olsson, U., and Mortensen, K. (1996). In preparation.
24. Strey, R., Schomäcker, R., Roux, D., Nallet, F., and Olsson, U. (1990). *J. Chem. Soc., Faraday Trans. I*, **79**, 2253.
25. Olsson, U., Würz, U., and Strey, R. (1993). *J. Phys. Chem.*, **97**, 4535.
26. Lichtenfeld, F., Schmeling, T., and Strey, R. (1986). *J. Phys. Chem.*, **90**, 5762.
27. Goodstein, D. L. (1985). *States of matter*. Dover, New York.
28. Carnahan, N. F. and Starling, K. E. (1969). *J. Chem. Phys.*, **51**, 635.
29. Björling, M. (1992). *Macromolecules*, **25**, 3956.
30. Beenakker, C. W. J. and Mazur, P. (1984). *Physica*, **126A**, 349.
31. Medina-Noyola, M. (1988). *Phys. Rev. Lett.*, **60**, 2705.
32. Megen, W. v. and Underwood, S. M. (1989). *J. Chem. Phys.*, **91**, 552.
33. Agterof, W. G. M., Van Zomeren, J. A. J., and Vrij, A. (1976). *Chem. Phys. Lett.*, **43**, 363.
34. Vrij, A., Nieuwenhuis, E. A., Fijnaut, H. M., and Agterof, W. G. M. (1978). *Faraday Discuss. Chem. Soc.*, **65**, 101.
35. Cazabat, A. M., Langevin, D., and Pouchelon, A. (1980). *J. Colloid Interface Sci.*, **73**, 1.
36. Cazabat, A. M. and Langevin, D. (1981). *J. Chem. Phys.*, **74**, 3148.
37. Candau, S. J., Hirsch, E., and Zana, R. (1984). *J. Phys.*, **45**, 1263.
38. Huang, J. S. (1985). *J. Chem. Phys.*, **82**, 480.
39. Kotlarchyk, M. and Chen, S.-H. (1983). *J. Chem. Phys.*, **79**, 2461.
40. Milner, S. T. and Safran, S. A. (1987). *Phys. Rev. A*, **36**, 4371.

41. Socoli, F., Langevin, D., Lee, L. T., and Monkenbusch, M. (1993). *Progr. Colloid Polym. Sci.*, **93**, 105.
42. Baxter, R. J. (1968). *J. Chem. Phys.*, **49**, 2770.
43. Baxter, R. J. (1970). *J. Chem. Phys.*, **52**, 4559.
44. Robertus, C., Philips, W. H., Joosten, J. G. H., and Levine, Y. K. (1989). *J. Chem. Phys.*, **90**, 4482.
45. Robertus, C., Joosten, J. G. H., and Levine, Y. K. (1990). *Phys. Rev. A*, **42**, 4280.
46. Zulauf, M. and Eicke, H. F. (1979). *J. Phys. Chem.*, **83**, 480.
47. Schurtenberger, P., Peng, Q., Leser, M., and Luisi, P. L. (1993). *J. Colloid Interface Sci.*, **156**, 43.
48. Christ, S. and Schurtenberger, P. (1994). *J. Phys. Chem.*, **98**, 12708.
49. Ricka, J., Borkovec, M., Hofmeier, U., and Eicke, H.-F. (1990). *Europhys. Lett.*, **11**, 379.
50. Prins, W. and Hermans, J. J. (1955). *J. Phys. Chem.*, **59**, 576.
51. Corti, M. and Degiorgio, V. (1981). *J. Phys. Chem.*, **85**, 711.
52. Neal, D. G., Purich, D., and Cannell, D. S. (1984). *J. Chem. Phys.*, **80**, 3469.
53. Hamaker, H. C. (1937). *Physica*, **4**, 1058.
54. Hunter, R. J. (1986). *Foundations of colloid science*. Clarendon Press, Oxford.
55. Mukerjee, P. (1972). *J. Phys. Chem.*, **76**, 565.
56. Missel, P. J., Mazer, N. A., Benedek, G. B., Young, C. Y., and Carey, M. C. (1980). *J. Phys. Chem.*, **84**, 1044.
57. Hayashi, S. and Ikeda, S. (1980). *J. Phys. Chem.*, **84**, 744.
58. Missel, P. J., Mazer, N. A., Benedek, G. B., and Carey, M. C. (1983). *J. Phys. Chem.*, **87**, 1264.
59. Imae, T. and Ikeda, S. (1984). *J. Colloid Interface Sci.*, **98**, 363.
60. Candau, S. J. (1987). *Surfactant science series* (ed. R. Zana), Vol. 22, p. 167. M. Decker, New York.
61. Magid, L. (1993). In *Dynamic light scattering: the method and some applications* (ed. W. Brown). Oxford Science Publications, Oxford.
62. Mahanty, J. and Ninham, B. W. (1976). *Dispersion forces*. Academic Press, New York.
63. D'Aguanno, B. and Klein, R. (1991). *J. Chem. Soc. Faraday Trans.*, **87**, 379.
64. D'Aguanno, B., Klein, R., Méndez-Alcaraz, J. M., and Nägele, G. (1993). In *Complex fluids* (ed. L. Garrido), p. 149. Springer-Verlag, Berlin.
65. Gisler, T., Schulz, S. F., Borkovec, M., Sticher, H., Schurtenberger, P., D'Aguanno, B., and Klein, R. (1994). *J. Chem. Phys.*, **101**, 9924.
66. Krause, R., Nägele, G., Karrer, D., Schneider, J., Klein, R., and Weber, R. (1988). *Physica A*, **153**, 400.
67. Pusey, P. N. (1991). In *Liquids, freezing and the glass transition* (ed. J. P. Hansen, D. Levesque and J. Zinn-Justin), p. 763. North-Holland, Amsterdam.
68. Ortega, F., Bacaloglu, R., McKenzie, D. C., Bunton, C. A., and Nicoli, D. F. (1990). *J. Phys. Chem.*, **94**, 501.
69. Mazer, N. A., Benedek, G. B., and Carey, M. C. (1976). *J. Phys. Chem.*, **80**, 1075.
70. Gravsholt, S. J. (1976). *J. Colloid Interface Sci.*, **57**, 575.
71. Young, C. Y., Missel, P. J., Mazer, N. A., Benedek, G. B., and Carey, M. C. (1978). *J. Phys. Chem.*, **82**, 1375.
72. Porte, G., Appell, J., and Poggi, Y. (1980). *J. Phys. Chem.*, **84**, 3105.
73. Ikeda, S., Ozeki, S., and Tsunoda, M. (1980). *J. Colloid Interface Sci.*, **73**, 27.
74. Ikeda, S., Hayashi, S., and Imae, T. (1980). *J. Phys. Chem.*, **84**, 744.
75. Appell, J. and Porte, G. (1981). *J. Colloid Interface Sci.*, **81**, 85.
76. Porte, G. and Appell, J. (1981). *J. Phys. Chem.*, **85**, 2511.
77. Ozeki, S. and Ikeda, S. (1982). *J. Colloid Interface Sci.*, **87**, 424.

78. Hoffman, H., Rehage, H., Platz, G., Schorr, W., Thurn, H., and Ulbricht, W. (1982). *Colloid Polym. Sci.*, **260**, 1042.
79. Hoffmann, H., Kalus, J., Thurn, H., and Ibel, K. (1983). *Ber. Bunsenges. Phys. Chem.*, **87**, 1120.
80. Appell, J. and Porte, G. (1983). *J. Phys. Lett.*, **44**, L-689.
81. Candau, S. J., Hirsch, E., and Zana, R. (1985). *J. Colloid Interface Sci.*, **105**, 521.
82. Olsson, U., Södermann, O., and Guérin, P. (1986). *J. Phys. Chem.*, **90**, 5223.
83. Candau, S. J., Hirsch, E., Zana, R., and Adam, M. (1988). *J. Colloid Interface Sci.*, **122**, 430.
84. Marignan, J., Appell, J., Bassereau, P., Porte, G., and May, R. P. (1989). *J. Phys. France*, **50**, 3553.
85. Imae, T. (1989). *Colloid Polym. Sci.*, **267**, 707.
86. Khatory, A., Kern, F., Lequeux, F., Appell, J., Porte, G., Morie, N., Ott, A., and Urbach, W. (1993). *Langmuir*, **9**, 933.
87. Tausk, R. and Overbeek, J. T. G. (1976). In *Colloid and interface science* (ed. M. Kerber), Vol. 2, pp. 379–386. Academic Press, New York.
88. Mishic, J. R. and Fisch, M. R. (1990). *J. Chem. Phys.*, **92**, 3222.
89. Van De Sande, W. and Persoons, A. (1985). *J. Phys. Chem.*, **89**, 404.
90. Schmidt, M. (1984). *Macromolecules*, **17**, 553.
91. Grob, M. C., Schurtenberger, P., and Suter, U. Q. (1995). *Makromol. Chem. Phys.*, **196**, 1391.
92. Schurtenberger, P. and Cavaco, C. (1994). *Langmuir*, **10**, 100.
93. Kirste, R. G. and Oberthür, R. C. (1982). In *Small angle X-ray scattering* (ed. O. Glatter and O. Kratky), p. 387. Academic Press, London.
94. Schurtenberger, P., Magid, L. J., King, S., and Lindner, P. (1991). *J. Phys. Chem.*, **95**, 4173.
95. Pedersen, J. S., Egelhaaf, S. U., and Schurtenberger, P. (1995). *J. Phys. Chem.*, **99**, 1299.
96. Hoffmann, H., Platz, G., Rehage, H., and Schorr, W. (1982). *Adv. Colloid Interface Sci.*, **17**, 275.
97. Egelhaaf, S. U. and Schurtenberger, P. (1994). *J. Phys. Chem.*, **98**, 8560.
98. Yamakawa, H. (1971). *Modern theory of polymer solutions*. Harper & Row, New York.
99. Huber, K. and Stockmayer, W. H. (1987). *Macromolecules*, **20**, 1400.
100. Carale, T. R. and Blankschtein, D. (1992). *J. Phys. Chem.*, **96**, 459.
101. de Gennes, P. G. (1979). *Scaling concepts in polymer physics*. Cornell University Press, Ithaca, New York.
102. Doi, M. and Edwards, S. F. (1986). *The theory of polymer dynamics*. Oxford University Press, Oxford.
103. Brown, W. and Nicolai, T. (1990). *Colloid Polym. Sci.*, **268**, 977.
104. Daoud, M., Cotton, J. P., Farnoux, B., Jannink, G., Sarma, G., Benoit, H., Duplessix, R., Picot, C., and de Gennes, P. G. (1975). *Macromolecules*, **8**, 804.
105. Imae, T. (1988). *J. Phys. Chem.*, **92**, 5721.
106. Makhloifi, R., Hirsch, E., Candau, S. J., Binana-Limbele, W., and Zana, R. (1989). *J. Phys. Chem.*, **93**, 8095.
107. Brown, W., Johansson, K., and Almgren, M. (1989). *J. Phys. Chem.*, **93**, 5888.
108. Appell, J. and Porte, G. (1990). *Europhys. Lett.*, **12**, 185.
109. Imae, T. (1990). *J. Phys. Chem.*, **94**, 5953.
110. Schurtenberger, P., Scartazzini, R., Magid, L. J., Leser, M. E., and Luisi, P. L. (1990). *J. Phys. Chem.*, **94**, 3695.
111. Terech, P., Schaffhauser, V., Maldivi, P., and Guenet, J. M. (1992). *Langmuir*, **8**, 2104.

112. Zhou, Z., Georgalis, Y., Liang, W., Li, J., Xu, R., and Chu, B. (1987). *J. Colloid Interface Sci.*, **116**, 473.
113. Eastoe, J., Steytler, D. C., Robinson, B. H., Heenan, R. K., North, A. N., and Dore, J. C. (1994). *J. Chem. Soc. Faraday Trans.*, **90**, 2497.
114. Scartazzini, R. and Luisi, P. L. (1988). *J. Phys. Chem.*, **92**, 829.
115. Schurtenberger, P., Scartazzini, R., and Luisi, P. L. (1989). *Rheol. Acta*, **28**, 372.
116. Schurtenberger, P., Magid, L. J., Penfold, J., and Heenan, R. (1990). *Langmuir*, **6**, 1800.
117. Ott, A., Urbach, W., Langevin, D., Schurtenberger, P., Scartazzini, R., and Luisi, P. L. (1990). *J. Phys.: Condens. Matter*, **2**, 5907.
118. Schurtenberger, P., Magid, L. J., Lindner, P., and Luisi, P. L. (1992). *Progr. Colloid Polym. Sci.*, **89**, 274.
119. Schurtenberger, P., Magid, L. J., King, S. M., and Lindner, P. (1991). *J. Phys. Chem.*, **95**, 4173.
120. Schurtenberger, P. and Cavaco, C. (1993). *J. Phys. II (France)*, **3**, 1279.
121. Utiyama, H., Tsunashima, Y., and Kurata, M. (1971). *J. Chem. Phys.*, **55**, 3133.
122. Koyama, R. (1973). *J. Phys. Soc. Jpn*, **34**, 1029.
123. Schmidt, M., Paradossi, G., and Burchard, W. (1985). *Makromol. Chem., Rapid Commun.*, **6**, 767.
125. Sharp, P. and Bloomfield, V. A. (1968). *Biopolymers*, **6**, 1201.
126. Yamakawa, H. and Fujii, M. (1974). *Macromolecules*, **7**, 649.
127. Yoshizaki, T. and Yamakawa, H. (1980). *Macromolecules*, **13**, 1518.
128. Hjelm, R. P., Thiagarajan, P., and Alkan-Onyuksel, H. (1992). *J. Phys. Chem.*, **96**, 8653.
129. Long, M. A., Kaler, E. W., Lee, S. P., and Wignall, G. D. (1994). *J. Phys. Chem.*, **98**, 4402.
130. Fujita, H. (1988). *Macromolecules*, **21**, 179.
131. Schurtenberger, P. and Cavaco, C. (1994). *J. Phys. Chem.*, **98**, 5481.
132. Schurtenberger, P. and Cavaco, C. (1994). *J. Phys. II (France)*, **4**, 305.
133. Sharp, P. A. and Bloomfield, V. A. (1968). *J. Chem. Phys.*, **49**, 4564.
134. Domb, C., Gillis, J., and Wilmers, G. (1965). *Proc. Phys. Soc. (London)*, **85**, 625.
135. Domb, C. (1963). *J. Chem. Phys.*, **38**, 2957.
136. Peterlin, A. (1955). *J. Chem. Phys.*, **23**, 2464.
137. Peebles, J. L. H. (1971). *Molecular weight distributions in polymers*. Interscience Publishers, New York.
138. Richtering, W. H., Burchard, W., Jahns, E., and Finkelmann, H. (1988). *J. Phys. Chem.*, **92**, 6032.
139. Ohta, T. and Oono, Y. (1982). *Phys. Lett.*, **89A**, 460.
140. Koper, G. J. M., Cavaco, C., and Schurtenberger, P. (1995). In *25 Years of non-equilibrium thermodynamics* (ed. M. Rubi). Springer-Verlag, Berlin.
141. Schurtenberger, P., unpublished results.
142. Nakanishi, A. and Ohta, T. (1985). *J. Phys. A*, **18**, 127.

Scattering from block copolymer micellar systems

Zdeněk Tuzar and Pavel Kratochvíl

10.1 Introduction

Block and graft copolymers in solution in selective solvents, that are good for one block and poor for the other, self-associate forming multimolecular micelles, the cores of which consist of insoluble blocks, while the soluble blocks are located in protective shells. A typical association number (i.e. the number of copolymer molecules in a micelle) is from tens to hundreds. These micelles, with a narrow molar mass and size distribution, are in dynamic equilibrium with molecularly dissolved copolymer molecules (unimers). Unlike aqueous micellar systems of soaps and surfactants, block copolymer micellar systems in both organic and aqueous selective solvents have very low, usually imperceptible, critical micelle concentrations (CMC). The structure and various properties of these micelles have been studied by numerous physico-chemical methods and the results have been reviewed several times.^[1-4]

Static light scattering (hereinafter SLS) is an efficient technique for studying block copolymer micelles, especially in combination with other methods. SLS alone is the best tool available for the molecular characterization of block and graft copolymers, i.e. for the determination of molar mass, the apparent value of the radius of gyration and, sometimes, the heterogeneity of chemical composition. Due to the relatively small size of the micelles (hundreds of Å), only the micellar molar mass, the association number and, for sufficiently large micelles, an apparent value of the radius of gyration can be measured by SLS. In combination with small-angle X-ray or neutron scattering, the geometrical radius of the core and of the whole micelle, as well as average segment densities in the core and shell, can also be determined. In combination with the sedimentation velocity method, the unimer/micelle mass ratio in a particular selective solvent at a given temperature and concentration of the copolymer can be determined, and the nature of the association (usually the closed association mechanism) can be established. Simultaneous employment of SLS and dynamic light scattering provides information on the hydrodynamic behaviour of the micelles. Unique data on the kinetics of micelle formation and dissociation have been obtained by the stopped-flow technique with SLS detection. SLS is very useful in monitoring the onset of micellization

(CMC or critical micelle temperature, CMT), as well as of the so-called 'anomalous micellization' in the vicinity of micellar critical conditions.

In this chapter, experimental studies on the structure and properties of block and graft copolymer micelles are reviewed, in which the SLS method plays a major role.

10.2 Molecular characterization of block and graft copolymers

SLS has been recognized as the optimal method for determination of the mass-average molar mass, M_w , the radius of gyration, R_g , and the heterogeneity of chemical composition of block and graft copolymers. Although the topic has been reviewed several times,^[5,6] a brief survey is given in this section.

The weight-average molar mass, M_w , of a copolymer can be evaluated from the equation

$$KC/R(q=0) = M_w^{-1} + 2A_2C, \quad (10.1)$$

where K is the optical constant containing the square of the refractive index increment, $(dn/dC)^2$, C is the solute concentration (usually in g ml^{-1}), $R(q=0)$ is the Rayleigh ratio, proportional to the intensity of light scattered by the solute and extrapolated to zero value of the magnitude of the scattering vector, q , and A_2 is the second virial coefficient. Refractive indices of the blocks (in the case of a block copolymer) or of a backbone and grafts (in the case of a graft copolymer) generally differ. Due to an almost inevitable heterogeneity in chemical composition,^[7,8] refractive indices and refractive index increments of individual molecules in a given copolymer sample also differ. As has been shown,^[5] M_w determined for a chemically heterogeneous copolymer by SLS is an apparent value only, depending on the refractive index of the solvent used:

$$M_{w,app} = M_w + 2P[(v_A - v_B/v_C)] + Q[(v_A - v_B)/v_C]^2. \quad (10.2)$$

v_A , v_B and v_C are the refractive index increments of the copolymer parts A and B and of the copolymer sample in a given solvent, respectively. Q and P are parameters characterizing the broadness and the asymmetry of the distribution of chemical composition. To obtain the true values of M_w , Q and P , measurements of $M_{w,app}$ in at least three solvents differing in refractive index are necessary. An analysis of the results of numerical model calculations showed that the three solvents should most suitably be chosen to meet the following criteria:^[9]

- (1) $|v_A|$ and $|v_B|$ large, sign v_A = sign v_B ;
- (2) $|v_A|$ large, $v_B = 0$;
- (3) $v_A = 0$, $|v_B|$ large.

It has also been shown that these criteria can relatively easily be fulfilled by employing multicomponent solvents.^[9] In such a case, however, the v values must be measured under the condition of osmotic equilibrium between the

polymer solution and the given mixed solvent.^[10] It should be stressed that the main source of heterogeneity in a diblock copolymer is the presence of a homopolymer or, in the case of a triblock copolymer, the presence of both homopolymer and a diblock copolymer. With graft copolymers, the heterogeneity in chemical composition is generally caused by a varying number of grafts per backbone, due to the statistical nature of reactions by means of which the copolymers are prepared.

If the copolymer molecules are of such a size that the q^2 -dependence of the intensity of scattered light is measurable, an apparent value of the radius of gyration, $R_{g,app}$, can be determined. $R_{g,app}$ is defined as

$$R_{g,app} = v_c^{-2} [w_A^2 v_A^2 R_{g,A} + (1 - w_A)^2 v_B^2 R_{g,B}^2 + 2x_A(1 - w_A)v_A v_B R_{g,AB}^2], \quad (10.3)$$

where the symbols v_i have the same meaning as in eqn (10.2), w_A is the mass fraction of the copolymer part A , and $R_{g,A}$ and $R_{g,B}$ are the radii of gyration of parts A and B , respectively, of a copolymer molecule about their centres of mass. The mixed term

$$R_{g,AB}^2 = (R_{g,A}^2 + R_{g,B}^2 + l^2)/2 \quad (10.4)$$

contains the mean square distance, l^2 , separating the centres of mass of the copolymer parts A and B . Unlike $M_{w,app}$, $R_{g,app}$ also depends on the thermodynamic quality of the solvent. Further, if v_A and v_B are of opposite sign, a negative $R_{g,app}^2$ may result. Thus, an estimate of the size of copolymer molecules from SLS data is rather involved. Only if one copolymer part is optically masked (i.e. isorefractive with the solvent), can the true R_g of the non-isorefractive part of the copolymer be determined.

10.3 Unimer \rightleftharpoons micelle equilibrium

All experimental data gathered^[1-4] so far have shown that, under given conditions, block and graft copolymer micelles are stable in time and their structure and properties are well reproducible. It has become clear that micellization of block and graft copolymers is, as a rule, a reversible and dynamic process, i.e. an association.

There are two limiting cases of association, open and closed.^[11] Open association assumes a broad distribution of unimers, dimers, trimers, etc., up to n -mers and can be described by a series of corresponding equilibrium constants. Closed association is characterized by an equilibrium between unimers and n -meric micelles with a narrow molar-mass and size distribution. Unlike the model of open association, closed association implies the existence of a CMC. Theoretical calculations of the concentration dependencies of the reciprocal values of the mass-average molar mass comprising all solute particles present in solution can be represented by the curves in Fig. 10.1.

According to Elias,^[11] the CMC does not represent a thermodynamically important property of a given micellar system. He only gave it the

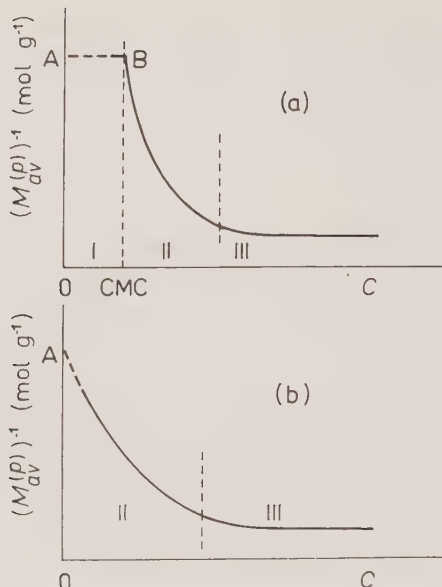


FIG. 10.1. Model concentration dependencies of the reciprocal value of an average molar mass comprising all solute particles for closed (a) and open (b) association. A equals the reciprocal value of unimer molar mass, and B marks the observable onset of micellization; for I, II and III, see the text. After ref. 11.

phenomenological meaning of a concentration at which micelles are just detectable by a given method. This explains why different methods give different CMC values for the same system. With a few exceptions only (see, e.g., ref. 12), soaps and surfactants in water follow the closed association dependence shown in Fig. 10.1(a).

Since the values of CMC for block and graft copolymers are usually much lower than those for soaps and surfactants, the experimental dependencies following the pattern of Fig. 10.1(a) may be detected by osmotic (M_n) rather than by SLS (M_w) measurements, where only parts II and III are measurable.^[14,13] Assuming the open association model, part II of the curves in Fig. 10.1 represents a steadily increasing micellar molar mass with increasing concentration, while in the closed association model, $M^{(m)}$ should not change and only the unimer/micelle mass ratio decreases with increasing concentration. Supposing that in SLS measurements a value of $KC/R(q = 0)$ at a finite copolymer concentration corresponds to a good approximation to the reciprocal mass-average molar mass of the system, $(M_w^{(p)})^{-1}$ (i.e. assuming that A_2 is close to zero, as can be substantiated by thermodynamic reasoning^[13,14]) we may write

$$M_w^{(p)} = M_w^{(u)}w(u) + M_w^{(m)}(1 - w^{(u)}), \quad (10.5)$$

where $w^{(u)}$ is the mass fraction of unimer and $M_w^{(u)}$ is its mass-average molar

mass that can be measured in any good solvent. To calculate $M_w^{(m)}$ in the concentration region II in Fig. 10.1(a), $w^{(u)}$ and $w^{(m)} (=1-w^{(u)})$ must be determined independently. Two methods can be employed here, viz. DLS and sedimentation velocity. In the first method, the mass fractions of unimer and micelles can be determined from the amplitudes corresponding to the decay rates of each species.^[15] This method is suitable in principle, since the decay rates (i.e. the diffusion coefficients) of unimer and micelles are sufficiently separated in most cases and the experimental correlation function can be evaluated by a double-exponential fitting procedure. Unfortunately, the intensity of the scattered light from the unimer is too low (since $M_w^{(u)} \ll M_w^{(m)}$), especially at low $w^{(u)}$, and thus the method is generally not reliable for this purpose.^[15]

In the sedimentation velocity method, both species, unimer and micelles, provide two concentration boundaries (the positions of which are proportional to the respective sedimentation coefficients) that are for physical reasons much better separated from each other than the diffusion coefficients. In a standard experimental arrangement, the sedimentation diagram is represented as a dr/dC vs. r dependence, where r is the distance in the sedimentation cell from the axis of rotation. In micellar systems, two well separated peaks are observed. In an ideal case of two independent species differing in sedimentation coefficients, the areas under the two peaks would be proportional to the masses of the corresponding type of particles. In most of the micellar systems, unimer and micelles are in a dynamic equilibrium. Fortunately, according to Gilbert's theory,^[16,17] for fast rates of unimer \rightleftharpoons micelle equilibration and for association numbers larger than about ten (which is the case for most block and graft copolymer micellar systems), unimers and micelles behave in a sedimentation experiment as independent species.

Constant values of $M^{(m)}$, independent of concentration, have been experimentally found for polystyrene *block*-polybutadiene-*block*-polystyrene ($M_w = 1.4 \times 10^5$ g mol⁻¹, $w^{PS} = 0.52$) dissolved in a solvent mixture of isopycnic and isorefractive components, tetrahydrofuran/allylalcohol.^[18] In several mixtures, differing in composition, and at different temperatures, the SLS data followed the pattern of parts II and III in Fig. 10.1. With increasing C , $w^{(m)}$ grew, and the limiting $M^{(m)}$ was constant for a given solvent and temperature. To give an example, in the mixture tetrahydrofuran/46 vol.% allylalcohol at 35°C, $w^{(m)}$ increased with increasing C (from 1×10^{-3} to 4×10^{-3} g ml⁻¹) from 0 to 0.38, and $M_w^{(p)}$ increased from 2×10^5 to 2.4×10^6 g mol⁻¹, while $M_w^{(m)}$ remained practically constant, equal to 6.2×10^6 g mol⁻¹ \pm 5%.

10.4 Static parameters of micelles

Static parameters include the molar masses of the core, $M^{(core)}$, of the shell, $M^{(shell)}$, and of the whole micelle, $M^{(m)}$, and the corresponding radii of gyration, $R_g^{(core)}$, $R_g^{(shell)}$ and $R_g^{(m)}$. Due to the practically uniform molar mass and size of micelles, the averaging is intentionally omitted here.

SLS is evidently the most reliable method for the determination of $M^{(m)}$, provided that the measurements are performed with copolymer concentrations at which the unimer \rightleftharpoons micelle equilibrium is shifted in favour of micelles, i.e. where the $KC/R(q = 0)$ vs. C dependence is horizontal (Fig. 10.1). The value of $M^{(m)}$, calculated from eqn (10.1), is a real value in spite of a potential heterogeneity in chemical composition of the copolymer. Statistical reasoning leads to a picture of uniform micelles, each containing copolymer molecules with nearly the same distribution in chemical composition.

Due to generally different refractive index increments of the core and the shell, $R_g^{(m)}$, if measurable (i.e. larger than ca. 120 Å), is only an apparent value

$$KC/R(q) = (M^{(m)})^{-1}(1 + q^2 R_{g,app}^{(m)}/3). \quad (10.6)$$

Since the core and the shell are concentric and thus have the same centre of mass, $R_{g,app}^{(m)}$ equals^[19]

$$(R_{g,app}^{(m)})^2 = Y^{(core)}(R_g^{(core)})^2 + Y^{(shell)}(R_g^{(shell)})^2. \quad (10.7)$$

where $Y^{(core)} = w^{(core)}v^{(core)}/v^{(m)}$ and $Y^{(shell)} = (1 - w^{(core)})v^{(shell)}/v^{(m)}$. $w^{(core)}$ is the mass fraction of the core-forming blocks and v is the refractive index increment. Equation (10.7) can be rewritten in terms of geometrical radii:

$$(R_{g,app}^{(m)})^2 = 0.6 Y^{(core)}(R^{(core)})^2 + 0.6 Y^{(shell)} \frac{(R^{(m)})^5 - (R^{(core)})^5}{(R^{(m)})^3 - (R^{(core)})^3}. \quad (10.8)$$

Fortunately, $R^{(core)}$ can relatively easily be obtained from small-angle X-ray (SAXS) or small-angle neutron (SANS) scattering, from the position of the side maximum on the scattering curve.^[19] The geometrical radii of the shell and the whole micelle, as well as the average volume fractions of polymer segments, φ , in the core, shell, and the whole micelle, can be calculated. Typical results obtained with a commercial triblock copolymer Kraton G-1650 (Shell Co.), polystyrene-block-hydrogenated polybutadiene-block-polystyrene ($M_w = 74 \times 10^6$ g mol⁻¹, mass fraction of styrene units 0.28) in 1,4-dioxane, where uniform micelles with aliphatic cores and polystyrene shells are formed, are introduced here.^[19] Measured values are as follows: $M_w^{(m)} = 5.1 \times 10^6$ g mol⁻¹, $R_{g,app}^{(m)} = 150$ Å, $R_g^{(core)} = 125$ Å. Calculated values are as follows: $R^{(m)} = 225$ Å, $R_g^{(m)} = 150$ Å, shell thickness = 100 Å, $\varphi^{(m)} = 0.18$, $\varphi^{(core)} = 0.75$, $\varphi^{(shell)} = 0.06$.

Some interesting features of these results should be commented on:

1. All three φ values confirm the dense character of micelles. For comparison, φ values for typical polymer coils are ca. 0.03–0.04.
2. The $\varphi^{(core)}$ value indicates that the cores contain a relatively high amount of the thermodynamically poor solvent. This finding has been corroborated by some other experimental data on block copolymer micelles in selective organic solvents.^[20,21] Only strongly hydrophobic cores of micelles in aqueous media are solvent-free. It has been shown recently that polystyrene cores of micelles with poly(methacrylic acid) shells may become glassy in 1,4-dioxane/water mixtures rich in water and in aqueous buffers, while in water-poor mixtures the cores are partially swollen.^[22,23]

3. Hydrodynamic radii obtained from DLS (197 Å) and from the combined SLS and viscosity data (194 Å)^[19] were not far from the calculated geometrical radius (225 Å), indicating that the micelles studied behave like hydrodynamic hard spheres. Moreover, the hydrodynamic radius and the calculated geometrical radius (150 Å) fitted well to the relationship for hard spheres, $R^{HS} = (5/3)^{1/2} R_g$.

10.5 Hydrodynamic behaviour of micelles

The very similar values for the hydrodynamic and geometric radii of Kraton G-1650 micelles in 1,4-dioxane discussed above, and which indicate the hydrodynamic hard sphere behaviour of these micelles, stimulated a more systematic study. The most urgent question was as follows: How does shell swelling influence the hydrodynamic character of micelles? The experiment with micelles having aliphatic cores and polystyrene shells in 1,4-dioxane discussed above was extended by employing the mixed solvent 1,4-dioxane/heptane.^[24] 1,4-Dioxane is a selective solvent for the polystyrene shell, while heptane is a selective solvent for the aliphatic core. An increase in heptane content in a solvent mixture leads to the swelling of the core and deswelling of the shell. Experimental SLS and DLS data in solvent mixtures containing 10, 20 and 30 vol.% heptane are shown in Table 10.1. SLS gave $M^{(m)}$ and A_2 , while DLS gave $R_h^{(m)}$ and the diffusion virial coefficient, k'_D . The last value, k_D , has been obtained from the concentration dependence of the diffusion coefficient, D_C :

$$D_C/D_0 = 1 + k_D \phi = 1 + k'_D C, \quad (10.9)$$

where D_0 is the diffusion coefficient at infinite dilution, ϕ is the volume fraction of the micelles and k_D is a value which is not directly accessible from experiment but can be calculated (see below).

Only small changes in the values of $M^{(m)}$ and $R_h^{(m)}$ with an increase in the amount of heptane in the solvent mixtures in Table 10.1 indicate that the effects of swelling of the core and deswelling of the shell compensate each other.

Table 10.1. SLS and DLS data for micelles of polystyrene–block–hydrogenated polybutadiene–block polystyrene in 1,4-dioxane. $M_w^{(m)}$ is the micellar molar mass, A_2 is the second virial coefficient, and $R_h^{(m)}$ is the hydrodynamic radius of the micelles; A_2^{HS} , k'_D and k_D are calculated values (for definitions see text). After ref. 24.

Heptane (vol.%)	$M_w^{(w)} \times 10^{-6}$ (g mol ⁻¹)	$R_h^{(m)}$ (Å)	$A_2 \times 10^6$ (cm ³ g ⁻² mol)	$A_2^{HS} \times 10^6$ (cm ³ g ⁻² mol)	k'_D (cm ³ g ⁻¹)	k_D
0	4.80	192	2.1	3.07	4.02	1.09
10	4.44	223	4.2	5.66	6.63	1.05
20	4.20	232	7.5	7.19	7.54	1.01
30	3.77	249	12.7	10.97	11.95	1.15

However, an increase in A_2 and k'_D means that the effect of core swelling predominates.

The evidence for hard sphere behaviour of micelles in all solvent mixtures in Table 10.1 is provided by the good agreement between the experimental values of A_2 and values for the hard sphere model, A_2^{HS} . The latter has been calculated from the relation

$$A_2^{HS} = 4N_A V/(M^{(m)})^2, \quad (10.10)$$

where V is the excluded volume of a micelle, $V = 4\pi(R_h^{(m)})^3/3$.

Even more convincing proof of the hard sphere behaviour can be seen in the almost perfectly constant value of k_D , which was calculated from the relation

$$k_D = k'_D/\bar{v}, \quad (10.11)$$

where \bar{v} is the partial specific volume of the swollen micelles, approximated by their volume per unit of $M^{(m)}$, defined as $N_A V/M^{(m)}$. Using again, as in eqn (10.10), R_h for the calculation of V , eqn (10.11) can be written as

$$k_D = 3k'_D M^{(m)} / [4\pi N_A (R_h^{(m)})^3]. \quad (10.12)$$

The k_D value from Table 10.1 (1.08 ± 0.07), which is independent of the solvent composition, is close to the value 1.3, obtained experimentally for a dispersion of silica particles^[25] which may be considered as being close to hard spheres.

In spite of the evidence of hydrodynamic hard sphere behaviour of block copolymer micelles given in ref. 24 and discussed above, it can be expected that micelles with extremely loose shells, such as those with relatively small cores and long ('hairy') shell-forming blocks or micelles with polyelectrolyte shells, may show different hydrodynamic behaviour.

10.6 Kinetics of micelle formation and dissociation

So far, there has been only one study on the kinetics of the formation and dissociation of block copolymer micelles.^[26] The method employed was stopped flow with SLS detection. The micellar systems were a diblock copolymer polystyrene–block–hydrogenated polyisoprene–block–polystyrene ($M_w = 105 \times 10^3$ g mol⁻¹, $w^{PS} = 0.4$) and a triblock copolymer polystyrene–block–hydrogenated polybutadiene–block–polystyrene ($M_w = 74 \times 10^3$ g mol⁻¹, $w^{PS} = 0.28$), both in 1,4-dioxane and in a mixture of 1,4-dioxane/20 vol.% heptane. The characteristics of these micelles with aliphatic cores and polystyrene shells in both copolymers are shown in both solvents in Table 10.2.

Micelle formation was achieved by fast mixing of the molecular copolymer solution ($C = 1 \times 10^{-2}$ g ml⁻¹) in a thermodynamically good solvent mixture, 1,4-dioxane/40 vol.% heptane, with the same amount of 1,4-dioxane. The resulting solution contained micelles in the mixture 1,4-dioxane/20 vol.% heptane. Dissociation of micelles was realized by mixing a micellar solution ($C = 1 \times 10^{-2}$ g ml⁻¹) in 1,4-dioxane with the same amount of heptane. The

Table 10.2. Characteristics of two micellar systems used in a kinetic investigation. $M_w^{(m)}$ is the micellar weight-average molar mass, n is the association number, PS is the polystyrene block, and hPB is the hydrogenated polybutadiene block. After ref. 26.

Copolymer	1,4-Dioxane		1,4-Dioxane/20 vol.% heptane	
	$M_w^{(m)} \times 10^{-6}$ (g mol ⁻¹)	n	$M_w^{(m)} \times 10^{-6}$ (g mol ⁻¹)	n
PS-block-hPI	20.7	197	18.0	171
PS-block-hPb-block-PS	5.1	69	4.8	65

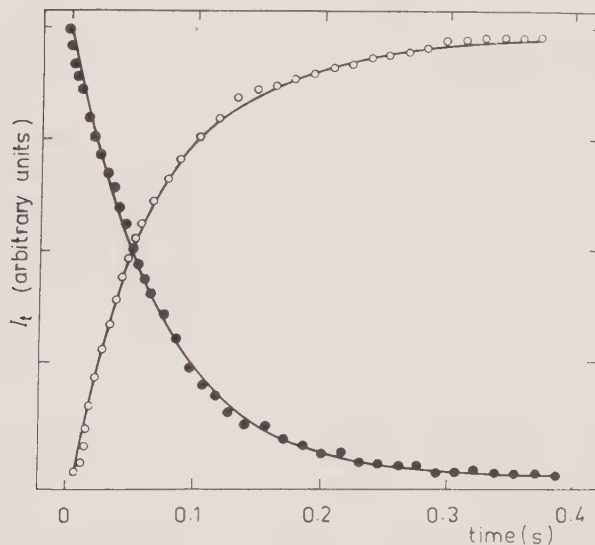


FIG. 10.2. The time dependence of the intensity of scattered light, I_t , after mixing: 1 mass-% micellar solution of a triblock copolymer polystyrene-block-hydrogenated polybutadiene block-polystyrene in 1,4-dioxane with an equal amount of heptane (●), or 1 mass-% unimer solution of the same copolymer in 1,4-dioxane/40 vol.% heptane with an equal amount of 1,4-dioxane (○). After ref. 26.

resulting solution in 1,4-dioxane/50 vol.% heptane contained only molecularly dissolved copolymer.

The dead time (i.e. the time between the mixing of a solvent and a solution, and the start of the SLS measurement) of the instrument used^[26] was 1 ms. Micelle formation was monitored as the increase in the intensity of the scattered light and micelle dissociation as the decrease in the intensity of scattered light. It has been found that the decay curves (Fig. 10.2) could best be fitted by a

double-exponential function

$$S(t) = a_1 e^{-t/\tau_1} + a_2 e^{-t/\tau_2}, \quad (10.13)$$

where a_1 and a_2 are the normalized amplitudes, τ_1 and τ_2 are relaxation times, and $S(t)$ is $(I_\infty - I_t)/I_\infty$ and I_t/I_0 for micelle formation and dissociation, respectively. Without giving τ_1 and τ_2 any specific physical interpretation, the double-exponential representation was used as an acceptable approximation of apparently continuous spectra of relaxation times, and the mean value $\tau = a_1\tau_1 + a_2\tau_2$ was taken to characterize the rates of micelle formation, τ_F , and dissociation, τ_D (Table 10.3). The quantity W , defined as

$$W = (a_1\tau_1^2 + a_2\tau_2^2)^{1/2}/\tau \quad (10.14)$$

was used as a measure of the width of the relaxation time distribution.

Table 10.3 illustrates differences between the kinetics of formation and dissociation of diblock and triblock copolymer systems. The similar values of τ_F and the very different values of W in both systems have been explained as follows. Micelle formation proceeds in two stages. In the first stage, a good solvent is changed to a selective one by mixing and copolymer molecules, with one block collapsed, aggregate and form a system of polydisperse particles. In the second stage, collapsed unsolvated blocks relax into entropically more favourable conformations. In this process the core-forming blocks may become entangled. Simultaneously, the particles equilibrate by exchanging unimers, which results in a system of nearly uniform micelles. While τ_F reflects only the first stage, W monitors the equilibration process, which is obviously more complex in the case of a triblock copolymer system.

Analogous reasoning also holds for the data on micelle dissociation in Table 10.3. Here, the first step would be a fast influx of solvent molecules into the micellar core and the second step a solvent-assisted separation of copolymer molecules from a micelle. The small value of τ_D (< 1 ms) for the diblock copolymer can be explained by an easy escape of unimer molecules from a micelle, since each core-forming block crosses the core/shell interface only once. In the case of a triblock copolymer, any unimer molecule crosses the core/shell

Table 10.3. Kinetics of block copolymer micellization. τ_F and τ_D are relaxation times of micelle formation and dissociation, respectively, and W is the width of the relaxation time distribution. PS is a polystyrene block, hPI is an hydrogenated polyisoprene block, and hPB is an hydrogenated polybutadiene block. After ref. 26.

Copolymer	τ_F (ms)	W	τ_F (ms)	W
PS-block-hPB	43	0.02	1	—
PS-block-hPB-block-PS	69	0.57	137	0.83

interface twice. It is obvious that this process involves disentanglements that are slowed down by unfavourable interactions between non-compatible blocks. As a result, the relaxation time of triblock copolymer dissociation is at least two orders of magnitude slower than that of diblock copolymer micelles.

10.7 Anomalous micellization

The first appearance of micelles at the CMC or CMT can be monitored sensitively as a sudden increase in the intensity of the scattered light. The CMC values obtained in this way have been used for the thermodynamic characterization of block copolymer micellization.^[27,28]

'Anomalous micellization' has been reported several times, for numerous and various block copolymer micellar systems.^[29-34] It usually consists of the appearance of a milky opalescence at the onset of micellization, i.e. in the vicinity of CMC or CMT, indicating the presence of particles orders of magnitude larger than ordinary micelles. Often, milky solutions then macrophase separate. In some cases the effect (large particles) disappeared when the conditions (solvent composition, temperature) were shifted further from the CMC or CMT towards conditions more favourable for micelle formation.^[29,35]

The present authors investigated the anomalous micellization of polystyrene-block-polybutadiene-block polystyrene in a selective solvent of polystyrene, isopropyl acetate, by SLS and sedimentation velocity.^[35] The milky opalescent solutions showed high values of the dissymmetry of scattered light, the effect becoming more pronounced with the decreasing concentration of the copolymer (Fig. 10.3.). Sedimentation diagrams and the q^2 - (i.e. angular) dependence of the reciprocal intensity of scattered light $KC/R(q)$ (Fig. 10.4) show that in a clear solution at 37 °C only unimer is present, while at 35 °C large particles appear in an amount imperceptible with the ultracentrifuge optics, but identifiable by a distinctly curved q^2 -dependence of $KC/R(q)$. In a strongly turbid solution at 30 °C, large spherical particles were present, as indicated by a maximum on the scattering curve at higher q^2 . The sedimentation diagram with a faster moving front showed the presence of polydisperse heavier particles. At 23 °C a bluish opalescent solution, indicating the presence of regular micelles, could be observed. The SLS pattern was typical of micellar systems free of any anomalous large particles, and the sedimentation diagram showed slower and faster moving well-separated peaks, corresponding to unimer and micelles. A further drop of temperature to 20 °C caused only an increase in the micellar molar mass and in the mass fraction of micelles.

Several attempts have been made to interpret the anomalous micellization. Price *et al.* identified large particles as metastable worm-like objects^[33,36] and substantiated their existence by thermodynamic reasoning.^[2] Utyama found that the large particles are ellipsoidal in shape.^[30] The present authors performed SLS and sedimentation experiments with block copolymer micellar systems, intentionally contaminated with a homopolymer, chemically identical

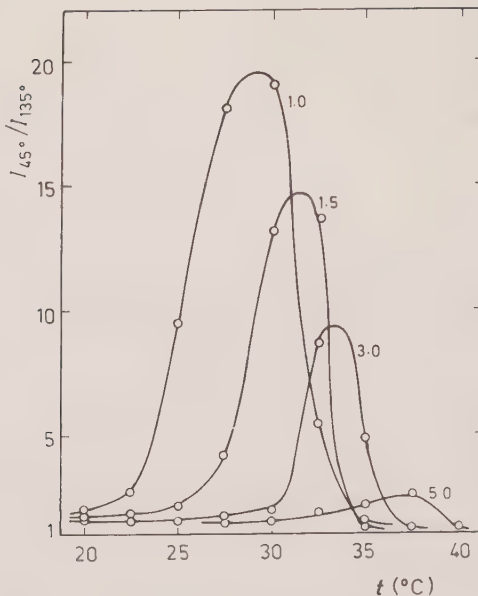


FIG. 10.3. The temperature dependence of the dissymmetry of scattered light for a triblock copolymer, polystyrene-block-polybutadiene-block-polystyrene, in isopropyl acetate. The curves are labelled by the copolymer concentration in $10^{-3} \text{ g ml}^{-1}$. From ref. 35.

with core-forming blocks.^[37] SLS data, closely resembling those in Fig. 10.4, were obtained when either (a) a small amount of a homopolymer with molar mass higher than that of the core-forming blocks or (b) a larger amount of a homopolymer with molar mass lower than that of the core-forming blocks was present in the system. Under conditions for the onset of micellization or, in other words, when the unimer \rightleftharpoons micelle equilibrium is shifted towards the unimer, the homopolymer precipitates, giving rise to large particles that are only partially stabilized by unimers. When conditions change in favour of micelle formation, lower-molar-mass homopolymer is incorporated (solubilized) into the micellar cores, without substantially influencing the micellar size and association number. Larger-molar-mass homopolymer cannot be solubilized, and it either coexists with micelles in the form of large particles or it undergoes macrophase separation.

Not only a homopolymer, but also copolymer molecules with a higher mass ratio of core-forming monomer units can cause an anomalous micellization, as has been demonstrated by Zhou and Chu^[38,39] in their light scattering studies of aqueous solutions of an ethylene oxide/propylene oxide block copolymer, which is strongly heterogeneous in chemical composition.

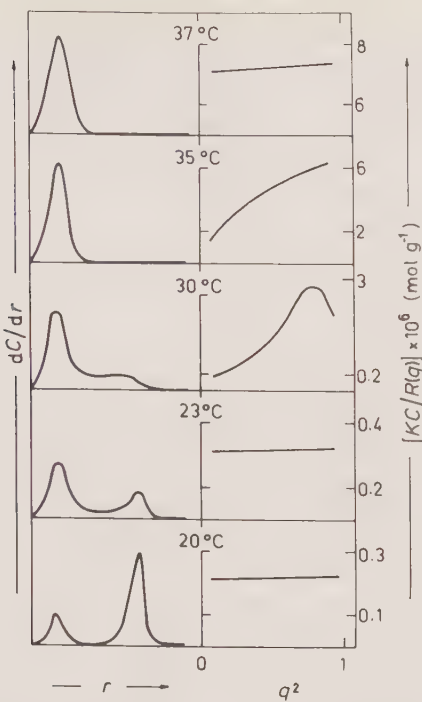


FIG. 10.4. Schematic temperature dependencies of sedimentation diagrams (concentration gradient, dC/dr , vs. distance from the axis of rotation, r), and of angular (q^2) dependence of the reciprocal intensity of scattered light $KC/R(q)$ for polystyrene-block-polybutadiene-block-polystyrene in isopropyl acetate. $C = 1.5 \times 10^{-3} \text{ g ml}^{-1}$. After ref. 35.

10.8 Block copolymer micelles in aqueous solutions

Until a few years ago, most of the studies on polymeric micelles were done in organic selective solvents. In recent years, more attention has been paid to micelles of hydrophilic/hydrophobic block copolymers in water. The reasons for this delayed interest could have been, for example, a belief that block copolymer micelles in aqueous media can add nothing substantially new to the classical surfactants, the experience that many hydrophilic/hydrophobic block copolymers fail to form micelles upon dissolution in water and also some complicating effects in micellar systems of some commercial materials, such as those already mentioned.^[33,39]

Copolymers studied in recent years can be divided into two groups: poly(ethylene oxide)-block-poly(propylene oxide)-block-poly(ethylene oxide) (abbreviated PEO-PPO-PEO) copolymers, known under the commercial names of Pluronics or Poloxamers, and laboratory prepared di- and triblock copolymers AB and ABA, where A is a hydrophilic block as poly(methacrylic acid) or poly(ethylene oxide) and B is polystyrene.

PEO-PPO-PEO copolymers represent a bridge between classical surfactants and block copolymers. Due to relatively low molar masses (a few thousands) and temperature-dependent phase transitions, these copolymers can form, depending on temperature and concentration, true solutions, micelles of different shapes or physical gels of various structures.^[40-42] PEO-PPO-PEO copolymers have found widespread industrial applications as detergents, lubricants, emulsifiers and foaming agents.^[43]

Since PEO-PPO-PEO micelles are generally small, the only information from SLS concerns the values of molar mass and second virial coefficient. As has been demonstrated, the CMC can be rather high, up to several per cent,^[38, 40, 44] unlike the other block copolymer systems discussed in the previous sections. Thus, to obtain the micellar molar mass, values of $C - C_{CMC}$ and $R - R_{CMC}$ should be used in eqn (10.1) instead of C and R , respectively.

SLS is the simplest method for the detection of the CMC. These values can be used for the determination of the standard Gibbs energy, enthalpy, and entropy of micellization. Like the micellization of soaps and surfactants in water, and unlike the micellization of block copolymers in organic selective solvents,^[1, 2] the micellization of PEO-PPO-PEO in water was found to be an entropy-driven process.^[45] Association of PPO-PEO-PPO results in micelles, the cores of which are formed by the outer blocks and the shells by the solvated inner blocks. Due to the entropy loss arising from the PEO loop geometry in micellar shell, the driving force for micellization is weaker. It has been shown^[46] that in this system the Gibbs energy of micellization was less negative and the CMC much larger than in the case of a similar PEO-PPO-PEO sample.

Although SLS proved to be a useful tool for the investigation of dilute PEO-PPO-PEO solutions, other scattering methods (DLS, SAXS and SANS) were found to be more appropriate for studies of structure and properties of these copolymers in both dilute and concentrated solutions.^[40-42, 44-47]

Micelles of block copolymers of type AB or ABA, where B is polystyrene and A is either poly(ethylene oxide) or poly(methacrylic acid), show quite different behaviour from both Pluronic type micelles and block copolymer micelles in organic selective solvents. Due to the strongly hydrophobic character of polystyrene, these copolymers form micelles by direct dissolution in water only when their molar mass is no higher than ca. 20×10^3 g mol⁻¹ and the mass fraction of polystyrene blocks does not exceed a value of ca. 0.15. Otherwise, the copolymers are non-dispersable in water.^[43] It is possible, however, to prepare aqueous micellar solutions with copolymers having molar mass up to 70×10^3 g mol⁻¹ and mass fraction of polystyrene up to 0.80. First, a given copolymer must be dissolved in a mixture of water and a cosolvent; e.g. dioxane. Copolymer molecules spontaneously associate to micelles with swollen polystyrene cores. These micelles, which are in a dynamic equilibrium with unimers, can be transferred to organic-solvent-free aqueous solutions by a stepwise dialysis. Naturally, during this process, the dynamic equilibrium becomes frozen and micelles with glassy polystyrene cores behave like stable particles. Changes in the molar mass and the size of the micelles during the

dialysis were monitored by SLS and DLS, respectively.^[22,48] Refractive index increment values in various mixed solvents were determined under osmotic equilibrium between the solution and the given mixed solvent prior to refractometric measurements,^[10] as described in Section 10.2.

Acknowledgement

This work has been supported by the Grant Agency of the Czech Republic (Grant No. 203/93/1058).

References

1. Tuzar, Z. and Kratochvíl, P. (1976). *Adv. Colloid Interface Sci.*, **6**, 201.
2. Price, C. (1982). In *Developments in block copolymers* (ed. I. Goodman), Vol. 1, p. 39. Applied Science Publishers, London, New York.
3. Riess, G., Hurtrez, G., and Bahadur, P. (1985). In *Encyclopedia of polymer science and engineering* (eds H. F. Mark, N. M. Bikales, Ch. G. Overberger, and G. Menges), 2nd edition, Vol. 2, p. 324. John Wiley, New York.
4. Tuzar, Z. and Kratochvíl, P. (1993). In *Surface and colloid science* (ed. E. Matijevic), Vol. 15, p. 1. Plenum Press, New York.
5. Benoît, H. and Froelich, D. (1972). In *Light scattering from polymer solutions* (ed. M. B. Huglin), p. 397. Academic Press, London.
6. Kratochvíl, P. (1987). *Classical light scattering from polymer solutions* (ed. A. D. Jenkins). Elsevier, Amsterdam.
7. Kotaka, T., Donkai, N., and Min, T. I. (1974). *Bull. Inst. Chem. Res., Kyoto Univ.*, **52**, 332.
8. Stejskal, J. and Kratochvíl, P. (1987). *Makromol. Chem.*, **182**, 2435.
9. Tuzar, Z., Kratochvíl, P., and Straková, D. (1970). *Europ. Polym. J.*, **6**, 1113.
10. Tuzar, Z. and Kratochvíl, P. (1967). *Collect. Czech. Chem. Commun.*, **33**, 3358.
11. Elias, H.-G. (1972). In *Light scattering from polymer solutions* (ed. M. B. Huglin), p. 397. Academic Press, London.
12. Ray, A. (1971). *Nature*, **231**, 313.
13. Sikora, A. and Tuzar, Z. (1983). *Makromol. Chem.*, **184**, 2049.
14. Pouchlý, J. and Sikora, A. (1979). International Symposium on Macromolecules, Mainz, Preprints, Vol. II, p. 935.
15. Tuzar, Z., Stěpánek, P., Koňák, Č., and Kratochvíl, P. (1985). *J. Colloid Interface Sci.*, **105**, 372.
16. Gilbert, G. A. (1955). *Discuss. Faraday Soc.*, **20**, 68.
17. Cann, J. R. (1970). *Interacting macromolecules*. Academic Press, New York. Chapters 3 and 4.
18. Tuzar, Z., Petrus, V., and Kratochvíl, P. (1974). *Makromol. Chem.*, **175**, 3181.
19. Tuzar, Z., Pleštil, P., Koňák, Č., Hlavatá, D., and Sikora, A. (1983). *Makromol. Chem.*, **184**, 2111.
20. Spěváček, J. (1982). *Makromol. Chem., Rapid Commun.*, **3**, 697.
21. Candau, F., Haetley, F., Price, C., and Stubbersfield, R. B. (1984). *Europ. Polym. J.*, **20**, 685.
22. Tuzar, Z., Webber, S. E., Ramireddy, C., and Munk, P. (1991). *Polym. Preprints*, **32**(1), 525.
23. Tian, M., Qin, A., Ramireddy, C., Webber, S. E., Tuzar, Z., Munk, P., and Procházka, K. (1993). *Langmuir*, **9**, 1741.

24. Koňák, Č., Tuzar, Z., Štěpánek, P., Sedláček, B., and Kratochvíl, P. (1985). *Progr. Coll. Polym. Sci.*, **71**, 15.
25. Kops-Werkhoven, M. M. and Fijnaut, H. M. (1981). *J. Chem. Phys.*, **74**, 1681.
26. Bednář, B., Edwards, K., Almgren, M., Tormod, S., and Tuzar, Z. (1988). *Makromol. Chem., Rapid Commun.*, **24**, 785.
27. Price, C., Kendal, K. D., Stubbersfield, R. B., and Wright, B. (1983). *Polym. Commun.*, **24**, 326.
28. Price, C. (1983). *Pure Appl. Chem.*, **55**, 1563.
29. Lally, T. P. and Price, C. (1974). *Polymer*, **15**, 325.
30. Utyiama, H., Takenaka, K., Mizumori, M., Fukuda, M., Tsunashima, Y., and Kurata, M. (1974). *Macromolecules*, **7**, 515.
31. Mandema, W., Zeldenrust, H., and Emais, C. A. (1979). *Makromol. Chem.*, **180**, 1521.
32. Mandema, W., Emais, C. A., and Zeldenrust, H. (1979). *Makromol. Chem.*, **180**, 2163.
33. Canham, P. A., Lally, T. P., Price, C., and Stubbersfield, R. B. (1980). *J. Chem. Soc., Faraday Trans. I*, **76**, 1857.
34. Price, C., Briggs, N., Quintana, J. R., Stubbersfield, R. B., and Robb, I. (1986). *Polym. Commun.*, **27**, 292.
35. Tuzar, Z., Sikora, A., Petrus, V., and Kratochvíl, P. (1977). *Makromol. Chem.*, **178**, 2743.
36. Price, C., Chan, E. K. M., Hudd, A. L., and Stubbersfield, R. B. (1986). *Polym. Commun.*, **27**, 196.
37. Tuzar, Z., Bahadur, P., and Kratochvíl, P. (1981). *Makromol. Chem.*, **182**, 196.
38. Zhou, Z. and Chu, B. (1987). *Macromolecules*, **20**, 3089.
39. Zhou, Z. and Chu, B. (1988). *Macromolecules*, **21**, 2548.
40. Brown, W., Schillén, K., Almgren, M., Hvilsted, S., and Bahadur, P. (1991). *J. Phys. Chem.*, **95**, 1850.
41. Mortensen, K., Brown, W., and Nordén, B. (1992). *Phys. Rev. Lett.*, **68**, 2340.
42. Schillén, K., Brown, W., and Johnsen, R. M. (1994). *Macromolecules*, **27**, 4825.
43. Bahadur, P. and Riess, G. (1991). *Tenside Surf. Det.*, **28**, 173.
44. Pospíšil, H., Pleštík, J., and Tuzar, Z. (1993). *Collect. Czech. Chem. Commun.*, **58**, 2428.
45. Alexandridis, P., Holtzwarth, J. F., and Hatton, T. A. (1994). *Macromolecules*, **27**, 2414.
46. Zhou, Z. and Chu, B. (1994). *Macromolecules*, **27**, 2025.
47. Mortensen, K., Brown, W., and Jørgensen, E. B. (1994). *Macromolecules*, **27**, 5654.
48. Tuzar, Z., Kratochvíl, P., Procházka, K., and Munk, P. (1993). *Collect. Czech. Chem. Commun.*, **58**, 2362.

Light scattering by block copolymer liquids in the disordered and ordered state

Petr Štěpánek and Timothy P. Lodge

11.1 Introduction

Block copolymers form a very important class of materials and are attracting increased attention because of their unique and widely variable properties. Block copolymers are macromolecules built of sequences of distinct repeat units. The number and chemical nature of the blocks can be varied but, most frequently, only two blocks, A and B, or three blocks A, B and C, are utilized. These can be used to generate a variety of chain architectures of which the most common types, both in laboratory experiments and in industrial applications, are AB diblock or ABA triblock copolymers. Less frequently, block copolymers of type ABC or $(A-B)_n$ are utilized.

Various polymerization methods can be used to synthesize block copolymers, e.g.^[1] condensation, Ziegler Natta or anionic polymerization. Living polymerizations produce monodisperse block copolymers with well-defined architectures. The resulting block and overall molecular weight distributions are rather narrow, typically $M_w/M_n < 1.1$ (M_w and M_n denote the weight- and number-average molar masses).

Light scattering and transmission are powerful non-invasive tools which can yield valuable information about block copolymer liquids that is not easily accessible by other techniques. In this chapter, we shall address the properties of light transmitted through and scattered by a diblock copolymer, either in bulk or in solution in a neutral solvent, i.e. in a solvent which is equally good for both blocks. Properties of block copolymers in selective solvents are discussed in Chapter 10.

11.2 Block copolymer liquids and the order-to-disorder transition

Since the two blocks are of different chemical nature, there is a thermodynamic interaction between the repeating units of the blocks. The net interaction is generally repulsive and, depending on its strength, the block copolymer system can have either a homogeneous structure, i.e. be in a disordered state, or form a microscopically ordered structure. The phase behaviour of a bulk block copolymer is governed by three parameters: the overall degree of polymerization, N , the composition f (the volume fraction of one component with

respect to both components) and the Flory–Huggins interaction parameter^[2], χ ,

$$\chi = \frac{a}{T} + b, \quad (11.1)$$

between the segments A and B. Here, T is the absolute temperature, and a and b are constants for the particular A–B pair. Let us recall that in the case of a solution of a block copolymer we consider only the case in which the solvent is equally good for both blocks, so that the interaction parameter between the copolymer and the solvent has no influence on the behaviour described in this chapter. The effect of the solvent will be described later, once the basic properties have been established for the case of a bulk diblock copolymer. The magnitude of χ is determined by the selection of the monomers A and B; the quantities N and f , which influence the translational and configurational entropies, are determined by the polymerization conditions.

The product χN determines the phase behaviour of the block copolymer. Decreasing temperature, i.e. increasing χ according to eqn (11.1), favours a reduction in A–B contacts which, for a sufficiently large N , may be accomplished by local ordering with some loss of translational and configurational entropy. Figure 11.1 represents such a case in detail for a symmetric diblock copolymer.

For other compositions, f , different ordered morphologies can be created, which are summarized in the general phase diagram shown in Fig. 11.2. This phase diagram was derived by Leibler^[3] in the framework of the mean-field theory (Fig. 11.2(a)) and subsequently extended by Fredrickson and Helfand^[4] to include the effects of fluctuations (Fig. 11.2(b)), which are always present in the vicinity of phase transition. In mean-field theory, the phase diagram presents an upper critical solution temperature (UCST) for $f = 0.5$ when

$$(\chi N)_c = 10.5. \quad (11.2)$$

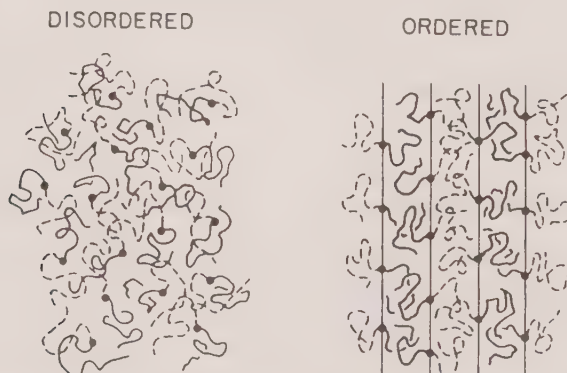


FIG. 11.1. The disordered (left) and ordered lamellar or microphase-separated (right) structure of a symmetric diblock copolymer. After ref. 1.

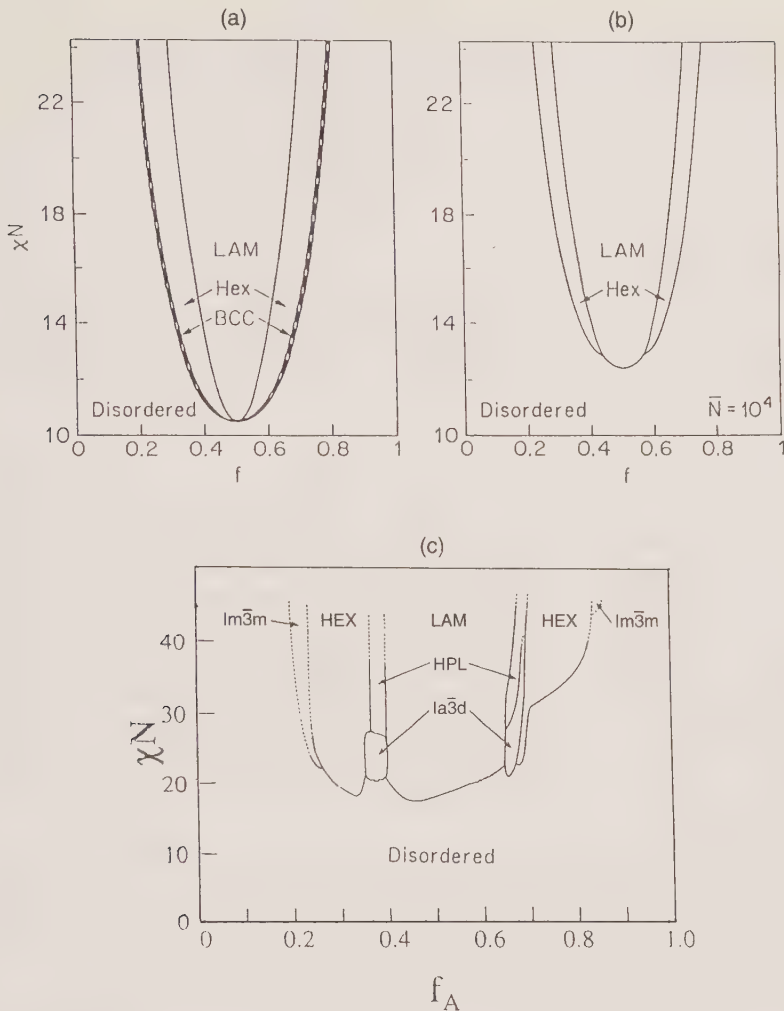


FIG. 11.2. (a) The theoretical mean-field phase diagram for diblock copolymers, after ref. 3. (b) The fluctuation-corrected phase diagram, according to ref. 4. (c) The experimental phase diagram determined for a PI-PS diblock copolymer ($\bar{N} = 1.1 \times 10^3$); $\text{Im}3\text{m}$ is a cubic phase, HEX is a hexagonal phase, HPL is a phase of hexagonally perforated lamellae, LAM is a lamellar phase, and $\text{Ia}3\text{d}$ is a bicontinuous cubic phase. The solid lines delimit the experimentally covered range. After ref. 7.

This point is a critical point at which the system undergoes a second-order phase transition from the disordered (high-temperature) phase into the ordered (low-temperature) lamellar phase. The order-to-disorder transition (ODT) is a major feature of block copolymer materials; sometimes it is referred to as the microphase separation transition (MST). At off-symmetrical compositions, $f \neq 0.5$, the block copolymer system exhibits an order-disorder transition into

other morphologies, generally a hexagonal or cubic structure at temperatures at which $\chi N > (\chi N)_c$. A variety of other structures has been found,^[5] mainly located in the vicinity of the ODT line in Fig. 11.2. Temperature-induced order-order transitions (OOT) between different ordered structures are also possible: e.g. in Fig. 11.2(b) and for $f = 0.65$ the material will first undergo an ODT from the disordered state into an hexagonal morphology, and then at a lower temperature an OOT from the hexagonal morphology into a lamellar structure.

The mean-field theory is not entirely correct for a system with critical composition $f = 0.5$ where large fluctuations in composition exist. It has been shown^[6] that in such a case the second-order phase transition is replaced by a weak first-order phase transition induced by fluctuations. The modified phase diagram^[4] shown in Fig. 11.2(b) exhibits a UCST at a higher and N -dependent value of the variable χN :

$$(\chi N)_c = 10.5 + 41.0 \bar{N}^{-1/3}, \quad (11.3)$$

where \bar{N} is proportional to the copolymer molecular weight, $\bar{N} = 6^3(R_g^3\rho_c)^2$, and ρ_c is the number density of copolymers in the melt. The fluctuation corrections to the phase diagram can be quite substantial, since \bar{N} is typically 10^3 – 10^4 , leading to values of $(\chi N)_{\text{ODT}} \approx 12$ – 13 . This lowers the temperature of the ODT by several tens of degrees, as compared to the mean-field predictions. The phase transition is called ‘weak’, because the order parameter is only weakly discontinuous at the transition; the associated pre-transitional effects in the disordered phase are illustrated, for example, in Fig. 11.5 below. Experimentally, it is found that the phase diagram is asymmetric and that additional ordered phases are present; an example reproduced from a recent review^[7] is shown in Fig. 11.2(c).

The phase diagram shown in Fig. 11.2 is, in principle, applicable not only to block copolymer melts but also to solutions. The usual approach consists^[8,9] in adopting the ‘dilution approximation’, which states that the phase diagram of a neutral copolymer solution can be obtained from the corresponding melt phase diagram by replacing χ by $\phi\chi$, where ϕ is the polymer volume fraction in solution. Such an approach suffers, however, from at least two problems. The first is the neglect of excluded-volume interactions, which are important in particular in semi-dilute solutions. The second difficulty is that the dilution approximation does not take into account possible inhomogeneities in solvent concentration, which can be present in ordered phases. For example, an excess of solvent at the interfaces between domains can screen the energetically unfavourable A–B interactions at a small entropy cost, thereby lowering the free energy.

For any practical investigation of block copolymer material, it is very important to know the exact location of the ODT. Two methods have been widely used to determine this transition: small angle neutron or X-ray scattering, and dynamic rheology.

Static neutron scattering is a direct observation of the structure in reciprocal space, but in many cases requires the synthesis of deuterium labelled copolymers

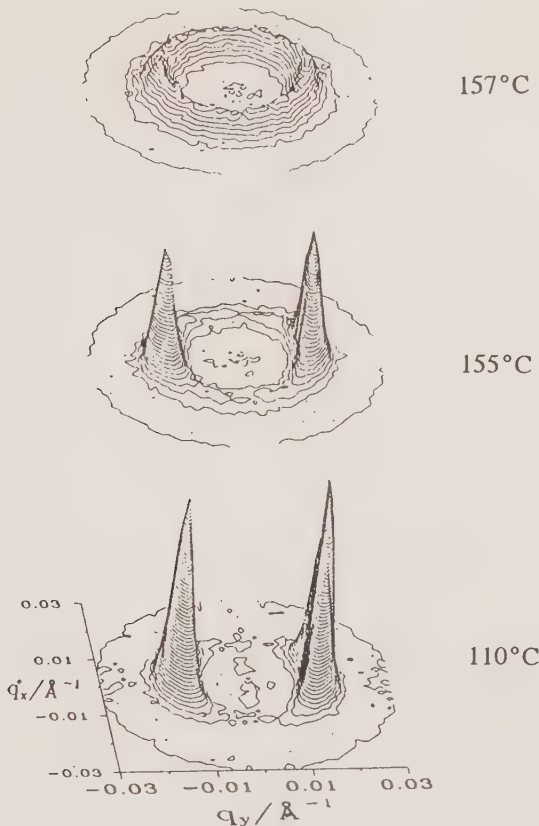


FIG. 11.3. Two-dimensional small-angle neutron scattering data (beam direction along the Z-axis) obtained on a shear-oriented sample of a PEP-PEE-7 diblock copolymer ($M_w = 107\,000$, $f_{\text{PEP}} = 0.77$) heated from 110°C to the indicated temperatures. After ref. 10.

to ensure sufficient contrast between the two blocks. Figure 11.3 reproduces neutron scattering data obtained^[10] on a symmetric PEP-PEE-7 diblock copolymer (poly(ethylenepropylene-*b*-ethylethylene), $M_n = 107\,000$, $f_{\text{PEP}} = 0.77$), which was shear-oriented in the lamellar ordered phase below $T_{\text{ODT}} = 155^\circ\text{C}$. The disappearance of order when heated from below T_{ODT} to above T_{ODT} is clearly evident in Fig. 11.3.

A very common method of detecting and studying the ODT is dynamic rheology. Figure 11.4 shows the temperature dependence of the storage modulus G' for the block copolymer PEP-PEE-2 at a single low frequency.^[12] A sharp drop in G' is observed at the temperature $T = 96^\circ\text{C}$, corresponding to the ODT.

Alternatively, the storage and loss moduli G' and G'' can be measured as a function of frequency for several temperatures and the time-temperature superposition principle applied for the high-frequency, high-temperature part of the data. Typical curves obtained^[11,12] in this way are presented in Fig. 11.5

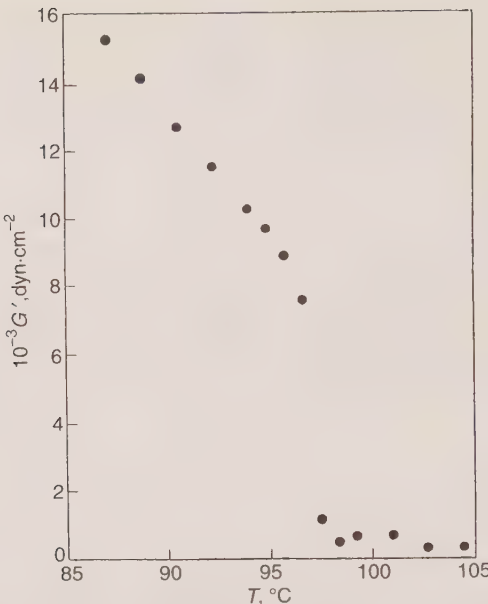


FIG. 11.4. The temperature dependence of G' for the block copolymer PEP-PEE-2 ($M_w = 50\,000$), obtained at a single frequency $\omega = 1.0$ rad/s and a strain amplitude of 2%. After ref. 12.

for the storage modulus G' . It can be seen that the time-temperature superposition principle fails even in a certain temperature range above the ODT. This is a consequence of the fluctuation effects observed above the ODT in the homogeneous phase.

Neutron scattering facilities are inconvenient for routine ODT determinations, and rheological measurements require that large frequency and temperature ranges be accessible. Optical techniques, on the other hand, are easily set up and can be equally sensitive to the ODT. The next section describes static birefringence and diffraction methods for determining the ODT, whereas the effect of the ODT on dynamic light scattering, will be discussed later in this chapter.

11.3 Static birefringence and small angle scattering of light

When a block copolymer liquid is cooled under quiescent conditions below the ODT a spontaneous ordered system emerges. The order is, however, not long-ranged; rather, the material is arranged in grains that are ordered inside with random orientation. Electron micrographs demonstrate that such a material is 'polycrystalline',^[13] which is schematically represented in Fig. 11.6; contrary to the sketch,^[10] the boundaries between the grains are probably rather diffuse and the director can vary smoothly. Experiments show that,

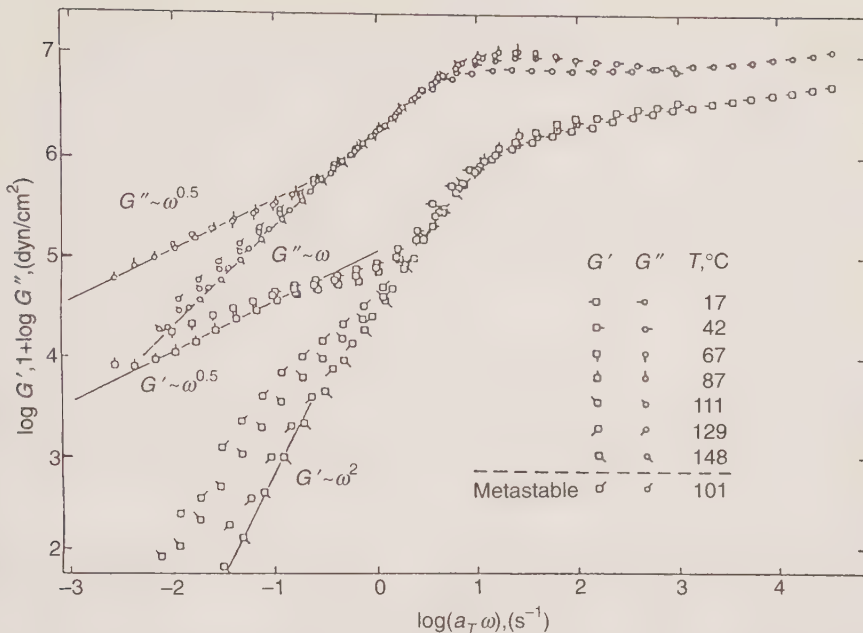


FIG. 11.5. The reduced dynamic storage and loss moduli for a block copolymer 1,4-polybutadiene-*b*-1,2-polybutadiene, $N = 1300$, $f_{1,4} = 0.38$. The G'' data have been shifted vertically by one decade. a_T is the shift factor. T_{ODT} is ca. $106 {}^\circ\text{C}$. After ref. 12.

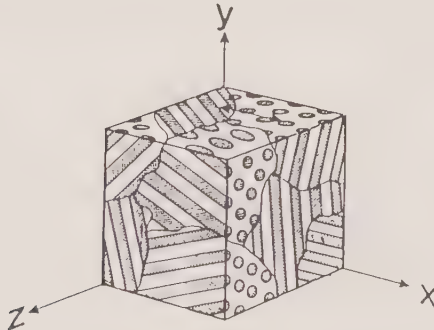


FIG. 11.6. A sketch of the grain structure of a block copolymer melt. After ref. 10.

when a laser beam passes through such a structure, a significant birefringence of the signal is observed, even though in the polycrystalline material the randomly oriented grains have no preferred orientation. This birefringence disappears when the material is heated from the ordered phase into the disordered region. Figure 11.7 demonstrates this effect with a styrene-isoprene diblock copolymer solution;^[14] B_∞ is proportional to the steady state birefringence. A remarkable

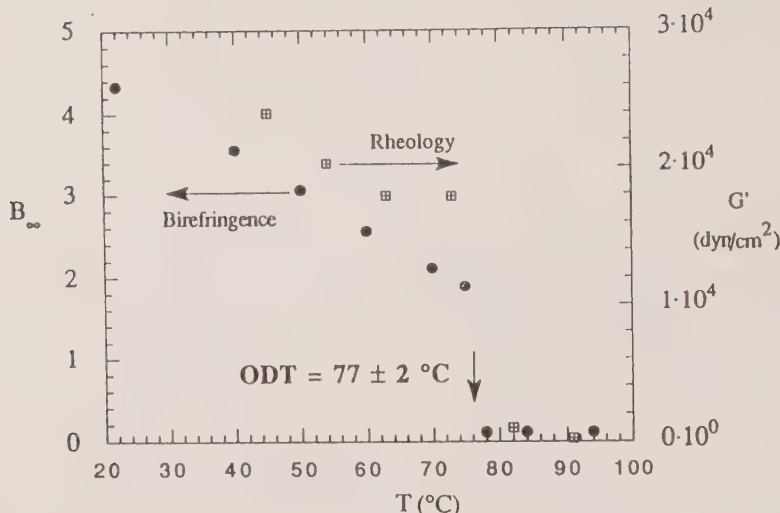


FIG. 11.7. The temperature dependence of G' obtained from rheology and the asymptotic value of birefringence, B_∞ , for a solution of PS-PI diblock copolymer ($M_w = 31\,000$, $w = 0.508$) in diethylphthalate. After ref. 14.

decrease in B_∞ is observed at the same temperature at which the ODT is determined from rheological data. Balsara *et al.*^[15] have quantitatively evaluated this effect and have shown that the observed birefringence arises from random changes in the polarization state of the transmitted beam. The fraction of incident light intensity that passes through a sample located between crossed polars can be estimated as

$$\frac{I}{I_0} = \frac{4\pi^2}{15} (\Delta n)^2 \frac{L l_{av}}{\lambda^2}, \quad (11.4)$$

where Δn is the difference in the refractive indices of light polarized parallel and perpendicular to the optical axis of a single grain, L is the sample thickness (path length of the laser beam), l_{av} is the average characteristic size of the grains, and λ is the wavelength of light. The average grain size can thus be measured, provided that Δn is known. In refs 15 and 16, Δn was estimated to be $|\Delta n| \approx 10^{-3}$ for the styrene-isoprene block copolymer also used in Fig. 11.7 above. The resulting average size of the grains is of the order of several microns, and depends substantially on thermal history: larger grains are formed when the sample is annealed only a few degrees below the ODT temperature, while smaller grains (though still in the micron range) exist when the sample is rapidly brought well below the ODT.

The above treatment deals with the intensity of light transmitted through crossed polarizers at zero angle. A different, and more complete, approach to the interaction between light and a randomly birefringent medium, specifically

including scattering effects, was worked out by Balsara *et al.*^[17] We have seen that typical observed grain sizes are of several μm , i.e. about an order of magnitude larger than the wavelength of light; the relevant scattering is therefore restricted to small angles.

If light propagates through the sample along the z direction (x is the polarizer direction and y the analyzer direction), then light scattered at small angles will be described in terms of a transverse coordinate $\rho = (x^2 + y^2)^{1/2}$. Experiments show^[17] that the observed far-field distributions of intensity $I(\rho, L)$ at a distance L from the sample to the detector plane are well approximated by Gaussian functions

$$I(\rho, L) = I(0) \exp[-\frac{1}{2}(\rho/w_{ff})^2]. \quad (11.5)$$

In such cases the correlation function that characterizes the statistical properties of the grains is also Gaussian with width w_{av} . The width of the Gaussian in the far field, w_{ff} , is related to w_{av} and to average grain size l_{av} by

$$l_{av} = (2\pi)^{1/2} w_{av} = \left(\frac{2}{\pi}\right)^{1/2} \frac{\lambda L}{w_{ff}}. \quad (11.6)$$

Using this relation it is possible to determine the average grain size l_{av} which, unlike in eqn (11.4), is independent of Δn . Used on the same sample, eqns (11.4) and (11.6) yield, to within 10–20%, the same value of l_{av} . Even though the small angle scattering measurement provides an estimate of the transverse dimension of the grain and the birefringence measurement an estimate of the longitudinal dimension, the two estimates should be comparable, as was indeed observed, because of the random orientation of the grains. Conversely, the good agreement of these two values can be used to estimate Δn .

Experiments have shown that the grains may have a slight preferred orientation in the sample, induced, perhaps, by the surfaces of the sample cell or a small temperature gradient. A proper experimental set-up allowing for the removal of this non-random component must thus include^[15, 17, 18] a quarter-wave retardation plate as a compensator. Appropriate rotation of the compensator and analyser to give the minimum transmitted intensity then permits cancellation of any non-random component in the depolarized signal.

Use of two-dimensional CCD detectors as well as other polarization geometries could allow extraction of further information^[17] from the scattered intensity distributions on ordered block copolymer materials and other random anisotropic media.

11.4 Principles of dynamic light scattering from disordered block copolymer liquids

Compared to static light scattering and transmission discussed above, dynamic light scattering yields a broader, different and much more complex description of block copolymer systems.

The current description of the dynamics of disordered block copolymer

systems is founded on two complementary theoretical approaches. The first, due to Benmouna *et al.*,^[19,20] is based on the linear response formalism for multicomponent systems of Akcasu *et al.*^[21,22] and utilizes a dynamical mean-field (random-phase approximation) assumption. Two dynamic modes are predicted for block copolymer solutions: a cooperative diffusion mode, reflecting relaxation of fluctuations in concentration (as is also observed in homopolymer solutions) and an internal chain mode arising from the relative translational motion of centres of gravity of the two blocks. This theory makes several simplifying assumptions: (a) the monomers of both blocks are characterized by the same friction constant ζ ; (b) the two blocks have the same radius of gyration R_g ; and (c) the two blocks have the same number of monomers with the same volume.

The second theory, due to Semenov,^[23] takes into account the fact that, experimentally, assumption (c) can never be satisfied, namely that all real polymers exhibit heterogeneity in composition, i.e. fluctuations in f from chain to chain. This permits fluctuations in relative block concentration of arbitrarily long wavelength, and generates in block copolymer solutions a third mode, governed by the translational diffusion of the whole chains. In some references, in particular in Semenov's original work,^[23] this mode is called the polydispersity mode, which could be erroneously interpreted to mean that the mode is due to the overall polydispersity in molecular weight of the block copolymers. This mode is analogous to the mode generated by polydispersity in scattering power, as described by Pusey *et al.*^[24] for hard spheres which differ in optical scattering power.

The dynamic structure factor for a solution of a diblock copolymer in a neutral good solvent can thus be written in the following form:

$$\frac{S(q, t)}{S(q, 0)} = A_I \exp(-\Gamma_I t) + A_C \exp(-\Gamma_C t) + A_H \exp(-\Gamma_H t), \quad (11.7)$$

where the subscripts, I , C , and H denote the internal, cooperative, and heterogeneity modes, respectively. This relation assumes that the three modes are uncoupled. As will be detailed below, block copolymer melts and solutions differ in that the cooperative mode does not exist in the melt, and that the amplitudes and relaxation rates of the modes in solution depend on concentration.

11.4.1 Block copolymer melts

In a monodisperse melt, a fluctuation in composition can be created only by shifting the centre of mass of block A relative to the centre of mass of block B. The corresponding relaxation process is characterized by a decay rate Γ_I which, for $qR_g \ll 1$ and to within a constant of order unity, is

$$\Gamma_I \approx \tau^{-1}, \quad (11.8)$$

where τ_1 is the longest viscoelastic relaxation time of the chain. Here, R_g is the

radius of gyration of the block copolymer and q is the scattering vector, $q = (4\pi n/\lambda) \sin^2(\theta/2)$, where λ is the wavelength of light and θ is the scattering angle. In the limit $qR_g \ll 1$ thermodynamic effects are not important,^[23] so that for low molecular weights in the Rouse regime, τ_1 is the Rouse time:

$$\tau_1 = \tau_R = \tau_0 N^2, \quad (11.9)$$

where τ_0 is the characteristic microscopic time for one segment and N is the number of segments in the chain. On the other hand, in the entanglement regime the reptation time^[25] provides a better estimate

$$\tau_1 \approx 5\tau_0 N^3/4N_e, \quad (11.10)$$

where N_e is the number of segments between entanglements. This relation is based on reptation theory; experimental data generally follow more closely the relation $\tau_1 \sim N^{3.4}$.

The amplitude of the internal mode is given by

$$A_I \sim \frac{2}{3} N v (n_A^2 - n_B^2)^2 f^2 (1-f)^2 (qR_g)^2, \quad (11.11)$$

where n_A and n_B are the refractive indices of the blocks A and B, and v is the segment volume.

This internal mode is the only dynamic process predicted by the Benmouna theory for a block copolymer melt which is *monodisperse* both in composition and in overall molecular weight. Real polymers always exhibit some polydispersity in molar mass and some heterogeneity in composition. Composition heterogeneity has the consequence that fluctuations in relative concentration of A and B segments can exist at all wavelengths, even if there is no polydispersity in molar mass. For $qR_g < 1$ such fluctuations will relax by exchange of A-rich and B-rich chains, i.e. by translational diffusion of the whole chain. It is not trivial to measure the compositional heterogeneity in a block copolymer directly, but for anionically synthesized, narrow molar mass distribution samples, Semenov^[23] has made the reasonable assumption that the molar mass polydispersities of the two blocks are statistically independent. The heterogeneity factor

$$\kappa = \frac{\langle N_A^2 \rangle \langle N_B^2 \rangle - \langle N_A N_B \rangle}{N^2 \langle (N_A + N_B)^2 \rangle}, \quad (11.12)$$

with $N = \langle N_A + N_B \rangle$, can then be expressed in terms of the polydispersity in overall molar mass,

$$\delta = 1 - M_w/M_n, \quad (11.13)$$

as

$$\kappa = 2\delta \frac{f^2(1-f)^2}{f^2 + (1-f)^2}. \quad (11.14)$$

The heterogeneity mode is then characterized by a decay rate

$$\Gamma_H = D_H q^2, \quad (11.15)$$

where the diffusion coefficient, D_H , of the heterogeneity mode is related to the self-diffusion coefficient, D_s , of the block copolymer by

$$D_H = D_s(1 - 2\chi N\kappa) \quad (11.16)$$

where χ is the Flory–Huggins interaction parameter.

The amplitude of the heterogeneity mode is then predicted^[23] to be

$$A_H \sim (n_A^2 - n_B^2)^2 \frac{\kappa N v}{1 - 2\chi N\kappa}. \quad (11.17)$$

Comparing eqns (11.11) and (11.17), it can be found that the amplitude of the heterogeneity mode is stronger than that of the internal mode, $A_H > A_I$, when

$$\delta > (qR_g)^2/6. \quad (11.18)$$

If we accept $\delta \sim 0.1$ as a typical value for anionically synthesized polymers, then for a typical magnitude of the scattering vector $q \sim 2.75 \times 10^5 \text{ cm}^{-1}$, the heterogeneity mode dominates for $R_g < 28.6 \text{ nm}$, which corresponds to $M_w < 340\,000$ for a styrene–isoprene type of copolymer.

11.4.2 Block copolymer solutions

The presence of a neutral solvent introduces two main differences into the dynamic light scattering from disordered block copolymer systems: (a) the amplitudes and decay rates of the internal and heterogeneity modes have to be renormalized owing to the presence of the solvent; and (b) an additional cooperative diffusion mode will exist.

Let us consider the changes to the first two modes. If g is the number of monomeric units per blob^[26] in a copolymer chain and ϕ is the volume fraction of the diblock copolymer in solution, the following renormalizations will account for the presence of solvent:^[25,26]

$$v \rightarrow \phi gv, \quad N \rightarrow N^* = N/g. \quad (11.19)$$

Then χ also has to be replaced by

$$\chi^* = \chi g^z \quad (11.20)$$

to take into account the fact that the mean number of contacts between neighbouring blobs in a good solvent is of order g^z . The best estimate for z is^[27] $z = -0.17$. Then χN should be replaced by

$$\chi^* N^* \cong \chi N \phi^{(1-z)/(3v-1)} \cong \chi N \phi^{1.53}, \quad (11.21)$$

where we have used the commonly accepted value of the Flory exponent, $v = 0.59$. Then eqns (11.16) and (11.17) for the diffusion coefficient and

amplitude of the heterogeneity mode are replaced by

$$D_H = D_s(N, \phi)(1 - 2\chi N \kappa \phi^{1.53}), \quad (11.22)$$

$$A_H \sim (n_A^2 - n_B^2)^2 \frac{\kappa N v \phi}{1 - 2\chi N \kappa \phi^{1.53}}. \quad (11.23)$$

The heterogeneity diffusion coefficient behaves essentially as the self-diffusion coefficient, since the correction in the parentheses in eqn (11.22) is very small: for typical values $\chi = 0.01$, $N = 10^3$, $\phi = 0.1$ and $M_w/M_n = 1.1$, we obtain D_H smaller than D_s by 1.5%.

Similarly, the properties of the internal mode for a disordered solution of a diblock copolymer as calculated using the original theory of Benmouna *et al.*^[19,28] are:

$$A_I \sim \frac{2}{3}(n_A^2 - n_B^2)^2 \phi^x v f^2 (1 - f)^2 N(qR_g)^2, \quad (11.24)$$

where $x = 1$ for dilute solutions and $x = 0.77$ (using $v = 0.59$) for semi-dilute solutions, and

$$\Gamma_I^{-1} = \tau_b(N/g)^2 \sim \tau_0 N^2 \phi^{0.30} \quad (11.25)$$

in the case of Rouse chains, or

$$\Gamma_I^{-1} = \tau_b(N/g)^3 \sim \tau_0 N^3 \phi^{1.60} \quad (11.26)$$

in the case of reptating entangled chains; τ_b is the local jump time of the blob, $\tau_b = \eta \xi^3/kT$, where ξ is the correlation length of the semi-dilute solution.

In general, however, one does not observe a clear Rouse-like or reptation-like regime in semi-dilute solutions, particularly for moderate molecular weight polymers. For comparison of theory with experiment, it is thus probably more appropriate to determine $\tau_1(\phi)$ directly via viscoelastic or flow birefringence measurements or to estimate its concentration dependence on the basis of established empirical relations such as^[29]

$$\tau_1 \cong \tau_1(\phi = 0) e^{\alpha \phi [\eta]}, \quad (11.27)$$

where $[\eta]$ is the intrinsic viscosity and α is a parameter of order 0.4.

The ratio Γ_I/Γ_H may also be estimated using an approach described later in the experimental Section 11.5.3.1.

The cooperative mode specific to copolymer solutions is essentially identical to that observed in homopolymer solutions, and is thus, at least to a first approximation, independent of the copolymer nature of the chain.^[19,20,23] In dilute solution,

$$\Gamma_C = q^2 D_C = q^2 D_0(1 + k_d \phi + \dots), \quad (11.28)$$

whereas in semi-dilute solution,

$$\Gamma_C = q^2 \frac{kT}{6\pi\eta_s \xi} \sim \phi^{0.75}, \quad (11.29)$$

where ξ is the correlation length and η_s is the solvent viscosity. The amplitude scales as^[30]

$$A_C \sim (\langle n \rangle^2 - n_s^2)^2 \phi N \quad (11.30)$$

in dilute solution, and

$$A_C \sim (\langle n \rangle^2 - n_s^2)^2 \phi g \sim (\langle n \rangle^2 - n_s^2)^2 \phi^{-0.25} \quad (11.31)$$

in semi-dilute solutions, where $\langle n \rangle$ is the average refractive index of the copolymer and n_s is the solvent refractive index. This mode reflects mutual diffusion of polymer and solvent, with amplitude and rate increasing with ϕ in the dilute regime, but with amplitude decreasing with ϕ in the semi-dilute regime. A very important practical consequence of eqn (11.31) is that the amplitude of the cooperative mode can be varied by varying the refractive index n_s of the solvent. In particular, by an appropriate selection of the solvent and measurement temperature, a 'zero average contrast' condition can be achieved, where $A_C = 0$. This is of great advantage in masking the (otherwise strong) contribution from cooperative diffusion, if one wishes to study the weaker internal and heterogeneity modes.

11.5 Review of experiments

Due to their complex chemical structure, the names of block copolymers are very long, and to avoid cumbersome repetitions, we often refer to them by abbreviations. Full names may be found in the 'List of symbols and abbreviations' in Appendix 11.A at the end of this chapter. Also, when referring to work published elsewhere in the literature, we use interchangeably the relaxation time, τ , and the decay rate, Γ , with $\Gamma^{-1} = \tau$, or a distribution of relaxation times, $A(\tau)$ and a distribution of decay rates $G(\Gamma)$. For the equal area representation appropriate when the horizontal axis of a correlation function is logarithmic, the relation $\Gamma G(\Gamma) = \tau A(\tau)$ is valid.

11.5.1 Polarized dynamic light scattering from diblock copolymer melts

Although the theoretical predictions for polarized dynamic light scattering from disordered diblock copolymer melts, as detailed above, seem to be quite clear, there has not been so far much experimental activity in this area. Suitable copolymers consist of two blocks having sufficiently different refractive indices, but that at the same time are reasonably compatible so that their ODT exists in an accessible temperature range for interesting molecular weights. The glass transition temperatures of both blocks also should be sufficiently below the interesting temperature range, so that the dynamics of fluctuations in density^[31] do not obscure the dynamics of composition fluctuations.

Several diblock copolymer materials have been examined: poly(ethyl-methyl-siloxane-*b*-dimethylsiloxane) [PEMS-PDMS], poly(ethylenepropylene-*b*-ethyl-ethylene) [PEP-PEE], poly(ethylene-*b*-ethylethylene) [PE-PEE], and poly(styrene-*b*-isoprene) [PS-PI].

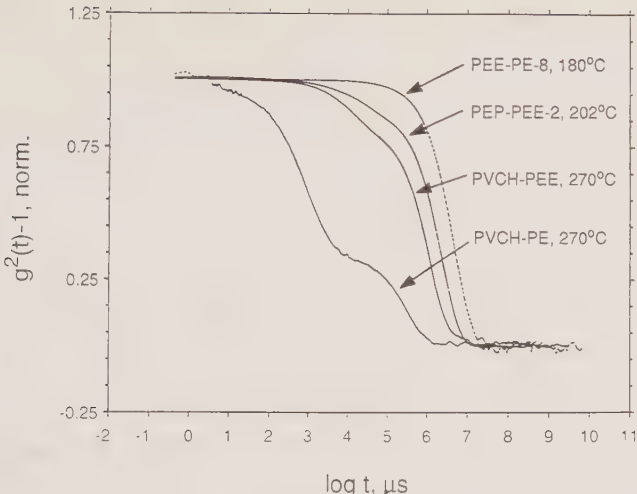


FIG. 11.8. Correlation functions obtained on block copolymer melts for the materials and temperatures indicated in the legend; full names of copolymers are identified in Appendix 11.A. For better comparison, the correlation functions are normalized to have an intercept of unity; t is correlator delay time.

Polarized dynamic light scattering from these systems reveals a complex correlation curve from which, using inverse Laplace transformation (ILT),^[32,33] several components of the spectrum of relaxation times can be extracted. In all cases examined so far a very slow mode has been observed, which is not predicted by theory; this mode resembles that found in glass-forming liquids, in certain semi-dilute solutions and in plasticized polymers,^[41] which is variously ascribed to clusters, long-range density fluctuations or heterogeneities. We shall first describe this mode which is apparently unrelated to the theoretical predictions. Figure 11.8 shows representative correlation functions obtained on several polyolefin block copolymer melts,^[34] (the polymers are identified in the caption). Figure 11.9 reproduces^[36] similar data for the siloxane copolymers.

A decay corresponding to a 'cluster' mode is always observed at delay times comparable to, or longer than 1 s. The relative amplitude of this process varies for the various systems and depends on temperature: it is almost negligible at 120 °C for the PDMS-PEMS copolymer in Fig. 11.9, whereas it is dominant for the PE-PEE copolymer in Fig. 11.8, to the extent that no other dynamics can be observed for that particular correlation curve. This process is diffusive, as can be concluded from Fig. 11.10: the relation $\Gamma = Dq^2$ is satisfied for both cases shown, and the slope of the straight lines gives the diffusion coefficient of the cluster mode.

If we assume that this cluster diffusion obeys the Stokes-Einstein relation,

$$D = kT/6\pi\eta R_h, \quad (11.32)$$

where η is the viscosity of the medium in which the cluster moves, we can

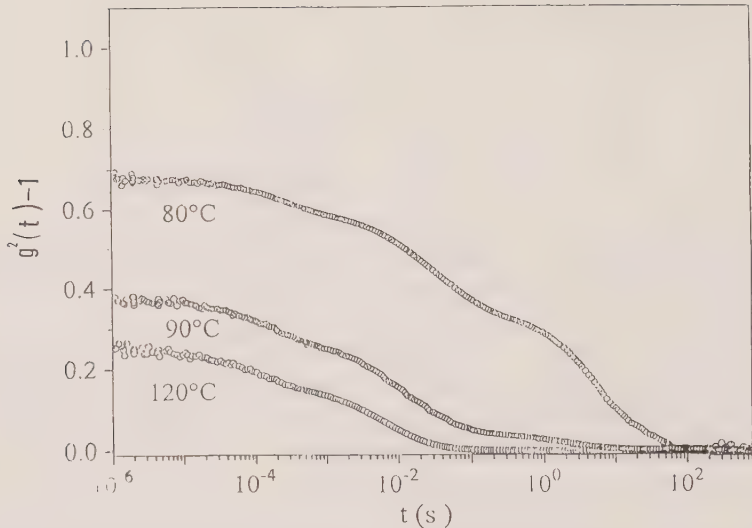


FIG. 11.9. Correlation functions obtained on the block copolymer of PDMS-PEMS ($M_n = 95\,000$) at the temperatures indicated. After ref. 36.

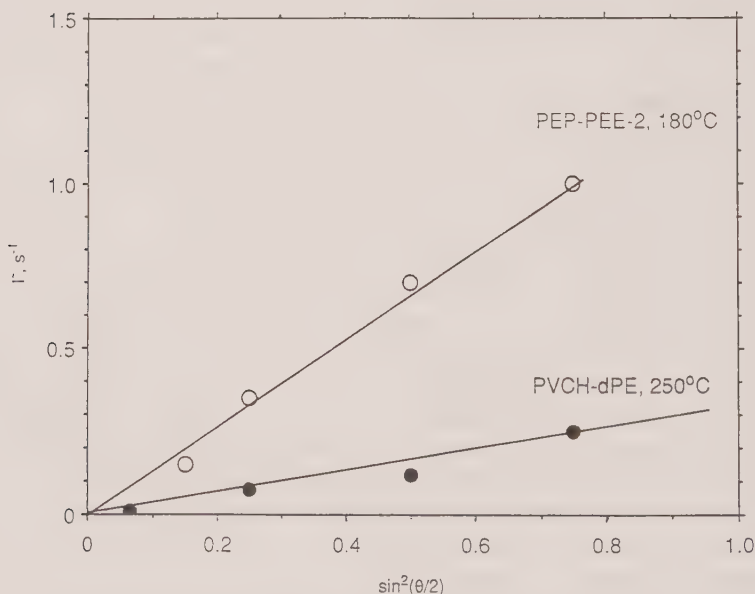


FIG. 11.10. The dependence of the decay rate, Γ , of the cluster mode on $\sin^2(\theta/2)$; for copolymer names, see Appendix 11.A.

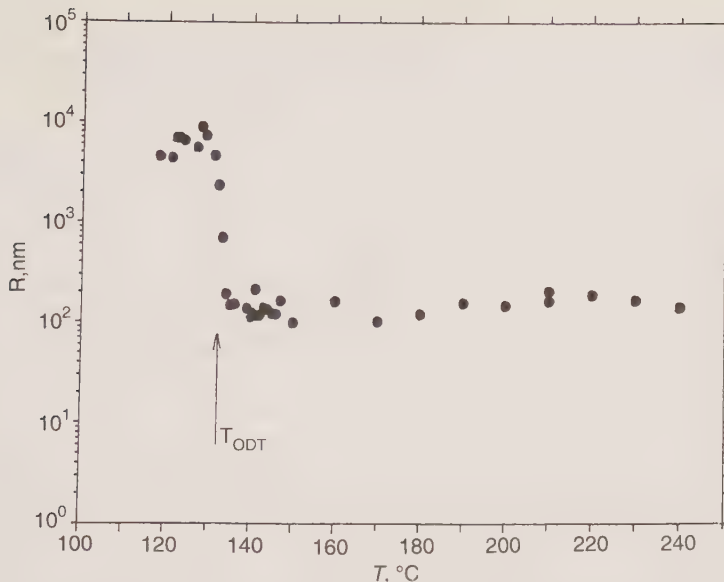


FIG. 11.11. The dependence of the hydrodynamic radius R_h corresponding to the cluster mode for the block copolymer PE-PEE-8 ($M_w = 25\,000$). For this sample, $T_{ODT} = 132\text{ }^\circ\text{C}$; the size is approximately constant above this temperature.

estimate the hydrodynamic size of the cluster, R_h . For example, for the block copolymer PE PEE the macroscopic viscosity can be determined in the disordered phase from the known loss modulus^[37] using the usual^[43] relation $G'' = \eta\omega^2$. The temperature dependence of the size of the clusters obtained in this way is shown in Fig. 11.11. R_h is approximately constant in the disordered phase and of the order of 100 nm. Below the ODT temperature, R_h represents only an apparent size, since the concept of a single value of the macroscopic viscosity loses its meaning in an ordered phase. In any case, the increase of R_h by two orders of magnitude simply represents a dramatic slowing down of the macroscopic dynamics of the system below the ODT. This could be used for a relatively easy determination of the ODT temperature for strongly asymmetric block copolymers, which produce an ordered phase with spherical symmetry. These systems do not become birefringent below ODT, so that the techniques described in Section 11.3 above cannot be used. For the other system for which the block copolymer bulk viscosity is known, PEP-PEE-2, a value of $R_h \sim 60$ nm was obtained.

The exact origin, structure and properties of the clusters observed by dynamic light scattering have not yet been fully established. They can, however, be related to other theoretical and experimental work. Fried and Binder^[38] have predicted the existence of a large-scale mesostructure in the disordered phase resulting in a partial compositional segregation of the block copolymer due to stretching of the polymer chains. Stühn *et al.*,^[39,40] have claimed, based on NMR and

dielectric normal mode spectroscopy, that for SI block copolymers, crossing the ODT from the ordered phase does not lead to homogeneous mixing of both blocks, and that local order remains even above the ODT over an extent of ca. 70 nm. These observations and possible explanations of clusters are related to the block copolymer nature of the material. It is, however, important to remember that clusters, possibly generated by a different physical mechanism, are also observed in other homopolymer systems and even in low-molecular-weight glass-forming systems. For example, an extensive static and dynamic light scattering study has been recently presented by Fischer *et al.*^[41] on poly(methyl-*p*-tolylsiloxane) over a wide temperature range. Large-scale heterogeneities have also been inferred^[42] from NMR measurements on a polyethylene melt above its crystallization temperature. Cluster formation is also briefly discussed in Chapter 5 of this volume.

In the remainder of this section on block copolymer melts we shall ignore the presence of this, not yet well understood, cluster mode. As we have seen in the theory section above, the two main dynamic processes predicted for a block copolymer melt are the internal relaxation and the heterogeneity mode. Figure 11.12 shows a spectrum of relaxation times obtained by ILT on a

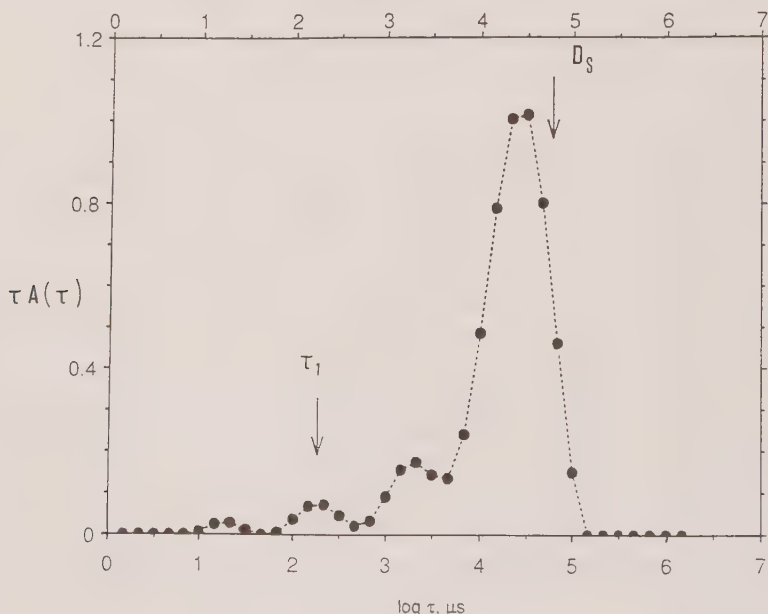


FIG. 11.12. The spectrum of relaxation times obtained on the copolymer PEP-PEE-2 ($M_w = 50\,000$) at 180°C and a scattering angle of 90° by inverse Laplace transformation from the corresponding correlation function shown in Fig. 11.8. The dominant decay corresponding to the cluster mode has been subtracted from the $g^2(t)$ prior to performing the inversion. Relaxation times corresponding to the internal mode τ_1 as determined from rheology and to self-diffusion as determined from forced Rayleigh scattering are indicated.

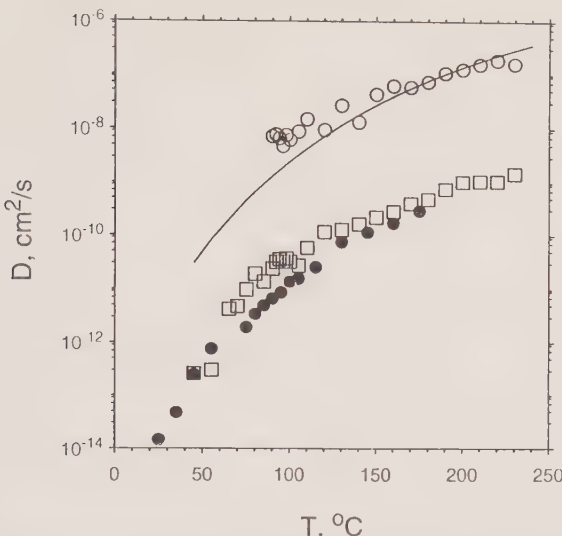


FIG. 11.13. The temperature dependence for the copolymer PEP-PEE-2 of the diffusion coefficients of self-diffusion (\square), DLS heterogeneity mode (\bullet), DLS internal mode (\circ) and internal mode determined by rheology (full line). For the purpose of this diagram, the decay rates of the angle-independent internal mode were replaced by Γ/q^2 .

block copolymer melt of PEP-PEE-2, in the disordered phase. The component corresponding to the cluster mode was subtracted from the correlation function before performing the final ILT; the subtraction technique is described in more detail in ref. 33. Attempts to recover weak components from a correlation function in the presence of a strong decay may yield unreliable and unstable results. Nevertheless, recent results show that in favourable circumstances subtraction is a powerful technique when multiple modes are present in the decay spectrum.

The arrow marked τ_1 on Fig. 11.12 indicates the relaxation time of the internal mode as determined from dynamic rheology; the established relation^[43] $\omega\tau_1 = 1$ is used, where ω is the frequency at which the straight lines $G' \sim \omega$ and $G'' \sim \omega^2$ cross in diagrams similar to Fig. 11.4. The arrow marked D_S corresponds to a decay time that would be generated by self-diffusion at the particular scattering angle. Values of D_S on the same system were measured by forced Rayleigh scattering.^[44] Reasonable agreement is observed in Fig. 11.12, allowing us to assign the fastest component to the internal mode and the slowest component to the heterogeneity mode; the correction due to the quantity κ in eqn (11.22) is negligible, and thus $D_H \sim D_S$. The intermediate component in the distribution in Fig. 11.12 cannot be explained at the present time; it may be an artifact caused by the so-called δ -effect^[33,45,46] in the Laplace inversion. Figure 11.13 shows a more extensive comparison, as a function of temperature, of the internal and heterogeneity modes with τ_1 and D_S . Almost quantitative agreement is observed over the common temperature range.

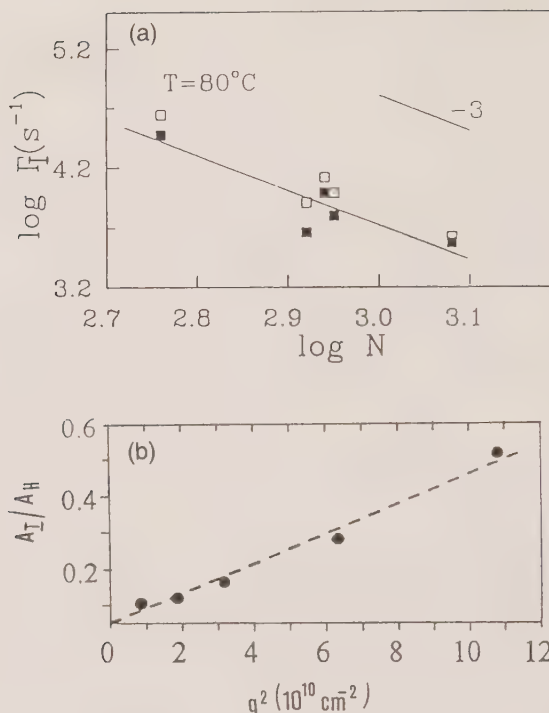


FIG. 11.14. (a) The dependence of the decay rate Γ_I of the internal mode on the polymerization index, N , for PDMS-PEMS symmetric block copolymers, at 80 °C. (b) The angle dependence of the ratio of amplitudes of the internal and heterogeneity modes A_I/A_H for a PDMS-PEMS-4 block copolymer ($M_n = 95\,000$) at 120 °C. After ref. 36.

The molecular weight dependence of the relaxation rates of the internal and heterogeneity modes has been tested on the PDMS-PEMS copolymers.^[36] Equation (11.10) shows that in the entanglement (reptation) regime the relaxation rate Γ should vary as N^{-3} . Figure 11.14(a) displays the dependence of Γ_I on N for a series of entangled PDMS-PEMS copolymers. Within experimental error the data points follow the predicted dependence. As to the amplitude of the internal mode A_I , it should increase with q^2 for a given polymer, according to eqn (11.11). Figure 11.14(b), reproduced from ref. 36, shows that the ratio of amplitudes A_I/A_H varies as q^2 , which confirms the predicted behaviour of A_I , since it will be shown below that A_H is independent of angle.

The diffusion coefficient of the heterogeneity mode is, except for a generally negligible correction, numerically equal to the self-diffusion coefficient, D_S (see eqn (11.16)). In the entangled regime the self-diffusion coefficient is predicted^[25,26] to behave as

$$D_S \sim N^{-2}. \quad (11.33)$$

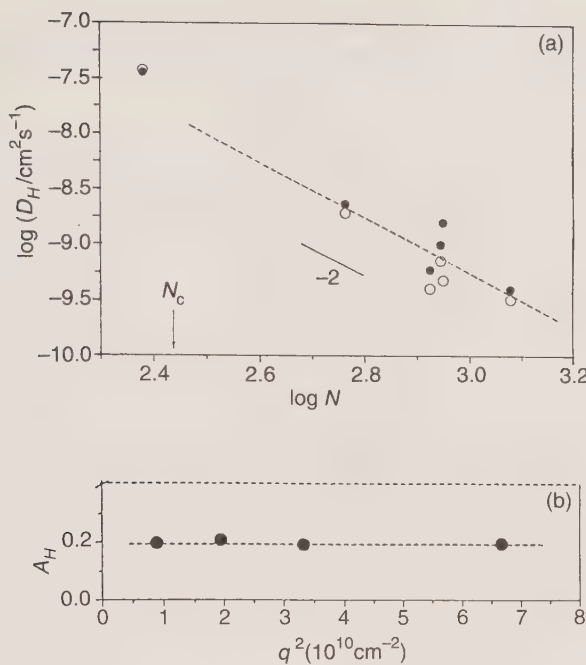


FIG. 11.15. (a) The dependence of the diffusion coefficient of the heterogeneity mode, D_H , on the polymerization index, N , for PDMS–PEMS block copolymers at 80 °C. The slope of -2 is the prediction from reptation theory; see eqn (11.33). (b) The angle dependence of the amplitude of the heterogeneity mode, A_H . After ref. 36.

The experimental data presented in Fig. 11.15(a) are somewhat scattered but still follow the predicted dependence reasonably well. Equation (11.17) shows that the amplitude of the heterogeneity mode should not depend on scattering angle, which is confirmed by the experiments on the PDMS–PEMS block copolymers, shown in Fig. 11.15(b).

11.5.2 Depolarized dynamic light scattering from diblock copolymer melts

Depolarized dynamic light scattering yields information about the system on a different scale than the polarized scattering discussed so far; it is a useful tool for studying the segmental dynamics of polymers. This local motion of chain segments (often corresponding to the so-called α -process) is strongly dependent on temperature, and in particular on the distance to the glass transition temperature, T_g , of the polymer. The time scale of segmental motions comes into the window of dynamic light scattering in a temperature interval several tens of degrees wide and starting slightly above T_g . For temperatures that are, for example, 100 °C above T_g , the segmental motions are too fast to be seen by dynamic light scattering. For temperatures close to T_g , they are too slow.

As a rule, the distribution of relaxation times in these experiments is very broad and the field correlation function is conveniently approximated by the Williams–Watts form

$$g^1(t) = A \exp[-(t/\tau_w)^\beta] + C, \quad (11.34)$$

where τ_w is an average relaxation time, independent of the scattering angle, and the parameter β measures the width of the relaxation spectrum; A and C are constants. For homopolymer melts, a typical value of $\beta \approx 0.3$ is obtained ($\beta = 1$ corresponds to a single exponential relaxation).

For block copolymers, the main difference is that generally the two blocks have different glass transition temperatures, so that two (possibly overlapping) relaxation peaks should be observed in the disordered phase. This has indeed been observed by Stühn *et al.*^[47,48] and Fytas *et al.*^[49–51] on poly(styrene-*b*-isoprene) copolymers. Figure 11.16, reproduced from ref. 50, shows an example of a correlation function of depolarized scattered light obtained on these polymers; the two peaks are well resolved in the corresponding distribution of relaxation times in Fig. 11.16(b). Depending on the relative positions of the

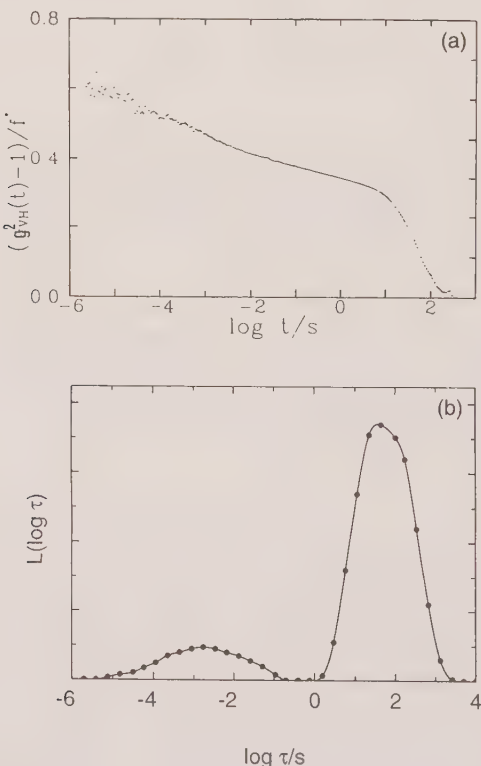


FIG. 11.16. (a) The correlation function of depolarized light for a PS PI block copolymer ($M_n = 5710$, $f_{PI} = 0.61$) at -27°C . (b) The distribution of relaxation times corresponding to the correlation function in (a). After ref. 50.

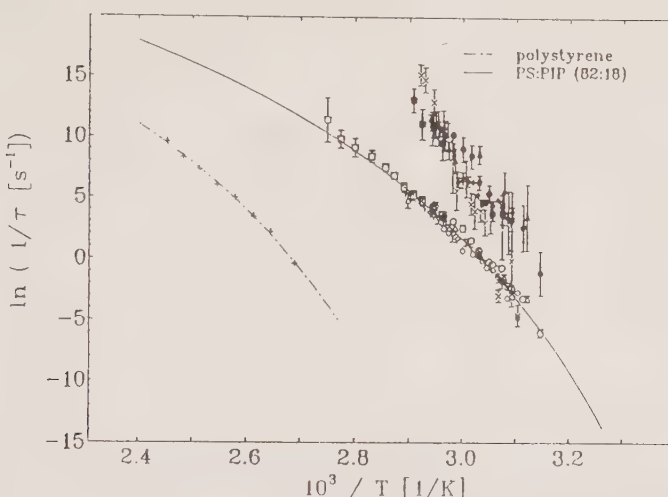


FIG. 11.17. The temperature dependence of the relaxation time τ of depolarized scattered light obtained on bulk polystyrene (dashed dotted curve), and of relaxation times of the polystyrene-rich and polyisoprene-rich phases of PS-PI block copolymer (full line for PS-rich phase). After ref. 47.

T_g -values of the two blocks, the two components may either overlap or be too distant, so that they are not clearly resolved in a single experiment. These experiments have been conducted in the disordered region of the phase diagram, and suggest that some local segregation persists even in the homogeneous phase.

The fluctuations in composition identified by many other techniques in block copolymer liquids in the vicinity of the ODT manifest themselves in depolarized light scattering experiments in two ways:

1. The distribution functions of segmental relaxation times are shifted in the block copolymer when compared to the same distributions obtained on the parent homopolymers under identical conditions; Fig. 11.17 displays such a comparison.

2. The widths of these distribution functions are generally broadened in the vicinity of the ODT, although a narrowing has also been observed.^[50] An example of such an effect is shown on Fig. 11.18, where the widths of these distributions are compared to that for a homopolymer melt, as a function of temperature; the excess broadening was described as resulting from fluctuations in composition.

11.5.3 Polarized dynamic light scattering from block copolymer solutions

11.5.3.1 Neutral solvent with general refractive index. Polarized dynamic light scattering from block copolymer solutions has been the subject of more activity in recent years than the case of block copolymer melts. As we have seen above,

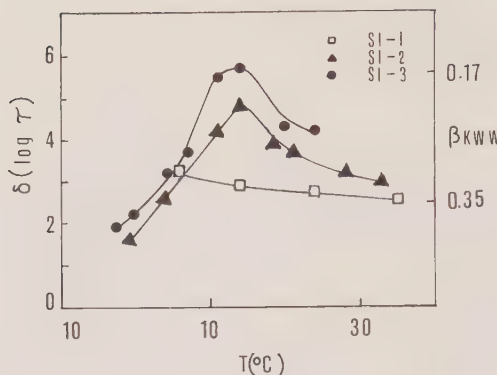


FIG. 11.18. The temperature dependence of the width $\delta(\log \tau)$ and of the Williams-Watts parameter β of the distribution function of relaxation times of depolarized scattered light according to eqn (11.34) for PS-PI copolymers ($M_n = 3930, 4420$ and 5710 for SI-1, SI-2 and SI-3, respectively). Note that β decreases as $\delta(\log \tau)$ increases. After ref. 50.

the presence of solvent in the system introduced an additional mode, the cooperative mode, equivalent to that observed in homopolymer solutions, and it also introduces one more variable, the concentration of polymer in the solution. Figure 11.19 shows typical polarized correlation functions obtained^[30] on a solution of poly(styrene isoprene) symmetric diblock copolymer (total molecular weight 340 000) in toluene, at the indicated concentrations. As the concentration increases, the complexity of the correlation function also increases. The corresponding distributions of decay times are displayed in Fig. 11.20, for two samples with total molecular weights differing by a factor of 10, $M_w = 35\,000$ and $M_w = 340\,000$. The two modes observed in Fig. 11.20(a) are both diffusive and can be identified as the cooperative (fast) and heterogeneity (slow) modes.

Figure 11.21 compares the diffusion coefficient obtained by pulsed field gradient NMR to that of the heterogeneity mode. A very good agreement is observed, confirming that for anionically synthesized polymers the magnitude of the term with κ in the parentheses in eqn (11.16) is less than the experimental error in D_H and D_C . The cooperative diffusion coefficient (the upper curve in Fig. 11.21) behaves as in homopolymer solutions, and can be described by a relationship $D_C \sim \phi^{0.7}$ for concentrations larger than the overlap concentration, independent of the molecular weight.

According to eqns (11.23) and (11.31), the ratio of amplitudes of the heterogeneity and cooperative modes should, in the semi-dilute regime, follow the relation

$$(\langle n \rangle^2 - n_s^2)^2 \frac{A_H}{A_C} \frac{1}{N} \propto c^{1.25}. \quad (11.35)$$

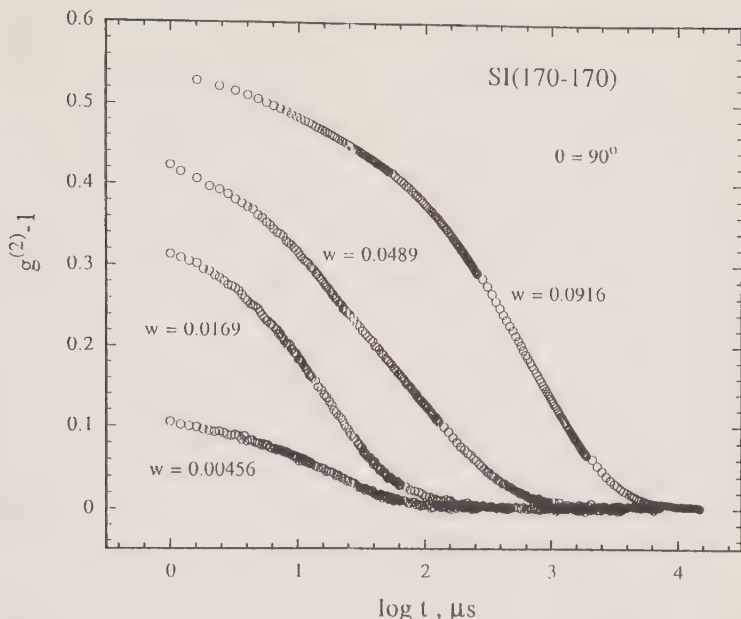


FIG. 11.19. Correlation functions of polarized scattered light obtained on solutions in toluene of a PS-PI symmetric block copolymer ($M_w = 340\,000$), at 30°C , at a scattering angle of 90° and for the indicated weight fractions, w . From ref. 30.

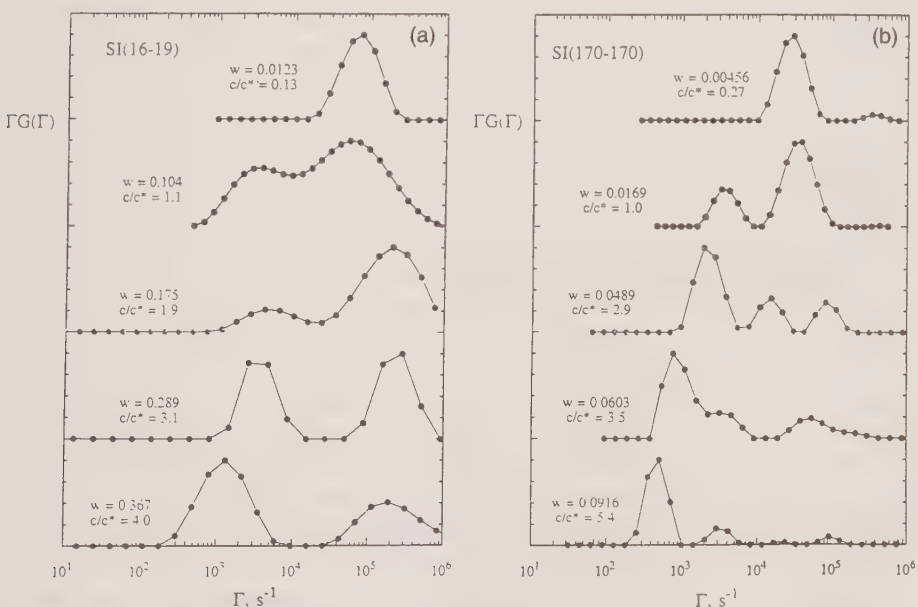


FIG. 11.20. Distribution functions of relaxation times obtained on toluene solutions of a PS-PI block copolymer, at 30°C , at a scattering angle of 90° , and for the weight fractions indicated: (a) $M_w = 35\,000$; (b) $M_w = 340\,000$. From ref. 30.

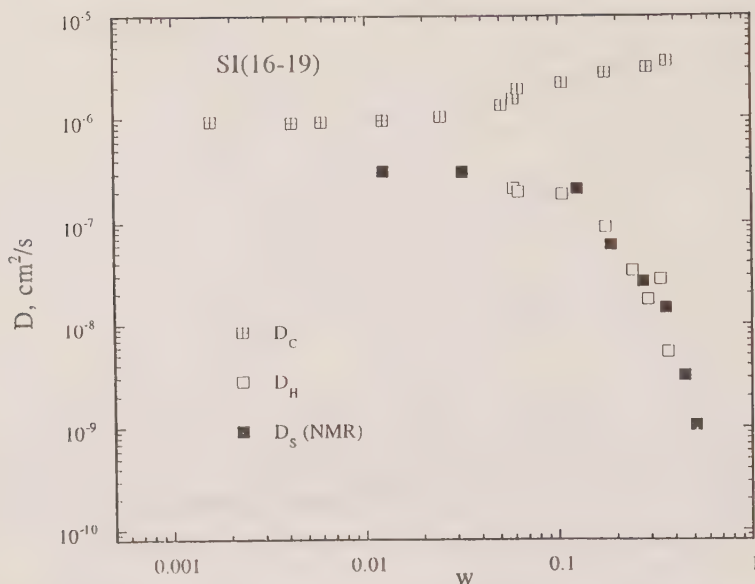


FIG. 11.21. Concentration dependencies of D_C and D_H obtained by polarized DLS, and D_S , obtained by NMR for toluene solutions of a PS-PI copolymer ($M_w = 35\,000$), at 30°C and at a scattering angle of 90°. From ref. 14.

Figure 11.22 demonstrates that for several molecular weights of the block copolymer and for various solvents, the ratio of amplitudes, A_H/A_C , is well described by the scaling law in eqn (11.35).

Figure 11.20(b) shows that for larger molecular weights an additional third mode exists in the distribution of relaxation times. As can be seen in Fig. 11.23, the decay rate of this mode is almost independent of angle, which leads to its assignment as the internal mode. The internal mode is, however, difficult to resolve, since its relaxation time is very close to that of the cooperative mode.

The magnitude of Γ_I can be estimated from Γ_H as follows; since the Zimm, Rouse and reptation theories all predict that^[25]

$$D_s \tau_1 / R_g^2 \approx 0.2, \quad (11.36)$$

where the ratio $D_s \tau_1 / R_g^2$ is dimensionless, we can estimate R_g of the copolymer used in Fig. 11.20(b) to be 21 nm. Then we obtain for the ratio $\Gamma_I/\Gamma_H \sim 40$, which is in good agreement with the positions of the peaks in Fig. 11.20(b). The accuracy of the determination of the amplitude is not sufficient to permit a quantitative evaluation of the angular dependence of A_I , according to eqn (11.24). We shall, however, show in the next section that the internal mode can be comfortably resolved and studied when a ‘zero-average contrast’ solvent is used (see also Chapter 8).

In recent years, dynamic light scattering measurements have been reported on a variety of copolymer systems. The characters of the modes observed

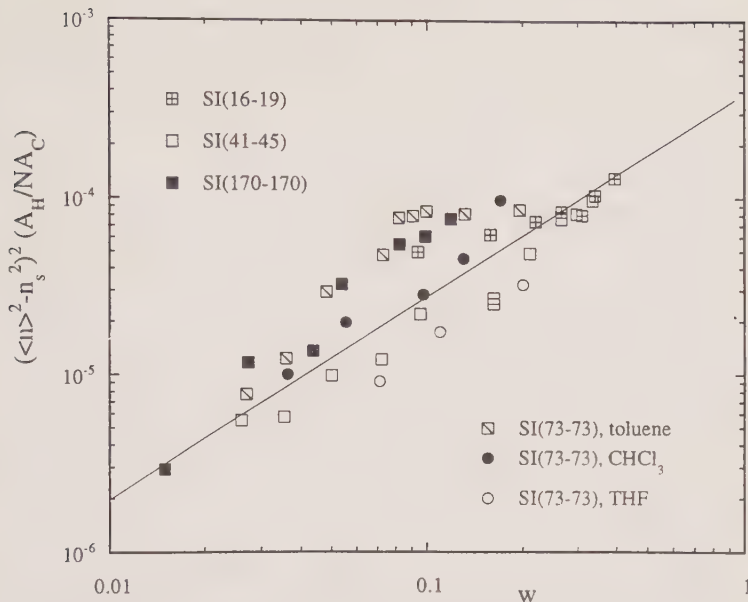


FIG. 11.22. Relative amplitudes of the heterogeneity and cooperative modes, normalized according to eqn (11.35), for several PS-PI copolymers in toluene, chloroform and tetrahydrofuran. The straight line is a guide for the eye and has a slope of 1.25. From ref. 30.

and the tentative interpretations advanced varied considerably. We feel, however, that it is now possible to reconcile all these findings.

Borsali *et al.*^[27] examined a poly(styrene-*b*-methylmethacrylate) (PS-PMMA) diblock copolymer ($M_w = 7.8 \times 10^5$) in toluene for $c \approx 5c^*$. Two modes were clearly evident, and both decay rates were roughly q^2 -dependent; in addition, the faster mode was comparable with D_C for a polystyrene homopolymer solution. The interpretation of the slower mode was uncertain, because it was diffusive, and thus did not fit the character of the expected internal mode. However, we can now say that its magnitude (ca. $7 \times 10^{-8} \text{ cm}^2/\text{s}$) is close to that expected for translational diffusion. Thus D_C and D_H were probably observed in this work, while Γ_I was presumably unresolvable because it overlaps D_C for this concentration and, moreover, D_C and D_H were only a factor of five apart.

Duval and coworkers presented two studies of a PS-PMMA copolymer in toluene, one^[52] with $M_w = 6.4 \times 10^5$ and the other^[53] with $M_w = 3.4 \times 10^5$. The former study involved one concentration, $c = 1.6c^*$, and two modes were seen. The slower mode was diffusive, and numerically consistent with D_C . The faster mode was attributed to Γ_I . The latter study included a range of semi-dilute solutions, and two diffusive modes were observed. The faster was again D_C , but the slower was attributed to 'superstructures'. However, its magnitude and concentration dependence are consistent with D_H , and this seems the more likely

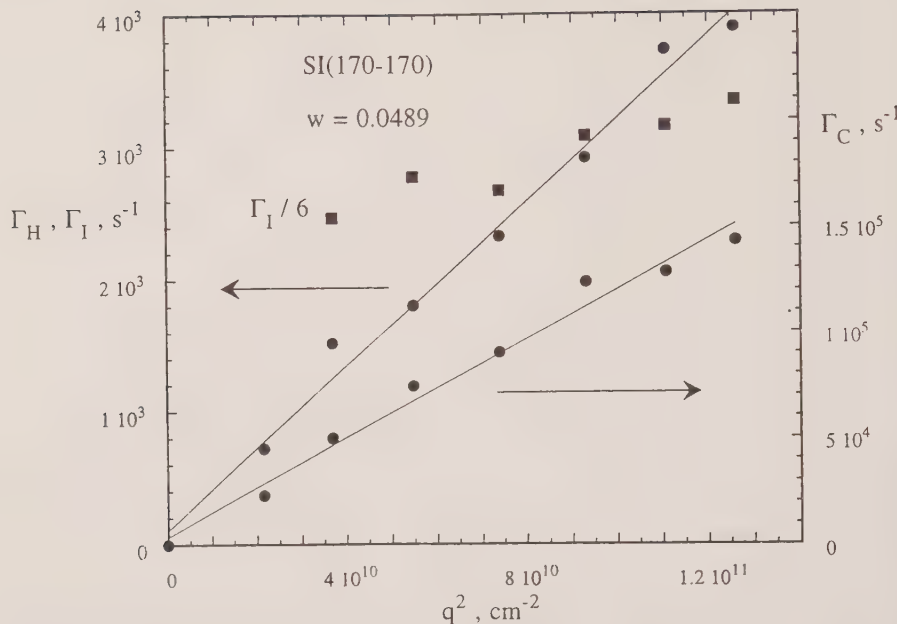


FIG. 11.23. The angle dependence of the decay rate for the three modes observed in Fig. 11.20(b), for a toluene solution of PS-PI copolymer ($M_w = 340\,000$) with weight fraction $w = 0.049$. The decay rate of the internal mode Γ_I was divided by six to bring it onto the scale of the heterogeneity mode. From ref. 30.

interpretation. The higher M_w and lower concentration in the former study presumably account for the observation of Γ_I and not Γ_H . These workers also noted the presence of an even slower mode that disappeared with time, and that was apparent at higher concentrations.

Koňák and Podesva^[54] examined a poly(styrene-*b*-isoprene) (PS-PI) diblock ($M_w = 1.8 \times 10^5$) in 1,2-diphenylethylene; four concentrations up to $c = 8c^*$ were employed. They noted two modes, and attributed the faster to Γ_I and the slower to D_C , on the basis of the q -dependence of the decay rates. However, the magnitude of the slower mode ($3\text{--}6 \times 10^{-8} \text{ cm}^2/\text{s}$) is at least an order of magnitude too low for D_C , and is therefore more likely to reflect D_H , even though it increased slightly with concentration. The appearance of a still slower mode was noted, particularly at high concentrations.

Balsara *et al.*^[55] examined a PS-PI diblock with $M_w = 3.1 \times 10^4$ in toluene; five rather high concentrations were employed ($w = 0.08\text{--}0.60$). As a consequence of this wide concentration range, these were the first DLS measurements to traverse the ODT. Two modes were consistently seen, the faster mode being diffusive and the slower having Γ close to q^3 -dependent. A comparison with forced Rayleigh scattering and NMR measurements led the authors to the suggestion that the diffusive mode corresponded to translational diffusion, a

then novel speculation that now has both theoretical and experimental support. Interestingly, the diffusivity was apparently unaffected by the ODT, in agreement with more recent results in melts.^[44] The slower mode was attributed to incipient grains, especially as it was found to slow down dramatically near the ODT. It is worth noting that these solutions were measured within a few days of their preparation. Consistent with some of the other results above, this slow mode may be attributed to a non-equilibrium state. The absence of Γ_I and Γ_C in this work is a consequence of the low molecular weight and high concentrations involved.

Tsunashima *et al.*^[56] examined a PS-PMMA diblock ($M_w = 1.5 \times 10^6$) in very dilute benzene solution. Two modes were seen, the slower clearly identified as D_C and the faster possibly as Γ_I ; the latter interpretation was uncertain because a q -independent regime was not detected as $q \rightarrow 0$. However, as the authors pointed out, the asymmetry of the sample ($f_{PS} = 0.39$) can compromise the simple assignment of modes in the mean-field theory.

Koňák *et al.*^[57] also examined a PS-PMMA diblock in toluene, but of low molecular weight ($M_w = 8 \times 10^4$) and of higher concentrations ($w = 0.005\text{--}0.04$). The faster mode observed was consistent with D_C ; the slower mode, which was also diffusive, was ascribed to aggregation induced by crystallization of stereo-regular sequences of the PMMA chain. It should, however, be pointed out that the magnitude of this diffusion coefficient ($4 \times 10^{-8} \text{ cm}^2/\text{s}$) is comparable to D_H .

Jian *et al.*^[67] examined the DLS properties of two PS-PI copolymers in toluene. One sample was asymmetric, and the other symmetric with total molecular weight of 1.6×10^5 . Three modes were found, and attributed to Γ_C , Γ_H , and Γ_I . The magnitudes and q -dependencies are comparable to those reported at the beginning of this section. An additional slow mode was found consistently, and was interpreted as being due either to clusters of copolymer chains, or to long-range density fluctuations.

11.5.3.2 Neutral, zero-average-contrast solvent.

The amplitude A_C of the cooperative mode observed in semi-dilute polymer or copolymer solutions is given by eqn (11.28), showing, as we have discussed above, that $A_C = 0$ if the average refractive index of the copolymer is equal to that of the solvent. Using such a 'zero average contrast' (ZAC) solvent masks the cooperative diffusion, and renders much easier the examination of other, weaker dynamic processes in the solution. This approach was previously used with a similar aim in a solution of two different polymers in a ZAC solvent.^[58,59]

Liu *et al.*^[60] reported the first DLS experiments of this kind on a solution of a diblock copolymer. A symmetric styrene-isoprene diblock copolymer was used, having a total molecular weight of $M_w = 340\,000$ (the same as for data shown in Fig. 11.20(b) above) dissolved in a mixed solvent of toluene and 1-chloronaphthalene. Differential refractometer measurements showed that ZAC conditions are achieved for this polymer-solvent system at a weight fraction of toluene in the mixed solvent of $w_{tol} = 0.48$. Figure 11.24 shows the distributions of relaxation times obtained at various angles on a typical solution

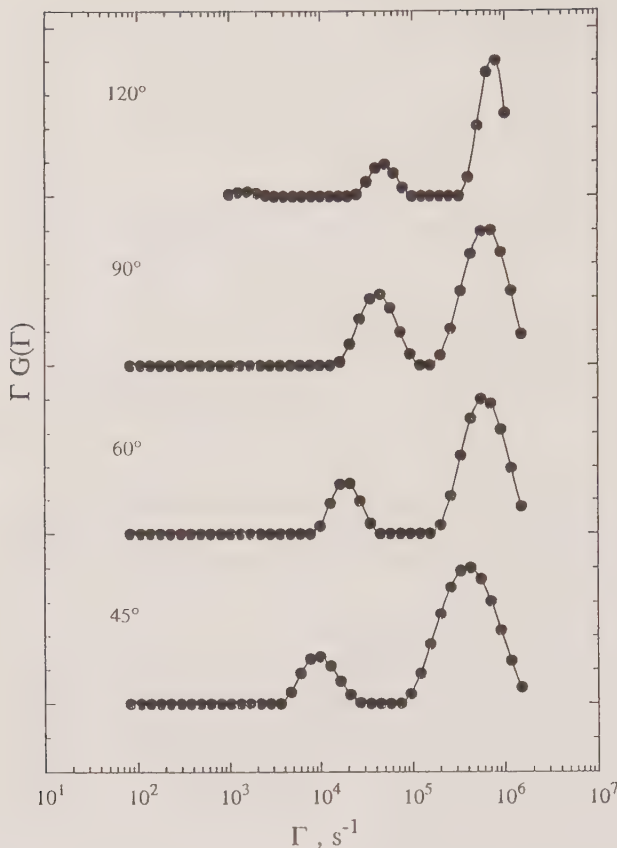


FIG. 11.24. The angle dependence of the distributions of relaxation times for a solution of PS-PI copolymer ($M_w = 340\,000$) at a weight fraction $w = 0.002$ and temperature 30°C , in a mixed solvent toluene/1-chloronaphthalene in ZAC conditions. From ref. 60.

under ZAC conditions. Although the same polymer is used as in Fig. 11.20(b), only two modes are seen: the cooperative mode is not present. In Fig. 11.24 the decay rate of the faster mode is clearly angle-independent and corresponds to the internal relaxation of the copolymer chain, whereas the decay rate of the slower mode depends on angle and has been shown^[60] to be diffusive. Figure 11.25 shows in more detail the angular dependence of the decay rate Γ_I of the internal mode, for several concentrations.

The theory predicts that, to zeroth order, Γ_I does not depend on the scattering vector, for $qR_g < 1$; see eqn (11.25). To first order, however, the following expression can be calculated^[60] from the theory of Benmouna *et al.*:^[19]

$$\Gamma_I = \frac{6kT}{N\zeta_0 R_g^2} (1 + \frac{3}{8}q^2 R_g^2 + \dots). \quad (11.37)$$

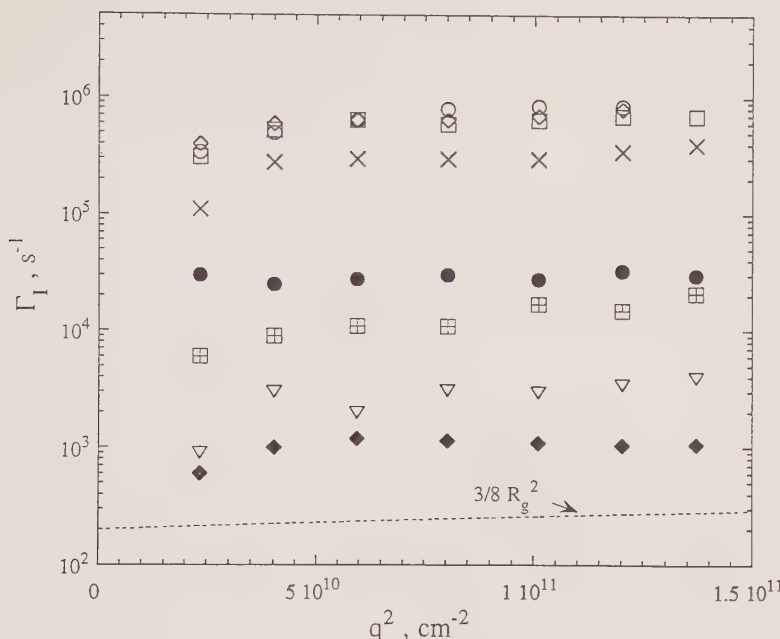


FIG. 11.25. The angle dependence of Γ_I in ZAC solutions, as a function of weight fraction: from top to bottom, $w = 0.002, 0.007, 0.008, 0.013, 0.054, 0.060, 0.075$ and 0.118 . The predicted q -dependence corresponding to eqn (11.37) is shown as the dotted curve. From ref. 60.

where ζ_0 is the monomeric friction coefficient. The dotted line in Fig. 11.25 shows the predicted dependence of Γ_I corresponding to eqn (11.37), which is in reasonable agreement with the data.

Figure 11.26 shows the concentration dependence of the diffusion coefficient of the heterogeneity mode and of the relaxation rate of the internal mode, presented as Γ_I/q^2 . Also shown are the measurements of D_S in chloroform by PFG-NMR, confirming that $D_H \approx D_S$; D_S has been scaled by the ratio of solvent viscosities. The concentration dependence of the internal mode has been modelled using eqn (11.27), a semi-empirical expression^[61–63] that has been shown to describe oscillatory birefringence, viscoelasticity, and dielectric relaxation data very well.^[29,64–66] The value of A obtained by the fit shown in Fig. 11.26 is 0.46, in excellent agreement with values between 0.4 and 0.5 obtained for polystyrene ($M > 10^5$) in Aroclor.^[29,64,65]

The intensities of the internal and heterogeneity modes are plotted as a function of concentration in Fig. 11.27. In dilute solution, $A_I > A_H$, but then A_H supersedes A_I near $c^* \approx 0.01$. The prediction for dilute solutions is^[60] that both A_I and A_H should increase linearly with c , but only A_H follows this prediction. In the semi-dilute regime, Jian *et al.*^[67] predict that A_I scales as $c^{0.75}$, which is not observed either. Above $c \approx 0.05$, both A_I and A_H increase very

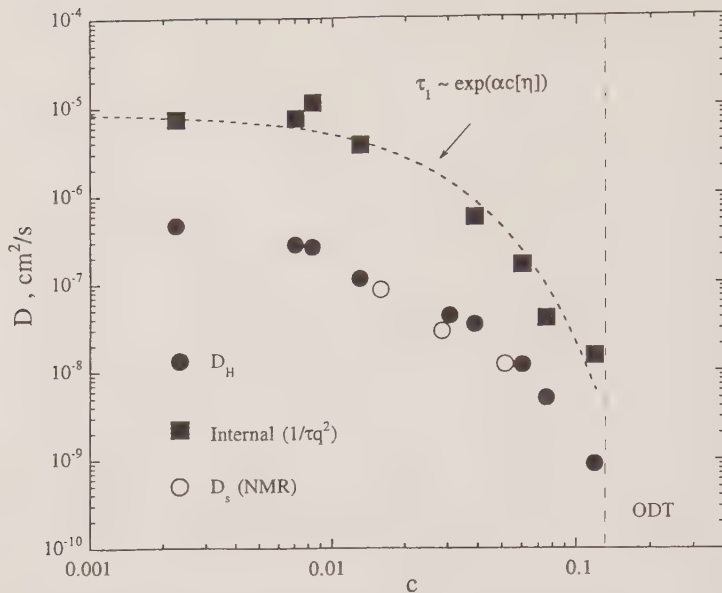


FIG. 11.26. The concentration dependence of D_H and D_s from PFG-NMR and Γ_I/q^2 (at 90°) for PS-PI copolymer ($M_w = 340\,000$) in ZAC solvent. The vertical line denotes the order-disorder transition, and the dashed line a fit of Γ_I to the exponential relation given in eqn (11.27). From ref. 60.

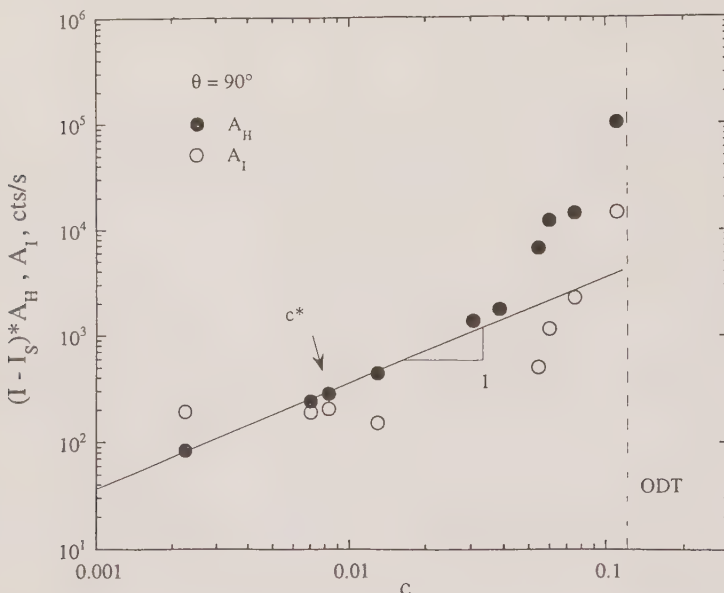


FIG. 11.27. The concentration dependence of the absolute amplitudes of the heterogeneity and internal modes for the PS-PI copolymer ($M_w = 340\,000$) in ZAC solvent. From ref. 60.

strongly (note the logarithmic axes on Fig. 11.27). Equation (11.17) includes the possibility of a divergence at high concentration, i.e. $1 - 2\kappa\chi Nc^{1.53} \rightarrow 0$, if the heterogeneity factor κ is sufficiently large. However, given that $\chi Nc^{1.53} \sim 10$ at ODT and $\kappa \sim 0.02$ for this block copolymer, eqn (11.17) cannot describe the strength of the observed increase in A_H . This extra intensity is more likely to correspond to the onset of large-amplitude fluctuations in composition.

The zero average contrast technique was also used in neutron spin echo measurements by Borsali *et al.*^[68] A poly(styrene-*b*-perdeutero-styrene) diblock copolymer was used in an appropriate mixed solvent of benzene and perdeutero-benzene. The internal mode was cleanly resolved, and it was shown that it has a Rouse-like character.

11.5.4 Depolarized dynamic light scattering from block copolymer solutions

In principle, one can expect to observe in depolarized dynamic light scattering the same segmental orientational mobility as we have discussed in Section 11.5.2 for block copolymer melts. For example, at a constant temperature, the glass transition temperatures and thus the peaks in the distribution of decay times should be shifted by the presence of the solvent in similar way to that observed in homopolymer solutions.^[69] To our knowledge, such studies have not yet been performed.

On the other hand, a different effect has been observed, in depolarized dynamic light scattering on a block copolymer solution just below the ODT. Jian *et al.*^[70] have used an asymmetric styrene-isoprene diblock copolymer ($M_w = 43\,000$ for the styrene block and 86 000 for the isoprene block) in toluene. At 25 °C and a concentration of 21% where static birefringence measurements (see Section 11.3) indicated the order-disorder transition, they have observed a substantial depolarized dynamic signal. An example of the correlation function is shown in Fig. 11.28(a). The shape of the correlation functions is almost single-exponential (β in the Williams-Watts relation (see eqn (11.34)) is ca. 0.9), and the decay rate depends linearly on q^2 , as shown Fig. 11.28(b). This process is thus completely different from the local segmental orientation normally investigated by depolarized light scattering, and was attributed in ref. 70 to the formation of grains of coherently ordered cylinders in the micro-structured solution which move by translational motion. Efforts should be made in imagining other mechanisms that better explain this effect. When this solution was heated from 25 °C to 45 °C, no correlation was observed again. The total depolarized intensity also increases substantially when the depolarized mode appears in the correlation function.

11.6 Conclusions

The aim of this chapter was to describe basic, yet exciting features of block copolymer liquids as observed by static and dynamic light scattering. These include, in particular, the ordering phenomenon, the grainy structure of the

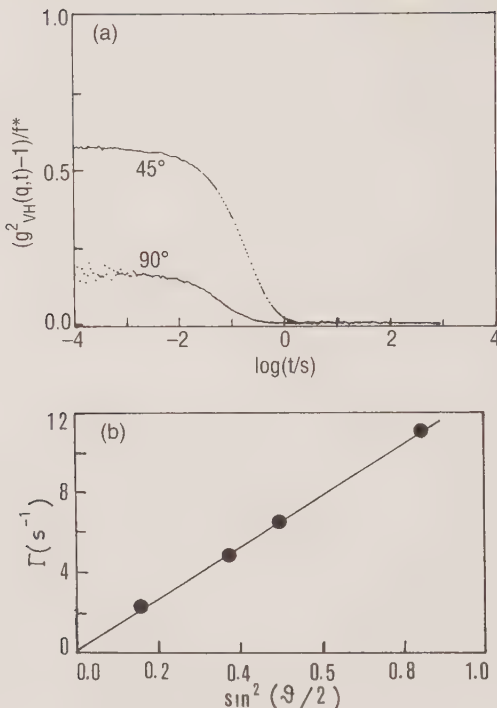


FIG. 11.28. (a) The correlation function of depolarized scattered light from a toluene solution of a PS PI asymmetric block copolymer ($M_w = 129\,000$, $f_{PS} = 0.31$), at 25°C and at weight fraction $w = 0.21$. After ref. 70. (b) The angle dependence of the decay rate, Γ , extracted from the correlation functions shown in Fig. 11.28(a). After ref. 70.

ordered phase, the existence of several dynamic modes and the insensitivity of some of them to the order-to-disorder transition. These properties are often quite complex, and one can only imagine that triblock and multiblock copolymers will be even more intricate.

Acknowledgement

We acknowledge the support of this work by the National Science Foundation through grant CHE-9203173 from the NSF Division of International Programs (a US–Czech Cooperative Research award).

Appendix 11.A: list of symbols and abbreviations

Often used symbols

c	concentration of polymer in solution (g/ml)
f	composition of a diblock copolymer: volume fraction of one component with respect to both components
g	number of monomers per blob
$g^2(t)$	intensity correlation function
n	refractive index
q	scattering vector
t	correlator delay time
v	segment volume
w	weight fraction of polymer in solution
B_∞	asymptotic birefringence
G'	storage modulus
G''	loss modulus
M_w	weight-average molecular weight
M_n	number-average molecular weight
N	degree of polymerization
R_g	radius of gyration
T	absolute temperature
T_g	glass transition temperature
T_{ODT}	temperature of the order-disorder transition
β	Williams-Watts parameter of a stretched exponential
Γ	decay rate of correlation function
δ	polydispersity parameter
η	viscosity
θ	scattering angle
κ	heterogeneity factor
λ	wavelength of light
τ	relaxation time
τ_1	relaxation time of the first internal mode of a polymer chain
ϕ	volume fraction of polymer in solution
χ	Flory-Huggins interaction parameter
ω	frequency

Abbreviations

DLS	dynamic light scattering
ILT	inverse Laplace transformation
MST	microphase separation transition
ODT	order-to-disorder transition

OOT	order-to-order transition
SANS	small-angle neutron scattering
UCST	upper critical solution temperature

Polymers

The first line gives the usual name, and the second line the rigorous name according to the IUPAC nomenclature:

PEP-PEE	poly(ethylpropylene- <i>block</i> -ethylethylene) poly(1-ethyl-1-methylethane-1,2-diyl)-poly(1-ethylethane-1,2-diyl)
PE-PEE	poly(ethylene- <i>block</i> -ethylethylene) poly(methylene)-poly(1-ethylethane-1,2-diyl)
PVCH-PE	poly(vinylcyclohexane- <i>block</i> -ethylene) poly(1-cyclohexylethane-1,2-diyl)-poly(methylene)
PVCH-PEE	poly(vinylcyclohexane- <i>block</i> -ethylethylene) poly(1-cyclohexylethane-1,2-diyl)-poly(1-ethylenethane-1,2-diyl)
PDMS-PEMS	poly(dimethylsiloxane- <i>block</i> -ethyl-methylsiloxane) same
PS-PI	poly(styrene- <i>block</i> -isoprene) same
PS-PMPS	poly(styrene- <i>block</i> -methyl-phenylsiloxane) same

References

1. Bates, F. S. and Fredrickson, G. H. (1990). *Ann. Rev. Phys. Chem.*, **41**, 525.
2. Flory, P. J. (1953). *Principles of polymer chemistry*. Cornell University Press, Ithaca, New York.
3. Leibler, L. (1980). *Macromolecules*, **13**, 1602.
4. Fredrickson, G. H. and Helfand, E. (1989). *J. Chem. Phys.*, **87**, 697.
5. Hamley, I. W., Koppi, K. A., Rosedale, J. H., Bates, F. S., Almdal, K., and Mortensen, K. (1993). *Macromolecules*, **26**, 5959.
6. Brazovskii, S. A. (1975). *Soviet. Phys. JEPT*, **41**, 85.
7. Bates, F. S., Schulz, M. F., Khandpur, A. K., Förster, S., Rosedale, J. H., Almdal, K., and Mortensen, K. (1994). *J. Chem. Soc., Faraday Disc.*, **98**, 7-18.
8. Fredrickson, G. H. and Leibler, L. (1989). *Macromolecules*, **22**, 1238.
9. Lodge, T. P., Xu, X., Jin, X., and Dalvi, M. C. (1994). Diffusion, rheology, and flow birefringence in block copolymer liquids near the ordering transition. *Makromol. Chem., Macromol. Symp.*, **74**, 87.
10. Almdal, K., Bates, F. S., and Mortensen, K. (1992). *J. Chem. Phys.*, **96**, 9122.
11. Rosedale, J. H. and Bates, F. S. (1990). *Macromolecules*, **23**, 2329.
12. Bates, F. S. (1984). *Macromolecules*, **17**, 2607.
13. Herman, D. S., Kinning, D. J., Thomas, E. L., and Fetter, L. J. (1992). *Macromolecules*, **20**, 2940.

14. Balsara, N. P., Perahia, D., Safinya, C. R., Tirell, M., and Lodge, T. P. (1992). *Macromolecules*, **25**, 3896.
15. Balsara, N. P., Garetz, B. A., and Dai, H. J. (1992). *Macromolecules*, **25**, 6072.
16. Lodge, T. P. and Fredrickson, G. H. (1992). *Macromolecules*, **25**, 5643.
17. Garetz, B. A., Newstein, M. C., Dai, H. J., Jonnalagadda, S. V., and Balsara, N. P. (1993). *Macromolecules*, **26**, 3151.
18. Amundson, K., Helfand, E., Patel, S., Quan, X., and Smith, S. D. (1992). *Macromolecules*, **25**, 1935.
19. Benmouna, M., Benoit, H., Borsali, R., and Duval, M. (1987). *Macromolecules*, **20**, 2620.
20. Benmouna, M., Duval, M., and Borsali, R. (1987). *J. Polym. Sci., Polym. Phys. Ed.*, **25**, 1839.
21. Akcasu, A. Z., Benmouna, M., and Benoit, H. (1986). *Polymer*, **27**, 1935.
22. Akcasu, A. Z., Hammouda, B., Lodge, T. P., and Han, C. C. (1984). *Macromolecules*, **17**, 759.
23. Semenov, A. N., Fytas, G., and Anastasiadis, S. H. (1994). *Polym. Prepr. (Am. Chem. Soc., Div. Polym. Chem.)*, **35**(1), 618.
24. Pusey, P. N., Fijnaut, H. M., and Vrij, A. (1982). *J. Chem. Phys.*, **77**, 4270.
25. Doi, M., and Edwards, S. F. (1986). *The theory of polymer dynamics*. Clarendon Press, Oxford.
26. de Gennes, P. G. (1979). *Scaling concepts in polymer physics*. Cornell University Press, Ithaca, New York.
27. Joanny, J. F., Leibler, L., and Ball, R. (1984). *J. Chem. Phys.*, **81**, 4640.
28. Borsali, R., Fischer, E. W., and Benmouna, M. (1991). *Phys. Rev. A*, **45**, 5732.
29. Lodge, T. P. and Schrag, J. L. (1982). *Macromolecules*, **15**, 1376.
30. Pan, C., Maurer, W., Liu, Z., Lodge, T. P., Štěpánek, P., von Meerwall, E. D., and Watanabe, H. (1995). *Macromolecules*, **28**, 1643–53.
31. See, e.g., Giebel, L., Meier, G., Fytas, G., and Fischer, E. W. (1992). *J. Polym. Sci., Polym. Phys. Ed.*, **30**, 1291.
32. Provencher, S. W. (1979). *Makromol. Chem.*, **180**, 201.
- 33a. Štěpánek, P. (1993). In *Dynamic light scattering: the method and some applications* (ed. W. Brown). Clarendon Press, Oxford.
- 33b. Štěpánek, P., Johnsen, R. M. (1995). *Collect. Czech. Chem. Communs*, **60**, 1941.
- 34a. Štěpánek, P., Lodge, T. P., and Bates, F. S. (1993). *Polym. Prepr. (Am. Chem. Soc., Div. Polym. Chem.)*, **35**(1), 616.
- 34b. Štěpánek, P., Lodge, T. P. (1996). In Dynamic light scattering from block copolymer melts near the disorder transition. *Macromolecules*, in press.
35. Papadakis, C., Brown, W., Johnsen, R. M., Posselt, D., Almdal (1996). *J. Chem. Phys.*, **104** (4), 1611.
36. Vogt, S., Anastasiadis, S. H., Fytas, G., and Fischer, E. W. (1994). *Macromolecules*, **27**, 4335.
37. Rosedale, J. H., Bates, F. S., Almdal, K., Mortensen, K., and Wignall, G. (1995). *Macromolecules*, **28**, 1429.
38. Fried, H. and Binder, K. (1991). *Europhys. Lett.*, **16**(3), 237.
39. Stuhn, B. and Stickel, F. (1992). *Macromolecules*, **25**, 5306.
40. Fleischer, G., Fujara, F., and Stuhn, B. (1994). *Macromolecules*, **27**, 3335.
41. Kanaya, T., Patkowski, A., Fischer, E. W., Seils, J., Glaser, H., and Kaji, K. (1994). *Acta Polym.*, **45**, 137.
42. Bremner, T. and Rudin, A. (1992). *J. Polym. Sci., Polym. Phys. Ed.*, **30**, 1247.
43. Ferry, J. D. (1970). *Viscoelastic properties of polymers*. John Wiley, New York.
44. Dalvi, M. C. and Lodge, T. P. (1994). *Macromolecules*, **27**, 3487.

45. Jakes, J. (1988). *Czech. J. Phys.*, **38**, 1305.
46. Provencher, S. W. (1992). In *Laser light scattering in biochemistry* (ed. S. E. Harding, D. B. Sattelle and V. A. Bloomfield). Royal Society of Chemistry.
47. Hoffmann, A., Koch, T., Schuler, M., Stickel, F., and Stuhn, B. (1993). *Progr. Colloid Polym. Sci.*, **91**, 61.
48. Holzer, B., Lehmann, A., Stuhn, B., and Kowalski, M. (1991). *Polymer*, **32**, 1935.
49. Fytas, G., Anastasiadis, S. H., Karatasos, K., and Hadjichristidis, N. (1993). *Phys. Scripta*, **T49**, 231.
50. Rizos, A. K., Fytas, G., and Roovers, J. E. L. (1992). *J. Chem. Phys.*, **97**, 6925.
51. Kanetakis, J., Fytas, G., Kremer, F., and Pakula, T. (1992). *Macromolecules*, **25**, 3484.
52. Duval, M., Haida, H., Lingelser, J. P., and Gallot, Y. (1991). *Macromolecules*, **24**, 6867.
53. Haida, H., Lingelser, J. P., Gallot, Y., and Duval, M. (1991). *Makromol. Chem.*, **192**, 2701.
54. Koňák, Č. and Podesva, J. (1991). *Macromolecules*, **24**, 6502.
55. Balsara, N. P., Štěpánek, P., Lodge, T. P., and Tirrell, M. (1991). *Macromolecules*, **24**, 6227.
56. Tsunashima, Y. and Kawamata, Y. (1993). *Macromolecules*, **26**, 4899.
57. Koňák, Č., Vlcek, P., and Bansil, R. (1993). *Macromolecules*, **26**, 3717.
58. Giebel, L., Benmouna, M., Borsali, R., and Fischer, E. W. (1993). *Macromolecules*, **26**, 2433.
59. Benmouna, M., Fischer, E. W., Ewen, B., and Duval, M. (1992). *J. Polym. Sci., Polym. Phys. Ed.*, **30**, 1157.
60. Liu, Z., Pan, C., Lodge, T. P., and Štěpánek, P. (1995). *Macromolecules*, **28**, 3221–9.
61. Adler, R. S. and Freed, K. F. (1978). *Macromolecules*, **11**, 1058.
62. Muthukumar, M. and Freed, K. F. (1978). *Macromolecules*, **11**, 843.
63. Muthukumar, M. (1983). *J. Chem. Phys.*, **79**, 8.
64. Amelar, S., Eastman, C. E., Morris, R. L., Schmeltzly, M. A., Lodge, T. P., and von Meerwall, E. D. (1991). *Macromolecules*, **24**, 3505.
65. Martel, C. J. T. (1983). *Faraday Symp. Chem. Soc.*, **18**, 173.
66. Patel, S. S. and Takahashi, K. M. (1992). *Macromolecules*, **25**, 4382.
67. Jian, T., Anastasiadis, S. H., Semenov, A. N., Fytas, G., Adachi, K., and Kotaka, T. (1994). *Macromolecules*, **27**, 4762.
68. Borsali, R., Benoît, H., Legrand, J. F., Duval, M., Picot, C., Benmouna, M., and Farago, B. (1989). *Macromolecules*, **22**, 4119.
69. Brown, W., Johnsen, R. M., Koňák, Č., and Dvoranek, L. (1991). *J. Chem. Phys.*, **95**, 8568.
70. Jian, T., Anastasiadis, S. H., Fytas, G., Adachi, K., and Kotaka, T. (1993). *Macromolecules*, **26**, 4706.

12

Low angle light scattering and its applications

Francesco Mallamace and Norberto Micali

12.1 Introduction

The length scale ranging from some hundreds of Ångstroms to micrometers is relevant in many different research areas of physics, chemistry and biology, and in particular in the interdisciplinary field of complex systems. The characteristic properties of these latter systems, i.e. polymers, polymer solutions, gels, charged colloids, microemulsions, micelles, liquid crystals, proteins, DNA solutions, living cells, etc., reflect structures or superstructures (cluster networks built up by precise aggregation phenomena) that fall in a length interval termed the mesoscopic region.^[1–3] In addition, many of these systems arrange themselves in extended networks with self-similar long-ranged structures characterized by scaling laws.^[2] A more complete understanding of such systems can be obtained by exploring many orders of magnitude in length.

In this respect, as is well known, scattering experiments constitute a powerful tool. In fact, using the different available techniques (X-rays, neutrons and light), and changing in a suitable way the probe wavelength, it is possible to study system properties ranging from atomic sizes to several microns, i.e. some seven orders of magnitude. X-rays and neutrons give deeper information on the microscopic scale; these techniques are used extensively in order to study dynamical and structural properties as reflected by the local molecular organization.

The mesoscopic scale includes phenomena mainly driven by interactions between supramolecular aggregates, macromolecules or colloidal particles of large size. These can arrange themselves in superstructures that are strongly dependent on the chemical nature of the basic units, the thermodynamic state of the system and on the strength of the interactions. Many of the resulting aggregates show a complex structural organization and their dynamics can be described using scaling concepts. These arguments, developed for complex fluids by de Gennes, give us the possibility of a conceptually important understanding of the system.^[2] Their main properties are determined by self-similarity, scaling and universality and involve, for all the different physical phenomena, behaviour describable by power laws. Analysis of the related power-law relations provides a simple and accurate method for determining their structural and dynamical properties. In other words, these systems are characterized by particular geometrical features of their structure, which is generally fractal in character.

This property is utilized to characterize the physical properties, in particular the dynamical ones, in terms of scaling and universality.^[3] More simply, fractal geometry allows a description of the physical phenomena in these systems on purely geometrical grounds, showing that it is not necessary to make reference to statistical mechanics.^[2,3]

Many of these phenomena are suitably investigated using light scattering. In particular, systems characterized by very large structures, sizes or characteristic correlation lengths (larger than some microns), can be studied using very small scattering angles. In fact, working in this spectral region makes it possible to obtain a quantitative understanding of the physical phenomena characteristic of the mesoscopic scale. The subject of this chapter is to detail this latter technique, mainly giving information about the theoretical foundations and their application. Firstly, we describe the use of small angle light scattering to the study of particle sizes, and subsequently we shall consider applications to the study of processes characterized by long-range order.

The simultaneous use of conventional scattering techniques and small angle light scattering allows accurate analysis of the scaling properties of such systems. In conclusion, we detail an application of the present scattering technique, developed in recent years, for the study of processes strongly dependent on the temporal variable. This novel technique is conventionally named ‘time-resolved spectroscopy’ and can be successfully applied to gain insight into the slow relaxation processes typical of complex systems: e.g. the kinetics of aggregation processes that characterize self-assembling systems, and the behaviour of quantities related to systems outside thermodynamic equilibrium; an example of this latter phenomenon is the kinetics of phase separation processes or spinodal decomposition.

12.2 Historical background

The scattering process is basically due to the interaction between light with matter. When an electromagnetic field of light impinges on matter it induces a response in the system. This is directly related to the polarization of the electrons in the molecules, which in turn depends on their structure and quantum mechanical properties.^[4] The incident field is said to polarize the medium, and the polarization magnitude is dependent upon the amplitude of the applied electric field. The ability of the system to be distorted is referred to as the polarizability; a quantity usually represented as a tensor denoted by $\underline{\alpha}(\mathbf{r}, t)$.^[5] Accelerated charges of the excited molecules emit radiation and behave as secondary sources of light giving rise to the scattered radiation. From electrodynamics the single molecule is considered to be the basic scattering unit. On this basis condensed matter can be viewed as a collection of scattering units. Therefore the properties of scattered light, i.e. the frequency shift, the polarization, the angular distribution and the intensity, are strongly dependent on the molecular organization inside the scattering material. These properties are in fact determined by the size, shape and molecular interactions inside the system.

Thus, by using theories of statistical mechanics and electrodynamics it is possible to obtain information about the physical properties of the scattering medium by analysing the scattered spectrum. The structure and dynamics of many different physical systems (solid, liquid or gaseous) can in principle be studied by light scattering techniques.

The scattered field depends basically on the spatial arrangement of scattering centres and on the coupling between the incident light and matter that can strongly change its magnitude and phase.^[4,5] Although light scattering can give information regarding the degrees of freedom of the molecule (translational, rotational, vibrational and electronic) for our purposes we consider only the light scattered by translational and rotational degrees of freedom. The coupling between matter and the electric field can determine an energy transfer from the field to the matter and vice versa. In such a case the scattering process can be accomplished by absorption. However, the dominant part of the scattered radiation will have the same frequency as the incident field ($v_s = v_i$). This type of scattering is referred to as *elastic*. The remainder of the scattered radiation will have frequencies higher or lower than the incident ($v_s \neq v_i$), and in this case we have *inelastic scattering*. In the following we shall mainly consider elastic scattering or scattering from physical processes dominated by very slow dynamics (long relaxation times). In terms of statistical physics, scattering phenomena are basically dependent on the ensemble and time-averaged properties of the scattering medium. We consider here only processes which are weakly dependent or independent of time.

Pioneering studies in this field are due to Tyndall,^[6] Lord Rayleigh,^[7] Debye^[8] and Gans.^[9] These studies concern scattering from assemblies of non-interacting particles of any size and is described by considering each scattering centre as an independent dipole oscillator with a fixed phase relation between the waves scattered from different points of the same particle. This type of scattering is commonly referred to as *Rayleigh-Debye* or *Rayleigh-Gans scattering*.^[5]

Scattering from pure liquids and complex systems can be described in the framework of the 'fluctuation theory of light scattering'. This theoretical model, developed by Smoluchowski,^[10] Einstein^[11] and Debye,^[8] considers the system as a continuous medium in which small thermal fluctuations give rise to local inhomogeneities, and thereby to density and concentration fluctuations. The intensity of the scattered field can be obtained from the mean square fluctuations in density and concentration. In this case the intensity of light is obtained without considering the molecular structure of the medium and depends only on the spatial arrangement or correlations of the scattering centres. In the framework of this model, it has been possible to detail many properties of condensed matter: i.e. the behaviour of critical systems,^[12] properties of macromolecules and polymers in solutions, their molar masses, sizes, shapes and interaction^[13] and hypersound propagation.^[14]

The situation is far more complex when the relative magnitude and phase of the incident field is modified by the scattering centre. In such a case the scattered field is strongly dependent upon the location of the molecule inside the

scattering particle. This is the situation for large particles (i.e. large compared to the scattering wavelength) of refractive index much different from unity. This type of scattering is referred as *Mie scattering*. Although, in principle, this scattering considers the general physical situation only for scattering particles having a spherical shape, a complete analytical solution exists.^[15] However, it is routinely used to study the shapes and sizes of large scattering particles in particle size analysis where studies can be made of the angular dependence and polarization of the scattered light. Because small angle light scattering involves both type of scattering, we shall consider the basic expressions in the following.

12.3 Mie scattering

Any scattering or light propagation problem can be solved by considering the basic Maxwell equations of electrodynamics.^[4,16] In particular, the scattered field amplitude can be obtained if the four components of the scattering matrix $S(\phi, \theta)$ are known for each individual aggregate of scatterers for the particular way in which it is oriented in space (ϕ and θ are the azimuthal angles in spherical coordinates). More precisely, knowledge of the scattering matrix allows us to write the intensity and state of polarization of the scattered wave in any direction when radiation of arbitrary intensity and polarization impinges on the scattering particle.

Mie theory describes the general form of $S(\phi, \theta)$ for a scattering system of spheres, giving the solutions of Maxwell equations inside and outside of a scattering particle which satisfy the boundary conditions due to the optical discontinuity at the edge of each particle.^[16] In particular, for the calculation of the scattering matrix, it takes into account the general situation in which the coupling between system and probe modifies the phase and amplitude of the incident electric field. In this situation the scattered field is dependent on the relative size of the scattering particles compared with the field wavelength (or the wavelength-independent size parameter) $k \times a = 2\pi a/\lambda$ (a denotes the particle radius) and the complex refractive index m . Because of the symmetry of spherical scatterers, the scattering matrix depends only on θ and $S_3(\theta) = S_4(\theta) = 0$.^[16] $S_1(\theta)$ and $S_2(\theta)$ are complex numbers with different phases; the scattered light is elliptically polarized even if the incident light has a linear polarization. We give only the final results of the calculations of the scattering amplitudes $S_1(\theta)$ and $S_2(\theta)$ in the far field approximation (i.e. when the scattering field is collected at a very large distance, r , from the scattering sphere) and recommend to the reader the impressive book by van de Hulst on the present subject.^[16] The relevant information on this subject is summarized there. In particular, from the Mie theory of light scattering we have

$$\left. \begin{aligned} S_1(\theta) &= \sum_{n=1}^{\infty} \frac{2n+1}{n(n+1)} \{a_n \pi_n(\cos \theta) + b_n \tau_n(\cos \theta)\} (-1)^{n+1}, \\ S_2(\theta) &= \sum_{n=1}^{\infty} \frac{2n+1}{n(n+1)} \{a_n \tau_n(\cos \theta) + b_n \pi_n(\cos \theta)\} (-1)^{n+1} \end{aligned} \right\} \quad (12.1)$$

where the angular functions are

$$\pi_n(\cos \theta) = \frac{P_n^1(\cos \theta)}{\sin \theta}, \quad \tau_n(\cos \theta) = \frac{d}{dt} P_n^1(\cos \theta) \quad (12.2)$$

and P_n^1 is the associated Legendre function of the first kind. The scattering coefficients a_n and b_n are given in terms of m and $\zeta = \mathbf{k} \times \mathbf{a}$; in particular, they are expressed by means of a combination of Riccati–Bessel functions with m and ζ as parameters. The resulting components of the scattered field are

$$\left. \begin{aligned} E_\theta &= H_\phi = -\frac{i}{kr} e^{ikr+i\omega t} \cos \phi S_2(\theta), \\ -E_\phi &= H_\theta = -\frac{i}{kr} e^{ikr+i\omega t} \sin \phi S_1(\theta), \end{aligned} \right\} \quad (12.3)$$

where E and H indicate the electric and magnetic field, respectively. The corresponding intensities are

$$\left. \begin{aligned} I_\phi &= \frac{\lambda^2}{4\pi^2 r^2} \sin^2 \phi |S_1(\theta)|^2 = \frac{\lambda^2}{4\pi^2 r^2} i_1 \sin^2 \phi, \\ I_\theta &= \frac{\lambda^2}{4\pi^2 r^2} \cos^2 \phi |S_2(\theta)|^2 = \frac{\lambda^2}{4\pi^2 r^2} i_2 \cos^2 \phi, \end{aligned} \right\} \quad (12.4)$$

where i_1 and i_2 are the intensity functions. These components are perpendicular and parallel to the scattering plane which contains the directions of the incident and scattered waves (θ, ϕ) . Each of these components can be thought of as arising from the component of the incident beam which is polarized in the same sense. I_ϕ is due to an incident field polarized perpendicularly to the scattering plane and I_θ to the beam polarized parallel to the scattering plane. The phase difference between these components of the scattered intensity is given by:

$$\delta = \tan^{-1} \left\{ \frac{\operatorname{Re}(S_1) \operatorname{Im}(S_2) - \operatorname{Re}(S_2) \operatorname{Im}(S_1)}{\operatorname{Re}(S_1) \operatorname{Re}(S_2) - \operatorname{Im}(S_2) \operatorname{Im}(S_1)} \right\}, \quad (12.5)$$

where Re and Im refer to the real and imaginary parts of the indicated complex amplitude function. Considering the two possible choices of the scattering plane, i.e. the $y-z$ and $x-z$ planes, the direction of the incident electric vector is, respectively, perpendicular ($\phi = 90^\circ$) or parallel ($\phi = 0^\circ$) to the scattering plane, and:

$$I_\phi = I_1 = \frac{\lambda^2}{4\pi^2 r^2} i_1, \quad I_\theta = I_2 = \frac{\lambda^2}{4\pi^2 r^2} i_2, \quad (12.6)$$

Similarly, we can consider the conventional scattering geometry, where $x-z$ is the horizontal scattering plane and y is the vertical direction. The incident polarization in the $x-y$ plane is defined by the angle χ between the electric

vector of the incident radiation and the x -axis. In this case:

$$I_1 = I_V(\chi) = \frac{\lambda^2}{4\pi^2 r^2} i_1 \sin^2 \chi, \quad I_2 = I_H(\chi) = \frac{\lambda^2}{4\pi^2 r^2} i_2 \cos^2 \chi, \quad (12.7)$$

where $I_V(\chi)$ and $I_H(\chi)$ designate the vertical and horizontal components of the intensity of the scattered radiation in units of incident intensity radiation polarized along χ . For unpolarized incident radiation of unit intensity, the scattered intensity is

$$I_U = \frac{\lambda^2}{8\pi^2 r^2} (i_1 + i_2) \quad (12.8)$$

and the degree of polarization is given by

$$P = \frac{|i_1 - i_2|}{|i_1 + i_2|}. \quad (12.9)$$

Quite generally, the computational problem involved in Mie scattering is the calculation of i_1 , i_2 and the phase difference δ as functions of the scattering angle θ .

Next we consider an approximation based only on mathematical considerations. When the arguments, m and ζ , of the Bessel function giving the scattering amplitudes are small (i.e. small particle radius and small complex refractive index), the expansions of these functions as power series in the argument converge rapidly. On this basis the first terms in the series expansions of the first three scattering coefficients are^[17]

$$a_1 = \frac{2}{3}i \left(\frac{m^2 - 1}{m^2 + 2} \right) \zeta^3, \quad a_2 = \frac{1}{15}i \left(\frac{2m^2 - 1}{2m^2 + 3} \right) \zeta^5, \quad b_1 = \frac{1}{45}i(m^2 - 1)\zeta^5. \quad (12.10)$$

The remaining coefficients are proportional to still higher powers of ζ . When both ζ and m are sufficiently small, the term containing a_1 becomes the leading term in the expression of the amplitude functions and we have

$$\pi_1(\cos \theta) = 1 \quad \text{and} \quad \tau_1(\cos \theta) = \cos \theta, \quad (12.11)$$

so that the scattered intensity is

$$I_U = \frac{8\pi^4 a^6}{r^2 \lambda^4} \left| \frac{m^2 - 1}{m^2 + 2} \right|^2 (1 + \cos^2 \theta). \quad (12.12)$$

This expression is the same as the well-known Rayleigh formula, the only difference being that m may be complex. This result illustrates the generality of Mie's theory. However, it is a laborious task to calculate the spherical harmonics needed for the field expansion. Only in recent years, with the facilities of powerful computational methods, have Mie calculations been applied to obtain exact solutions for the scattering (and absorption) of large ellipsoids and cylinders of revolution of arbitrary refractive index and size. Such solutions can be extended to other types of particles.^[18] In particular, they have been

used to study the size, shape, polydispersity and internal radial polarizability of systems containing particles in the micron range.^[19] At present Mie scattering theory is extensively applied in many different fields of research.

However, simplified expressions of this scattering model have given significant physical insight into the behaviour and properties of particles, especially those in the mesophase region. In this respect it is interesting to consider a useful survey of the simplifications that arise in the limits when m and ζ have large or small values. All general expressions for Mie scattering are written in terms of the two significant parameters m and ζ . The refractive index may range from values smaller than 1 to ∞ . Values smaller than 1 are sometimes encountered in the laboratory if the medium surrounding the scattering particle is not a vacuum. The size parameter ζ may have values from 0 to ∞ (for non-spherical particles, a is the major semi-axis). We consider the schematic diagram in Fig. 12.1 in which any combination of m and ζ is represented as a point within a square. More specifically, the two scattering parameters and the combination of both in the phase shift ($2\zeta|m - 1|$), allow us to identify the domains within the plane in which simplified theories can be used to understand the scattering and absorption by a particle. This plane is characterized by three main areas and allows a clear physical interpretation of the scattering process. The first zone is related to the size of the scattering sphere, the second zone is defined by the value of m and the third is defined by the phase shift. There is a gradual change from typical scattering properties of small spheres to those of large spheres. The importance of the area due to ζ is evident from the Mie scattering formulae. Also, in the second zone there is a gradual transition from small m values (well-known) to $m = \infty$ (total reflectors). The characteristics of the

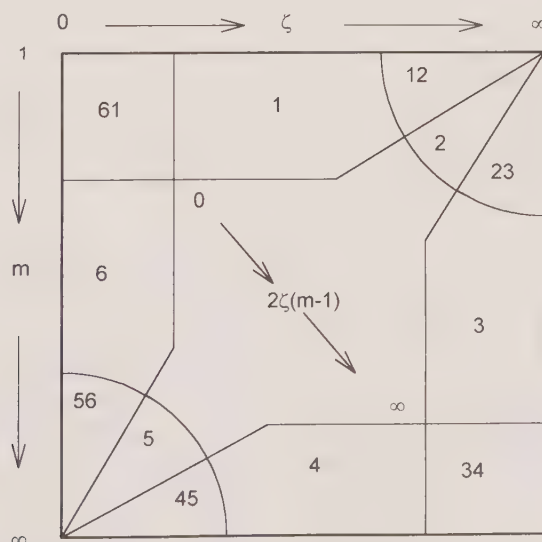


FIG. 12.1. Regions of different scattering processes in the m - ζ domain.

scattering processes change completely depending on the circumstance that the phase shifts are small (the well-known Born approximation) or large compared to unity. The dividing line is approximately the diagonal of the square. The clearest physical interpretation with the simplest mathematical reductions of the scattering expressions is obtained for points in the $m-\zeta$ plane that satisfy at least two of the following inequalities:

$$\begin{aligned}\zeta \ll 1 &\quad \text{or} \quad \zeta \gg 1, \\ m - 1 \ll 1 &\quad \text{or} \quad m - 1 \gg 1, \\ \zeta|m - 1| \ll 1 &\quad \text{or} \quad \zeta|m - 1| \gg 1.\end{aligned}$$

The possibilities for this to occur are shown in the following table, in which the related simplified theories are also reported ('arb' denotes the arbitrary situation):

Simplified theory	Region	Relative size	Refractive index	Phase shift
Rayleigh–Debye	1	arb	$ m - 1 \ll 1$	$\zeta m - 1 \ll 1$
Total reflectors	4	arb	$ m - 1 \gg 1$	$\zeta m - 1 \gg 1$
Anomalous diffraction	2	$\zeta \gg 1$	$ m - 1 \ll 1$	arb
Surface modes	5	$\zeta \ll 1$	$ m - 1 \gg 1$	arb
Rayleigh	6	$\zeta \ll 1$	arb	$\zeta m - 1 \ll 1$
Geometrical optics	3	$\zeta \gg 1$	arb	$\zeta m - 1 \gg 1$

12.3.1 Particle size analysis

An example of the application of Mie theory is represented by the scattering of very large particles ($\zeta \gg 1$); i.e. particles with a mean size larger than the probe wavelength λ . We consider this type of scattering in some detail here because it is readily investigated by means of SALS. Technically, this scattering is referred to as *particle size analysis* and is of widespread use in many different areas of research and in technological applications.

For scattering particles with a very large size parameter ζ the angular distribution of the scattered intensity is dominated by the forward contribution. In fact in this experimental situation ($\zeta \gg 1$) Mie theory accounts for the intensity as a sum of reflection, refraction and diffraction contributions. This latter contribution dominates the intensity scattered at very low scattering angles. More precisely such a contribution is completely described by Mie theory in terms of the well-known Fraunhofer diffraction. In this case, for a single spherical scatterer we have the scattering matrix $S(\theta, \phi)$ (with $S_3(\theta, \phi) = S_4(\theta, \phi) = 0$ and $S_1(\theta, \phi) = S_2(\theta, \phi) = S(\theta, \phi)$):^[16]

$$S(\theta, \phi) = \frac{\zeta^2}{2} F(\zeta \sin \theta) = \frac{\zeta^2}{2} \frac{2J_1(\zeta \sin \zeta)}{\zeta \sin \theta} = \frac{\zeta J_1(\zeta \sin \theta)}{\sin \theta}, \quad (12.13)$$

where J_1 is the Bessel function of the first kind of order unity, so that the related intensity is

$$I(\theta) = I_0 a^2 \left[\frac{J_1(\zeta \sin \theta)}{\sin \theta} \right]^2, \quad (12.14)$$

where I_0 is the incident light intensity. Working at small angle, where $\sin \theta \approx \theta$ (i.e. $\theta \leq 8^\circ$), we can write

$$I(\theta) = I_0 a^2 \left[\frac{J_1(\zeta \theta)}{\theta} \right]^2. \quad (12.15)$$

In the real case of an assembly of polydisperse particles with a size distribution function $f(a)$, the intensity profile is

$$I(\theta) = I_0 \int_0^\infty f(a) \left[\frac{a^2 J_1(\zeta \theta)}{\theta} \right]^2 da. \quad (12.16)$$

This equation shows that the range of particle sizes a about which information can be obtained from a single measurement is limited by the information content of the observed scattered intensity pattern, by deviations from the scattering theory and by measurement errors. The latter effects are related to the experimental apparatus, so that here we give the related information.

The experimental set-up that can be used for particle size analysis is the same as that used in the other studies described in this chapter and therefore we discuss here its details and possibilities. Figure 12.2 represents a typical experimental set-up for small angle light scattering; it performs an optical Fourier transform. This is based on a linear sensitive detector with 1024 channels, but a square CCD or a diode array can also be used. The scattered spectrum is converted into a digital signal by means of an A/D converter and stored in a

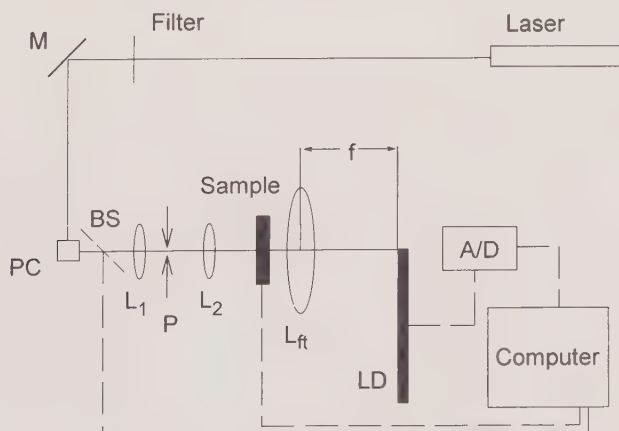


FIG. 12.2. A typical experimental set-up for small angle light scattering which is suited for optical Fourier transformation.

personal computer. The obtained signal has a dynamical range of 16 bits and each spectrum can be stored every 30 msec, after which it is processed. This is the typical simple experimental apparatus for SALS; however, we stress that great attention must be devoted to the optical alignment.

Methods for inverting the scattering pattern to retrieve $f(a)$ from the measured $I(\theta)$ may be divided into two classes: iterative techniques relying on numerical quadrature and integral transform methods. We discuss both these methods, considering first the integral transform inversion of the forward scattered light. The analytical inversion of eqn (12.16) is based on a Titchmarsh transform^[20] and was derived by Chin^[21] and Shifrin,^[22] giving

$$a^2 f(a) = \frac{-4\pi^2}{\lambda} \int_0^\infty \left((\zeta\theta) J_1(\zeta\theta) Y_1(\zeta\theta) \frac{d}{d\theta} (\theta^3 I_\theta) \right) d\theta, \quad (12.17)$$

where Y_1 is the Bessel function of the second kind of order unity, and $I_\theta = I(\theta)/I_0$. Equation (12.17) has been widely used in many experiments, although an obvious limitation is imposed by the requirement that the integral must be performed over the angular range $0 < \theta < \infty$, whereas the Fraunhofer diffraction result (eqn (12.13)) is valid only for a small range of scattering angles near $\theta = 0$. The truncation of the integral of eqn (12.17) at some angle θ_{\max} leads to noise in the inverted spectrum. This noise can be reduced by the use of the apodization function $A(\theta)$ is used, which ensures that $I(\theta)$ approaches zero smoothly as $\theta \rightarrow \theta_{\max}$. The form of $A(\theta)$ is

$$A(\theta) = \left(1 - \frac{\theta^2}{\theta_{\max}^2} \right)^2. \quad (12.18)$$

The effect of the apodization technique is to eliminate unwanted oscillations in the calculated size spectrum $f(a)$. Using such a procedure for direct inversion of the intensity data may result in considerable computational difficulties and non-physical solutions because of the large dynamic range of the data and of the related coefficients.

An alternative approach for the calculation of $f(a)$ considers the energy falling onto an annular ring from a distribution of particles defined by their weight distribution. By the use of planar detectors such as a square CCD, the scattered intensity can be monitored on computer-selected circular rings. The widths of the rings can be increased radially. This, together with an increase in the circumferential length, results in a substantial increase in the area of successive detector elements (rings) with the radius. In practice, the dynamic range of the data is compressed in the desired way. With the use of recent A/D converters and CCD drivers this can be obtained using simple software. From eqn (12.13) and the recurrence relations for the Bessel functions, the energy scattered by a distribution of spheres $f(a)$ in a forward cone of angle θ is given by

$$E = C \int_0^\infty a^2 f(a) \left[1 - J_0^2 \left(\frac{2\pi a\theta}{\lambda} \right) - J_1^2 \left(\frac{2\pi a\theta}{\lambda} \right) \right] da, \quad (12.19)$$

where C is a constant. Therefore the energy E_n scattered on to the n th ring of the detector and subtending an angular range $\theta_i^n < \theta < \theta_f^n$ is given by

$$E = C \int_0^\infty a^2 f(a) \left[J_0^2 \left(\frac{2\pi a \theta_i^n}{\lambda} \right) + J_1^2 \left(\frac{2\pi a \theta_i^n}{\lambda} \right) - J_0^2 \left(\frac{2\pi a \theta_f^n}{\lambda} \right) - J_1^2 \left(\frac{2\pi a \theta_f^n}{\lambda} \right) \right] da \quad (12.20)$$

and it is this quantity rather than $I(\theta)$ that is recorded by the detector array. The average intensity over the angular range covered by each detector is calculated by dividing each of the recorded energies by the area of the detector element. Therefore eqn (12.13) can be written as

$$a^2 f(a) = \frac{-4\pi^2}{\lambda} \left\{ \sum_{n=1}^{N_{\text{det}}} I_n \int_{\theta_i^n}^{\theta_f^n} \left((\zeta \theta) J_1(\zeta \theta) Y_1(\zeta \theta) \frac{d}{d\theta} (A(\theta) \theta^3) \right) d\theta \right. \\ \left. + \sum_{n=1}^{N_{\text{det}}-1} \int_{\theta_f^n - \delta}^{\theta_i^{n+1} + \delta} \left((\zeta \theta) J_1(\zeta \theta) Y_1(\zeta \theta) \frac{d}{d\theta} (A(\theta) \theta^3) I_n \right) d\theta \right\}, \quad (12.21)$$

where N_{det} is the number of detectors (rings) over which the integration is to be performed, and I_n is the average value of I associated with the n th detector. The first summation of eqn (12.21), considering the apodization function, can be written as

$$\sum_{n=1}^{N_{\text{det}}} I_n \int_{\theta_i^n}^{\theta_f^n} \left(\left(\frac{3(\zeta \theta)^3}{\zeta^3} - \frac{10(\zeta \theta)^5}{\zeta^5 \theta_{\max}^2} + \frac{7(\zeta \theta)^7}{\zeta^7 \theta_{\max}^4} \right) J_1(\zeta \theta) Y_1(\zeta \theta) \right) d\theta,$$

i.e. an integral that can be solved analytically.^[23] The second term of eqn (12.21) may be integrated by parts to obtain

$$\sum_{n=1}^{N_{\text{det}}-1} I_n \left\{ [(\zeta \theta) J_1(\zeta \theta) Y_1(\zeta \theta) A(\theta) \theta^3 I_n]_{\theta_f^n}^{\theta_i^{n+1}} \right. \\ \left. - \int_{\theta_f^n}^{\theta_i^{n+1}} A(\theta) \theta^3 I_n \frac{d}{d\theta} ((\zeta \theta) J_1(\zeta \theta) Y_1(\zeta \theta)) d\theta \right\}$$

and the second of these terms vanishes as $\theta_f^n \rightarrow \theta_i^{n+1}$. In this way the Chin-Shifrin inversion may be expressed in a form that does not require the experimental data to be differentiated numerically.

Not all the detector elements that fall within the detector-subtended angular range from θ_{\min} to θ_{\max} contain useful information for particle size analysis. Analytical inversion is strongly sensitive to the choice of θ_{\max} . For a particle of radius a , most of the diffracted energy is contained in the forward scattering angular cone $\theta_{\max}(a) \propto a^{-1}$, so that extending the inversion integral to $\theta > \theta_{\max}$ can only degrade the calculated size distribution by introducing unwanted noise. A suitable choice of the limiting angle to be used in particles sizing is $\theta \leq 15.47/\zeta$.^[24] Such a condition is applied separately at each value of ζ at which $f(a)$ is evaluated and is independent of the distribution of sizes in the

sample; in addition, it corresponds to the inclusion of 96% of the diffracted light in the calculation of $f(a)$.

As previously mentioned, another method of inverting the scattered pattern is to retrieve $f(a)$ from the measured $I(\theta)$ by iterative techniques. For this the following relation can be used:

$$[I(\theta)] = [K(\theta, a)] \cdot [f(a)], \quad (12.22)$$

where $[I(\theta)]$ is a vector of m elements (the number of detectors, i.e. the number of diodes or pixels in the diode array and in a CCD camera, respectively), $[f(a)]$ is a vector of m elements representing the unknown distribution function to be determined and $[K(\theta, a)]$ is a matrix of $m \times n$ elements which defines the intensity distribution curve for each particle. Relation (12.22) represents a system of equations that can be solved algebraically; however, due to the large dynamical range of the coefficients, large errors may be present. A good method is to guess an initial form of $f(a)$, which is subsequently rearranged by means of many numerical iterations with least squares under the condition of positive or zero values for the related coefficients (negative values represent a non-physical situation). Such an algorithm, widely used in quasi-elastic light scattering for the study of the size distribution function of particles with sizes in the sub-micron range, is named NNLS (non-negative least squares). Figure 12.3 shows typical results for the size distribution function, obtained using such a procedure, for water solutions of spherical latex particles with a radius of $11.9 \mu\text{m}$ and $26.6 \mu\text{m}$, with a standard deviation, σ , of $5.6 \mu\text{m}$ and $1.9 \mu\text{m}$, respectively. Figures 12.3(a) and 12.3(b) shows for comparison, typical results obtained by using the two different methods for a solution of particles with $a = 26.6 \mu\text{m}$ ($\sigma = 5.6 \mu\text{m}$). Figure 12.3(c) shows the result for $f(a)$ obtained by the use of analytical inversion in a mixture of particles having two different mean sizes.

12.4 Fluctuation theory of light scattering

We describe the scattering phenomena that fall in the area of the Rayleigh and Rayleigh-Debye scattering using the general formalism of *linear response theory*.^[25-27] In this model, scattering is considered from a molecular viewpoint and involves direct use of the correlation functions of the significant physical quantities. Thus the scattering problem is treated with a large generality independent of the probe wavelength used (neutrons, X-ray and light). The model can be applied when the coupling between system and probe is weak. In this condition it is only necessary to know how radiation and matter behave in the absence of coupling in order to describe the way in which one system responds to the other. This response is completely accounted for in terms of the correlation functions of the proper variables. Correlation functions, widely used in statistical mechanics, provide a simple method for expressing the degree to which physical properties are correlated in space and time.^[26,27] Their basic properties are relevant in order to explain cooperative phenomena by scattering studies. Linear response theory can be applied to scattering processes when the

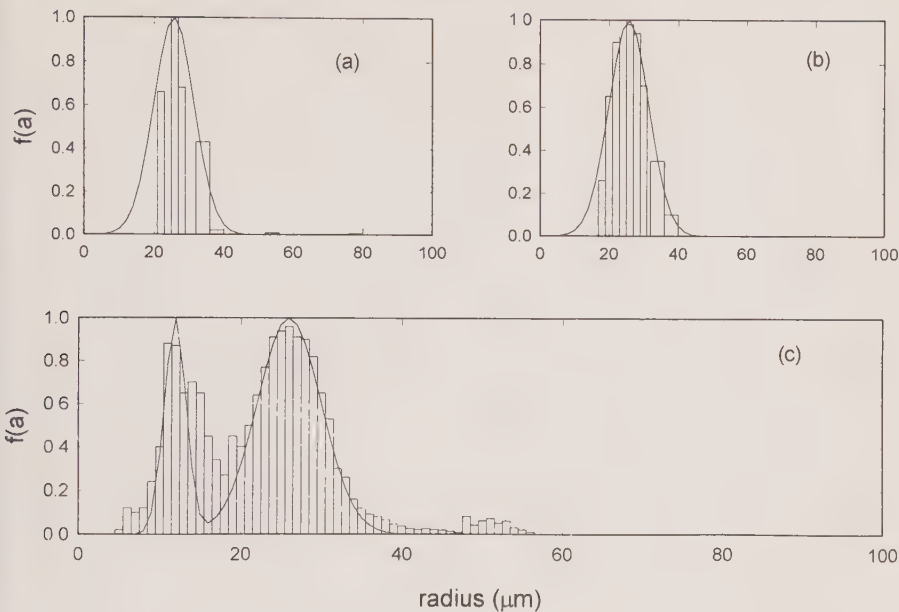


FIG. 12.3. Typical results for the size distribution function, obtained for water solutions of spherical latex particles with radii of 11.9 μm and 26.6 μm with standard deviations σ of 5.6 μm and 1.9 μm , respectively. (a, b) Typical results obtained by using the two different methods for a solution of particles with $a = 26.6 \mu\text{m}$ ($\sigma = 5.6 \mu\text{m}$) are shown for comparison. The result for $f(a)$ obtained by means of the analytical inversion in a mixture of particles with two mean different sizes.

Born approximation holds (for light, as previously mentioned, when the phase shift is small). This scattering formalism was applied for the first time in neutron scattering by van Hove,^[28] who gave the correct relationship between the scattered intensity and the density-density correlation function at the scattering wavevector \mathbf{k} and frequency ($k = (4\pi m/\lambda) \sin(\theta/2)$). The scattering wavevector is $\mathbf{k} = \mathbf{k}_i - \mathbf{k}_s$, where \mathbf{k}_i is the wavevector of the incident electric field and \mathbf{k}_s the scattered wavevector. In particular, the dynamic structure factor or power spectrum $S(\mathbf{k}, \omega)$, proportional to the scattered intensity, is the Fourier transform of the generalized pair correlation function $G(\mathbf{r}, t)$:

$$S(\mathbf{k}, \omega) = (2\pi)^{-1} N \int d\mathbf{r} dt \exp[i\mathbf{k}\mathbf{r} - t] G(\mathbf{r}, t), \quad (12.23)$$

with

$$G(\mathbf{r}, t) = N^{-1} \left\langle \sum_{i,j}^N \delta(\mathbf{r} + \mathbf{r}_i(0) - \mathbf{r}_j(t)) \right\rangle. \quad (12.24)$$

This latter equation well clarifies the meaning of $G(\mathbf{r}, t)$ as the probability that a particle will reside at time t at point \mathbf{r} , if another arbitrary particle is at

$\mathbf{r} = 0$ at time $t = 0$. In the static approximation, $t = 0$, this quantity becomes

$$G(\mathbf{r}, 0) = N^{-1} \left\langle \sum_{i,j}^N \delta(\mathbf{r} + \mathbf{r}_i(0) - \mathbf{r}_j(0)) \right\rangle \quad (12.25)$$

or

$$G(\mathbf{r}, 0) = \delta(\mathbf{r}) + N^{-1} \sum_{i,j}^N \langle \delta(\mathbf{r} + \mathbf{r}_i - \mathbf{r}_j) \rangle = \delta(\mathbf{r}) + g(\mathbf{r}), \quad (12.26a)$$

according to the definition of the conventional pair correlation function $g(\mathbf{r})$. The meaning of the latter equation is that the correlation function $G(\mathbf{r}, 0)$ can be partitioned into a self and a distinct part. By considering the system to be composed of distinguishable particles, G splits into two contributions referring, respectively, to correlations of positions of the same particle at different times and of pairs of distinct particles:^[28]

$$G(\mathbf{r}) = \delta(\mathbf{r}) + \rho g(\mathbf{r}) = G_s(\mathbf{r}) + G_d(\mathbf{r}). \quad (12.26b)$$

Thus

$$S(\mathbf{k}) = (2\pi)^{-1} N \int d\mathbf{r} \exp[i\mathbf{k}\cdot\mathbf{r}] G(\mathbf{r}, 0) = 1 + \rho \int d\mathbf{r} [g(\mathbf{r}) - 1] \exp[i\mathbf{k}\cdot\mathbf{r}], \quad (12.27)$$

where ρ is the number density of individual scatterers in the sample. The function

$$F(\mathbf{r}, t) = N^{-1} \sum_{i,j}^N \langle \exp(-i\mathbf{k}\cdot\mathbf{r}_i(0)) \exp(i\mathbf{k}\cdot\mathbf{r}_j(t)) \rangle \quad (12.28)$$

that corresponds to the space Fourier transform of $G(\mathbf{r}, t)$ is called the intermediate scattering function. For light scattering in the Rayleigh–Debye approximation it is easy to show that the scattered intensity can be written in terms of these two latter functions.

Considering the molecular polarizability $\underline{\alpha}_l$ the electric field scattered by the l th molecule at large distance \mathbf{r} is given by^[4,5,29]

$$\mathbf{E}_{sl}(r_l, t) = \frac{-k_s^2 E_0}{r_l} \exp(i\mathbf{k}_s r_l - \omega_i t) (\mathbf{n}_s \cdot \underline{\alpha}_l(t) \cdot \mathbf{n}_i) \exp(i\mathbf{k}\cdot\mathbf{r}_l), \quad (12.29)$$

where E_0 is the field amplitude, \mathbf{n}_i and \mathbf{n}_s are unit vectors indicating the directions of the incident and scattered electric fields (i.e. the polarization vectors), and \mathbf{r}_l is the position of the centre of mass of the considered molecule. The total intensity scattered by an assembly of N molecules at a distance R from the scattering volume is^[5,29]

$$\begin{aligned} I_s(\mathbf{r}, \omega) = & \left[\frac{I_0 k^4}{R^2} \right] \frac{1}{2\pi} \int_{-\infty}^{+\infty} dt \left\langle \sum_{i,j}^N (\mathbf{n}_s \cdot \underline{\alpha}_l(0) \cdot \mathbf{n}_i) (\mathbf{n}_s \cdot \underline{\alpha}_j(t) \cdot \mathbf{n}_i) \right. \\ & \times \exp i\mathbf{k}\cdot(\mathbf{r}_l(t) - \mathbf{r}_j(0)) \left. \right\rangle \exp i\omega t. \end{aligned} \quad (12.30)$$

The averaged quantity represents the intermediate scattering function of light $J(\mathbf{r}, t)$, and its time Fourier transform $T(\mathbf{r}, \omega)$ is the power spectrum. It is seen from eqn (12.30) that light scattering reflects molecular motion through the fluctuations of position (translation) and the fluctuation of the polarizability tensor (rotations and vibrations). Considering that the molecular polarizability tensor depends on the charge distribution in the molecules and that this distribution changes when the molecules vibrate, it is possible to split this into two contributions. The polarizability can be written in terms of the normal coordinates, \mathbf{q}^v , of the vibrational state as

$$\underline{\alpha} = \underline{\alpha}^0 + \sum_v \underline{\alpha}^v \mathbf{q}^v \quad \text{with} \quad \underline{\alpha}^v = (\partial \underline{\alpha} / \partial \mathbf{q}^v)_{\mathbf{q}^v=0}. \quad (12.31)$$

$\underline{\alpha}^0$ is the permanent polarizability tensor and $\underline{\alpha}^v$ the derivative polarizability tensor corresponding to the vibration v that, as is well-known, leads to Raman scattering. Considering only the contribution arising from $\underline{\alpha}^0$, the correlation function relevant for Rayleigh scattering is^[29]

$$J_{00}(\mathbf{k}, t) = \left\langle \sum_{l,j}^N (\mathbf{n}_s \cdot \underline{\alpha}_l^0(0) \cdot \mathbf{n}_i)(\mathbf{n}_s \cdot \underline{\alpha}_j^0(t) \cdot \mathbf{n}_i) \exp i\mathbf{k} \cdot (\mathbf{r}_l(t) - \mathbf{r}_j(0)) \right\rangle. \quad (12.32)$$

If translation and rotation are uncorrelated, for example if they appear on different time scales, it is reasonable to separate the two averages in the last equation. In addition, it is possible to split the permanent tensor $\underline{\alpha}^0$ into an isotropic $\alpha^0 \mathbf{I}$ (\mathbf{I} being the unit tensor) and an anisotropic part $\underline{\beta}^0$. With a suitable choice of the polarization directions \mathbf{n}_s and \mathbf{n}_i we can pick up out different aspects of the motion and can split this scattering contribution into depolarized $J_{00}^{VV}(\mathbf{k}, t)$ and polarized $J_{00}^{VH}(\mathbf{k}, t)$ parts:

$$J_{00}^{VV}(\mathbf{k}, t) = \sum_{l,j}^N \langle \alpha_l^0 \alpha_j^0 \rangle \langle \exp i\mathbf{k} \cdot (\mathbf{r}_l(t) - \mathbf{r}_j(0)) \rangle, \quad (12.33)$$

$$J_{00}^{VH}(\mathbf{k}, t) = \sum_{l,j}^N \langle \beta_{l,yz}^0(0) \beta_{j,zx}^0(t) \rangle \langle \exp i\mathbf{k} \cdot (\mathbf{r}_l(t) - \mathbf{r}_j(0)) \rangle. \quad (12.34)$$

β_{yz} are the relevant tensor components in the laboratory frame. The polarized intermediate scattering function is formally identical to that for neutron scattering: see eqns (12.24) and (12.28). This means that VV Rayleigh light scattering and coherent neutron scattering contain *a priori* the same kinds of information about collective translational motion in the system, the difference being the different k -ranges which can be explored. Since space and time scales (due to better energy resolution) are larger with light than with neutrons, light scattering is more suitable than neutrons to test slow and large length-scale phenomena. Finally, in the case of optically isotropic molecules ($\underline{\alpha}_l = \alpha$) the

intensity of the scattered light is

$$I_s(\mathbf{k}, \omega) = \left[\frac{I_0 k^4}{R^2} \right] \frac{N_i^2 \alpha^2}{2\pi} \int_{-\infty}^{+\infty} dt \left\langle \sum_{l,j}^N \exp i\mathbf{k} \cdot (\mathbf{r}_l(t) - \mathbf{r}_j(0)) \right\rangle \exp i\omega t, \quad (12.35)$$

where N_i represent the number of scattering molecules.

The intermediate scattering function in Rayleigh scattering can be used to investigate the properties of complex liquids. In this case the great majority of molecules are arranged in supramolecular aggregates.^[1-3] Focusing our interest on the structural properties of such networks, we first consider the static approximation for isotropic scattering. We limit the discussion to isotropic scattering only for simplicity, although we stress that the following considerations can also be applied also with polarized scattering. In this case we consider time-independent phenomena, so that the intermediate scattering function function can be written as

$$J_{is}(\mathbf{k}) = J_{is}(\mathbf{k}, 0) = N_i^2 \alpha^2 \left\langle \left| \sum_l^N \exp(i\mathbf{k} \cdot \mathbf{r}_l) \right|^2 \right\rangle. \quad (12.36)$$

This result can be redefined without losing generality, by considering separately scattering from molecules and aggregates as macromolecules, colloids and polymers. The scattering system can be thought of as partitioned into N_p cells (aggregates) each containing N_i molecules.^[30] Such a picture is represented in Fig. 12.4. Relabelling molecules with the subscripts i and j , we have

$$J_{is}(\mathbf{k}) = N_i^2 \alpha^2 \left\langle \left| \sum_{i=1}^{N_p} \sum_{j=1}^{N_i} \exp(i\mathbf{k} \cdot \mathbf{r}_{ij}) \right|^2 \right\rangle, \quad (12.37)$$

where \mathbf{r}_{ij} is the position of the j th molecule contained in the i th cell. If \mathbf{R}_i denotes the position of the centre of mass of the aggregate and \mathbf{x}_j the relative position of a molecule at \mathbf{r}_{ij} , we can write

$$J_{is}(\mathbf{k}) = N_i^2 \alpha^2 \left\langle \left| \sum_{i=1}^{N_p} \exp(i\mathbf{k} \cdot \mathbf{R}_i) \cdot \sum_{j=1}^{N_i} \exp(i\mathbf{k} \cdot \mathbf{x}_j) \right|^2 \right\rangle. \quad (12.38)$$

If we define the quantity

$$F_i(\mathbf{k}) = \sum_{j=1}^{N_i} \exp(i\mathbf{k} \cdot \mathbf{x}_j) \quad (12.39)$$

as the form factor $F_i(\mathbf{k})$ of the i th particle or aggregate, we have

$$J_{is}(\mathbf{k}) = N_i^2 \alpha^2 \left\langle \sum_{i=1}^{N_p} \sum_{i'=1}^{N_p} F_i(\mathbf{k}) F_{i'}^*(\mathbf{k}) \exp[i\mathbf{k} \cdot (\mathbf{R}_i - \mathbf{R}_{i'})] \right\rangle. \quad (12.40)$$

$F_i(\mathbf{k})$, also called the field amplitude, is connected with the individual scattering lengths b_{ij} of the scatterers in the cell containing the i th aggregate,

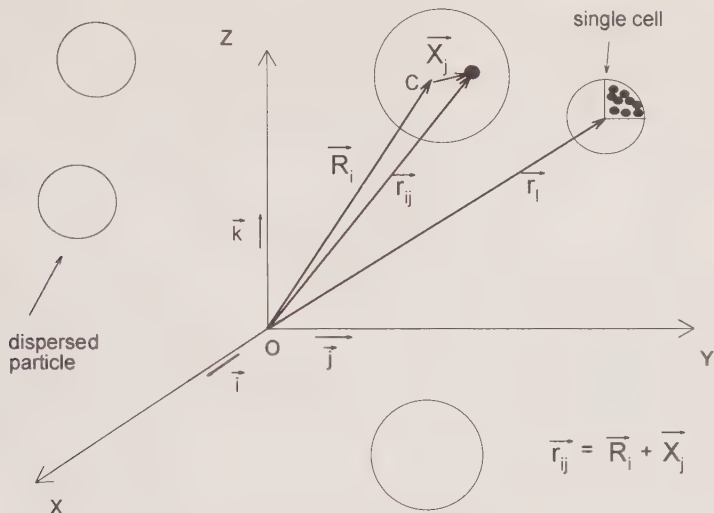


FIG. 12.4. A schematic representation of a scattering process for disperse supramolecular aggregates. The scattering system is partitioned into N_p cells (aggregate) each containing N_i molecules.

and can be defined as the Fourier transform of the scattering length densities. In fact, defining the scattering-length density at position \mathbf{r} of the i th cell as

$$\rho_i(\mathbf{r}) = \sum_j^{N_i} b_{ij} \delta(\mathbf{r} - \mathbf{x}_j), \quad (12.41)$$

the form factor can be rewritten as

$$F_i(\mathbf{k}) = \int_{\text{cell } i} d\mathbf{r} \rho_i(\mathbf{r}) \exp(i\mathbf{k} \cdot \mathbf{r}). \quad (12.42)$$

Considering the last integral performed over the aggregate volume only, it follows that

$$F_i(\mathbf{k}) = \int_{\text{agg } i} d\mathbf{r} [\rho_i(\mathbf{r}) - \rho_s] \exp(i\mathbf{k} \cdot \mathbf{r}) + \rho_s \int_{\text{cell } i} d\mathbf{r} \exp(i\mathbf{k} \cdot \mathbf{r}), \quad (12.43)$$

where ρ_s is the scattering-length density of the solvent. Since the second integral is simply a function centred at $\mathbf{k} = \mathbf{0}$,

$$F_i(\mathbf{k}) = \int_{\text{agg } i} d\mathbf{r} [\rho_i(\mathbf{r}) - \rho_s] \exp(i\mathbf{k} \cdot \mathbf{r}), \quad \text{for } \mathbf{k} \neq \mathbf{0}. \quad (12.44)$$

The quantity $[\rho_i(\mathbf{r}) - \rho_s]$ is often called the contrast. The above form factor represents a general expression for a disperse solution, and constitutes a standard result which is used extensively in neutron scattering. The contrast

defines the difference between the scattering properties of the dispersed aggregates, measured through the density ρ_i of the particles and the equivalent quantity corresponding to the solvent treated as a continuum. The scattering density, depending on the scattering technique, is related to different physical quantities, and in light scattering it is identified with the molecular polarizability ($\alpha_i = \alpha$ in the present case). With X-rays it is proportional to the atomic number Z and is a function of the interaction between the electromagnetic field and the electron cloud. For neutron scattering it is connected to the coherent scattering length b_i which, being dependent on the nucleus, is characteristic of each isotope. This latter situation makes it possible to isolate different parts of a given molecule by means of isotopic substitution. In a neutron experiment, which is usually performed at small angles (SANS – small angle neutron scattering), care must be taken in order to subtract the constant background due to incoherent scattering.

It is important to consider that, in general, a complex liquid system is made up of polydisperse structures, i.e. the form factor can be different for different aggregates. In such a case the intermediate scattering function becomes

$$J_{is}(\mathbf{k}) = N_i^2 \alpha^2 \left\langle \sum_{i=1}^{N_p} \sum_{i'=1}^{N_p} \langle F_i(\mathbf{k}) F_{i'}^*(\mathbf{k}) \rangle \exp[i\mathbf{k} \cdot (\mathbf{R}_i - \mathbf{R}_{i'})] \right\rangle, \quad (12.45)$$

where the angle brackets represent an average weighted by the distribution of aggregate sizes. The last expression can be written down, assuming weak correlation of aggregate size and aggregate position. On the basis of this approximation, and considering that

$$\langle F_i(\mathbf{k}) F_{i'}^*(\mathbf{k}) \rangle = \langle |F(\mathbf{k})|^2 \rangle \quad \text{for } i = i',$$

and

$$\langle F_i(\mathbf{k}) F_{i'}^*(\mathbf{k}) \rangle = |\langle F(\mathbf{k}) \rangle|^2 \quad \text{for } i \neq i',$$

we have

$$\langle F_i(\mathbf{k}) F_{i'}^*(\mathbf{k}) \rangle = |\langle F(\mathbf{k}) \rangle|^2 + [|\langle F(\mathbf{k}) \rangle|^2 - |\langle F(\mathbf{k}) \rangle|^2] \delta_{ii'}, \quad (12.46)$$

where $\delta_{ii'}$ is the Kronecker delta. In this situation $J_{is}(\mathbf{k})$ becomes

$$\begin{aligned} J_{is}(\mathbf{k}) = N_i^2 \alpha^2 N_p & \left\{ [|\langle F_i(\mathbf{k}) \rangle|^2 - |\langle F_i(\mathbf{k}) \rangle|^2] \right. \\ & \left. + |\langle F_i(\mathbf{k}) \rangle|^2 \left\langle \sum_{i=1}^{N_p} \sum_{i'=1}^{N_p} \exp[i\mathbf{k} \cdot (\mathbf{R}_i - \mathbf{R}_{i'})] \right\rangle \right\}. \end{aligned} \quad (12.47)$$

Defining the interparticle structure factor, eqn (12.23), as

$$S(\mathbf{k}) = N_p^{-1} \left\langle \sum_{i=1}^{N_p} \sum_{i'=1}^{N_p} \exp[i\mathbf{k} \cdot (\mathbf{R}_i - \mathbf{R}_{i'})] \right\rangle, \quad (12.48)$$

eqn (12.45) becomes

$$J_{is}(\mathbf{k}) = \alpha^2 N_i^2 N_p \{ [|\langle F_i(\mathbf{k}) \rangle|^2 - |\langle F_i(\mathbf{k}) \rangle|^2] + |\langle F_i(\mathbf{k}) \rangle|^2 S(\mathbf{k}) \}. \quad (12.49)$$

The scattered intensity will be

$$I_s(\mathbf{k}) = \frac{I_0 k^4 N_i^2 N_p \alpha^2}{R^2 V} [P(\mathbf{k}) + |\langle F(\mathbf{k}) \rangle|^2 (S(\mathbf{k}) - 1)] \quad (12.50a)$$

or, in more compact form,

$$I_s(\mathbf{k}) = \frac{I_0 k^4 N_i^2 N_p \alpha^2}{R^2 V} P(\mathbf{k}) \cdot \tilde{S}(\mathbf{k}), \quad (12.50b)$$

where V is the sample volume.

In eqn (12.50a) the scattered intensity is split into two contributions due, respectively, to the *self* and *distinct* parts (eqns 12.26a and 12.26b). Equation (12.50b) shows that the scattered intensity has, as an effect of the polydispersity, the following *effective solution structure factor*:

$$\tilde{S}(\mathbf{k}) = 1 + \frac{|\langle F(\mathbf{k}) \rangle|^2}{\langle |F(\mathbf{k})|^2 \rangle} [S(\mathbf{k}) - 1], \quad (12.51)$$

while the form factor $F(\mathbf{k})$ is related to $P(\mathbf{k})$ through

$$P(\mathbf{k}) = \langle |F(\mathbf{k})|^2 \rangle. \quad (12.52)$$

When the system is made by an arrangement of monodisperse aggregates, we have

$$|\langle F(\mathbf{k}) \rangle|^2 = \langle |F(\mathbf{k})|^2 \rangle \quad \text{and} \quad \tilde{S}(\mathbf{k}) = S(\mathbf{k}), \quad (12.53, 12.54)$$

so that

$$I_s(\mathbf{k}) = \frac{I_0 k^4 N_i^2 N_p \alpha^2}{R^2} P(\mathbf{k}) \cdot S(\mathbf{k}). \quad (12.55)$$

In conclusion, we observe that eqn (12.50b) correctly represents the elastic scattered intensity for a complex liquid system. Next, we consider the form factor $P(\mathbf{k})$ and the structure factor $\tilde{S}(\mathbf{k})$, which give information about their calculation for different systems in many different physical situations, in particular when the system is arranged in structures of large size.

12.4.1 Form factor

Depending on the characteristic geometries of the supramolecular aggregates, the above integration can be carried out to give the correct form factor. In the following, we give the results of such a calculation for aggregates of different shape that are representative of real systems that can be studied in light scattering experiments.^[5,31] We shall then consider as an example the effect of polydispersity for spherical and spheroidal particles.

(a) *Homogeneous sphere* of radius R and density ρ :

$$F_i(\mathbf{k}) = F_i(kR) = V(\rho - \rho_s) \frac{3j_1(kR)}{kR}, \quad (12.56)$$

where $j_1(R)$ is the first-order spherical Bessel function,

$$j_1(kR) = \frac{\sin(kR) - kR \cos(kR)}{(kR)^2}. \quad (12.57)$$

(b) *Hollow sphere* with radius R and inner radius R_I :

$$F_i(\mathbf{k}) = F_i(X) = V(\rho - \rho_s) \left[\frac{3}{X^3(1 - \gamma^3)} \{ \sin(X) - \sin(\gamma X) \right. \\ \left. - X \cos(X) + \gamma X \cos(\gamma X) \} \right]^2, \quad (12.58)$$

where $X = kR$ and $\gamma = R_I/R$.

(c) *Thin rod* of length L , with $X = kL$:

$$F_i(\mathbf{k}) = F(X) = V(\rho - \rho_s) \frac{2}{X} \int_0^X \frac{\sin Z}{Z} dZ - \left[\frac{2}{X} \sin \frac{X}{2} \right]^2. \quad (12.59)$$

(d) *Infinitely thin disc* with a radius R and $X = kR$:

$$F_i(\mathbf{k}) = F_i(kR) = V(\rho - \rho_s) \frac{2}{X} \frac{1 - j_1(2X)}{X}. \quad (12.60)$$

(e) *Circular cylinder* of length L and radius R , with $X = kL \cos(\beta)$ and $Y = kR \sin(\beta)$:

$$F_i(\mathbf{k}) = F_i(kR) = V(\rho - \rho_s) \int_0^{\pi/2} \frac{\pi}{X} \left[\frac{2j(1/2)j_1(Y)}{Y} \right]^2 \sin(\beta) d\beta. \quad (12.61)$$

(f) *Gaussian coil* with radius of gyration R_G and $X = kR_G$:

$$F_i(\mathbf{k}) = F_i(kR) = V(\rho - \rho_s) \frac{2}{X^4} [\exp(-X^2) + X^2 - 1]. \quad (12.62)$$

In these cases, when the system is nearly monodisperse and very dilute, the solution can be considered as ideal, and particle-particle correlation is essentially absent, $S(\mathbf{k}) \approx 1$ and $I(\mathbf{k}) \propto P(\mathbf{k})$. The measured intensity $I(\mathbf{k})$ reflects the size, shape and internal features of the particles, and can be described by means of the distribution of the mean length density. For example, for monodisperse non-interacting spheres,

$$I(\mathbf{k}) \propto P(\mathbf{k}) = V^2(\rho - \rho_s)^2 \left\{ 3 \frac{\sin(kR) - kR \cos(kR)}{(kR)^3} \right\}^2. \quad (12.63)$$

It is illustrative in this case to verify the behaviour of the function $P(\mathbf{k})$ at small and large values of the scattering wavevector \mathbf{k} which defines the explored length range.

(a) For $kR \ll 1$ expansion of eqn (12.63) yields

$$P(\mathbf{k}) = V^2(\rho - \rho_s)^2 \left\{ 1 + \frac{R^2 k^2}{5} \right\}. \quad (12.64)$$

This result is the well-known Guinier approximation,^[32,33] and is suitably applied to spheres in which the gyration radius R_g is connected to the effective radius through the relation $R_g = \sqrt{3/5} R$, and

$$P(\mathbf{k}) = V^2(\rho - \rho_s)^2 \left\{ 1 + \frac{R_g^2 k^2}{3} \right\} \cong V^2(\rho - \rho_s)^2 \exp \left\{ -\frac{R_g^2 k^2}{3} \right\} \quad (kR \ll 1). \quad (12.65)$$

(b) For large k ($kR \gg 1$) the average $P(\mathbf{k})$ decreases as k^{-4} , and from eqn (12.63), putting $\sin^2 x = \cos^2 x = 1/2$,

$$P(\mathbf{k}) = \frac{9V^2(\rho - \rho_s)^2}{2} \frac{1}{(kR)^4}. \quad (12.66)$$

This is the so-called Porod law,^[32,33] which characterizes the scattered intensity of a system where the two densities ρ and ρ_s are separated by a sharp boundary. The general form of the Porod law obtained with a more detailed treatment is

$$P(\mathbf{k}) = \frac{2\pi S(\rho - \rho_s)^2}{k^4}, \quad (12.67)$$

where S is the total surface of the boundary. In Fig. 12.5 we plot with a solid line $P(\mathbf{k})$, normalized to $V^2(\rho - \rho_s)^2$, versus kR as calculated from eqn (12.63) in the above case, i.e. a homogeneous sphere of radius R and density ρ . In the same figure the dot-dash line is obtained from eqn (12.66), which gives the same quantity in the Porod regime, and shows the k^{-4} dependence.

For polydisperse homogeneous spheres it is illustrative to show the analysis reported in the work of Kotlarchyk and Chen,^[30] where the form factors for different colloidal systems are given. In that paper, in particular, the properties of non-spherical particles are also discussed, and it is shown that the orientational average yields similar effects in the effective interparticle structure factor $\tilde{S}(\mathbf{k})$, at least qualitatively, to those observed in polydispersity. It is shown in terms of different real examples that such an analysis has wide applicability. A variety of systems have been studied, including homogeneous polydisperse colloids, as water-in-oil microemulsions far from a phase boundary (weakly interacting system), water-in-oil microemulsions near a critical point (strongly attractive), ionic micellar solution (a strongly repulsive system) and aqueous solutions of the globular protein bovine serum albumin which are known to constitute a

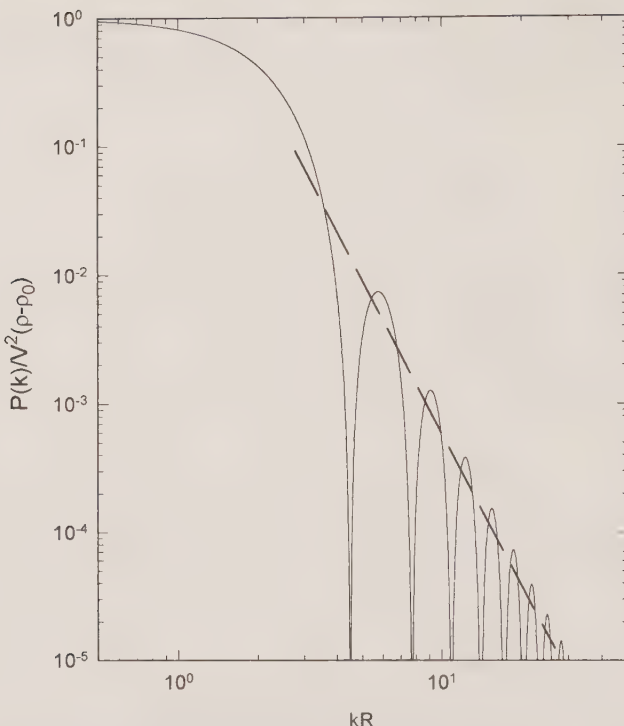


FIG. 12.5. A log-log plot of the form factor $P(\mathbf{k})$ normalized to $V^2(\rho - \rho_s)^2$ (continuous line), versus kR as obtained from eqn (12.63) for an homogeneous sphere of radius R and density ρ . The dotted-dashed line (eqn (12.66)), gives the same quantity in the Porod regime.

strongly repulsive system with non-spherical particles. Figure 12.6 shows some characteristic SANS data together with the corresponding results of the analysis performed in these different polydisperse colloids.^[30] This work is instructive because it provides a useful way of regarding SANS spectra, and it provides unusually exact models for polydispersity in the presence of specific interparticle interactions.

The approximations in such a procedure for calculation of the differential cross-sections are made essentially by considering correlations between the particle orientation and the particle position to be absent. In the case of polydisperse homogeneous spheres, the averages for computing the scattered cross-section are

$$\langle |F(\mathbf{k})|^2 \rangle = \int_0^\infty |F(\mathbf{k})|^2 f(R) dR \quad (12.68)$$

and

$$|\langle F(\mathbf{k}) \rangle|^2 = \left| \int_0^\infty F(kR) f(R) dR \right|^2, \quad (12.69)$$

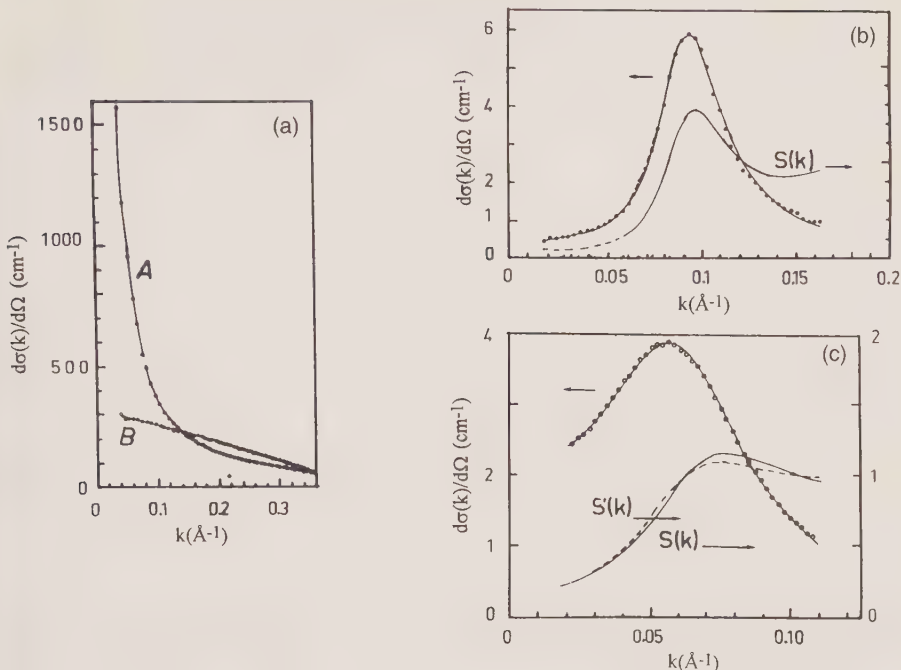


FIG. 12.6. SANS spectra and best fit curves obtained considering size polydispersity, respectively, for water-in-oil microemulsions near a critical point (a), ionic micellar solution (b) and aqueous solutions of bovine serum albumin (a globular protein) (c) (Figs 4, 6 and 8 respectively of ref. 30).

where $F(kR)$ is given by eqn (12.56) and $f(R) dR$ is the probability of a sphere having a radius between R and $R + dR$. The above integrals have been computed for a rectangular distribution and for the more realistic Schulz distribution,^[34] for which $f(R)$ is given by the following expression:

$$f(R) = \left[\frac{u+1}{\bar{R}} \right]^{u+1} R^u \exp \left[- \left[\frac{u+1}{\bar{R}} R \right] \right] \frac{1}{\Gamma(u+1)}, \quad u > -1, \quad (12.70)$$

where \bar{R} is the mean of the distribution, u is the width parameter and $(u+1)$, the gamma function. For large u the distribution approaches a Gaussian form, and a delta function at $R = \bar{R}$ as u approaches infinity. The corresponding root mean square deviation from the mean is

$$\sigma_R = (\bar{R}^2 - \bar{R}^2)^{1/2} = \bar{R}/(u+1)^{1/2}. \quad (12.71)$$

The j th moment of the Schultz distribution is easily calculated as

$$\langle R^j \rangle = \frac{\Gamma(u+j+1)}{\Gamma(u+1)} \left[\frac{\bar{R}}{u+1} \right]^j. \quad (12.72)$$

To study non-spherical particles, useful averages of the form factor are

$$\langle |F(\mathbf{k})|^2 \rangle = \int_0^1 |F(k, a, b, \mu)|^2 d\mu, \quad (12.73)$$

$$|\langle F(\mathbf{k}) \rangle|^2 = \left| \int_0^1 F(k, a, b, \eta) d\mu \right|^2 \quad (12.74)$$

and

$$F(k, a, n, \eta) = V(a, b)(\rho - \rho_s) \frac{3j_1(x)}{x}, \quad (12.75)$$

where $F(k, a, b, \mu)$ is the form factor for a spheroid with semi-major axis a and semi-minor axis b . The integration variable μ is the cosine of the angle between \mathbf{k} and the direction of the spheroid major axis. For a prolate spheroid,

$$x = k[a^2\mu^2 + b^2(1 - \mu^2)]^{1/2}, \quad V(a, b) = (4\pi/3)a^2b \quad (12.76)$$

and for an oblate spheroid,

$$x = k[a^2(1 - \mu^2) + b^2\mu^2]^{1/2}, \quad V(a, b) = (4\pi/3)a^2b. \quad (12.77)$$

Using these equations, $P(k)$ can be explicitly calculated for light scattering^[30] (at least for spherical suspensions) with a Schultz polydispersity.

12.4.2 The structure factor

Statistical mechanics and current theories for liquids give us powerful methods to use in order to calculate the structure factor $S(\mathbf{k})$. At the present time for a large class of complex fluids (microemulsions, micelles, colloids and polymer solutions) calculation of this quantity and comparison with experimental results is routine. In addition, from eqn (12.50b) the importance of the calculation of the structure factor $S(\mathbf{k})$ to obtain $\tilde{S}(\mathbf{k})$, in order to clarify the interparticle properties and the effects of polydispersity, is clear. In particular, polydispersity may arise from different system properties. It is well known that the properties of charged colloids are determined by size and charge polydispersity, and the same occurs in polyelectrolyte solution or in gels. For a polydisperse system, partial structure factors $S_{ij}(\mathbf{k})$ are usually determined by solving the matrix form of the Ornstein-Zernike equation for the pair potential U_{ij} between particles with hard-core diameters σ_i and σ_j . But the developed formalism ignores correlations between droplet size and position, and therefore it is necessary to deal with the average structure factor $S(\mathbf{k})$ which can be calculated by means of the actually used microscopic theories of liquids.

It is reasonable^[30,35] to approximate $S(\mathbf{k})$ with a structure factor calculated from the one-component Ornstein-Zernike equation,^[12] using an effective potential with a physically meaningful value for the hard-core diameter. We will describe this procedure because it represents, at this time, the most widely used and valid method for studying colloidal particles, and also because it

represents the most significant method developed from liquid state physics concepts for the calculation of the structure factors. In this calculation it is assumed that the colloidal spheres interact via an interparticle potential function made up of a hard core of range σ plus an attractive Yukawa tail:

$$\frac{U_a(x)}{k_B T} = -\gamma \frac{\exp[-k'x]}{x}, \quad x > 1, \quad (12.78)$$

where $x = r/\sigma$, $k' = k\sigma$ and r is the interparticle separation. The range of the attractive tail is given by k'^{-1} and the contact potential is $\gamma \exp(-k)$, with $\gamma > 0$. The structure factor $S(k)$ can be calculated by first solving the Ornstein-Zernike equation for the net correlation $h(x)$,

$$h(x) = C(x) + \frac{N_p}{V} \sigma^3 \int h(x - \xi) C(\xi) d\xi^3, \quad (12.79)$$

and subsequently, taking the Fourier transform,

$$S(k) = 1 + 4\pi \frac{N_p}{V} \sigma^3 \int_0^\infty dx x^2 h(x) \frac{\sin(k\sigma x)}{k\sigma x}. \quad (12.80)$$

For this calculation, an approximate closure relating $h(x)$ with $C(x)$ and the pair potential is necessary. The *ansatz* of the mean spherical approximation (MSA)^[36]

$$h(x) = -1 \quad \text{for } x < 1, \quad (12.81)$$

$$C(x) = -\frac{U_a(x)}{k_B T} \quad \text{for } x > 1, \quad (12.82)$$

allows eqn (12.79) to be solved. This approximation (MSA) has been successfully applied to colloidal particles with a repulsive potential ($\gamma < 0$)^[37] and for the analysis of critical scattering from non-ionic micelles which interact through an attractive potential.^[38] These studies, together with a number of works mentioned previously, indicate that the MSA is valid for an attractive potential where the system is not too close to the critical point. In this latter case it is well known that the experimental data can be analysed by means of the modified Ornstein-Zernike^[12] form, valid in the small k region,

$$S(k) = 1 + \chi(T)[1 + k^2 \xi(T)^2]^{-1}, \quad (12.83)$$

for which the limit

$$\lim_{k \rightarrow 0} S(k) = n_p k_B T \chi_T = 1 + \chi(T) \cong \chi(T) \quad (12.84)$$

can be taken (ξ is the correlation length of critical fluctuations and χ is connected with the isothermal osmotic compressibility χ_T).

For more complex situations, for example charged systems or other potential forms, different closure equations can be used. Together with the MSA^[36] typical examples are the Percus-Yevik (PY)^[39] and the more sophisticated

hypernetted chain (HNC)^[40] approximations. Although MSA yields analytical solutions both for the monodisperse case and mixtures, and the PY is appropriate for hard core potentials, these closure schemes are not thermodynamically consistent. The corresponding values of the isothermal compressibility χ_T depend on the calculation route. χ_T can be derived from either the compressibility or the virial equations of state. The thermodynamic consistency and the improvement of structural quantities can be obtained from a ‘mixing’ of the PY and HNC as has been done by Rogers–Young (RY).^[41] This calculation procedure works well for repulsive potentials; an extension to potentials with attractive parts has been developed by ‘mixing’ HNC and MSA. These arguments, for charged polydisperse colloids, are reported in the work of Klein^[42] and summarized in Chapter 2 of the present volume. The obtained spectra can be analysed in this way, and the closure equation for $S(k)$, together with the averages for the form factor, can give an accurate method of calculation. In Fig. 12.6 the results of MSA for microemulsions are summarized and Fig. 12.7 shows the results of a calculation for a charged colloidal solution that consider both the size and charge polydispersity.^[42] Obviously, in deriving the spectra some quantities are used as fitting parameters, such as \bar{R} and u for the form factor, with ξ and χ for critical phenomena. In the normal phase regions the parameters used in the MSA are k' , σ and $\gamma \exp(-k')$, which give detailed information about the physical properties of the system. In addition, these arguments on the structure factor must be considered as very useful and instructive in order to test, by means of the comparison of experimental data with calculations, the properties of colloidal systems at very low k , i.e. in the hydrodynamic regime where many cooperative phenomena remain unclear.

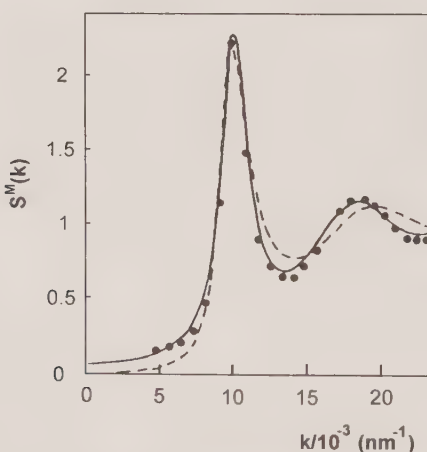


FIG. 12.7. A comparison of two different fittings of an experimentally measured structure factor obtained for a charged, monodisperse (dotted line) and, polydisperse (continuous line) colloidal solution. The calculation considers both the size and charge polydispersity (Fig. 12 of ref. 42).

Studies of charged colloidal solutions in this regime by means of SALS can furnish deeper insights into their properties.

12.4.3 Applications of light scattering to macromolecules and polymers

Equations (12.50a) and (12.50b) give the integrated intensity of the scattered light from disperse systems. Next, we discuss some applications that are representative of many physical situations. In eqn (12.50a) the intensity is partitioned as the sum of two parts: i.e. the *self* (proportional to the form factor) and the *distinct* (proportional to the structure factor) contributions. $N_i^2 N_p$ terms contribute to the *self* part, whereas in the *distinct* contribution we have $N_i^2 N_p(N_p - 1)$ terms. In addition, it is well known that the polarizability α can be related to both the mean refractive indices of the solution, m_s , and the solvent, m_0 , and the aggregate concentration^[43,44] by:

$$\alpha = \frac{m_0(m_s - m_0)}{2\pi(N_p N_i/V)} \cong \frac{m_0[c_p(\partial m_s/\partial c_p)_{T,\mu'}]}{2\pi(N_p N_i/V)}, \quad (12.85)$$

where $c_p = (M_p N_p / N_A V)$ (in g/cm³) is the concentration of the dispersed medium, M_p is the corresponding molar mass, N_A is Avogadro's number, μ' is the chemical potential of the remaining species in solutions and N_p/V is the number density of the particles. In these terms, putting

$$S'(\mathbf{k}) = |\langle F(\mathbf{k}) \rangle|^2 (S(\mathbf{k}) - 1), \quad (12.86)$$

we have

$$I_s(\mathbf{k}) = I_0 k^4 \left[\frac{m_0(\partial m_s/\partial c_p)_{T,\mu'}}{2\pi R^2} \right]^2 \left[\frac{M_p c_p V P(\mathbf{k})}{N_A} + c_p^2 V^2 S'(\mathbf{k}) \right]. \quad (12.50c)$$

In order to have a separation of instrumental parameters from molecular ones, this equation is rearranged considering the Rayleigh ratio R and a quantity H that contains only known quantities (such as N_A) or measurable ones (such as the refractive index increment at constant temperature and chemical potential μ'). The parameter H is defined as^[5,16]

$$H = \frac{[2\pi m_0(\partial m_s/\partial c_p)_{T,\mu'}]^2}{\lambda^4 N_A} \quad (12.87)$$

and the Rayleigh ratio as^[44]

$$R_\theta = F(\theta) \frac{I_s(\theta)}{VI_0} R^2, \quad (12.88)$$

where $F(\theta)$ is a term that includes all geometrical corrections. In fact, it takes into account the geometric relationship between the polarization of the incident light and the dependence of the scattering volume on the scattering angle. In particular, considering only the polarization correction,^[44] we have for VV polarization $F(\theta) = 1$, whereas for unpolarized light, $F(\theta) = 2/[1 + \cos^2 \theta]$.

A practical way to obtain R is to take values of R , V and I_0 from literature data for the Rayleigh ratio (R) corresponding to a simple liquid (benzene or toluene) with a scattered intensity I_R , so that $R = (I_s/I_R)R$.^[5,45] In such a case it is also important to consider the correction for the ratio between the refractive index of the sample and the reference fluid.^[45] The measured intensity data (eqn (12.40c)) are represented by

$$\frac{Hc_P}{R_g} = \frac{1}{M_p P(k) + N_A c_p V S'(k)}. \quad (12.89)$$

This equation can be applied to many different situations, depending on the size of the dispersed particles or on their concentration and interaction. In particular, it is used in a variety of systems, such as, for example, colloidal solutions, micelles and microemulsions and polymer solutions, and it has been put in different equivalent forms. For this we consider some limiting situations.

12.4.3.1 Small, non-interacting particles. In this situation we have $\mathbf{k} \cdot \mathbf{r} \ll 1$, so that $P(k) \sim 1$, and $S'(k) \sim 0$. Non-interaction between scattering particles means that scattering centres are completely uncorrelated. In this situation

$$Hc_P/R_\theta = 1/M_p \quad (12.90a)$$

or, considering some polydispersity in the dispersed macromolecular aggregates or polymer,

$$Hc_P/R_\theta = 1/\langle M_p \rangle_W, \quad (12.90b)$$

where $\langle M_p \rangle_W$ is the ‘weight-average’ molar mass:

$$\langle M_p \rangle_W = \left(\sum_i N_i M_i^2 \right) / \left(\sum_i N_i M_i \right). \quad (12.91)$$

Equation (12.90b) has been extensively used in the study of dilute solutions of very small (some tens of Å) macromolecules such as proteins, enzymes and polymers.

12.4.3.2 Large, non-interacting particles. When $\mathbf{k}\mathbf{r} \sim 1$, i.e. the sizes of the macromolecules are comparable with the probe wavelength and the solution is sufficiently dilute ($c_p \rightarrow 0$, and $S'(k) \sim 0$), we can write

$$\left. \frac{Hc_P}{R_g} \right|_{c_p \rightarrow 0} \frac{1}{M_p P(k)}. \quad (12.92)$$

This result can be used to obtain the particle form factor $P(k)$ from light scattering measurements. In particular, eqn (12.92) is used to explore the situations described in Section 12.4.3.1. Obviously, it represents a typical situation in which light scattering experiments must be performed at small angles (e.g. with large polymers or large colloids such as deoxyribonucleic acid (DNA) having a root-mean-square radius of gyration of about 7000 Å).^[46]

12.4.3.3 *Small, interacting particles.* In this situation ($P(k) \sim 1$) we can write eqn (12.89) as

$$\frac{Hc_P}{R_\theta} = \frac{1/M_P}{[1 + N_A c_P VS'(k)/M_P]}. \quad (12.93)$$

In the low concentration limit, this becomes

$$\left. \frac{Hc_P}{R_\theta} \right|_{c_p \rightarrow 0} \approx \frac{1}{M_P} - \frac{N_A c_P VS'(k)}{M_P^2}. \quad (12.94)$$

In order to use the two latter equations, the calculation of the quantity $VS'(k)$ considering the correct form of the interaction potential between the macromolecules is important. For example, in the case of identical macromolecules it is possible to write eqn (12.80) as

$$S(k) = 1 + 4\pi \frac{N_p}{V} \sigma^3 \int_0^\infty dx x^2 [g(x) - 1] \frac{\sin(k\sigma x)}{k\sigma x}. \quad (12.80a)$$

Considering eqns (12.86) and (12.53), we have

$$VS'(k) = V(S(k) - 1) = 4\pi N_p \sigma^3 \int_0^\infty dx x^2 [g(x) - 1] \frac{\sin(k\sigma x)}{k\sigma x}. \quad (12.80b)$$

In the limit where pairwise correlations are dominant (a situation obtained in the low density limit, i.e. $c_p \rightarrow 0$) the two-body correlation function and the integral in eqn (12.80b) are directly related to the second virial coefficient, B_2 .^[40]

$$B_2 = -\frac{1}{2} \int_0^\infty dx x^2 [g(x) - 1]. \quad (12.95)$$

Therefore eqn (12.94) becomes

$$\left. \frac{Hc_P}{R_\theta} \right|_{c_p \rightarrow 0} \approx \frac{1}{M_P} + \frac{N_A 2B_2}{M_P^2} c_p. \quad (12.96)$$

The second virial coefficient can be calculated using current methods of statistical mechanics.^[40] In fact, it is well known that in the low density limit

$$g(r)|_{c_p \rightarrow 0} \approx \exp\left[-\frac{U(r)}{k_B T}\right]$$

which, for weak interactions, becomes $g(r) \approx 1 - U(r)/k_B T$. Considering the correct potential form $U(r)$ for the specific system, for example, eqn (12.78) in the case of dilute microemulsions, B_2 can be calculated.

12.4.3.4 *Large, interacting particles (Zimm plot).* In such a situation, for moderate concentrations, the total intensity cannot be separated into self and distinct contributions, so that the studied system can only be described by means of the general expression in eqn (12.50b), and the effective structure

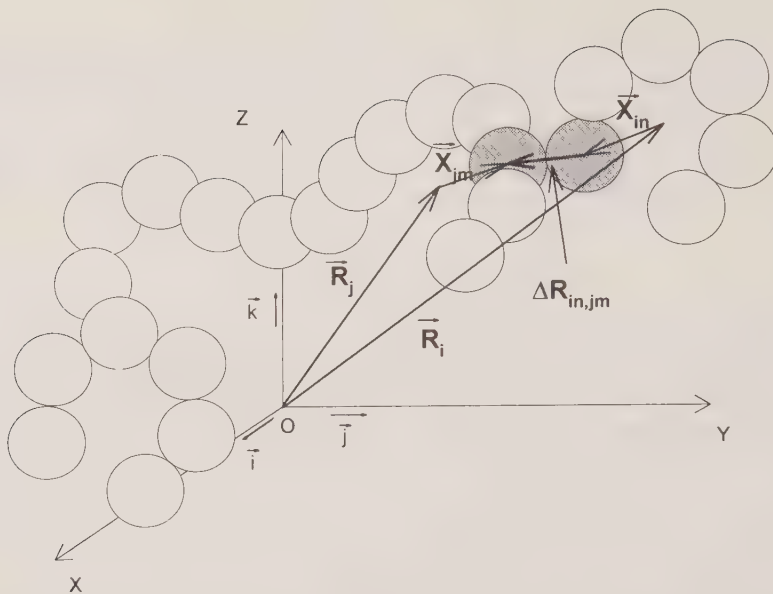


FIG. 12.8. A one-contact Zimm model for flexible coil molecules^[47] (or macromolecules aggregating in coil clusters).

factor must be calculated considering the real physical situation. In the following paragraphs we discuss this for some physical phenomena in which the structure factor can be obtained by means of well-defined scaling properties of the system.

Here we describe an example using an approximation that has been successfully applied to the study of polymer solutions; this is referred to as the *one contact approximation* and is due to Zimm;^[47] more precisely, the special case in which only one segment from each chain is in real physical contact is considered. This model is represented in Fig. 12.8 for flexible coil molecules (or macromolecules aggregating in clusters). As can be seen, the distance between the contact segments is $\mathbf{R}_{in,jm} = (\mathbf{R}_i + \mathbf{X}_{in}) - (\mathbf{R}_j + \mathbf{X}_{jm})$, where \mathbf{R}_i denotes the centre-of-mass position of the i th segment. Obviously, such a term in the limit of dilute solution can be associated with the second virial coefficient (eqns (12.48), (12.51) and (12.80b)) and eqn (12.89) can be written as

$$\frac{Hc_P}{R_\theta} = \frac{1}{M_P P(k)} \frac{1}{1 - [2B_2 N_A c_P P(k)/M_P]} \quad (12.97)$$

and for very small scattering angles one has

$$\begin{aligned} \frac{Hc_P}{R_\theta} &\approx \frac{1}{M_P} + \frac{16\pi^2 m_0^2 \langle R_G^2 \rangle}{3\lambda_0^2 M_P} \sin^2\left(\frac{\theta}{2}\right) + \frac{2B_2 N_A}{M_P^2} c_P \\ &= \frac{1}{M_P} + A \sin^2\left(\frac{\theta}{2}\right) + Bc_P. \end{aligned} \quad (12.98)$$

A plot of Hc_P/R versus $A \sin^2(\theta/2) + Bc_P$, with A and B as arbitrary constants, is referred to as a Zimm plot. The contact models constitute a powerful tool in the study of polymeric systems, whereas the single-contact model (and the Zimm plot) give deeper information for flexible polymers. Multiple-contact models have been studied for more complex systems such as copolymers and homopolymer mixtures. In these latter systems the effective structure factor $\tilde{S}(k)$ has been studied extensively.^[42,48]

12.5 Scattering function for self-similar systems

The structure factor introduced in eqn (12.17) defines the spatial distribution of scattering particles and, as shown previously, in the scattering theory $S(k)$ is connected to the pair correlation function $g(\mathbf{r})$, eqn (12.16), by

$$S(\mathbf{k}) = 1 + \rho \int d\mathbf{r}[g(\mathbf{r}) - 1] \exp[i\mathbf{k} \cdot \mathbf{r}]. \quad (12.17a)$$

From eqn (12.55) and (12.63) we obtain the limiting behaviour of the scattered intensity $I(k)$. For small k , in the Guinier regime, where $kR \ll 1$ (R again represents the particle radius), $P(k) \cong 1$ and $I(k) \cong S(k)$. On the contrary, in the Porod regime at large k ($kR \gg 1$), in a disordered system $g(r) \cong 1$, $S(k) \cong 1$ and $I(k) \cong \rho P(k)$. Therefore one expects for $k \sim 1/R$ a crossover from a region in which $I(k)$ depends entirely on $S(k)$ to a region in which it depends only on $P(k)$.

The scattering function for fractal (self-similar) objects can be obtained by combining the results of scattering theory and the definition of fractals. Fractals can be classified into two main categories, random and non-random.^[49] Fractals in physics belong to the first category, although the most commonly reported example of these structures is the well known Sierpinski gasket, which is a non-random fractal defined, as is well known, by a simple iterative process.^[34,49]

In a random fractal structure, all physical properties behave as powers of a relevant length scale. This behaviour crosses over to a homogeneous one on length scales larger than a certain correlation length ξ . This latter quality may represent the aggregate dimension, or the correlation length in a critical phenomenon or in a percolation process.^[50,51] Fractals in nature are not fractals at all length scales; in fact, there is always a length above which the structure starts to show homogeneous behaviour. Since ξ is the relevant length scale of the problem, the dependence of the examined physical properties on any other length l should be considered only in terms of the ratio l/ξ . Depending on this ratio, one thus obtains two different behaviours, for $l/\xi \ll 1$ (fractal) and $l/\xi \gg 1$ (homogeneous) respectively. This effect can be described by a scaling law of the form $I^\chi f(l/\xi)$. All observable structural and dynamical properties of self-similar systems follow this characteristic general law. One example of this is the well-known scaling property of mass density in polymers and colloidal systems that is representative of such long-ranged systems, and constitutes

one of the first applications of fractals to the description of condensed matter. Another example, related to the main topics of this chapter, is the kinetics of aggregation processes and in particular the time-dependence of the cluster size, which obeys the following scaling form:^[52]

$$N_s(t) \approx s^{-2} f(s/S(t)). \quad (12.99)$$

Here $N_s(t)$ represents the number of clusters of size s at time t and $S(t)$ is the ‘mean cluster size’:

$$S(t) = \sum_{s=1}^{\infty} s^2 N_s(t) / \sum_{s=1}^{\infty} s N_s(t). \quad (12.100)$$

Aggregates due to flocculation or polymerization phenomena usually have large dimensions, so that their properties can be directly studied by means of SALS. This experimental procedure is based on the well-established power-law relations among the number of particles constituting the aggregate, i.e. the corresponding mass density. In particular, it is based on the Mandelbrot^[53] definition of the fractal dimension d_f :

$$N(R) = (R/R_k)^{d_f}, \quad (12.101)$$

where $N(R)$ is a quantity obtained by measuring a fractal medium with a *gauge* R_k . In our case $N(R)$ can be identified as the number of particles of radius R_0 which lie within a sphere of radius R centred on an arbitrary particle. This latter form reveals the validity of the fractal nature of many physical phenomena.

Considering fractal aggregates in real space, the density–density correlation function plays a relevant role in mass scaling. This quantity is directly related, as will be shown in the following sections, to the previously defined density–density correlation function

$$G(r) = \frac{1}{V\rho} \int_V dr' \langle \rho(r') \rho(r+r') \rangle, \quad (12.25a)$$

where the integral extends over the whole sample volume. As previously shown in eqn (12.26b), the correlation function $G(r)$ is related to the pair correlation function $g(r)$ and can be partitioned into self and distinct parts.^[28] This separation into self, $G_s(r)$ (points for which $r=0$), and distinct, $G_d(r)$, parts, is a fundamental property of the density correlation function and implies the simple conditions $g(0)=0$ and $\lim_{r \rightarrow \infty} g(r)=1$. Since fractal objects are self-similar structures, the geometrical properties of which are scale-invariant, the pair correlation function is homogeneous:^[54]

$$\langle \rho(\lambda r_1) \rho(\lambda r_2) \rangle = \lambda^{-A} \langle \rho(r_1) \rho(r_2) \rangle, \quad (12.102)$$

where the exponent A is related to the fractal dimension. This implies that

$$\langle \rho(r_1) \rho(r_2) \rangle - \rho^2 \approx |r_2 - r_1|^{-A}. \quad (12.103)$$

From the definition of $g(r)$, the total number $N(r)$ of particles within a spherical

volume of radius R is

$$N(R) = \int_0^R \rho g(r) d^d r, \quad (12.104)$$

where the exponent d is the Euclidean space dimension. Thus

$$N(R) = \int_0^R d^d r \langle \rho(0) \rho(r) \rangle / \langle \rho \rangle \approx \int_0^R d^d r r^{-A} \approx R^{d-A} = R^{d_f}. \quad (12.105)$$

In addition, considering that the mass M of the cluster is

$$M = \int_0^R g(r) d^d r, \quad (12.106)$$

we obtain

$$M \approx R^{d_f}. \quad (12.107)$$

This relationship confirms the above considerations regarding scaling properties and means that a logarithmic representation of the correlation function $G(r)$ as a function of r will be a straight line with slope A related to the fractal dimension d_f .

The scattering function for self-similar objects can be calculated from the definition of the pair correlation function, since the number of particles in a sphere of radius r is

$$N(R) = \rho \int_0^r g(r) 4\pi r^2 dr \quad (12.108a)$$

or

$$dN(r) = \rho g(r) 4\pi r^2 dr. \quad (12.108b)$$

Differentiation of eqn (12.101) yields

$$dN(R) = dN(r) = \frac{d_f}{R_k} \left(\frac{r}{R_k} \right)^{d_f-1} dr. \quad (12.109)$$

Combining the last two equations, the form of the pair correlation function for fractals becomes

$$g(r) = \frac{1}{\rho} \frac{d_f}{4\pi} (R_k^{d_f})^{-1} r^{(d_f-3)}. \quad (12.110)$$

The structure factor $S(k)$ is obtained from the Fourier transform of $g(r) - 1$, and on the basis of the resulting ‘scaling forms’ it is easy to obtain the following general expression:

$$S(k)_M = S(kR_k), \quad (12.111)$$

where S_M is the structure factor for a cluster of mass M . In a d -dimensional

expansion:

$$S(kR_k) = 1 - \frac{k^2 R_k^2}{d} \quad \text{for } kR_k \ll 1, \quad (12.112\text{a})$$

$$S(kR_k) = (kR_k)^{-d_f} \quad \text{for } kR_k(r) \gg 1. \quad (12.112\text{b})$$

Therefore, in the Porod region, where $kR_k \gg 1$, direct measurement of the fractal dimension d_f is possible (only for distances small compared with the radius of gyration of the fractal). The measured intensity $I(k)$ is

$$I(k) \approx S(k) \approx k^{-d_f} \quad (12.113)$$

and this simple relationship can be used to measure d_f .

However, we expect for our system that the constitutive droplets from aggregates having a finite range of correlation ξ . The term 1 is introduced in eqns (12.27) and (12.83) in order to remove the δr function corresponding to the limiting value of $g(r)$ at large distances.^[55] For fractal structures this problem can be overcome by introducing a cut-off length in the same way, as is usually done in critical phenomena, putting^[56,57]

$$|g(r) - 1| = \frac{1}{\rho} \frac{d_f}{4\pi} (R_k^{d_f})^{-1} r^{(d_f - 3)} \exp\left[-\frac{r}{\xi}\right]. \quad (12.114)$$

Substituting this expression into eqn (11.27) the structure factor becomes

$$S(k) = 1 + \frac{d_f}{R_k} \int_0^\infty dr \exp\left[-\frac{r}{\xi}\right] r^{(d_f - 1)} \frac{\sin(kr)}{kr} \quad (12.115)$$

which, after integration, yields the form

$$S(k) = 1 + \frac{1}{(kR_k)^{d_f}} \frac{d_f \Gamma(d_f - 1)}{(1 + 1/(k\xi)^2)^{(d_f - 1)/2}} \sin[(d_f - 1) \arctg(k\xi)], \quad (12.116)$$

where $\Gamma(x)$ is the gamma function. This form of the structure factor can be used for the simultaneous determination of the fractal dimension and the size of the constitutive monomer of the cluster.

In summary, the intensity scattered from a fractal aggregate, with colloidal particles (or monomers of a polymer structure) as the constitutive ‘monomer’, can be calculated from eqns (12.44), (12.50), (12.51), (12.52) and (12.55). The so-obtained intensity is strongly dependent on k . In fact, for k large compared with the single particle radius ($kR_k \gg 1$), eqn (12.116) again gives $S(k) \approx 1$ and, as expected, the experiment is sensitive to the individual scatterers by measuring its form factor, $I(k) \approx \rho P(k)$. For k in the range $1/\xi < k < 1/R_k$, it is $P(k) \approx 1$ and $I(k) \approx S(k)$. In addition, assuming that under these conditions the aggregate cluster spans the entire scattering volume, for example, in a percolating

system,^[58] we obtain

$$\begin{aligned} \lim_{\xi \rightarrow 0} S(k) &= 1 + \frac{1}{(kR_k)^{d_f}} d_f \Gamma(d_f - 1) \sin[(d_f - 1)\pi/2] \\ &= 1 + \frac{1}{(kR_k)^{d_f}} \cong (kR_k)^{-d_f} \quad \text{for } kR_0 \ll 1. \end{aligned} \quad (12.117)$$

This result has been extensively used in a direct study of the scattered intensity for fractal systems and has been derived for the first time on the basis of scaling laws only,^[59] but is not reliable for the evaluation of the fractal dimension outside the limits $k \gg 1$ and $kR_k \ll 1$. For percolation processes eqn (12.116) represents an exact result.

For small k ($k\xi \ll 1$) the expansion of eqn (12.116) clarifies the physical meaning of the cut-off length ξ ; in fact

$$\lim_{\xi \rightarrow 0} S(k) = \Gamma(d_f - 1) \left(\frac{\xi}{R_k} \right) \left[1 - \frac{d_f(d_f + 1)}{6} (k\xi)^2 \right] \quad (12.118)$$

and ξ reflects the finite overall size of the system. It is interesting that the asymptotic behaviour of eqn (12.116) at $k \rightarrow 0$ for the fractal dimension is $d_f = 2$. In fact, it is easy to see that, under these conditions, the Ornstein-Zernike form (eqn (12.83)) is obtained:

$$S(k) \approx \frac{1}{(1 + k^2 \xi^2)}. \quad (12.119)$$

Using eqn (12.116), analysis of experimental data obtained from light, X-ray or neutrons, can simultaneously give information about ξ , R_0 (assuming that $R_0 = R_k$) and d_f if the form factor is known. For a better understanding of results connected with eqn (12.116) we show in Fig. 12.9(a) a plot (on a logarithmic scale) of the structure factor calculated from this form for the percolation case,^[58,60] i.e. $d_f = 2.5$ and for different ratios ξ/R_0 as a function of $k\xi$. The measured scattered intensity, eqn (12.55), is the product of this function and the form factor $P(k)$, which for $kR_k < 1$ is almost equal to unity. From this graphic representation of $S(k)$, the scattered intensity is seen to be linear in a log-log plot in the range defined by the significant points $k = 1/\xi$ and $k = 1/R_k$, i.e. $1/\xi < k < 1/R_k$. It is worth noticing that this linear interval, with slope equal to d_f , is larger for large values of the ratio ξ/R_0 or $1/R_k$. In Fig. 12.9(b) we show results obtained from SANS measurements^[57] on the protein (BSA)/detergent complexes (LDS) in D₂O (1 wt% of BSA in D₂O; curves 2 and 3 refer, respectively, to samples containing 2 and 3 g of LDS in 100 g of protein solution). As can be observed, eqn (12.116) reproduces the experimental data well.

In conclusion, we observe that for systems in which the constitutive 'monomers' give rise to large structures, these results can be usefully monitored only by small angle light scattering measurements.

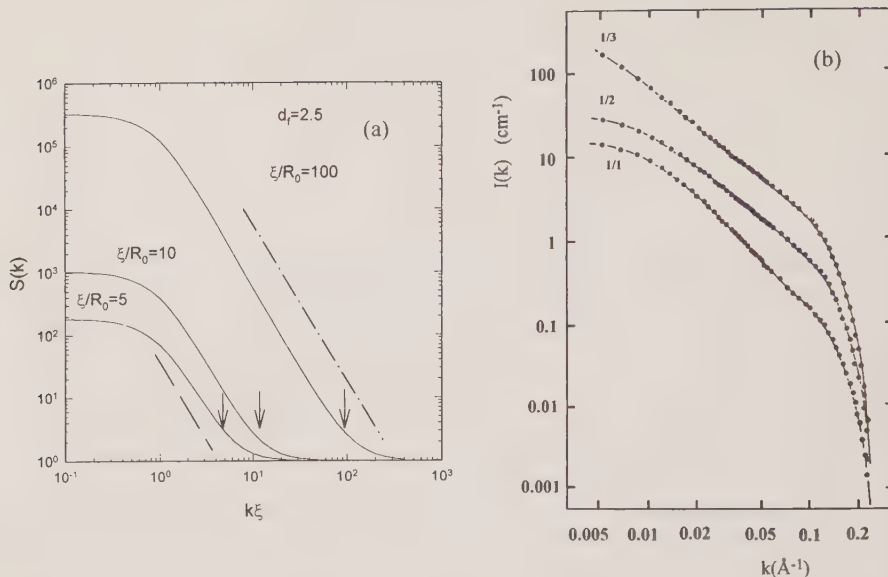


FIG. 12.9. A log-log plot of the structure factor $S(k)$ versus k calculated using eqn (12.116) for the case of percolation ($d_f = 2.5$) and for different ξ/R_0 ratios. (b) The measured scattered intensity, $I(k)$ versus k , obtained from SANS experiments^[57] on protein (BSA) detergent complexes (LDS) in D_2O on a log-log diagram. Dots, experimental points; solid lines, best theoretical fits to eqn (12.116) (Fig. 3 of ref. 57).

12.5.1 Scattering function and aggregation kinetics

Recent comprehensive works^[61] extend the reported model for the intensity measured by static light scattering in aggregating systems and show how typical interrelated features of aggregation processes determine such a quantity. These features are cluster structure, their anisotropies and the extent and form of the cluster mass distribution. With this model, together with simulation on computer-generated structures under the conditions of Diffusion Limited Cluster Cluster Aggregation^[54, 62, 63] and Reaction Limited Aggregation,^[64–66] using for the cluster mass distribution that obtained from the Smoluchowski equation for irreversible growth,^[67] it is possible to calculate $I(k)$ and from this quantity to gain information on the kinetics of aggregation. In fact, considering $N_M(t)$ as the number of clusters of mass M in the scattering volume at aggregation time t , if interactions among clusters are negligible, the total intensity can be represented as

$$I(k) = \sum_M N_M(t) I_M(k), \quad (12.120)$$

where $I_M(k)$ is the intensity contribution from clusters with mass M . Introducing the corresponding structure factor $S_M(k)$ for clusters of mass M gives $I_M(k) = M^2 S_M(k)$. This latter equation is obtained on the basis of simple

considerations about the length scale of the probe k^{-1} and the radius of gyration R_g of the clusters. Therefore,

$$I(k) = \sum_M N_M(t) M^2 S_M(k) \quad (12.121)$$

and from eqn (12.27)

$$S_M(k) \approx \int d^3r g_M(r) \exp[-ikr]. \quad (12.27b)$$

$g_M(r)$ is the density correlation function which, for self-similar objects, scales as $g(r) \sim r^{d_f - 3}$. The introduction of a cut-off function, $h(r/R_g)$, yields

$$g(r) \sim r^{d_f - 3} \tilde{h}(kR_g) \quad (12.122)$$

and from eqn (12.27b) it follows that

$$S_M(k) \approx (kR_g)^{-d_f} \tilde{h}(kR_g). \quad (12.123)$$

Such a result emphasizes that fact that the measured intensity $I(k)$ is strongly dependent upon the form of the cut-off function $h(x)$. From numerical analysis of $S_M(k) = S_M(kR_k)$ (eqn (12.123)) for computer-generated clusters from both DLCCA and RLA condition,^[68] it is shown that the best form for $h(x)$ is a stretched exponential.

Since the scattered intensity $I(k)$ is a convolution of $S_M(k)$ and the cluster mass distribution, another important quantity determining the scattered intensity is $N_M(t)$. The effects of $N_M(t)$ on $I(k)$ can be quantified by solving^[69] the Smoluchowski equation,^[67] written in terms of the same quantity

$$\frac{dN_k}{dt} = \frac{1}{2} \sum_{i+j=k}^{\infty} K_{ij} N_i N_j - N_k \sum_{j=1}^{\infty} K_{jk} N_j, \quad (12.124)$$

where $N_k = N_{M_k}(t)$ and K_{ij} have the usual meaning of reaction rates for the aggregation of clusters of mass M_i and M_j . Assuming the scaling relationship $N_M(t) = u(t) \Psi(M/\tilde{M}_n)$, with $\tilde{M}_n(t) = M^{(n)}/M^{(n-1)}$, and $M^{(n)} = \sum_M N_M(t) M^n$, with \tilde{M}_n representing the n th reduced moment of $N_M(t)$, from mass conservation it follows that

$$N_M(t) = \frac{1}{\tilde{M}_n^2(t)} \Psi(M/\tilde{M}_n(t)). \quad (12.125)$$

The time-dependence of the cluster mass distribution is entirely contained in the moments $\tilde{M}_n(t)$, while the scaling function $\Psi(x)$ is time-independent. The moments $\tilde{M}_n(t)$ characterize the mass of an average cluster of the distribution at time t (usually $n = 2$ is chosen). At this stage of the analysis it is important to consider the form of $\tilde{M}_2(t)$, which depends on the kernels of the Smoluchowski equation. If these are homogeneous, $K_{ai,aj} = a^\lambda K_{ij}$ and it follows that

$$\tilde{M}_2(t) = \exp[t/\tau] \quad \text{for } \lambda = 1, \quad \tilde{M}_2(t) = [1 + t/t_0]^z \quad \text{for } \lambda \neq 1, \quad (12.126)$$

where $z = (1 - \lambda)^{-1}$. The case $\lambda = 1$ (an exponential growth of clusters) corresponds to RLA.^[70] For the DLCCA case^[67] the kernels have the form $K_{ij} = (4\pi\sigma_{ij})(D_i + D_j)$, with $\sigma_{ij} = (R_i + R_j)$.

Considering that the hydrodynamic radius R_{hi} scales as the gyration R_{gi} ,^[71] the translation diffusion coefficient D_i scales as

$$D_i \sim (R_{hi})^{-1} \sim (R_{gi})^{-1} \sim (M_i)^{-1/d_f}.$$

Assuming that $\sigma_{ij} = (R_{gi} + R_{gj})$, we find that

$$K_{ij} \approx 2 + (M_i/M_j)^{-1/d_f} + (M_j/M_i)^{-1/d_f}.$$

Thus K_{ij} is homogeneous with $\lambda = 0$ and it may be approximated by a constant. In such a case the cluster mass distribution is^[72]

$$N_M(t) = \frac{N_0}{\tilde{M}_1^2(t)} \left(1 - \frac{1}{\tilde{M}_1(t)}\right)^{M-1}. \quad (12.127)$$

This result corresponds to a broad cluster mass distribution with a fairly sharp cut-off for large clusters; N_0 represent the total number of constitutive particles. On the basis of the previous considerations, $\lambda = 0$, $z = 1$, and $\tilde{M}_1(t) = [1 + t/t_0]$, where $t_0 = 3\eta V/(8k_B T)N_0$, with η the solvent viscosity and N_0/V the initial concentration, we find that the average cluster mass grows linearly. Defining the radius of the average clusters as $\bar{R}_g = a(\bar{M}_1(t))^{1/d_f}$, asymptotic behaviour for long times will be $\bar{R}_g \approx (t/t_0)^{1/d_f}$. Furthermore, the total number of clusters at time t , $N_T(t) = \sum_M N_M(t)$, decreases as t^{-1} for $t > t_0$.

In the RLA case, when the cluster masses are comparable,^[70] the kernels scale as $K_{ij} \sim M_i^\lambda$, while for $M_i \gg M_j$ they behave as $K_{ij} \sim M_i M_j^{\lambda-1}$ in both cases. On this basis, the time-dependence of the cluster distribution can be determined and a power-law distribution with an exponential cut-off^[69,70] is obtained:

$$N_M(t) \approx M^{-\tau} \exp[-M/2\tilde{M}_2(t)], \quad (12.128)$$

with $\tau = 1.5$. Computer simulations have been used to test these predictions, based on the Smoluchowski equation, and good agreement was found. Different studies suggest different expected values for τ ; one^[73] gives $\tau \sim 1.5$, while another^[74] gives an increasing value of τ up to 2 for large times.

As a concluding example, the performed analysis using this model with the experimental data for the scattered intensity as a function of k at different aggregation times t , obtained for colloidal gold particles aggregated under DLCCA and RLA conditions^[61] is shown in Fig. 12.10. As can be seen, the calculation, employing the appropriate form for $N_M(t)$, reproduces exactly the observed kinetics and the corresponding fractal dimensions. In particular, for long times the scattered intensity is entirely due to clusters for which $kR_g \sim kR_k > 1$, and the data in the experimental k range are well represented by eqn (12.116).

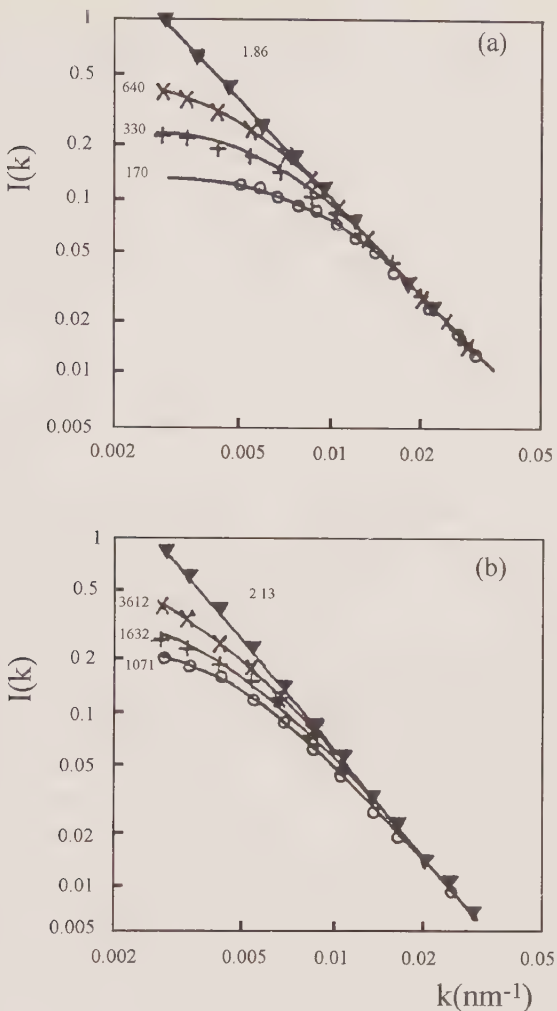


FIG. 12.10. The scattered intensity as a function of k at different aggregation times t , obtained for colloidal gold particles aggregated under DLCCA (a) and RLA (b) conditions. The solid curves correspond to the calculation, and the values of $\tilde{M}_2(t)$ obtained from the data fitting label each curve (Fig. 1 of ref. 61).

12.5.2 Phase separation and spinodal decomposition

A large number of studies have dealt with the dynamics of phase separation. Examples of well studied systems are binary mixtures, alloys and polymer blends. The dynamics of phase separation in all these systems, following a thermal quench into the unstable coexistence region, proceeds either by nucleation growth or spinodal decomposition.^[75,76] Immediately after the quench, small domains, with a local concentration roughly corresponding to

that of the two main phases, form spontaneously and grow with time, and finally result in complete phase separation. As the mixture evolves towards equilibrium, the strong non-linearity of the decomposition produces an interconnected morphology that coarsens with time. From the viewpoint of both universality and dynamical scaling concepts, the time evolution of spinodal decomposition in a system near its critical point has attracted much attention because of the dynamics of the ordering process. Recently, attention has been focused on the dynamics of glasses, polymer melts, gels and microemulsions, which are generally called 'complex fluids'. In such systems the dynamics, reflecting their complex interconnected phenomena that can interfere with phase separation. However, the characteristic relaxation times for complex systems, being larger than those occurring in simple fluids, allows investigation of spinodal decomposition over a much greater range of phase space than for liquid mixtures.

The entire time behaviour of spinodal decomposition can be characterized by means of three different stages, namely early, intermediate and late stages.^[78] Linearized theory,^[79] scaling concepts^[80] and recently MD simulations^[81-84] have greatly contributed to the study of the growth and the time evolution of component fluctuations in such systems. Whereas the early and the intermediate stages show universal behaviour well accounted for by theoretical models and experimental results, the late-time behaviour is strongly dependent on the system properties. In this stage simple binary mixtures and complex fluids show different behaviour. In particular, in complex systems, well defined slowing-down^[81] and pinning phenomena^[83] in the structure factors can be observed due to strong interactions or to the presence of a persistence length. Careful attention has been devoted to the study of spinodal decomposition in binary mixtures containing surfactant or polymeric solutions; in fact, depending on the surfactant amount (or on the length of the polymer chain), such systems can show behaviour that ranges from that of a simple critical mixture to that of a complex system. It is well known that such systems, depending on the surfactant (or polymer) concentration, present many different structural arrangements.

The best experimental technique for studying phase separation is small angle light scattering. In particular, the kinetics of the process can be completely described by means of the analysis of the temporal evolution of the scattered intensity function. In this section we describe the basic concepts of the phase separation process, showing that current theories can account for the phenomenon with a wide generality; i.e. the time behaviours of different systems, if scaled in a proper way, show common features that are independent of their main physical properties. Critical binary mixtures, alloys, polymer solutions, gels, glasses, micelles and microemulsions removed from thermodynamic equilibrium behave in an analogous manner. Furthermore, we show how small angle light scattering can fully describe all the physical properties of the phenomenon.

Phase separation may occur by either nucleation or spinodal decomposition.

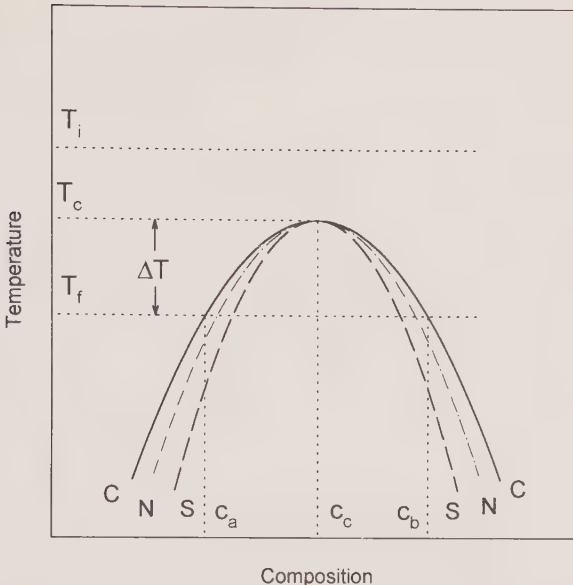


FIG. 12.11. The phase diagram of a binary mixture. The solid curve indicates the coexistence curve (C–C), where T_c and c_c refer, respectively, to the critical temperature and concentration respectively. The dashed-dotted curve indicates the nucleation (N–N) and the broken curve the spinodal line S–S. The initial and final temperatures are T_i and T_f , and the quench depth is ($\Delta T = |T_c - T_f|$).

Nucleation is associated with metastability (i.e. the existence of a finite energy barrier and the occurrence of a rare but large energy fluctuation). Spinodal decomposition refers to phase separation in an initially unstable system (in which even the smallest fluctuation will grow because the energy barrier is negligible or zero). Therefore, the term *spinodal* indicates the limit of the meta-stability, beyond which no thermodynamically stable phase can exist. Figure 12.11, showing a temperature-composition phase diagram for a binary mixture, explains such a situation well. The solid line indicates the coexistence curve (C–C), where T_c and c_c refer, respectively, to the critical temperature and concentration respectively. For $T < T_c$, the two phases (A and B) are in thermal equilibrium and contain c_A and c_B molecules/ml of one of the components. As $T \rightarrow T_c$, the two phases become equivalent. The nucleation line, shown as N–N, has a dynamic rather than a thermodynamic definition. A system which is supercooled to a temperature T lying just above the N–N line may take long times (hours, weeks or years) to form droplets of the stable phase, whereas a slight temperature decrease below the nucleation line results in an instantaneous and copious production of droplets. The spinodal line S–S, encloses a region within which the system is thermodynamically unstable to the growth of composition fluctuations. In a binary mixture this line is defined by the

following condition on the susceptibility

$$\chi_c^{-1} = (\partial c / \partial \mu)_{P,T}^{-1} = 0,$$

where μ is the difference in the chemical potential of the two components. Such a quantity is negative within the spinodal region. In simple fluids the spinodal line is described by means of the isothermal compressibility χ . In an experiment, phase separation is obtained by quenching the sample from the initial temperature T_i to the final ΔT_f ($T = |T_i - T_f|$), with $T_f < T_{SP}$ (the spinodal line temperature), and T_f is the temperature at which the fluid is quenched. This quench can be very deep or very shallow, i.e. $T_f \ll T_{SP}$ or $T_f \approx T_N$ (the nucleation line temperature). Usually the experiments are performed with a *critical quench*, i.e. the sample of critical concentration is cooled through the critical point (see Fig. 12.11). In such a case the system does not have to pass through intermediate metastable states.

In a light scattering experiment spinodal decomposition appears as a ring of scattered light just after the quench. In the early stage the radius of the ring remains constant and the intensity of the ring increases with time. After this stage where the Cahn and Hilliard^[79] theory, based on the linearization of a generalized diffusion equation, describes the behaviour of composition fluctuations, the wavenumber of the most dominant fluctuation decreases with time whereas the corresponding intensity increases. As a typical example, Figure 12.12 shows the time evolution of the measured scattering functions for

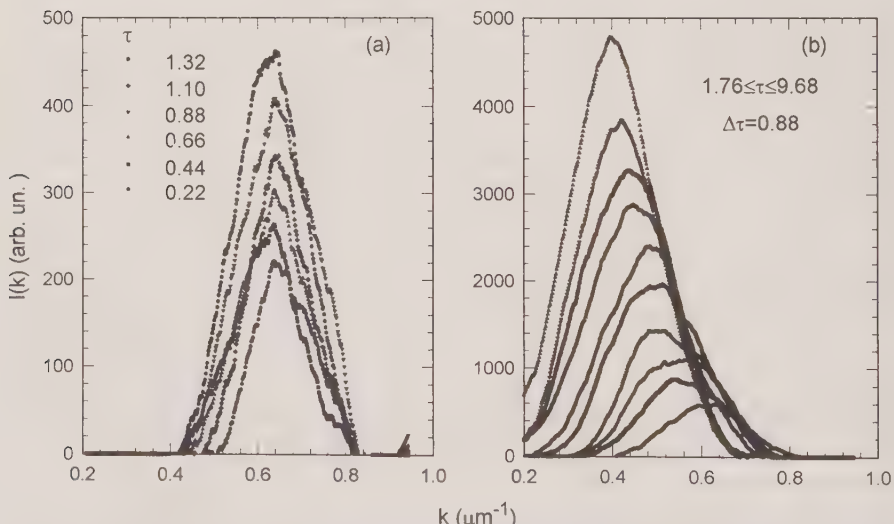


FIG. 12.12. The time-evolution of the scattering intensity distribution following a quench of depth $\Delta T = 0.05$ K for a microemulsion system (a pseudobinary critical system^[85]). (a) Intensities corresponding to the early stage. (b) Those for the intermediate and late stages (Fig. 2 of ref. 85).

$\Delta T = 0.05$ K of a microemulsion system (a pseudo-binary critical system^[85]) in the early and intermediate stages. One can see from Fig. 12.12 the behaviour corresponding to the early stage; i.e. the scattered intensity increases with time and there is almost no change in the wavenumber at the maximum intensity.

Whereas in the early stage the decomposition mechanism is explained in terms of the negative curvature of the free energy, which makes the diffusion constant negative (particles move from rare to dense regions), in the latter, intermediate, stage the driving force for droplet growth is the surface tension. In this stage the use of scaling concepts is determinant in the description of the growth rate of coalescing domains.^[80] In particular, scaling behaviour of the measured structure factor suggests the existence of a single-length parameter describing the formation of self-similar structures in the phase separating system and is related to the k -dependence of the dominating peak of the fluctuation modes.

Now we consider the basic equation of the linearized theory of Cahn and Hilliard^[79] for spinodal decomposition. This, as shown in the following, accounts well for the system behaviour in the early stage. This theory assumes that domain growth takes place because the composition diffusivity D (cm²/sec) is negative. In particular, this follows by considering the relationship between D and the susceptibility χ :

$$D = M\chi_c^{-1} = M(\partial\mu/\partial\eta)_{P,T}^{-1} \quad (12.129)$$

where the atomic mobility M is always positive, and μ is the chemical potential.

In a binary mixture the local composition $\eta(\mathbf{r}, t)$, which represents the order parameter, obeys the Fick's first law of diffusion

$$\mathbf{J}(\mathbf{r}, t) = -D\nabla\eta(\mathbf{r}, t), \quad (12.130)$$

where $\mathbf{J}(\mathbf{r}, t)$ is the interparticle flux. By combining with the continuity equation

$$\frac{\partial\eta(\mathbf{r}, t)}{\partial t} + \nabla \cdot \mathbf{J} = 0 \quad (12.131)$$

we have

$$\frac{\partial\eta(\mathbf{r}, t)}{\partial t} = D(T_f)\nabla^2\eta(\mathbf{r}, t) = 0, \quad (12.132)$$

where $D(T_f)$ represents the diffusivity at the quench temperature T_f . Considering $\eta(\mathbf{k}, t)$ as the Fourier component of $\eta(\mathbf{r}, t)$, we find that eqn (12.132) has the solution

$$\eta(k, t) = \eta(k, 0) e^{-\Gamma(k)t} \quad \text{with} \quad \Gamma(k) = D(T_f)k^2. \quad (12.133)$$

Since $D < 0$ in the spinodal region, all Fourier components $\eta(k, t)$ will grow at an exponential rate. The intensity $I(k)$ of light scattered by the mixture will be, in the frame of validity of the Born approximation, proportional to $|\eta(k, t)|^2$, where k is now the scattering wavevector. From the last equation it is possible to understand why the quenched fluid scatters light in the form of a ring in

spinodal decomposition. In particular, we consider eqn (12.129) as an oversimplification, since it does not take into account the k -dependence of D . In a real system one might expect k , and hence $D(k)$, to become positive, because rapid spatial variations in $\eta(k, t)$ are energetically costly to produce. For this reason, Fourier components of η with large k (say, k greater than some value k_c) would be expected to decrease exponentially rather than to grow with time, so that when $k \gg k_c$, $D > 0$ and fluctuations decay. When $k \ll k_c$, $\eta(k, t)$ will grow very slowly because $\Gamma(k) \propto -k^2$. Consequently, the scattering will be dominated by the intermediate k -values.

Cahn's treatment is given in terms of the Ginzburg–Landau free energy density,

$$f_{\text{GL}}(r, t) = f(\eta) + 2\kappa(\nabla\eta(r, t))^2, \quad (12.134)$$

where

$$f = \text{constant} + \chi^{-1}(\eta - \eta_c)^2 + A(\eta - \eta_c)^4 \quad (12.135)$$

and A and κ are constants. In these terms we have

$$\mathbf{J}(\mathbf{r}, t) = -M\nabla \frac{\partial F}{\partial \eta(\mathbf{r})} = -M\nabla[\tilde{\mu} - 2\kappa\nabla^2\eta], \quad (12.136)$$

where $\tilde{\mu} = \partial f / \partial \eta$ is the local chemical potential and F is the volume integral of f_{GL} . Linearizing over the average concentration $\bar{\eta}$, putting $u = \eta - \bar{\eta}$, and combining eqn (12.132) with eqn (12.136):

$$\frac{\partial u}{\partial t} = M\nabla^2 \left[\left(\frac{\partial \tilde{\mu}}{\partial \eta} \right)_{P,T} - 2\kappa\nabla^2 u \right]. \quad (12.137)$$

After Fourier analysis, solving for the component $\eta(k, t)$, we obtain the decay rate Γ as

$$\Gamma(k) = D(k)k^2 = \{M[\chi^{-1}(T_f) + 2\kappa k^2]\}k^2. \quad (12.138)$$

Inside the spinodal region, $\chi(T_f) < 0$, so that Γ changes sign at $k = k_c = (2\kappa\chi)^{-1/2}$. The most rapidly growing Fourier component $\eta(k_m, t)$ can be obtained by differentiation, and its wavenumber will be $k_m = k_c/\sqrt{2}$. This is the wavenumber at which the growth rate has a maximum value and should coincide with the wavenumber corresponding to the peak intensity, $k_m(t)$ at $t = 0$. Thus:

$$\Gamma(k) = D^* \{1 - k^2/2k_m^2(0)\}k^2 \quad (12.139)$$

and $k_m(0) = \frac{1}{2}[D^*/M\kappa]^{1/2}$. In these terms the quantity $(\xi^*)^{-1} = k_c = k_m(0)$ is the relevant length scale.

Considering thermal noise effects,^[87] the scattering function $I(k, t)$ obtained from linearized theory is

$$I(k, t) = I_x(k) + [I_0 - I_x(k)] \exp(2\Gamma(k)t). \quad (12.140)$$

$I_x(k)$ is the virtual intensity arising from the thermal noise, and I_0 is the intensity at time $t = 0$ (the elapsed time after the quench). This latter expression describes

well the early stages of spinodal decomposition. The temporal evolution of the system after this initial stage is different: the wavenumber of the most dominant fluctuation decreases with time whereas the intensity shows a marked increase. This can be accounted for by considering non-linear contributions in eqn (12.137). However, beyond the early stages, the attention of experiments and theories is focused on the time-evolution of the *ring diameter* $k_m(t)$ and the *ring intensity* $I_m = I(k_m(t), t)$.

Although linear theories give a complete description of the early stages of spinodal decomposition, the other stages of the phase separation process, in particular the late stage, are not yet completely understood and represent challenging problems in the field of non-equilibrium statistical physics. The different theoretical models proposed for these stages (namely intermediate and late) can be arranged in two main categories: i.e. non-linear and 'mean field' scaling theories.

The first theoretical approach in terms of the non-linearity of the free energy is due to Langer, Baron and Miller;^[86] after this contribution many papers were devoted to generalizing or extending their theory. In this framework, important applications that consider the effect of the flow of matter (and of inertia) and of surface tension are due to Kawasaki and Ohta^[87] and Siggia,^[88] respectively. The use of scaling concepts is due to the work of Binder and Stauffer,^[89] de Gennes,^[90] Pincus^[91] and Furukawa.^[80] More precisely, Binder and Stauffer proposed a model based on Smoluchowski-type aggregation kinetics (i.e. diffusional in character) for droplet coarsening. Therefore the coalescence process is considered in a self-similar way. More precisely, each droplet is regarded as a Brownian particle which freely diffuses until another is met. When two particles meet, they coalesce into a larger droplet and so on. This process continues until complete phase separation is obtained. For polymer systems and polymer blends in particular, de Gennes and Pincus^[90,91] made calculations by adapting the original Cahn–Hilliard theory developed for low molecular weight systems. The de Gennes–Pincus and Binder–Stauffer theories, although introducing different viewpoints to describe fluctuations with wavelengths smaller than the dimensions of a polymer coil, lead (for length scales larger than the polymer coil) to essentially the same results as linearized theories. Both use the Flory–Huggins description for the free energy term^[92] with modification for the interfacial free energy density of the square gradient term (eqns (12.134)–(12.137)).

There are many review articles^[75, 76, 80, 92, 93] in the field of spinodal decomposition that treat the subject in detail giving all the related information, so we will not make a deeper analysis of the properties and results of the different models used. We restrict our interest to scaling theories taking into account how the use of scaling concepts can explain the growth and time-evolution of component fluctuations of the system and the overall behaviour of the corresponding structure functions. Our main interest is to stress how small angle light scattering can be fruitfully used for the investigation of phase-separating systems.

Scaling concepts for the kinetics of phase separation have been considered in all the theoretical models characterizing the behaviour of $k_m(t)$ and $I_m(t)$ with time. In fact, $k_m(t)$ and $I_m(t)$ are expressed by simple power-law relations as:^[180]

$$k_m(t) \sim t^{-\alpha} \quad \text{and} \quad I_m(t) \sim t^\beta. \quad (12.141\text{a}, \text{b})$$

In particular, the scaling idea was extended to a later stage at which a self-similar structure develops in the system and a single length describing such structure exists. More specifically, the temporal evolution of the quantities characterizing the spinodal decomposition is described using the dimensionless variable:

$$\tau = t/t_c \quad \text{with} \quad t_c = 1/D^* k_m^2(0). \quad (12.142)$$

Here t_c is the characteristic time of the process and is therefore related to ξ^* and to the interdiffusion coefficient D^* . The relevant length scale ξ^* and D^* are determined by the early stage behaviour, using a well established procedure proposed by Sato and Han.^[194] This procedure considers the following $\frac{1}{3}$ -power plot of eqn (12.140) to obtain in an accurate way the growth rate Γ :

$$\{t/[I(k, t) - I(k, 0)]\}^{1/3} = \{2\Gamma[I(k, 0) - I_x(k)]\}^{-1/3} [1 - \frac{1}{3}\Gamma t + \frac{1}{8}\Gamma^3 t^3 + \dots]. \quad (12.143)$$

The Γ values obtained from this equation at different k are plotted as R/k^2 vs. k^2 . The intercept of the abscissa gives $2^{1/2}k_m$ and that of the ordinate gives D^* . In Fig. 12.13 we show a typical result for such a procedure. ξ^* and D^* are expected to behave similarly to the correlation length and the diffusion coefficient in the stable one-phase region.

Finally, by means of t_c and k_c , the time-evolution of phase separation is expressed by the dimensionless scaled relation, as

$$k_m(\tau) = \frac{k_m(t)}{k_m(0)} \sim \tau^{-\alpha}, \quad (12.144)$$

$$I_m(\tau) \sim \tau^\beta. \quad (12.145\text{a})$$

In critical binary mixtures, where hydrodynamic effects are also considered, the exponent α can change from 0 to 1 corresponding to the early and the late stages of spinodal decomposition.^[75–78] In the intermediate stage in which Brownian coagulation occurs, $\alpha = \frac{1}{3}$. Its deviation from 0 denotes the onset of the intermediate stage in which $\beta > 3\alpha$. In the late stage, where the system dynamics are dominated by mass flow, α changes from $\frac{1}{3}$ to 1. In this stage $\beta = 3\alpha$ and

$$k_m(\tau)^3 I_m(\tau) \sim \tau^0. \quad (12.146)$$

Figure 12.14 shows the scaled time-evolution of $k_m(\tau)$ (Fig. (12.14(a)) and of $I_m(\tau)$ (Fig. 12.14(b)) in a critical microemulsion system^[85] for a given quench depth ΔT . The results in Fig. 12.14(a) confirm the existence of the time domain in which the linearized theory of SD is valid and well characterizes kinetic

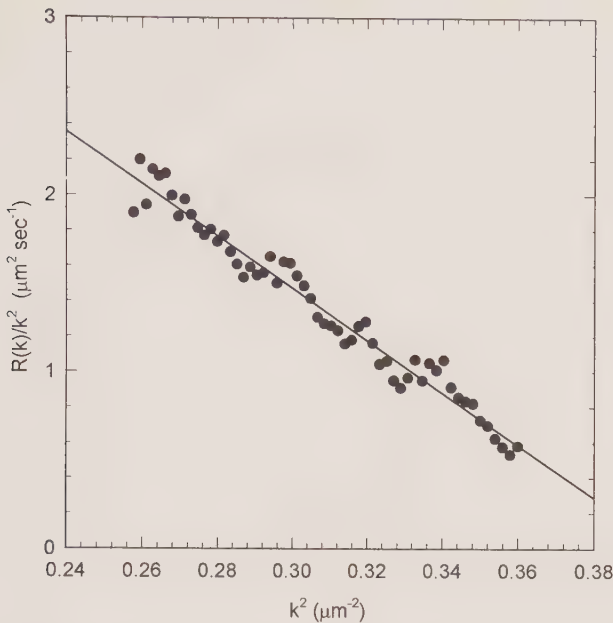


FIG. 12.13. The growth rate R obtained from the $\frac{1}{3}$ -power of $I(k, t)$ plotted as R/k^2 versus k^2 . The intercept of the line with the abscissa gives $2(\xi^*)^{-2}$ and with the ordinate gives D^* (Fig. 3 of ref. 85).

properties of the SD discussed above. The curves for the scaled time of $k_m(\tau)$ for different ΔT coincide. The change of α from 0 to $\sim \frac{1}{3}$ occurs at $\tau \sim 1$ in complete agreement with other experimental results in simple critical mixtures^[78] and theoretical models.^[75, 76, 84] The master curve shows no evidence of pinning or slowing down at large, as proposed by MD simulations.^[81, 83] On the contrary we can observe for $\tau \sim 20$ the $\alpha = 1$ growth law behaviour characteristic of the late stage in binary fluid systems quenched into a regime in which there are interconnected domains. The full line in Fig. 12.14(a) represents the theoretical result for a large crossover regime for critical concentration fluid mixtures in which inertia and gravitational effects are neglected. In particular, such a continuous line is obtained by fitting the experimental data with an analytical equation frequently used in the literature, i.e. the Furukawa equation (eqn (8.6) of ref. 80):

$$(k_m^{-1} - 1) - \{(A/B)^{1/2} [\tan^{-1}(k_m^{-1}(B/A)^{1/2})] - \tan^{-1}[(B/A)^{1/2}]\} = B\tau, \quad (12.145b)$$

where A and B are constants. Usually the parameter A is set close to 0.1 in order to recover the behaviour predicted by the hydrodynamic theory of Kawasaki and Ohta.^[87] On this basis in the intermediate stage the Furukawa equation is coincident with the Kawasaki and Ohta^[87] curve. From data-fitting,

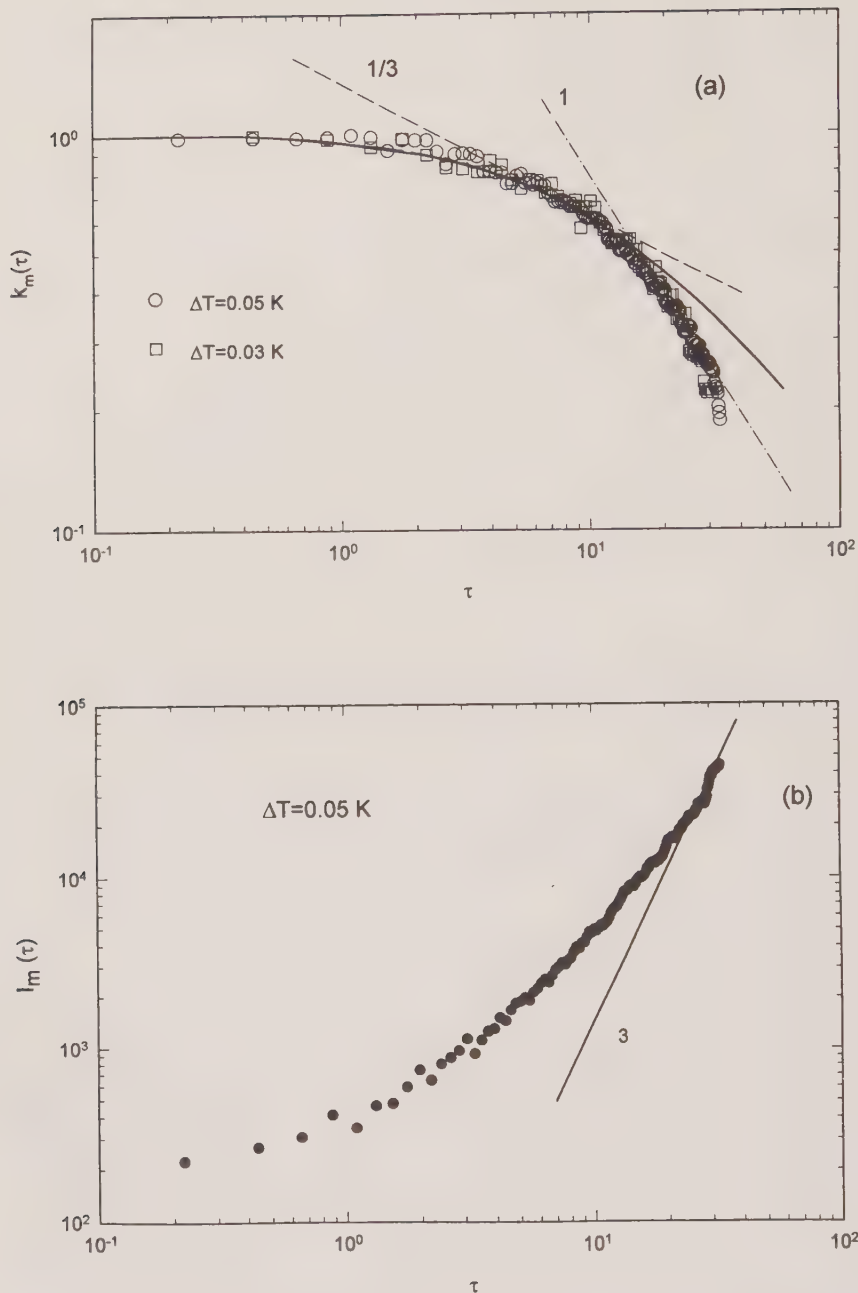


FIG. 12.14. The scaled-time evolution of the scaled wavevector at the peak intensity $k_m(\tau)$ (a) and the peak intensity $I_m(\tau)$ (b) for the critical microemulsion system^[85] for $\Delta T = 0.05 \text{ K}$ and $\Delta T = 0.03 \text{ K}$. The continuous line represents the fit of the data in the intermediate stage with the Furukawa equation^[80] (Figs 4 and 5 of ref. 85).

$B = 0.054$ is obtained, a value that is of the same order of magnitude for critical mixtures ($0.02 < B < 0.1$).^[78,80,98]

As can be observed from Fig. 12.14(b), $I_m(\tau)$ reaches the slope $\beta = 3$ in the time range of $\tau \geq 20$, whereas in the intermediate stage $1 < \tau < 20$ the inequality $\beta > 3\alpha$ holds. The feature $\beta = 3\alpha$ with $\alpha = 1$ means that the self-similar structure which is characteristic of the ordering process in the late stage is formed. At such a late stage, hydrodynamic effects determine the kinetics of phase separation.^[87,88] The same behaviour has also been observed for different critical binary mixtures.^[78,95] A comparison of the obtained data in the late stage with the main results of a recent MD simulation,^[81] carried out for binary mixtures containing surfactant, indicates that in such a microemulsion system the separation occurs through formation of irregular bicontinuous-like domains. This result is interesting because it reflects the structural properties of the system in the stable region. In fact, the studied microemulsion system has a percolation point just above the critical one.^[85] The percolation phenomenon is explained by means of a structure very similar to a bicontinuous one.^[95]

Another important feature of scaling concepts applied to spinodal decomposition is given by the suggestion that, at stages where self-similar structures are developed, the dynamical structure factor $S(k, t)$ for the system can be expressed by the scaling law

$$S(k, t) = (k_1^3)^{-1} F(k/k_1), \quad (12.147)$$

where $F(X) = F(k/k_1)$ is a universal scaling function,^[89] and k_1 is the first moment of the scattering function. Since the scattering function $S(k, t)$ is proportional to the measured intensity $I(k, t)$ we have

$$k_m^3(\tau) I_m(\tau) \sim F[k/k_m(\tau)] \quad (12.148)$$

In order to compare the scaled structure factor $F(X)$ obtained at different stages (i.e. at different elapsed times τ) and at different quench depths, the scaled structure factor is usually normalized as^[80,97]

$$\overline{F(X)} = F(X) \left/ \int F(X) X^2 dX \right. \quad \text{with} \quad X = k/k_m(\tau). \quad (12.149)$$

The integration factor in the denominator corrects the difference in the equilibrium fluctuations (density or concentration) between the two phases at different quench depths, thus removing adjustable parameters in the structure factor.

Different forms have been proposed for the normalized structure factor^[80,96-99] in order to have a universal form completely independent of τ and ΔT . The scaling properties of the structure function were tested and demonstrated by numerical simulation^[100,101] and for real materials^[78,96-98] including systems in which the order parameter is conserved (or not conserved). In systems in which the order parameter is conserved the following behaviour of the structure function was observed. The early stage shows a time-independent k^{-2} tail, which reflects the initial structure before quenching.^[86]

As time proceeds there is a crossover from k^{-2} to k^{-4} and the k^{-4} tail is connected with the appearance of a well-developed droplet interface. In particular, it is observed that the crossover in the kinetic exponent is accompanied by a crossover of the scaling structure function.^[100] The observed structure function becomes sharper as the time proceeds, exhibiting initially the k^{-4} dominated tail, followed by a k^{-6} dominated tail, as predicted by Furukawa.^[80] A very important result of numerical simulation experiments^[81,82,101] is that the scaling in $F(X)$ is dependent on the volume fraction of the minor phase. An additional feature of the scattering functions in the late stage is the presence of a shoulder in the larger scattering-angle region of the dominant peak. This shoulder was theoretically predicted by taking into account long-range hydrodynamic interactions^[77] and has been observed in different systems.^[79] Furthermore, the tail of such a shoulder approaches the form $F(X) \sim X^{-4}$ (the Porod law) with increasing elapsed time. The scattering function at such a shoulder is slightly time-dependent, indicating that the global structure evolves with a self-similar growth of the local structure.

Furukawa^[80] has proposed, for the range of self-similarity in the structure, the simple form

$$F(X) \sim X^\delta / (\gamma/\delta + X^{(\gamma+\delta)}). \quad (12.150)$$

This form gives $\overline{F(X)} \sim X^\delta$ for $X \ll 1$, and $\overline{F(X)} \sim X^{-\gamma}$ for $X \gg 1$. In the late stage of decomposition the tail of the structure factor (large k) follows the Porod law; in fact it behaves as k^{-4} , indicating the formation of a sharp interface ($\gamma = 4$). For conservative systems, in three-dimensional space, $\delta = 4$ is predicted (when thermal fluctuations are not effective; otherwise $\delta = 2$). Therefore an X^{-6} dependence is predicted for $X > 1$.

The scaled structure factors defined by eqn (12.149) are shown in Fig. 12.15 for $\Delta T = 0.05$ at different τ in order to cover the range from the intermediate to the late stage where dynamical scaling holds. These stages are considered separately. The overall shape and the k^2 behaviour are the same as observed in previous measurements on critical mixtures.^[95] In Fig. 12.15(a) the scaled structure factors for all the elapsed times in the range $14 < \tau < 17.6$ (intermediate stage of SD) are shown. As can be observed, the wavevector scaling behaviour agrees with the Furukawa predictions and, in particular, we have $\overline{F(X)} \sim X^2$ for $X \ll 1$ ($\delta = 2$) and $\overline{F(X)} \sim X^{-6}$ for $X \gg 1$ ($\gamma = 6$). The scaling behaviour is different in the late stage, as seen in Fig. 12.15(b), for $26.4 < \tau < 29.7$. Whereas for small k ($k < k_m$) we again have a k^2 -dependence, for $k > k_m$ we can observe the onset of the shoulder peak located at $k \sim 2.5k_m$ and an overall Porod behaviour (k^{-4}). The k^{-6} scaling can be observed for $1.5 < k/k_m < 2$. Thus, the theoretical predictions based on scaling behaviour also hold in this stage.

In conclusion, we note that in the early and intermediate stages, the phase separation process seems to have a universal time behaviour (independent of the system), whereas the late stage depends on system properties and more specifically on its structure. An example of such behaviour is shown in Figs 12.16 and 12.17 where the results for three different systems are reported: i.e. a

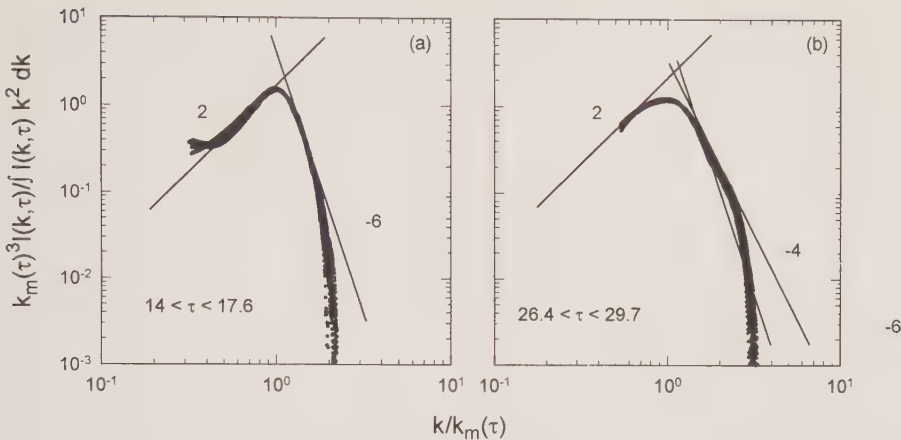


FIG. 12.15. The scaled structure factors (about 30 of them) measured in the scaled time intervals (a) $14 < \tau < 17.6$ (the intermediate stage of SD) (b)), and $26.4 < \tau < 29.7$ (late stage). In both figures, the scaled intensities show the universal behaviour predicted by the theoretical models based on scaling concepts^[80] (Figs 6 and 7 of ref. 85).

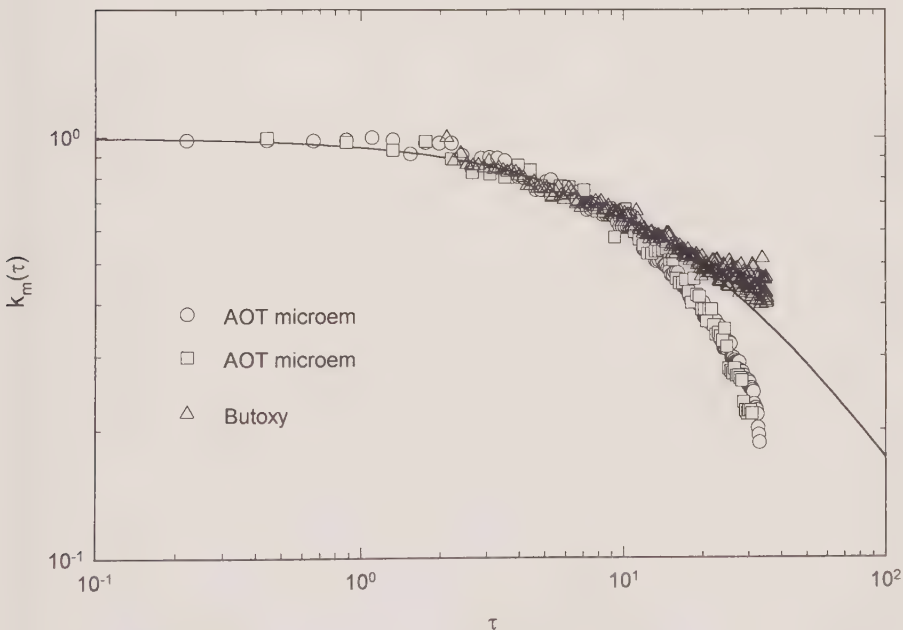


FIG. 12.16. A comparison of the scaled-time evolution of the scaled wavevector at the peak intensity $k_m(\tau)$ for a microemulsion and a micellar-like system (water–butoxyethanol).^[85] The continuous line represents the fit of the data in the micellar system with the Furukawa equation^[80] (Fig. 8 of ref. 85).

microemulsion (the same as previously discussed), a micellar (water–butoxyethanol) suspension^[85] (Fig. 12.16) and a gel (gelatin–water–methanol) which is undergoing a sol–gel transition simultaneously with phase separation (Fig. 12.17(a)).^[102] The continuous line in Fig. 12.16 represents the data fitting of the micellar mixture with eqn (12.145b), with $A = 0.1$ and $B = 0.015$. As can be observed, these three systems have three different types of behaviour in the late stage. In particular, the microemulsion exhibits behaviour dominated by the bicontinuous structure and hydrodynamic effects. In the micellar mixture phase separation is due to droplet structure.^[85] For both systems good agreement with MD simulation^[81] is observed.^[85] In the gel a strong dependence of the kinetics of the phase separation on the quenching temperature and a marked pinning phenomenon (k_m constant in time) is evident. The kinetic behaviour was explained using a Ginzburg–Landau-type model for a mixture undergoing a sol–gel transition (non-conserved order parameter) simultaneously with phase separation (conserved-order parameter).^[103] From a structural point of view the basic properties of such a model are the following: phase separation produces domains which grow to some finite size and then become ‘pinned’ due to gelation, which manifests itself as a crossover in the structure factor from a time-dependent to a time-independent behaviour. Approaching the sol–gel transition, this crossover moves towards smaller times and larger k values. Figure 12.17(b) shows the results of such a model in comparison with the experimental data for an analogous system.

We now consider some aspects of colloidal aggregation that are in some way related to phase separation. This can be considered as a representative example of the interconnection between the properties of the physical phenomena in complex systems, which can be studied with the use of SALS. It was recently observed that colloidal aggregation and spinodal deconvolution show some common characteristics.^[104] By SALS measurements performed on charged colloidal aqueous solutions (latex spheres of $0.095\text{ }\mu\text{m}$ in radius, at isodensity conditions, with a volume fraction in the range $3 \times 10^{-5} < \phi < 10^{-3}$). During the aggregation process a finite wave vector peak k_m in the scattering function was observed. The time behaviour of such a peak is similar to that observed in spinodal deconvolution Fig. 12.18(a). The peak height increases in time and its position moves to smaller k values. In addition, the intensity curves collapse onto the same asymptotic line at high k (behaviour similar to that shown in Fig. 12.10), which gives the fractal dimension of the cluster ($d_f = 1.9 \pm 0.1$). For the aggregation processes it is possible to distinguish three different stages. In the first stage the peak intensity grows very rapidly while the peak position moves slowly. In the second intermediate stage the scattering function scales according to the universal law represented by eqns (12.147) or (12.148) with d_f instead of 3 in the exponent of k_m (see Fig. 12.18(b)). The third terminal stage of the aggregate is characterized by the fact that, for the more concentrated solutions, the aggregation stops as soon as the peak position reaches a terminal value k^* . It has been also observed that this final position of k_m depends on the monomer concentration.

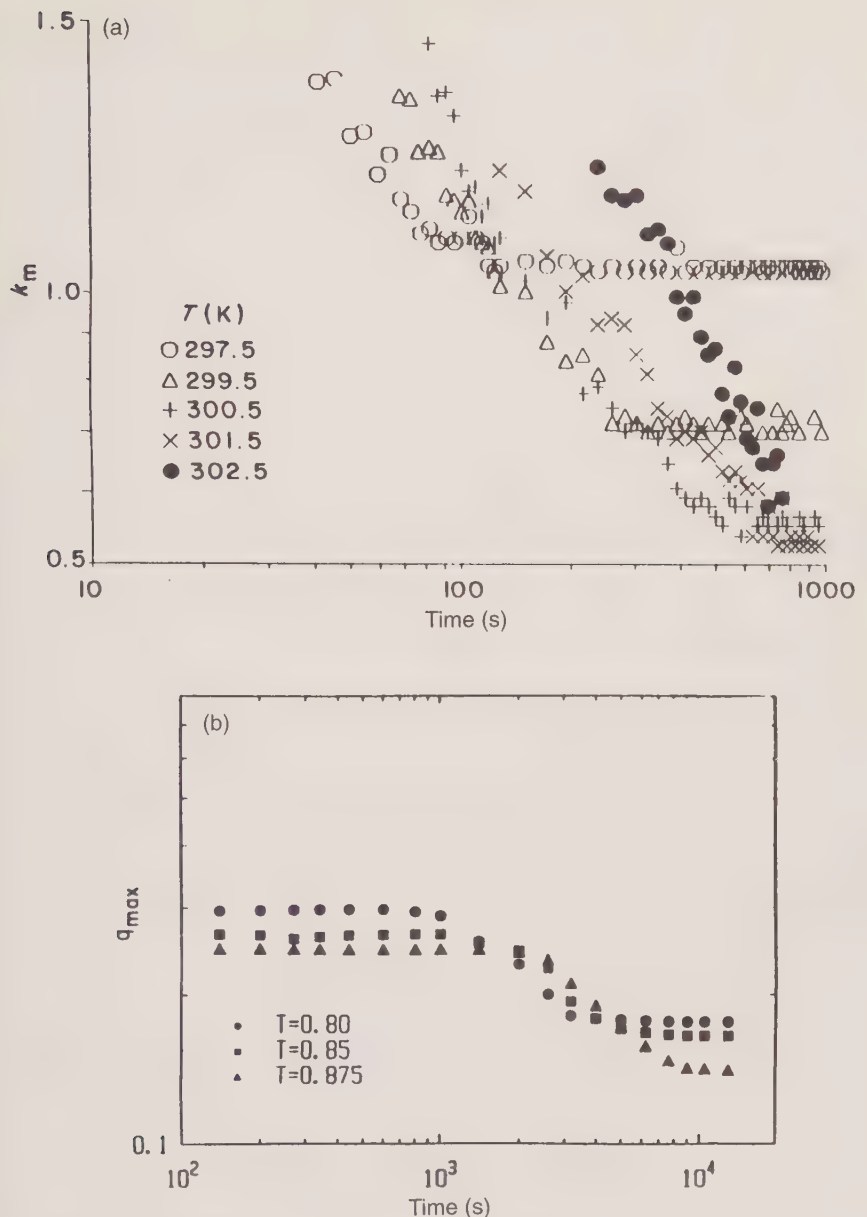


FIG. 12.17. (a) The time dependence of k_m (in units of 10^4 cm^{-1}), at the different quench temperatures indicated in the figure, for the gel system (gelatin water-methanol) (Fig. 4a of ref. 102). (b) The time-dependence of k_m obtained from predictions of the Ginzburg-Landau-type model (Fig. 3 of ref. 103).

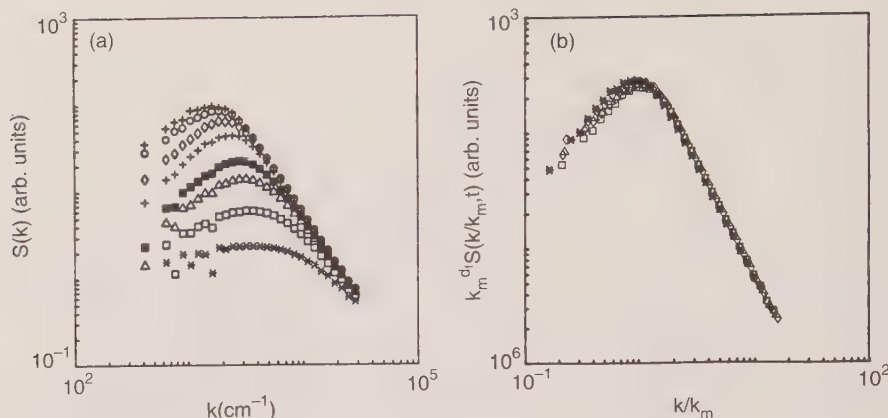


FIG. 12.18. (a) A log-log plot of the intensity distribution for a colloidal solution taken at various times during the aggregation. (b) A log-log plot of the scaled functions $k_m^{d_f} S(k/k_m, t)$ (Figs 2 and 3 of ref. 104).

12.6 Conclusions

In this chapter we have presented physical principles, pertinent equations and a survey of recent applications of small angle light scattering, to complex liquid systems in particular. However, this account is not intended as an exhaustive review of the wide field of phenomena that can be studied using this scattering technique. For example, one may consider solutions of large polymers near and above the gel transition and glassy systems above T_g which, in our opinion, deserve closer attention. In fact, in the field of complex systems, these constitute promising areas of pure and applied research. In addition, although SALS is a potentially powerful technique for investigating the behaviour of systems that show scaling properties on the mesoscopic scale, the results obtained so far lead to many open questions (more unanswered questions than answered ones). The structure factor of colloids in the hydrodynamic regime (see, e.g., the contribution of Klein and D'Aguanno in Chapter 2 and related works), the kinetics of aggregation (including percolation) in colloidal solutions, the late stage of phase separation, gels at high crosslinking contents, dense systems (such as charged colloids, proteins and polyelectrolytes) are some examples. In addition, we note that some of the phenomena presented here, as reported for the colloidal aggregation and spinodal decomposition, are in some ways interconnected, so that in the near future we should see novel improvements in the theoretical models, with many new suggestions for experimentalists.

Finally, we stress that combining SALS with other techniques that are sensitive either within the same (e.g. quasi-elastic light scattering in the same k region) or in a different (SANS and SAXS) length interval, should help to elucidate many of the above questions. Typical of this situation are the gels and

and structural networks which, as is well known, when formed by precise crosslinking mechanisms, have a swelling pressure and a statistical distribution of the component polymer chains that are characterized by many different correlation lengths falling into different scales (from microscopic to mesoscopic). Considering this, we note that for such systems there is, at the moment, lack of a general theory of scattering taking into account the effects of the presence of multiple correlation lengths, i.e. which would allow combination in a unique way of the results of static light scattering and SANS.

We conclude our *escursus* on the study of small angle light scattering in complex fluids by emphasizing that the properties of such systems are rich and varied and provide new and important insights in this field of the science, where many interdisciplinary interests meet and play important roles.

Acknowledgements

The authors are indebted to Professor R. Bansil, Professor S. H. Chen, and Professor R. Klein for numerous discussions and suggestions, and in particular to Professor Wyn Brown for the opportunity to participate in writing this book. We are also grateful for Dr C. Vasi and S. Trusso for helpful comments and to the Consiglio Nazionale delle Ricerche for financial support to our research.

References

1. Chen, S. H., Huang, J. S., and Tartaglia, P. (eds) (1992). *Structure and dynamics of strong interacting colloids and supramolecular aggregates in solutions*. Kluwer Academic, Dordrecht, Nato ASI Vol. 369; Degiorgio, V. and Corti, M. (eds) (1985). *Physics of amphiphiles, micelles, vesicles and microemulsions*. North-Holland; Schick, M. J. (ed.) (1987). *Nonionic surfactants: physics and chemistry*. Dekker, New York.
2. de Gennes, P.-G. (1979). *Scaling concepts in polymer physics*. Cornell University Press, Ithaca, New York.
3. Stanley, H.-E. and Ostrowsky, N. (eds) (1986). *On growth and form*. Nato ASI series. Nijhoff, Dordrecht.
4. Jackson, J. D. (1965). *Classical electrodynamics*. John Wiley, New York.
5. Berne, B. and Pecora, R. (1976). *Dynamic light scattering*. John Wiley, New York.
6. (a) Tyndall, J. (1869). *Phil. Mag.*, **37**, 384.
(b) Tyndall, J. (1869). *Phil. Mag.*, **38**, 156.
7. (a) Rayleigh, Lord (1871). *Phil. Mag.*, **51**, 107, 274, 447.
(b) Rayleigh, Lord (1881). *Phil. Mag.*, **12**, 81.
(c) Rayleigh, Lord (1899). *Phil. Mag.*, **47**, 375.
(d) Rayleigh, Lord (1910). *Proc. R. Soc.*, **A84**, 25.
(e) Rayleigh, Lord (1918). *Proc. R. Soc.*, **A94**, 296.
8. (a) Debye, P. (1909). *Ann. Phys.*, **30**, 755.
(b) Debye, P. (1915). *Ann. Phys.*, **46**, 809.
(c) Debye, P. (1947). *J. Phys. Coll. Chem.*, **51**, 18.
9. Gans, R. (1925). *Ann. Phys.*, **76**, 29.
10. von Smoluchowski, M. (1908). *Ann. Phys.*, **25**, 156.
11. Einstein, A. (1910). *Ann. Phys.*, **33**, 1275.

12. (a) Ornstein, L. S. and Zernike, F. (1914). *Proc. Acad. Sci. Amst.*, **17**, 793.
(b) Ornstein, L. S. and Zernike, F. (1916). *Proc. Acad. Sci. Amst.*, **19**, 1312, 1321.
(c) Ornstein, L. S. and Zernike, F. (1926). *Phys. Z.*, **27**, 761.
13. (a) Zimm, B. H. (1946). *J. Chem. Phys.*, **14**, 164.
(b) Zimm, B. H. (1948). *J. Chem. Phys.*, **16**, 1093, 1099.
(c) Zimm, B. H. (1956). *J. Chem. Phys.*, **24**, 269.
14. (a) Brillouin, L. (1914). *C.R. Acad. Sci., Paris*, **158**, 1331.
(b) Brillouin, L. (1922). *Ann. Phys.*, **17**, 88.
15. Mie, G. (1909). *Ann. Phys.*, **25**, 377.
16. van de Hulst, H. C. (1951). *Light scattering by small particles*. John Wiley, New York.
17. Stratton, J. A. (1941). *Electromagnetic theory*. McGraw-Hill, New York.
18. Mungnai, A. and Wiscombe, W. J. (1986). *Appl. Opt.*, **25**, 1235.
19. (a) Glatter, O., Hofer, M., Jorde, C., and Einger, W. D. (1985). *J. Colloid Interface Sci.*, **105**, 577.
(b) Glatter, O. and Hofer, M. (1988). *J. Colloid Interface Sci.*, **127**, 484.
20. Titchmarsh, E. C. (1925). *Proc. Lond. Math. Soc.* 2, **23**, XXII–XXIV.
21. Chin, J. H., Sliepecevich, C. M., and Tribus, M. (1955). *J. Chem. Phys.*, **59**, 841.
22. Shifrin, K. S. (1956). *Trudy VZLTI, Leningrad*, **2**, 153.
23. Watson, G. N. (1922). *A treatise on the Theory of Bessel functions*, p. 136. Cambridge University Press, London.
24. Knight, J. C., Ball, D., and Robertson, G. N. (1991). *Appl. Opt.*, **30**, 4759.
25. Kadanoff, L. P. and Martin, P. C. (1963). *Ann. Phys. (N.Y.)*, **24**, 419.
26. Zwanzig, R. (1965). *Ann. Rev. Phys. Chem.*, **16**, 67.
27. Martin, P. C. (1968). *Measurements and time correlation functions*. Gordon and Breach, New York.
28. Van Hove, L. (1954). *Phys. Rev.*, **95**, 249.
29. Volino, F. (1977). *Micro structure and dynamics of liquids* (ed. J. Dupuy and A. J. Dianoux). Plenum Press, New York.
30. (a) Kotlarchyk, M. and Chen, S. H. (1983). *J. Chem. Phys.*, **79**, 2461.
(b) Kotlarchyk, M., Chen, S. H., and Huang, J. S. (1984). *Phys. Rev. A*, **29**, 2054.
31. Glatter, O. and Kratky, L. (1983). *Small angle X-ray scattering*. Academic Press, New York.
32. Guinier, A. and Fournet, G. (1955). *Small angle scattering of X-rays*. John Wiley, New York.
33. Egelstaff, P. A. (1971). *Thermal neutron scattering*. Academic Press, New York.
34. Sheu, E. G., Chen, S. H., Huang, J. S. and Sung, J. C. (1989). *Phys. Rev. A*, **39**, 5867.
35. Aragon, S. R. and Pecora, R. (1976). *J. Chem. Phys.*, **64**, 2395.
36. Lebowitz, J. L. and Percus, J. K. (1966). *Phys. Rev.*, **144**, 251.
37. Hansen, J. P. and Hayter, J. B. (1982). *Mol. Phys.*, **46**, 561.
38. Hayter, J. B. and Zulauf, M. (1982). *Colloid Polym. Sci.*, **260**, 1023.
39. Van Beurten, P. and Vrij, A. (1981). *J. Chem. Phys.*, **74**, 2744.
40. Hansen, J. P. and McDonald, I. R. (1976). *Theory of simple liquids*. Academic Press, London.
41. Rogers, F. J. and Young, D. A. (1984). *Phys. Rev. A*, **30**, 999.
42. D'Aguanno, B. and Klein, R. (1991). *J. Chem. Soc. Faraday Trans.*, **87**, 379.
43. Flory, P. J. (1953). *Principles of polymer chemistry*. Cornell University Press, Ithaca, New York.
44. Fabelinskii, I. L. (1969). *Molecular scattering of light*. Plenum Press, New York.
45. Chu, B. (1974). *Laser light scattering*. Academic Press, New York.
46. Harpst, J. A. (1980). *Biophys. Chem.*, **11**, 295

47. (a) Zimm, B. H. (1946). *J. Chem. Phys.*, **14**, 164.
(b) Zimm, B. H. (1948). *J. Chem. Phys.*, **16**, 1093.
48. (a) Benmouna, M. and Benoît, H. (1983). *J. Polym. Sci., Polym. Phys. Ed.*, **21**, 1227.
(b) Benoît, H. and Benmouna, M. (1984). *Macromolecules*, **17**, 535.
(c) Benoît, H., Benmouna, M., and Wu, W. (1990). *Macromolecules*, **23**, 1512.
49. Stauffer, D. and Stanley, H. E. (1990). *From Newton to Mandelbrot*. Springer-Verlag, Berlin.
50. Stauffer, D. (1979). *Phys. Rep.*, **54**, 1.
51. Stauffer, D. (1985). *Introduction to percolation theory*. Taylor and Francis, London.
52. Vicsek, T. and Family, F. (1984). *Phys. Rev. Lett.*, **52**, 1669.
53. Mandelbrot, B. (1977). *Fractals, form and dimensions*. Freeman, San Francisco.
54. Witten, T. A. and Sander, L. M. (1981). *Phys. Rev. Lett.*, **47**, 1400.
55. (a) Placzek, G. (1952). *Phys. Rev.*, **86**, 377.
(b) Wick, G. C. (1954). *Phys. Rev.*, **94**, 1228.
56. Teixeira, J. (1986). In *On growth and form* (ed. H.-E. Stanley and Ostrowsky, N.). Nato ASI series. Nijhoff, Dordrecht.
57. Chen, S. H. and Teixeira, J. (1986). *Phys. Rev. Lett.*, **57**, 2583.
58. Stauffer, D. (1986). In *On growth and form* (ed. H.-E. Stanley and Ostrowsky, N.). Nato ASI series. Nijhoff, Dordrecht.
59. Martin, J. E. and Ackerson, J. (1985). *Phys. Rev. A*, **31**, 1180.
60. Aharony, A. (1980). *Phys. Rev. B*, **22**, 400.
61. Klein, R., Weitz, D. A., Lin, M. Y., Lindsay, H. M., Ball, R. C., and Meakin, P. (1990). *Progr. Colloid Polym. Sci.*, **81**, 161.
62. Kolb, M., Jullien, R., and Botet, R. (1983). *Phys. Rev. Lett.*, **51**, 1123.
63. (a) Meakin, P. (1983). *Phys. Rev. Lett.*, **51**, 1119.
(b) Meakin, P. (1983). *Phys. Rev. A*, **27**, 1495.
64. Jullien, R. and Kolb, M. (1984). *J. Phys. A*, **17**, L369.
65. Kolb, M. and Jullien, R. (1984). *J. Phys. Lett.*, **46**, L977.
66. Weitz, D. A., Huang, J. S., Lin, M. Y., and Sung, J. (1984). *Phys. Rev. Lett.*, **53**, 1657; (1985). **54**, 1123.
67. (a) von Smoluchowski, M. (1916). *Phys. Z.*, **17**, 557.
(b) von Smoluchowski, M. (1916). *Phys. Z.*, **17**, 585.
(c) von Smoluchowski, M. (1917). *Z. Phys. Chem.*, **92**, 129.
68. Mountain, R. G. and Molholland, G. W. (1988). *Langmuir*, **4**, 1321.
69. Van Dongen, P. G. J. and Ernst, M. H. (1985). *Phys. Rev. Lett.*, **54**, 1396.
70. Ball, R. C., Weitz, D. A., Witten, T. A., and Leyvraz, F. (1987). *Phys. Rev. Lett.*, **58**, 274.
71. Hess, W., Frish, H. L., and Klein, R. (1986). *Z. Phys. B*, **64**, 65.
72. Choen, R. J. and Benedek, G. B. (1982). *J. Phys. Chem.*, **86**, 3696.
73. Brown, W. D. and Ball, R. C. (1985). *J. Phys. A*, **18**, L527.
74. (a) Meakin, P. and Family, F. (1988). *Phys. Rev. A*, **38**, 2110.
(b) Meakin, P. and Family, F. (1987). *Phys. Rev. A*, **37**, 5498.
75. Binder, K. (1990). In *Material science and technology: phase transformation in materials* (ed. P. Haasen), Vol. **5**, pp. 405–471, VCH, Weinham.
76. Goldburg, W. I. (1981) In *Scattering techniques applied to supramolecular and nonequilibrium systems* (eds S. H. Chen, B. Chu and R. Nossal). Plenum Press, New York.
77. Onuki, A. and Kawasaki, K. (eds) (1989). *Dynamics and patterns in complex fluids*. Springer, Heidelberg; Kawasaki, K., Tokuyama, M., and Kawakatsu, T. (eds) (1992). *Slow dynamics in condensed matter*. American Institute of Physics, New York.

78. (a) Kubota, K., Kuwahara, N., Eda, H., Sakazume, M., and Takiwari, K. (1992). *J. Chem. Phys.*, **97**, 9291.
(b) Kubota, K., Kuwahara, N., Eda, H., Sakazume, M., and Takiwari, K. (1992). *Phys. Rev. A*, **45**, R3377.
79. Cahn, J. W. and Hilliard, J. E. (1958). *J. Chem. Phys.*, **28**, 258.
80. Furukawa, H. (1985). *Adv. Phys.*, **34**, 703.
81. Kawakatsu, T., Kawasaki, K., Furusaka, M., Okabayashi, H., and Kanaka, T. (1993). *J. Chem. Phys.*, **99**, 8200.
82. Shinokazi, A. and Oono, Y. (1993). *Phys. Rev. A*, **48**, 2622.
83. Glotzer, S. C., Gyure, M. F., Sciortino, F., Coniglio, A., and Stanley, H. E. (1994). *Phys. Rev. E*, **49**, 247.
84. Laradji, M., Mouritsen, O. G., Toxvaerd, S., and Zuckermann, M. J. (1994). *Phys. Rev. E*, **50**, 1243.
85. Mallamace, F., Micali, N., Trusso, S., and Chen, S. H. (1995). *Phys. Rev. E*, in press.
86. Langer, J. S., Bar-on, M., and Miller, H. D. (1975). *Phys. Rev. A*, **11**, 1417.
87. (a) Kawasaki, K. and Ohta, T. (1978). *Progr. Theor. Phys.*, **59**, 362.
(b) Ohta, T. and Nozaki, H. (1989). In *Space-time organization in macromolecular fluids* (eds F. Tanaka, M. Doi and T. Ohta). Springer, New York; Koga, T. and Kawasaki, K. (1991). *Phys. Rev. A*, **44**, 817.
88. Siggia, E. D. (1979). *Phys. Rev. A*, **20**, 295.
89. (a) Binder, K. and Stauffer, D. (1974). *Phys. Rev. Lett.*, **33**, 1006.
(b) Binder, K. and Stauffer, D. (1976). *Adv. Phys.*, **25**, 343.
(c) Binder, K. (1983). *J. Chem. Phys.*, **79**, 6387.
90. de Gennes, P. G. (1980). *J. Chem. Phys.*, **72**, 4756.
91. Pincus, P. (1981). *J. Chem. Phys.*, **75**, 1996.
92. Gunton, J. D., San Miguel, M., and Sahni, P. S. (1983). In *Phase transition and critical phenomena* (eds C. Domb and J. L. Lebowitz), Vol. 8, Academic Press, New York.
93. Hashimoto, T. (1988). *Phase Transitions*, **12**, 47.
94. Sato, T. and Han, C. C. (1988). *J. Chem. Phys.*, **88**, 2057.
95. (a) Cametti, C., Codastefano, P., Tartaglia, P., Rouch, J., and Chen, S. H. (1990). *Phys. Rev. Lett.*, **64**, 1461.
(b) Ku, C. Y., Chen, Rough, J., and Tartaglia, P. (1995). *Int. J. Thermophys.*, to appear.
96. Knobler, K. and Wong, N. C. (1981). *J. Chem. Phys.*, **85**, 1972.
97. Komura, S., Osamura, K., Fujih, H., and Takeda, T. (1985). *Phys. Rev. B*, **31**, 1278.
98. Maro, J., Lebowitz, J. L., and Kalos, M. H. (1979). *Phys. Rev. Lett.*, **43**, 282.
99. Chou, Y. C. and Goldburg, W. L. (1981). *Phys. Rev. A*, **23**, 858.
100. Furusaka, M., Ishikura, Y., and Mera, M. (1985). *Phys. Rev. Lett.*, **54**, 2612.
101. Lebowitz, J. L., Marro, J., and Kalos, M. H. (1982). *Acta Metall.*, **30**, 297.
102. Bansil, R., Lal, J., and Carvalho, B. (1992). *Polymer*, **33**, 2961.
103. Sciortino, F., Bansil, R., Stanley, H. E., and Alström, P. (1993). *Phys. Rev. E*, **47**, 4615.
104. (a) Carpineti, M. and Giglio, M. (1992). *Phys. Rev. Lett.*, **68**, 3327.
(b) Carpineti, M. and Giglio, M. (1993). *J. Phys. (Paris)*, **3**, 43.

Combined static and dynamic light scattering

Walther Burchard

13.1 Introduction

Dynamic light scattering (DLS) has been applied in polymer and colloid science for about 30 years^[1,2] and many review articles and several books have been published on the topic.^[3-11] Although the theory is well developed, there are probably several reasons why another review is timely. The first is that research in polymer science has been mainly concerned with flexible linear chains or with rigid rods in the dilute and semi-dilute solution regimes. Recently, however, polymer scientists have become increasingly interested in the behaviour and characterization of other polymeric architectures such as semi-flexible or worm-like chains, cyclic macromolecules, star-branched macromolecules, randomly branched and hyper-branched structures, but systematic studies have not been made and an overview has not yet appeared. A review is also desirable for systems which undergo reversible association or irreversible aggregation in semi-dilute and concentrated solutions. In these cases the architecture that is formed under the influence of strong special interactions cannot be reliably predicted. Interpretation of such structures would certainly be greatly simplified if the dynamic behaviour of the mentioned covalently bound architectures was known and well understood.

Another reason why an overview may be useful follows from the observation that recent investigations have considered the dynamics alone without checking which equilibrium structure the system has adopted. This tendency relegates light scattering techniques to the stage of mechanical rheology: both techniques are essentially ‘blind’ and data interpretation relies on theories which in turn, are based on the assumption of particular models. Probably most of the present controversial discussions have their root in the assumption of specific models which have not been proven to be valid for the system.

Static LS, however, is not a ‘blind’ method. It reflects the equilibrium structure, not directly in space but as its Fourier transform which refers to the structure in reciprocal space. These static properties are, in principle, also contained in the data from dynamic light scattering which are used to construct the time correlation function (TCF) of the scattering intensity. Experimentally, the static data can be obtained simultaneously with the dynamic data, although extreme care has to be taken in instrument alignment.

Moreover, the time correlation function of the electric field $g_1(q, t)$ obtained from the intensity TCF is the dynamic structure factor $S(q, c, t)$, normalized by the static structure factor $S(q, c)$:

$$g_1(q, c, t) = S(q, c, t)/S(q, c). \quad (13.1)$$

This fact makes it clear that valuable knowledge is neglected when the static structure factor is not taken into account. Because of the great care required in the optical alignment of the photogoniometer, it is often advisable to record the static scattering data separately in a different set-up for which the scattering volume is much larger than in the dynamic LS equipment, and where a longer accumulation time is used. In recent developments the scattered intensity is immediately converted into frequencies which are proportional to the intensity.^[1,2] This design has immensely improved the accuracy and reliability of the measured data, since counting frequencies in a given time interval is very accurate and drastically reduces the noise. In fact, this counting much resembles photon-counting employed in modern autocorrelators. Simultaneous recording of static and dynamic data becomes imperative when time-dependent systems are studied, i.e. aging of slowly associating or dissociating ensembles. In such experiments, exact reproducibility of the measurements is often not feasible, while separately measured static and dynamic scattering data will not reflect identical conditions.

In dynamic LS the scattered intensity is detected over very short time intervals and results in strong fluctuations that are mostly due to the concentration fluctuations. Polymeric chains are often rather flexible and therefore two different types of motion mainly contribute: (i) the translational motion of the centre of mass of the individual particles; and (ii) the internal modes of motion of segments with respect to their centres of mass. Both types can be distinguished in experiments by the fact that translational diffusion always exhibits a well-defined angular dependence of the relaxation time, while the internal motions are independent of the scattering angle.

To avoid parallel reading of other reviews, some basic relationships of dynamic LS will be briefly given. The new quantities that are obtained by combination of static and dynamic LS data are then discussed in more detail with regard to various molecular architectures. The review then turns to larger architectures, and in particular to flexible chains and the yet unsolved problem of internal mobility. The final part deals with semi-dilute and more concentrated solutions, emphasizing systems which under these conditions undergo reversible association or irreversible aggregation.

13.2 Time correlation functions of the scattered intensity and electric field^[6]

In dynamic LS the scattered intensity originating from a very small scattering volume is measured within short time intervals, Δt . The resulting strong fluctuations are converted into a smooth time correlation function by the following manipulations that are performed by an autocorrelator: The scattering

intensity of two time intervals that are separated by j time intervals are multiplied, and this process is repeated about 10^6 times to give a good average. These procedures are performed for a large number of delayed times $t = j\Delta t$ ($j = 1, 2, 3, \dots, n$) which eventually represents the time correlation function (TCF) of the scattered intensity

$$\langle i(0)i(t) \rangle = G_2(q, t) = B(1 + \beta|g_1(q, t)|^2), \quad (13.2)$$

where B is a baseline that corresponds to the square of the average scattering intensity, β is an efficiency factor and $g_1(q, t)$ is the normalized TCF of the scattered field:

$$g_1(q, t) = S(q, c, t)/S(q, c), \quad (13.3)$$

with $q = (4\pi/\lambda) \sin(\theta/2)$ the value of the scattering vector at scattering angle θ . $S(q, c, t)$ is the dynamic structure factor, written explicitly as

$$S(q, c, t) = \langle \exp[iq|r_j(0) - r_k(t)|] \rangle. \quad (13.4)$$

The static structure factor $S(q, c)$ has the same form but does not depend on time. The sum is taken over all pairs (j, k) of segments in the scattering volume.

Figures 13.1(a) and (b) show examples of a TCF in two different plots. In Fig. 13.1(a) the logarithm of the TCF, $\ln g_1(t)$, is plotted against the delay time t . This curve has an initial linear decay that at larger times deviates to a weaker decay. In Fig. 13.1(b) the same TCF is plotted linearly against the logarithm of time. The dotted line represents the behaviour of a single exponential TCF (the dotted straight line in Fig. 13.1(a)) where both curves have the same initial decay. Figure 13.1(a) immediately shows the deviation from a single exponential, which is of essential relevance for the system. However, the deviation can become very strong and such an appreciable decay can only be observed after some decades of time; for this reason Fig. 13.1(b) is to be preferred.

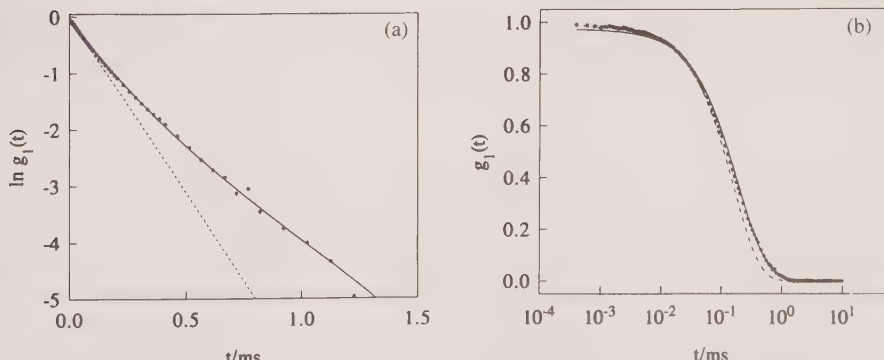


FIG. 13.1. The time correlation function of the scattered electric field plotted (a) as $\ln g_1(t)$ against delay time t and (b) as $g_1(t)$ against $\log t$. Measurements made on a polyetherketone in concentrated sulphuric acid at 20°C.

The most important operation in eqn (13.4) is indicated by the brackets $\langle \rangle$ which means the average over all positions of the scattering elements in the time interval t . This operation requires knowledge of the space-time correlation (or distribution) function and is the main problem in the theory of dynamic LS.

13.3 Small particles

As a first example, a dilute solution of small particles may be considered. Here ‘dilute’ means a concentration which is so low that two particles have only a very low probability of colliding within the time interval of observations. ‘Small particles’, on the other hand, refers to particles which are still large compared to the volume of a solvent molecule but are small compared to the wavelength of the applied light ($R_g < \lambda/10$). Under these conditions the dynamics of the particles can be considered to be that of Brownian motion. Einstein^[13] showed that the motion of these Brownian particles can be described by a differential equation which becomes identical to that of the diffusion equation by setting

$$D = kT/(6\pi\eta_0 R_h). \quad (13.5)$$

(Note, however, that the common diffusion equation describes macroscopic transport for a return to thermodynamic equilibrium, while the Einstein approach is based on a *molecular ensemble in thermodynamic equilibrium*.) The Stokes–Einstein relationship given in eqn (13.5) is strictly valid only for hard spheres but is used also to define a hydrodynamically effective sphere to describe macromolecules or colloidal particles which may strongly deviate in shape from a hard sphere.

The diffusion differential equation allows the derivation of the desired space-time distribution. The average required in eqn (13.3) is easily performed and gives^[6]

$$g_1(q, c, t) = \exp(-\Gamma t) = \exp(-q^2 D t). \quad (13.6)$$

Hence the translational diffusion coefficient D and consequently the hydrodynamic radius R_h may be easily measured at an arbitrary scattering angle by plotting $-\ln[g_1(q, t)]$ against the delay time t , the slope of which gives Γ and the diffusion coefficient D .

13.4 Polydispersity and determination of molar mass distributions

Reality, however, is more complex than set out in the previous section, because in general the curves deviate from a straight line at longer delay times, as was indicated in Fig. 13.1. These deviations are caused by polydispersity and, for large particles, as discussed below, by internal modes of motion. The effect of polydispersity can be expressed by the equation

$$g_1(q, c, t) = \int M_w(M) \exp(-q^2 D t) dM/M_w = \int A(M) \exp(-q^2 D t) dM, \quad (13.7)$$

where $w(M)$ is the mass distribution of molar masses, D is the translational diffusion coefficient of a particle with molar mass M , and M_w represents the weight-average molar mass. The translational diffusion coefficient often displays power-law behaviour with respect to M ,

$$D = KM^{-v}, \quad (13.8)$$

such that D (or M) can be expressed in terms of M (or D). Usually eqn (13.6) is written as

$$g_1(q, t) = \int A(\tau) \exp(-t/\tau) d\tau, \quad q^2 D = 1/\tau. \quad (13.9, 13.10)$$

Equation (13.9) represents $g_1(q, t)$ as a Laplace transformation of the relaxation time spectrum. Inversion gives the desired distribution $A(\tau)$ and, together with eqns (13.7) and (13.8), the molar mass distribution $w(M)$. Inversion, for instance by means of the CONTIN program of Provencher,^[14] yields good agreement with SEC/LALLS detection for unimodal distributions. Figure 13.2 shows as an example the distribution obtained by Laplace inversion from the TCF shown in Fig. 13.1, and this result is compared with the SEC result.^[15] The distribution could be well fitted with the logarithmic normal distribution and gave a polydispersity of $M_w/M_n = 2.6$. Much broader size distributions are obtained with randomly branched materials, for which the polydispersity index M_w/M_n is expected to increase proportionally to the degree of polymerization. Percolation theory predicts^[16] power-law behaviour for such systems near the gel point

$$w(M) = AM^{1-p}f(M/M^*) \quad (13.11)$$

with a cut-off function, $f(M/M^*)$, at the upper end where the distribution decays

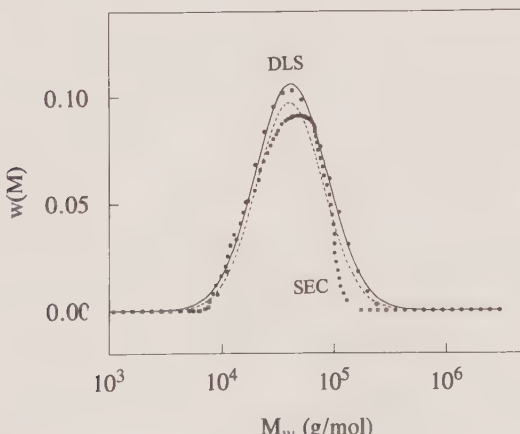


FIG. 13.2. The molar mass distribution for the same sample as in Fig. 13.1, determined by dynamic LS (symbols) and by SEC/LALLS (full line).^[15b]

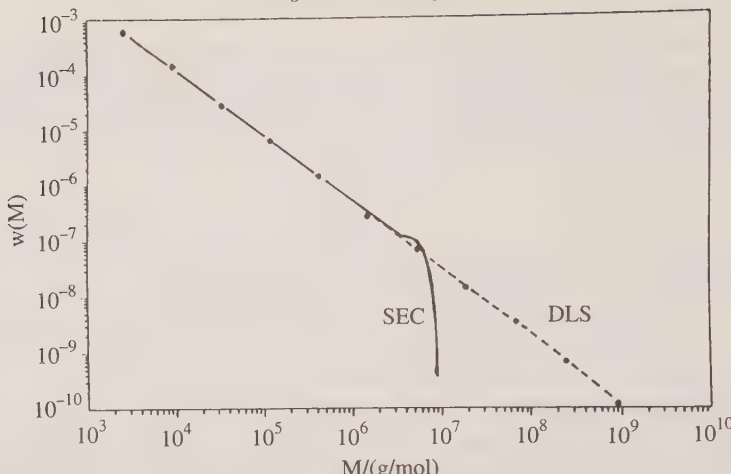


FIG. 13.3. The molar mass distribution of a highly branched polycyanurate near the gel point, determined by dynamic LS (symbols) and by SEC/LALLS (full line) in THF. The sharp decay at large M results from the upper SEC exclusion limit.^[9,10]

more strongly. The A value of $\tau_p = 2.2$ is predicted, and was indeed found for various systems. At the gel point the cut-off function becomes unity, and power-law behaviour is expected over the whole molecular mass region. Even this power-law behaviour of randomly branched polymers is correctly obtained using the inversion technique, as is demonstrated in Fig. 13.3 with a randomly branched polycyanurate obtained by polycyclotrimerization.^[17] Many other examples appear in the literature.

13.5 Large particles

Both static and dynamic LS exhibit an angular dependence with large particles and this is usually expressed in terms of the static and dynamic structure factors. As is well known, the static structure factor $S(q, c)$ can be factorized as follows:^[18,19]

$$S(q, c) = P(q)S'(q, c), \quad (13.12)$$

where $P(q)$ denotes the particle scattering factor that describes the shape of the individual macromolecules, and $S'(q, c)$ describes the order of arranging the particles in space and is related to the centre of mass. Similar factorization may also be used as an approximation for the dynamic structure factor $S(q, c, t)$, such that

$$g_1(q, c, t) = [P(q, t)S'(q, c, t)]/[P(q)S'(q, c)]. \quad (13.13)$$

This approximation helps greatly to derive principal conclusions without employing detailed mathematics.

13.6 Special examples

13.6.1 Hard spheres

Two types of motion have to be considered: (i) the translational diffusion of the centre of mass; and (ii) the rotation of the sphere during this diffusion process. The centre-of-mass diffusion can be described by the already mentioned equation

$$S'(q, c, t)/S'(q, c) = \exp(-q^2 D_c t)[S'(0, c)/S'(q, c)] \quad (13.14)$$

with

$$D_c = D_0(1 + k_D c). \quad (13.15)$$

From Fig. 13.4 we notice that rotation does not correspond to a change in shape of the particle. Thus

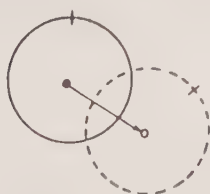
$$P(q, t) = P(q)$$

and

$$g_1(q, c, t) = S'(q, c, t)/S'(q, c) = [\exp(-q^2 D_c t)][S'(0, c)/S'(q, c)]. \quad (13.16)$$

Equation (13.16) is commonly used in colloid science even for irregularly structured aggregates, and is also a rather good approximation for geometrically anisotropic particles.^[20] At low concentrations the second factor in eqns (13.14) and (13.16) becomes unity, but at large concentrations a liquid-like ordered packing occurs, and the static structure factor now develops the characteristic maxima and minima related to the number of neighbouring particles in the highly concentrated solution. Thus, for low concentrations eqn (13.16) predicts no angular dependence of $D_c = \Gamma/q^2$ for homogeneous spheres, even for particles which display a very strong angular dependence in static LS. This fact has been proved using monodisperse polystyrene particles. The result is demonstrated in Fig. 13.5. The strong decay at large q -values has been diagnosed as an artefact caused by the weak reflection of the primary beam at the water/glass surface. Further details are given in the original paper.^[21]

Hard spheres:



translation



rotation, no change
in shape

FIG. 13.4. Hard spheres: the influence of the two types of motion on the apparent shape of the object.

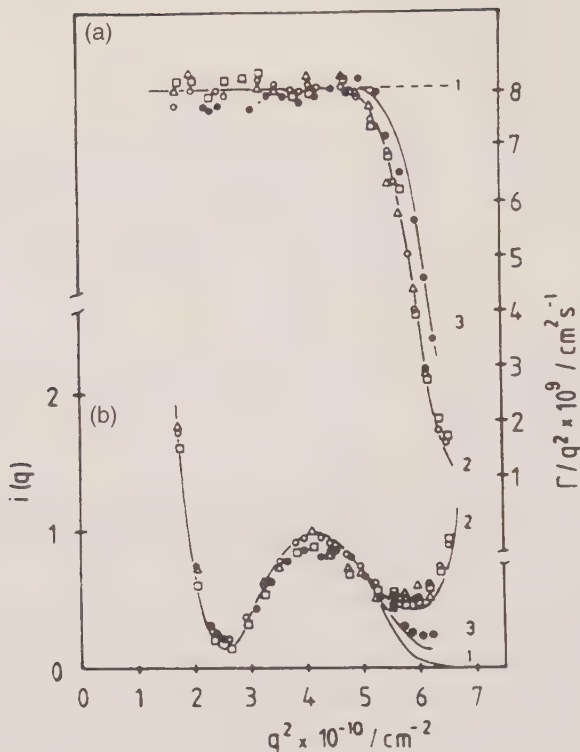


FIG. 13.5. Angular dependencies of the static LS (a) and the diffusion coefficient $D_c = \Gamma/q^2$ (b) for a polystyrene latex of $R = 405$ nm. The strong decay of D_c at large q values results from back reflection.^[21]

13.6.2 Rod-like rigid particles

For geometrically anisotropic particles, $P(q, t)$ measured for a rod that has rotated by a certain angle differs from the averaged particle scattering factor over a long time t . Hence, the erratic rotation of the rods can be calculated, and this may be done using the differential equation for rotational diffusion. The averaging procedure with the so-derived orientational distribution eventually leads to^[6,22]

$$g_1(q, t) = [\exp(-q^2 D t)] : \sum_i P_i(qR_g) \exp[-i(i+1)D_{rot}t], \quad i = 0, 2, 4, 6, \dots \quad (13.17)$$

In general, only the first two relaxation times can be measured, which are

$$(1/\tau_1) = q^2 D \quad \text{and} \quad (1/\tau_2) = (q^2 D + 6D_{rot}).$$

Hence both diffusion coefficients can be determined. However, the two relaxation times can be observed only at rather large qR_g . In this region the first term $P_0(qR_g)$ has decreased strongly, but the prefactor of the second mode still remains fairly small.^[6,11] Once the two diffusion coefficients are known, the

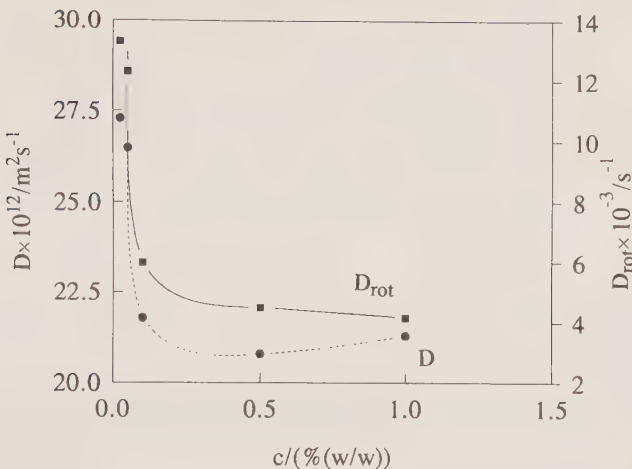


FIG. 13.6. The concentration dependence of the translational (D) and rotational (D_{rot}) diffusion coefficients for an $\text{EO}_n\text{-PO}_m\text{-EO}_n$ triblock copolymer in water.^[25]

dimensions of the anisotropic particles can be obtained. For prolate ellipsoids, for instance, one has^[23]

$$D = [kT/(6\pi\eta_0 r)]G(s), \quad (13.18a)$$

$$D_{rot} = [3kT/(16\pi\eta_0 r^3)][(2-s)G(s)-1]/[1-s^2] \quad (13.18b)$$

with

$$G(s) = (1-s^2)^{-1/2} \ln[1 + (1-s^2)^{1/2}/s], \quad (13.18c)$$

where $s = b/a$ is the inverse axial ratio of the ellipsoid and $r = (4ab^2)^{1/3}$. Equations (13.18a-c) can be solved for s and r , and from these parameters the absolute values of a and b can be derived. Similar, but slightly more complicated, relationships have also been derived for cylinders.^[24] This technique has successfully been applied to the characterization of micellar structures of ethylene oxide-propylene oxide triblock copolymers ($\text{EO}_n\text{-PO}_m\text{-EO}_n$) in aqueous media.^[25] Figure 13.6 shows the obtained concentration dependence of the translational and rotational diffusion coefficients, both of which decrease as a result of growth in rod length. Another technique of determining the rod length will be discussed in Section 13.7.1. See also chapter 12 of ref. 11 for a more detailed discussion.

13.6.3 Flexible chains

Here again, $P(q, t)$ differs from $P(q)$, as is illustrated by Fig. 13.7. A solution of the problem is possible for the bead-spring model. The result of the eigenvalue problem is very similar to that of the rigid rod and is given by the relationship^[6]

$$S'(q, c, t)P(q, t) = P_0(qR_g)\exp(-q^2Dt) + \sum_i P_i(qR_g)\exp[-(D_c q^2 + 1/\tau_i)t]. \quad (13.19)$$

The first four relaxation times may be determined, and the result will be discussed later in connection with the first cumulant.

Flexible chains:

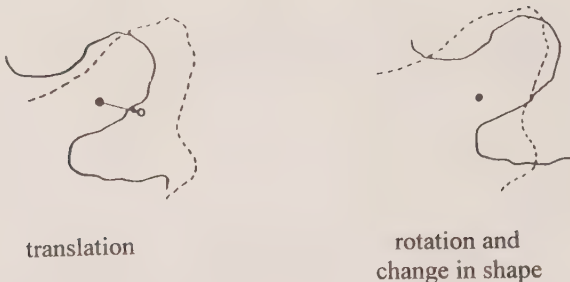


FIG. 13.7. Flexible chains: the influence of the two types of motion on the shape of a flexible object. During translational and rotational diffusion a change in shape occurs.

13.7 First cumulant

The first cumulant is defined by the initial slope of the logarithmic TCF:

$$\Gamma_1 = -\partial \ln g_1(q, t)/\partial t, \quad \text{at } t = 0. \quad (13.20)$$

Applied to eqn (13.19) this gives

$$D_{app}(q) \equiv \Gamma_1/q^2 = D_c \{P_0(qR_g) + \sum P_i(qR_g)/\tau_i\}. \quad (13.21)$$

Two limiting relationships can be found without referring to special architectures:^[26]

$$D_{app}(q) = D_c(1 + Cq^2R_g^2 - \dots), \quad \text{for } qR_g < 2, \quad (13.22)$$

$$D_c = D_0(1 + k_D c) \quad [\text{eqn (13.15)}]$$

and^[26,27]

$$D_{app}(q) \rightarrow \Gamma^*(\eta_0/kT)q, \quad \text{for } qR_g \gg 1, \quad (13.23)$$

where C is a coefficient which, like the parameter $\rho = R_g/R_h$ discussed below, depends on the macromolecular architecture.^[26] Actually, the C -parameter is determined by the slowest internal mode of motion in the particle and thus also depends on particle polydispersity.^[26,28]

13.7.1 Dynamic Zimm plot

A comparison of eqn (13.22) with the common static LS equation,

$$Kc/R_\theta = [1 + \frac{1}{3}q^2R_g^2]/M_w + 2A_2c + \dots, \quad (13.24)$$

reveals a close similarity. Thus the dynamic LS first cumulant data can be plotted in the same manner as a Zimm plot for the static measurements. Examples of static and dynamic Zimm plots are given in Fig. 13.8. Other examples have been discussed previously.^[21,26,29] Hence, in favourable circumstances six molecular parameters may be obtained,^[30] i.e. the two intercepts

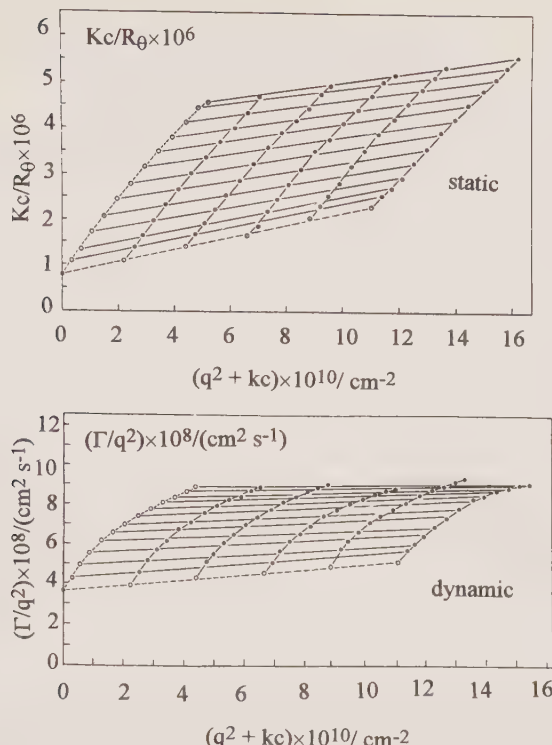


FIG. 13.8. Static and dynamic Zimm plots from a bacterial polysaccharides synthesized by *Rhizobium trifoli* strain TA-1. The intercepts give the molar mass and the translational diffusion coefficient; the initial slopes give the angular dependencies and the radius of gyration; and the parameter C in eqn (13.22) and the slopes of the concentration dependencies give the second virial coefficient A_2 and the correspondent dynamic interaction parameter k_D .^[42]

$1/M_w$ and D , respectively, the two slopes at $c = 0$ resulting in R_g and the coefficient C , and the two other slopes at $q = 0$ which give the interaction parameters A_2 and k_D . Applying the Stokes-Einstein relationship, one obtains the hydrodynamic radius R_h and, together with R_g , the ρ parameter, which is defined as

$$\rho = R_g/R_h. \quad (13.25)$$

The structural dependence of the parameters and C has been demonstrated previously^[4, 21, 28-30] with many examples and here only with two instructive examples will be set out. Table 13.1 gives a list of C and ρ for some selected structures.

The results in Fig. 13.20(b) below were obtained with microgels obtained by emulsion polymerization of polyvinylacetate on addition of increasing amounts of 1,4-butyldivinylether, which acts as a crosslinker. At low crosslinker

Table 13.1. The ρ parameter and the C parameter for selected structures.

Architecture	ρ	C
Homogeneous sphere	0.778	0
Random coil, monodisperse		
Theta conditions	1.50	0.173
Good solvent	1.78	—
Random coil, polydisperse, $z = 1$		
Theta conditions	1.73	0.200
Good solvent	2.05	—
Regular stars		
Theta conditions, $f = 4$	1.33	0.148
Theta conditions, $f \gg 1$	1.079	0.098
Rigid rod		
Monodisperse	> 2.0	0.042
Polydisperse, $z = 1$	> 2.0	0.16

concentrations, undercritical branching occurs and the ρ parameter corresponds to that for randomly branched clusters. With increasing crosslinker concentration the clusters grow in size until they reach the gelation point. The clusters can then no longer grow in radius, and the action of the crosslinker results in intramolecular network formation. The ρ parameter displays a clear transition to a lower value, which is smaller than that for hard spheres but is characteristic of microgels. Measurements have been made in methanol after removing the soap.

The reason for the decrease in the ρ parameter is schematically demonstrated in Fig. 13.9 for a linear chain and a microgel having the same radius of gyration. The radius of gyration is geometrically defined, while the hydrodynamic radius is also determined by the hydrodynamic interaction, which increases with the segmental concentration. During the translational motion of the particles, the solvent can penetrate deeply into the fairly open coil. However, solvent prefers to circumvent the obstacle if the particle is highly compact and then only the outer shell is drained.

The great value of the ρ and C parameters is that information on the structure can be obtained using a single sample, whereas conclusions on the shape of the particles are generally made from the molar mass dependence of the radii or the intrinsic viscosity. This fact is of particular relevance in the study of biological macromolecules, which adopt a unique well-defined supramolecular structure in addition to associated or aggregated structures which change with concentration. A few examples are discussed in Sections 11.3 and 12.2, which deal with concentrated solutions.

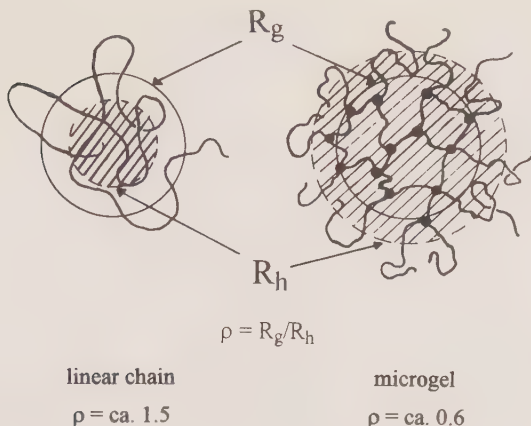


FIG. 13.9. A demonstration of the effect of draining on the hydrodynamic radius of particles. The fairly open structure of a flexible linear chain is compared with that for a microgel having the same radius of gyration (full lines). Because of its high segment density the microgel is drained only at its periphery (large R_h), whereas the solvent can drain the coil far more deeply (low R_h).

13.7.2 Asymptotic behaviour

Assuming flexible chain behaviour for the sub-chains, the asymptotic behaviour of the first cumulant can be rigorously calculated using Gaussian statistics or the blob model, respectively.^[27,32] Renormalization group theory (RG) was subsequently developed and allows derivation of the first cumulant over the whole range of qR_g values.^[31] The theoretical values and the experimentally observed asymptotic data are listed in Table 13.2.

Experimentally data measured by different groups^[33–37] agree remarkably well (see Fig. 13.10) but the agreement with theory is poor, especially with the prediction of the RG theory; the trend, however, is correctly predicted. Recently, Shiwa and Tsunashima^[38] have suggested a possible explanation. Since

$$\Gamma^* = (\Gamma/q^3)(\eta_0/kT) \quad (13.26)$$

they argue that the local solvent viscosity η_{eff} cannot be expected to equal

Table 13.2. A comparison of theoretically predicted and experimentally observed $\Gamma^*(\infty)$ values.

Solvent type	$\Gamma_{sb}^*(\infty)$ ^[23]	$\Gamma_{RG}^*(\infty)$ ^[22]	$\Gamma_{exp}^*(\infty)$ ^[24–22]
Good solvent	0.071	0.02669	0.062
Theta solvent	0.053	0.01292	0.044

sb = spring-bead model; RG = renormalization group theory; exp = experiment.

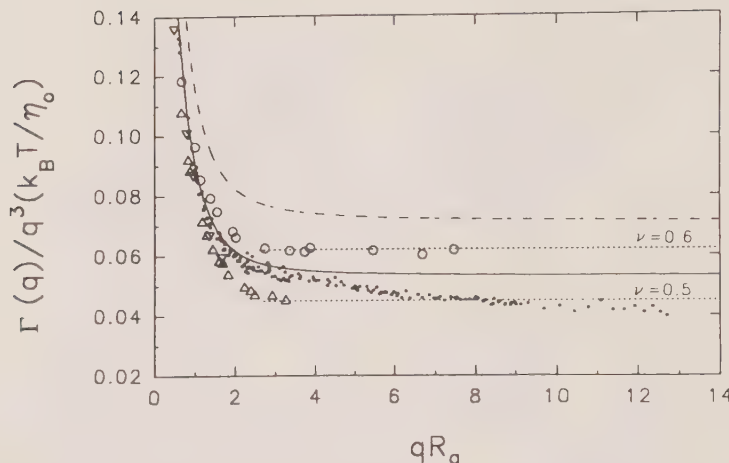


FIG. 13.10. A plot of $\Gamma^* = \Gamma/[q^3(kT/\eta)]$ against qR_g for linear chains^[24–28] in a good solvent (open circles), linear chains in a theta solvent (open triangles), and for branched polyesters^[30] near the gel point in a good solvent (filled points). The heavy lines correspond to theory, and the dotted ones to experimental estimates.

the macroscopically observed viscosity η_0 . Thus Shiwa introduces a factor λ_0^2 and writes

$$\Gamma^*(\infty) = \lambda_0^2 \Gamma_{RG}^*(\infty), \quad \lambda_0^2 = \eta_0 / \eta_{eff}. \quad (13.27a, b)$$

This λ_0 parameter is an empirical quantity so far not predicted by theory. It would be of interest to measure the local viscosity separately by another technique. To fit the experimental data one has to assume that the local viscosity is lower by a factor of 2.3–3.5 than the macroscopic solvent viscosity.

13.8 Alternative explanation

Recent experiments by Chi Wu *et al.*^[40] with high molar mass polystyrenes cast new light on this unresolved problem. The authors studied the TCF at small $qR_g < 0.4$ values, on the one hand, and the first cumulant at large qR_g values, on the other. The inversion of the TCF in the latter case always revealed two relaxation modes. The second mode was normalized with respect to the diffusion coefficient, giving a common plot for the three different molar masses, which can be expressed by

$$1/(D\tau_{2 exp}) = 1 + 1/(D\tau_i^{sb}). \quad (13.28)$$

These τ_i^{sb} values are related to those of the spring-bead model. Table 13.3 shows the first four relaxation times as predicted by the Pecora theory^[6] and the values that have been experimentally observed.

Table 13.3. Predicted and experimentally observed relaxation times for polystyrene.

	$1/\tau_1 \text{ exp}$	$1/\tau_2 \text{ exp}$	$1/\tau_3 \text{ exp}$	$1/\tau_4 \text{ exp}$
Pecora ^[1,6]	$2/\tau_1^{\text{sb}}$	$1/\tau_2^{\text{sb}}$	$4/\tau_1^{\text{sb}}$	$2/\tau_2^{\text{sb}}$
Observed ^[31]	$2/\tau_1^{\text{sb}}$	$2/\tau_2^{\text{sb}}$	$2/\tau_3^{\text{sb}}$	$2/\tau_4^{\text{sb}}$

sb = spring-bead model.

The reasons for these deviations are as yet unknown but the fact that some of the energetically possible relaxation modes are not observed by dynamic LS has a clear consequence for the height of the asymptotic plateau $\Gamma^*(\infty)$ in eqn (13.26): the missing relaxation modes must lead to a reduced value for this plateau, as in fact is observed.

13.9 Branched macromolecules

The effect of internal motions has so far been investigated only with monodisperse linear and flexible chains. Figure 13.10 shows the result for randomly crosslinked (vulcanized) monodisperse polyester chains.^[39] Three samples close to the gel point are plotted here in a common graph. Three essential observations can be made: (i) the measurements at different extents of cross-linking (different cluster sizes) asymptotically approach a common master curve; (ii) the curve decreases even when $qR_g > 8$; (iii) a plateau may eventually be approached at very large qR_g values, but this plateau is then much lower than the value of $\Gamma^*(\infty)$ observed for linear chains in a theta solvent.

The steady decrease of Γ^* is probably the result of the large polydispersity of these materials. This has the consequence, for large clusters, that internal modes can be seen with $\Gamma \sim q^3$.

The number of smaller particles in the distribution is still too small for observation of the internal motions, and only translational diffusion is observed with $\Gamma \sim q^2$, which leads to a dependence of $\Gamma^* \sim 1/q$. For sufficiently large qR_g values, internal motion should nonetheless become observable. The much lower $\Gamma^*(\infty)$ value found by experiment can only mean that several of the internal modes of motions are suppressed. This may be the result of a reduced internal flexibility of the subchains due to branching (i.e. a deviation from Gaussian statistics), but it could also be a result of the constraints of the fixed ends in a network, which would suppress a number of modes that are possible in the freely moving linear chain. Probably both reasons contribute, but this awaits suitable theory.

Another observation is worth mentioning. The plot of $\Gamma^*(q)$ as a function of qR_g is not universal for various randomly branched clusters.^[39] This is demonstrated by Fig. 13.11(a), which shows the measurements from the already

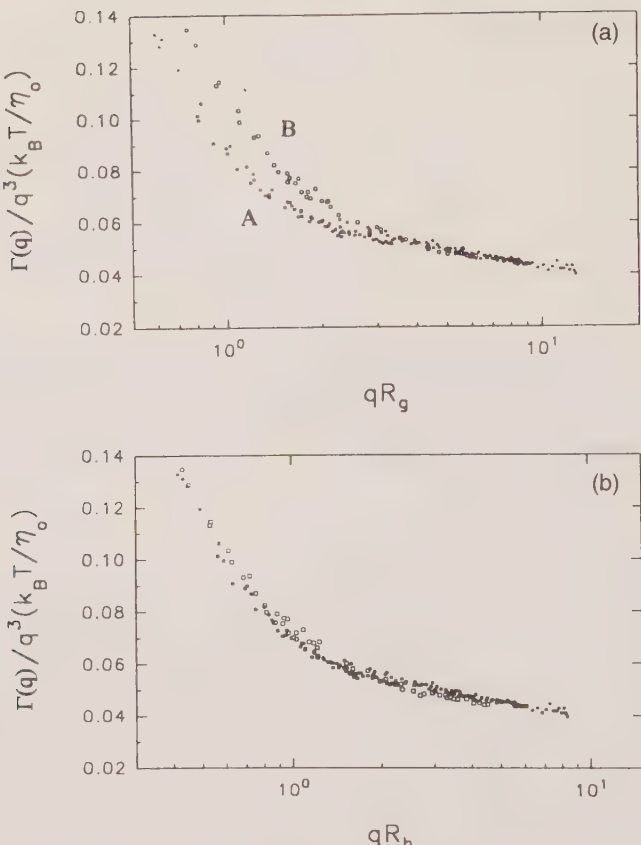


FIG. 13.11. (a) A plot of $\Gamma^*(q)$ as a function of qR_g for randomly vulcanized polyester chains (filled symbols) and for trifunctional polycyanurates (open symbols). (b) The same $\Gamma^*(q)$ data, but plotted against qR_h .^[39]

mentioned vulcanized polyesters compared with those from trifunctional polycyanurates. However, if qR_h is used the two curves collapse into a master curve (Fig. 13.11b).^[39]

13.10 Shape function

Equations (13.22) and (13.23) indicate that the first cumulant can be written in the universal scaled form

$$(q)/(D_0 q^2) = D_{app}(q)/D_0 = f(qR_g), \quad (13.29)$$

a result which is also predicted by the RG theory.^[31] This result holds for different polymer architectures but contains no explicit size dependence. Akcasu *et al.*^[27b] have observed that not only the first cumulant but also the whole

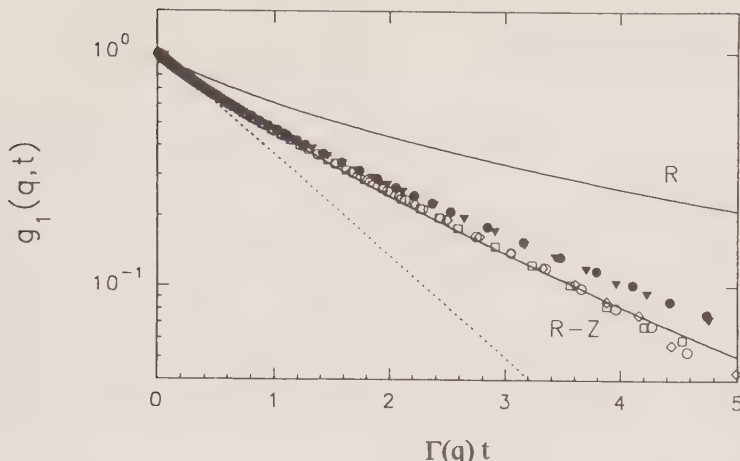


FIG. 13.12. A scaled plot of the TCF against $\Gamma(q)t = t/t^*$ (the *shape function*), for three different highly branched polyesters in THF. Filled symbols, measurements at various large angles such that $qR_g > 2$; open symbols results obtained with $qR_g < 1$. Full lines; R, Rouse model; R-Z Rouse-Zimm model. Dotted line, single exponential behaviour.^[39]

TCF can be expressed in an universal manner if $qR_g \gg 1$, where scaling is now performed with respect to time:

$$g_1(q, t) = g_1(t/t^*), \quad t^* = 1/\Gamma(q). \quad (13.30, 13.31)$$

This means that the strong angular dependence of the time correlation functions yields a common universal curve when the first cumulant is chosen as a scaling parameter. Akcasu has called this curve the *shape function*.^[27b] This fact has been observed earlier with linear chains.^[40,42] Figure 13.12 shows the result for branched clusters^[39] which, surprisingly, gives a value for the shape function that agrees satisfactorily with that predicted for linear chains on the basis of the bead-spring model with hydrodynamic interactions (the Zimm-Rouse model^[43-45]). We conclude from this observation that the bead-spring concept in its essential features remains valid at least as regards universal scaling behaviour. The prefactors $P_1(qR_g)$ in eqn (13.19) and $\Gamma^*(\infty)$ in eqn (13.26) are not universal, however, and depend on the particular constraints in the polymer architecture. Roughly speaking, one can say in an oversimplified manner that a decrease in the plateau value $\Gamma^*(\infty)$ means a reduction in internal flexibility.

It should be emphasized, however, that such universal behaviour is obtained only in the asymptotic region, i.e. when $qR_g \gg 1$, and at least larger than 4. This fact is demonstrated by the curve with open symbols for the clusters of the already mentioned randomly vulcanized polyesters. A clear angular dependence remained when $qR_g < 2$ (see Fig. 13.12). Here the translational diffusion coefficient has still a dominant influence.

13.11 Semi-dilute solutions

13.11.1 Some general remarks

Because of the large volume that an individual macromolecule has in solution, the particles already start to touch each other at a rather low concentration, c^* . At higher concentrations, two limiting alternatives are possible: either the segment clouds of the macromolecules interpenetrate each other, or the highly swollen particles become compressed into a smaller volume. Flexible chain molecules clearly show evidence of full interpretation, eventually leading to transient network formation.^[46] ‘Transient’ means that entanglement points are not locally fixed; the motion of chains transverse to the chain contour is strongly inhibited, but motion through slip links along the contour length still remains possible. The latter point is of importance when special interactions causing complex formation are effective.

If coil interpenetration occurs and a transient network is formed, then the properties of the solution change markedly and become independent of the chain length^[46,47] and, consequently, also of the polydispersity. The behaviour is now governed by the correlation length ξ corresponding to the mesh size of the net or to the length between two points of entanglement. This concept, developed mainly by de Gennes,^[46] has been very successful in the interpretation of the properties of linear chains in the semi-dilute regime and leads to the conclusion that all measurable quantities of such solutions can be scaled in terms of c/c^* . No predictions have so far been made for the solution behaviour of branched materials in which full interpenetration is no longer possible.

It is important to note that in most cases the overlap concentration cannot be uniquely defined. This is a consequence of the Gaussian-like shape of the segment distribution about the centre of mass, which has no well-defined surface. Large differences can result depending on whether c^* is defined by a static or a dynamic quantity. Our considerations will be confined to good solvent conditions, and here it has become common to define c^* either using thermodynamic or hydrodynamic interactions, i.e.^[48]

$$c_{A_2}^* = [A_2 M_w]^{-1} \quad \text{static}, \quad c_\eta^* = [\eta]^{-1} \quad \text{dynamic}. \quad (13.32, 13.33)$$

For linear chains the ratio $c_{A_2}^*/c_\eta^* = 1.04$ ^[49,50] but increases up to a factor of 2 for branched macromolecules. In general the ratio is not a constant but only asymptotically approaches the value of 2 at high molecular mass.^[39,50] The following discussion is based on A_2 , if not otherwise stated, and c/c^* is expressed as $A_2 M_w c = X$.

13.11.2 Static and dynamic scaling of linear chains

The concentration dependence of the diffusion coefficient in the entanglement region, i.e. $X = A_2 M_w c \gg 1$, was predicted by de Gennes^[46] to follow a power law $D_c/D_0 = AX^{0.75}$, where A is a structure-dependent prefactor. As previously

discussed by Brown and Nicolai,^[51] the exponents vary between 0.60 and 0.73 even for polystyrene in good solvents. This variation may be attributed to concentrations which are not high enough to ensure the condition $X \gg 1$. The following data, however, demonstrate that this variation has another source.

The essential point for universality is that the properties of the solution depend on $X = A_2 M_w c$, and that the same master curve is obtained whether c is varied for a fixed molar mass or whether the molar mass is also varied and, to some extent, also the second virial coefficient.

Figure 13.13 shows values of D_c/D_0 for three polystyrene samples in toluene,^[4] where M_w varies between 15 000 and 7.8×10^6 . Clearly, the anticipated universality is not observed. This finding stands in contrast to the static properties for which, for example, the reduced osmotic modulus is written in the scaled form as

$$M_w Kc/R_{\theta=0} = (M_w/RT)(\partial\pi/\partial c) = 1 + 2X + 3g_A X^2 + \dots = f(X). \quad (13.34)$$

Figure 13.14 shows (for the same samples) that universality is nicely fulfilled in this case, with a slightly higher exponent of 1.40^[4,48] instead of the value of 1.25 predicted by scaling arguments and also by the RG theory. The factor g_A allows one to express the third virial coefficient in terms of the square of the second virial coefficient. Its value is characteristic of the particular structure of the particles.^[48]

Irreversible thermodynamics show that^[52]

$$D_c/D_0 = [f_0/f(c)][(M_w RT)(\partial\pi/\partial c)][1 - (v_2 c)^2], \quad (13.35)$$

where v_2 is the partial specific volume of the macromolecule. Since the reduced osmotic modulus can be measured by static light scattering, the combination

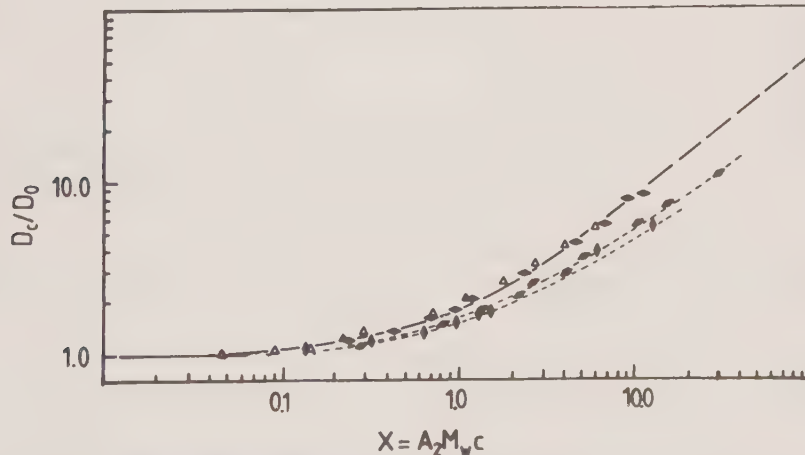


FIG. 13.13. A plot of D_c/D_0 against the reduced concentration $X = A_2 M_w c$ for three molar masses of polystyrene in toluene: $M_w = 155\,000$ (lower curve), $M_w = 1.08 \times 10^6$ (middle curve) and $M_w = 7.8 \times 10^6$ (upper curve).^[4,48]

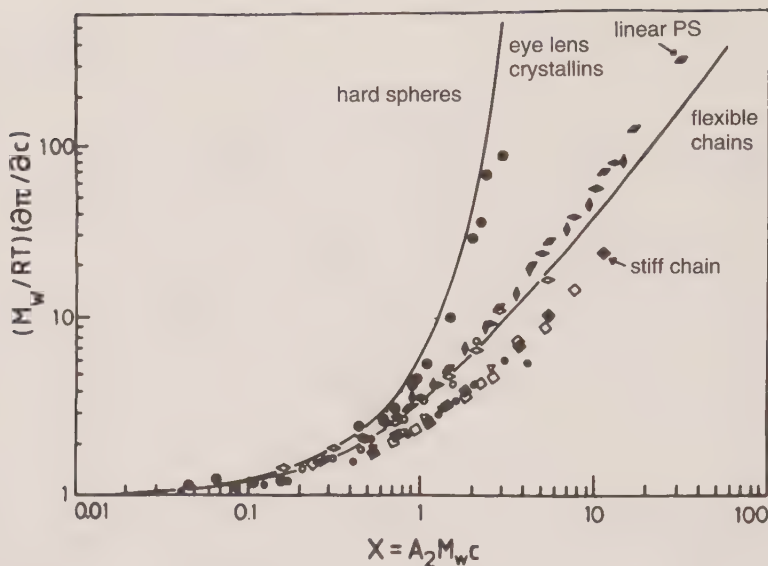


FIG. 13.14. The reduced osmotic modulus (M_w/kT) $(\partial\pi/\partial c)$ as a function of the reduced concentration X for three different molecular architectures. The full line corresponds to theories of Carnahan and Starling^[53] (spheres), of Ohta and Oono^[54] (flexible linear chains) and of Cotter and Martire^[55] (stiff chains). Measurements are those of Delaye and co-workers^[56] (eye lens crystallines), Burchard^[4] (polystyrene chains) and Coville et al.^[41,42] (stiff chains).

of static with dynamic light scattering leads to an X dependence of the reduced frictional coefficient. Figure 13.15 reveals that it is the dynamic part of D_c that violates universality. As was also shown by Weill and des Cloiseaux, asymptotic behaviour of dynamic quantities is always reached more slowly than the corresponding static properties, as a result of different weighting on forming the averages. In fact, the data in Fig. 13.15 indicate that the asymptotic limit is eventually reached for molar masses larger than 10^7 . In other words, the static properties attain the asymptotic limit where the corresponding hydrodynamic properties are still in the non-universal crossover region. Similar observations have also been made with randomly crosslinked or vulcanized polyester chains. Here it is has also been possible to observe the crossover region for the osmotic modulus, as shown in Fig. 13.16.

13.11.3 Influence of special architectures

13.11.3.1 Static behaviour. As well as the reduced osmotic moduli for flexible linear chains, Figure 13.14 also contains the curve for hard spheres and stiff, infinitely thin rods, as predicted by theory.^[53-57] These curves have been experimentally verified.^[4,41,42,56] The data refer to a few selected examples

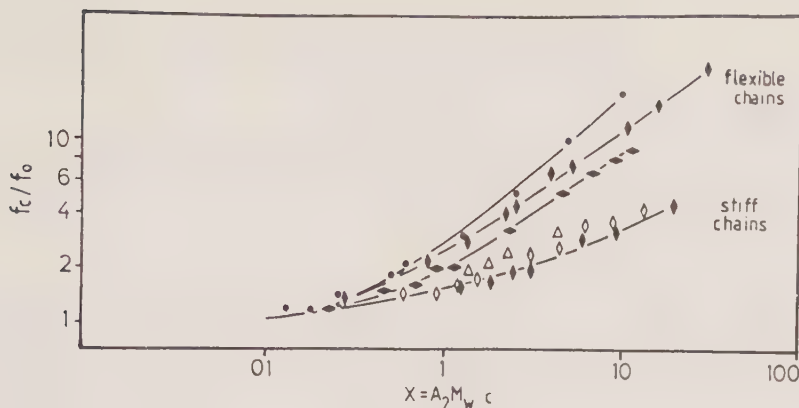


FIG. 13.15. The reduced frictional coefficient $f(c)/f_0$ as a function of X for polystyrene⁽⁴⁾ and stiff chain molecules^[41,42] of differing molar mass.

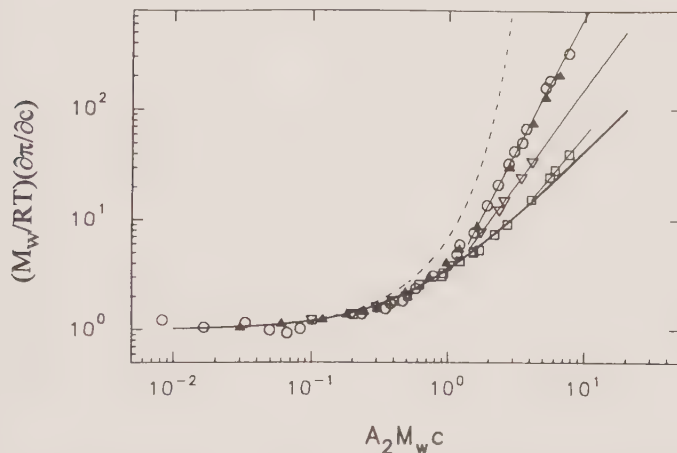


FIG. 13.16. The reduced osmotic modulus as a function of X for anhydride-cured epoxies (branched polyesters) of differing molar mass.^[39]

only; many others, for spherical micelles for example, are known from the literature. The effect of branching has also been demonstrated. As would be expected, the curves for star-branched macromolecules are shifted towards that for hard-sphere behaviour but never attain this limit.^[48,57] This, of course, arises because coil interpenetration becomes increasingly hampered as the number of arms increases but still remains possible to some extent even for very large numbers of arms.

The situation will be different for regular multiply-branched clusters such as, for instance, the recently much considered dendrimers. Here coil interpenetration is possible only for the outer chains of the outermost branching generation and,

if the chain length of these chains is small compared to the cluster diameter, hard-sphere behaviour should be observed. However, experimental data are not yet available.

Randomly branched materials show behaviour which asymptotically resembles that of star-branched macromolecules (Fig. 13.16). This result is the effect of the very large polydispersity, which increases with molar mass and which partly balances the effect of branching.

13.11.3.2 Dynamic behaviour. At this point the question arises as to whether the various architectures have a similar effect on the cooperative diffusion coefficient. Since irreversible thermodynamics hold in the same manner for all types of molecular architectures, eqn (13.35) remains valid. Consequently D_c should also display the same shape dependence as the reduced osmotic modulus. However, the observed phenomena are more complex, since the reduced frictional coefficient not only depends on the parameter $X = c/c^*$ but also on the shape of the molecule, although in a different manner than the reduced osmotic modulus. In fact, the frictional coefficient is governed by the hydrodynamic interactions which depend on how deeply a macromolecular object is drained by the solvent. These interactions can increase with concentration more strongly, but sometimes more weakly, than the corresponding thermodynamic interactions between particles. Cooperative diffusion is controlled by the ratio of both types of interactions and, in the region of entanglement, this can result in rather unusual non-linear effects. For instance, initially the thermodynamic effect may be larger than hydrodynamic interaction, as is usually the case. This results in the commonly observed increase in the cooperative diffusion coefficient with concentration. At higher concentrations, however, the friction will increase more strongly than the osmotic modulus, which will cause a reversal from the initial increase in D_c to a strong decrease (see also Chapter 5, Fig. 5.5). Figure 13.17 shows an example that will be discussed in more detail and interpreted in Section 13.2.3.

13.12 Association and aggregation

13.12.1 Definitions and general comments

Association and aggregation processes usually occur at concentrations above c^* , but occasionally also below c^* . For the following it is essential to distinguish between association and aggregation. The former refers to a true thermodynamic equilibrium and can be described by the law of mass action. Aggregation, on the other hand, is likewise induced by an increased concentration but, in contrast to association, a supramolecular structure, once formed, does not easily dissociate into its unimers when the concentration is lowered or the temperature is changed within certain limits. Dissociation shows typical hysteresis effects, i.e. the structure formed, for instance, on cooling needs a much higher energy to be broken into less organized unimers. In some cases the aggregated structure

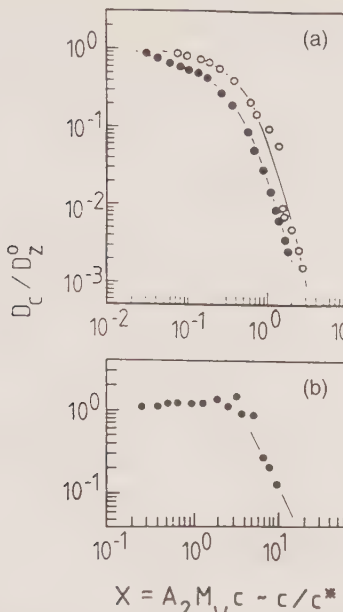


FIG. 13.17. The change in the normalized cooperative diffusion coefficients with increasing concentration for cellulose 2.5-acetate (CA) (a) in acetone^[58a] and cellulose tri-carbanilite (CTC) (b) in dioxane.^[39]

cannot be disrupted again at temperatures below the material's decomposition temperature; the structure closely resembles permanently linked clusters. Quite a few types of polysaccharides, with their ample possibilities for H-bond formation, belong to this group.^[58-67]

Associating and aggregating systems differ from semi-dilute solutions due to the fact that the entanglement points are now fixed, for a short time in associating processes, but quasi-permanently in aggregating systems which remain in a metastable state. Obviously, the lifetime of a particular complex governs the dynamic behaviour. These time effects have not been well investigated and are poorly understood.

13.12.2 Aggregation

13.12.2.1 Characterization by global cluster quantities. Because of their quasi-permanent but not covalently bound structures, these systems are not easily differentiated from true macromolecules. Extremely high molar masses usually provide the first indication of such aggregates and a number of unusual effects should then be taken seriously and not discarded as impurity side-effects. Such effects are: (i) unusually high radii of gyration when compared with the molar mass, indicating high chain stiffness; (ii) a low ρ parameter, indicating a rather compact structure; (iii) violation of scaling laws among the various exponents

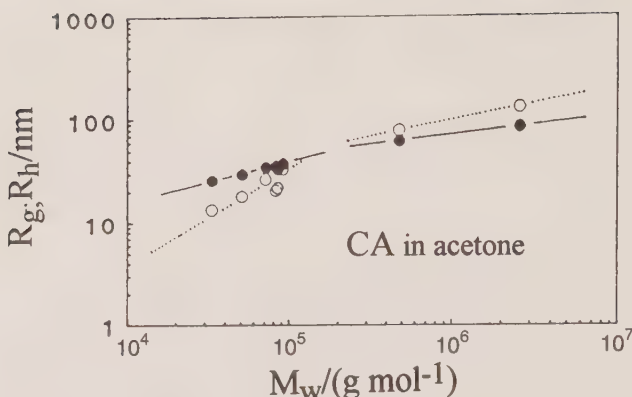


FIG. 13.18. The molar mass dependence of R_g (●) and R_h (○) for cellulose 2.5-acetate (CA) in acetone.^[58a]

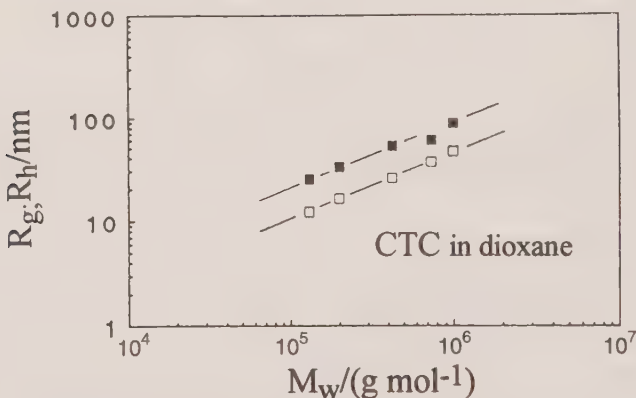


FIG. 13.19. The molar mass dependence of R_g (■) and R_h (□) for CTC in dioxane.^[29]

when the molar mass dependence is studied; and (iv) the observation of no power-law behaviour at all.

Cellulose 2.5-acetate (CA) in acetone or THF may serve as an example.^[58a] Figure 13.18 shows the results of R_g and R_h measurements as a function of the molar mass and these are compared in Fig. 13.19 with those for cellulose tri-carbanilate (CTC) in dioxane.^[29] The properties of the fully substituted CTC are similar to those for polystyrene in a good solvent. In contrast to this common behaviour, CA displays two significant deviations. (i) The radius of gyration exhibits no power-law behaviour: the curve starts with an exponent of $v_{low} = 0.5$, then flattens off and approaches an asymptotic exponent of $v_{high} = 0.28$. (ii) The hydrodynamic radius starts with a value that is lower than R_g , crosses the R_g curve and eventually becomes larger than R_g , finally

Table 13.4. Exponents v_{app} in the relationship $R_g = KM_w^{v_{app}}$ for various polymer solvent systems.

Polymer	Solvent	Exponent v_{app}
CTC ^a	Dioxane	0.60
AC ^b	Acetone	0.34 ($M_w > 10^5$)
AC ^b	Acetone	0.27 ($M_w > 10^5$)
CMC ^c	0.1 M NaCl	0.28
Na-Alginate	0.1 M NaCl	0.28
MHPC ^d (low DS)	Water	0.22
MHPC ^d (high DS)	Water	0.26
MHEC ^e	Water	0.22

^a CTC = cellulose tri-carbanilate; ^b CA = cellulose 2,5-acetate; ^c CMC = carboxymethyl-cellulose; ^d MHPC = methyl-hydroxypropyl cellulose; ^e MHEC = methylhydroxyethyl cellulose.

approaching the same asymptotic slope. Similar behaviour was also found for carboxymethyl cellulose (CMC) in 1 M NaCl aqueous solution^[58b] and for solutions of various other cellulose ethers in water and in trifluoroethanol (TFE).^[58b, 59] Table 13.4 gives a list of the asymptotic slopes for such systems.

The strikingly different molar mass dependencies of R_g and R_h give a variation in the ρ parameter as a function of M_w , as shown in Fig. 13.20(a). The data are compared with those of microgels in the pre-gel and post-gel states in Fig. 13.20(b). The initial value at low M_w is close to that for linear chains, while the asymptotic value corresponds to that of an intramolecularly crosslinked microgel.

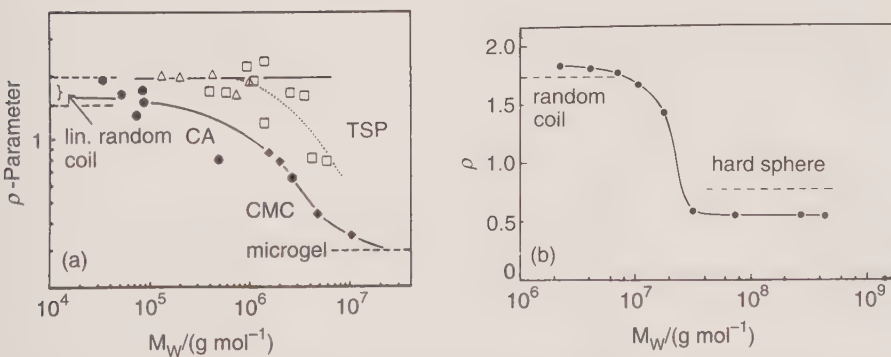


FIG. 13.20. The variation of the ρ parameter with molar mass: (a) for CA in acetone, CMC in 1 N NaCl and CTC in dioxane; (b) for microgels in the pre-gel and post-gel states. The microgels were prepared by emulsion polymerization of vinyl acetate in the presence of a crosslinker. Measurements were made in methanol after removing the soap.^[69]

Furthermore, in most common systems the exponent v is related to the fractal dimension of self-similar objects:

$$\langle d_f \rangle = 1/v, \quad (13.36)$$

where the fractal dimension is defined by

$$M_w \sim R_g^{\langle d_f \rangle}. \quad (13.37)$$

For randomly branched or cross-linked clusters this average fractal dimension has to be corrected for the very broad size distribution, since the polydispersity increases with M_w . According to percolation theory this correction is^[16]

$$d_f = \langle d_f \rangle / (3 - \tau), \quad (13.38)$$

in which the exponent $\tau = 2.2$ occurs in the molecular mass distribution of the clusters,

$$w(M) = A M^{1-\tau} f(M/M^*), \quad (13.39)$$

where $f(M/M^*)$ is a cut-off function that causes a stronger decay of $w(M)$ than the power-law function $M^{1-\tau}$ (note that $f(M/M^*) \rightarrow 1$ when $M^* \rightarrow \infty$).^[16,65]

Applying eqn (13.36) to these systems in a naive manner would result in fractal dimensions between 3.6 and 4.6 which would be physically meaningless, since a value of 3.0 cannot be exceeded for mass fractals. The decrease of the ρ parameter with increasing M_w gives a hint that the true fractal dimension may have changed from a value smaller than 2.0 (linear chains) to values as large as 2.5 (non-swollen branched clusters). This conjecture was confirmed by evaluating the asymptotic slope of the angle-dependent scattered intensity in a double logarithmic plot. This slope again gives the average fractal dimension of the clusters. Values ranging from 1.8 to 2.2 were found when a polydispersity correction was not performed.^[66]

In fact, the rather weak increase of R_g , whereas M_w has grown strongly, can be explained by a model in which several chains aggregate laterally (i.e. side-by-side), since this will change the radius of gyration only slightly, whereas the mass can increase strongly.^[58,59,62-64,67] Figure 13.21. shows two stages of a fringed micelle model. Indeed, the latter can reconcile the apparent high stiffness of the observed objects (because of the rigid stem) and the low ρ parameter indicating a microgel. The aggregation number of the CA samples was determined from measurements in cuoxam (copper ammonium complex) and was found to vary between 15 and 22. The acetyl groups are saponified in this alkaline solvent, and the remaining cellulose is readily dissolved in this Schweizer's reagent.^[68]

13.12.2.2 Change of internal flexibility with concentration. Other aspects of the suggested fringed-micelle model still have to be proven, e.g. the flexible character of the outer chains. It may be worth emphasizing that truly rigid rods are in general not soluble because of a low entropy of mixing. The flexible outer chains increase the mixing entropy and are probably responsible for the

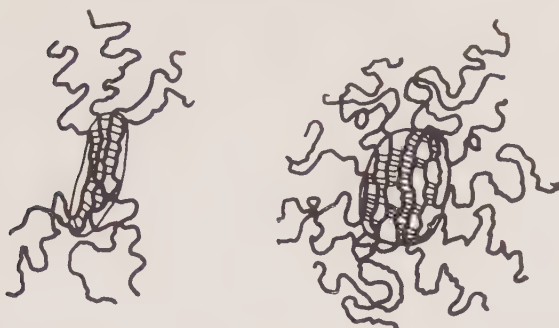


FIG. 13.21. Two stages of fringed micelles which are formed by lateral aggregation of chains.^[67]

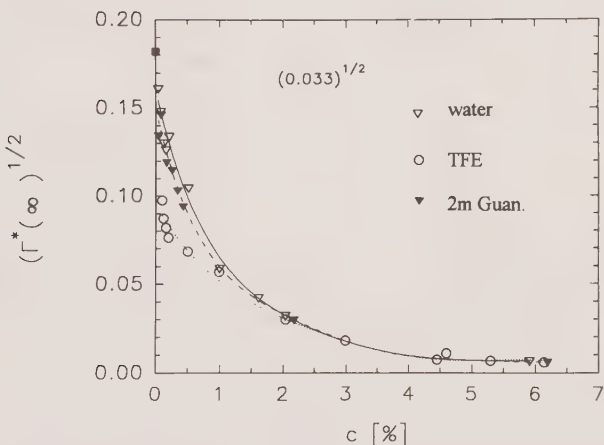


FIG. 13.22. The variation of $[\Gamma^*(\infty)]^{1/2}$ with increasing concentration of a methyl-hydroxyethyl cellulose (MHEC) in trifluoroethanol (TFE), in water and 2 M guanidine HCl (GuaHCl).^[66]

solubility of the objects. Thus proof of the existence of such flexible chains will be an important milestone.

The following observations made by dynamic LS may be interpreted along these lines. As was already outlined in Section 13.10, the asymptotic plateau value of $\Gamma^*(\infty) = (\Gamma/q^3)(\eta/kT)$ appears to be an indication of internal flexibility. The limiting $\Gamma^*(\infty)$ value has been measured for some cellulose ethers in water and in TFE as a function of concentration; the result is shown in Fig. 13.22. The data decreased strongly with concentration, as already indicated by the unusual shape of the dynamic Zimm plots shown in Fig. 13.23. We interpret this observation as due to a forced decrease in internal flexibility that

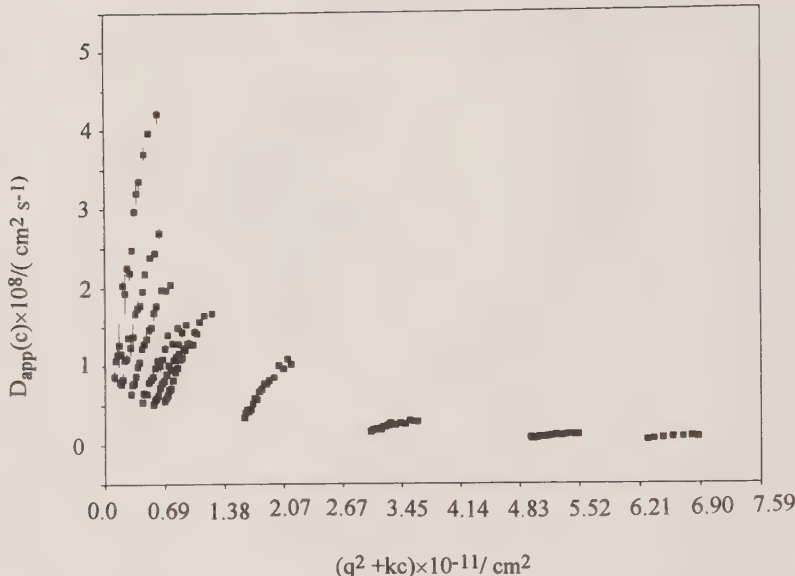


FIG. 13.23. A dynamic Zimm plot for MHEC in GuaHCl.^[66]

cannot occur with entangled polystyrene systems. Evidently, little particle interpenetration is possible and the clusters become compressed at concentrations larger than c^* , thus reducing the internal flexibility.

It remains to be explained why fully substituted derivatives of the (1,4) glycosidic bond type do not form such fringed-micelle structures. For cellulose there is a simple explanation. We know that even activated cellulose contains a high fraction of crystallinity. On chemical reaction, substitution first takes place in the amorphous regions and will then proceed as much as is possible in the more highly ordered regions. Finally, a chain is obtained with a block-like derivatization and some sections will probably remain which are not substituted at all. These sections can form bundles of laterally aggregated strands, while the highly substituted chain sections can dissolve and move fairly freely.

13.12.3 Association

13.12.3.1 Detection of association and the formed cluster sizes. Association phenomena are most convincingly recognized from the fully reversible change of measurable quantities when the concentration is varied. The apparent molar mass is of particular importance since it can be estimated by application of the law of mass action, but other quantities can also be considered, for instance the apparent radii R_g and R_h (or correlation lengths ξ and ξ_h) and the reduced viscosity. Such estimations are, however, only approximate, since all these global particle parameters are altered by non-specific interparticle interaction.

For good solvent conditions, the influence of the repulsive interactions can be separated by a recently developed approximation,^[30] but for this the cluster shape has to be known approximately.

Here it is of interest that the ratio $\rho_{app} = \xi/\xi_h$ is much less sensitive to the influence of the interactions than the radii themselves, since its influences on ξ and ξ_h occur in a similar manner and effectively cancel when the ratio is formed. Thus, to a first approximation, we get

$$\rho_{app}(c) \cong \rho(c = 0) \quad (13.40)$$

and the values provide an index of the structure as in the case of dilute solutions (see Table 13.1).

Even after correction for the true particle mass $M_w(c)$ at concentration c , calculation of the concentration dependence of the cluster molar mass via the law of mass action still remains rather complex. The mass law can be applied only to complex formation between two functional groups, but the influence of steric hindrance and cooperative complex formation, which is common with macromolecules, will cause a very involved treatment, that so far has not yet been proposed.

A further possibility of detecting how association clusters arise is by analysis of the time correlation function, which may display a slow motion. If this slow motion is correlated to an excess low angle scattering in the static LS experiment, then one can be sure that this slow mode is caused by clusters. Distinction from aggregates follow from the reversibility, i.e. the slow relaxation, and the excess low angle scattering will disappear again on dilution.

The various ways of characterizing association clusters may now be illustrated with some particular examples.

13.12.3.2 Micelles. The simplest case is that of the formation of spherical micelles. This type of highly cooperative association was treated earlier by Elias,^[71] who coined the term *closed* association for this case. This expression means that, beyond a critical concentration, called the critical micelle concentration (cmc), a large number of unimers cluster together into a monodisperse, often spherical, structure with a well-defined surface, such that no further association can take place as long as the micelles do not start to touch each other. This process typically leads to a concentration dependence of the reciprocal scattering intensity and the apparent molar mass as sketched in Fig. 13.24. The initial increase in $M_{app}(c)$ reflects the increase in the particle mass due to association. Because of the low concentration the influence of interparticle volume repulsion is very small and can be neglected. The decrease is caused by repulsive interaction between micelles, and its influence can approximately be corrected for as follows.

The hydrodynamic radius is first measured by dynamic LS. Since the concentration dependence of the diffusion coefficient is rather weak in this concentration regime, one obtains approximately the correct micelle radius which, for hard spheres, equals the hydrodynamic radius. The next step is to insert

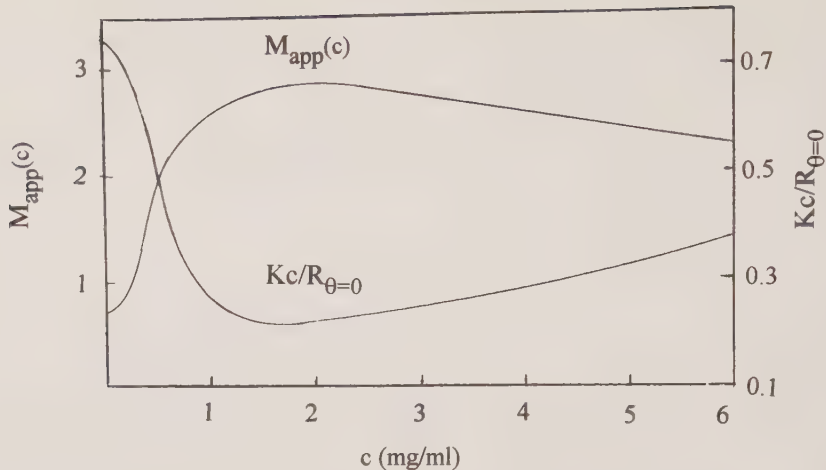


FIG. 13.24. A schematic plot of the concentration dependence of the reciprocal forward scattering $K_c/R_{\theta=0}$ (ordinate) and the apparent molar mass $M_{app}(c)$ (right-hand scale).

the micellar volume into the well-known relationship for the second virial coefficient,^[52] which gives

$$A_2 = 4N_A V_m / M^2, \quad (13.41)$$

with V_m being the volume of the molecule, M the corresponding molar mass and N_A Avogadro's number. With this value of A_2 , the correct $M(c)$ can be calculated using the Carnahan-Starling equation^[53] for the osmotic compressibility or, to a first approximation, by using only the first term in the virial expansion of eqn (13.24).^[30]

Micelles are a common feature of low molar mass surfactant systems. Similar structures are also found with block copolymers in selective solvents, in which one block is readily soluble while the other tends to phase separate. In these solvents, a star-shaped structure is obtained in which the less soluble blocks cluster together to form an amorphous, densely packed core, and the better soluble blocks stretch out into the solvent with freely moving segments. These structures have been intensely studied by Tuzar and Kratochvil, who review their characterization techniques and the results obtained by applying scattering methods in Chapter 10 of this volume and also in ref. 72.

Less known is the fact that proteins form similar micelles. Examples are found with the various casein components in milk micelles; these are, in fact, rather complex composite metastable aggregates. The main components are the α -, β - and κ -caseins. Only the κ -caseins are insensitive to the Ca^{++} ion concentration of the milk and stabilize its colloidal structure. The other two components are precipitated by Ca^{++} ions and have to be studied in calcium-free media.

In both cases the apparent molar mass exhibits the typical concentration dependence described above for closed association. A maximum is obtained

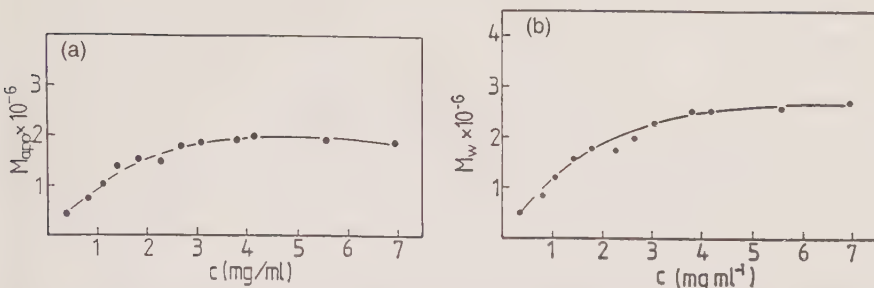


FIG. 13.25. The concentration dependence of the apparent molar mass of β -casein in calcium-free buffer and the corresponding dependence after applying a correction for the interaction as described by eqn (13.41).^[72]

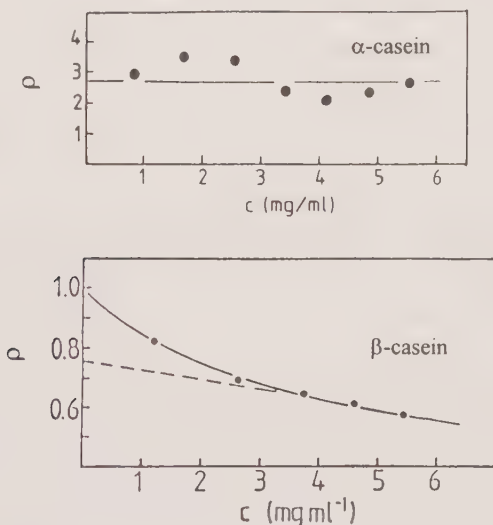


FIG. 13.26. The concentration dependence of $\rho_{app}(c) = \xi/\xi_h$ for α - and β -caseins at 20 °C.^[72-74]

at around 4 mg/ml, and the decrease in the apparent molar mass may be corrected in the manner described above. Figure 13.25 shows results for β -casein, and similar results were obtained for α -casein. A first hint regarding the structure of these micelles is given by the concentration dependence of the ρ_{app} parameter^[73-75] shown in Fig. 13.26. Extrapolation to zero concentration gives a value of $\rho \approx 1$ for β -casein, as expected for a star-shaped micelle, but a much higher value is found for the α -casein, indicating stiff or worm-like chains. Both the star-shaped micellar structure for β -casein and the worm-like filamentous chain character of α -casein were verified from the angular dependence of the static scattering of neutrons^[73] and visible light,^[74] respectively. A Kuhn

segment length of $l_k = 123$ nm was found for α -casein, indicating a rather high rigidity.^[74]

The formation of filamentous micelles is known for several surfactants and is explained by the volume requirement of the fairly long aliphatic chain as has been described, for example, by Israelachvili.^[72] Recently, similar micellization was found for the surfactant hexadecyl ammonium sulphate dissolved in 97% concentrated sulphuric acid.^[77] Because of the low refractive index increment, an accurate molar mass could not be measured. However, the determination of the radii R_g and R_h , can be carried out without knowing the particle weight. The rather high value of $\rho = 4.3$ was found, which is characteristic of stiff cylinders. After correction for the polydispersity,^[77,78] which was assumed to be $M_w/M_n = 2$ (the most probable distribution), an axial ratio of $p = 64$ was obtained which, together with the radius of gyration, gave rod length of 153 nm and a cylinder diameter of $d = 2.53$ nm. Another example, already discussed in Section 13.6.2, was given by Schillén and Brown^[25] for the $\text{EO}_n\text{-PO}_m\text{-EO}_n$ triblock copolymer, where relaxation times for both the rotational and translational components were evaluated from the TCF.

13.12.3.3 Open association. More frequent than closed association is the association process due to continuous growth with concentration. Elias^[71] calls this type *open* association. Only for a collinear association, which is fairly common with proteins as discussed in the literature,^[79] can the process be described by the law of mass action by taking into account the volume exclusion of rigid cylinders. Other effects are similar to the aggregation processes discussed above.

Association occurs with almost all chain molecules, even in good solvents, when the overlap concentration is exceeded. Figure 13.27 shows two typical examples,^[29,56] where the reduced osmotic modulus is plotted against the scaling parameter X . Up to a certain value of X , measurement of the static forward scattering follows the curves for the characteristic structures nicely but, beyond a certain X value, the curve displays a turn-over to a sharp decrease which eventually leads to a molar mass of $M_w \rightarrow \infty$, indicating reversible gelation. The simultaneous recording of the dynamic light scattering gave a similar turn-over of the first cumulant (Fig. 13.17), indicating a strong slowing down of the diffusion process. The cooperative diffusion coefficient often starts to decrease already in the dilute concentration regime, as shown in Fig. 13.17(a). This slowing down is usually accompanied by a strong low-angle excess scattering.

For systems having more than one relaxation process, the first cumulant represents the sum over these relaxations. These different relaxations are often directly distinguished in the time correlation function. Figure 13.28 shows TCF for the systems shown in Figs 13.17 and 13.27. Here the advantages of dynamic LS become apparent: while static LS and the first cumulant only allow determination of the sum of the contributions from the various components, the TCF displays these processes separately.

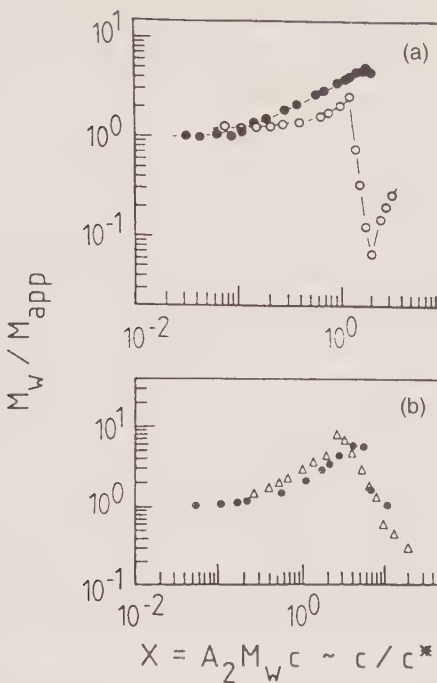


FIG. 13.27. The concentration dependence of the reduced osmotic modulus ($= M_{app}/M_w$) for two samples of cellulose 2.5-acetates (CA) in acetone^[58] and two samples of cellulose tri-carbanilate (CTC) in dioxane.^[29]

As a final example, the association of randomly crosslinked polyester clusters formed by the anhydride-curing of epoxies is discussed. Figure 13.29 shows that the slow motion becomes increasing well-separated as the concentration is increased.^[39] The effect is accompanied by a growing small-angle excess scattering, as shown in Fig. 13.30. The slow motion could be separately studied by fitting the TCF with Williams-Watts (stretched exponential) functions. From the evaluated relaxation time τ_{slow} , the translational diffusion coefficient D_c could be calculated ($D_{c,slow} = 1/(q^2 \tau_{slow})$). These data are plotted in Fig. 13.31 against the concentration and result in a curve that approaches zero translational mobility, which is indicative of a critical point of gelation. In fact, critical behaviour is found with a critical point at $c = 260$ mg/ml ($X = [\eta]c = 5.5$) with an unusually high exponent of $\gamma_D = 4.5$.^[39] These are the first results obtained with branched clusters known to the author, and a conclusive interpretation cannot yet be given. Simple association of the *hairy* but otherwise non-interpenetrable clusters may identify the critical point as the point of reversible gelation. Alternatively, the slowing down may result from the random close-packing of spheres, and the critical point would then be assigned to the glass transition point.

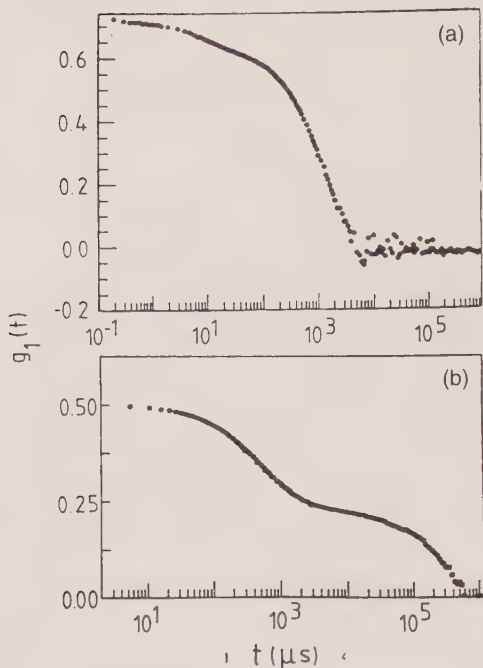


FIG. 13.28. A typical TCF (a) for CA in acetone ($M_w = 3.33 \times 10^4$, $c = 11.4\%$) and (b) CTC in dioxane ($M_w = 1 \times 10^6$) at concentrations $X \gg 1$ ($c \gg c^*$).^[58a]

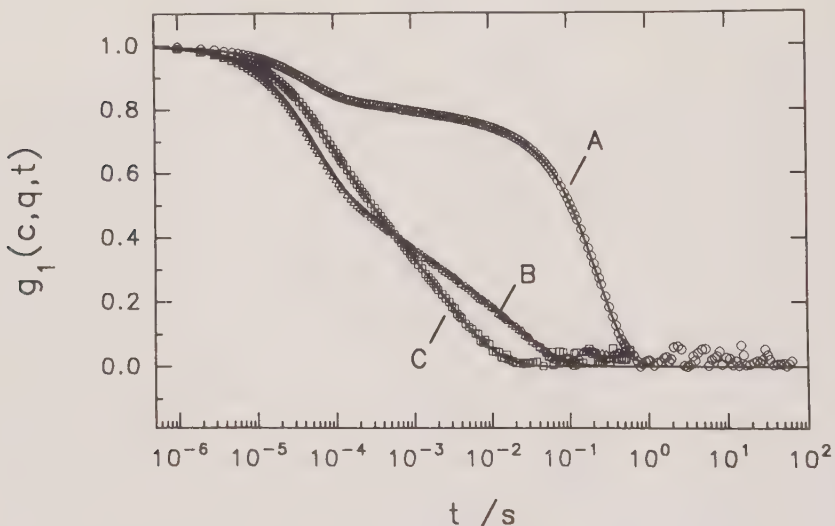


FIG. 13.29. The normalized TCF of a branched anhydride-cured epoxy ($M_w = 1.77 \times 10^6$) at three different concentrations. A, $c = 545.5 \text{ mg/ml}$; B, $c = 111.6 \text{ mg/ml}$; C, $c = 68.85 \text{ mg/ml}$ at $\theta = 50^\circ$ in THF for the same sample as in Fig. 13.28.^[39]

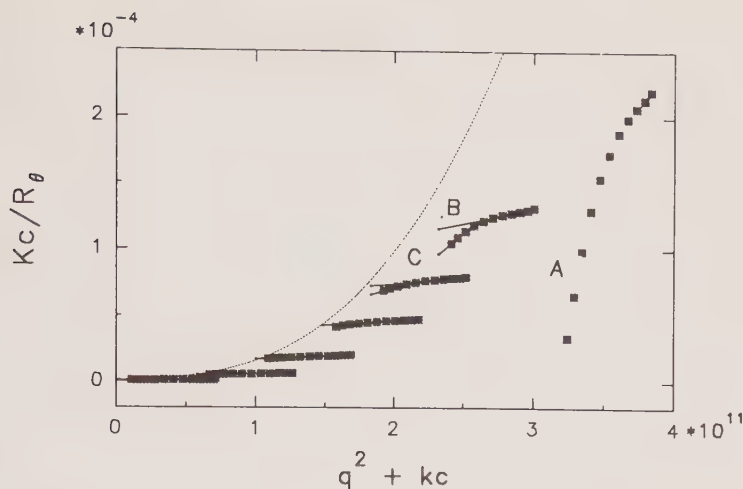
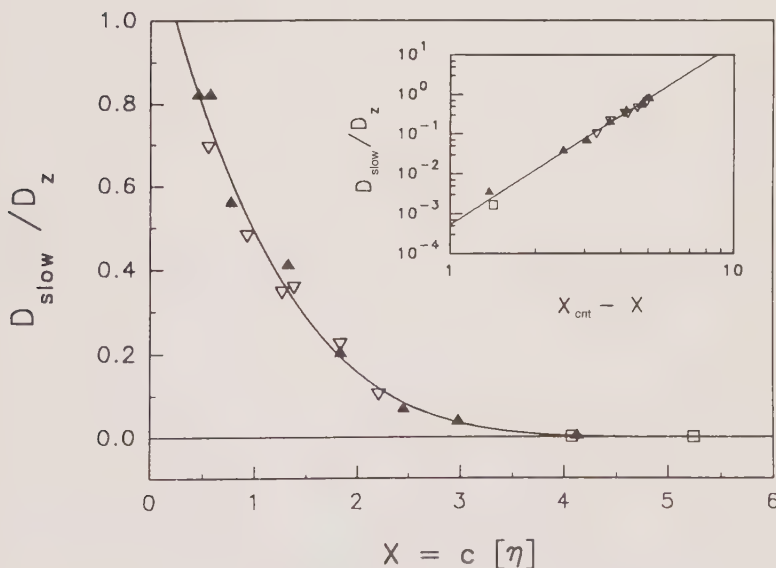


FIG. 13.30. A Zimm diagram for the same sample as in Fig. 13.29.

FIG. 13.31. A plot of $D_{\text{slow}}(c)/D_0$ against the parameter $X = c[\eta]$ for anhydride-cured epoxies ($M_w = 1.77 \times 10^6$ and $M_w = 1.72 \times 10^5$ g/mol). The solid lines correspond to the relationship $D_{\text{slow}}/D_0 = 3.3 \times 10^{-4}(5.5 - X)^{4.5}$.^[39]

Here a comment should be added concerning the discussion of a frequently observed slow mode which corresponds to the q -independent structural relaxation spectrum, which is only observed with significant amplitude in semi-dilute theta solutions which are, moreover, entangled; see, for example, Chapters 5 and 6 in

Ref. [11], and also Chapter 5 of this volume for further discussion. A coupling of the diffusion process, resulting from Brownian motion, with the frequency-dependent rheology of the entangled network has been assumed. The frequencies which can be observed correspond to the internal vibrations of the transient network and are limited to a spatial corelation length which is far too short to give an angular dependence in static light scattering. The slowing down may then be interpreted as an increase in the macroscopic viscosity. This leads to the important conclusion that this type of coupling should only be found when no low-angle excess scattering is observed. Here again it becomes obvious that a conclusive interpretation is only possible if the static properties have also been studied. Rheological coupling will, of course, occur with associating systems in which the crosslinks are short-time fixed. The theoretical derived properties are then, however, strongly dominated by the translational motion of the clusters and will be no longer detectable.

Acknowledgements

The author wishes to thank Dr Chi Wu, Chinese University of Hong Kong, and Dr Y. Tsunashima, Institute for Chemical Research, Kyoto, for fruitful discussions and for providing preprints of recent papers prior to publication.

References

1. Pecora, R. (1964). *J. Chem. Phys.*, **40**, 40?1604.
2. Cummins, H. Z., Knable, N., and Yeh, Y. (1964). *Phys. Rev. Lett.*, **12**, 150.
3. Burchard, W. (1985). *Chimia*, **39**, 10.
4. Burchard, W. and Richtering, W. (1989). *Progr. Colloid Polym. Sci.*, **80**, 151.
5. Štěpánek, P. and Koňák, Č. (1984). *Adv. Colloid Interface Sci.*, **21**, 195.
6. Berne, B. J. and Pecora, R. (1976). *Dynamic light scattering*. John Wiley, New York.
7. Chu, B. (1974). *Laser light scattering*. Academic Press, New York.
8. Cummins, H. B. and Pike, E. R. (eds) (1974). *Photon correlation spectroscopy*. Plenum Press, New York.
9. Pecora, R. (ed.) (1985). *Dynamic light scattering*. Plenum Press, New York.
10. Schmitz, K. S. (1990). *Dynamic light scattering by macromolecules*. Academic Press, New York.
11. Brown, W. (ed.) (1993). *Dynamic light scattering*. Clarendon Press, Oxford.
12. Baur, G. (1989). Unpublished. Instrumental development at Freiburg University.
13. Einstein, A. (1905). *Ann. Phys.*, **17**, 549.
14. (a) Provencher, S. W. (1979). *Makromol. Chem.*, **180**, 201.
(b) Provencher, S. W. (1979). *Computer Phys. Commun.*, **27**, 229.
15. (a) Burchard, W., Bauer, J., and Lang, P. (1992). *Makromol. Chem., Macromol. Symp.*, **61**, 25.
(b) Jenne, F. and Burchard, W. unpublished data.
16. Stauffer, D. (1982). *Introduction to percolation theory*. Taylor & Francis, Philadelphia.
17. Bauer, J., Lang, P., Burchard, W., and Bauer, M. (1991). *Macromolecules*, **24**, 2634.
18. Guinier, A. and Fournet, G. (1955). *Small angle scattering of X-rays*. Chapman & Hall, London.
19. Zimm, B. H. (1948). *J. Chem. Phys.*, **16**, 1068.

20. (a) Schulz, S. F., Maier, E. E., Krause, R., Hagenbüchle, H., Deggelmann, M., and Weber, R. (1990). *J. Chem. Phys.*, **92**, 7080.
(b) Krause, R., Maier, E. E., Deggelmann, M., Hagenbüchle, H., Schulz, S. F., and Weber, R. (1989). *Physica*, **A160**, 135.
21. Bantle, S., Schmidt, M., and Burchard, W. (1982). *Macromolecules*, **15**, 1604.
22. (a) Pecora, R. (1968). *J. Chem. Phys.*, **48**, 1036.
(b) Pecora, R. (1968). *J. Chem. Phys.*, **49**, 4168.
23. (a) Perrin, F. (1936). *J. Phys. Radium*, **5**, 497.
(b) Perrin, F. (1934). *J. Phys. Radium*, **7**, 1.
24. Broersma, S. (1981). *J. Chem. Phys.*, **74**, 6989.
25. Schillén, K. and Brown, W. (1994). *Macromolecules*, **27**, 4825.
26. Burchard, W., Schmidt, M., and Stockmayer, W. H. (1980). *Macromolecules*, **13**, 580, 1265.
27. Akcasu, Z. A., Gurol, H. (a) (1976). *J. Polym. Sci., Polym. Phys. Ed.*, **14**, 1; Akcasu, A. Z., Benmouna, H., and Han, C. C. (b) (1980). *Polymer*, **21**, 866; Akcasu, Z. A. and Benmouna, H. (1980). *Macromolecules*, **11**, 1183.
28. Burchard, W. (1983). *Adv. Polym. Sci.*, **48**, 1.
29. Wenzel, M., Burchard, W., and Schätzel, K. (1988). *Polymer*, **27**, 1.
30. Burchard, W. (1988). *Makromol Chem., Macromol Symp.*, **18**, 1.
31. Shiwa, Y. J. (1991). *Phys. A: Math. Gen.*, **24**, L575.
32. Benmouna, M. and Akcasu, A. Z. (1978). *Macromolecules*, **11**, 1187.
33. Han, C. C. and Akcasu, Z. A. (1989). *Macromolecules*, **14**, 1080.
34. Chu, B., Wang, Z., and Xu, J. (1991). *Macromolecules*, **24**, 6832.
35. Tsunashima, Y., Nemoto, N., and Kurata, M. (1983). *Macromolecules*, **16**, 1184.
36. Nemoto, N., Tsunashima, Y., and Kurata, M. (1984). *Macromolecules*, **17**, 425.
37. Tsunashima, Y., Hirata, M., Nemoto, N., and Kurata, M. (1987). *Macromolecules*, **20**, 1992, 2862.
38. Shiwa, Y. and Tsunashima, Y. (1993). *Physica A*, **197**, 47.
39. Trappe, V. (1994). Ph.D. Thesis, Freiburg University; manuscript in preparation.
40. Chi Wu, Chem, K. K., and Xia, K.-Q. (1995). *Macromolecules*, **28**, 1032.
41. Dentini, M., Covello, T., Burchard, W., and Crescenzi, V. (1988). *Macromolecules*, **21**, 3312.
42. Covello, T., Burchard, W., Dentine, M., and Crescenzi, Y. (1987). *Macromolecules*, **20**, 1102.
43. Zimm, B. H. (1956). *J. Chem. Phys.*, **24**, 269.
44. de Gennes, P.-G. (1967). *Physics*, **3**, 37.
45. Dubois-Violeye, E. and de Gennes, P.-G. (1967). *Physics*, **3**, 1281.
46. de Gennes, P.-G. (1979). *Scaling concepts in polymer physics*. Cornell University Press, Ithaca, New York.
47. des Cloixeaux, J. (1985). *J. Phys. (Paris)*, **36**, 281.
48. (a) Burchard, W. (1990). *Makromol. Chem., Macromol. Symp.*, **39**, 179.
(b) Burchard, W., Lang, P., Schulz, L., and Covello, T. (1992). *Makromol. Chem., Macromol. Symp.*, **58**, 21.
49. Freed, K. F. (1987). *Renormalization group theory of macromolecules*. John Wiley, New York.
50. Bauer, J. and Burchard, W. (1993). *Macromolecules*, **26**, 3103.
51. Brown, W. and Nicolai, T. (1993). In *Dynamic light scattering*. Clarendon Press, Oxford.
52. Yamakawa, H. (1971). *Modern theory of polymer solutions*. Harper & Row, New York.
53. Carnahan, N. F. and Starling, K. E. (1969). *J. Chem. Phys.*, **51**, 625.

54. Ohta, T. and Oono, Y. (1982). *Phys. Lett.*, **89A**, 460.
55. Cotter, M. A. and Martire, D. C. (1970). *J. Chem. Phys.*, **52**, 1909.
56. (a) Delaye, M. and Tardieu, A. (1983). *Nature*, **306**, 45.
(b) Delaye, M. and Gromiac, A. (1983). *Biopolymers*, **22**, 1203.
57. Merkle, G., Burchard, W., Lutz, P., Freed, K. F., and Gao, J. (1993). *Macromolecules*, **26**, 2736.
58. (a) Burchard, W. and Schulz, L. (1989). *Das Papier*, **43**, 665.
(b) ibid. (1992). *Das Papier*, **47**, 1.
59. Burchard, W. (1994). *Das Papier*, **48**, 755.
60. Clark, A. and Ross-Murphy, S. B. (1987). *Adv. Polym. Sci.*, **83**, 57.
61. Phillips, G. O., Wedlock, D. J., and Williams, P. A. (eds) (1988). *Gums and stabilizers for the food industry 4*. IRL and Press, Oxford.
62. Burchard, W. (1993). In *Plant polymeric carbohydrates* (eds F. Meuser, D. J. Manners and W. Seibel). Royal Society of Chemistry Publishers, Cambridge.
63. Ebringerova, A., Hromadkova, Z., Dolega, R., Burchard, W., and Vorwerg, W. (1994). *Carbohydr. Polym.*, **34**, 161.
64. Lang, P. and Burchard, W. (1991). *Macromolecules*, **24**, 314.
65. Daoud, M. and Martin, J. E. (1989). In *The fractal approach to heterogeneous chemistry* (ed. D. Avenir). John Wiley, New York.
66. Schulz, L. (1995). *Ph.D. Thesis*, University of Freiburg; manuscript in preparation.
67. Burchard, W. (1993). *Trends in Polymer Science (TIPS)*, **1**, 192.
68. (a) Seger, B. and Burchard, W. (1993). *Makromol. Chem., Macromol. Symp.*, **83**, 291.
(b) Seger, B. (1992). *Diploma Thesis*, University of Freiburg.
69. Schmidt, M., Nerger, D., and Burchard, W. (1979). *Polymer*, **20**, 582.
70. Fengel, D. and Wegener, G. (1989). *Wood*. de Gruyter, Berlin.
71. Elias, H.-G. (1972). *Makromoleküle*. Hüting K Wpf, Basel, Lehrbuch.
72. Tuzar, Z. and Kratochvíl, P. *Adv. Colloid Interface Sci.*, **6**, 201.
73. Thurn, A., Burchard, W., and Niki, R. (1987). *Adv. Colloid Interface Sci.*, **265**, 653.
74. Thurn, A., Burchard, W., and Niki, R. (1987). *Adv. Colloid Interface Sci.*, **265**, 899.
75. (a) Burchard, W. (1992). In Harding, S. E., Sattelle, D. B., and Bloomfield, V. A. (ed.): *Laser light scattering in biochemistry*. Royal Society of Chemistry Publishers, London.
(b) (1994). In Ross-Murphy, S. B. (ed.) *Physical techniques in the study of food biopolymers*. Chapman & Hall, London.
76. Israelachvili, J. (1992). *Intermolecular and surface forces*. Academic Press, New York, 3rd edition.
77. Müller, A. and Burchard, W. (1995). *Colloid Polym. Sci.*, **273**, 866.
78. Schmidt, M. (1984). *Macromolecules*, **17**, 553.
79. (a) Lehninger, A. L. (1975). *Biochemistry*. Worth, New York.
(b) Alberts, B., Bray, D., Lewis, J., Raff, M., Roberts, K., and Watson, J. D. (1989). *Molecular biology of the cell*. Garland, New York.

Size distributions from static light scattering

F. Ross Hallett

14.1 Introduction

A knowledge of particle size distributions is central to innumerable scientific and applied problems in analytical chemistry,^[1] chemical physics and biophysics,^[2,3] atmospheric sciences^[4] and a host of other disciplines. A wide variety of techniques has been used to measure particle sizes.^[1] These include dynamic light scattering (DLS), static light scattering (SLS), turbidimetry, small angle diffraction, optical particle counting, velocimetry, small angle X-ray and neutron scattering, size exclusion chromatography, electron microscopy, sedimentation and sieving/filtering. No one technique is suited for all particles and all conditions. In most situations the application of several techniques often serves to enhance the confidence in the results. Different techniques often measure different particle properties and these differences can yield complementary information about the size, structure and interactions of particles in suspension. In some cases the properties and concentration of the sample can preclude the use of a technique and favour others. The analysis of particle size distributions by SLS should be viewed as one of the methods in the arsenal of particle sizing techniques, having its own set of advantages and limitations.

The determination of the size distribution of a suspension of particles by non-invasive means has been a goal of several light scattering laboratories. In principle, complete information on size distributions is present in either the angular dependence of the scattered light intensity (static light scattering (SLS)) or in the intensity autocorrelation function (dynamic light scattering (DLS)). In both cases the recovery of the size distribution is difficult because of the ill-conditioned nature of the mathematical inversion that is required. However, a large body of literature on inversion techniques such as non-negative least squares (NNLS) exponential sampling, regularization, and maximum entropy, is now available, and these methodologies have gained fairly wide acceptance, especially in the analysis of DLS data.^[3] Unlike the usual DLS apparatus where measurements can involve a single scattering angle and no special calibration techniques, SLS requires precise intensity measurements, with calibration, over a broad range of scattering angles. For these reasons there are few size analysis studies based on the inversion techniques to SLS data and much is yet to be learned. It will be shown in this chapter that the SLS approach has advantages over DLS in speed and resolution. In some cases SLS provides complementary

information. This chapter will be limited to a discussion of particle size distributions obtained from the inversion of static light scattering data acquired over a broad range of scattering angles and where either the Rayleigh–Gans–Debye criteria are satisfied or where Mie theory can be applied. Typically this is for particle sizes between about 50 nm and 5 μm . Not covered is a discussion of the fast developing literature on recovering larger particle sizes from low angle scattering using the diffraction approximation.^[5,6] Low angle light scattering is dealt with comprehensively in Chapter 12 of this volume.

14.2 Light scattering geometry

Figure 14.1 illustrates a typical SLS experimental arrangement in which vertically polarized incident light passes through the sample, and defines the direction from which the scattering angle θ is measured. Although the angular dependence of the scattered intensity is determined as a function of θ , it is usually expressed as a function of the momentum transfer vector or scattering vector, q , the magnitude of which is related to θ by

$$q = \frac{4\pi n_0}{\lambda} \sin\left(\frac{\theta}{2}\right), \quad (14.1)$$

where n_0 is the refractive index of the medium surrounding the scatterers, and λ is the wavelength *in vacuo* of the incident light. q^{-1} sets the length scale that is sampled by the light scattered at an angle θ . For most experiments (assuming a helium neon wavelength of 0.632 μm) this length scale varies from about 0.05 to 0.5 μm . This clearly shows that, relative to X-ray and neutron scattering, SLS is a rather coarse tool, best suited for determining the gross size and structural features of aggregates and large particulates.

14.3 Theory

The basic concepts underlying the scattering of light by a suspension of particles can be found in a number of excellent books.^[7–9] The angular dependence of the intensity of light, $I_s(q)$, is obtained by measuring the differential cross-section

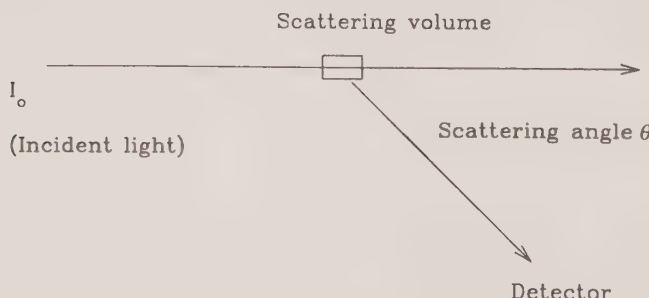


FIG. 14.1. The scattering geometry of an SLS experiment.

of light scattered from a dilute suspension of identical particles, and is described by the expression

$$I_s(q) = I_0 k N M^2 P(q, m, r) S(q), \quad (14.2)$$

where I_0 is the incident light intensity, k is an experimental constant, N is the number of scattering particles and M is the particle mass. The parameter r is related to the size of the scatterer (e.g. the radius) and m is its relative refractive index (i.e. for a particle of refractive index, n , in a medium of refractive index, n_0 , $m = n/n_0$). The intraparticle scattering factor $P(q, m, r)$ arises from interference effects within the scatterer and contains information on the particle's size, shape and internal structure. The interparticle scattering factor, $S(q)$, describes the angle dependent interference arising as light is scattered from different particles. In well ordered arrays, $S(q)$ leads to the diffraction pattern, but it also can provide a measure of interaction potentials when scatterers are weakly attracted. Some authors have performed SLS for the particular purpose of extracting radial distribution functions and interaction potentials from $S(q)$.^[10,11] The presence of $S(q)$ in eqn (14.2) is a complicating factor for particle size analysis, because it acts to distort the scattered intensity, especially at low scattering angle when the sampling distance q^{-1} is of the same order of magnitude as the interparticle spacing. Strictly, $S(q)$ is unity only when the scatterers are dilute and electrically neutral. In practice, however, and unless the scatterers are highly charged, $S(q)$ can usually be assumed to be unity for the scattering angles commonly used in SLS experiments, and at the concentrations normally employed (i.e. sufficiently dilute to avoid multiple scattering effects). In some cases pH adjustment and modification of ionic strength can minimize effects due to $S(q)$. For this discussion it is assumed that interparticle interactions can be neglected and $S(q) = 1$. In addition, the angle dependent scattering can be normalized to unity when $q = 0$. Therefore, the normalized angle dependent scattered intensity $i_s(q)$ is

$$i_s(q) = \frac{I_s(q)}{I_s(0)} \approx M^2 P(q, m, r). \quad (14.3)$$

If several populations of discrete sizes are present in the suspension, then the resulting angle dependent intensity is the weighted sum of their respective scattering functions:

$$i_s(q) = \omega_1 M_1^2 P_1(q, m, r_1) + \omega_2 M_2^2 P_2(q, m, r_2) + \dots \quad (14.4)$$

Since $\omega_1, \omega_2, \dots$ are the fractions of each population,

$$\sum_{j=1} \omega_j = 1. \quad (14.5)$$

Most samples of interest, however, do not contain a number of discrete sizes of particles but consist of one (unimodal) or more (multimodal) smooth distributions. If the distribution of sizes is represented by the number density

function, $G(r)$, then

$$i_s(q) = \int_0^\infty M^2(r)P(q, m, r)G(r) \, dr. \quad (14.6)$$

Once good quality scattering data is obtained in the form of $i_s(q)$, the principle problem is to recover the size distribution function by inverting eqn (14.6). However, this inversion belongs to a class of functions known as Fredholm integrals of the first kind that are recognized to be ill-posed or ill-conditioned, and are well known in the analysis of data in a variety of spectroscopies. Ill-conditioned means that the recovered solution for $G(r)$ is notoriously unstable, and extremely sensitive to the presence of noise and truncation errors. That is, the recovered solution is unique only in the ideal case corresponding to the absence of noise, rounding errors and truncation effects. A relatively large literature is available on the problem and on a variety of methods for circumventing difficulties. Some of this literature was developed for the analysis of DLS data where a similar ill-conditioned inversion must be employed to obtain particle size distributions from experimentally obtained autocorrelation functions.^[3,12,13] Constrained regularization, CR,^[13,14] exponential sampling with non-negative least squares, EXNNLS,^[15-17] and maximum entropy, MEM,^[18] techniques have all been applied in DLS analysis. The literature relating to the inversion of SLS data to recover particle size distributions has been mostly theoretical. One of the first computational studies was performed by Dave,^[19] and this led to a number of further numerical investigations,^[20-26] many with application to atmospheric scattering. A method has also been suggested for recovering the moments of $G(r)$ in the select case of vesicles,^[27] using the thin shell approximation (see eqn (14.9) below) and in the general case of spherical particles.^[28] The latter of these approaches requires measurement of the integral of the scattered intensity over all scattering angles, and this is difficult to achieve experimentally. Recently, Ho and Allen^[29] have described a theoretical study of the inversion of scattering data from ellipsoidal particles.

Successful application of inversion methods such as CR, EXNNLS, and MEM to SLS data requires that considerable '*a priori*' information is known about the scattering particles. Of fundamental importance is the knowledge of the particle's shape and structure so that the functional form of $P(m, q, r)$ can be specified. If the particle radius and the relative refractive index are sufficiently small that the Rayleigh–Gans–Debye criteria

$$\frac{r^2}{\lambda^2} (m^2 - 1) \ll 1 \quad (14.7)$$

holds, it is possible to obtain $P(m, q, r)$ for a variety of particular structures (Schmitz^[30]) and for vertical polarization of the incident light. Most studies

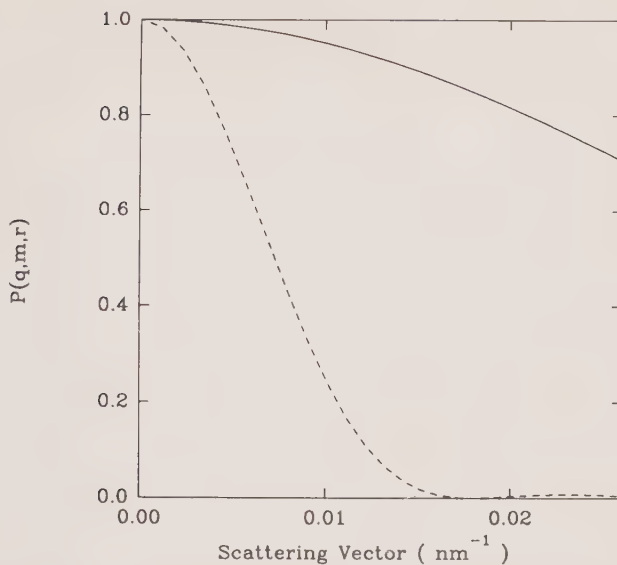


FIG. 14.2. The scattering vector (q) dependence of $P(q, m, r)$ calculated, using eqn (14.8), for uniform spheres of radius 50 nm (solid line) and radius 250 nm (dashed line).

have been applied to spherical particles of uniform index. In this case,

$$P(q, m, r) = \left[3 \frac{(\sin(qr) - qr \cos(qr))}{(qr)^3} \right]^2. \quad (14.8)$$

Figure 14.2 shows the q dependence of $P(q, m, r)$, calculated according to eqn (14.8) for uniform spheres having radii of 50 nm and 250 nm. There has also been significant interest in the size analysis of vesicle systems and other hollow shell particles. The scattering factor for a thin spherical shell is

$$P(q, m, r) = \left[\frac{\sin(qr)}{qr} \right]^2. \quad (14.9)$$

Often a particle has a structure that can be represented by a coated sphere. If r_1 is the inner radius, r_2 is the outer radius, m_1 is the relative refractive index of the core, m_2 is the relative refractive index of the coat and $f = r_1/r_2$, then the corresponding scattering factor becomes

$$P(q, m_1, m_2, r_1, r_2) = \left[(m_2 - 1) \left[\frac{3J_1(qr_2)}{qr_2} + 3f^3 \frac{m_1 - m_2}{m_2 - 1} \frac{J_1(fqr_2)}{fqr_2} \right] \right]^2. \quad (14.10)$$

Figure 14.3 shows the expected q dependence for a 50 nm radius vesicle calculated using eqn (14.9) and a 50 nm radius coated sphere calculated with eqn (14.10) and with values $f = 4$ nm, $m_1 = 1.021$ and $m_2 = 1.066$. Rayleigh Gans-Debye scattering factors for rods, cylinders, discs and Gaussian coils

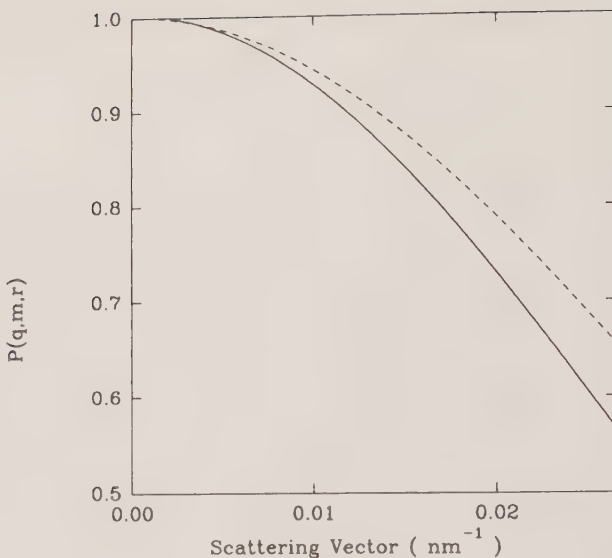


FIG. 14.3. The scattering vector (q) dependence of $P(q, m, r)$ calculated, using eqn (14.9), for a thin spherical shell of radius 50 nm (solid line) and calculated, using eqn (14.10), for a coated sphere of radius 50 nm (solid line). The coat thickness is 4 nm, and the relative refractive indices are 1.021 for the core and 1.066 for the coat.

are known^[30] and, in principle, can be used to recover particle size information. To date little has been published on the use of SLS for these cases.

When particles are too large to satisfy the condition in eqn (14.7), it is still possible to compute, using Mie theory, scattering factors for uniform spheres, hollow shells and coated spheres. For vertically polarized incident light, the angle dependence of the scattered light is contained in the S_{11} component of the Mueller matrix:

$$S_{11}(\cos \theta, m, r) = \sum_{j=1}^{\infty} \frac{2j+1}{j(j+1)} (a_j \pi_j + b_j \tau_j), \quad (14.11)$$

$$\pi_j = \frac{P_j^1 \cos(\theta)}{\sin(\theta)} \quad \text{and} \quad \tau_j = d \frac{P_j^1 \cos(\theta)}{d\theta}, \quad (14.12)$$

where $P_j^1 \cos(\theta)$ is the associated Legendre polynomial. The scattering coefficients, a_j and b_j , for uniform spheres, hollow shells and coated spheres are given elsewhere.^[8, 9] It is usually assumed that light absorption (i.e. due to the imaginary part of the refractive index) by the particles can be neglected.

In addition to the *a priori* knowledge of the shape and structure of the scattering particles, the use of inversion techniques requires that a set of predetermined trial radii be identified. In the case of DLS the minimum and maximum radii can be obtained from the initial and final slopes of the

experimental intensity autocorrelation function, because it could be reasonably assumed that these slopes provide an indication of the extrema of $G(r)$. The slopes of $i_s(q)$ at small and large values of q can also be used to obtain crude estimates of the largest and smallest particles present in the sample. However, because of flare and specular reflections at low and high scattering angles, the measured intensities at low and high angles are the least reliable. Spectrometers have been specifically designed for small angle use, but these devices are often not suited for wide angle measurements. A limitation of SLS arises, therefore, because there is no completely reliable way of predetermining the extrema (r_{\min} and r_{\max}) of the set of trial radii from the SLS signal itself. While a judicious 'guess' can be made, it is usually preferable to obtain the information from alternative techniques, such as DLS. Fortunately, as long as the quality of the data is high, most inversion techniques such as CR, EXNNLS, and MEM yield results for the recovered distributions that are relatively insensitive to the specific values of r_{\min} and r_{\max} , as long as these extrema do indeed encompass the real distribution.

The complete set of trial radii can easily be computed once the band limits r_{\min} and r_{\max} , have been determined. Both the number (N) of trial radii and their spacing must be determined in advance of the actual fit to the data. The number of trial radii must, as closely as possible, match the resolution of the data and the signal to noise ratio associated with each data point. In other words, the more data points and the better their quality, the larger the number of trial radii that can be specified. In the analysis of data from both uniform spheres and vesicle systems we have found, in our laboratory, that higher quality fits to the data were obtained using exponential or geometric spacing,

$$r_n = r_{\min} \left[\left(\frac{r_{\max}}{r_{\min}} \right)^{1/N} \right]^{n-1}, \quad (14.13)$$

but linear spacing has been regularly employed as well.^[25,31] After the set of $P_n(q, m, r)$ are calculated for each value of q and r_n , the objective is to find the set of ω_n that minimize the function VAR ,

$$VAR = [i_s(q) - \omega_n P_n P(q, m, r_n)]^2 \quad (14.14)$$

subject to the constraints of non-negativity and parsimony. Non-negativity means that the set of ω_n is required to be all positive, and parsimony is a secondary constraint requiring that the set of ω_n describe a simple smooth histogram with no abrupt discontinuities. A multimodal solution containing two or more smooth distributions is allowed, however. Lack of parsimony is an indication that too many preset values of r have been chosen relative to the quality of the data and as a result the fitting routine has started to fit some of the noise. The best fits are deemed to be the ones having the largest number of preset values of r , but yield smooth distributions that approach zero at both extrema.

14.4 Experimental considerations

Detailed descriptions of SLS apparatus optimized for particle size analysis have been published elsewhere.^[31–35] This section will provide only a brief discussion of the basic principles, compromises, and limitations of different experimental designs. Unlike DLS, where collimating pin-holes need to be quite small (about 200 µm) so that approximately one coherence area falls on the detector face, collimation in SLS is simply to define q adequately. In most spectrometers pinholes or slits as large as 1 mm are usually sufficient to limit the acceptance angle to 0.03° or less. These larger pinholes allow more light to be collected from a larger scattering volume, and reduce the time required to obtain reliable intensity measurements at each scattering angle. As long as proper calibration is performed it is sometimes useful to increase slit sizes with θ to maintain a constant Δq .^[33] This is especially useful in back scattering where the scattered intensities can be low, and where q changes only slowly with angle (see eqn (14.1)). In addition, if pinholes or slits are too small, fluctuating intensities can sometimes be present at small scattering angles, due to the diffusive motion of dust and larger aggregates in the sample.

In order to recover size distributions from SLS experiments, the apparatus must be accurately calibrated at each angle by monitoring the light scattered by a standard scatterer. While measurement of absolute scattered intensities is not necessary for the determination of size distributions, one must still have excellent knowledge of the relative scattering at one angle compared to the next. Among the best standard scatterers for this purpose are small latex spheres such as the 0.096 µm diameter spheres (Duke Scientific Corp., Palo Alto). These particles are highly monodisperse and because of their small size they scatter strongly over all accessible scattering angles. The expected $i_s(q)$ function for these particles can be calculated accurately using eqn (14.8). Other standard scatterers such as toluene or benzene have been used,^[32] but the intensity levels are often several orders of magnitude less than those obtained from particulate systems. Because many detectors exhibit some degree of non-linearity over their dynamic range, it is usually best when the intensity of the scattered light from the standard is within two or three orders of magnitude of that from the sample. Jones *et al.*^[34] have developed a spectrometer that measures size distributions of airborne particles, and have developed a novel calibration procedure using a freon gas.

The need for calibration can also seriously affect the design of the SLS apparatus. Many spectrometers (Type 1) have a detector mounted on an arm that can be rotated to allow an infinite number of scattering angles in the scattering plane.^[31,32] This approach has the advantage of flexibility in setting scattering angles and is ideal for maximizing the angular resolution, but also requires mechanical translation of the detector, either manually or automatically. Since this has to be done twice for each angle (i.e. standard and sample), then both the sample positioning and the mechanical translation must be extremely precise and reproducible. Other (Type 2) spectrometers^[33,34] have

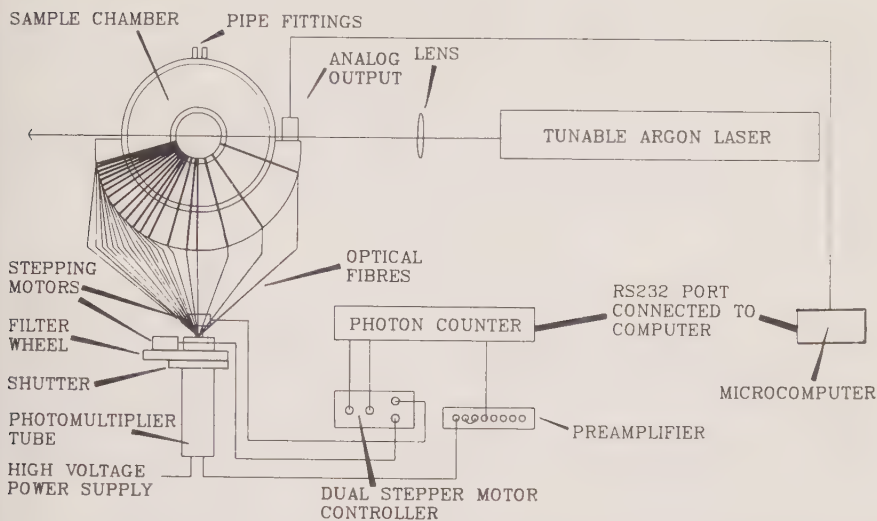


FIG. 14.4. A schematic design of a Type 2 spectrometer using fibre optic cables placed at fixed scattering angle. From ref. 33.

used fibre optics or fixed optics^[35] placed at fixed scattering angles (see Fig. 14.4). This type of apparatus is very fast to calibrate and to use. However, due to spatial limitations arising from the physical size of the fibre optic cables and the fact that each fibre optic must have its own set of collimating slits, intensities at only a few (about 20) fixed scattering angles can be monitored.

In both Type 1 and Type 2 instruments, but especially Type 2 devices, the design of the apparatus can limit the size of particles that can be studied. In Section 14.2 the minimum length scale or particle size that can be seen by an SLS experiment was shown to be determined by the wavelength of the incident radiation and the maximum scattering angle. The wavelength is of greater significance, however, because the magnitude of q varies only slightly at large scattering angles. For helium-neon incident light scattering from particles in an aqueous environment the minimum size is about 0.05 μm . Below this the scattered light becomes isotropic (independent of q), and lacks sufficient information to allow recovery of size distribution information. The maximum particles sizes recoverable are determined by another set of instrumental constraints arising from the fact that larger particles tend to scatter light predominantly in the forward (small q) direction. For particles larger than 1 μm most of the light is scattered at angles less than 30°, and the $i_s(q)$ curve can exhibit several small peaks and valleys over the complete range of accessible angles. Therefore, a relatively large number of scattering angles is needed to obtain the angular resolution so as to meaningfully extract size distribution information. For this reason Type 2 instruments are basically limited to the study of particles with radii between 0.05 and 1 μm , whereas the corresponding

range for Type 1 instruments is from 0.05 to about 5 μm . The study of even larger particles requires high quality low angle data, and the presence of flare and specular reflections at low angle can make these measurements difficult. If size information on particles larger than about 5 μm is desired then other spectrometer designs incorporating low angle position sensitive detection and the diffraction approximation are more appropriate.^[5,6]

14.5 Discussion

A criticism of much of the literature on the recovery of size distributions from SLS is that many papers describe the application of inversion techniques to simulated data with simulated noise rather than real data. Nevertheless, these studies have been useful in the development of smoothing techniques (regularization), non-negativity constraints, and in the choice of the appropriate spacing of the trial radii. In the following we will be primarily concerned with studies involving real SLS data.

Some of the first attempts to recover size distribution information from $i_s(q)$ were plagued with the problems that characterize the ill-conditioned nature of the inversion. Dave^[19] performed numerical simulations to show that recovery of size distributions was possible, and demonstrated that considerable *a priori* information is needed to obtain a unique solution. Desai and Vaidya,^[36] in a computational investigation, noted broadening effects and other distortions as they tried to recover size information from the forward scattered radiation from spherical particles using both Mie theory and the diffraction approximation. House^[20] attempted to recover information on $S(q)$ and aggregate sizes from the Fourier inversion of light scattered from coagulating latex particles. He noted large oscillations in the resulting particle distribution owing to the truncation of the data set, and suggested an exponential modification function to partially suppress the problem. The first attempt to perform an indirect inversion of the SLS data for the specific purpose of obtaining size distributions was by Glatter *et al.*^[37] Figure 14.5 shows their scattering data from latex particles, the nominal radius of which was 240 nm and Figure 14.6 shows the resulting function for $G(r)$. Glatter *et al.*, in a series of publications^[25,32,38,39,40] developed several improvements to an indirect transform method in which $G(r)$ is represented as a weighted sum of basis functions, in this case cubic splines. The detailed form of the basis functions provided a measure of the resolution of the distribution. The relative weights were obtained by a procedure similar to eqn (14.14), but included constraints to prevent oscillations and a stabilization factor. The procedure was tested by simulations, as well as on real scattering data from oil–water emulsions^[40] and on relatively large (nominal radius 1450 nm) latex particles.^[32] Rather than recover the number distribution, $G(r)$, for the latex particles these authors performed a similar inversion of

$$i_s(q) = \int_0^\infty D_v(r) \frac{P(q, m, r)}{P(0, m, r)} dr \quad (14.15)$$

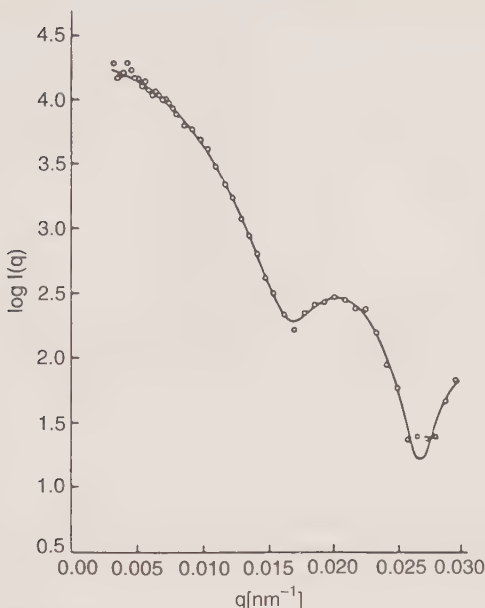


FIG. 14.5. The scattering function of 240 nm radius latex spheres: \circ , experimental data points; —, fit by the indirect transformation procedure. Reproduced from Glatter *et al.*^[37]

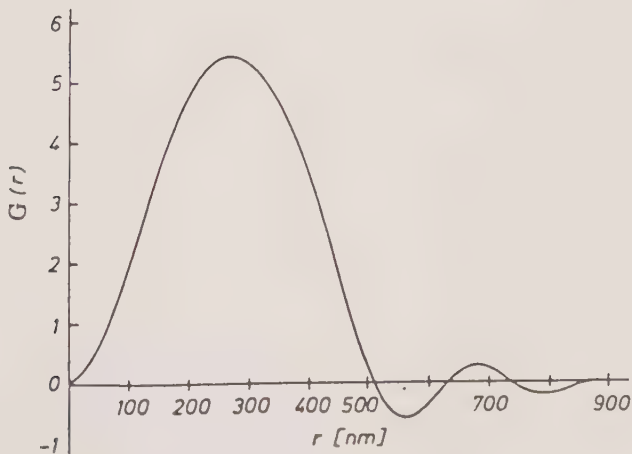


FIG. 14.6. The $G(r)$ function computed from the experimental data points in Fig. 14.5, using the method of Glatter *et al.*^[37]

to obtain the volume distribution function, $D_v(r)$. Figures 14.7 and 14.8 show the scattering data and $D_v(r)$ respectively. These studies represent some of the most sophisticated work performed to date. In some of their recent studies, Schnablegger and Glatter^[32] have begun numerical investigations on recovering size distributions of ellipsoidal particles from simulated SLS data.

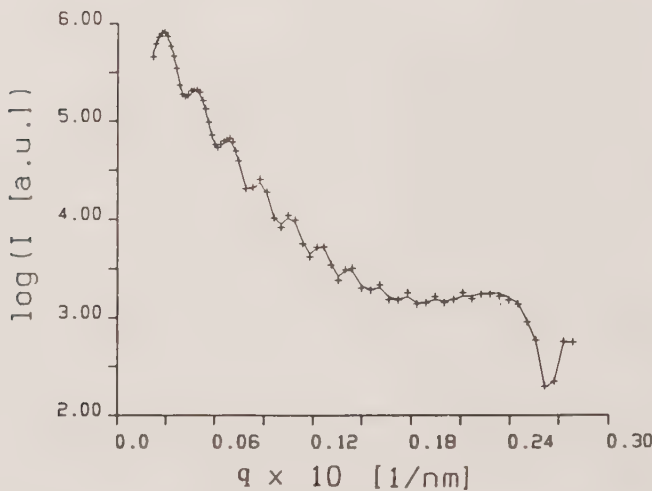


FIG. 14.7. The scattering function of 1450 nm radius latex spheres: +, data points; —, fit using the inversion procedures of Schnablegger and Glatter.^[32]

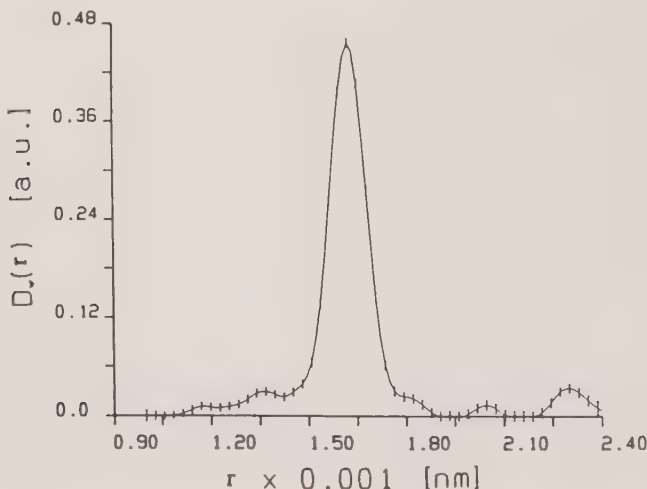


FIG. 14.8. The volume distribution function $D_v(r)$ computed from the experimental data in Fig. 14.7. From Schnablegger and Glatter.^[32]

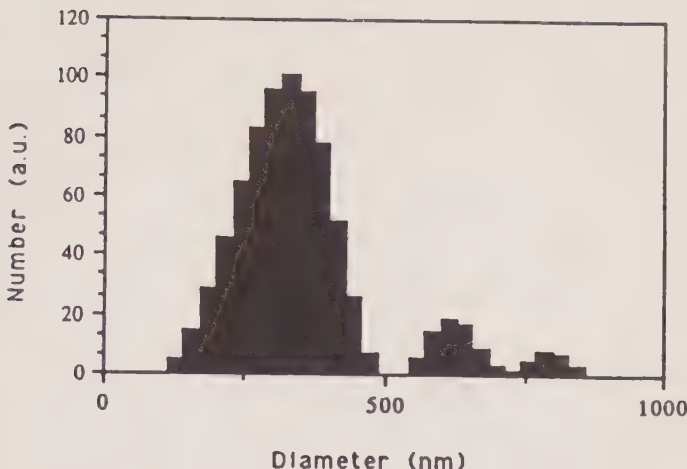


FIG. 14.9. $G(r)$ obtained, using the CR inversion technique, on SLS data from a multimodal sample of spherical butadiene particles. From Finsy *et al.*^[31].

Finsy *et al.*^[31] compared maximum entropy (MEM) and constrained regularization (CR) methods in a study involving both simulated and real data. The emphasis of this investigation was to test the relative ability of these two inversion schemes to recover size distribution information on unimodal, bimodal and trimodal distributions of latex suspensions ranging in radius from 50 nm to 2000 nm. The CR methods appears superior in analysis of data from the smaller sized particles. The ability to recover the sizes of particles even in the trimodal cases was extremely good, although there were large errors in recovering the relative abundance of each population (see Fig. 14.9). They also demonstrated that the recovery of good results from the larger particles requires high angular resolution in the $i_s(q)$ data. Strawbridge and Hallett^[41] performed similar studies using the exponential sampling and non-negative least squares (EXNNLS) inversion method in a comparative study by DLS and SLS (a Type 2 spectrometer) on unimodal and bimodal suspensions of solid and hollow latex particles with radii from 48 nm to 135 nm. The resolution obtained by the SLS inversion was consistently better than that obtained by DLS (see Fig. 14.10). This increased resolution allowed cleaner separations of the particle size distributions recovered from multimodal samples, an effect also noted by Finsy *et al.*^[31] In recent studies by DLS and SLS on the same preparation of phospholipid vesicles Strawbridge *et al.*^[42] noted that consistently smaller sizes were obtained by SLS than by DLS. There may be occasions, therefore, when the hydrodynamic radius as measured by DLS differs from the effective structural radius as measured by SLS. This difference could be especially pronounced with particles the surface of which contains loosely bound fibres or polymeric strands. The enhanced resolution of the SLS experiment, coupled with the fast data acquisition times available on a fibre-optic (Type 2) system

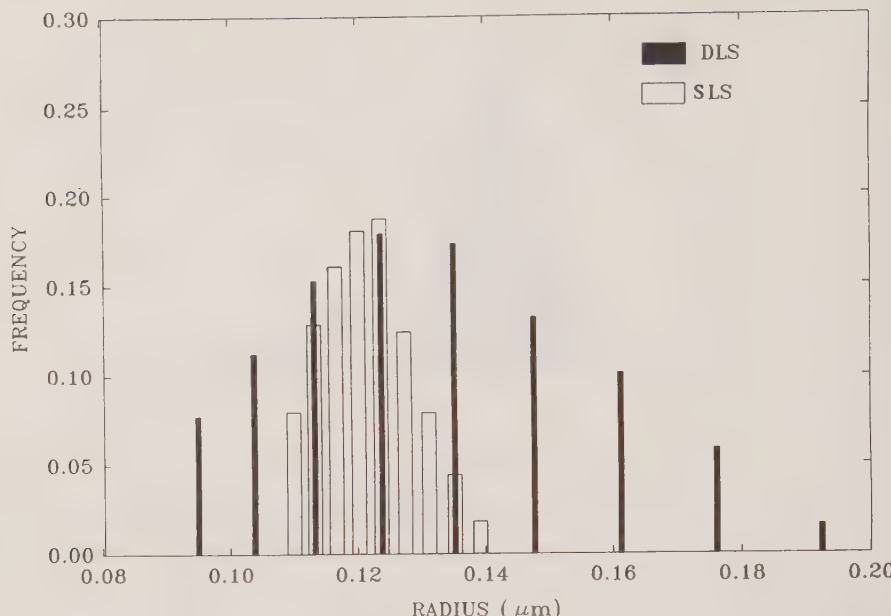


FIG. 14.10. A comparison of SLS and DLS results obtained by EXNNLS inversion methods on the sample sample of latex spheres of nominal radius 135 nm. From Strawbridge and Hallett.^[41]

allowed Strawbridge *et al.*^[42] to observe the small increases in radius of a lipid vesicle as molecules of the peptide colicin E1 were incorporated into the membrane (see Fig. 14.11). By analysing this change in radius as the number of incorporated peptides was increased, it was possible to determine the effective amount of phospholipid displaced per peptide and obtain an estimate of the membrane bound size of the peptide. Although attempts were made, the relatively long data acquisition times and the lower resolution associated with DLS precluded its use on time-sensitive samples such as this.

14.6 Conclusions

As a technique for determining particle sizes and particle size distributions, SLS has some distinct advantages and some disadvantages. It is non-invasive and involves minimal sample treatment other than dilution to prevent multiple scattering. The mean sizes obtained by SLS compare well with other techniques. Sometimes the difference in mean sizes obtained by SLS and other techniques (e.g. DLS) is a source of complementary information, such as a comparison of the 'dry' particle size to its hydrodynamic size. SLS appears to be intermediate between DLS and electron microscopy in terms of the relative resolution in recovered size distributions. Fibre-optic based SLS spectrometers allow for data recovery that is significantly faster than most other sizing techniques, but has

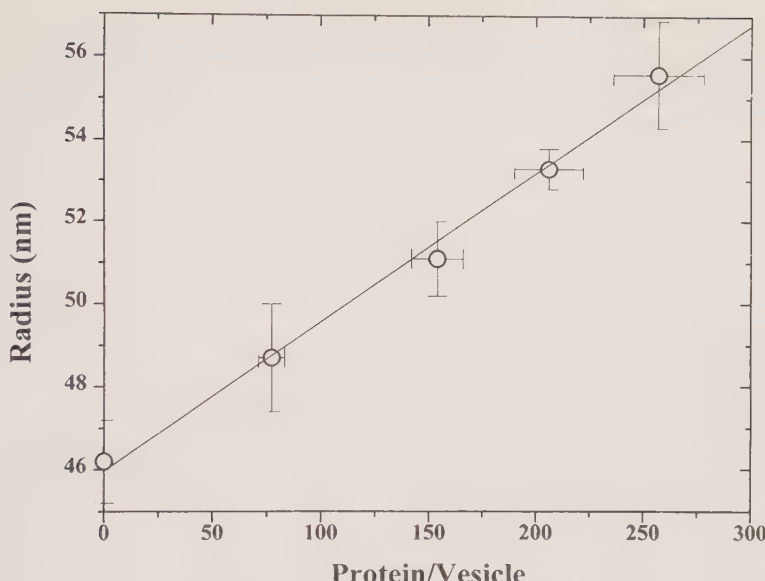


FIG. 14.11. The expansion of a phospholipid vesicle with the addition of colicin E1, a membrane-bound protein. From Strawbridge *et al.*^[42]

limited angular resolution. This type of apparatus is, therefore, best suited for analysis of particle suspensions in which the maximum particle radius is less than 1 µm. SLS spectrometers that have a detector mounted on an arm that can be rotated about the sample have the angular resolution needed to analyse particle sizes up to 5 µm or slightly higher. In either case, SLS is limited to the study of particle radii greater than about 25 nm because the angular dependence of light vanishes for light scattered by smaller particles. An inherent disadvantage of the SLS approach is that good data quality requires accurate calibration of the spectrometer. At the moment SLS is best suited to the study of spherical particles, although it has the potential for obtaining the sizes of particles having other shapes. Further studies will be necessary to define the limits of its performance for this purpose.

References

1. Barth, H. G. and Sun, S.-T. (1993). Particle size analysis. *Analyt. Chem.*, **65**, 55R–66R.
2. Dahneke, B. E. (ed.) (1983). *Measurement of suspended particles by quasi-elastic light scattering*. John Wiley, New York.
3. Štěpánek, P. (1993). Data analysis in dynamic light scattering. In *Dynamic light scattering: the method and some applications*, Monographs on the Physics and Chemistry of Materials (ed. W. Brown), pp. 177–241. Oxford Science Publications, Oxford.
4. Shifrin, K. S. and Tonna, G. (1993). Inverse problems related to light scattering in the atmosphere and ocean. *Adv. Geophys.*, **34**, 175–252.

5. Kusters, K. A., Wijers, J. G., and Thoenes, D. (1991). Particle sizing by laser diffraction spectrometer in the anomalous regime. *Appl. Opt.*, **33**, 4839–4847.
6. Bassini, A., Musazzi, S., Paganni, E., Perini, U., Ferri, F., and Giglio, M. (1992). Optical particle sizer based on the Chahine inversion scheme. *Opt. Engng*, **31**, 1112–1117.
7. Kerker, M. (1969). *The scattering of light and other electromagnetic radiation*. Academic Press, New York.
8. Van de Hulst, H. C. (1957). *Light scattering by small particles*. John Wiley, New York.
9. Bohren, C. F. and Huffman, D. R. (1983). *Absorption and scattering of light by small particles*. John Wiley, New York.
10. Salgi, P. and Rajagopalan, R. (1993). Polydispersity in colloids: implications to static structure and scattering. *Adv. Colloid Interface Sci.*, **43**, 169–288.
11. Rajagopalan, R. (1992). Probing interaction forces in colloidal fluids through static structural data: the inverse problem. *Langmuir*, **8**, 2898–2906.
12. McWhirter, J. G. and Pike, E. R. (1978). On the numerical inversion of the Laplace transform and similar Fredholm integral equations of the first kind. *J. Phys. A, Math. Gen.*, **11**, 1729–1745.
13. Provencher, S. W. (1982). A constrained regularization method for inverting data represented by linear algebraic or integral equations. *Comput. Phys. Communns*, **27**, 213–227.
14. Provencher, S. W. (1982). Contin: a general purpose constrained regularization program for inverting noisy linear algebraic and integral equations. *Comput. Physics, Communns*, **27**, 229–242.
15. Pike, E. R., Watson, D., and Watson, F. M. (1983). Analysis of polydisperse scattering data II. In *Measurement of suspended particles by quasi-elastic light scattering* (ed. B. E. Dahneke), pp. 107–128. John Wiley, New York.
16. Herb, C. A., Berger, E. J., Chang, K., Morrison, I. D., and Grabowski, E. F. (1987). Particle size distribution: assessment and characterization. In *ACS Symposium Series 332* (ed. T. Provder), pp. 89–104.
17. Hallett, F. R., Craig, T., Marsh, J., and Nickel, B. (1989). Particle size analysis: number distributions by dynamic light scattering. *Can. J. Spectrosc.*, **34**, 63–70.
18. Skilling, J. (ed.) (1989). *Maximum entropy and Bayesian methods*, Kluwer, Dordrecht.
19. Dave, J. V. (1971). Determination of size distribution of spherical polydispersions using scattered radiation data. *Appl. Opt.*, **10**, 2035–2044.
20. House, W. A. (1978). Fourier inversion of light scattering intensity data from coagulating dispersions. *J. Chem. Soc., Faraday Trans. 1*, 1112–1124.
21. Alger, T. W. (1979). Polydisperse-particle-size-distribution function determined from intensity profile of angularly scattered light. *Appl. Opt.*, **18**, 3494–3500.
22. Heintzenberg, J. (1980). Polydisperse-particle-size-distribution function determined from intensity profile of scattered light: comments. *Appl. Opt.*, **19**, 1894–1895.
23. Curry, Bill P. (1989). Constrained eigenfunction method for the inversion of remote sensing data: application of particle size determination from light scattering measurements. *Appl. Opt.*, **28**, 1345–1355.
24. Arridge, S., van der Zee, P., Delpy, D. T., and Cope, M. (1989). Particle sizing in the Mie scattering region: singular-value analysis. *Inverse Prob.*, **5**, 671–689.
25. Schnablegger, H. and Glatter, O. (1991). Optical sizing of small colloidal particles: an optimized regularizatin technique. *Appl. Opt.*, **30**, 4889–4896.
26. Jones, M. R., Curry, Bill P., Brewster, M. Q., and Leong, K. H. (1994). Inversion of light-scattering measurements for particle size and optical constants: theoretical study. *Appl. Opt.*, **33**, 4025–4034.

27. Wang, J. and Hallett, F. R. (1995). Vesicle sizing by static light scattering: a Fourier cosine transform approach. *Appl. Opt.*, **34**, 5010–5015.
28. Mroczka, J. (1993). Method of moments in light scattering data inversion in the particle size distribution function. *Optics Commun.*, **99**, 147–151.
29. Ho, K. C. and Allen, F. S. (1994). An approach to the inverse obstacle problem from the scattering Mueller matrix. *Inverse Prob.*, **10**, 387–400.
30. Schmitz, K. S. (1990). *An introduction to dynamic light scattering by macromolecules*, pp. 21–24. Academic Press, New York.
31. Finsy, R., Deriemaeker, L., Gelade, E., and Joosten, J. (1992). Inversion of static light scattering measurements for particle size distributions. *J. Colloid Interface Sci.*, **153**, 337–354.
32. Schnablegger, H. and Glatter, O. (1993). Simultaneous determination of size distribution and refractive index of colloidal particles from static light-scattering experiments. *J. Colloid Interface Sci.*, **158**, 228–242.
33. Strawbridge, K. R., Hallett, F. R., and Watton, J. (1991). Rapid determination of $I(Q)$ using a fibre-optic based integrated light scattering spectrometer. *Can. J. Spectrosc.*, **36**, 53–60.
34. Mones, M. R., Leong, K. H., Brewster, M. Q., and Curry, Bill P. (1994). Inversion of light scattering measurements for particle size and optical constants: experimental study. *Appl. Opt.*, **33**, 4035–4041.
35. Haller, H. R., Destor, C., and Cannell, D. S. (1983). Photometer for quasi-elastic and classical light scattering. *Rev. Scient. Instruments*, **54**, 973–984.
36. Desai, J. N. and Vaidya, D. B. (1975). Particle size analysis by forward scattering. *J. Colloid Interface Sci.*, **51**, 527–531.
37. Glatter, O., Hofer, M., Jorde, C., and Eigner, W.-D. (1985). Interpretation of elastic light-scattering data in real space. *J. Colloid Interface Sci.*, **105**, 577–586.
38. Glatter, O. and Hofer, M. (1988). Interpretation of elastic light scattering data in real space II: nonspherical and inhomogeneous monodisperse systems. *J. Colloid Interface Sci.*, **122**, 484–495.
39. Glatter, O. and Hofer, M. (1988). Interpretation of elastic light scattering data III: determination of size distributions of polydisperse systems. *J. Colloid Interface Sci.*, **122**, 496–506.
40. Hofer, M., Schurz, J., and Glatter, O. (1989). Oil-water emulsions: particle size distributions from elastic light scattering data. *J. Colloid Interface Sci.*, **127**, 147–155.
41. Strawbridge, K. B. and Hallett, F. R. (1994). Size distributions obtained from the inversion of $I(Q)$ using integrated light scattering spectroscopy. *Macromolecules*, **27**, 2283–2290.
42. Strawbridge, K. B., Palmer, L. R., Merrill, A. R., and Hallett, F. R. (1995). Integrated light-scattering spectroscopy, a sensitive probe for peptide–vesicle binding: application to the membrane-bound colicin E1 channel peptide. *Biophys. J.*, **68**, 131–6.

Light scattering and chromatography in combination

Linda L. Lloyd, John F. Kennedy, and Charles J. Knill

15.1 Introduction

The need to understand the relationships between the physicochemical characteristics of macromolecules has been the driving force for the development of instrumentation for the characterization of such molecules. Polymer chemists and biochemists have constantly strived for analytical instrumentation and methods which enable molecular weight and structure information to be generated, as it has long been recognized that these are fundamental properties which influence the physical properties of polymeric materials. Many methods have been utilized, such as thermogravimetric analysis, osmometry, viscometry, and light scattering, which provide information on the bulk characteristics of a material, and separation systems, such as liquid chromatography, which attempt to separate the molecules prior to characterization. By combining the separation methodologies with the characterization methods, an exceptionally powerful method becomes available for determining not just bulk characteristics but also distributions of these characteristics. Such a system involves the combination of liquid chromatography and laser light scattering to obtain information on the distribution of molecular weight and size of a polymeric material. This is the technique which is described in this chapter and gives unparalleled information on the characteristics of the separated macromolecules.

15.2 Chromatographic techniques

Liquid chromatography is a technique which has long been recognized as a tool that can be used by polymer chemists and biochemists to gain some insight into the relationship between molecular weight/structure and functionality. The liquid chromatography system separates macromolecules according to a given characteristic. In the case of size exclusion chromatography (also termed gel filtration chromatography or gel permeation chromatography), which is a non-destructive, non-interactive technique, the separation mechanism is based on molecular size in solution, whereas with the interactive techniques such as ion exchange, reversed phase, hydrophobic interaction, and affinity, a given characteristic or characteristics of the molecule, charge, hydrophobicity, or

biological affinity are exploited to achieve resolution. The former technique is applicable to both synthetic and biopolymer analysis, whereas the interactive techniques are utilized more frequently for high resolution separations of biopolymers or, in the case of reversed phase chromatography, for small molecule analysis.

15.2.1 Size exclusion chromatography

The separation of molecules based on size is a technique utilized by scientists working with both natural and synthetic macromolecules, although the two groups of scientists have tended to develop the technique independently. The pioneering work in the separation of biological macromolecules, proteins, was carried out by Porath and Flodin,^[1] who called the technique 'gel filtration chromatography', whereas the comparable work with synthetic macromolecules was instigated by Moore,^[2] who used the 'term gel permeation chromatography' to describe this form of liquid chromatography. Neither name adequately describes the technique, because the mechanism of separation is not filtration and the column packing materials are not gels. As the separation of molecules is based exclusively on their hydrodynamic volume, or size in solution, a more accurate term to describe the technique is 'size exclusion chromatography'. The simplest non-mechanistic approach to understanding size exclusion chromatography is to consider only two assumptions; firstly that there is a stagnant phase of liquid of volume V_i in the column and, secondly, that there is a differential solute permeability into the stagnant phase based on the size in solution of the molecules. Theoretical descriptions have also been published which relate solute dimensions to pore geometry and size but which, by necessity, are mathematical models. A full description of the theoretical aspects of size exclusion chromatography is beyond the scope of this chapter, but the reader is referred to the book of Yau, Kirkland, and Bly^[3] for further information.

In size exclusion chromatography the retention volume of a given molecule (V_e) is explained in terms of three variables: (1) the stationary phase volume, considered to be the liquid in the pores of the particles (V_i); (2) the mobile phase volume or volume of liquid outside the pores and located in the interstitial volume, considered to be the elution volume of a non-retained peak (V_0); and (3) the distribution coefficient (K_d), which defines the portion of V_i accessible to a solute and may be defined as $V_e = V_0 + K_d V_i$. The value of V_i is therefore less than 1. In summary, the elution order in size exclusion chromatography is based on molecular size in solution (hydrodynamic volume) with large molecules which are unable to permeate the particle porous structure eluting at the column void volume (V_0), whereas molecules which can totally permeate into the pores elute at the totally included or permeation volume (V_i), which equals $V_0 + V_i$. Molecules of intermediate size will be fractionated based on their permeability into the porous particle, with those least able to permeate eluting first. It is therefore clear that the molecular size in solution of a given molecule can be

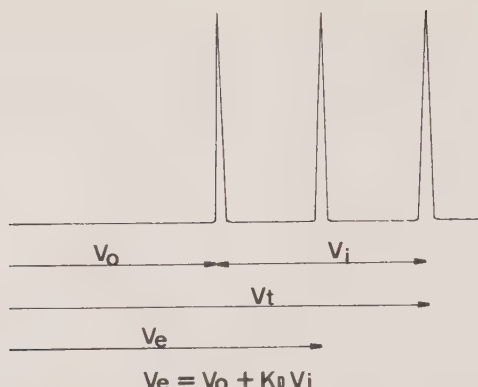


FIG. 15.1. A schematic representation of the terms used to define a size exclusion chromatography separation.

related to its elution volume, which is dependent in turn upon column dimensions, or to the distribution coefficient, which is independent of column dimensions. This is summarized in Fig. 15.1, which gives a diagrammatic representation of these parameters. In its standard form size exclusion chromatography is carried out using a concentration dependent detector which monitors the concentration of material in the eluent stream as it exits the column. The most common detector is the differential refractometer, which monitors the refractive index difference between the eluent stream as it exits the column and a reference sample of the eluent. Alternatively, if the molecules have a suitable chromophore, on-line UV detectors can be used. A typical size exclusion chromatogram is shown in Fig. 15.2.

When concentration detectors are used in order to convert elution volume to molecular weight, the separation system must be calibrated. In an ideal size exclusion chromatography system, where there is no interaction between the solute and the porous particles, calibration curves of molecular weight against elution volume or distribution coefficient can be produced using

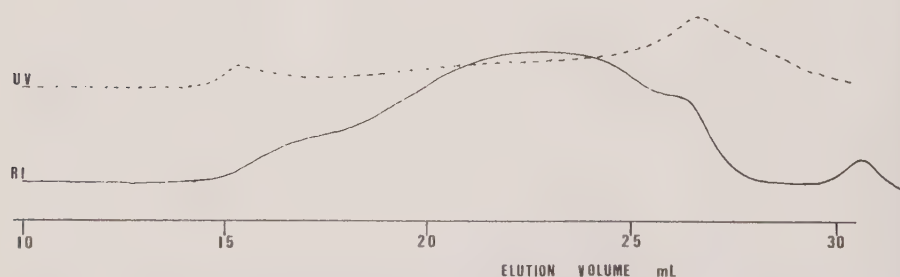


FIG. 15.2. A typical size exclusion chromatogram: elution profiles of pectin extracted from citrus, showing data obtained using RI and UV, 235 nm detectors.

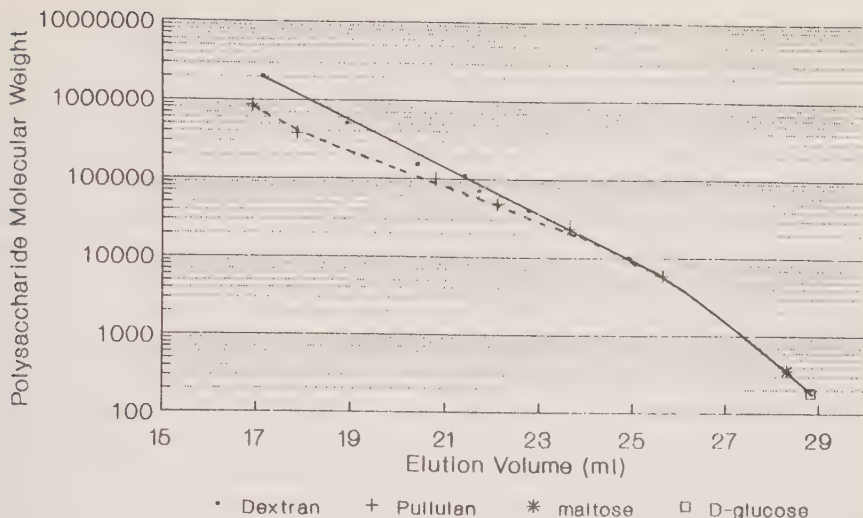


FIG. 15.3. Size exclusion calibration curves produced using dextran and pullulan polysaccharide reference materials.

standards of known molecular weight (see Fig. 15.3). However, the separation mechanism is based on solution size hydrodynamic volume, and not molecular weight, and therefore to determine the molecular weight of a polymer the system must be calibrated with standards of the same chemical/molecular type; otherwise large errors may occur due to differences in molecular conformation, i.e. different types of polymer may have the same molecular weight but different solution sizes and hence elution volumes under a given set of chromatographic conditions. This is clearly evident in Fig. 15.3, in which the calibration curves for the two polysaccharides, pullulan and dextran, are displaced due to different conformations in solution. Non-ideal size exclusion behaviour may also occur, particularly in eluents with an aqueous base, where a mixed mode separation occurs, owing to size and solute/column packing interaction. These problems can be overcome if an absolute molecular weight detector such as one of the laser light scattering detectors is used, as it does not require calibrating to relate elution volume to molecular weight. It is an absolute detector.

15.2.2 Interactive chromatography

In addition to size exclusion chromatography, solute molecular characteristics, charge and hydrophobicity being the most common, can also be exploited to achieve a separation. The early separations of proteins were achieved using an anion exchange material, diethylaminoethyl derivatized cellulose,^[4] and subsequently using carboxymethyl derivatized cation exchangers. However, it was not until the 1970s that reversed phase HPLC was routinely used for the analysis of small molecules and subsequently biological macromolecules. In

in interactive chromatography the elution order of a series of molecules is determined by the strength of the interaction between the packing material and the solutes and is only related to size in exceptional circumstances, e.g. for an homologous series such as cellulose or polystyrene oligomers. Therefore when a concentration detector is used with interactive chromatographic techniques information on molecular size and conformation cannot readily and reliably be obtained. Except in some instances of copolymer compositional characterization, synthetic polymers are not normally characterized using these types of chromatography. Biological macromolecules such as proteins are, however, routinely purified and characterized using these techniques. Figure 15.4 shows a typical chromatogram of a reversed phase separation of a standard protein mixture. The macromolecular environment and surface interactions can have a significant effect on the three-dimensional structure of biological macromolecules: therefore, when interactive chromatography is performed on such a molecule, the tertiary structure responsible for the three-dimensional architecture may be disrupted and multiforms observed. The use of an on-line absolute molecular weight detector enables such chromatographic or process-induced changes to be observed and the molecular weight and conformation data of the individual components to be obtained, even when the elution order is not related to size.

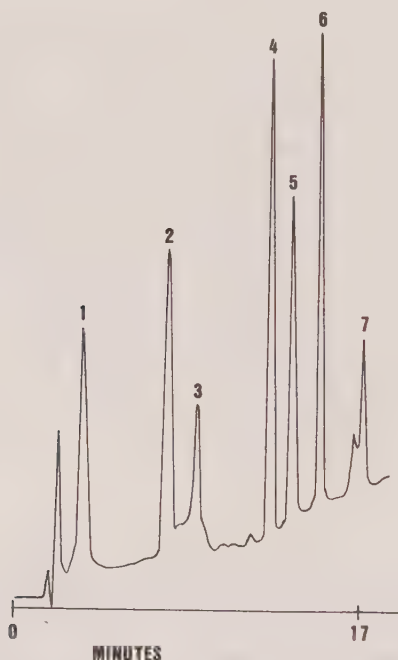


FIG. 15.4. The reversed phase HPLC separation of a standard protein mixture: 1, ribonucleases; 2, insulin; 3, cytochrome C; 4, lysozyme; 5, bovine serum albumin; 6, myoglobin; 7, ovalbumin.

15.3 Information obtainable

Static light scattering, where the intensity of scattered light due to the presence of molecules in solution (excess Rayleigh ratio) is measured as a function of the observation angle, is used in the characterization of polymers in solution. The technique was historically one of the only methods available for the determination of the absolute molecular weight and radius of gyration for both synthetic and natural polymers. The data from such an experiment is normally presented in the form of a Zimm plot; see Fig. 15.5 for a typical example. By extrapolation of the intensities of scattered light to zero angle and concentration, the weight average molecular weight of the sample is obtained. The square mean radius of the polymer is also obtained from this plot by determining the initial angle dependent slope at zero concentration. Consideration of the zero concentration line and the second virial coefficient provides conformational information. In the early 1970s a fundamentally different design of light scattering instrument was introduced, low angle laser light scattering (LALLS), which measures light scattering at very low angles, typically 3° – 10° .^[5] The assumption was made that extrapolation to zero angle was not required and hence data manipulation was simplified. Although originally developed for static determinations of molecular weight, it was subsequently used as an on-line detector coupled to a size exclusion chromatograph for the routine determination of molecular weight and molecular weight distributions. The radius of gyration and associated information could not be obtained.^[6] The theory and data processing associated with the LALLS instrument have been discussed elsewhere.^[7]

More recently, instrumentation has become commercially available to enable scattering measurements to be performed over a broad range of scattering angles in combination with a liquid chromatography. The utilization of multi-angle laser light scattering (MALLS) instrumentation has enabled many important deductions of light scattering theory to be applied for the first time to on-line measurements. In addition to the molecular weight distribution and cumulative distribution, the mean square radius and its averages, molecular conformational and structure, and branching ratios can be calculated. A more thorough characterization, particularly of copolymers, can be achieved. The details of how the molecular parameters are derived from the experimental data with the MALLS detector are beyond the scope of this chapter, but have been well presented by Wyatt.^[8]

The third variant of laser light scattering instrumentation is the right angle laser light scattering detector (RALLS). This detector is a single angle instrument, as is the LALLS, and therefore similar information can be obtained. However, to date applications of the RALLS detector have been as one component in a triple detector SEC instrument with an on-line viscometer and refractive index detector. Combining the data from the RALLS and viscometer, it is possible to obtain the radius of gyration.

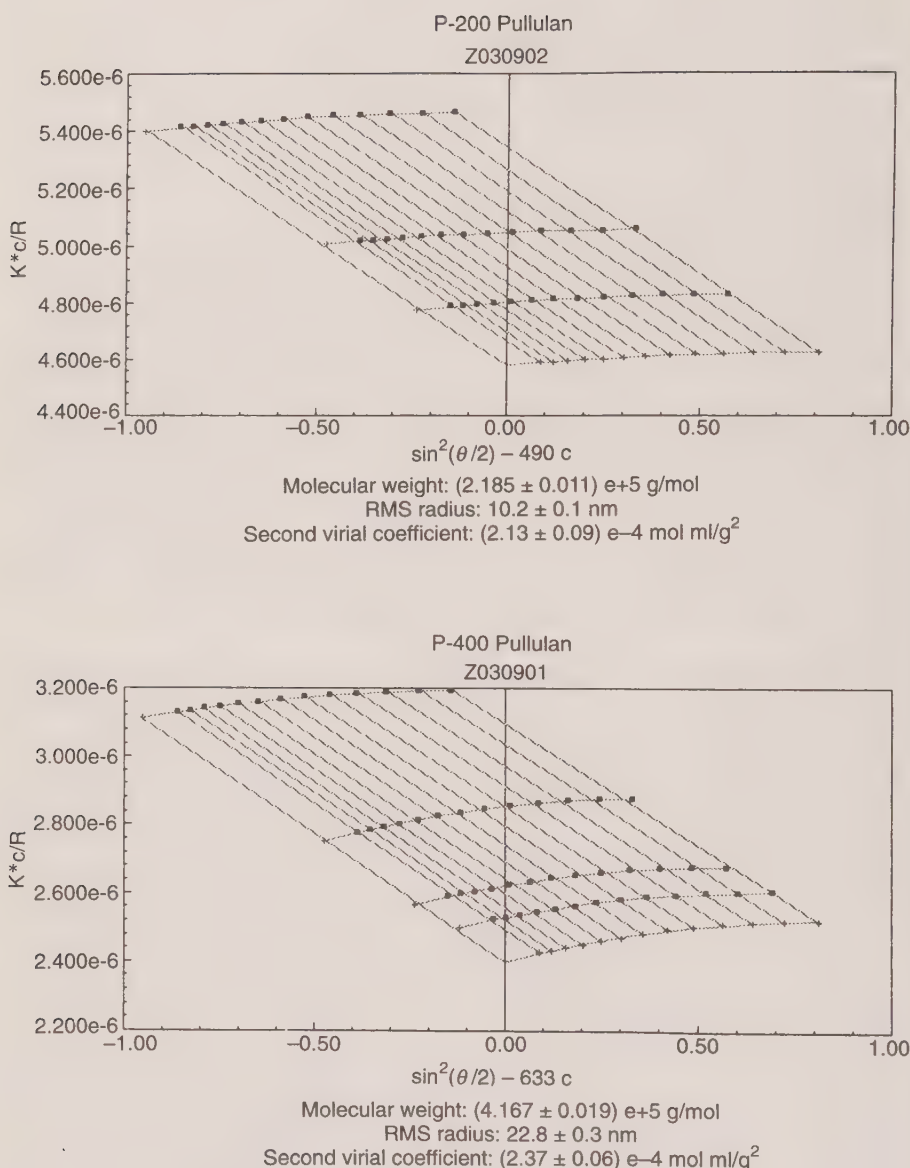


FIG. 15.5. Zimm plots of pullulan polysaccharides.

15.4 Instrumentation

A typical configuration of the liquid chromatography system required for the analysis of polymers by on-line light scattering is shown in Fig. 15.6. Standard chromatographic components, a degasser, a pump, a pressure damper, a concentration detector, and data recording/handling, are used, with the light scattering detector placed between the columns and the concentration detector to minimize the back pressure on the concentration detector sample cell. The most commonly used concentration detector is the differential refractometer, although if the polymers to be analysed contain a suitable chromophore, UV detection is often used as this can be more sensitive than refractive index. A limited number of applications have also been published using an on-line viscometer and high temperature organic phase size exclusion chromatography with an infrared concentration detector. As the majority of analyses are performed to obtain molecular weight information, size exclusion columns, where the separation mechanism is based on molecular size in solution, are most commonly used, although reversed phase and ion exchange columns have been used for some biological applications, e.g. protein aggregation studies. The requirement for sample characterization by on-line laser light scattering is a discriminating separation of the individual components by whatever mechanism is appropriate, including mixed mode.

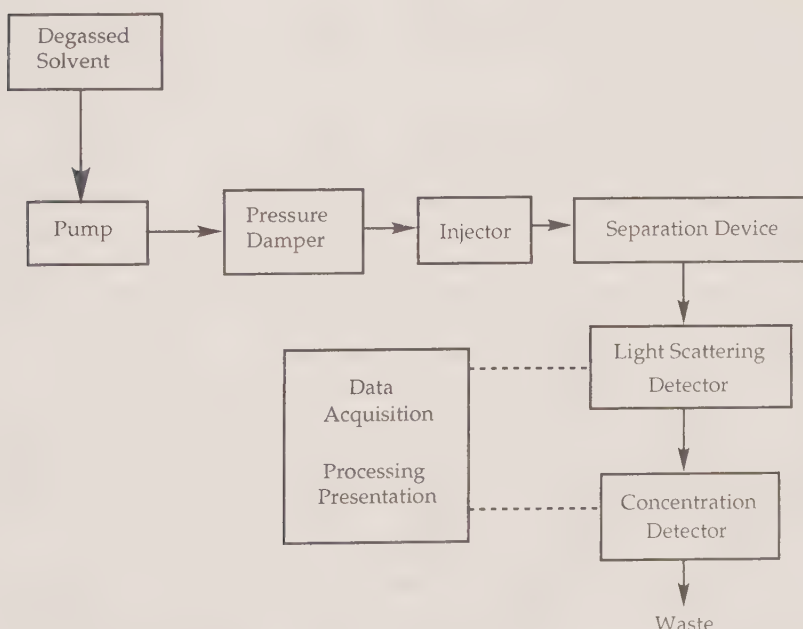


FIG. 15.6. A schematic representation of a size exclusion chromatography system incorporating a laser light scattering detector.

15.4.1 Low angle laser light scattering detectors (*LALLS*)

As previously mentioned, the first light scattering detector to be coupled with a liquid chromatography system was the low angle laser light scattering photometer, the best known example being the LDC/Milton Roy Chromatix™ KMX-6. With this detector absolute molecular weight distributions are calculated from the concentration detector response and the LALLS measurement of the excess Raleigh factor, R_θ . The instrument uses a 2 mW, 633 nm He–Ne laser light source with a patented optical design, as illustrated in Fig. 15.7. The cell, with a scattering volume of 0.1 μl , is formed between two fused silica windows and the scattered light is measured at a low angle, typically 3°–7°, to the incident beam. The standard instrument for on-line SEC/LALLS is fitted with a 5 mm, 10 μl stainless cell, but there is also an option of a high temperature cell assembly which permits operation within the temperature range 30–165 °C. For accurate measurement of absolute molecular weights by SEC/LALLS the differential change of solution refractive index with solute concentration at infinite dilution (dn/dc) must be known, as it is a squared term in the calculation. To ensure accuracy in its determination LDC/Milton Roy have a complementary stand-alone instrument, the KMX-16 laser differential refractometer, with a similar 633 nm He–Ne laser, for determining this parameter. Typical elution curves obtained with a differential refractive index detector and LALLS detector are shown in Fig. 15.8. The different responses to high and low molecular weight components in the sample can be clearly seen. The scattered light intensity is proportional to molecular weight and concentration and responds to molecular mass, and the RI responds to the concentration of the sample.

More recently, an alternative low angle laser light scattering instrument for both batch and on-line analysis, PL-LALS, has been commercialized by Polymer Laboratories Ltd. This instrument measures the scattered light intensity at a single angle of 5° from a 0.1 μl scattering volume for molecular weight determinations in the range of 10 000–10 000 000 daltons. The light source is also a 633 nm He–Ne laser but with a higher power rating of 5 mW. The optical pathway is somewhat different with this instrument, as it continuously monitors the incident beam to compensate automatically for fluctuations in laser intensity and has an integrated refractive index detector at the same wavelength (650 ± 30 nm); see Fig. 15.9. According to the manufacturer, having the refractive index detector incorporated into the LALLS instrument allows both on-line concentration detection together with dn/dc determination. The PL-LALS instrument can be supplied with an alternative built-in concentration detector, a single wavelength UV detector, but obviously dn/dc measurements are then not possible with the same instrument.

Both of these LALLS instruments have data collection and manipulation software to maximize the information that can be obtained from the analysis of polymers.

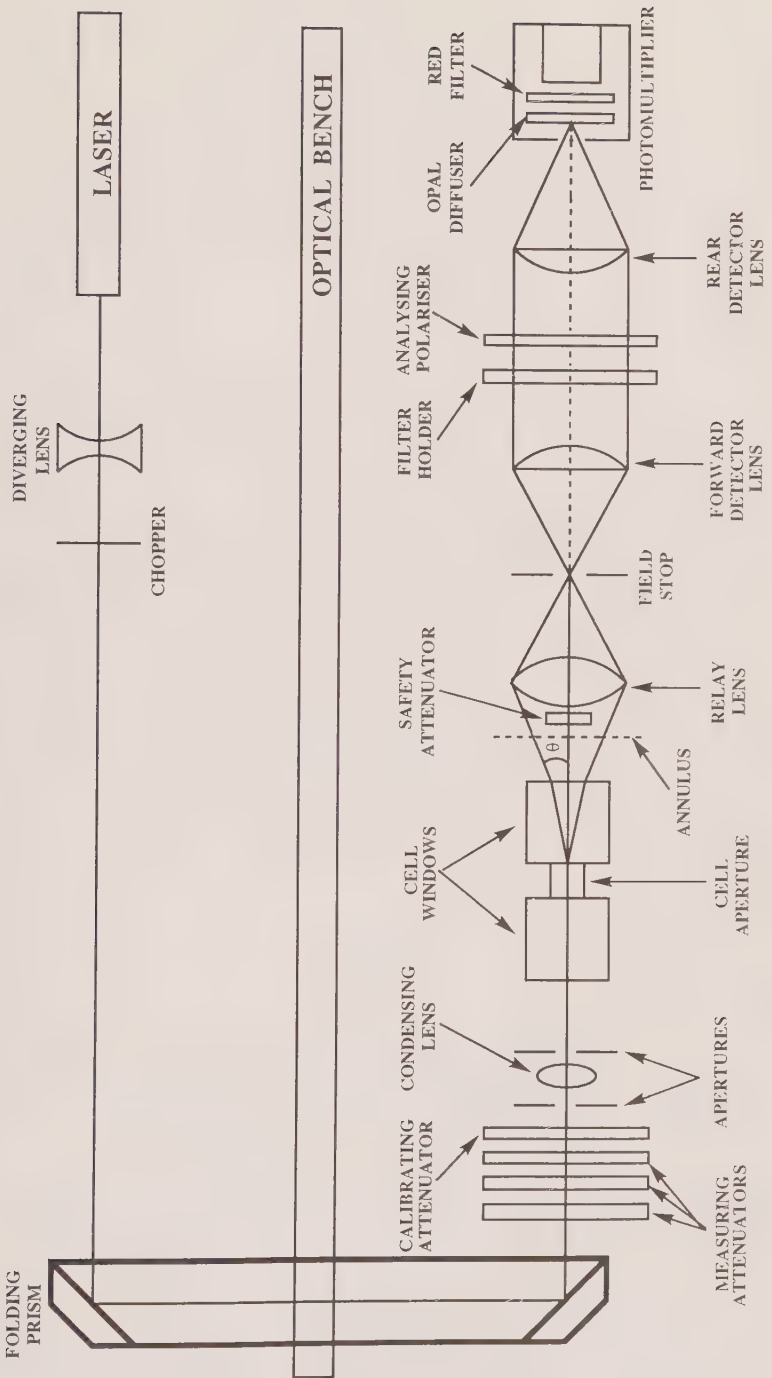


FIG. 15.7. A representation of the optical pathway of the KMX-6 low angle light scattering detector.

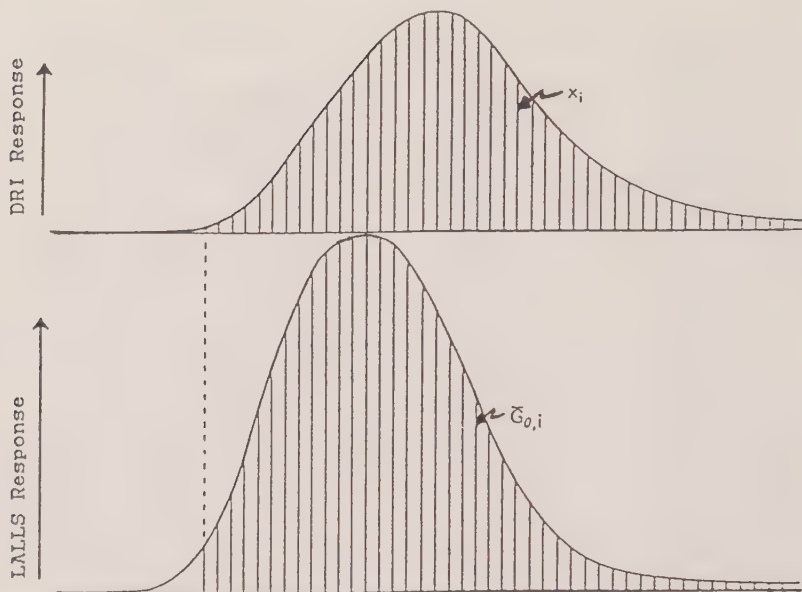


FIG. 15.8. Elution curves, corrected for interdetector volume, generated by an RI and low angle laser light scattering detector.

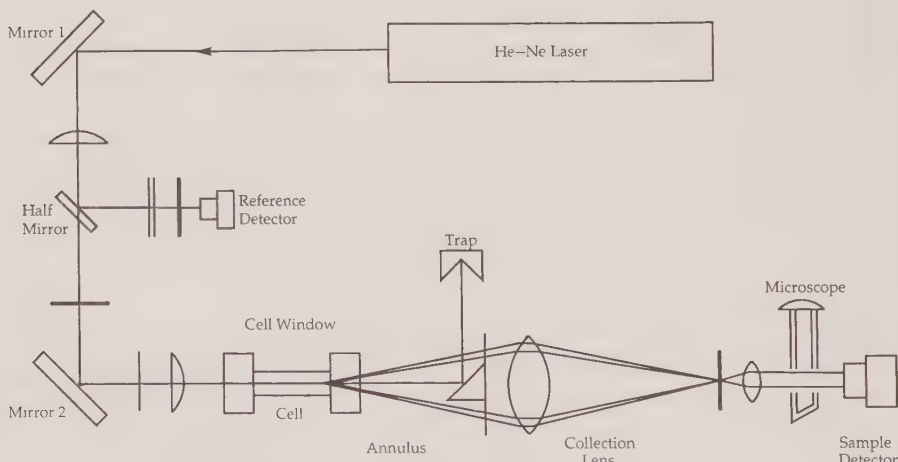


FIG. 15.9. A representation of the optical pathway of the PL-LALS low angle laser light scattering detector.

15.4.2 Multi-angle laser light scattering detectors (MALLS)

The first multi-angle laser light scattering photometer was constructed in 1978 and was fully commercialized in 1986 as the DAWN™ Laser photometer by Wyatt Technology Corporation. This instrument has undergone further

refinements, with the latest model being the DAWN™ DSP. It can be used on-line as a liquid chromatography detector or off-line to produce classical light scattering measurements. In the on-line mode it is possible to determine molecular weights in the range 1000–10 000 000 daltons and r.m.s. molecular radii of 10–500 nm. The design of this instrument is very different from that of the LALLS detectors. There are 18 discrete photodetectors located around the flow cell (although only 17 are used with the flow-through cell) which simultaneously measure light intensity over a broad range of angles, 15°–160°. A schematic of the multi-detector geometry is shown in Fig. 15.10. There is also a solid optical bench where the flow cell, read head and laser are bolted together, which gives exceptional electro-optical stability to the instrument and also means that no realignment is needed when the cell is replaced after cleaning. One of the major problems which users of the older LALLS instruments encountered, particularly when working with aqueous eluents and biological macromolecules, was that of cell window contamination. The patented cell design of the DAWN™ DSP MALLS instrument incorporates cell windows which protrude into the eluent stream at the entrance and exit manifolds, which is reported to assist in keeping the cell and interfaces clean of precipitates and coatings. The light source is a 5 mW He–Ne linearly polarized laser of 632.8 nm wavelength, although for very high sensitivity applications, very low concentrations or molecular weights, there is an option of a 10–40 mW argon ion laser which operates at 488 nm or 514 nm, with a scattering volume of 0.5 µl. In addition to an ambient temperature, instrument options are available for high temperature (150 °C), ultra high temperature (210 °C), and cooled/heated (−15 °C to 80 °C) operation, to enable analysis of polymers with high temperature solubility and temperature sensitive biological macromolecules. The Dawn™ DSP has digital signal processing which gives a digital output from the

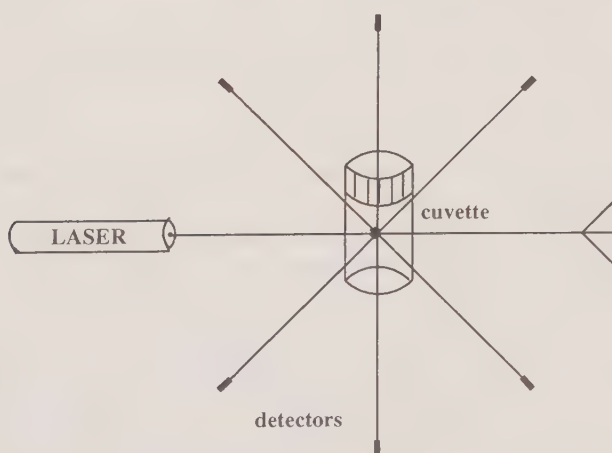


FIG. 15.10. A schematic representation of a multi-angle laser light scattering detector system, showing a sample surrounded by an array of detectors.

detector to a computer via the RS-232 serial port. There is a complementary software package, ASTRATM, for both IBMTM PC and AppleTM Macintosh formats to produce molecular weight and molecular weight versus volume plots, differential molecular weight and molecular size distributions, cumulative molecular weight and molecular size distributions, branching ratio calculations and graphs, conformational plots of $\log M$ versus $\log R_g$, and three-dimensional plots of the normalized Rayleigh excess ratio as a function of scattering angle and elution volume.

The Wyatt Technology Corporation also produce an instrument called the miniDAWN which, according to the manufacturer, has been designed primarily as a light scattering detector for liquid chromatography. It can, however, still be used as an off-line instrument for stand-alone batch-type measurements of polymer solutions. This instrument has a fixed triple angle detector array (see Fig. 15.11), which measures at 45°, 90°, and 135° the intensity of the scattered light from the 20 mW semiconductor laser of 690 nm wavelength. These angles were reportedly chosen to maximize the range of angles while at the same time minimizing any sample noise. The scattering volume in this instrument is the lowest of all the commercially available detectors, being 0.02 μ l. Although the range of polymers which can be characterized using this instrument is less than that of the DAWNTM DSP, being molecular weights in the range of 1000–1 000 000 daltons and molecular sizes of 10–50 nm, it is still an exceptionally useful instrument for polymer characterization and an alternative for routine work to the more expensive, larger MALLS detector, the DAWNTM DSP. The computer interface is also via RS-232 after digital signal processing and it has its own software, ASTRetteTM, for simultaneous collection and processing of data files.

An interferometric refractometer, Optilab 903TM, is also available from the Wyatt Technology Corporation, and can be used as an on-line concentration detector and off-line to determine the refractive index increment, $d\eta$, for a change of solute concentration, dC , for the determination of absolute molecular weights using the MALLS detectors. The refractometer is normally supplied for detection at the He-Ne laser wavelength of 633 nm, but it may also be specified for other laser wavelengths as required to match the light scattering detector being used, e.g. 488 nm and 514 nm to match the argon ion laser option in the DAWNTM DSP.

A research group at the University of Maine, France, have recently developed a multi-angle light scattering and viscosity detector^[19] which has been evaluated for the characterization of polydisperse solutions of branched poly(methyl-methacrylate).^[1,0] The instrument was developed from the premise that with a viscometry detector a better signal-to-noise ratio can be obtained with batch measurements than with continuous measurement, and that with size exclusion chromatography long column sets give better resolution than short sets, although the analysis time is longer. To maximize the amount of information that can be obtained from the light scattering/viscosity measurements, the group have placed the emphasis on complete and accurate results rather than

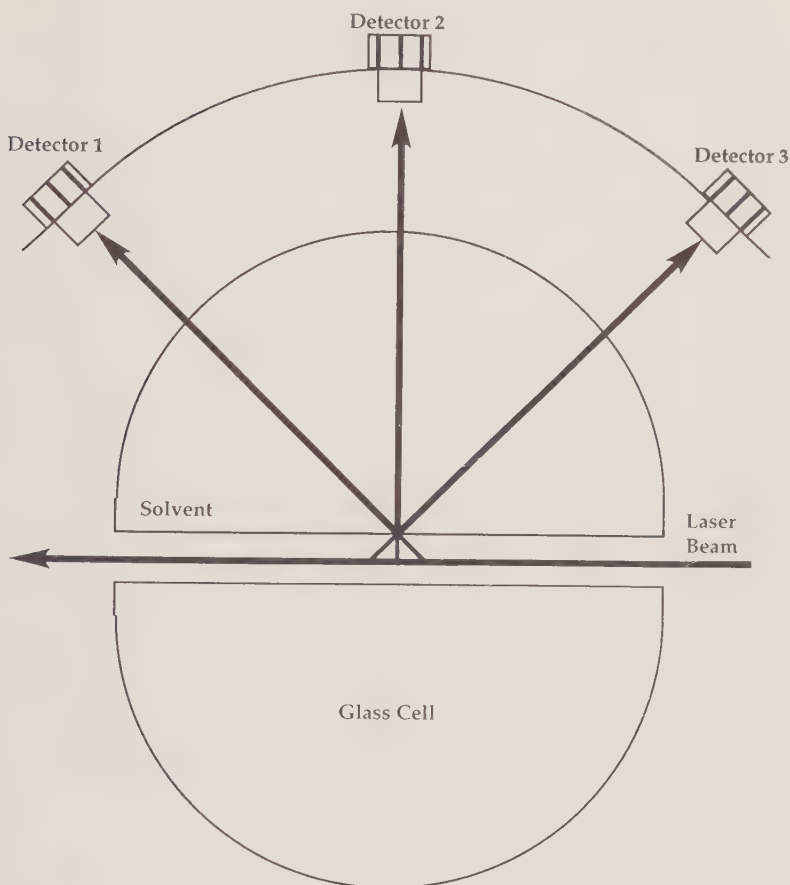


FIG. 15.11. A representation of the detector geometry of the miniDAWN multi-angle laser light scattering detector.

rapid results, and therefore decided that measurements should be performed on discrete 1 ml aliquots of the eluent, collected after it exits from the refractive index concentration detector. The eluent is collected in a reservoir before being transferred to the light scattering detector cell, where measurements of the scattered light from a 5 mW He-Ne laser at 633 nm are made at 11 angles, 7.5°, 15°, 30°, 45°, 60°, 75°, 90°, 105°, 120°, 135°, and 150°. The lowest angle is, however, not used for on-line measurements. After the measurements have been made, the aliquot is transferred to the capillary viscometer. Using this equipment it is reported to be possible to obtain weight average molecular weights, the Z-average radius of gyration, the second virial coefficient, the intrinsic viscosity, and the Huggins constant and—when coupled to an SEC system—the relationship between intrinsic viscosity, molecular weight, and radius of gyration as a function of elution volume can be determined.

15.4.3 Right angle laser light scattering detector (RALLS)

Recently, a triple detector for size exclusion chromatography has been commercialized by Viscotek Corporation.^[11] This detector combines refractive index, viscometry, and light scattering, where the light scattering component is a right angle laser light scattering detector. It is claimed that with this instrument the light scattering molecular weight (MW) information can be combined with the intrinsic viscosity (η) information from the viscometer to determine the polymer molecular size, otherwise termed the radius of gyration (R_g). When used in combination with SEC columns, the intrinsic viscosity and radius of gyration can be determined at every volume step across the chromatogram. This then enables the relationship between polymer molecular weight, intrinsic viscosity, and radius of gyration to be determined and differences in polymer branching or conformation can be identified for different samples. In the triple detector SEC system the right angle laser light scattering detector is used in preference to a low or multi-angle laser light detector. For the determination of the radius of gyration, when a viscosity detector is also used, only the molecular weight and size are needed—as can be determined by the light scattering detector—and this requires information at only a single scattering angle. The RALLS is preferred to the LALLS, as the signal-to-noise ratio is reported to be optimum for a 90° scattering angle. The optimum sensitivity at this angle is achieved due to there being no error from liquid–glass refraction correction to determine the actual scattering angle, minimal stray light, noise from particulates and air bubbles, and minimal cell surface refraction. The RALLS instrument was specifically designed as a component for the triple detector SEC system and uses opaque glass to mask the scattered light and minimize background noise and a hybrid photo-op detector for high sensitivity. A laser diode of wavelength 670 nm is used as the light source. For accurate determination of molecular weights using this system, it is necessary to consider the angular dissymmetry factor $P(90)$ of the scattering function, measured at the 90° angle. This is the ratio of the scattering intensity at 90° divided by the scattering intensity at the 0° scattering angle and is less than or equal to 1. A value of 1 indicates that no angular dissymmetry correction of the 90° scattering intensity is required, which indicates that the sample is a small molecular weight isotropic scatterer. With polybutadiene samples the molecular weight above which the correction must be applied has been shown to be 22 000 daltons and an 11% correction is needed for a molecular weight of 272 000 daltons. The software used with triple detector SEC system automatically performs the dissymmetry correction using the R_g values calculated from intrinsic viscosity and the molecular weight information derived from the viscometer and light scattering detectors. It is claimed that with this system molecular weights in the range from 1000 to several million daltons can be accurately determined. Apart from the price advantage of this triple detector SEC system compared with a MALLS instrument, its other main benefit is its ability to measure polymer R_g values down to 1 nm, this being significantly

lower than is reported to be possible using a MALLS detector. A detailed examination of the theory of operation of this instrument is beyond the scope of this chapter, but may be found in the paper by Yau *et al.*^[12] It is considered worthwhile to include a brief description for those less familiar with the triple detector SEC instrument, as it relates to the quantitative determination of polymer branching and chain conformation. Quantification is dependent upon the measurement of the Mark–Houwink exponent a in the intrinsic viscosity molecular weight relationship, as given by $\eta = KM^a$. The precision in determining this parameter is high, as the intrinsic viscosity and molecular weight are determined experimentally using the three detectors. The Mark–Houwink exponent a is a polymer conformation parameter and decreases with increasing molecular compactness: extended rod-like molecules have a value of greater than 1, random coil molecules have a value between 0.8 in a good solvent and 0.5 in a poor solvent, and for some globular proteins the value may be very close to zero. Where random coil molecules have long chain branching, the value of the a parameter decreases depending upon the amount of branching.

In summary, it is clear that there are now available three types of laser light scattering instruments which are used as on-line detectors in liquid chromatography: the low angle laser scattering instrument (LALLS), which is used for the determination of absolute molecular weights and sizes; the multi-angle laser light scattering detector (MALLS), which can be used not only for absolute molecular weight determinations but also to obtain conformational information; and the right angle laser light scattering detector (RALLS), which is incorporated in the triple detector SEC system and provides molecular weight, intrinsic viscosity, and branching information via the Mark–Houwink exponent a .

15.5 Applications

Light scattering in combination with chromatography can and has been used for the characterization of both synthetic and biological macromolecules. However, the approaches required for these two types of polymers and the information obtained/required may differ due to the special features associated with biopolymers. Biopolymers often have an associated biological activity which is attributed to a unique solution conformation. This conformation may exist only within a narrow band of temperature and/or solvent composition, outside of which the shape may change and biological activity would be lost, i.e. the biological macromolecule is denatured. Analytical conditions must therefore be carefully chosen according to the information required. It must also be remembered when dealing with biopolymers that the defined tertiary solution structure is stabilized by intramolecular interactions involving polar and non-polar main chain side groups. In dilute solutions, the interactions will be intramolecular, but as the solution concentration increases so the possibility of intermolecular interactions increases. Non-specific association may occur, leading to random clusters, or in many cases the interactions are very specific, producing organized supramolecular structures. The non-specific interactions

and the defined association of biologically active macromolecules are of significant importance.

The choice of the laser light scattering instrument used for a given application—low angle, single (right) angle, or multi-angle—will depend upon the information which is required from the experiment. All three forms of light scattering detector can be used to determine the number, weight, and Z-average molecular weights and distributions when used as an on-line detector in size exclusion chromatography. It has been shown that the size of a molecule may affect the angular variation of scattered light intensity, and therefore detectors which measure the intensity of scattered light at a single angle are only suitable for the determination of the size of a molecule when the molecule is compact and small, i.e. there is little or no angular variation in the intensity of the scattered light. The multi-angle laser light scattering detector measures the intensity of scattered light at a number of different angles and is therefore able to determine the molecular root mean square (r.m.s) radii from approximately 8 nm to approximately 1000 nm. The direct determination of branching ratios also requires the use of a multi-angle laser light scattering detector, since the molecular mean square radius must be known for the calculation.

Representative examples of the use of laser light scattering detectors in various application areas are given below.

15.6 Macromolecular interaction and aggregation

Dynamic light scattering is a technique which can be used to study macromolecular interactions in solution. All macromolecules can be studied, as monitoring does not rely on distinct chromophores. Therefore, in addition to protein–protein interactions it is possible using dynamic light scattering also to investigate the interactions of proteins with other types of solutes, including carbohydrates, lipids, and nucleic acids, and the formation of detergent micelles. Such interactions are not restricted to biopolymers: synthetic polymers can also exhibit interactions in the form of aggregation/gel formation.

Perhaps the most important application area for the characterization of aggregation is in biotechnology. Protein-based products for pharmaceutical applications are by necessity strictly controlled in terms of composition and purity. Analytical techniques which are capable of detecting ‘nothing’ in ‘something’ are needed for the quality control and monitoring of such therapeutics. This is particularly so with aggregation, as although an aggregate may be only a very small percentage of the total sample, its large size may—and often does—cause an immunogenic response. Often, in a gel filtration separation of a protein or mixture of proteins when the normal concentration detector is used, UV or RI, a small perturbation is seen in the baseline prior to the elution of the solutes. This is often interpreted merely as baseline noise or drift, a common problem with RI detectors in particular. However, if in addition to the concentration detector a laser light scattering detector is also used to monitor column eluent, then it is immediately apparent that the baseline

perturbation is indeed a peak due to the presence of aggregates. Figure 15.12 shows the chromatograms, RI and light scattering at the 90° angle, of a mixture of protein standards, and Fig. 15.13 the UV and light scattering at the 90° angle for the therapeutic Interleukin-2, which has aggregated during storage to a level of approximately 2%.

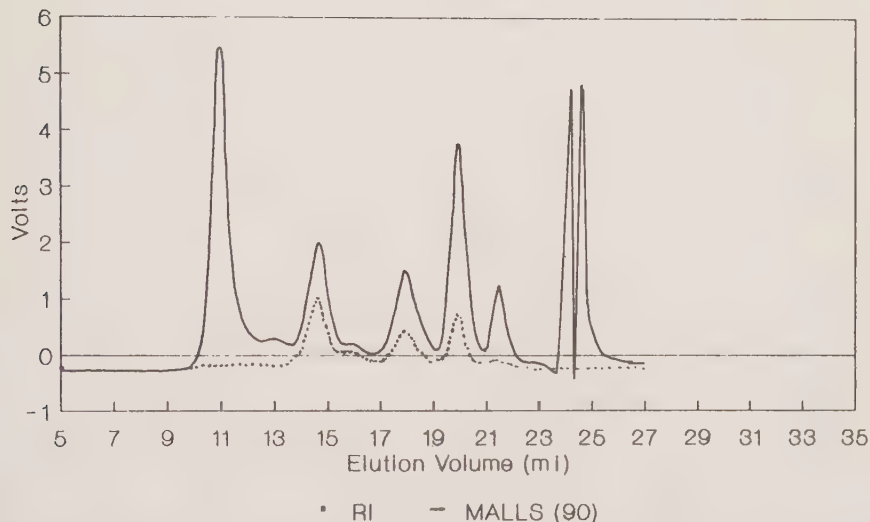


FIG. 15.12. The separation of a protein standard mixture, monitored by RI and MALLS (90°).

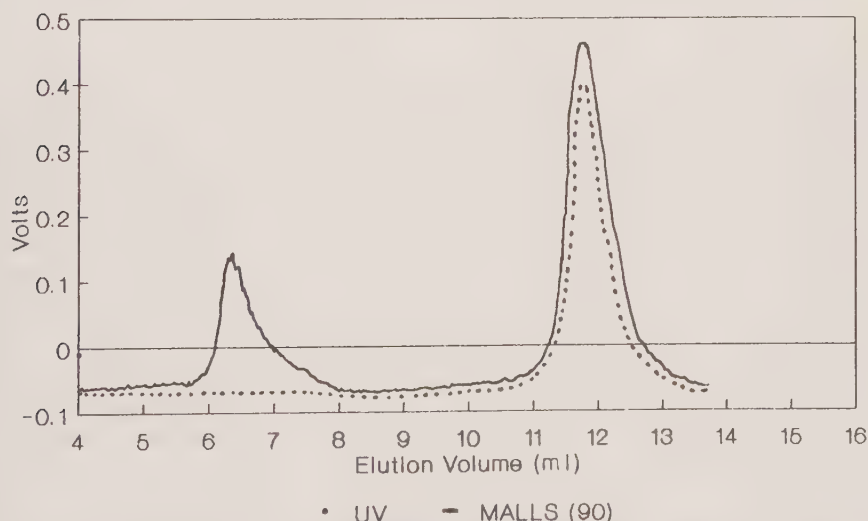


FIG. 15.13. The separation of Interleukin-2, monitored by UV and MALLS (90°).

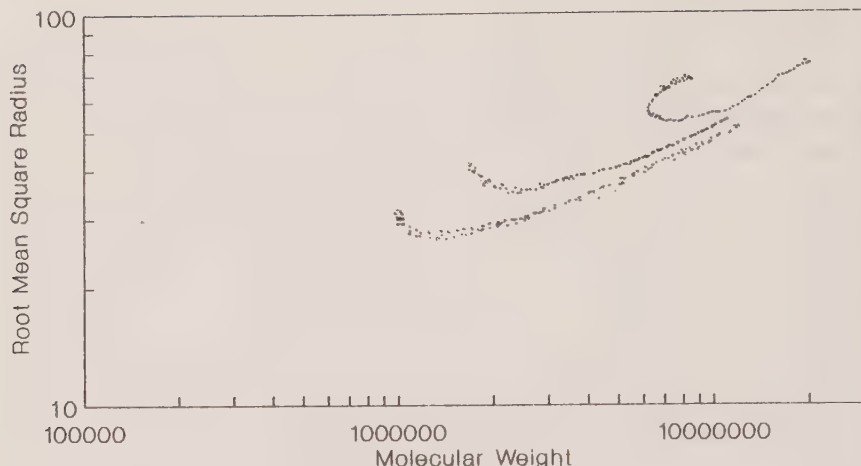


FIG. 15.14. A log-log plot of R_g versus M_w for three samples of polystyrene which contain microgel.

This type of phenomenon is not limited to natural polymers such as proteins: it is also evident in synthetic materials, although with the synthetic polymers the process is normally the formation of microgels. The log-log plot of R_g versus M_w should be a straight line for macromolecules with a random coil conformation. Figure 15.14 shows a plot obtained for three high molecular weight polystyrene polymers, where there is a departure from the expected straight line. Matsumoto^[13] has postulated a theory which explains the type of curves seen in Fig. 15.14 as being due to microgel formation.

15.7 Branching

Branching is a polymer characteristic which has long been recognized as having a significant effect on the physical properties of the material. The degree and distribution of branching will effect both the solubility and strength characteristics of a polymer. The molecular weight analysis of branched polymers is very difficult and often inaccurate when SEC is used with a concentration detector. A branched polymer of a given molecular weight has a smaller hydrodynamic volume than a linear, unbranched, molecule of the same molecular weight. Therefore, for a valid calibration, calibrants of not only the same composition but also having the same degree of branching and conformation must be used to obtain the elution volume plot. However, when a multi-angle light scattering detector is used with a size exclusion chromatograph, absolute molecular weights can be obtained and from this the branching parameter, g_M , and the branching frequency can also be calculated. The branching ratio is the ratio of the mean square radius of the branched polymer to that of the linear polymer of the same molecular weight: $g_M = \langle r^2 \rangle_b / \langle r^2 \rangle$.

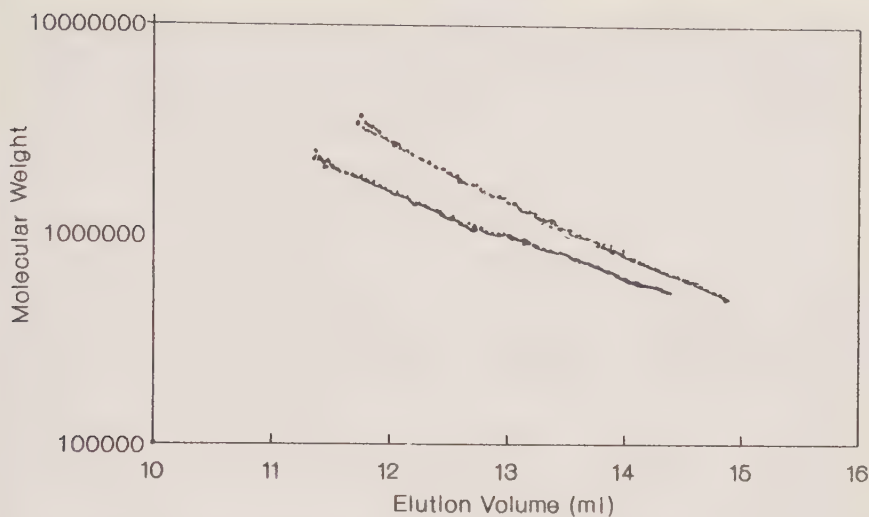


FIG. 15.15. Plots of elution volume versus molecular weight for a branched and a linear sample of polymethylmethacrylate. The branched material elutes after the linear polymer.

Figure 15.15 shows a plot of elution volume versus molecular weight for two samples of polymethylmethacrylate obtained using size exclusion chromatography/light scattering. The displacement in elution volume for the same molecular weight is due to the branching present in the one sample and hence it has a smaller hydrodynamic volume. By plotting $\log M$ versus $\log R_g$ it is confirmed that the branched polymer has a smaller R_g for the same molecular mass and hence a tighter binding within the molecule (see Fig. 15.16).

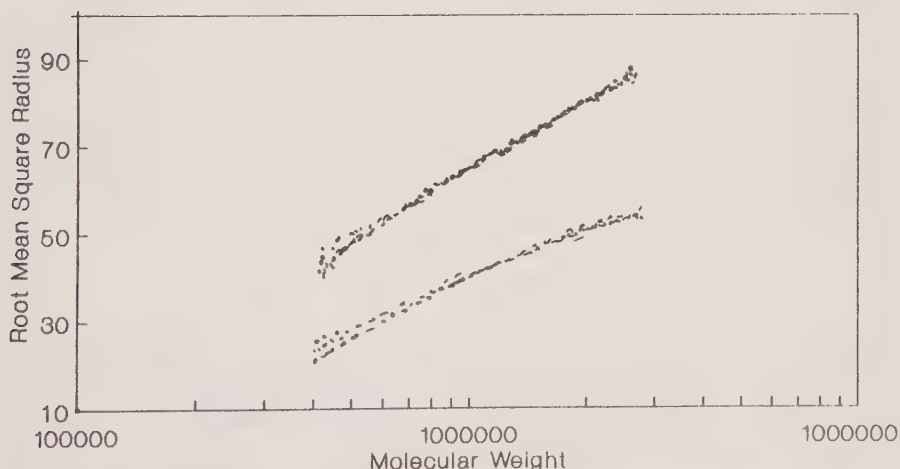


FIG. 15.16. Conformation plots of branched and linear polymethylmethacrylate.

The slope of the log–log plot can also be used to give an indication of conformation branching. When considering compact homogeneous spherical molecules the slope would be expected to be of the order of 0.33, but if the slope is less than this for broad polymers produced by an anionic polymerization process then branching is implied. It is, however, important not to oversimplify the characterization of polymer branching. In some applications the situation can become quite complex; for example, long chain branching in polyethylene.^[14] In the side chain analysis reported ethyl and hexyl side chains were not quantified as long chains, but chains of 16 carbons in length were. A particularly interesting characteristic which was determined from this work was the dependence of branching frequency on molecular weight. At low molecular weight the low chain branching frequency was highest in low density polyethylene.

15.8 Copolymer analysis

The problems encountered in the molecular weight characterization of copolymers are very similar to those for branched polymers. Without the use of an absolute molecular weight detector for size exclusion chromatography, the analyst is dependent upon the calibration curve to obtain molecular weight data. Again, for this to be meaningful the calibrants must be of the same chemical type and composition as the material under investigation. This can be even more difficult when the type and distribution, block or random, of monomers in a copolymer must be considered. The copolymer styrene–butyl acrylate has been characterized using low angle laser scattering in combination with size exclusion chromatography and valid results have been obtained.^[15] There is the added complication with copolymers that there is a possibility of the composition and monomer ratios changing as a function of molecular weight: if this is indeed the case then concentration detectors such as RI and UV may give an incorrect value for the concentration, as the response may be dependent upon composition. To overcome this it would be necessary also to determine the composition of the copolymer as a function of molecular weight, to adjust the concentration detector response for the changes in response due to changes in composition. This would then enable an accurate measurement of solute concentration as a function of elution volume to be achieved for absolute molecular weight calculations.

15.9 Synthetic polymers

Polymer chemists have long used the technique that is referred to as gel permeation chromatography (size exclusion chromatography) to obtain characterization information which can then be related to the physical properties of the material. As these materials become more and more complex so the information needed becomes more difficult to obtain and the techniques used more sophisticated. From the earlier sections dealing with macromolecular

interactions, branching, and copolymer analysis, it is evident that significant information can be achieved by combining liquid chromatography and laser light scattering. There are, however, a number of synthetic polymer analyses which are worthy of individual inclusion in this chapter.

15.9.1 Polystyrene analysis

Polystyrenes are possibly the best recognized and most utilized of all the synthetic polymers. They are used as bulk polymer for plastic compound manufacture and are produced as highly characterized materials for use as calibrants. In fact, the most used types of calibrant for size exclusion chromatography are the polystyrene reference materials, which have a narrow polydispersity. Because of this they are often used as examples of successful size exclusion chromatography and as a means of evaluating any new column or instrument/data handling. An example has been given in an earlier section on the detection of microgel in polystyrene solutions using size exclusion chromatography with on-line laser light scattering.

15.9.2 High temperature size exclusion chromatography

The requirement for ultrahigh performance polymers has led to the development of a whole series of materials engineered to have exceptional strength. As a consequence of this, there is a class of polymers that can only be dissolved in aggressive solvents at elevated temperature and, indeed, will precipitate if the solution is allowed to cool outside a narrow temperature band. Polyethylene and polypropylene are two such types of polymer with which we are all familiar. The determination of the molecular weight of these polymers is very difficult by conventional size exclusion chromatography with a concentration detector: often infrared detectors are the only option, and then the solvent must be chosen so that it is not only a good solvent for the polymer to be characterized but also transparent. These polymers are often optimized and engineered to possess unique conformations, so making it impossible to source suitable calibrants of the same conformation/chemical type, particularly in the case of the thermoplastic polypropylene. For the analysis of this type of polymer researchers have often been forced to prepare and characterize their own SEC calibrants for use with concentration detectors. Many of the light scattering detectors which can be used on-line with a size exclusion chromatograph have high temperature cell options, which means that they can be utilized for the determination of the absolute molecular weight of polymers at high temperature. Figure 15.17 shows the response from refractive index and light scattering detectors at the 90° angle as a function of elution volume for a sample of highly branched polyethylene. It is evident that the RI hardly detects the presence of the high molecular weight, highly branched material which is clearly detected by the light scattering instrument.

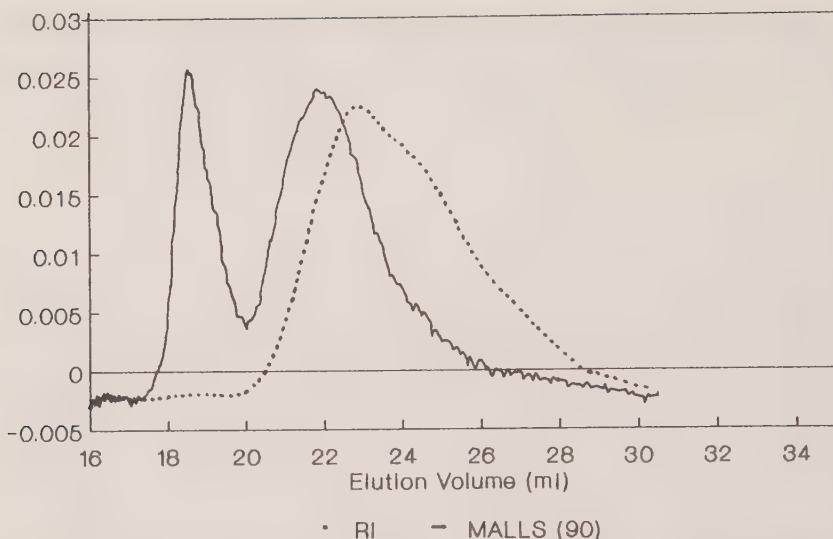


FIG. 15.17. The separation of polyethylene, monitored by RI and MALLS (90°).

15.9.3 Polycyanurate characterization

Polycyanurates are trifunctional randomly branched polymers prepared by the polycyclotrimerization of difunctional aromatic cyanates. Early work^[16] has shown that they can be used as models for understanding trifunctional randomly branched polymers. In a more recent paper,^[17] the same group has investigated the scaling behaviour of this polymer as a function of the molecular weight distribution, the intrinsic viscosity, and the second virial coefficient. The work was accomplished using size exclusion chromatography with on-line low angle laser light scattering and viscometry detectors and off-line measurements using static light scattering and viscometry. Analysis using these three techniques enabled the researchers to determine the broad molecular weight distribution of the whole polymer and fractionate and subsequently to characterize the fractions to determine the structure of the individual clusters. Although the authors rightly point out that more experimental data are required to interpret their results fully, it is obvious that such powerful techniques are moving our understanding of complex polymer systems forward by leaps and bounds.

15.10 Biological macromolecules

Much of the earlier discussion on the suitability of liquid chromatography and on-line laser light scattering for the determination of macromolecular interactions and aggregation, branching, and copolymer analysis is equally applicable to both synthetic polymers and biological macromolecules, proteins,

nucleic acids and polysaccharides. However, it is worthwhile in this chapter considering the analysis of the three main types of biological macromolecules, proteins, nucleic acids, and polysaccharides, and to provide some key examples of where the technique of light scattering in combination with liquid chromatography can provide a significant amount of information which otherwise would be difficult or very time-consuming to obtain.

15.10.1 *Proteins and nucleic acids*

The separation and analysis of biopolymers has in recent years become an area of major importance. One has only to look in the literature for publications relating to the development of new methods, instrumentation and columns to realize that this is a major growth area. Although there have been considerable advances in the development of HPLC packing materials, often developed and optimized specifically for the macromolecular separations, detection methods have not progressed so rapidly. The normal concentration detectors, RI and UV, provide very little information on the characteristics or even the type of biomolecule which is present. Refractive index is the least specific of all; indeed, it is often referred to as a universal detector, responding only to differences in refractive index between a reference aliquot of eluent and the eluent stream as it exits the column. It is also very insensitive and can normally only be used with an isocratic liquid chromatography instrument. The alternative UV detector is somewhat more selective, monitoring specific chromophores according to the wavelength selection, but it is still not possible to distinguish the type of biomolecule being resolved. For example, liquid chromatographic analysis of proteins is routinely carried out with a UV detector at 280 nm, but it is not possible at this wavelength to distinguish between proteins and nucleotides, which are present in many samples as contaminants. However, if a light scattering detector is used on line with a liquid chromatograph, then the protein components can be distinguished from the nucleotides which, being small molecules, have no light scattering response. This is illustrated in Fig. 15.18, a gradient HPLC separation of two proteins, bovine serum albumin and pyruvate kinase, and a nucleotide, guanosine monophosphate.

Although many protein and nucleic acid separations are carried out using size exclusion chromatography (see Fig. 15.12), this is not a high resolution technique for what are essentially monodispersed macromolecules. A given protein has a defined amino acid sequence which by definition implies a specific molecular weight, unlike synthetic polymers which have a distribution of polymer chain lengths of the same composition. High resolution techniques such as reversed phase and ion exchange HPLC are therefore often employed for the analysis of proteins and nucleic acids. Unlike size exclusion chromatography, these are interactive separation mechanisms and are single column techniques, often requiring eluent gradients for sample elution. It may be anticipated that the change in eluent composition as a function of time may prohibit the use of an on-line laser light scattering detector for such analyses.

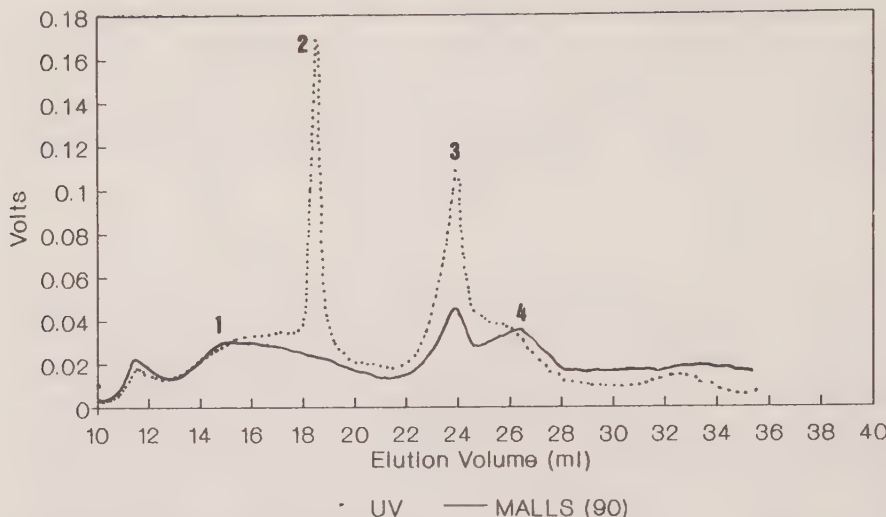


FIG. 15.18. The separation of proteins (1, pyruvate kinase; 2, bovine serum albumin; 4, bovine serum albumin aggregated) and a nucleotide (3, guanosine monophosphate) monitored by UV and MALLS (90°).

It has, however, been demonstrated that a low angle laser light scattering detector can be used on line for the determination of protein molecular weights with a gradient in hydrophobic character and reversed phase.^[18,19] This is indeed an extremely important application as protein molecular size/conformation and hence elution position in a chromatographic system may vary according to concentration, eluent, and column packing characteristics, and therefore component identification can be greatly assisted by absolute molecular weight information.

One particular example of the usefulness of an on-line light scattering detector is in the analysis of gelatin (see Fig. 15.19). This is a particularly difficult protein to characterize. The influence of branching must be considered, and when analysed by size exclusion chromatography it is very difficult to eliminate solute column packing interactions, i.e. non-size exclusion effects dominate. The chromatograms in Fig. 15.19 clearly demonstrate this phenomena. Although the UV trace appears to be a typical molecular size versus elution volume plot, it is evident from the light scattering data that non-size exclusion effects also occur, and that the molecular weight increases with increasing elution volume.

15.10.2 Polysaccharides

Polysaccharides are considerably more difficult to characterize than the other types of biological macromolecules, proteins, and nucleic acids. This is because the repeat units, monosaccharides, in the polysaccharide molecules have several possible attachment sites for the linkage to the next unit. This gives rise to

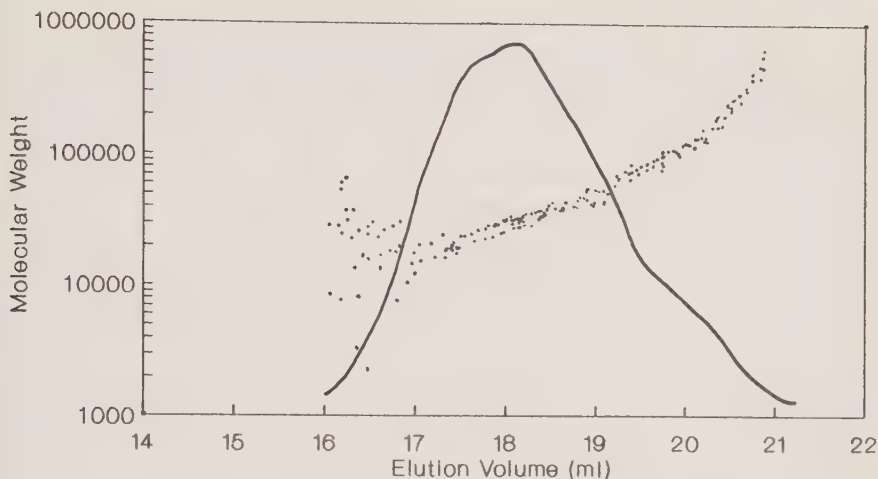


FIG. 15.19. The separation of gelatin using size exclusion chromatography columns, monitored using UV and MALLS (90°) detectors. Interaction between the column packing and the gelatin is clearly shown from the MALLS data.

branching and therefore the possibility of numerous structures. Light scattering is one way of obtaining information on the relationship between polysaccharide structure and functionality. For the characterization of polysaccharides, information is needed on molecular weight, branching, size and shape—and this is obtainable using laser light scattering detectors.

15.10.2.1 Starch. Starch is a very common polysaccharide which has many uses in the food industry, including as a starting material for the production of high fructose corn syrups and as a gelling agent. It is composed of two types of glucose polysaccharides: amylose, which is a linear polymer of α -D-glucopyranose units linked by a 1–4 glycosidic linkage; and amylopectin, which is a highly branched molecule having a backbone of 1–4 linked α -D-glucopyranose units and 1–6 branch points. The proportions, structures, and properties of these two components determine the ease with which it can be hydrolysed and are therefore industrially important. Much work has been carried out to develop methodologies, including size exclusion chromatography with on-line laser light scattering detectors. Hizukuri and Takagi have pioneered much of the early work in the use of SEC/LALLS for the determination of the molecular size distributions of amylose and compared the degree of polymerization as a function of source.^[20,21] There is still a great deal of work to be done in the analysis of starch, including the development of suitable solvent systems for liquid chromatography. Yu and Rollings used 0.5 M NaOH, but then there is the possibility of alkaline degradation.^[22] The insolubility of starch and its ability to form gels in solutions is a notorious problem for those working with this industrially important polysaccharide, which still has to be satisfactorily resolved.

15.10.2.2 *Pectin.* Pectins are structural polysaccharides, present in the cell walls of all higher plants and of commercial value as gelling agents. Pectin is mainly composed of 1–4 linked α -D-galacturonic acid residues in either free acid (salt) or methyl ester form. In addition to the acidic polysaccharide backbone there are neutral sugar side chains, distributed in varying densities along the backbone. The gelling mechanism is dependent upon the molecular weight, the degree of esterification, and the distribution of methoxyl groups, and therefore analytical methods are required which can assist in the determination of these characteristics both in a research environment and in industrial quality control laboratories. Many research groups have used chemical methods and enzyme specificity to elucidate the composition of the pectin,^[23] but this does not assist with the determination of molecular weight. Liquid chromatography, including ion exchange and size exclusion, is used for the determination of the methoxyl group distribution and molecular weight of the polysaccharide. With a polymer which is so variable in composition, the determination of absolute molecular weight has proved to be quite a challenge. There is a tendency for non-ideal behaviour through the formation of aggregates and solute column packing interactions, and even if these problems are overcome then there is the question of the selection of the appropriate molecular weight calibrants given the variation in the composition of the pectin. The degree of esterification and the distribution of the methoxyl groups along the polysaccharide backbone would be expected to have a significant effect on the molecular size in solution and hence the apparent molecular weight as determined using a calibrated SEC instrument. There is little alternative for the determination of the absolute molecular weight distribution of pectin samples than to use an on-line laser light scattering detector. Brigand *et al.*^[24] have shown that SEC/LALLS can be used to obtain realistic values of the molecular weight and molecular weight distribution of pectin and that the presence of aggregates can be easily identified. Molecular weight fractionations were performed and compositional analysis of the fractions carried out to determine the effect of molecular weight on composition. Differences between pectins from different sources were easily identified.

15.10.2.3 *Chitosan.* Another polysaccharide of commercial importance, and which also illustrates the diversity in the chemical nature encountered in the polysaccharide family of biological macromolecules, is chitosan ((1–4)-2-amino-2-deoxy- β -D-glucan). This amino polysaccharide is a cationic polymer prepared by deacetylation of chitin which is particularly abundant in Crustacea, and due to its method of preparation samples have variable degrees of acetylation and distribution of acetyl groups. As with the analysis of pectin, this heterogeneity causes many problems in obtaining reliable molecular weight data. Nine chitosan samples differing in their degree of acetylation and molecular weight were characterized using SEC/MALLS.^[25] The results obtained for both the molecular weight and the radius of gyration were reproducible and, according to the authors, accurate and reliable.

15.10.2.4 Carrageenan. This important polysaccharide, extracted from seaweed and used in the food industry as a gelling agent, is composed of alternating $\alpha(1-3)$ and $\beta(1-4)$ linked D-galactosyl residues. Much work has been carried out to investigate the molecular weight of this polysaccharide, as it was at one time thought that the presence of a low molecular weight component could have a toxic effect when used as a gelling agent in foodstuffs. Rochas and Landry^[26] used SEC/LALLS to investigate the structure of carrageenans and found that κ -carrageenan existed as a helical structure. Some of the problems associated with carrying out aqueous size exclusion chromatography are illustrated in Fig. 15.20, which shows the apparent size separation of carrageenan. The analysis was performed at two different flow rates, 1.0 ml/min and 0.5 ml/min, with only a small difference in the elution profiles as monitored by RI. However, when the differential molecular weight distributions as determined by on-line laser light scattering are compared, a dramatic difference is observed. The carrageenan molecules are rod-like rather than spherical, and at 1 ml/min stream through the SEC column as an aligned block without any size differentiation: the width of the observed RI peak is due to column band spreading effects. At 0.5 ml/min the forces responsible for the molecular streaming within the column are reduced and a molecular size separation occurs. Without the on-line light scattering detector this flow rate phenomenon would not have been identified.

15.11 Conclusions

The rapid development in equipment and computers has enabled what was originally a technique available to only a few research laboratories to become widely accessible. By coupling laser light scattering detectors to liquid chromatography instruments, absolute molecular weight and molecular weight distributions can be obtained, and if a multi-angle system is used radii of gyration and branching ratios can also be calculated. By necessity, this chapter has but scratched the surface of what can be—and has been—achieved by the utilization of this valuable tool for the characterization and measurement of absolute molecular weights of polymers.

It is hoped that through the choice of applications the versatility of the technique has been demonstrated and its applicability to the analysis of both synthetic and biological macromolecules demonstrated. Although the majority of the publications using liquid chromatography and laser light scattering have used size exclusion chromatography, one of the most exciting future developments will be the coupling of these detectors to other forms of liquid chromatography and indeed separation systems, for although the information generated relates to molecular weight, conformation, size, and branching, a separation technique in which elution is dependent upon size is not required.

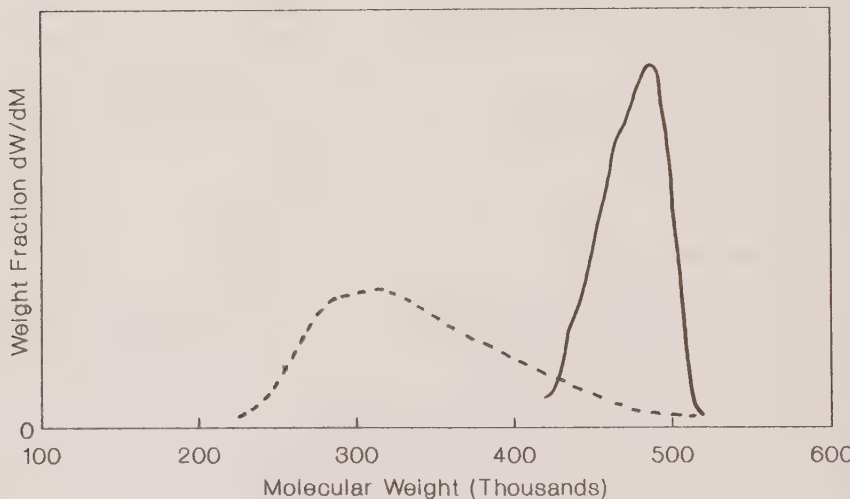
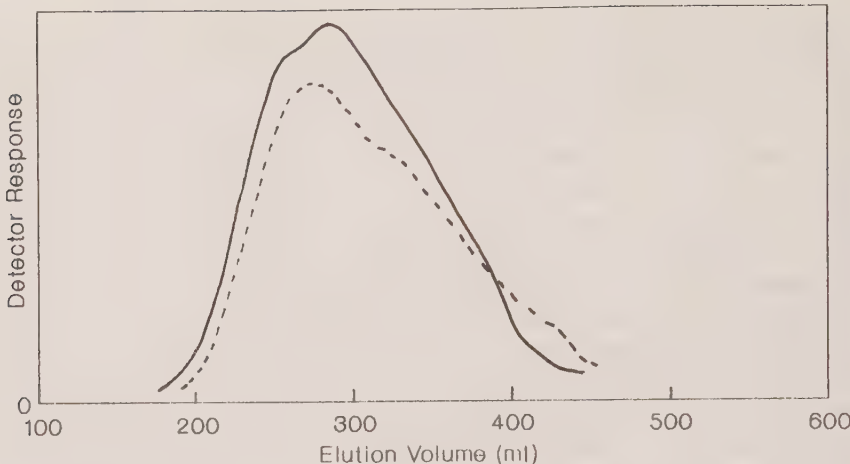


FIG. 15.20. Size exclusion chromatography of carrageenan, run at 1.0 ml/min (—) and 0.5 ml/min (----).

Acknowledgements

The authors wish to express their thanks to the manufacturers of light scattering detectors who have provided the technical information used in the preparation of this chapter. Particular thanks are extended to Mr Robin Sanders for useful discussions during the preparation of this chapter and to the Wyatt Technology Corporation for supplying the data used to prepare Figs 15.5 and 15.12–15.20.

References

1. Porath, J. and Flodin, P. (1959). *Nature*, **183**, 1657.
2. Moore, J. C. (1964). *J. Polym. Sci.*, **A2**, 835.
3. Yau, W. W., Kirkland, J. J., and Bly, D. D. (1979). In *Modern size exclusion chromatography*. John Wiley, New York.
4. Sober, H. A. and Peterson, E. A. (1954). *J. Am. Chem. Soc.*, **76**, 1711.
5. Kaye, W., Havlik, A., and McDaniel, J. B. (1971). *Polym. Lett.*, **9**, 695.
6. Quano, A. C. (1976). *J. Chromatogr.*, **118**, 303.
7. Jumel, K., Browne, P., and Kennedy, J. F. (1992). In *Laser light scattering in biochemistry* (ed. S. E. Harding, D. B. Sattelle, and V. A. Bloomfield). The Royal Society of Chemistry, Cambridge.
8. Wyatt, P. J. (1993). *Analyt. Chim. Acta*, **272**, 1.
9. Busnel, J.-P., Degoulet, C., Nicolai, T., Woodley, W., and Patin, P. (1996). *Measurement Sci. Technol.*, in press.
10. Degoulet, C., Nicolai, T., Durand, D., and Busnel, J.-P. (1996). *Macromolecules*, in press.
11. Haney, M. A., Mooney, C. E., and Yau, W. W. (1993). *Int. Labmate*, **IV**, 31.
12. Yau, W. W. and Rementer, S. W. (1990). *J. Chromatogr.*, **13**, 627.
13. Matsumoto, A. (1990). ACS National Meeting, Washington, DC.
14. Rudin, A., Grinshpun, B., and O'Driscoll, K. F. (1984). *J. Liq. Chromatogr.*, **7**, 1809.
15. Malih, F. B., Kuo, C. Y., and Provder, T. (1984). *J. Appl. Polym. Sci.*, **29**, 925.
16. Bauer, J., Lang, P., Burchard, W., and Bauer, M. (1991). *Macromolecules*, **24**, 2634.
17. Bauer, J. and Burchard, W. (1993). *Macromolecules*, **26**, 3103.
18. Krull, I. S., Stuting, H. H., and Krzysko, S. C. (1988). *J. Chromatogr.*, **442**, 29.
19. Mhatre, R., Krull, I. S., and Stuting, H. H. (1990). *J. Chromatogr.*, **502**, 21.
20. Takagi, T. and Hizukuri, S. (1984). *J. Biochem.*, **95**, 1459.
21. Hizukuri, S. and Takagi, T. (1984). *Carbohydr. Res.*, **134**, 1.
22. Yu, L. P. and Rollings, J. E. (1987). *J. Appl. Polym. Sci.*, **33**, 1909.
23. Rombouts, F. M. and Thibault, J. F. (1986). *Carbohydr. Res.*, **154**, 189.
24. Brigand, G., Denis, A., Grall, M., and Lecacheux, D. (1990). *Carbohydr. Polym.*, **12**, 61.
25. Beri, R. G., Walker, J., Reese, E. T., and Rollings, J. E. (1993). *Carbohydr. Res.*, **238**, 11.
26. Rochas, C. and Landry, S. (1987). *Carbohydr. Polym.*, **7**, 435.

Index

- α -relaxation 196
aggregation 201, 460
 kinetics 416
 number 214
anisotropic particles 147, 310, 445
anisotropy fluctuations 180
anomalous micellization 337
Arrhenius fit 198
association 460
 number 327
- β -lactoglobulin 220
 β -relaxation 196
backbone degradation 22
bead-spring model 447
Bhatia-Thornton structure factors 47
bicontinuous cubic phase 345
binary interactions 170
binary mixtures 57
biological macromolecules 516
birefringent medium 350
Bjerrum length 103, 124
block copolymer
 melts 346
 solutions 354
 systems 327
block and graft copolymers 328
Born approximation 50, 423
branched aggregate 220
branched polymers 8, 453
branching 224, 512
bulk elastic modulus 178
- Carnahan-Starling equation 66, 298, 468
carageenan 521
centre-of-mass diffusion 445
charge-charge structure factor 47
charge fluctuations 104
charged spherical micelles 304
chitosan 520
chromatography 494
closed association 329, 467
- clusters 213, 416
distribution 222
formation 194
mass distribution 417
mode 357
networks 381
coil-coil interactions 239
coil
 draining 246
 interpenetration 456
 shrinkage 251
collective diffusion 298
colloidal aggregation 432
colloidal suspensions 30
complex micellar systems 293
composition fluctuations 255
compositional segregation 359
compressibility structure factor 47
compressible mixtures 16
concentrated polymer solutions 166
concentration fluctuations 4, 126, 171, 287
connectivity 217
constrained regularization 480
CONTIN 264
contour length 312
contrast 397
 factors 25
cooperative diffusion coefficient 177, 366
cooperative mode 270, 352
copolymerization 224
correlation function 182, 202
correlation hole 147
Coulomb energy 104
counterion condensation 124
critical exponents 23
critical fluctuations 19
critical micellar concentration (CMC) 296, 327
critical microemulsion 426
critical point of gelation 471
critical quench 422
critical temperature 25
crosslinked network 176
cubic phase 345
cut-off function 169, 208, 212, 443
cylindrical micelles 309
cylindrical reverse micelles 314

- Debye function 6, 168, 205
Debye–Hückel approximation 107
Debye–Hückel screening length 81, 123
Debye screening length 105
degree of interpenetration 312
density fluctuations 46, 127, 183
depolarized correlation function 182
depolarized dynamic light scattering 363
depolarized light scattering 190
depolarized Rayleigh spectrum 192
dialysis 132
diblock copolymers 255, 343
 melts 356
dielectric spectroscopy 191
diffusion virial coefficient 237
diffusion-limited cluster aggregation (DLCA) 212, 416
disordered block copolymer liquids 351
disordered region 349
dissociation of micelles 334
DLVO theory 122, 305
DNA 110, 149
domains 149
Donnan equilibrium 129
double layer 108
draining 451
dynamic clusters 176
dynamic light scattering 173
dynamic scattering function 237
dynamic structure factor 258
dynamic Zimm plot 448
- effective solution structure factor 399
elastic longitudinal modulus 176
electrostatic excluded volume theories (EEV) 10
electrostatic interactions 122
electrostatic persistence length (EPL) 10
end effects 110
entanglement network 317
entanglement regime 362
entanglements 176, 353
entanglement threshold 312
equivalent hard sphere 238
excess scattered intensity 4, 127, 148
excluded volume 140, 166, 218, 246, 313
 parameters 262
expansion factor 170
exponential sampling 480
external cut-off function 203
- Fabry–Perot interferometer 191
filamentous micelles 470
first cumulant 448
flocculation 213, 412
- Flory–Huggins free energy 15
Flory–Huggins interaction parameter 14, 258, 344
Flory–Huggins mean field theory 170, 257
fluctuation theory 383
fluorescence recovery after photobleaching (FRAP) 269
- forced Rayleigh scattering 370
form factor 6, 58, 279, 398
- fractal aggregates 202
fractal dimension 219, 464
fractal domain 221
fractal objects 411
Fredholm integral 480
free volume 179
friction coefficient 237
fringed micelles 465
- Gauss-GEX analysis 190
gel point 212, 450
gelation 211
 time 213
gelling systems 201
general exponential distribution (GEX) 211
giant flexible micelles 310
globular proteins 220
grain size 351
grain structure 349
grand canonical ensemble 35
Green function 49
growth process 211
- hard sphere
 behaviour 334
 interaction 246
 systems 64, 89
Hartree approximation 104
heat-induced denaturation 220
heterogeneity
 factor 353
 mode 276, 352
hexagonal phase 345
high temperature size exclusion chromatography 515
homopolymer mixtures 255
hydrodynamic correlation length 315
hydrodynamic interactions 175, 237, 273
hydrodynamic radius 333
hypernetted chain (HNC) 31, 60, 308, 406
hysteresis effects 460

incoherent scattering 57
 interaction
 length 238
 parameter 268
 potential 305
 interactive chromatography 497
 interdiffusion 255
 internal cut-off 203
 internal mode 248, 274, 352
 internal relaxation 360
 interparticle interactions 128
 interparticle potential 305
 interparticle scattering factor 479
 interpenetration function 246
 intra-coil modes 248
 intraparticle interference 127
 intraparticle scattering factor 479
 inversion methods 480
 ion exchange 133
 ionomer 161
 Ising critical temperature 24
 isoionic dilution 142
 isothermal compressibility 38, 127, 422
 isotropic liquid phase 294

jumping unit 179

kinetics of copolymer micellization 336
 Kohlrausch–Williams–Watts (KWW)
 model 197, 375
 Kuhn length 168

lamellar liquid crystalline phase 294, 345
 linear diblock copolymer 274
 linear response theory 103, 255
 liquid chromatography 494
 liquid microemulsion phase 294
 local viscosity 452
 long-range density fluctuations 194, 371
 long-range interactions 128
 long-range order 382
 longest viscoelastic relaxation time 352
 Lorentzian fit 191
 loss modulus 347
 low angle laser light scattering (LALLS) 499
 low angle light scattering 381

macromolecular aggregation 510
 macroscopic solvent viscosity 452
 Manning parameter 8
 maximum entropy 480
 Maxwell's equations 48, 384

mean-field theory 104, 344
 mean spherical approximation (MSA) 60, 405
 measured structure factor 55
 mesoscopic scale 381
 micellar dispersion 293
 micellar growth 308
 micellar molar mass 327
 micellar systems 293, 327, 467
 micelle
 dissociation 336
 formation 335
 microemulsion 293
 microgels 449
 microphase separation 288
 microphase separation transition (MST) 280,
 345
 microstructure 30
 Mie scattering 52, 384, 482
 molar mass distributions 442
 molecular polarizability 394
 Monte Carlo simulation 108, 228
 multi-angle laser light scattering (MALLS) 499
 multicomponent systems 31, 128
 multicomponent polymeric systems 257, 293
 multistranded polymer 20

network 312
 non-interacting particles 408
 non-negative least squares 480
 nucleation 420
 number–number structure factor 46

one-contact Zimm model 410
 Oosawa–Manning theory 124
 open association 329, 470
 optical bidispersity 57
 optical contrast variation 302
 optical excess polarizability 301
 optical Fourier transformation 389
 optical match point 299
 optical polydispersity 56
 optical theta condition (OTC) 14, 265, 273
 order-to-disorder transition (ODT) 345
 ordered phase 343, 349
 Ornstein–Zernike equation 1, 31, 308, 404
 Oseen tensor 260
 osmotic coefficient 159
 osmotic compressibility 159, 181, 297, 319
 osmotic pressure 159
 overlap concentration 284

pair correlation function 168, 204
 pair distribution function 305
 parsimony 483

- partial static structure factors 55, 258
particle form factor 149
particle size analysis 388, 477
pectin 520
percolating cluster 219
percolation theory 211, 443
Percus–Yevick approximation (PY) 60
Percus–Yevick (PY) closure 31
Percus–Yevick theory 298
persistence length 125, 309
phase separation 255, 419
Poisson–Boltzmann equation 12, 104
polydisperse aggregates 207
polydisperse hard spheres 72
polydispersity 32, 210, 299, 442
mode 276, 352
polyelectrolyte solutions 8
polyelectrolytes 103, 120
poly(ethylene oxide) 243
polymer
blends 23
interpenetration 241
segmental motion 186
polymer-like micelles 315
polymer–polymer interaction 232
poly(methylmethacrylate) 224
polysaccharides 518
poly(urethane) 225
probe polymer 265
prolate ellipsoid 447
pseudobinary critical system 422
- quenched system 218
- radial distribution function 58, 152
radius of gyration 10
random degradation 20
random phase approximation (RPA) 1, 255, 352
randomly branched clusters 450
Rayleigh–Debye–Gans scattering 50, 383, 481
Rayleigh ratio 297
reaction-limited cluster aggregation (RLCA) 212, 416
reduced osmotic modulus 457
refractive index increments 132
relaxation time spectrum 443
relaxational modes 261
renormalization group theory 169, 319, 451
reorientational dynamics 187
reptation 257, 353
reverse micelles 301
reversed phase separation 498
rheology 347
ring diblock copolymer 277
rod-like particles 57, 103
rod-like micelles 310
- Rogers–Young (RY) closure 62
rotation 445
Rouse–Zimm model 257
- scaling of linear chains 456
scaling theories 166, 219
scattering
cross-section 303
function 234
length 265
vector 183
Schulz distribution 67
screened Coulomb potentials 61
screening 142
length 123, 166
second virial coefficient 128, 233, 263, 319, 328
second-order phase transition 346
sedimentation velocity 331
segmental motions 363
segmental reorientational relaxation 180
segregation limit 278
self-consistent potential 108
self-diffusion 178, 265, 296, 361
self-similar systems 221, 411
semi-dilute polyelectrolyte solution 142
semi-dilute solutions 125, 166, 311, 456
separation of proteins 518
shape function 454
shear 18
shear elastic modulus 178
side-chain degradation 22
Siegert relation 264
single contact approximation (SCA) 1
single-particle form factor 127
single-particle properties 57
size distribution function 393
size exclusion chromatography (SEC) 221, 495
Sogami potential 123
sol-gel transition 201, 432
solvent
mobility 178, 186
self-diffusion 186
spatial resolution 308
sphere-to-rod transition 293
spherical micelles 296
spinodal decomposition 255, 419
spontaneous curvature 308
standard scatterers 484
star-branched macromolecules 459
static birefringence 348
static correlation length 311
static light scattering 1, 126, 216, 232
static structure factor 146, 202, 258, 298
sticky hard sphere potential 299
Stokes–Einstein equation 175, 357
storage modulus 47
structure factor 103, 404
structural relaxation 176

- sub-theta systems 243
supramolecular aggregates 397
surfactants 293
- temperature-shifting 176
temporal aggregates 149
ternary interactions 170
ternary mixtures 265
ternary polymer solution 24, 255
thermal noise 424
third virial coefficient 110
time correlation function 440
transient network 176, 456
- worm-like chain 10, 312
- Yukawa interaction potential 72
- universal time behaviour 430
upper critical solution temperature (UCST) 344
- Zero Average Contrast (ZAC) 265, 356
Zimm plot 14, 134, 236

PROPERTY OF THE U. S. GOVERNMENT
SPACE TELESCOPE SCIENCE INSTITUTE
BALTIMORE, MARYLAND

DEC 4 1996

